AN EXPERIMENTAL STUDY ON THE COLLAPSE OF AN AIR-FILLED CYLINDRICAL CAVITY UNDER DYNAMIC LOADING

BY

GALINA V. SHPUNTOVA

DISSERTATION

Submitted in partial fulfillment of the requirements
for the degree of Doctor of Philosophy in Aerospace Engineering
in the Graduate College of the
University of Illinois at Urbana-Champaign, 2018

Urbana, Illinois

Doctoral Committee:

Professor Craig J. Dutton, Chair
Professor Joseph Shepherd, California Institute of Technology
Professor Daniel Bodony
Professor John Lambros

ABSTRACT

A model system was designed and investigated experimentally to gain insight into the interactions of an air-filled cylindrical bubble immersed in hydrogel, a compliant boundary, and a transient loading wave. This combination is an analog of processes that occur in biomedical applications such as shockwave lithotripsy. No-boundary, rigid boundary, and two-boundary cases were also investigated. A transient pressure wave of 20 MPa peak magnitude generated by projectile impact was used to initiate bubble collapse. Ultra high-speed video recordings of the process showed the development of a re-entrant jet characteristic of asymmetric bubble collapse in the no-boundary case, but less frequent occurrence of this behavior in cases with boundaries. Void interface velocity in excess of 200 m/s was detected, which is sufficient to cause pressures in the hundreds of megapascals and possibly damage tissues. However, an alternative damage mechanism is also proposed based on the significant deformation of the upstream boundary during the collapse time.

Flowfield data for all cases were acquired by a particle image velocimetry technique to elucidate the causes of boundary deformation, the suppression of jet formation, and the extreme velocities on the upstream void interface. An analytical model for the flow was developed to describe these flowfields, incorporating three components: the free-stream flow, a source flow, and a doublet flow. Parameters of the model were determined by fitting to data. The model represented the data to within 5 m/s on average—this was approximately equal to the 1-pixel PIV system noise threshold, and 5% of the maximum flowfield velocity. The variation of model parameters over the course of the collapse was investigated to give the model predictive as well as descriptive value. The source strength agreed well with predictions based on symmetrical collapse relations. The doublet strength was consistent with the generation of vorticity on the bubble boundary due to interaction with a weak shock.

For my grandparents.

ACKNOWLEDGMENTS

I would like to offer my deepest and most humble thanks to the following people and organizations for assistance, encouragement, and support that they offered me over the years it took to complete this doctoral project.

First, to my advisor, Prof. Joanna Austin, for guiding and supporting my work and my graduate career for all these years, and always remaining upbeat and optimistic. Also to Prof. Joseph Shepherd, for co-advising me this past year through the writing process, and for lending his invaluable expertise and insight over my entire time at Caltech. His guidance, encouragement, and good humor were absolutely indispensable to completing this project, and his time, commitment, and energy are appreciated beyond words. Additionally, deepest regards to my committee, Professors Craig J. Dutton, Daniel Bodony, and John Lambros at UIUC. Thank you for your time and your instruction.

For their financial support, I thank the NSF CAREER program that initially sponsored this project, and California Institute of Technology for their support since our group's relocation here. I also thank the College of Engineering at Illinois for their support through the Carver Fellowship and the Mavis Future Faculty Fellowship.

I greatly appreciate the efforts of the administrative staff that have worked with me over the years, helping solve logistical problems of all calibers. At Caltech, Denise Ruiz, Christine Ramirez, Tess Legaspi, Barbara McKinzie-Slater, and Dimity Nelson. At Illinois, Staci Tankersley, Barb Bohlen, Kendra Lindsey, Laura Gerhold, and Diane Jeffers. I greatly appreciate the technical advice, instruction, and assistance received from Bahram Valiferdowsi and John Van Deusen in issues of manufacturing. For manufacturing the gas gun, I thank all the shop staff at Illinois, and particularly Greg Milner.

I always tell aspiring grad students to find a good group as well as a good advisor; these are the people who walk the journey with you every day. Thanks for teaching me the ropes, and for learning with me as I went, fellow students Andy, Bill, Ryan, Dave, Andrew, Matt, Nelson, Mallory, Joel, and Ryan and also our postdoc Ilan! I immensely appreciate our discussions, your help, and proofreading! I also extend great appreciation to our summer students, Anurag and Hector, for their assistance on this project. Extra special thanks to Jean-Christophe Veilleux for his help with strain gauges and teaching me LS-DYNA!

Finally, no major project gets done without good preparation and the ongoing backing of friends and family. Thank you to all my teachers and professors, and especially to Professors Candace Wark and David

Williams at the Illinois Institute of Technology, who gave me my first taste of research, without which I may never have attempted graduate school. Thank you to my friends, Anna, Vlada, Joy, Nicole, Bindu, Laura, Jenn, Rose, Natalie, and Rachel, for keeping it in perspective for me and reminding me that I could when I forgot! Thanks to my parents, for preparing me well for grad school and for life, and for being my safety net and my biggest supporters. And of course, thank you Matthew, for moving across the country, for building a life with me, for your patience, and love, and encouragement, and for all the little things, too. I couldn't have done it without you.

TABLE OF CONTENTS

LIST OF ABBREVIATIONS

2B	Two-boundary
ALE	Arbitrary Lagrangian-Eulerian
DB	Downstream boundary
DBA	Downstream boundary with aluminum
FEA/FEM	Finite element analysis or method
fps	Frames per second
FSI	Fluid-structure interaction
NB	No boundary
PAA	Polyacrylamide
PDMS	Polydimethylsiloxane
PIV	Particle Image Velocimetry
PMMA	Polymethylmethacrylate (Acrylic)
PSV	Particle Shadow Velocimetry (type of PIV)
UB	Upstream boundary
SWH	Shock Wave Histotripsy
SWL/ESWL	(Extracorporeal) Shock Wave Lithotripsy
SWT	Shock Wave Therapy
UTS	Ultimate Tensile Strength

LIST OF SYMBOLS

Latin

a	Sound speed
A	Area
$\mathrm{C_p}$	Specific heat at constant pressure
$\mathrm{C_v}$	Specific heat at constant volume
D	Diameter
$\boldsymbol{e}$	Unit vector
E	Elastic (Young's) modulus
$\mathscr{E}$	Energy
g	Acceleration due to gravity
G	Shear modulus
h	Linear dimension of fixture
H	Enthalpy
H/W	Height divided by width of bubble (aspect ratio)
k	Conductivity
K	Doublet flow strength
N	Number of tests
P	Pressure
Q	Source (or sink) flow strength
r	Radial coordinate
R	Bubble radius
S	Surface tension coefficient
t	Time
u	Velocity, as a local variable
U	Velocity, as a constant or parameter
V	Volume
x	Horizontal or longitudinal coordinate.
y	Vertical or transverse coordinate.
Z	Acoustic impedance (ρA)

Greek

γ	Ratio of specific heats
Γ	Circulation
ϵ	Strain
λ	Wavelength
θ	Azimuthal coordinate
μ	Dynamic viscosity, or mean of data
ν	Kinematic viscosity
ρ	Density
σ	Standard deviation of data

Subscripts & Superscripts

a	Ambient fluid
A	Actual
b	Bubble fluid
c	At end of collapse
d	Downstream
f	Finite or final
g	In Gas
j	Of jet
I	Impact
L	In Liquid
M or max	Maximum
o	Initial state
p	Of particle
r	In radial direction
s	Of shock
u	Upstream
w	Of wave
x	In x-direction
y	In y-direction
z	In z-direction
θ	In azimuthal direction
∞	In free-stream
*	Nondimensionalized quantity
$\dot{X}$ and $\ddot{X}$	First and second time derivative of X

CHAPTER 1

INTRODUCTION

The fluid dynamics of collapsing voids is a topic of study applicable across a large range of scientific fields, perhaps even surprisingly so. Initially investigated as the mechanism of cavitation damage on watercraft propellers and in pumps [1–3], this phenomenon has also been found applicable to detonation initiation in energetic materials [4, 5], damage to spillways at dams and reservoirs [6, 7], the breakup of kidney stones in shock wave lithotripsy [8–10], and traumatic brain injury [11–13]. The phenomenon has been harnessed in ultrasonic cleaning devices [14, 15], and efforts are underway to take advantage of it in medical settings. Cavitation is one mechanism responsible for damaging and killing cancer cells using ultrasound (oncotripsy [16]), and other tissues (such as blood clots and arterial plaques) can be removed through ablation by ultrasound-induced bubble clouds (histotripsy [17, 18]) in a minimally invasive way. In supporting these efforts toward progressively less invasive surgical techniques, as well as continuing work on mitigating cavitation damage in both biological and industrial settings, understanding the behavior of collapsing bubbles and voids in a large variety of settings is of great importance [18–21].

1.1 Early Work

The phenomenon of cavitation was first observed and reported by Professor Osborne Reynolds in 1894 [22] but did not find practical application for about 25 years, until used by Lord Rayleigh to describe damage observed on Royal Navy steamboat propellers in 1917 [23]. Rayleigh's work neglected viscosity and surface tension, but was eventually extended into the quintessential Rayleigh-Plesset equation for the dynamics of a bubble in an infinite incompressible fluid [24, 25]:

$$R\ddot{R} + \frac{3}{2}\dot{R}^2 + \frac{4\nu_L}{R}\frac{dR}{dt} + \frac{2S}{\rho_L R} = \frac{P_B - P_\infty}{\rho_L}. \tag{1.1}$$

Here, R is bubble radius, ν_L is liquid kinematic viscosity, S is liquid surface tension, ρ_L is liquid density, and p_∞ and p_B are ambient and intra-bubble pressure respectively. Lord Rayleigh also calculated a relation for pressure distribution assuming isothermal compression of gas in the cavity (rather than vacuum or constant pressure) [23]:

$$\frac{P(r)}{P_\infty} = 1 + \frac{R}{3r}\left(\frac{V_o}{V} - 4\right) - \frac{R^4}{3r^4}\left(\frac{V_o}{V} - 1\right), \tag{1.2}$$

where $P(r)$ is pressure at radial coordinate r, and V_o and V are initial and instantaneous bubble volume. This relation demonstrates that once bubbles collapse to a very small fraction of their original size, the maximum pressure occurs at approximately 1.587 R, and that this pressure can rise to a thousand times ambient when bubble radius collapses to just below $R_o/10$. The work of Stanley S. Cook took the same derivation a step further, suggesting that pressure generated by impact on solid surfaces would be better modeled by imagining the moving liquid boundary encountering a solid sphere at the center of the bubble [26]. This predicted even higher pressures than Rayleigh's methodology. Together, these two methods were accepted explanations of cavitation pitting on watercraft propellers, and only incremental progress was made for almost two decades.

By the mid-1940s, some questions arose about the assumptions made by the Rayleigh theory [1]. Kornfeld and Suvorov argued that in order to achieve the pressures on the order of thousands of atmospheres required to damage structural materials (such as steel), Rayleigh's theory predicted velocities on the order of 1 km/s, which would violate the assumption of incompressibility. Accounting for compressibility and viscosity of the liquid and the interior pressure of the bubble would decrease the pressure generated below that predicted by Rayleigh, by an amount indeterminable at the time [1]. However, advances in imaging technology since the turn of the century allowed Kornfeld and Suvorov to image bubble dynamics in a Gaines oscillator, including changes in shape, zig-zag motion, breakup, and re-coalescence. Their observations led them to first theorize that near a boundary (such as the container wall), bubbles experience asymmetric collapse and water jetting, and that this jetting behavior could be responsible for the damaging effects of cavitation [1]. However, imaging resolution was not yet sufficient to actually capture this proposed behavior itself, as opposed to inferring it from its effects. Interest in the problem persisted, and evidence of jetting continued to accrue. In 1961 a series of experiments by Naud and Plesset were able to demonstrate that a bubble collapsing adjacent to a photoelastic CR39 boundary experienced a definite loss of sphericity, and a stress wave propagating into the CR39 apparently from a single point of impact was imaged, providing strong support for the jetting theory, even though a jet still could not be directly observed [27].

It was 5 years later, in 1966, that a carefully designed experiment by Benjamin and Ellis photographically recorded the jet in action. The experiment involved sub-millisecond imaging of the expansion and collapse of small seed bubbles directly adjacent to a solid wall, and a small distance from one, under ambient pressure of about 4% of atmospheric [28]. The relatively large size of the bubbles (with radii on the order of a centimeter) and the low ambient pressure resulted in a relatively long collapse time (roughly 5 ms), which made the temporal and spatial resolution of contemporary cameras sufficient to capture the collapse in great detail, including the formation of a jet toward the solid wall. The theory was subsequently given a quantitative and theoretical basis by Plesset and Chapman in 1970. They used the method of images to derive potential flow equations for the flow about a collapsing vapor bubble both adjacent and proximate to a solid wall, then solved them computationally to obtain bubble surface profiles for approximately 100 timesteps during the collapse process [29]. If scaled to reflect water at 1 atm, their results predict a jet velocity of 128 m/s in a spherical bubble initially touching a solid wall. The equation for water hammer pressure of a liquid jet with velocity u_j is:

$$P_{\mathrm{WH}} = \rho_L a_L u_j. \tag{1.3}$$

Using this expression, Plesset and Chapman determined pressures of almost 200 MPa could be achieved on the wall, albeit for very short durations limited by jet diameter, tentatively confirming jet impact as a damage mechanism. They also proposed considering the stagnation pressure of the jet $P_s = \frac{1}{2}\rho_L u_j^2$ as a lower pressure but longer duration mechanism, since the timescale of stagnation pressure scales with the jet length [29].

1.2 Detonation Initiation

Simultaneously with studies on the jetting behavior of collapsing bubbles, interest was growing in the interaction between collapsing bubbles and shock waves. While this situation could be applicable to the effect of underwater explosions on watercraft, the primary motivation in studying this phenomenon was its applicability to detonation initiation. It was known for some time that homogeneous energetic materials, such as degassed liquids and single crystals, required much larger shock pressures to initiate detonation than did compressed powders and fluids that had not been degassed [4]. The presence and behavior of gas bubbles was identified as a major contributor to initiation behavior, though other mechanisms were also proposed and could potentially coexist with bubble dynamics, e.g. viscous heating. A 1974 paper by Chaudhri and Field describes a series of experiments conducted to elucidate the specific mechanism relevant to detonation initiation. Ultimately, they concluded that it is heating from gas compression that is responsible after eliminating other mechanisms, including jet impact and rebound shock, as possible causes [30]. To make the final distinction between jet impact and gas heating as the cause, they devised a method wherein a cylindrical air bubble was trapped between two glass microscope slides and penetrated by the needle-shaped crystal of silver azide. Thus, the jet development and propagation was not obscured by bubble interface curvature, and could be clearly observed.

This setup likely influenced a future series of experiments conducted by John Field with Neil Bourne and John P. Dear in the 1980-90s, wherein a cavity geometry of choice was cast in a thin (3 mm) layer of gelatin sandwiched between glass, PMMA, or solid gelatin plates, then observed as the cavities were collapsed by a strong shock wave (up to 10 GPa), generated by either flyer plate impact or an explosive plane wave generator. Geometries included single cavities of various diameters, arrays of circular (cylindrical) cavities, cavities near particles, and non-circular cavities [31–33]. Observing a single 12 mm diameter cavity collapsing under a 0.26 GPa shock, they were able to capture not only the deformation of the material interface, but also dynamics of the shock inside the air-filled cavity—it could be observed crossing the cavity 6 times before becoming indistinguishable in available resolution.

The upstream cavity interface (which eventually formed a transverse jet) appeared to maintain a constant velocity of 130±5 m/s throughout the collapse. By performing the experiment with different cavity diameters and pressures, Bourne and Field deduced that jet velocity increased not only with incident shock strength, as expected, but also with decreasing cavity size. At a planar interface, the reflection of a shock off a free surface is expected to produce flow speed of twice the post-shock particle velocity, but for strong shocks and small cavities, the jet velocity could easily exceed this value. This was explained by the focusing effect of the curved cavity interface [33]. Furthermore, for even stronger shocks, the jet was demonstrably exceeding the incident shock velocity (the tip of the jet was observed in front of the leading edge of the shock). Measured jet velocities ran as high as 8±4 km/s, and the extreme conditions suggested by this are further confirmed by observed sonoluminescence in strong shock (1.9 GPa) tests on a 3 mm cavity [33]. For the 0.26 GPa shock tests, in which area could be reliably tracked, Bourne and Field also found that the nondimensional area-time relationship for the void is quite strictly linear, and that this also holds for two earlier studies under significantly different conditions of void size and shock pressure [34, 35].

One of the conditions investigated by Bourne and Field, that of a 6 mm cavity under a 1.9 GPa shock loading, was subsequently simulated by Ball et al. using a Free-Lagrange approach [36]. The simulation matched well with geometric features of the experiments (within experimental accuracy), such as collapse time, jet velocity, and location of gas luminescence after jet impact. In light of this agreement, it is reasonable to interpret simulation results as a prediction of collapse properties that were poorly resolved or inaccessible for measurement in the experiment. Most notably, the behavior of a shock propagating within the air-filled cavity could be resolved, including the pressures and temperatures produced by repeated reflections of the shock from the moving air-water interface of the cavity. These properties were computed based on shock relations, whereas experimentally only a lower limit for these values could be obtained from an adiabatic compression calculation. Dear and Field noted from experimental results that luminescence occurs when bubble area has been reduced to 10% or less of the initial area, which would indicate a temperature of at least 750 K, but admit the actual value would require simulating shock behavior [32]. Bourne and Field note that the presence of luminescence suggests temperatures exceeding 800 K [37]. Ball et al. calculate the temperature achieved by adiabatic compression as 755 K, then observe that the conditions achieved in simulation (at 10% area ratio) are both higher and spatially variant: 1800 K and 4 MPa in front of the shock inside the void and 5900 K and 35 MPa behind the shock. Shock reflections and cavity compression during the subsequent 0.8 μs further increase the predicted temperature to as high as 12000 K and pressure as high as 300 MPa by the time the cavity achieves minimum volume. However, Ball et al. emphasize that heat transfer and real gas effects are neglected in this simulation, making these extreme values only a pessimistic upper bound. It is worth noting that this simulation examines the results of applying an extremely strong incident shock. The resulting shock in air is much weaker, but it still generates a pressure ratio of about

27 even before focusing and gas cavity compression are considered (both would strengthen the compression even further). This definitely plays a role in the high pressures and temperatures achieved; however, the multiplicative effect of repeated shock processing plays a large role as well. Unfortunately, Ball et al. do not comment on the evolution of this effect under applied shocks of different strengths.

The experimental setup of Field and coworkers was further adapted by Swantek and Austin, and used to investigate the interactions of arrays of bubbles [5]. Such interactions were of great interest for their potential to alter shock propagation speed through a bubbly liquid, focus a shock, and/or create "hot spots" that could lead to ignition. The experiment of Swantek and Austin, like those of Field and coworkers, used a thin sheet of hydrogel contained between PMMA blocks, and a compressed air gas gun to generate a loading wave. The pressure in the gel due to the impact was estimated from impact conditions as 421 atmospheres (or 42 MPa). A key aspect of this experiment was that in addition to high-speed shadowgraph video of the collapse, they were able to collect velocity field data using a particle image velocimetry (PIV) technique. This clearly demonstrated the diffraction of a loading wave around the void, the development of a high-speed jet, and the shock generated by jet impact and void rebound. When additional voids were introduced, it was clear how voids linearly downstream were initially shielded from the incident wave, but subsequently collapsed by the shock emitted at the end of collapse. Finally, it was clear how the diffracted shock led to the formation of liquid jets at an angle in off-axis voids downstream of the first one. These behaviors were all observed by Dear and Field [32], but velocity measurements clarified their origins.

1.3 Biomedical Applications

In the 1980s, a revolutionary new technology came to market for treating kidney stones. Instead of exposing patients to a risky and invasive surgery, extracorporeal shock wave lithotripsy (ESWL) allowed large kidney stones to be fragmented with focused shock waves [38, 39]. The apparatus consisted of a large tub filled with water, containing a spark gap electrode at one focus of an ellipsoidal reflector, located at one end of the tub. The patient, under general anesthesia or epidural, was precisely positioned at the opposite end, with the kidney stone at the second focus of the ellipse (F2) as confirmed by imaging technology (e.g. x-ray). Treatment consisted of a series of shock waves generated by the spark gap and focused by the ellipsoidal reflector to a small region within the kidney (a cylinder 15 mm in diameter and 80 mm long [8]). The mechanism of action initially proposed was that the shock wave would pass harmlessly through soft tissues, which have a similar acoustic impedance to water, but reflect within a rigid stone and cause large tensile stresses sufficient to fracture the stone. After a series of pulses (about 500 to a few thousand), the stones were sufficiently pulverized to pass naturally with minimal pain. Clinical trials were so promising the treatment quickly attained FDA approval [39].

Unfortunately, within the first two decades of use, it became clear that ESWL was not as harmless as initially expected [8, 40]. In a number of patients, treatment led to reduced kidney function, chronic kidney disease, and/or hypertension; advanced age and small kidney size were two relevant risk factors [8]. Studies on pig kidneys elucidated a possible mechanism: that ESWL damages blood vessels in the kidney and leads to inflammation; subsequent healing of the damaged areas results in scar tissue, which affects kidney function even years after treatment [8, 40]. The blood vessel damage, in turn, was attributed to the newfound understanding that the wave profile produced by the lithotripter contained a significant tensile component as well as a compressive one [41]. The negative pressure induced the growth of cavitation bubbles, and the asymmetrical collapse of these under the next wave caused tissue damage, particularly after large numbers of applied shocks [42–45]. Further complicating the issue, numerous studies found evidence that the cavitation works synergistically with stress wave dynamics to break up stones [10, 44, 46], and therefore, the cavitation behavior needs to be optimized to maintain efficacy of ESWL while improving safety. With this end in mind, investigating the interactions between waves, bubbles, stones, and tissues remains an active area of research [46–48].

ESWL has changed little since its introduction; new shock wave emitters, imaging technologies, and more comfortable patient supports have been introduced [9, 48], but the salient features have remained much the same. Yet, a number of novel medical techniques have been developed in its footsteps that also take advantage of the destructive power of cavitation, or have to reckon with it as a side effect. One of the first was a direct application of ESWL to gallstones [49]. It never became the preferred treatment due to the availability of even safer options, and in time a high rate of stone recurrence among treated patients has put it even more out of favor [50]. Nonetheless, it motivated a broader perspective on shock wave treatment. Along similar lines, a modified form of extracorporeal shock wave therapy (ESWT) was developed in the late 1990s to treat painful musculoskeletal disorders including tendonitis and plantar fasciitis [51]. The mechanism of action of these methods is not yet well understood; it is suspected cavitation results in microscopic injuries to the affected tendons, which stimulate repair mechanisms in the body. The technique is under continuing development and study [52].

Another significant category of related methods are the focused ultrasound (FU) techniques, typically subdivided into the categories of "low-intensity" and "high-intensity" focused ultrasound (LIFU and HIFU) [48]. Instead of high amplitude shock waves with a slow repetition rate, as in ESWL, HIFU techniques apply a continuous stream of ultrasound waves to the tissue, focusing them to a small region as in ESWL. Depending on the specifics of the application, tissue at the focus can experience any combination of heating from the deposited energy, shear due to wave dynamics, and cavitation, all of which could contribute to the destruction of undesirable tissues (such as stones, cancers, clots, or plaques) or to collateral damage. Although FU techniques have been tested for breaking up kidney stones and other concretions, ESWL still remains the standard for kidney stone treatment. However, because FU techniques are not so dependent on differences in acoustic impedance, there is significant interest in developing them to non-invasively destroy troublesome soft tissues, a practice known as "histotripsy" [17, 18].

The range of low intensity ultrasound techniques ultimately merges with the well-established technique of diagnostic ultrasound, which has been medically applied to much of the human body over the past several decades [48, 53]. To improve resolution of the technique, biologically compatible “microbubbles” can be added; when these bubbles experience large, nondestructive oscillations in the ultrasound field, they enhance wave scattering and the resolution of the final image [54]. If ultrasound excitation slightly exceeds some acceptable intensity, microbubbles may begin to collapse catastrophically (i.e. the bubble shell will break); this phenomenon has been harnessed for targeted drug delivery. At even greater intensities, collapse of microbubbles begins to damage cell walls in a non-lethal way; this has been found to improve cell uptake of medication and thus improve effectiveness of chemotherapy, and also harnessed in gene therapy [55]. Further intensity increases would then enter a destructive regime, discussed above. By studying the biological response to waves with widely varying properties (such as amplitude, timescale, profile, and repetition rate), the limits of safe use for diagnostic ultrasound or drug delivery can be determined, even as the potential for damage is evaluated, to be applied when tissue removal is desired.

If all open questions about these many varieties of ESWT could be answered, including how to prevent collateral damage, and how to determine the best wave parameters for a given application, there is potential to use ultrasound and shock waves to truly revolutionize a segment of surgical medicine [56, 57]. Eliminating the need to cut through inches of flesh and sensitive organs to remove problem tissues could make surgery a viable treatment for conditions and patients for whom open surgery is not a safe or practical option. Moreover, it would be expected to drastically cut down on recovery time, complications, and thus medical expenses associated with these kinds of surgeries for all patients. Moving toward this amazing goal requires furthering our collective understanding of interactions between waves, tissues, and bubbles under a wide range of conditions [48].

1.4 Influence of Wave Profile

The waveform of the shock wave in ESWL has been of great interest to academic investigators since the earliest days of research on the process [41]. Measurements are typically made in a water bath without a body present, and often classified by the largest positive and negative pressures achieved (P^+ and P^-) and/or total acoustic energy detected. These values vary for each device depending on the voltage setting used: typical ranges are 10–30 kV for electrohydraulic (spark gap) or electromagnetic designs, and 1–10 kV for piezoelectric actuators [9]. Resultant P^+ can range from 10 to over 100 MPa, and P^- magnitudes tend to be between 15% and 25% of P^+ magnitudes [9, 41]. Different pressure magnitude outputs from the lithotripter may have significantly different effects on any cavitation bubbles formed. Ding and Gracewski investigated the effect of changing compressive shock pressure on bubble collapse behavior across a range of bubble sizes in a computational study [58]. They found that jetting behavior developed only in bubbles impacted by strong shocks, and that when it did, jets achieved very high velocity in excess of twice the post-shock particle velocity. Bubbles impacted by weak shocks collapsed virtually symmetrically; this was explained by the short transit time of the shock across the bubble relative to the duration of the bubble collapse process. The bubble was under a non-uniform pressure for a very small fraction of its total collapse in the weak shock cases, and a large portion of its collapse in the strong shock cases. The weak cases investigated were characterized by pressures of <30 MPa, whereas high pressure was defined as >500 MPa. The intermediate regime was not investigated, so it was not clear at what point or in what way weak shock behavior transitioned into strong shock behavior.

The pressure-time profiles generated by different types of devices exhibit the same general behavior, but the exact timescales of features can differ [9]. All profiles start with a sharp positive pressure peak (with rise time of about 30–100 ns and width 1–3 μs) followed by a longer-duration dip to P^- and eventual recovery through decaying oscillations [41]. The profiles may vary between different actuators in the width of the P^+ pulse, the rate of pressure drop, and most notably the timescale of oscillations; piezoelectric devices have distinctly higher-frequency oscillatory behavior that dips into negative pressures repeatedly. Since it is expected that the tension component of the wave causes cavitation bubble inception during ESWL, and compression waves can intensify their collapse, the timing and relative strength of these pressure extremes can influence the effectiveness of the lithotripsy process.

Although measurements of the wave profile in water are informative for classifying different devices, it is evident that propagation through the body will attenuate the wave. Cleveland et al. investigated the difference between *in vitro* lithotripsy waveforms in water and *in vivo* waveforms in porcine kidneys [59]. After installing hydrophones to measure pressure on the anterior and posterior kidney surfaces, they found that although the shape of the profile remained largely unchanged, the P^+ magnitude dropped by 35–50%, the rise time increased, the focal region broadened, and small fluctuations were smoothed out during travel through tissue. They attributed the changes to nonlinear properties of the tissues themselves, and the resulting nonlinear harmonic generation; acoustic heterogeneity, they argued, was sufficiently minor that it did not play a detectable role, evidenced by the minimal change in wave shape. They were not able to attain reliable measurements of the tensile portion of the wave; however, they argue that it would be even less susceptible to changes due to material nonlinearities or heterogeneity than the P^+ shock. With similar motivation, Cirovic et al. investigated the propagation of a radial shock wave therapy (rSWT) wave into two human cadaver feet (as for the treatment of plantar fasciitis) [52]. The rSWT wave is very different from the ESWL wave; it is lower in magnitude, has a sinusoidally decaying profile approximately symmetric about zero, and also allowed to dissipate radially rather than being focused like the ESWL wave. They observe a longer residence time than they expected, and emphasize the differences in wave magnitude at the treatment site in spite of identical stimulation. They attribute these differences to variations in foot geometry, though they do not distinguish what phenomenon is responsible: a difference in offset distance alone, or coupled with dissipation properties of the tissue. These studies suggest that while nominal wave profiles and characterization are important and informative, it is necessary to consider the attenuating effect of the body when considering the mechanics of the treatment processes.

Although the loading waves undergo some relatively small changes due to traveling through the body, researchers also intentionally introduce large variations in the loading wave profile. There are two major motivations for investigating lithotripsy under different waveforms: one is to isolate stimuli and behaviors to deduce causal relationships, the other is to work toward a waveform designed to maximize effectiveness and minimize collateral tissue injury. One of the first notable modifications was testing samples under elevated pressures, up to 120 atm, to decrease the tensile component of the wave or even eliminate it completely, stifling cavitation [46, 60, 61]. Samples consisted of red blood cells, gallstones, or model stones in pressurized vials or tubes. Damage to blood cells was significantly suppressed by even small overpressures (less than the P^- magnitude of the ESWL wave); stone breakup was also suppressed, though to a much lesser extent. These findings led to the conclusion that while cavitation was a major mechanism of cell damage, it was also instrumental to treatment effectiveness. This was further confirmed by a second wave modification: an insert was devised for the lithotripter reflector that essentially reversed the waveform in time, placing the tensile component before the shock [47, 62, 63]. This effectively suppressed cavitation by not providing enough time for bubbles to expand due to the tension wave before the arrival of the high-pressure shock. As with elevated hydrostatic pressure, this modification led to decreased cell injury but also some decreased stone comminution. This finding was further confirmed by testing the effectiveness of standard ESWL shocks on stones in cavitation-suppressing environments [10] or shielded by thin mylar membranes [64].

Recent work has primarily been aimed at designing a better waveform. Zhong and Zhou created an insert for the Dornier HM-3 lithotripter reflector dish that created a second, lower-amplitude shock wave trailing the first by 4 μs, which truncated the tensile portion of the wave [65]. Sokolov et al. proposed an alternate design using two confocal shock sources to double the generated pressures in an extremely localized area [66]. Devices to administer tandem shock waves, such that a second strong shock arrives tens or hundreds of microseconds after the first and intensifies cavitation bubble collapse have also been developed, and have attracted interest for application in cancer treatment as well as in ESWL [48, 67, 68]. It is notable that these studies focus on improved stone breakup and reduced treatment time, but do not address the potential for greater tissue injury with intensified cavitation. While many novel techniques attempt to shrink the focal region and increase shock intensity, it has been suggested that the optimum between effectiveness (stone breakup) and safety (tissue damage) may lie in returning to lower-pressure shocks, a broader instrument focus, and lower pulse repetition frequencies [9]. Ultimately, only extensive further study can provide the tools to design optimal waveforms for any application.

1.5 Bubble Collapse Near Solid Boundaries

Much of the earliest work on cavitation, and the damage it can impart on solid materials, as discussed above, is still relevant today when it is used to understand kidney stone comminution in ESWL. However, study on the phenomenon continues as sensor resolution improves, new techniques are devised, and the capabilities of computational systems exceed all previous expectations.

Akira Shima and coworkers conducted some of the most detailed experimental studies of the interactions between bubbles, waves, and neighboring surfaces in the 1980s. After starting with some theoretical analyses, [69], they subsequently investigated the behavior of a bubble in a water-filled tank under a variety of environmental and loading conditions [70–73]. Data were collected simultaneously by high-speed streak videography and a pressure transducer on the solid surface; in some experiments microscopy was used to subsequently examine surfaces to identify damage patterns. They initially investigated the behavior of a spark-induced cavitation bubble at or near the solid surface with no pressure loading, and observed a complicated relationship between collapse intensity and distance from the wall [74]. After measuring the initial velocity of the rebound shock, bubble interface velocities, and bubble rebound radius, they concluded that the most extreme collapse occurs in the free field; this case exhibited the strongest rebound shock and the fastest radial interface velocities. As the bubble was generated closer to the wall, shock intensity and bubble interface velocity decreased, and bubble centroid migration increased; the rebound radius also increased, indicating more energy remained in the system after the first collapse. This trend continued up to a bubble position of one bubble radius from the wall; as the bubble was generated closer than this, it became deformed by contact with the wall and multiple weak shocks were generated upon collapse, but as the bubble was generated even closer to the wall, sources of the multiple shocks became closely spaced, and coalesced into relatively stronger shocks.

Shima et al. continued their investigation by suspending a syringe-generated air bubble either just under a rigid wall, or off a fine iron wire in a water tank at a set distance from the wall [70, 71]. They then created a 5 MPa shock from below using electrode spark discharge. The bubbles were recorded at high magnification with high-speed video, and a pressure sensor on the wall measured the incident pressure. However, they emphasize that pressure measurements are fairly qualitative in nature because the pressure transducer is quite large relative to the experiment, and the non-uniform response distribution across the sensor area is unknown. Their work shows that bubbles within as much as 7 diameters of the wall had an amplifying effect on the pressure experienced by the wall; this effect was generally stronger for bubbles closer to the wall, but oddly enough dropped off significantly around 1–1.2 radii (i.e. a bubble just touching the wall), before increasing significantly for bubbles flattened against the wall. It is also of great interest that bubbles within about 5 radii of the wall experience displacement toward the wall during the collapse process as did the laser-induced cavitation bubble; this would indicate that wall pressure can increase over the course of multiple collapses, as experienced in medical applications.

As a final portion of their investigation, Tomita and Shima used a photoelastic material to capture wave propagation in the solid wall as well as using Schlieren imaging to image the wave in the fluid media [72]. They then compared the observed disturbance dimensions and behaviors to the microscopic features of a damage pit made in indium (a relatively soft metal). Their observations suggested that rather than the water jet directly causing material damage, the water jet caused the creation of a toroidal bubble, which broke into a circle of small spherical bubbles. The subsequent and very violent collapse of this ring of tiny bubbles was the mechanism they proposed for the creation of pitting on the indium (or other solid boundary).

These findings were confirmed by a detailed investigation by Philipp and Lauterborn [75]. They were able to capture very high resolution high-speed video of the topography of laser-induced cavitation bubbles collapsing within a few radii of a rigid boundary. They also examined the microscopic appearance of damage to aluminum and other metals. Damage was observed for bubbles closer than two maximum radii from the boundary; most extreme damage was for bubbles less than 0.3 radii from the boundary (flattened against it), and between 1.2–1.4 maximum radii away. The appearance of the damage varied with distance, from a single pit, to a small area filled with pits, to a ring of pits. The formation of a toroidal bubble due to jet formation, and the subsequent collapse of this ring against the surface, was observed in videos; the ring diameter varied with the maximum bubble diameter, further supporting the idea that the toroidal bubble cloud was responsible for damage in those cases. Pressures are cited in the study but they are estimated from water hammer pressure of observed liquid jets; no pressure measurements were made. Making highly precise pressure measurements to confirm predicted values remains a challenge because of the small size of collapsing bubbles of interest and relatively large pressure sensor areas.

Computational studies can provide greater insight at resolutions and locations unreachable by physical sensors, as well as into the dominant physical mechanisms at play. Johnsen and Colonius used a computational approach to investigate bubble collapse near rigid boundaries as compared to free-field collapse [76]. They chose to model a spherical air bubble in water near an ideally rigid boundary with infinite acoustic impedance. First, they considered the effect of offset distance and shock strength on peak wall pressure, and found that pressure drops off as the inverse of the offset and increases linearly with shock strength (Mach number). Presence of the bubble 2 radii away from the wall amplified wall pressure by a factor of about 6, in contrast with the results of Shima et al., who found a factor of about 2.5 for the same offset [71]. It is possible the maximum pressure measured in experiment was attenuated by an area-averaging effect of the sensor.

Johnsen and Colonius then investigated the effect of pulse width relative to bubble size on the collapse process [76]. The pulse profile was modeled after lithotripter profiles, with a shock compression peak (instantaneous rise) followed by a gradual expansion tail that includes negative pressure. The nominal wave width included both the compression and tension components of the profile. They found that as the pulse profile widened, jet velocity and wall pressure increased, and collapse time decreased, asymptotically approaching the response exhibited by the system to a step function input (i.e. a wave with infinitely long decay time). Based on visual inspection of plots, a pulse width of 750 times the bubble radius appears a reasonable threshold for the asymptotic assumption; pulses of 100–200 times the bubble radius produced 50% slower collapse and up to 60% lower wall pressure. Using the lithotripter pulse length scale of 6.75 mm calculated by Johnsen and Colonius from standard lithotripter parameters, this indicates that the pulse width can become a factor in the collapse of bubbles larger than about 9 μm, for a 35.3 MPa incident shock in water, which covers most of the range expected in ESWL [77]. The jet velocities calculated at this pressure ranged from about 660 m/s to 900 m/s; comparing expected water hammer pressure to the pressure detected in the fluid, Johnsen and Colonius find good agreement and damage potential, with pressures well in excess of 1 GPa. While there is precedent for jet velocities at that magnitude in shock-induced collapse [33, 78], those cases do not overlap precisely with the conditions applied by Johnsen and Colonius, making comparison difficult. Simulations performed at lower pressure ratios of 100–200 yielded jet velocities of 360–700 m/s, overpredicting the experimentally determined value of 150 m/s at the same pressure [79]. Johnsen and Colonius propose that finite rise time could depress the value, and that equipment limitations may prevent the true maximum velocity from being resolved in experiment, but it is unclear whether these factors completely explain the discrepancy.

The next study by Johnsen and Colonius assumed a shock with a step profile and analyzed the effects of pressure ratio on collapse in free-field and at various offset distances from a rigid boundary [80]. Both Rayleigh collapse, initiated by an instantaneous pressure change, and shock-induced collapse, initiated by a translating shock, were considered. Collapse time for shock induced collapse was increased only by the transit time of the shock across the bubble, and agreed with the collapse time calculated from the Rayleigh-Plesset equation. Free-field Rayleigh collapse was symmetric and exhibited interface velocities as high as 750 m/s for the highest pressure ratios; shock-induced and near-wall collapse exhibited asymmetry characterized by a high-speed jet, exceeding a velocity of 2000 m/s for shock-induced collapse near a wall. Jet diameter was found to increase with shock pressure from about 15% of the initial bubble radius to 27%; in conjunction with higher jet velocities, this creates higher kinetic energy in the jet. This, in turn, is used by Johnsen and Colonius to explain lower levels of radiated energy in asymmetrical bubble collapse. Water hammer pressure due to jet impact is found to be the main driver of high wall pressures, exceeding 2 GPa along the centerline at the highest pressure ratios. Wall pressure is found to drop off as $1/r$ with distance from the centerline, and to oscillate quickly in time due to wave reflections between bubble and wall. A simulation with parameters designed to match the experiment of Shima et al. exhibited good agreement in bubble migration distances, and reasonable agreement in wall pressure values. The overprediction of wall pressures by the simulation was reasonably explained by the assumption of an infinite-impedance boundary, whereas the Lucite boundary used by Shima et al. only had about twice the acoustic impedance of water and generated a lower pressure rise from wave reflections [71, 80].

1.6 Bubble Collapse Near Compliant Boundaries

The interaction of cavitation bubbles with rigid walls explains the damage observed on kidney stones and turbomachinery. However, it is not necessarily the case that the same mechanisms are involved in damage to soft tissues. A series of studies by Chen et al. demonstrates this. They were able to collect high-speed video of bubble interactions with the microvessels of *ex vivo* rat tissue, under single HIFU waves (1–10 MPa peak negative and positive pressures) [81, 82]. Commercially available contrast microbubbles, marketed to improve ultrasound imaging, were used as micrometer-sized cavitation nuclei; these microbubbles consist of nonreactive gas and contained in a polymer or lipid shell [54]. Microbubbles were circulated in a saline and dye solution through cleaned rat mesentery, a tissue that connects organs to the abdominal wall. The thinness of the mesentery allowed optical access to observe in detail the interactions of bubbles and vessel walls.

In sufficiently large vessels, with diameter greater than $4R_{\max}$ (where $R_{\max}$ is the bubble maximum radius), bubbles that were initially within $2R_{\max}$ of the nearest vessel wall were found to migrate away from this wall, with bubbles closest to the wall migrating the furthest (up to 20 μm). Bubbles close enough to contact the vessel walls upon full expansion would cause distension of the vessel wall during the growth phase, and in some cases form microjets through the bubble oriented away from the wall during collapse. These microjets were not observed to contact the opposite vessel wall even in relatively small vessels (diameter less than $4R_{\max}$), and no dye leakage was observed, suggesting the vessel was not damaged by the microjet. Migration away from the nearest wall was not as large in the small vessels, presumably because the space was not available. However, the bubbles in small vessels were observed to affect both boundaries during their expansion and/or collapse, in many cases causing invagination of the vessel walls—essentially pulling them in toward the center, creating an hourglass shape [82]. In another study, histological and TEM (transmission electron microscopy) analysis of the tissues was performed on vessels where invagination was observed, and this showed evidence of the endothelium of the vessel pulled away from the other tissues [81]. Endothelium separation was also one type of injury observed by Evan et al. in histological studies on pig kidneys treated with clinical doses of ultrasound as for ESWL [8].

Coralic and Colonius recently modeled a similar geometry to that studied by Chen et al. [83]. They modeled a small (micrometer-scale) air bubble within a water-filled cylindrical vessel 1.1–4 times the bubble diameter. The material surrounding the vessel was modeled as gelatin; however, viscosity and elasticity were neglected in the simulation, so gelatin properties were quite similar to those of water. A 40 MPa shock wave (step pressure increase) propagated through the system, perpendicular to the axis of the cylindrical vessel, and stimulated bubble collapse. Due to the similarity in acoustic properties of gelatin and water, the confinement did not have a strong effect on the bubble collapse; however, distinguishing the two materials allowed the researchers to track interface deformation and pressure on the interface, which both present potential for damage. They observed that in addition to jetting behavior causing distension of the vessel wall on the distal side of the bubble (relative to the shock), there was significant invagination of the vessel wall on the proximal side, which corresponded well to a potential sink flow model. Pressures as high as 450 MPa (over ten times the loading pressure) were also observed near the site of jet impingement.

These two studies suggest that either additional or entirely different mechanisms are responsible for soft tissue damage, compared to rigid surface damage. To further elucidate these mechanisms, additional experimental and computational studies on simple model systems are desirable, to allow independent control over variables such as tissue and fluid properties, bubble size, and loading wave profile. From these results, models with predictive value can hopefully be devised, to predict the potential for cavitation-induced damage in a wide range of biological as well as industrial settings.

In one experimental study similar in design to those of Shima et al., Kodama and Takayama used a syringe to place a bubble just underneath samples of various materials in a water bath; the materials included thin aluminum film, 10% gelatin, rat liver, rat abdominal aorta, and a PMMA (polymethylmethacrylate) plate [84]. A shock was generated below the bubble by detonation of a small pellet of silver azide, far enough that the shock was approximately planar by the time it reached the air bubble. The bubble collapsed under the shock impact, creating visible pitting, cracks or rupture of the boundary in all cases except PMMA. The shock had a compressive amplitude of about 10 MPa, but no measured tensile portion. In the absence of a bubble, it did not damage the boundary. High-speed video of the process showed a thin line, presumed to be a liquid microjet, penetrating into a gelatin boundary during the bubble collapse. The bubble then migrates along the same trajectory and re-expands, taking on a rounded conical shape and penetrating significantly into the boundary. The length of the jet formed was measured and found to scale with the bubble radius; the functional nature of the relationship was not quite clear, but for the range of bubble radii from 0.12 mm to 3.06 mm, the jet length was about equal to the bubble diameter. Penetration through thin aluminum foil, but not into a PMMA surface, was detected. Examining the gelatin and biological materials under a microscope after testing, Kodama and Takayama found that the nature of the damage pit differed in spite of nearly identical acoustic properties; the gelatin had a small damage pit, an order of magnitude smaller than the bubble size, whereas rat liver exhibited a larger area deformed by the impact, like a dent or a crater, with the damage pit at the center. They suggest the rat liver exhibits plastic deformation in response to bubble collapse, demonstrating how strength of the material contributes to its interaction with cavitation bubbles. Also observed under microscope were cells elongated in a particular direction; shear stresses from the high-speed jet flow were implicated in this effect.

Building on this study, Kodama and Tomita examined the behavior of air bubbles adjacent to gelatin of differing concentrations, collapsed by shock wave from below [85]. They also considered laser-induced cavitation bubbles at different offset distances from the gelatin surface (not under shock loading). Cavitation bubbles were observed to migrate away from the gelatin surface at a rate inversely proportional to the initial stand-off distance; this migration was less pronounced than similar migration away from a free surface. This behavior is in stark contrast to the observed migration of bubbles toward a rigid surface [71]. The period of motion (expansion and collapse) of the cavitation bubbles near gelatin boundaries (within 2 radii) was found to be higher than of bubbles near a free surface, and in fact differed less than 10% from that of bubbles far from the boundary. As in the study by Kodama and Takayama, air bubbles adjacent to the boundary were found to form liquid jets into the gelatin. However, higher concentrations of gelatin noticeably suppressed the jet velocity and penetration; instead, the bubbles flattened against the boundary much as they did near rigid boundaries [72, 75]. It is not yet definitively understood what property of higher-concentration gelatin suppresses jet penetration. While strength or stiffness seem an obvious choice for a material resisting deformation, a computational study by Freund et al. demonstrated that viscosity can also play a role in suppressing jet penetration into a medium. [86]. However, the simulations did not produce a case exhibiting a counterjet phenomenon observed in experiments [85]. After bubble expansion and jet penetration into the gelatin, the gelatin bounced back, and a jet aimed toward the water tank (counterjet) was visible in the photos. It was unclear if the jet consisted of air, water, or ejected gelatin; however, given the conventional understanding of viscosity as energy dissipation mechanism and elasticity as an energy storage mechanism, it seems likely elasticity was involved in this behavior.

Using boundaries of materials other than gelatin can allow investigation of a larger range of material properties. Brujan et al. performed extensive and detailed studies with laser-induced cavitation bubbles near polyacrylamide (PAA) boundaries [87, 88]. They varied the concentration of water in the PAA (thus the stiffness of the membrane) as well as the bubble offset distance, in order to identify correlations between these conditions and collapse behaviors. They were able to plot the parameter space based on PAA water concentration and bubble offset from the boundary, identifying regions with different jetting behavior. Unsurprisingly, for the stiffest boundary (E=2.03 MPa), the jetting was toward the boundary for almost all offsets; conversely, for the most compliant boundary (E=0.017 MPa), jetting was away from the boundary for almost all offsets less than 1.5 R_{max}. For an intermediate case with E=0.252 MPa and offsets less than R_{max}, the bubble developed jets oriented both toward and away from the boundary. Moreover, the jet toward the boundary would penetrate the PAA material for offsets in the 0.5–0.75 R_{max} range, and the jet directed away would entrain PAA material for offsets less than about 0.25 R_{max}; and in the intermediate 0.25–0.5 R_{max} range, both PAA penetration and entrainment would occur. For a stiffer membrane with E=1.04 MPa, dual jetting occurred for offsets less than 1.5 R_{max}, but neither penetration into the PAA, nor PAA ejection occurred. This variation of behaviors illustrates that for soft materials, in addition to the familiar damage mechanism of jetting against or into the material, there is a mechanism that can somehow "pull" material away from the boundary. The damage potential of this mechanism clearly depends on boundary material properties, but also likely on system properties like bubble size and loading condition, which were not investigated by Brujan et al.

The dual-jetting phenomenon deserves some additional comments. It is initially confusing to consider a bubble generating two jets during its collapse. Brujan et al. offer the following explanation for the phenomenon. During the expansion phase, the growing cavitation bubble can deform the elastic boundary. It then bounces back, flattening the bubble slightly and changing the local pressure and flow field conditions. The greater curvature at the so-called "equator" of the ellipsoid leads to more rapid acceleration of this fluid during collapse, and causes the bubble to assume an hourglass shape, if symmetrical, and a "mushroom" shape if asymmetrical. The waist of this shape is called an "annular jet" by Brujan et al.; fluid accelerating inward radially. When it inevitably collides at the axis, the fluid diverts into two axial jets, their relative speed and strength determined by the asymmetry of the collapse. As an additional effect, the annular jet effectively "pinches" the bubble into two halves (one closer to the boundary and traveling toward it, and one farther and traveling away). Bubble splitting was also observed by Sankin and Zhong in a study observing the interaction of a laser-induced cavitation bubble with a shock wave near a silicone rubber membrane [89]. Although the full parameter space was not presented, bubble splitting clearly occurred in 3 out of 4 high-speed image sequences included; with a membrane elastic modulus of 1.3 MPa and offset distances for laser-induced cavitation bubbles of 0.75–1.17 $R_{\max}$, all three cases fell into the bubble splitting region defined by Brujan et al. in spite of using different materials, bubbles with roughly half the maximum radius, and shock loading with 50 MPa peak compressive stress.

1.7 Analytical Approaches

As discussed in Section 1.1, Rayleigh was the first to propose a theory and a quantitative basis for describing the symmetrical collapse of a spherical bubble in a liquid environment [23] and it remains a standard for estimating collapse time [5, 80] and contextualizing new models [90]. One of the first criticisms of the Rayleigh-Plesset equation was that the conditions it predicted (velocities approaching sonic velocity in water) violated the assumptions it made (incompressibility) [1]. Gilmore resolved this conflict by applying the Kirkwood-Bethe approximation and proposed a first order model that included the effects of compressibility, viscosity, and surface tension, in terms of fluid enthalpy (H_o) [91].

$$R\ddot{R}\left(1-\frac{\dot{R}}{a}\right)+\frac{3}{2}\dot{R}^2\left(1-\frac{\dot{R}}{3a}\right)=H_o\left(1+\frac{\dot{R}}{a}\right)-\frac{2S+4\mu\dot{R}}{\rho_\infty R}\left(1+\frac{\dot{R}^2}{a^2}\right)-\frac{4\mu\ddot{R}}{\rho_\infty a}\left(1-\frac{\dot{R}}{a}\right) \tag{1.4}$$

Here, a is sound speed, S is surface tension, μ is dynamic viscosity, ρ is fluid density, and ∞ denotes liquid conditions in the far-field, away from the bubble.

Keller and Miksis derived an equation similar in form, but based upon pressure [92, 93]. This has become a standard in modeling bubble collapse where compressibility is of importance.

$$R\ddot{R}\left(1-\frac{\dot{R}}{a_\infty}\right)+\frac{3}{2}\dot{R}^2\left(1-\frac{\dot{R}}{3a_\infty}\right)=\frac{1}{\rho_\infty}\left[P_B(t)-P_\infty-P_v\left(t+\frac{R}{a_L}\right)\right]\left(1+\frac{\dot{R}}{a}\right)+\frac{R}{\rho_\infty a_\infty}\frac{dP_B(t)}{dt} \tag{1.5}$$

Here, $P_B(t)$ denotes the time-variable pressure within the bubble, while P_v is variable liquid pressure at the bubble location, in the absence of the bubble.

The above models all describe symmetrical behavior; unfortunately, some of the most interesting incidences and applications of cavitation involve asymmetrical collapse. Plesset and Chapman were the first to theoretically tackle the asymmetrical collapse, representing the collapse as a potential source flow and utilizing the method of images to represent the boundary [29]. In spite of the relatively simple model, numerical methods were required to solve the resulting equation and advance it in time. Using contemporary computational systems, they were able to simulate about 100 timesteps for each of two different bubble-wall distances, and provide a theoretical explanation for the asymmetry and jet formation observed in bubble collapse near rigid boundaries.

A recent computational study by Wang also solved for the behavior of a cavitation bubble near a planar rigid boundary based on a mathematical model [90]. The model was updated from the potential flow model used by Plesset and Chapman by assuming weakly compressible flow and using matched asymptotic expansion to reconcile near-field and far-field solution. The result is that the near-field solution (where $r \ll a_\infty t_c$) is essentially incompressible, whereas the far-field (for $r \gtrsim a_\infty t_c$) is acoustic, described by the wave equation. These equations are solved by the boundary integral method and the computed bubble outlines for a range of offset distances showed excellent agreement with the experimental photographs of Philipp and Lauterborn [75], as well as the volume-time history of Lauterborn and Ohl through the first rebound [94]. The applicability of such a solution does depend on the dimensions of the bubble relative to the collapse time and sound speed. Wang models 0.145 mm radius bubbles collapsing in 15 μs, which means $r/at_c \approx 0.006$ near the bubble surface. If a larger bubble collapses in the same time, this value increases, and the bubble takes up more and more of the incompressible region, limiting the extent around the bubble where incompressible flow can be assumed.

To the best of the author's knowledge, no theoretical work has been published on the interaction of gas bubbles in liquid with traveling shock waves or pressure gradients. Computational studies investigating these phenomena take a finite-element type approach, and thus do not yield a unified mathematical description for the flow field or bubble boundary. Such computational studies have been mentioned in the relevant sections above.

Typically, an infinite or "large" body of liquid is assumed when considering a theoretical explanation for bubble behavior; this assumption is still made if a bubble is confined, as long as the confinement dimensions are significantly larger than bubble diameter. Leighton challenged the range of applicability of this assumption by investigating the effect of confinement on the left-hand side of the Rayleigh-Plesset equation (i.e. $R\ddot{R} + \frac{3}{2}\dot{R}^2$) [25]. His argument is that a spherical bubble confined in a long tube or between large parallel plates will not be accelerating fluid in all directions as assumed in the derivation of the Rayleigh-Plesset equation. Leighton computes a correction factor for the Rayleigh-Plesset equation by considering changes to the volume of fluid that would be accelerated by bubble motion due to the containment, and finds that differences can become significant for long tubes, even for a tube diameter of 500 times the radial diameter (but particularly so if the tube is only 10 times the bubble radius). The effect also exists for a planar confinement geometry, but is significantly less extreme for spacing as large as 10 $R_{\max}$. However, there is experimental evidence that in planar gaps slightly larger than bubble diameter (gap of 2.77 $R_{\max}$)

the oscillation period of initially spherical bubbles deviates toward that of cylindrical bubbles, indicating influence of confinement on bubble dynamics [95].

The results of Leighton are somewhat at odds with the conclusions of Ilinskii et al., who provide one of the most complete discussions on the theoretical treatment of cylindrical bubble dynamics [96]. They begin by demonstrating the derivation of an equation analogous to the Rayleigh-Plesset equation, but in cylindrical coordinates. Starting with the conservation of mass, momentum, and energy, they obtain the following expression with a logarithmic singularity:

$$\left(R\ddot{R}+\dot{R}^2\right)\lim_{r_\mathrm{f}\to\infty}\left(\ln\frac{r_\mathrm{f}}{R}\right)-\frac{1}{2}\dot{R}^2=\frac{P_g-P_L}{\rho_L}\qquad\text{with}\qquad P_g=\left(\frac{R_o}{R}\right)^{2\gamma}Po \tag{1.6}$$

The singularity is resolved by comparing to a number of experimental studies reporting the collapse times of bubbles from the micrometer to the centimeter scales, and finding that integrating the expression out to $r_\mathrm{f}/R_o = O(10)$ results in good agreement across the wide range of scales [95, 97, 98]. At first glance, this would seem to be in contradiction to Leighton's finding that geometry outside the range of $10\,R_\mathrm{max}$ is significant; however, there are two additional factors to consider. One is that Leighton is considering modifications to a spherical geometry, whereas Ilinskii is dealing with a cylindrical formulation from the start. The second is that while Ilinskii et al. find a region with $r_\mathrm{f} = 10\,R_o$ is sufficient to model bubble collapse, they also find that for modeling small bubble oscillations, a much larger region is necessary, on the order of or $r_\mathrm{f} = 350\,R_\mathrm{max}$ (or more generally, 1/5 of the acoustic wavelength of the disturbance). Leighton does not consider different regimes of bubble oscillation.

The second approach taken by Ilinskii to model bubble collapse is to derive an analog to the Keller-Miksis equation based on Kedrinskii's generalization of the Kirkwood-Bethe approximation and Gilmore equation to an arbitrary number of dimensions [97]. The resulting Keller-Miksis type equation for cylindrical coordinates is as follows:

$$\left(1-\frac{\dot{R}}{a_o}\right)R\ddot{R}+\left(1-\frac{\dot{R}}{3a_o}\right)\cdot\frac{3}{4}\dot{R}^2=\left(1+\frac{\dot{R}}{a_o}+2\frac{R}{a_o}\frac{d}{dt}\right)\frac{P_g-P_L}{2\rho_L}. \tag{1.7}$$

By taking the incompressible limit of this expression ($a_o \to \infty$), the following expression is obtained:

$$R\ddot{R}+\frac{3}{4}\dot{R}^2=\frac{P_g-P_L}{2\rho_L} \tag{1.8}$$

Comparing this to equation 1.6, it is clear that it is identical to setting $r_\mathrm{f}/R_o = e^2 = 7.4$, which is in agreement, for earlier parts of the collapse, with the O(10) range determined empirically; once R/R_o is quite small, the behavior would diverge, but this also corresponds to higher velocities in the flow, where a compressible model may be more appropriate anyway. A plot presented by Ilinskii et al. demonstrates that the three models (compressible, incompressible limit, and Rayleigh-Plesset type) predict the same behavior early in the collapse, then diverge at a certain radius and velocity when conditions begin to violate initial assumptions.

It is important to recognize that all three models are estimates: the Rayleigh-Plesset type relies on an artificial outer radius, and both the Keller-Miksis type equations rely on the Kirkwood-Bethe approximation, which is far more tenuous for cylindrical geometry than for spherical. In fact, Kedrinskii has argued that this assumption makes the coefficient 3/4 in equation 1.8 somewhat arbitrary, and proposed that a coefficient of 1 better fits to data; Ilinskii et al. dismissed this adjustment on the grounds that it changes the collapse time by only about 5%, but did not consider the possible effects on maximum velocity and minimum volume predicted by the different models.

Ultimately, it is possible the most important takeaway from the theoretical models is not where they differ, but where they overlap. All three models predict similar behavior until the radius of the bubble becomes quite small; at this point, there are in any case additional real-world effects that greatly increase the complexity of the problem if considered quantitatively, such as heat transfer, phase changes, and real gas effects. Moreover, at such small radii experimental observation becomes much more difficult, and verifying theoretical or computational results presents additional challenges.

1.8 Origins and Role of Vorticity in Shock–Bubble Interaction

Vorticity and vortex formation have been mentioned by numerous authors in connection with asymmetric bubble collapse (e.g. [33, 58, 90]). However, most quantitative studies of the phenomenon have focused on gas inhomogeneities, with applications to vorticity generation for mixing efficiency [35, 99–103], while a few have investigated the motion of gas bubbles in a gravitational field, which involves much lower accelerations than those applied by shock waves [104, 105]. The latter two cases involve modest volume change of the bubble or gas inhomogeneity, and thus do not precisely qualify as "collapse" processes. However, the physical elements involved in both these problems are similar to those involved in shock–induced bubble collapse, and are thus worth reviewing for insights into the mechanics of the process.

At the core of all three problems, a fluid inhomogeneity interacts with a pressure gradient. The pressure gradient is very gradual in the case of only hydrostatic loading, but much steeper in shock-loaded experiments, even though fairly weak shocks (Mach number less than 2) have generally been used in studies of vorticity [35, 100, 101]. A range of ambient and inclusion fluids have been considered, spanning density ratios from about 1/1000 for air in water to about 3 for refrigerant-22 in air [35]. Cylindrical and spherical (i.e. 2D and axisymmetric) inclusion geometries have both been used. Wave propagation behavior will vary between these systems due to the differences in density and sound speed of substances involved, but the physics of vorticity generation are the same.

The vorticity equation is obtained by taking the curl of the compressible momentum equation, and describes the generation, stretching, dilatation, and dissipation of vorticity [106]. However, stretching is only relevant to 3D flows, dilatation only becomes significant in highly compressible flows, and dissipation can be neglected if viscosities are relatively low and timescales are short, which leaves only one term in the equation. This dominant term (for the three problems described above) is the so-called baroclinic vorticity term, which originates from the misalignment of the pressure gradient (associated with the shock wave or hydrostatic pressure field) and the density gradient around the edge of the inhomogeneity. Therefore, the vorticity in the system is effectively described by:

$$\frac{D\omega}{Dt} = \frac{1}{\rho^2}\left(\nabla P \times \nabla \rho\right) \tag{1.9}$$

and is produced along the boundary of the inhomogeneity. This distribution is nonuniform, and experimental as well as computational studies have shown that the regions of higher vorticity "roll up" the regions of lower vorticity, deforming the cylindrical inhomogeneity first into a kidney shape, then into a pair of counter-rotating vortices traveling downstream [35, 100, 101]. In the context of mixing of gases through this mechanism [35, 99, 101] or evaluating the applicability of bubbles for flow tracking [100], the parameters of interest are the strength, spacing, and velocity of the structure ultimately produced, rather than the time-dependent process of inhomogeneity deformation and area change which are of interest in the case of bubble collapse.

Getting the exact time-dependent vorticity distribution is challenging, because it is dependent on local pressure and density gradients, and these can change significantly during the interaction between loading wave and inhomogeneity. So far, this has only been obtained from finite volume simulations, rather than analytically derived expressions [99, 103]. A number of analytical expressions have been derived for the circulation of the vortices formed at the end of the interaction, as well as velocities and spacing of these features, which allow evaluating agreement with experiments [99, 100]. One of the latest suggested models was that of Yang et al., who wished to obtain an expression solely in terms of initial shock wave and inhomogeneity properties. To this end, they made a number of simplifying assumptions to allow them to integrate Equation 1.9 over the shock passage time and the upper half-plane of a 2-dimensional geometry. This resulted in the following expression for the circulation of one of the pair of counter-rotating vortices produced by the shock-bubble interaction:

$$\Gamma = \frac{2R_o}{U_s}\frac{\Delta P}{\rho_{\text{ref},1}}\frac{\Delta \rho}{\rho_{\text{ref},2}} \tag{1.10}$$

where U_s is the shock velocity, ΔP is the pressure difference across the shock, $\Delta\rho$ is the density difference across the interface, and $\rho_{\text{ref},1}$ and $\rho_{\text{ref},2}$ are reference density parameters, brought outside the integral with the assumption that suitably selected values can accurately represent the data [99]. They suggest taking the post-shock density of the ambient fluid as $\rho_{\text{ref},1}$ and the average of high and low density across the interface ($(\rho_H + \rho_L)/2$) for $\rho_{\text{ref},2}$; this yields good agreement with their simulation of the interaction of a shock wave with a helium jet in air. However, it is possible different values would yield better agreement under significantly different problem parameters (e.g. liquid ambient fluid, instead of gas).

Quirk and Karni critique this model presented by Yang et al., specifically its assumption that vorticity is deposited during the entire time of shock passage, and that the pressure gradient maintains the same magnitude and direction [103]. They argue that the pressure gradient significantly weakens after the wave passes the widest part of the bubble, and also that local deformation of the wavefront results in the pressure gradient acting tangentially to the bubble on the downstream interface. They also point out that vorticity generation terminates (and circulation magnitude stabilizes) after the wave passing through the lighter gas bubble arrives at the downstream interface; however, we note that for a gas bubble in liquid, this time is long relative to the shock passage time over the bubble ($2R_o/U_s$). Ultimately, Quirk and Karni are unable to suggest a superior model for circulation that does not depend on simulating local gradients, and propose that the circulation may be insensitive to the details of vorticity deposition, to explain the relative success of models presented by Yang et al. and others. However, the points raised in their critique highlight the ways in which the simple model may deviate from experimental observations.

1.9 Objectives and Overview

The goal of this study was to investigate the flowfields developed during the collapse of a single bubble, using a PIV technique, in order to further the understanding of damage mechanisms and damage potential of the system. Although a model system that featured no biological matter was used, the system was comprised of biomimetic materials and a loading wave within a reasonable range for biomedical applications was selected, to maximize applicability of results to understanding cavitation in biomedical environments. Two main concessions were made for experimental feasibility. First, a two-dimensional geometry with a cylindrical bubble was used to simplify the acquisition and interpretation of image data. Second, the radius of the bubble used was about 1 mm, which is larger than biologically relevant bubbles by at least a factor of 10. However, such a change can be justified as remaining in the same flow regime based on Reynolds number, such that relevant physical mechanisms are the same. Unlike smaller bubbles, this size could be repeatably created in the laboratory, and imaged at the necessary frame rates to capture collapse behavior.

The remainder of this document details the work that was done on an experimental study of cylindrical bubbles and the results achieved. Chapter 2 describes the equipment and materials used for the study, and the reasoning behind these choices. Chapter 3 describes in greater detail the design process for the experimental fixture using finite element analysis, and the resulting loading condition. Chapter 4 offers predictions of bubble behavior using an existing theoretical approach for symmetrical bubble collapse, and investigates the effect of time-variant pressure loading of a bubble based on theoretical relations. Chapter 5 presents the results of high-speed shadowgraph videography of collapsing bubbles, both in a homogeneous environment and near compliant boundaries. Features of the bubble and boundary deformation are measured and discussed. In particular, there is an extensive discussion regarding the evolution of the cross-sectional area of the bubble over time. Finally, Chapter 6 presents the flowfield data acquired for the same set of material boundary geometries, distributed over the collapse time. The section develops an analytical model that fits the entire observed flowfield within the accuracy of the diagnostic. The theoretical justification for this model is discussed, and it is used to compare the collapse process among different test cases. A summary of the study and potential future work directions are presented at the end of the document.

This work contributes a proposed analytical model for the flowfield around a cylindrical bubble collapsing in a pressure gradient, supported by well-resolved flowfields of a collapse process under these conditions. It also presents the theoretical response of a bubble to a symmetric, but time-varying pressure field, as well as qualitative and quantitative observations on the interaction between a collapsing bubble and a proximate compliant boundary.

CHAPTER 2

METHODOLOGY

2.1 Single-Stage Compressed-Air Gas Gun

A single-stage compressed air gas gun was constructed based on drawings provided by Professor John Lambros at the University of Illinois. However, they were modified by increasing flange width from 1 inch to 1.5 inches, to minimize gas leakage at higher pressures and allow for the possibility of using the gun with helium rather than air, although these capabilities were not ultimately utilized for this project. The gun has a reservoir volume of 6.9 L, a barrel length of 1.52 m and a honed inner diameter of 25.4 mm. Detailed drawings can be found in Appendix A. The rapid release of high pressure air from the cylinder through the barrel accelerates the projectile, a cylindrical maraging steel slug 25.3 mm in diameter and 38.1 mm long, with a mass of 155 g. Performance of the gun was characterized up to a pressure of 45 psi and a resultant velocity of 47 m/s. Higher-pressure conditions were destructive to the experiment test section and were deemed unnecessary, as the experiments were performed at a pressure of 15 psi, resulting in impact velocities of approximately 26 m/s.

The end of the gas gun barrel was instrumented with infrared sensors for measurement of projectile velocity and for triggering diagnostics. Located approximately 1 cm (to ±1 mm) in front of the end of the gas gun barrel (i.e. in the direction of projectile motion), a photodiode and matched LED pair (Honeywell SD1420-002L and SE1470-003L) were suspended on plastic mounts to allow precise sample placement (to ±0.01 mm) as well as impact detection for triggering diagnostics. On the gas gun barrel, at approximately 14 and 20 cm (to ±0.5 cm) from the gun barrel, pairs of Honeywell Optoschmitt detectors and matched LEDs (SD5610 and SE5455) were mounted at vent holes to create two beams across the barrel. These were used to determine the projectile velocity by measuring the width of the square pulse generated by projectile passage. The beam located at 14 cm was also used to trigger a Xenon flash lamp when performing the ultra-high speed shadowgraph diagnostic (described below), to allow the lamp adequate warm-up time.

Signals from the barrel sensors were passed through a custom signal conditioning circuit (see Fig. 2.1) before they were connected to an oscilloscope (Tektronix TDS2014C) for signal measurement, and/or triggered diagnostics devices. The custom circuit performed several functions, as follows. First, the photodiode signal (v_{in}) went through a comparator with hysteresis to determine if impact was imminent (if voltage dropped sufficiently low) and output a TTL-compatible 5 V or 0 V signal, accordingly. Hysteresis was employed to prevent electronic ringing. Second, this signal passed through a simple latch circuit to create a one-shot output and thus prevent retriggering. Finally, output from each Optoschmitt detector was passed through a NOR gate used as an inverter (not pictured); this was found to be the simplest way to change the signal's impedance characteristics so it could be used with the delay generator (Berkeley Nucleonics Model 577); the resulting time delay was on the order of tens of nanoseconds, negligible for the observed pulse widths on the order of a millisecond.

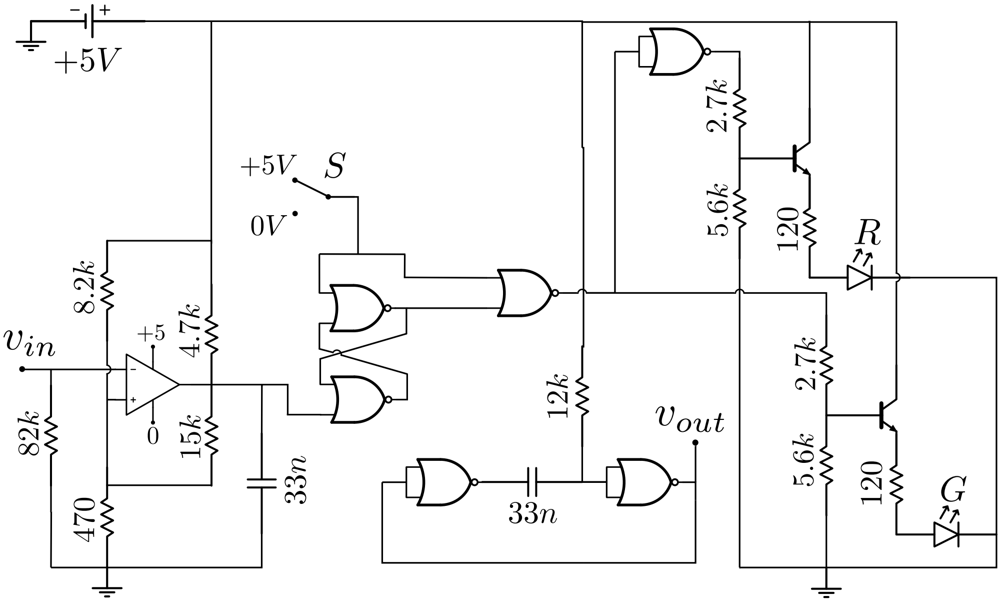

Figure 2.1: Schematic of custom signal conditioning circuit. Photodiode signal (v_{in}) goes through comparator, latch, and one-shot circuit to generate a pulse to trigger diagnostics (v_{out}). LEDs indicate status of latch for operator convenience.

2.2 Sample Fixture Construction

Two materials were used to create bubble geometries of interest: agarose hydrogel and three compositions of Sylgard 184 polydimethylsiloxane (PDMS) polymer by DOW Corning. The properties and process of synthesizing these materials will be expounded in Section 2.3. Four two-dimensional geometric configurations of these materials were investigated, shown in Fig. 2.2. These geometries were inspired by considering how a gas bubble in a biological fluid might be confined by nearby tissues in an anatomical environment (see Section 1.3).

First, a bubble in homogeneous agarose gel, 8.6 mm downstream of the edge of an aluminum striker plate (described below), served as a baseline case, sometimes referred to as the "no-boundary" case. Second, a 6 mm ($^1/_4$ in) wide layer of PDMS was inserted, spanning from the striker to 2.2 mm upstream of the bubble center; this will be referred to as the "upstream boundary" case. Third, all agarose from 2.2 mm

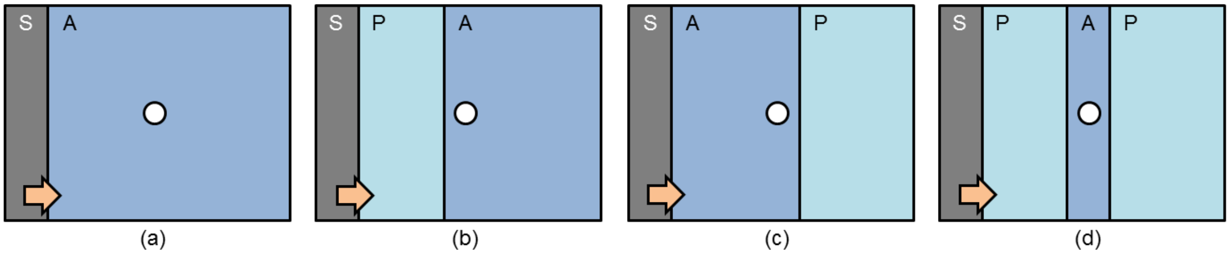

Figure 2.2: Geometries of interest. Arrow indicates direction of impact, striker motion, and prevailing flow. Elements of the geometry are labeled as S: striker, P: PDMS, and A: agarose gel.

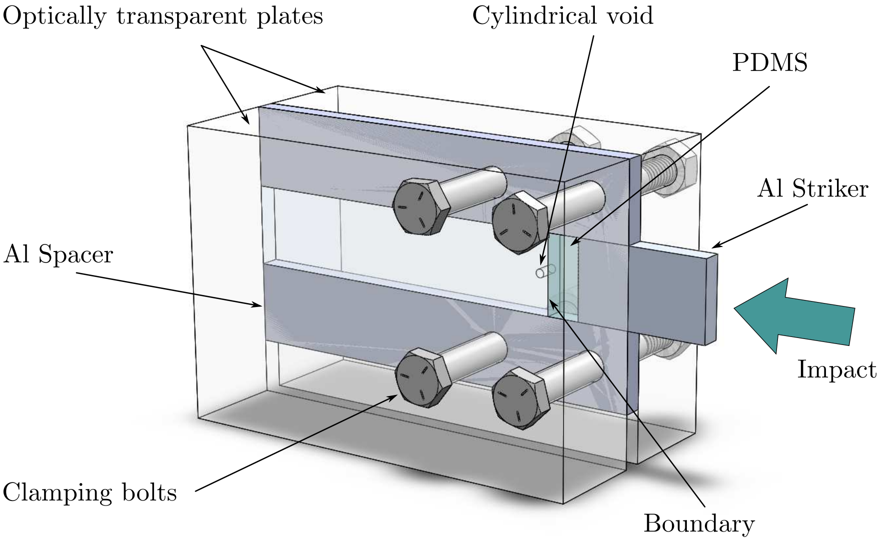

Figure 2.3: Schematic of the assembled experimental fixture filled with gel. Al striker is $^3/_4$ in wide by 1 $^1/_4$ in long by $^3/_{16}$ in thick. PMMA sample face plates are 2 $^3/_4$ in wide by 4 in long by 1 in thick. Additional dimensions are described in the text.

downstream of the bubble to the end of the sample was replaced with PDMS; this will be referred to as the "downstream boundary" case. The downstream boundary case was also performed with an aluminum bar replacing the PDMS, to consider the case of a comparatively rigid boundary. In the final geometry, two PDMS boundaries were combined, resulting in a sample with a 4.5 mm wide layer of agarose gel surrounded by PDMS; this will be referred to as the "two-boundary" case. The bubble was always located in agarose, because early tests demonstrated the strength and elastic modulus of PDMS were too great for the bubble to collapse to any significant degree under the loading pressures of interest, and that avenue of investigation was abandoned.

The 2-D geometry was assembled in a layer of gel and/or polymer $^3/_{16}$ in thick by $^3/_4$ in wide by 3 $^1/_2$ in long, and enclosed in a plastic and aluminum fixture as shown in Figure 2.3. The gel/polymer layer was sandwiched between nominally 1 in thick PMMA plates, 2 $^3/_4$ in wide by 4 in long. Aluminum spacers

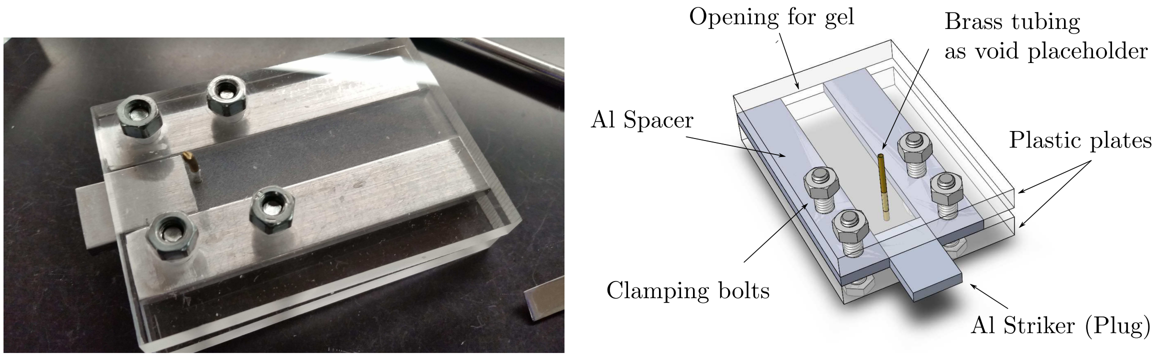

(a) Mold with gel.

(b) Mold design.

Figure 2.4: Gel casting mold.

($^{3}/_{16}$ in thick by $^{3}/_{4}$ in wide by 4 in long) along the outside edges of the gel provided containment in the transverse direction. Four $^{1}/_{4}$"-20 hex bolts were used to secure the assembly through holes in the PMMA plates and aluminum spacer bars. At one end of the sample, a 1 $^{1}/_{4}$ in long aluminum striker plate penetrated approximately $^{1}/_{2}$ in into the sample. Its role was to transfer the projectile impact into the gel layer with maximum uniformity and repeatability. High-speed videos with a large field of view indicated that the piston moved at constant velocity with minimal acceleration time through the end of the bubble collapse, alleviating concerns about multiple impacts and significant friction-based energy dissipation, and indicating that an impulsively started piston was an appropriate model for the striker-fluid interaction during this time.

To create the bubble in agarose, molds were created as shown in Fig. 2.4 with a piece of brass tubing holding the place of the bubble, and $^{3}/_{8}$ in thick PMMA plates serving as sidewalls. Spacers in both $^{3}/_{16}$ in and $^{1}/_{16}$ in thicknesses were available to allow casting of thin seeded layers for particle shadow velocimetry (see Section 2.5, below). Otherwise, the molds were very similar in structure to the test sample enclosure. A striker was inserted to plug one end, and could be adjusted to create the appropriate offset from the bubble to one nearby boundary (this varied between 2.2 mm and 8.5 mm). In the downstream boundary and two-boundary cases, where a second material boundary was required, it was created by manually trimming the sheet of gel to size with a razor blade after it had set. PDMS was cast in sizable sheets, and therefore all pieces were cut to desired size with a razorblade. For $^{1}/_{4}$ in (6 mm) wide sections, a tool was devised to hold two razorblades in parallel, in order to facilitate consistency, but for longer pieces a single blade was used to trim the material and ensure a flat, vertical edge free of bubbles in contact with agarose.

Once all pieces were cut to size, one of the 1 in PMMA plates and the aluminum spacers were assembled with bolts to create a channel; the agarose and PDMS pieces were then arranged in the channel. The faces of PDMS pieces were lubricated with glycerin during assembly to prevent sticking to the PMMA sidewalls, as that would significantly change the boundary conditions. Liquid dish detergent was superior to glycerin at preventing sticking and lubricating the PDMS-PMMA interface, but it was excessively prone to cavitation.

The cavitation bubbles on the material surface obstructed optical access, and this ultimately made dish detergent untenable as a lubricant for this application. Once the agarose and PDMS sections were arranged, the second PMMA plate and striker were added and bolts were hand-tightened. Then, gentle pressure was applied to the striker while the bolts were tightened further, to squeeze out any small air bubbles caught at the boundaries or on the sample surface, without deforming the bubble. Occasionally, multiple attempts at final assembly had to be made if air bubbles did become trapped, as they would cause detrimental visual aberrations during the test.

2.3 Sample Materials

Materials were selected to optimize experimental feasibility and applicability of the results to bubble collapse in biological environments. For the diagnostic techniques (particle image velocimetry and shadowgraph video) to be applicable, the samples needed to be optically transparent, which significantly limited material options. Since many repeat tests were required, it was also desirable that materials be reasonably inexpensive and quick to manufacture in the laboratory. Manufacturing in-lab was preferred so that the same materials could be manufactured with or without seeding particles, and the seeding process could be adapted as needed.

In order to maintain relevance of the model problem to biomedical applications, materials were selected that had a history of being used in a biomimetic capacity. Given the high water content of human tissues, hydrogels like ballistic gelatin make good model materials, and have been used for many decades to investigate tissue damage produced by ammunition [107, 108]. Agarose gel has similar properties to gelatin, which makes it an acceptable substitute; this will be discussed in greater detail in the following section. Agarose has also long been used as a substrate for cell cultures and tissue engineering [109, 110]. Polydimethylsiloxane (PDMS) is a silicone rubber that is biocompatible and has been used for biomedical implants and sensors [111]. It has also been used as a tissue surrogate to investigate mechanical damage of some tissues [112, 113]. There is ongoing interest in manipulating PDMS structure to optimize its properties for biomimetic applications [114]. However, it is important to note that any inanimate material is extremely unlikely to exactly match the response of a living tissue, given the vastly different structure and mechanisms at work in these substances at the microscopic level. The elastic moduli of most living tissues are reported on the order of 10–100 kPa with density and sound speeds typically close to those of water (within 5–10% of 1000 kg/m^3 and 1500 m/s respectively), though diverging for some tissues with particularly distinctive composition, such as lung or bone [115–117]. The reported properties of agarose gel and PDMS, discussed in detail in the sections below, were deemed sufficiently similar for a model problem.

2.3.1 Agarose

Agarose gel is a hydrogel, a substance composed primarily of water with gelling agent added. The quantity of the gelling agent needed may be very small. Molecules of the gelling agent (in the case of agarose, polysaccharrides) crosslink to form a network within the water, and attract the water through hydrogen bonds [118]. This structure can be visualized as similar to a household sponge, except on a molecular level—the solid structure holds the water within it, but the two phases are not chemically bonded, and water can be squeezed out by applied pressure. Given this structure, it is unsurprising to find that the density and sound speed of hydrogels like agarose gel or gelatin are very similar to water [119, 120], but the elastic modulus depends on gelling agent concentration and gel temperature [118, 121]. Agarose gel was preferred in this application over gelatin due to its better optical clarity, but also due to its stability at room temperature compared to gelatin. Gelatin has a melting point in the range of 22–31°C, whereas for agarose it is 69–80°C [121], which translates into much less variation in mechanical properties for agarose gel at room temperatures.

Agarose gel was prepared by mixing Genemate Agarose LE powder (BioExpress, Kaysville, UT) with distilled water in a ratio of 2.5±0.1% by weight at 295 K, heating to boiling, and cooling to 328 K in a water bath. 0.05 g of glass microspheres were then added for every 20.5 g batch of gel if particle shadow velocimetry was being performed (see Section 2.5), then gel was poured into the PMMA mold. It then set within 30 minutes. Due to its water-based nature, regions of the gel exposed to atmosphere visibly dry out within 24 hours, so air exposure was minimized by leaving the gel in the sample mold until needed. Agarose samples were used the same day they are created.

Agarose mechanical and acoustical properties are not widely available; however, they have previously been assumed to be similar to other hydrogels such as gelatin with great success [5]. Assumed agarose properties are presented in Table 2.1. The shock Hugoniot for agarose gel is assumed to be similar to that of gelatin: $u_s = a + 2u_p$ [120]. The Tait equation of state, with parameters applicable to water, was used successfully by Ball et al. to model the behavior of cylindrical bubbles in gelatin as observed by Bourne and Field [33, 36]. The equation is

$$\frac{p}{B} = \left(\frac{\rho}{\rho_R}\right)^n - 1 \tag{2.1}$$

with the parameters, ρ_R=999.96 kg/m^3, B=331 MPa, and n=7. This approach should be justifiable for agarose as well, given the similar structure of the two gels and the high proportion of water in the gel composition.

Table 2.1: Agarose properties. From [119, 120].

ρ	1060 kg/m^3
a	1500±10 m/s
E	38 kPa

2.3.2 PDMS

PDMS (polydimethylsiloxane) is from a different class of materials, the elastomers. These are a subset of polymers that generally exhibit low hardness, low elastic modulus, and high extensibility. PDMS can exist in a linear polymer form, which is a collection of polymer chains without cross-linking; this will act as a viscous liquid if composed of shorter polymer chains, as the molecules slide past each other in an amorphous mass [122]. Longer molecules exhibit more resistance to such motion (for example, through entanglement with each other) and thus viscosity of PDMS increases with molecular weight [123, 124]; at extremely large molecular weights, it may even behave as a solid as the long molecules become extremely entangled [122].

However, it is more typical to encounter PDMS solids with a cross-linked structure. A chemical agent and/or heat are introduced to the linear polymer to facilitate the formation of bonds between polymer chains [125]. These bonds begin to form a lattice in the PDMS, which can store energy through temporary deformation of bonds—that is, it begins to exhibit elastic behavior. Initially, the lattice is very sparse and irregular, so many molecules remain free to flow around it, resulting in viscoelastic material properties. However, as crosslink density increases, fewer molecules are free to flow and more are involved in the lattice, until elastic behavior dominates. Since the bonds restrict the relative motion of molecules, strength and stiffness (or storage modulus) of the material increase as crosslink density increases, but viscosity (or loss modulus) decreases as fewer molecules remain free to move [124, 126]. The crosslink density is controlled by the conditions of crosslink generation—the amount of chemical agent, the curing temperature, and other factors can both play a role in the strength, stiffness, hardness, and viscosity of the final product. The density, however, changes by only a small percentage as a result of cross-linking [127].

The PDMS used in these experiments was prepared from a commercial kit (Sylgard 184) by mixing the base provided with curing agent in the desired ratio by weight. While the recommended ratio is 10:1, varying this to investigate the effect of a range of properties is not uncommon in scientific applications [126, 128, 129]. The compositions used in this study were 20:1, 30:1, and 40:1 to reduce crosslink density and produce materials with lower stiffness (Young's modulus) and strength. The base fluid was measured out first in a weighing boat set on a precise balance, then curing agent was added to the same container. If necessary for particle shadow velocimetry (see Sec. 2.5 below), hollow glass microspheres were added at a ratio of 0.05 g per 20 g PDMS. The mixture was then agitated as carefully as possible until fully mixed. If particles were added, it was then allowed to rest for 1 hour to allow bubbles to escape. Then it was gently mixed once more to redistribute particles, poured into a 20 mL syringe and extruded into an 8 in long sample mold (note: the mold was previously covered by plastic cling film to aid subsequent PDMS removal). However, if no particles were added, there was no intermediate resting or syringing step; the PDMS was poured into flat frames adhered to a glass plate with clear RTV adhesive. In either case, the PDMS was then allowed to cure for at least 48 hours before use.

The density of PDMS is listed as 1030 kg/m^3 for 10:1 cured product, and 1110 kg/m^3 for the base [130].

Table 2.2: 10:1 PDMS elasticity and strength properties from various sources, with varying cure temperature, ambient test conditions, strain rate, and methods.

Source	Cure T(°C)	E (MPa)	UTS (MPa)	Notes
Carillo et al. 2005 [135]	25	2.04	–	Nanoindentation results also reported, values up to 1.5 MPa higher than compression results.
Mata et al. 2005 [126]	95	3.12	7.6	9:1 mix. E by nanoindentation, reported as G'=1.04 at 4 Hz. Increases to G'=1.40 at 256 Hz.
Khanafer et al. 2008 [129]	65	2.13-2.39	–	Varied shear rate, 5 mm/min to 500 mm/min
Schneider et al. 2008 [136]	150	1.8±.09	–	E increases linearly with ambient temp, up to 3.5 MPa at 190°C.
Wang 2011 [128]	65	2.66	–	
Johnston 2014 [134]	25	1.32±.07	5.13	
Johnston 2014 [134]	100	2.05±.12	6.25	

Density is expected to remain in this range for intermediate concentrations. Sound speed reported in literature varies only slightly. Tsou et al. investigated acoustic properties of three concentrations (5:1, 7:1, and 10:1 PDMS) [131]. They found sound speeds increasing gradually from 1077 m/s for 10:1 PDMS to 1119 m/s for 5:1 PDMS. Other authors report sound speeds from 1050 m/s [132] to 1100 m/s [133] for 10:1 PDMS. Therefore, it can be assumed with good confidence that sound speed in PDMS is 25-30% lower than that in water or hydrogel.

Greater variation is observed in the Young's modulus and tensile strength of PDMS, which can vary with mixing ratio, curing temperature, ambient pressure and temperature during test, and strain rate. This is demonstrated by the values presented in Table 2.2 for 10:1 PDMS, for which data is most readily available. Few sources investigate the elastic properties of significantly softer PDMS ratios; the Young's moduli presented by the two most comprehensive sources available are presented in Table 2.3. Wang presents moduli for a wide range of PDMS mixing ratios in his thesis, and proposes some functional fits to the data; unfortunately, his gels are cured at 65°C, which the work of Johnston [134] suggests will produce stiffer, stronger gels than those cured at room temperature. We apply two of the functional fits suggested by Wang (exponential with ratio, and linear with inverse of ratio) to the data of Carillo, whose PDMS was cured at 25°C, to predict stiffness and strength of room-temperature cured PDMS down to 40:1 mixing ratio.

The shock Hugoniot of PDMS, along with many polymers, exhibits a steeper slope at low pressures than at high pressures. This has most recently been explained by considering free volume present in the polymer

Table 2.3: Young's modulus of PDMS of various concentrations. Exponential fit equation is $E = 3.779e^{-.078R}$. Inverse fit equation is $E = 24.939R^{-1} - .4648$.

Ratio (R)	Wang 2011 [128]	Carillo et al. 2005 [135]	E(MPa) by exp fit	E(MPa) by inverse fit
5:1	3.588	–	2.57	4.41
7:1	2.91	–	2.20	3.02
10:1	2.66	2.04	1.74	1.97
15:1	–	1.03	1.18	1.16
16.7:1	1.21	–	1.03	1.00
20:1	–	0.76	0.80	0.75
25:1	0.98	0.50	0.54	0.51
30:1	–	0.42	0.37	0.35
33:1	0.56	–	0.29	0.27
40:1	–	–	0.17	0.15

structure that is "crushed" at a sufficiently high level of pressure [132, 137]. This means a Hugoniot fit to a large range of pressure data will not be valid for the lower pressures [137, 138], and a separate Hugoniot relation is required for relatively low pressure. A quadratic Hugoniot has also been proposed to describe this region [113, 139]. Some proposed Hugoniot relations are presented in Table 2.4 along with notes on their applicability. The linear, low-pressure relations proposed by Dattelbaum et al. and Appleby-Thomas et al. show good agreement in spite of being obtained by very different mechanisms, and thus inspire confidence.

While many mathematical models have been applied to PDMS structure and properties, the Tait equation (Equation 2.1) is certainly an accepted equation of state for this material [132, 137]. The empirical fit constants for low-pressure (<200 MPa) behavior found by Dattelbaum et al. are B=85 MPa and n=11.4; molecular dynamics simulations by Hooper et al. arrive at similar values of B=85.6 MPa and n=12.2. The reference density ρ_R can be safely equated to the nominal 1050 kg/m^3 as atmospheric pressure is negligible next to the value of B. For completeness, it is worth noting that for much higher pressure (order of GPa), the equation of state for PDMS changes much like the Hugoniot, and Dattelbaum et al. calculate the new constants as B=5.237 GPa and C=0.1415 (n=7.1).

Table 2.4: Shock Hugoniot of PDMS.

Source	Equation	Notes
Dattelbaum 2005 [137]	$U_s = 1.572 + 1.703U_p$	P>1.5 GPa, diamond anvil cell with impact data from Marsh 1980 [140]
	$U_s = 0.970 + 2.618U_p$	P<.2 GPa, by dilatometry
Appleby-Thomas 2014 [113]	$U_s = 1.03 + 2.45U_p$	Impact studies, $U_p < 1$ mm/μs
	$U_s = 0.96 + 3.03U_p + 0.68U_p^2$	Impact studies, $U_p < 1$ mm/μs
Winter 2003 [138]	$U_s = 1.63 + 1.66U_p$	Up to $U_p < 2$ mm/μs; uses data from Marsh 1980 [140].

2.3.3 Effect of Adding Seeding Particles on Material Properties

It is well established that the properties of a multiphase mixture can vary significantly from that of the base phase on its own, even for small fractions of additives; whether this occurs depends on the nature and quantity of the additive. Therefore, it is important to analyze the effect of adding the PIV seeding particles to agarose gel and PDMS, to verify that the properties of the materials are not significantly changed.

The seeding particles were purchased in bulk from McMaster-Carr (item number 1414T36), and are nominally 0.002 in or about 50 μm in diameter. The expected structure is a glass shell encircling a gas or vacuum phase. The average density, measured by mixing a known mass of particles into water and measuring the volume, is 0.24±0.02 g/mL. As the particles are added at a ratio of 0.05 g per 20±1 g of gel or PDMS, this amounts to 0.2% by mass or 1% by volume in both agarose and PDMS.

To predict the change in the elastic properties of the materials, the system can be considered as a relatively compliant base, or matrix, reinforced with rigid spherical particles. A classic approach to estimate properties of an elastomer reinforced with rigid particles is the Einstein equation:

$$E_c = E_m(1 + C_E V_p^*) \tag{2.2}$$

where E_c and E_m are the composite and matrix elastic modulus respectively, C_E is Einstein's constant dependent on particle shape (2.5 for spherical inclusions), and V_p^* is the particle volume fraction [141]. This relation was initially applied to material viscosity, but has been found to also apply to the shear and elastic moduli. For $V_p^* = 0.01$, this yields an expected increase in the elastic modulus of the material of only 2.5%, a minimal difference that is not expected to have significant impact on experimental results.

Einstein's formula does not account for interactions among particles; it is expected that with a low volume fraction of particles (e.g. 1%), these interactions can be neglected. To verify, a generalized relation proposed by Guth can be used, which includes an additional term to account for spherical particle interactions [141, 142]:

$$E_c = E_m(1 + 2.5V_p^* + 14.1V_p^{*2}). \tag{2.3}$$

The contribution of the additional term is only 0.14% of E_m, which confirms that the additional contribution of particle interactions is negligible, and the results of Einstein's formula are an appropriate estimate.

Understanding the effect on sound speed requires a slightly different analysis. Atkinson and Kytomaa investigated the acoustic wave speed in suspensions of small rigid particles in water [143]. They found that, as long as particle size is much smaller than disturbance wavelength, a volume-weighted average bulk modulus (K) and density (ρ) allow a good estimate for sound speed (a) to be calculated:

$$\frac{1}{K_c} = \frac{V_p^*}{K_p} + \frac{1 - V_p^*}{K_L} \tag{2.4}$$

$$\rho_c = V_p^* \rho_p + (1 - V_p^*)\rho_L \tag{2.5}$$

$$a_c = \sqrt{\frac{K_c}{\rho_c}} \tag{2.6}$$

where subscripts p, L, and c refer to the particle, liquid, and composite respectively. Bulk moduli of 30–100 GPa have been reported for various glasses and densities between 2200 and 4800 kg/m^3 have been measured, averaging about 3000 kg/m^3 [144]. Using approximate values of $K_L = 2.25$ GPa and $\rho_L = 1000$ kg/m^3 (which yield a $a_L = 1500$ m/s), $K_c = 2.27$ GPa (not very sensitive to K_p) and ρ_c ranges from 1012 to 1038 kg/m^3. This results in a maximum change in sound speed of 21 m/s or less than 1.5% ($a_c = 1478$ m/s).

It can be argued that solid particles are not a valid model for the microbubbles; after all, the above analysis assumes particles with the high density and sound speed of glass, whereas the composition of inclusions in the gel is over 90% air, which has low density and low sound speed. Substituting the average density of the bubbles (240 kg/m^3) in the above analysis for glass density suggests rigid particles that have a sound speed of 11 km/s, which is quite clearly not the case for air-filled spheres! It's then unsurprising that using average density and glass stiffness modestly increases the predicted material sound speed (to 1512 m/s), but it is nonetheless nonsensical. There is no physical mechanism that allows pockets of air, with low sound speed and low acoustic impedance ρa, to expedite sound wave travel through a material.

A different way to adjust the bulk modulus for lower-density inclusions is required. Zimmerman analyzed three different models for change in material moduli with the addition of both rigid inclusions and empty voids [145]. Although these models diverge for inclusion concentrations of over 20%, his results make clear that for small inclusion concentrations, the three models converge to $K_c/K_m = 1 - 2V_p^*$ for voids, and $K_c/K_m = (1 - 2V_p^*)^{-1}$ for rigid inclusions. This model is derived without considering bubble dynamics as would occur in a fluid medium, and therefore should be reasonable for bubbles that cannot deform due to their hard glass shell. Using this estimate for K_c and a volume-weighted average density, the resulting sound speed is $a_c = 1498$ m/s; even less of a predicted change than solid inclusions.

Although the actual gel-glass microsphere system is more complex than solid particle or non-deforming void inclusions, the foregoing analysis should be sufficient to demonstrate that the very low volume fraction of included particles only changes the material properties by a few percent; such a change is negligible with regards to the experiment.

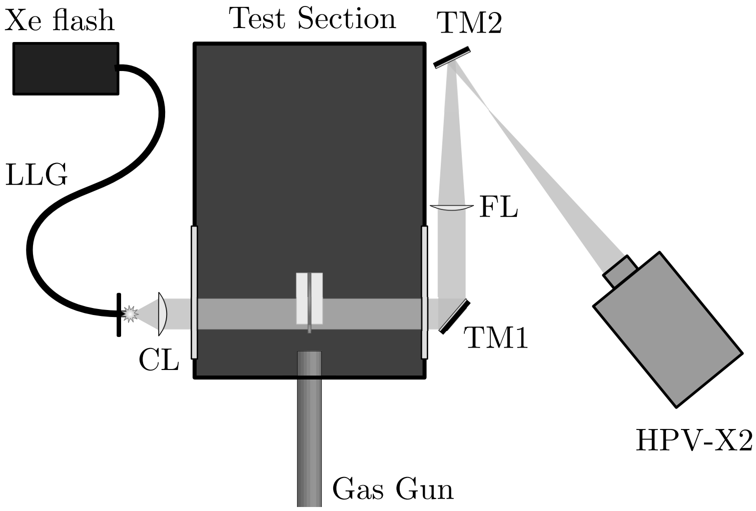

Figure 2.5: Schematic of shadowgraph imaging setup. LLG: liquid light guide. CL: collimating lens (60 mm focal length). FL: focusing lens (500 mm focal length). TM1,2: turning mirrors (flat). HPV-X2: Ultra High-Speed Camera.

2.4 Ultra-High Speed Shadowgraph Imaging

The objective of doing shadowgraph imaging was to acquire a full time series of the bubble interface motion and material boundaries deformation, as well as to capture the behavior of any waves generated at the end of collapse. The setup was designed around the required temporal resolution, spatial resolution, magnification, and good wave visualization through the shadowgraph effect.

Temporal resolution and spatial resolution entirely hinged on camera availability and/or selection. The Shimadzu HyperVision-X2 ultra-high speed camera (Shimadzu Corporation, Kyoto, Japan) allowed the acquisition of data at 5 million frames per second with a fixed exposure of 110 μs (though exposure is adjustable at lower frame rates). The output is 256 frames with 10-bit depth and 400x250 pixel resolution on a 12.7 mm wide sensor.

At these high frame rates and short exposure times, supplying sufficient lighting becomes a challenge. A Photogenic PL2500DR 1000 W-s Xenon flash lamp was used in a light-collecting housing designed and manufactured by Hadland Imaging (Santa Cruz, CA). The housing included a liquid light guide to supply the light to the optical system as a 5 mm spot.

A lens-based focused shadowgraph system was utilized in the final setup. A 60 mm focal length lens with 2 inch diameter was used to collimate light from the light guide, in order to maximize light captured; in fact, enough light was captured that an iris could be introduced to limit the size of the light source. Collimated light was passed through the sample, centered on the bubble. A 500 mm singlet lens was then used to focus the image and obtain the desired magnification at the sensor; the final magnification was 1.6x, imaging an area just over 2 bubble diameters across the height of the sensor. This setup is schematically illustrated in Figure 2.5.

The shadowgraph technique is dependent on the change in the index of refraction as light travels along an optical path; this could occur due to angled or curved material interfaces, changes in density due to thermodynamic effects, or both [146]. The deflection of light rays due to these changes results in variations in intensity in the captured image; for the shadowgraph technique, these intensity variations are proportional to the second spatial derivative (Laplacian) of n. For gases, the variation of index of refraction (n) with density is captured by the Gladstone-Dale relation:

$$n - 1 = k\rho \tag{2.7}$$

where k is the Gladstone-Dale coefficient, which ranges from 0.1 to 1.5 cm^3/g for various gases; it is 0.23 cm^3/g for air at standard conditions. The so-called refractivity ($n - 1$) for gases can range from 10^{-5} to 10^{-3}. Refractivity of liquids is generally several orders of magnitude higher; it is about 0.336 for water [147]. The functional form of refractivity with density is more complicated for liquids; one common model is the Lorenz-Lorenz equation:

$$\frac{n^2 - 1}{(n^2 + 2)\rho} = LL. \tag{2.8}$$

For water, LL varies relatively little (5–10%) across the visible spectrum and can be estimated as a constant, but it should be noted it can be highly variable for other materials and wavelength ranges [148]. The functional form of $n - 1$ is clearly nonlinear with density, but it is monotonic for the range of pressure, density, and temperature in the experiment, and exhibits changes on the order of 10^{-3} as pressure increases from 0.1 to 20 MPa at 20°C [147]. Using the Tait equation of state for water, this would correspond to a density change of 0.87%; the same change in air would result in a refractivity change of only 2.5×10^{-6}. Assuming disturbances of the same spatial extent, the shadowgraph system would be much more sensitive to disturbances in water than in air; the same is expected to hold true for most liquids and solids as compared to gases [146].

In theory, the sensitivity of the system could be adjusted to optimize it for waves in liquid, compromising the visibility of waves in the air-filled bubble. Focused shadowgraph sensitivity is adjusted by changing the focal plane; image intensity variations are caused by the nonuniform deflection of light rays such that they cluster in some regions (bright) and are absent from other regions (dark). Therefore, a system perfectly focused on the location of the disturbance will not show the disturbance; at that point, a light ray going through the disturbance has changed direction, but has not yet traveled away from its prior path. Shadowgraph must be slightly defocused in order to be viewed [146]. In practice, the distance the focal plane must be shifted along the optical path is extremely small, and finding the optimal sensitivity for viewing waves in liquid but not air was not possible, particularly considering the finite sample thickness.

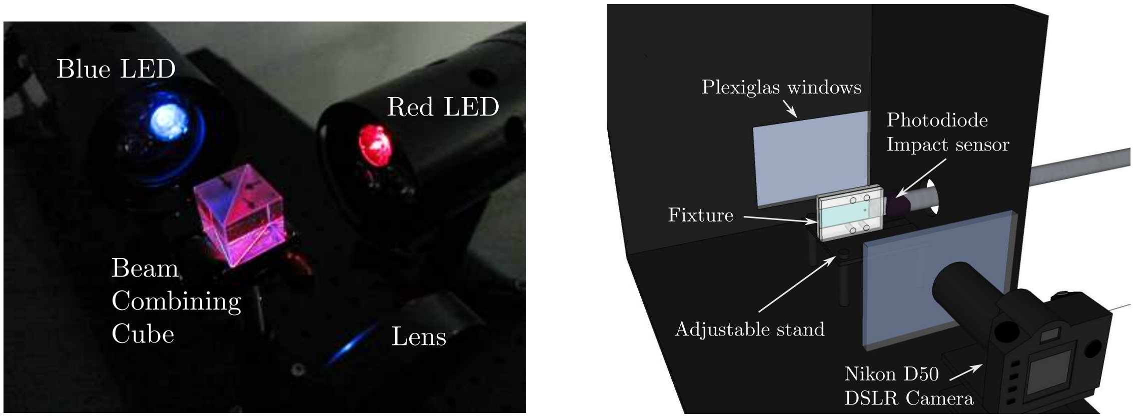

(a) LEDs and optics setup.

(b) Test section, IR sensors, and camera setup.

Figure 2.6: Schematics of the PIV imaging setup.

The system was instead adjusted to show a focused image of material boundaries, and to show a jet generated by a compressed-gas computer duster. To do this, a test sample fixture was constructed without one of the spacers, and with a thin straw sandwiched between the plastic sidewalls. The sample was aligned, then the duster can was used to create a small jet through the straw as a test flow in the exact location of the experiment. Since the system alignment was sufficient to show disturbances in the gas, it was extremely sensitive to disturbances in fluid and even very weak waves show up clearly. Discretion is necessary to identify important wave patterns and disregard the weak ones.

It is worth noting that initial attempts at shadowgraph utilized 4.25 inch $\lambda/8$, f/10.6 optical mirrors, but the 1143 mm focal length resulted in significant light loss. This limited feasible frame rate, made it extremely difficult to attain the required magnification, and overall degraded the image quality. Ultimately, it became clear that the advantages of mirrors and long focal lengths were limited for such a small region of interest, and a much simpler lens based system provided a higher quality image.

2.5 Particle Shadow Velocimetry

Particle Shadow Velocimetry (PSV), a form of Particle Image Velocimetry (PIV), was performed using a Nikon D50 color DSLR camera and two high-power, fast-response LED modules (LM2X-DMHP-RGB by Innovative Scientific Solutions Inc., Dayton, OH). The LED module heads each consisted of three separate LEDs in red, green, and blue; each configured to replicate a TTL/CMOS pulse pattern received at a corresponding BNC input on the module. This signal was created by a delay generator (Berkeley Nucleonics Model 577), which was in turn triggered by the signal from the photodiode impact sensor (see Sec. 2.1).

The arrangement of the optical components of the diagnostic is shown in Fig. 2.6. The two LED modules were aligned such that beams from a red and a blue LED passed through a 50/50 beam splitter cube

(Thorlabs BS013) oriented to function as a beam combiner. At this point, verifying that both LEDs have equal setback from the cube was important to ensure equal path length, therefore equal beam divergence, and therefore maximum beam overlap. The combined beams were then passed through a 60 mm focal length lens (Thorlabs LA1401) to narrow the beam and capture maximum light on the sample; the ideal lens offset was such that the beam was nearly, but not quite, collimated. If the beam was collimated, intensity variations following the shape of the emitter were observed, and since the goal was uniform illumination in the plane of the sample, this was unacceptable . The optics were positioned with the beam perpendicular to the gas gun barrel and offset to center the light spot approximately 1–2 mm downstream of expected bubble center (in anticipation of some bubble propagation during the test). The camera was used with a 105 mm prime lens and 42 mm of extension tubes, placed as close to the sample as the test section inset would allow (110–120 mm). The lens was aligned coaxially with the beam. Once optics were aligned, they were covered with black felt to block stray light from the lab and allow long exposure time of the camera. Direct overhead lights were also turned off as an additional precaution. Turning off all lights was found unnecessary as it did not have an appreciable effect on image quality and presented a safety hazard.

During the test, as for high-speed shadowgraph tests, the projectile was loaded into the gas gun barrel and the cylinder was pressurised; doing this after sample alignment would risk bumping the sample. Once the gun was ready, a seeded sample was positioned in the test section such that the striker was clipping the edge of the photodiode beam and resulting in a reading of 375±5 mV of a maximum voltage of 425–450 mV. The sample was oriented such that the seeded layer was closest to the camera to maximize magnification. Using manual controls on the delay generator, the setup was checked through the viewport of the camera, then camera height and/or focus adjusted as necessary to center the bubble vertically and bring particles into sharp focus. A pre-shot image was taken with camera focus and light pulse settings configured for the test. The oscilloscope and delay generator were then both set to trigger mode, to be activated by the photodiode impact sensor. The camera was activated manually with a 2 sec shutter time immediately before the gas gun was fired, also manually. Upon entry of the gas gun projectile into the photodiode beam (indicating imminent impact with the striker), the delay generator was triggered to send a 500 ns square pulse to each LED module, with a 1 μs delay between them, and a prescribed delay before the first one (10–50 μs, depending on the test). This resulted in two images with 1 μs delay recorded on the red and blue color channels respectively in the image, which can subsequently be separated and analyzed by dPIVB software (Innovative Scientific Solutions, Inc. Dayton, OH).

After the shot, if the focus was changed, a scale image was taken as a still shot, using all the same settings as the shot, with manual triggering. This was important because at such close range, magnification changes caused by focusing optics are significant. Pulse widths and projectile time of arrival were recorded from the oscilloscope for verifying consistency of impact conditions.

2.5.1 PSV System Accuracy

Each of the numerous components comprising the PSV system can contribute to the overall error of the system. While some considerations regarding the choice of each component and parameter are given below in Section 2.5.3, the overall accuracy of the system can be evaluated experimentally.

The procedure was as follows. First, a seeded sample was prepared, as for a regular bubble collapse PSV test. This sample was aligned in the test section, with the striker cutting off approximately half the photodiode beam (signal value of about 200±50 mV out of 425–450 mV). A still photo was taken the same way as pre-shot photos, by manually triggering the light system without projectile impact on the sample. To create a controlled (known) horizontal displacement, the translation stage was moved using the fine adjustment screw until the photodiode signal had increased by roughly 40–60 mV, indicating a displacement of 0.1–0.15 mm, or 20–30 px (this is the upper range of expected experimental values). To create a vertical displacement, a 0.005 in (0.127 mm) aluminum shim was inserted under the sample, and the sample was aligned to the same voltage as before, within 5 mV. Still photos were taken with horizontal, vertical, and diagonal (horizontal and vertical) displacement relative to the initial location. To create a constant-displacement (CD) image for testing the system, the red channel from the first image was combined with the blue channel from one of the displaced images. This was expected to produce the same displacement for all particles in the sample; the displacement can be predicted from the measured photodiode voltage, shim height, and image scale, or the displacement can be measured from a clear edge in the image (not a particle), like the bubble interface.

PSV is essentially a subtype of PIV, so the process of extracting vector data from images is the same in many ways. The CD images were analyzed with ISSI dPIVB software, and insights from research on PIV processing have been used to optimize the PSV results. The correlation and filter settings used on CD images were identical to those used on actual data (see Section. 2.5.2, below) with the exception that interpolation is disabled. Interpolation is useful to ensure continuous output data by filling in unsightly small gaps produced by filtering out inconsistent vectors (a standard practice in PIV [149]). However, for the purposes of error analysis, the average and spread of vectors produced by the correlation algorithm was of interest, and interpolation interferes with this distribution (if only slightly, since it does not contribute many vectors). The expected and computed values of displacement are presented in Table 2.5. It is apparent that expected values exhibit significant uncertainty and noticeably overestimate the observed motion of the sample, based on both manual tracking of prominent features, and the PIV results. The stated uncertainty indicated includes that from beam width and voltage, shim thickness, and image scale; an additional source of error could be small angular variations in positioning, in spite of using a fixed guide in the test section for sample alignment. Since the sample is not clamped and is positioned by hand, it is not unreasonable this could occur and cause image shifts in the tens of microns. The displacement that is measured manually in the resulting image agrees well with the PIV results, within uncertainty.

Table 2.5: Displacement of sample, in pixels, determined from change in photodiode signal and known shim thickness, measured directly from the CD image, and found through PIV processing (standard deviation in [ ]). Stated uncertainty accounts for photodiode beam width and voltage, shim thickness, and image scale, but not uncertainty in rotational placement of the sample.

Displacement:	From photodiode & shim		From image		Measured (PSV)	
Direction:	Δx	Δy	Δx	Δy	Δx	Δy
Horizontal	28.3±3.2	0.0	20±2	0±2	20.3 [0.6]	0.3 [0.4]
Vertical	0.4±3.2	24.4±3.7	8±2	17±2	8.2 [1.0]	16.2 [0.7]
Diagonal	28.8±3.2	24.4±3.7	26±2	17±2	28.3 [1.0]	16.1 [0.7]

In examining the error distribution, it became clear that there was a systematic component to it, creating disparities as large as 3 px along the edges and corners of the image. The pattern exhibited by these vectors was symmetrical and matched the vectors attained by processing a pre-shot image (i.e. a no-flow condition); it also did not move or change when alignment of optics was adjusted or the fixture was moved. This suggests it could be a chromatic aberration artifact of the camera lens, possibly exacerbated by the extension tubes used to achieve high magnification.

While it would have been ideal to crop the image and discard this data, it was highly desirable to have information about the flow far from the bubble, while also retaining high magnification of the bubble (see Chapter 6). Therefore, a procedure was devised to minimize this optical effect. Chromatic aberration would deflect red and blue light in different directions, but for constant illumination through the same optics, the offset in the shadow of a small particle in a given location under red and blue light should be constant. For small displacements, it is also reasonable to assume this offset is additive to actual particle motion. Therefore, the systematic noise was treated as a spatially variant signal bias at each point in the image; this bias was measured by analyzing the pre-shot image, smoothed with a polynomial fit, then subtracted from the actual data, point-by-point. The displacement values in each direction, δ_x and δ_y, were independently fit with a polynomial surface. For δ_x, the surface was cubic in x and linear in y, whereas for δ_y, it was cubic in y and linear in x. Applying this procedure lowered the variance of the controlled displacement data and no-motion data (see Table 2.6, below); furthermore, the remaining noise did not retain a consistent systematic character.

As a final metric for the accuracy of the PIV system, the statistical distribution of displacement values was investigated, using vector data with chromatic aberration correction applied, as described above. The expected behavior is roughly Gaussian in character, with most vectors close to the average value and progressively more with larger absolute error. However, histograms of the computed vectors exhibit distributions with multiple peaks, as shown in Figure 2.7. The peaks are characteristic of an undesirable effect known as peak-locking or pixel-locking, a tendency for PIV results to bias toward integer pixel displacement values [149]. A typical cause for peak-locking is using particles less than two pixels in size, but this is unlikely in this case, as the particles in this setup are more likely larger than optimal (see Section 2.5.3, below). The

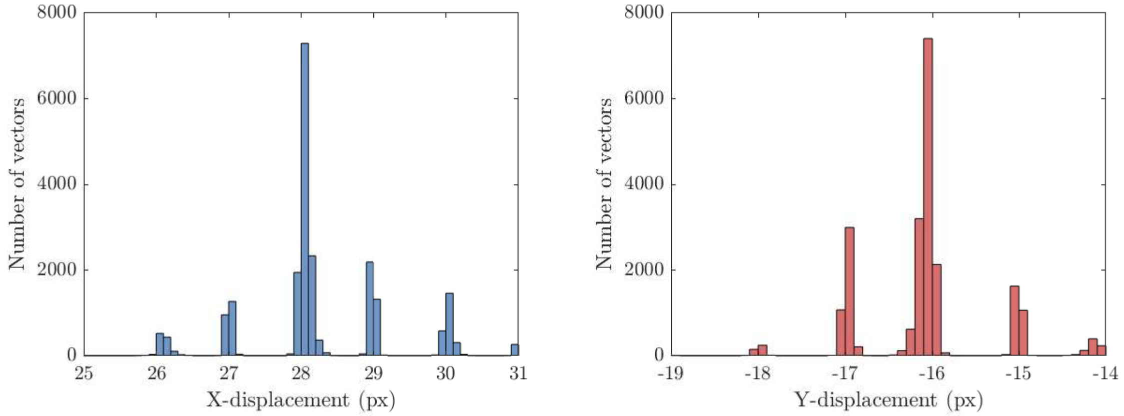

(a) Horizontal (x) displacement.

(b) Vertical (y) displacement.

Figure 2.7: Histograms of horizontal and vertical displacement measured in test with controlled diagonal displacement.

truncation of particle images by interrogation windows has also been implicated in this type of error [150].

A systematic investigation by undergraduate researcher Hector Ochoa varied many parameters of the PSV optical system and data processing techniques, seeking to optimize the arrangement [151]. Changes to the optical system, including beam angle and intensity of light, camera location (and thus field of view and particle size), and seeding density, did not significantly reduce the peak locking effect. However, increasing image contrast prior to analyzing the image in dPIVB was found to widen the bases of the individual peaks. Taken to its extreme, increasing contrast results in thresholding, or more generally, binarization: converting the image to black and white.

In this case, binarization is applied to the grayscale image obtained from each color channel, individually. Thresholding, a test for pixels below or above a particular gray level, is perhaps the simplest form of binarization, but it caused empty spots in place of small single particles in bright illumination and large agglomerations of particles in regions under marginally dimmer illumination. This can be circumvented by applying an unsharp mask filter prior to thresholding to enchance edges and small particles, and applying

Table 2.6: Measured displacement of sample, in pixels, for controlled-displacement tests in three directions. Column 1: No image pre-processing or vector post-processing. Column 2: No image pre-processing, vectors post-processed to remove chromatic aberration effect. Column 3: Image pre-processing with Gaussian-Unsharp-Threshold method and vector post-processing for aberration correction. Standard deviation of data given in [ ].

Displacement	No Processing		Aberration correction		Gaussian-Unsharp-Threshold	
Direction	Δx	Δy	Δx	Δy	Δx	Δy
Horizontal	20.3 [0.6]	0.3 [0.4]	20.0 [0.4]	0.0 [0.3]	20.0 [0.3]	0.0 [0.3]
Vertical	8.2 [1.0]	16.2 [0.7]	7.9 [0.8]	16.3 [0.6]	7.9 [0.6]	16.9 [0.5]
Diagonal	28.3 [1.0]	16.1 [0.7]	28.0 [0.8]	-16.3 [0.7]	28.0 [0.6]	-16.4 [0.6]

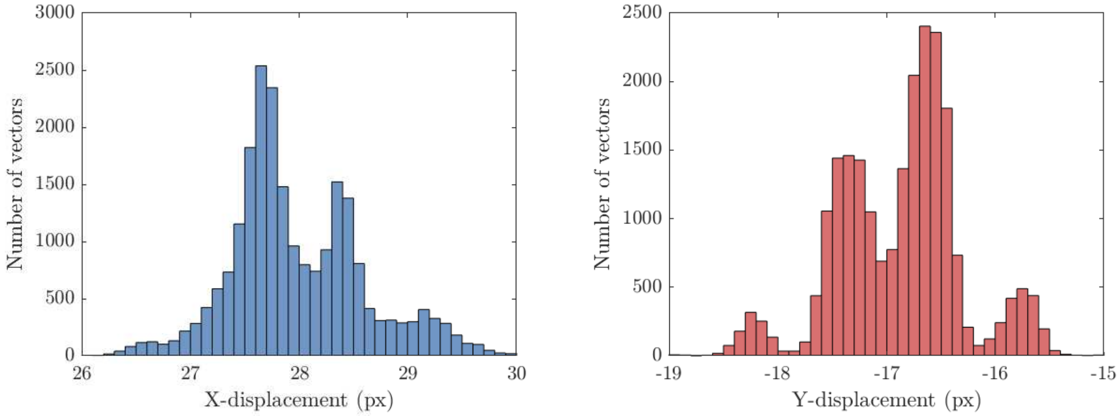

(a) Horizontal (x) displacement.

(b) Vertical (y) displacement.

Figure 2.8: Histograms of horizontal and vertical displacement measured in image controlled diagonal displacement, using Gaussian-Unsharp-Threshold algorithm to pre-process the images.

a Gaussian blur filter prior to that so as not to enchance any stray specks or noise. This Gaussian blur, unsharp mask, thresholding method largely resolved the peak-locking issue (Figure 2.8), and additionally lowered standard error in the data by a small amount (Table 2.6).

The fact that contrast enchancement reduces the peak-locking observed suggests the cause may be the presence of large, overlapping particles of varying intensity, as investigated by Nobach and Bodenschatz [152]. Although they consider intensity varying due to out-of-plane motion and varying light-sheet intensity, in this experiment both effects are minimal. However, the use of different colors for the two images and the tendency of particles to aggregate in clusters cause varying particle-background contrast across the image, and between the two frames. Applying sharpening filters and binarization imposes greater uniformity on particle images, at the cost of some increase in random error in the system [149]. In this case, the tradeoff is worthwhile to remove the bias error due to peak-locking, and overall error levels are reasonable for the vector magnitudes, most of which in the region of interest range from 30–100 m/s (see Chapter 6).

2.5.2 PSV Image Processing

In the process of quantifying error of the PSV system, a number of steps were added to the image processing procedure in an effort to minimize error from various sources. The finalized process for converting the digital images from each experiment to vector data is as follows.

The camera was computer-controlled with tethering software (TetherPro Lite), so images were automatically downloaded to the computer. Images were stored in the lowest-compression JPEG format; in early stages of the project this was compared to using the proprietary Nikon NEF format, and differences between the output vectors were minimal. The error analysis in the preceding section was done with JPEG images.

The raw images were imported into ImageJ software [153] and the color channels separated for pre-processing. As a first step for each channel, a Gaussian blur filter with radius 2 was applied to eliminate high-frequency sensor noise. Then, an unsharp mask filter, also of radius 2, was applied twice to sharpen particle images, particularly of the smallest particles. Subsequently, threshold binarization was applied to each color channel at the median image intensity value. Finally, processed image channels were recombined, and the image flipped horizontally so that flow was in the standard left-to-right direction.

These pre-processed images were then analyzed by dPIVB software. In a general sense, PIV processing works as follows: the two images are subdivided into small computational windows, and a cross-correlation function is applied to corresponding windows to determine the average linear spatial shift of the intensity pattern in each window during the delay time between images. Cross-correlation is typically performed using the computationally efficient fast Fourier transform (FFT), which effectively mandates that correlation window sizes are a power of 2, typically between 16x16 and 64x64 pixels. By virtue of the Nyquist criterion and decreasing correlation signal strength with decreasing overlap, the detectable displacement is typically limited to $^1/_4$ the window size. However, the technique can also be applied iteratively, decreasing window size during each iteration, but using the result of each iteration as an estimate for the next. This significantly improves final resolution while maximizing detectable displacement magnitude [149]. For this experiment, window size was stepped down from 256 px to 32 px over 4 iterations, with a maximum allowed shift (vector) of $^1/_4$ of window dimension. The initial iteration used non-overlapping windows, but subsequent iterations used a 50% overlap, resulting in final vector spacing of 16 px, which translates into 0.07–0.10 mm (varying with image scale). Vectors were numerically filtered at each step, excluding vectors deviating more than 2 standard deviations from the mean locally, or with correlation peaks less than 10^7 counts (these occurred over dark features in the image such as material boundaries and indicated a lack of data for a good correlation). Nearest-neighbor interpolation was used to fill in the resulting gaps to continue the iterative processing. As a final step, vectors over image features (boundaries and bubbles), as well as in compromised regions (e.g. in the presence of surface bubbles) were manually excluded before the vector data were saved.

In addition to performing this analysis on post-impact images, it was also performed on pre-shot images with a known velocity of zero to evaluate error (from the pre-processing image adjustments all the way to saving vectors). The only difference is that interpolation was not performed; any vectors removed by the numerical filters were not included in the data set. These data were used to evaluate and adjust for error in the PSV system believed to originate from chromatic aberration in the camera objective lens, as discussed in Section 2.5.1, above.

2.5.3 PSV System Parameters

While image sharpness and uniformity could to some degree be adjusted in pre-processing to improve correlation quality, many PSV (or PIV) image properties are set before image acquisition, in the configuration of the optical system. Some important image properties dependent on the system parameters include: particle image size, particle image density, uniformity of illumination, image contrast between background and particle, and persistence of particle image pairs (minimizing the incidence of particles traveling out-of-window or out-of-focus) [149]. As with virtually any experimental technique, achieving a truly optimal system may not be possible due to practical and budgetary considerations; therefore, the goal in selecting system parameters was to reduce error to acceptable levels within existing limitations. This section covers some of the choices involved.

It is important to keep in mind that this experiment is very fast; the test time is under 50 μs with velocities over 100 m/s occurring in a field of view of a few millimeters. It also contains steep velocity gradients, which means large velocity changes must remain detectable in small correlation windows, i.e. they must result in fairly small displacements. This requires small interframe times, on the order of 1 μs. In a two-color PSV system, this is quite easily accomplished, controlling exposure using the LED modules. However, this leaves the system vulnerable to noise—just a 1 pixel displacement is 5 m/s measurement error.

To capture a single image pair per experiment, using the LED modules to control exposure, a consumer-grade, color camera (Nikon D50) is sufficient for image capture. It must be enclosed to block out ambient light and triggered manually with a sufficiently long exposure to encompass the entire experiment (2 sec). This camera has 6 MP resolution in each color channel, adequate sensitivity to the LED illumination, and 8-bit per channel color resolution. Although increasing image bit depth from binary up to 4 or 6 bits decreases RMS noise in the data, further improvements in bit depth have vanishingly small effects; there is no reason to expect 8-bit resolution is insufficient [149]. It would certainly be desirable to instead capture multiple image pairs or color images during the experiment; unfortunately, no cameras currently on the market fulfil the resolution, frame rate, and image quality requirements to capture multiple image pairs usable for PIV in the time frame of this experiment. Therefore, camera frame rate was not an issue.

The LED modules used (Innovative Scientific Solutions, Dayton, OH) provide broadband, incoherent illumination, distinct from the monochromatic, coherent output of a laser. This makes them preferable for backlighting small particles in PSV, as they do not generate diffraction pattern artifacts in the image, which would interfere with PIV analysis. However, even when overdriven for short pulses, LEDs are low powered compared to available lasers; minimizing exposure time to avoid particle "smearing" must be balanced against maximizing illumination to ensure good contrast and high signal-to-noise ratio in the image. To maximize illumination, a 60 mm lens was introduced after the beam-combining cube in the optical path, to narrow the beam and capture maximum light into the region of interest on the sample. Collimated light would perhaps be ideal as refraction of rays at subsequent material interfaces (like test section windows and the sample enclosure) would be minimized. However, this resulted in significant nonuniformity of illumination as the 2x2 grid shape of the emitter was projected onto the image plane. Therefore, the lens was placed 130 mm from the emitters, creating a gradually convergent beam, which provided bright, uniform illumination in the region of interest. An image of the illumination alone has red and blue histograms with a mean gray value of 190 and 210, respectively, and standard deviation of 6 gray levels, indicating a well-lit background with minimal variation. Of course, a seeded sample blocks a significant portion of the light, resulting in lower average intensity, but a brightly lit background ensures good particle contrast and decreases error in the final measurement.

Using two colors in the system offers many advantages, but it should be noted that this choice essentially means two different sources and two different sensors are being used, which sacrifices uniformity of image appearance (compared to using two pulses of the same laser sheet and a high-speed or double-shutter camera). This is further exacerbated by using widely spaced wavelengths (red and blue light), which minimizes the chance of interference and "ghosting" on the sensor, but maximizes chromatic aberration of the two beams relative to each other at any of the material interfaces present in the test setup (light-spot focusing lens, test section windows, plastic sidewalls, and sample gel). These effects were discussed in greater detail in Section 2.5.1, above.

The volume illumination provided by the LEDs (as compared to sheet illumination typically used) requires some special consideration. Volume illumination is not always an option, as it can be blocked or scattered by particles in the flow outside the image plane, or include too many blurred particles for good PIV analysis. However, in this experiment the flow is fully contained between clear plastic plates; as a result, most of the illumination volume is transparent. In order to minimize optical aberrations (e.g. from scratches or smudges on windows or the exterior of the sample fixture), the depth of field was minimized by opening the camera aperture to maximum. To further ensure good contrast and minimize blurred particle images, only $^1\!/_3$ of the sample thickness is seeded with glass microspheres, and the other $^2\!/_3$ is cast as a clear gel or polymer. A positive side effect of sample geometry and of seeding only a thin layer is that particle loss is very low; there are only extremely minimal transverse displacements, and they do not take the particle suddenly out of focus or illumination. In-plane losses are minimized by iterative processing.

Because the particles are casting shadows under light from a distributed source, rather than scattering light, they are somewhat larger than what might typically be used; nominally 50 μm [5]. The size of the resulting images may vary from this, and precisely quantifying them is difficult, due to the dependence of this measurement on some kind of binary thresholding technique, and due to the tendency of particles to clump in the gel medium. Examining several arbitrary images after the pre-processing stage, and seeking out only particles with circularity of 0.9 or higher (to rule out clusters or pairs of particles whose images overlap), the median 50% of particle images fall between 2.7 px and 7.7 px in diameter; this is clearly higher than the optimal 2 px diameter suggested by Raffel and Willert for a 32 px correlation window; however, the RMS error predicted for even the largest sizes is below 0.1 px [149]. These values correspond to image sizes of 11 μm and 38 μm respectively; reasonable values for the size of a shadow of a 50 μm particle under a distributed light source. The larger size of the particles and images, as well as their tendency to clump, led to a compromise of halting analysis at 32x32 pixel windows; the finer resolution of 16x16 windows was desirable, but there were simply not enough particles per window, and adding more just caused bigger clusters. 32 pixel windows equate to 0.17±0.03 mm interrogation regions, or about 24 vectors across the bubble diameter.

2.5.4 Pressure Measurements in the Fixture

Pressure measurements in the gel inside the sample fixture were needed to verify pressure waveforms computed by FEA simulations (see Chapter 3) and estimated from high speed video data (see Chapter 5). There are numerous challenges to experimentally measuring pressure profile in these experiments. The gel layer thickness and the size of the area of interest are quite small compared to many available pressure sensors. Smaller sensors that are available tend to be limited to lower pressures and/or sensitive, fragile, and expensive; a liability when the loading wave is created by impact and the sample is unrestrained! Due to these challenges, it was unfortunately not possible to mount a sensor in such a way that pressure data could be obtained simultaneously with shadowgraph video or PSV data.

Instead, pressure data were acquired in a separate series of tests from a PCB 113A23 sensor mounted on a fixture sidewall, directly over the area where the bubble would be located, obstructing optical access. A $^1/_2$ in diameter steel adapter was available to hold the PCB sensor securely; the mount was screwed into a (nominally) 1 in thick polycarbonate plate threaded to accommodate it. Polycarbonate was substituted for the usual PMMA plate on the side of the pressure sensor for three reasons: 1) the greater fracture toughness of polycarbonate over acrylic was desired for threading the plastic to accommodate the PCB mount without breaking, 2) the density, elastic modulus, and sound speed of polycarbonate were very close to those of PMMA, so the change was not expected to noticeably change the pressure condition, and 3) unlike for photographic data, the tendency of polycarbonate plate to develop surface scratches did not prevent it being reused, making its higher unit cost manageable. A photo of the plate, mount, and PCB sensor is shown in Figure 2.9(a). A regular PMMA sidewall was used on the opposite side of the fixture.

A second oscilloscope was necessary for these experiments. Signals were routed as follows. The PCB was connected to a signal conditioning and power unit (PCB 480B02). The output from the signal conditioner was connected to an oscilloscope (Tektronix TDS2014C), along with the raw photodiode signal and the diagnostics trigger signal. The diagnostics trigger signal was connected to a second oscilloscope (Tektronix TDS2014) along with the outputs from the two projectile velocity sensors (Honeywell Optoschmitt SD5610), so that impact velocity could be determined the same way as during the shadowgraph and PSV tests. This arrangement is shown in a diagram in Figure 2.9(b). Pressure traces were stored on a USB drive and transferred to a PC for further processing and interpretation.

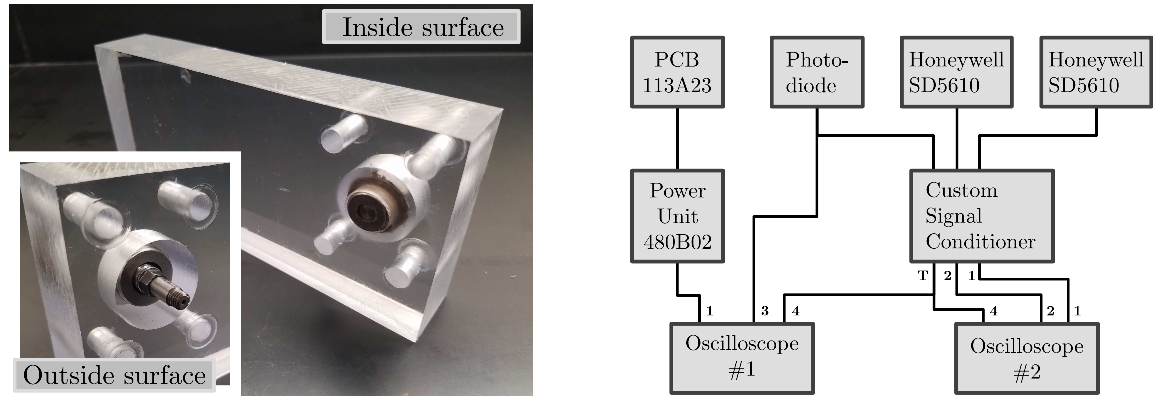

(a) Alternate sidewall for pressure measurements, with PCB 113A23 sensor in mount.

(b) Signal propagation for pressure measurements with PCB.

Figure 2.9: Fixture and electronics design for pressure measurements.

CHAPTER 3

FIXTURE MODELING AND DESIGN

Much of the setup for this experiment was adapted from previous studies on air-filled voids. However, when a seemingly small change was made to accommodate the addition of material boundaries, it resulted in surprising changes in void behavior in early tests. This prompted a thorough investigation of the internal state of the fixture using commercial finite element analysis (FEA) software LS-DYNA. Based on the results, the sample was re-designed to yield a pressure loading with desirable properties for the experiment. The software was also used to investigate the effect of added material boundaries on the pressure profile, and to perform a rough simulation of the collapse of an air-filled void. The computed pressure traces were also tested against pressures measured experimentally to evaluate the validity of the model.

3.1 First Generation Fixture

The sample fixture initially used for this experiment was based on the design used by Swantek and Austin [5, 154], and had thinner sidewalls ($^3\!/_8$ in), and a gel layer that was both thinner ($^1\!/_{16}$ in) and wider (1 $^1\!/_4$ in) than described in Section 2.2. In the previous study, the bubble was located within one diameter of the aluminum striker, but in order to investigate the effect of an upstream boundary, the bubble had to be located $^1\!/_4$ in–$^1\!/_2$ in farther downstream. Making this change elicited some unexpected behaviors, including cavitation bubbles that obscured view of parts of the sample (Figure 3.1(a)), and expansion of the bubble before collapse commenced (Figure 3.1(b)). Collapse time was at least double its previously measured value, and the profile of the particle velocity (U_p) through the sample did not simply translate but noticeably changed shape as it propagated through the sample, Figure 3.1(c).

From these observations, it was apparent that a tensile loading condition was occurring in the sample, which could not be explained by one-dimensional wave propagation, or the bubble collapse. This prompted a thorough investigation of the loading state within the fixture, an understanding of the factors at play, and an eventual redesign of the sample to reduce the complexity of the loading condition.

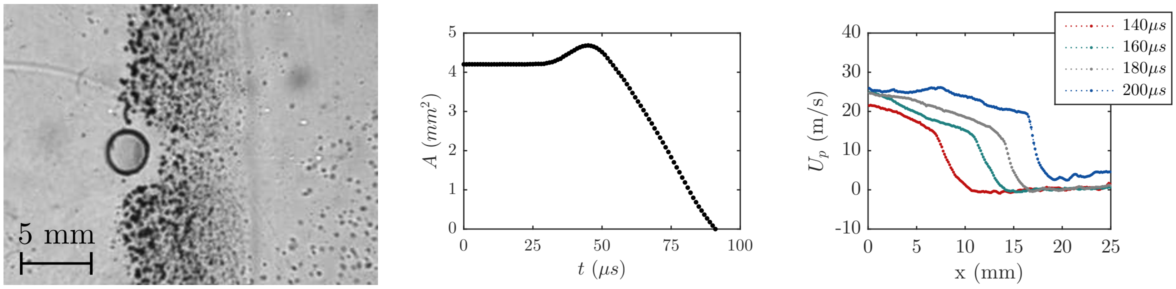

(a) Cavitation in sample.

(b) Expansion of bubble prior to collapse.

(c) Velocity profiles in old fixture (PSV data).

Figure 3.1: Problems with previous fixture design.

3.2 Finite Element Modeling in LS-DYNA

LS-DYNA is a commercial, multi-purpose finite element code developed by Livermore Software Technology Corporation (Livermore, CA) [155]. Its greatest benefit to this study was the capability to implement arbitrary Lagrangian-Eulerian (ALE) analysis in a straightforward way, in order to capture and analyze the fluid-structure interaction (FSI).

Since the goal was primarily to understand the loading on the bubble, rather then modeling the collapse itself, the bubble was omitted from the simulated system. Some additional modifications were made to reduce computational complexity; a snapshot of the objects comprising the resulting model is shown in Figure 3.2. They are meshed with cubic elements 0.2–0.4 mm long, although elements as large as 0.8 mm were used initially and elements as small as 0.1 mm were used to test mesh dependence. The details of the sidewall and spacer bar geometry were neglected; the containment was modeled as a solid acrylic box, one end blocked with the striker plate, and filled with gel. The striker plate was modeled as a rigid solid, a model in LS-DYNA that restricts deformation; however, it takes elastic properties into account when computing interactions between objects. Rigidity was needed to prevent spurious force oscillations that would arise due to the confinement of the striker in the acrylic block. The pressures expected in the fixture were not sufficient to cause much striker deformation, so losing that behavior in simulation was not a concern. Rigidity also prevented the software from modeling the propagation of reflected waves within the striker, and the propagation of these weaker waves into the gel downstream. However, analytical estimates (see Section 3.4, below) show that these disturbances would change gel velocity by at most 2.5 m/s (generally much less), causing a pressure change of less than 4 MPa, and experimental observations confirm no major fluctuations in the velocity of the leading edge of the striker (see Chapter 5). The projectile characteristics and velocity were measured more accurately and could be better-controlled than striker motion, and particularly the initiation thereof. Even so, the impact velocity was adjusted from 26 m/s as occurred in experiments to 23 m/s in simulations; this resulted in a match of gel particle velocity, likely because friction was not modeled between the different parts (and in particular the striker and acrylic).

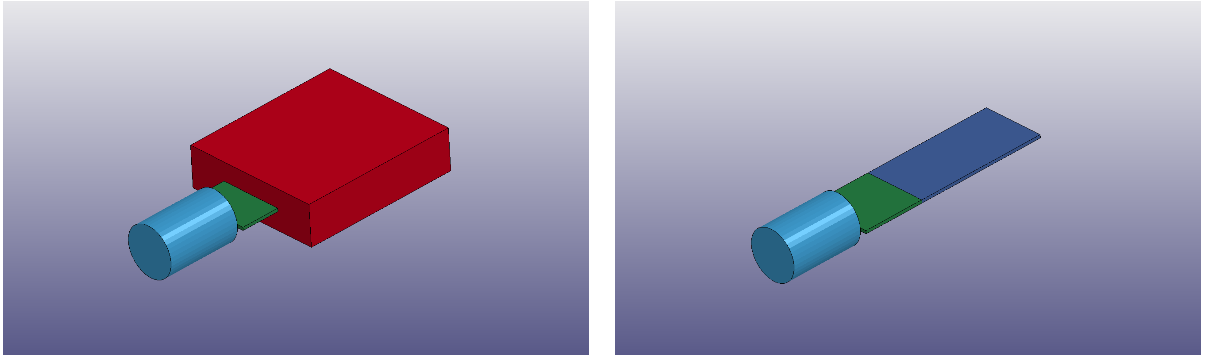

(a) Exterior components.

(b) Interior components.

Figure 3.2: Components of fixture model in LS-DYNA software, meshed with 0.2-0.4 mm elements. Materials modeled as described in Table 3.1.

The geometric and material properties of the model are presented in Table 3.1. Thermal behaviors were not of interest; therefore, the elastic and acoustic properties were of greatest interest, and it was important they were appropriately represented. Density, sound speed, and elastic modulus were sufficient to define all the solid material models. In addition to these properties, the Gruneisen model used for fluids additionally required the shock Hugoniot to be defined ($u_p = 1500 + 2u_s$ was used, see Section 2.3.1).

The simulation demonstrated fixture behavior as follows. The processes of impact between the projectile and the striker and the acceleration of the striker have a short, but measurable duration of about 5 μs. As the striker begins to move, the pressure in the gel immediately adjacent to the striker increases rapidly. Given the geometry of a thin layer of liquid contained by a solid, one might be tempted to assume rigid confinement of the fluid, and that the pressure continues increasing up to $P = \rho a U_p$, but this would be incorrect. The acoustic impedance (ρa) of acrylic is 3.2×10^6 Pa·s/m, just over twice that of water. The compressive (bulk) modulus is reported as only about 3 GPa [156], compared to 2.25 GPa (ρa^2) for water. This closeness in properties means that as pressure rises, compression and deformation occur to a significant extent in both materials. The plastic sidewall bends outward by fractions of a millimeter as the gel accelerates downstream. This deformation is on the order of 0.01 mm and not sufficient to be observable even in shadowgraph, but it relieves some of the developing pressure. This begins to happen even before the wave reaches the exterior of the sidewall and the expansion wave returns, an approximately 7 μs round trip.

The local pressure disturbance does more than just locally deform the plastic fixture. It initiates a

Table 3.1: Properties of the different parts of the LS-DYNA finite element model of the fixture and gel.

Material	Dimensions	Material Model	ρ (kg/m^3)	a (m/s)
Gel	32.0 mm x 187.2 mm x 1.6 mm	Gruneisen	1000	1500
PMMA	70.4 mm x 80 mm x 20.0 mm	Elastic solid	1180	2730
Al striker	32.0 mm x 32.0 mm x 1.6 mm	Rigid solid	2700	6300
Steel projectile	25 mm D x 38 mm L	Elastic Solid	8100	5800

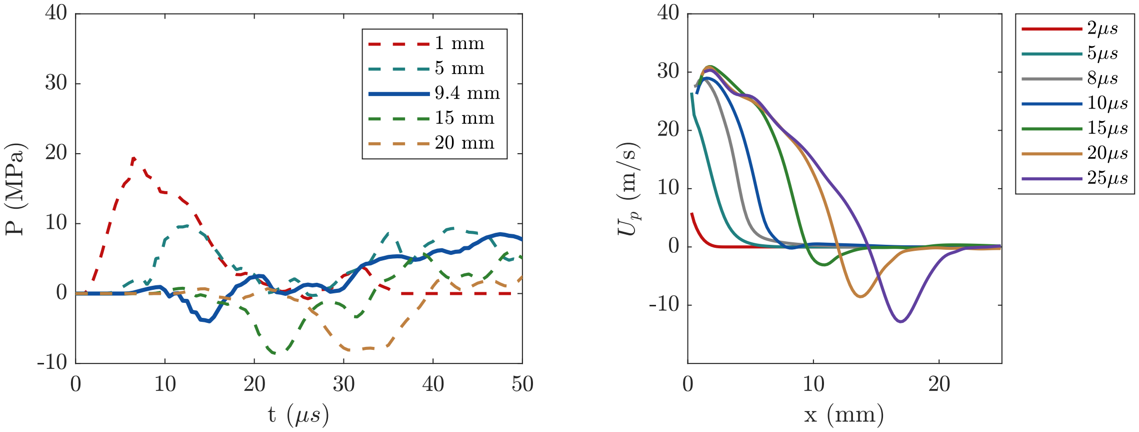

(a) Pressure traces in old fixture.

(b) Velocity profile development in old fixture.

Figure 3.3: Pressure traces in new fixture and the resulting velocity profiles. In the first 5 mm of gel, the pressure presents as a single positive peak returning to zero, with any secondary peaks occurring after 30 μs, and this generates a ramped velocity profile as expected. For locations more than 10 mm from the striker, the tensile precursor arrives first, and the resulting velocity profile for the first 25 mm of the sample goes through significant changes in form.

flexural wave that travels down the sidewall; this is more evident when extra thin sidewalls are modeled, as in Figure 3.4. The disturbance travels faster in PMMA than in the gel, so after some time, the inner surface of the sidewall begins to bend away from the gel significantly before the wave traveling through the gel (and the higher-pressure state it creates) arrives! This creates the tensile condition in the fixture and is known in FSI as the "tensile precursor" wave, which has also been observed in pipe flows [157]. This was not problematic for a bubble placed close to the striker, as the travel times for both waves were small, so the difference was not pronounced. However, when the bubble was shifted downstream by 6–12 mm, the tensile precursor was arriving well before the pressure rise, and causing cavitation in a layer of water on the surface of the gel. It was also in some cases sufficient to cause noticeable bubble expansion, before the high pressure arrived and initiated collapse. When the pressure trace in the gel is examined, it is apparent it undergoes extreme oscillations due to coupling with the dynamics of the plastic fixture.

It would seem that the solution to the deflection of the plate is to utilize more rigid containment, such as steel or perhaps glass. However, due to the larger speed of sound in these materials, simulations showed the oscillations would be even more extreme, as the disturbance would reflect repeatedly in the sidewall. Only the idealized case of a perfectly rigid boundary produced a one-dimensional wave without a tensile component, but of course this cannot be achieved in practice. Silicone rubber, the only transparent material found with a similar sound speed to water, was tried experimentally, but its deformation resulted in extreme image distortion. It was also apparent from the much slower bubble collapse that the rubber absorbed a large proportion of the impact energy, and therefore pressures achieved in the gel were low.

A solution that produces superior results for eliminating the excessive pressure oscillations is to make the

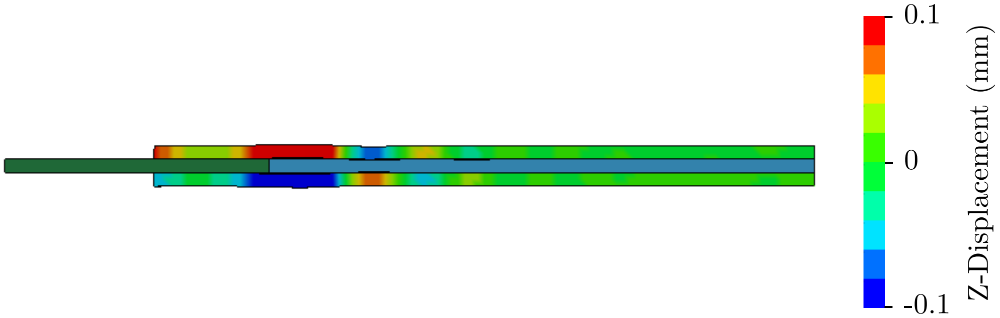

Figure 3.4: Cross-section through centerline of modeled sample design with extremely thin sidewalls at 50 μs, demonstrating development and propagation of flexural wave. Contours of element displacement in the thickness dimension.

sidewalls thicker. Thicker sidewalls resist bending, and also delay the return of the rarefaction wave from the outer surface of the sidewall. However, a compression disturbance still propagates along the inside surface and generates tension (observable as cavitation bubbles on the surface of the gel). This cannot be prevented, but its effect on the fluid is reduced by also increasing the thickness of the fluid layer. Combined, these changes push the onset of tension and cavitation in the fluid later in time and farther downstream, although coupling between the fluid and sidewalls persists. The peak pressure is reduced from the theoretical ideal, and yet the velocity achieved by the gel (or fluid) layer is close to what acoustic relations predict. Another observed effect is that, sufficiently far downstream, the pressure can begin to decrease and then increase again. This effect could not be explained by two-dimensional phenomena, but can be readily explained by the oscillation of fixture sidewalls in response to the high-pressure disturbance, and the perceived decoupling of pressure and velocity can likewise be explained by the fluid-structure interaction.

Due to the multiple interacting mechanisms at play in this system, it presents a unique possibility to intentionally control the profile of high-rate loading. The control is not absolute, but oscillations of a particular wavelength and magnitude can be created by changing fixture materials, dimensions, and actuation mechanism. The system might be actuated by a projectile impact as it is here, or perhaps changed to a device resembling a Hopkinson bar or an explosive plane wave generator as used by Bourne and Field [33]. Wedge-shaped sidewalls, either increasing or decreasing in thickness along the length of the sample, might also produce interesting results on the pressure state within. FEA or other computational modeling techniques are invaluable to any attempts to design the pressure state within the fixture in such a way, as these tools can resolve the complicated dependencies of the various parts of the system. As experience has made clear, even an adjustment as simple as translating the region of interest by a few millimeters can cause major changes and should be very carefully considered.

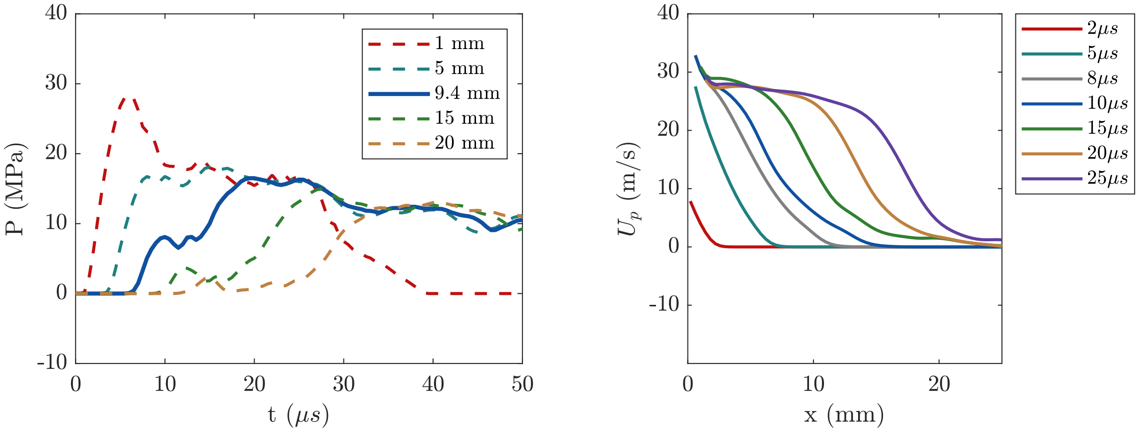

(a) Pressure traces in new fixture.

(b) Velocity profile development in new fixture.

Figure 3.5: Pressure traces in new fixture and the resulting velocity profiles. Except very close to the striker, the pressure tends to rise and then stabilize, without significant fluctuations or tension zones within the region or time of interest. The velocity develops a ramped profile that propagates downstream at 900 m/s (the lower wave speed, a consequence of the fluid-structure interaction).

3.3 New Fixture Dimensions and Behavior

The gel and the sidewalls were both approximately tripled in thickness in the new fixture design compared to the initial design (1 in sidewalls and $^3/_{16}$ in gel). Changing the sidewalls or gel thickness independently was not sufficient for the desired effect on the pressure waveform. The dimensions were selected by computationally investigating a range of thicknesses from half to quadruple the original; the effect on the pressure was not linear. Thinner layers resulted in more pressure oscillation and more coupling, whereas thicker ones yielded a smoother signal, as any oscillations had longer temporal and spatial scales. Doubling the thickness of both layers had a noticeable effect of reducing tension severity and moving it farther downstream, but the tension component still appeared within the first 20 mm and 50 μs (the experimental domain of interest). Tripling the thickness further reduced the magnitude of the tension that occurred and shifted the location further downstream, but quadrupling led to minimal additional changes in the region of interest. As such, (approximately) triple thickness was selected as using the least material to produce the desired changes.

In the resulting fixture, the pressure peaks at about 30 MPa near the striker plate, compared to the theoretical value of 45 MPa for the impact velocity and materials involved, and compared to about 20 MPa in the previous fixture design. However, the fluid accelerates to about 30 m/s, much higher than expected at the pressure achieved, but close to the value expected from acoustic relations for the theoretical maximum pressure. Farther downstream, the disparity is greater; even at only 5–10 mm from the striker the pressure doesn't reach 20 MPa, and yet the same velocities are attained. The initial pressure pulse, reflected as a rarefaction wave, is expected to return 18.6 μs after the peak of the pressure pulse, which is apparent in the sudden drop in the 1 mm pressure trace at this time (just short of 30 μs, as the peak does not occur

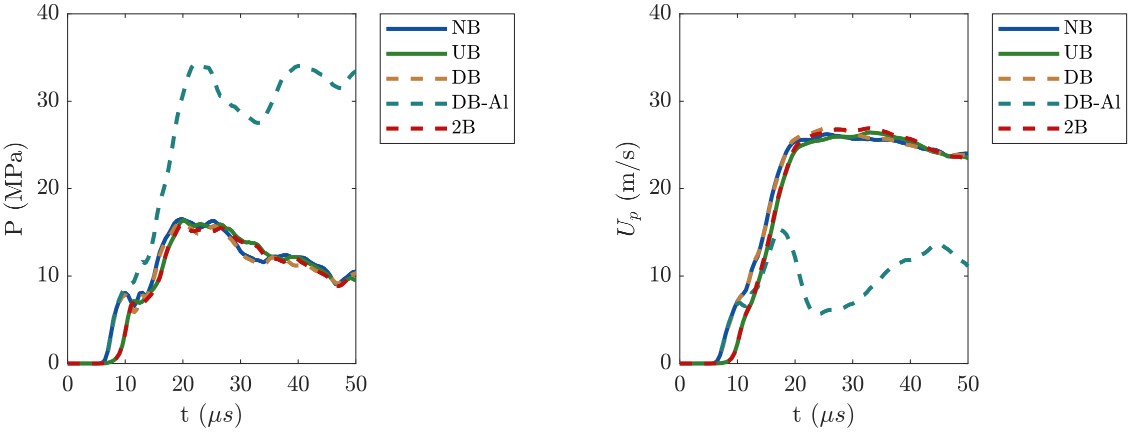

(a) Pressure traces in model with PDMS boundaries.

(b) Velocity traces in model with PDMS boundaries.

Figure 3.6: The pressure and velocity development in time at the bubble location (9.4 mm from striker). Upstream boundary (UB) delays the arrival of the pressure and velocity rise by a few microseconds (compared to no-boundary, NB). Downstream boundary (DB, 2B) does not seem to have much discernible effect. Aluminum downstream boundary results in large increase in pressure and drop in velocity relative to NB, DB cases.

until about 7 μs). The other traces experience a drop at almost the same time, since the rarefaction wave expands outwards in all directions, and travel times along the hypotenuse to the 5 mm and 9.4 mm locations differ only by fractions of a microsecond.

3.3.1 Model Behavior with Boundaries

The model was subsequently modified to accommodate multiple materials in the gel layer in order to predict the effect of PDMS boundaries on the pressure state in the fixture. After some consideration, PDMS was modeled with fluid elements in the ALE framework, using the Gruneisen equation of state (as for the agarose gel) with the appropriate Hugoniot parameters sourced from literature (see Sec. 2.3.2). While the strength of the PDMS may be an important aspect of its response to the bubble collapse flowfield, which involves shearing and extensional flows, it is expected that the pressure state is defined entirely by the acoustic properties of the material. It has been argued that these do not vary with crosslink density (in our case, the amount of curing agent used) and therefore with the physical state of the PDMS [137]; therefore, different compositions are not modeled. It should also be noted, the rigidity and strength of the PDMS (E≈1 MPa) is so low next to the other solids involved (e.g. PMMA, E≈3 GPa) that it can be neglected when considering the fixture system as a whole, and only the compressive and acoustic properties of the material considered.

Figure 3.6 shows the behavior of pressure and velocity at the anticipated bubble location (9.4 mm) in the absence of the bubble. The addition of an upstream boundary (UB) delays the beginning of pressure rise and flow acceleration by a few microseconds, as would be expected due to the lower sound speed in PDMS. The addition of a downstream boundary with PDMS to either the no-boundary (NB) or UB conditions to create the downstream boundary (DB) or two-boundary (2B) condition does not appear to have a discernible additional effect on the pressure and velocity traces. However, introducing the downstream boundary of aluminum (DBA), results in a doubling of pressure and significant reduction of velocity. This effect is also not unexpected, as the aluminum presents an effectively rigid boundary to the flow; the incident compression wave should reflect as a compression wave, doubling the pressure, and arresting the flow immediately at the boundary (the effect on velocity is not quite absolute at the bubble location).

3.3.2 Model Behavior with Bubble

The model was also modified to introduce the air-filled cylindrical bubble. It should be noted upfront that LS-DYNA is not the ideal tool for modeling this phenomenon; in fact, modeling the problem of bubble collapse with specialized codes is a research problem in its own right. In the absence of sophisticated techniques like boundary tracking or re-meshing, the resolution of geometric features (such as the boundary shape or the formation of a jet) is limited to the resolution of the grid. High pressure or velocity gradients are also averaged over the size of an element, yielding more moderate values of property extrema. On the other hand, in the absence of techniques to simplify and improve efficiency of computations, an extremely fine grid is excessively resource-intensive to run. Therefore, a moderate grid of 36 elements across the bubble diameter was used, and the results interpreted in light of the limitations of the system.

The second major limitation exhibited by the system, aside from resolution, is an inability to manage the immense pressure and rapid acceleration that occurs in the air cavity at the end of collapse. The air accelerates too quickly for the relation defining contact between air and plastic to keep the air confined. Increasing stiffness of the contact results in impractically short timesteps. Again, this problem can be circumvented, but it requires a specialized approach that was beyond the scope of this work.

Figure 3.7 presents some selected snapshots from the bubble collapse and flowfields as modeled by the software. While the resolution is limited, it is sufficient to capture the deformation of the boundary and even the formation of the jet. The incident wave moves quite linearly into the region of interest, laying to rest concerns that the unusual grid distorts the wave propagation. Immediately upstream of the bubble, the wave reflection off the free surface creates additional acceleration of the flow, whereas the region downstream of the bubble is effectively blocked from the effect of the bubble (the shock transmitted through the air-filled bubble is far too weak to create any discernible effect on the downstream interface). As the collapse progresses, the velocity upstream of the bubble exceeds 100 m/s, although a few radii away from the bubble laterally the velocities do not exceed 40 m/s. To investigate the area around the bubble in more detail, cross-sections of the flowfield are taken through the centroid, along the longitudinal and the transverse axes. The pressure along these is also shown.

Along the longitudinal centerline, it is apparent that not only does the flow velocity exceed 100 m/s, but it is expected to reach velocities as high as 300 m/s just before the end of collapse (23.5 μs). The extreme

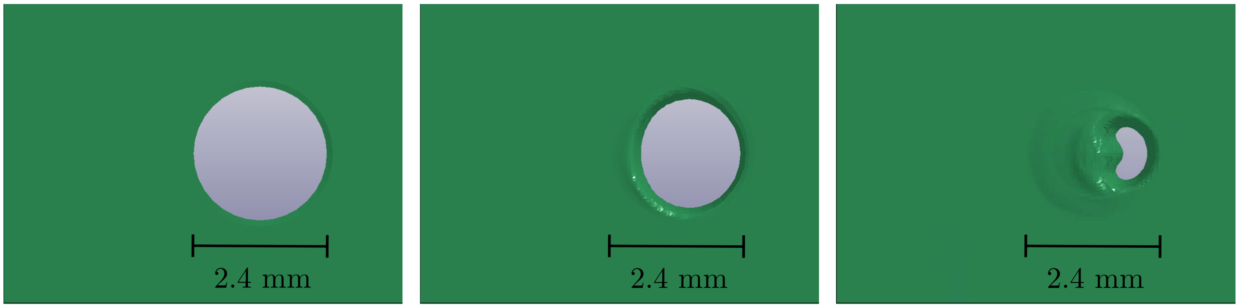

(a) Bubble boundary, 7.5 μs. (b) Bubble boundary, 17 μs. (c) Bubble boundary, 23 μs.

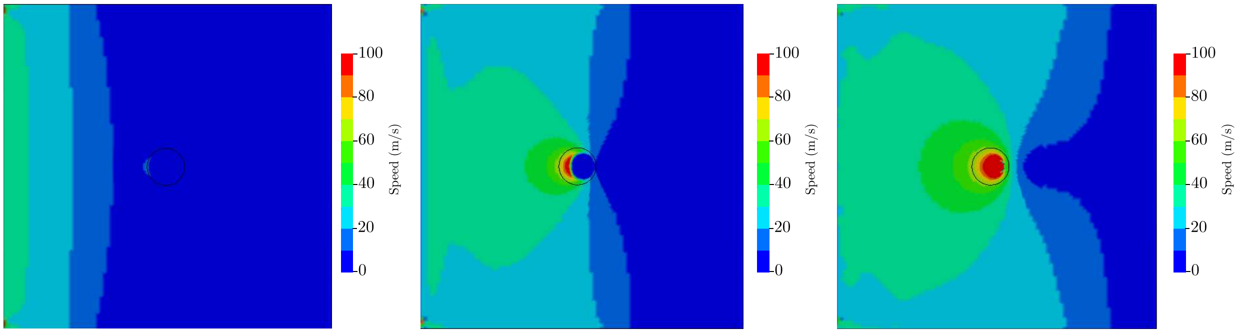

(d) Bubble contours, 7.5 μs. (e) Velocity contours, 17 μs. (f) Velocity contours, 23 μs.

Figure 3.7: Select images of bubble boundary and selected velocity contours in surrounding fluid, as modeled by LS-DYNA software. Asymmetry of collapse is evident, as is development of jet across the bubble. The wave is observed to diffract around the bubble, the downstream region shielded from the wave's effects. Upstream of the bubble, the flow accelerates to above 100 m/s.

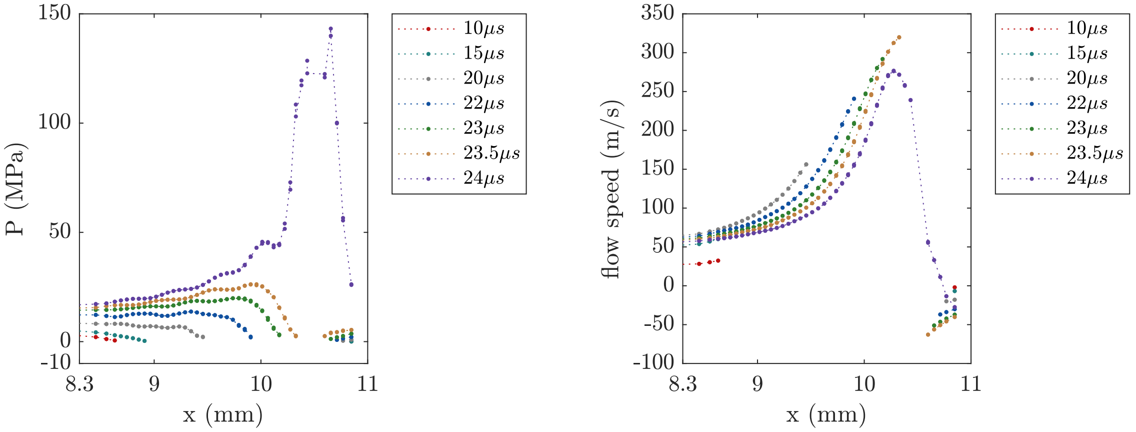

(a) Pressure, longitudinal cross section. (b) Flow speed, longitudinal cross section.

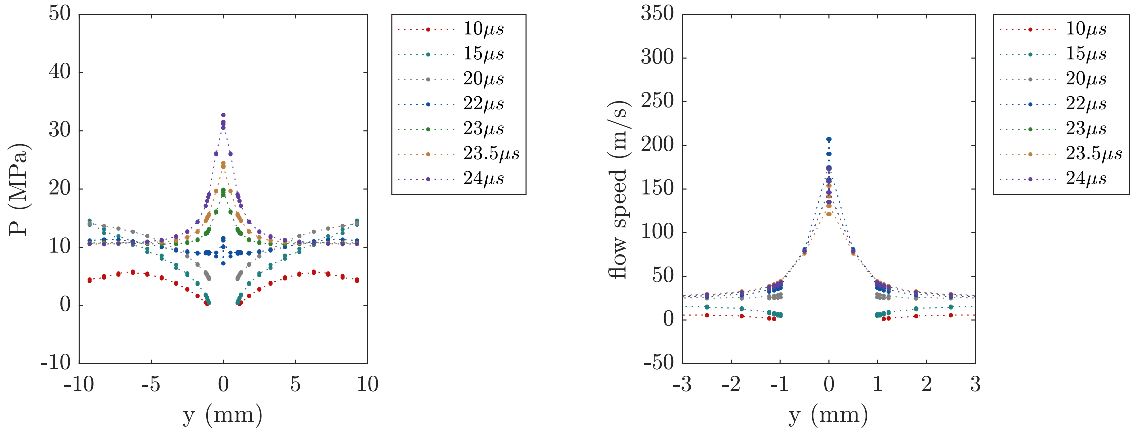

(c) Pressure, transverse cross section. (d) Flow speed, transverse cross section.

Figure 3.8: Pressure and longitudinal flow velocity along cross sections through the bubble centroid in the longitudinal (parallel to flow) and transverse (normal to flow) direction.

velocities are localized within the original radius of the bubble; at the upstream edge (8.4 mm) the velocities only reach about double the maximum free-stream velocity (∼60 m/s and ∼30 m/s respectively), and the velocity even drops with time, approaching 50 m/s toward the end of collapse. On the downstream bubble interface, negative velocities (directed upstream or toward the center of the bubble) develop, in excess of 50 m/s. However, these are very quickly reversed once the jet collides with the downstream interface, as is likely the case just before 24 μs.

This collision is expected to produce a pressure of $P_{\mathrm{WH}} = (U_u - U_d)\rho a = 600$ MPa. However, only 150 MPa is detected, for which there are three possible explanations. One is the very short time for which the water hammer pressure is expected to persist, which scales with the radius of the jet and the sound speed, giving $\dfrac{r_j}{a} = \dfrac{0.1\,\mathrm{mm}}{1500\,\mathrm{m/s}} = 0.07\,\mu s$ if the jet tip radius is estimated as a tenth of the original bubble radius. This would indicate a high likelihood the observed pressure is partially relieved by 24 μs. It is also possible the area where the jet tip makes contact is below the grid resolution, leading to some spatial averaging lowering the observed pressure. Finally, as was the case for pressure developed at the striker, the deformation of the fixture may contribute to greater pressure relief than would be expected in a two dimensional system. However, this pressure is measured at the centerline of the gel layer, so any rarefaction due to the fixture walls would take at least 1.6 μs to propagate, making this mechanism an unlikely candidate. It is likely that a combination of the other two factors discussed is at play.

Prior to the jet impact, pressures where the interface of the bubble was initially located remain in the range of those predicted from impact alone, 15–20 MPa. In the fluid near the bubble interface, low pressures persist. In the region traversed by the bubble interface, the pressure increases gradually to a maximum before decreasing again, as predicted by Rayleigh [23] for the spherical bubble. The maximum pressure remains below 30 MPa even when the collapse is imminent (23.5 μs), although the profile at 24 μs suggests it does increase locally to around 50 MPa in the short time before jet impact occurs. In the transverse direction, the increase in velocity and pressure along the centerline upstream of the bubble is also evident. The large, 150 MPa pressure spike has not reached the bubble centroid location (9.4 mm), but the pressure is observed to rise sharply around 22 μs, after the upstream bubble interface passes the cross-section location, then drop slightly as the collapse proceeds further, and the bubble interface continues to move farther downstream of the cross-section. At earlier times, the pressure at the edges of the domain only rises up to about 15 MPa with the passage of the wave, as it does in the absence of a bubble. The pressure gradually drops very low at the bubble interface. As in the longitudinal direction, extreme pressures and velocities in excess of what is observed in the absence of a bubble are confined to the initial bubble location ($|\,y\,| < R_o$).

Although the rebound of the compressed bubble and the motion of the water hammer shock cannot be simulated further, the computational investigation was informative. It demonstrated that although dynamics of the fixture lower the pressure developed within, high fluid velocities and re-entrant jet formation should be expected in this system. This jet subsequently has the potential to create pressures on the order of hundreds of MPa, although the duration will be short, and the spatial extent limited. The simulation also highlights that high velocities and velocity gradients tend to occur just upstream of the bubble, particularly toward the end of collapse, which suggests this area merits attention when it comes to potential for damage of soft tissues.

3.4 Wave Dynamics

Computational modeling of the experiment has shed light on the motion, deformation, and pressure field of the fixture, but the software is not optimal for quantitatively tracking wavefronts. Since the shadowgraph imaging diagnostic that was employed is extremely sensitive to even very small density (and thus pressure) fluctuations, it is useful to gain an understanding of the origins and propagation of disturbances in the system so that they can be identified.

It is clear that the most dominant effect will be the wave in the gel created by the initiation of striker motion, in turn caused by impact from the projectile. It is not immediately clear how best to model this impact, but simulation and experiment (see Chapter 5) both suggest that a perfectly inelastic collision, wherein the velocity of striker and projectile is equal after the interaction, underpredicts striker velocity only slightly (about 10% relative to experiment).

The propagation of a wave into the gel can be simply modeled by assuming the striker moving at constant velocity encountering the gel (or liquid) column. Graff solves the wave equation for an elastic wave through a solid in terms of particle displacement (ξ) [158]:

$$\xi = f(x - at) + g(x + at). \tag{3.1}$$

where f and g are waveforms to be solved for based on boundary and initial conditions, that are propagating rightwards and leftwards in the material respectively with wave speed a (sound speed). Based on definitions of strain (ϵ) and velocity (u) as spatial and temporal derivatives of displacement, they can be expressed as:

$$\epsilon = f'(x - at) + g'(x - at) \tag{3.2}$$

$$u = -af'(x - at) + ag'(x + at) \tag{3.3}$$

where $f'(z)$ denotes the derivative with respect to z. It should be noted that this result implies $\epsilon = u/a$. To model a free-flying striker plate moving from left to right with velocity u_i, the required initial condition is:

$$f_1' = -\frac{u_i}{2a} = -g_1', \tag{3.4}$$

so that initial velocity is u_i but initial strain (and thus stress) is 0.

Interaction with the fluid column generates a transmitted wave propagating into the fluid and a reflected wave propagating into the striker, as schematically illustrated in Figure 3.9(a). The transmitted wave increases fluid velocity by Δu_T and pressure by P_T. The reflected wave, traveling left, creates displacement $\xi_R = g_2(x + at)$ and associated strain ϵ_R and velocity change Δu_R in the aluminum. The reflected wave in the aluminum is superimposed with the pre-existing state, since the incident pulse is continuous rather than of finite length (f_1' and g_1' are constant). The two materials do not separate at the interface, so it is required that $\Delta u_T = u_i - \Delta u_R$. Forces must also balance if the interface is moving with a constant velocity, which with equal area means pressure in the liquid must equal compressive longitudinal stress in the aluminum. Graff uses a convention of compressive stress being negative, which requires a sign change to reconcile with

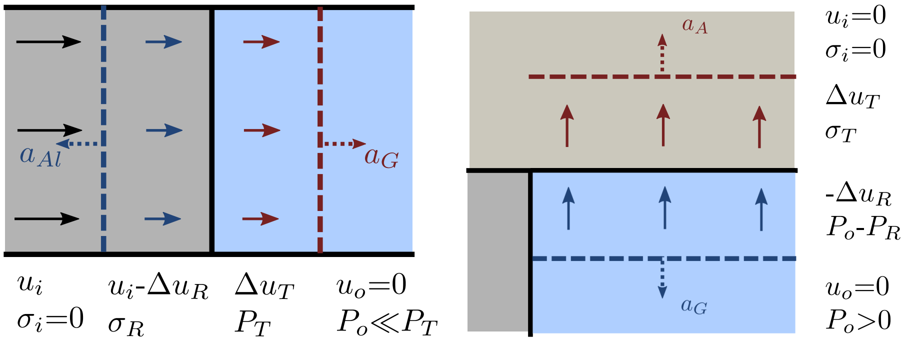

(a) Longitudinal (x) direction.

(b) Transverse (y,z) direction.

Figure 3.9: Schematic representation of the generation of waves in the longitudinal and transverse directions due to striker impact. For clarity, transverse velocities are omitted in (a) and longitudinal velocities are omitted in (b).

a convention of positive pressure indicating compression, and thus:

$$P_T = -(\sigma_i + \sigma_R) \quad \text{and} \quad 0 + \Delta u_T = u_i - \Delta u_R. \tag{3.5}$$

Substituting a linearized expression for pressure in the gel ($\rho a \Delta u$) and for stress in the aluminum ($\sigma = E\epsilon$),

$$\rho_G a_G \, \Delta u_T = 0 - E_{Al}\epsilon_R = -\frac{E_{Al}}{a_{Al}}(-\Delta u_R) = \rho_{Al} a_{Al} \, \Delta u_R \tag{3.6}$$

using the definition $a^2 = \sqrt{E/\rho}$ for solids to accomplish the last step. Solving with ρ_G=1000 kg/m^3, a_G=1500 m/s, ρ_{Al}=2700 kg/m^3, E_{Al}=70 GPa, and a_{Al}=5100 m/s yields $\Delta u_R = 0.109 \Delta u_T$. u_T can be reliably measured from video data and has a value of 25±2 m/s. This yields Δu_R of 2.7±0.2 m/s and u_i of 27.7±2 m/s (slightly higher than the impact velocity, as would be expected for a partially elastic collision). Pressure is predicted to be 37.5±3 MPa, obtained from the expression on the right-hand side of Equation 3.6. The same value is obtained from stress calculation for the reflected wave in the aluminum.

This computed pressure is significantly higher than pressures observed at any time in simulation, suggesting that mechanisms to release pressure play a significant role. One of these mechanisms is the deformation of the acrylic face plates and aluminum spacers due to the pressure rise within the sample. Assuming that rise is instantaneous, as described by the striker-gel interaction above, the same relations can be used to find the initial velocities and pressure changes in the acrylic and aluminum, after the incident wave propagates a small distance into the gel, as illustrated in Figure 3.9(a) . Starting with elevated pressure in the fluid (P_G)

and zero velocities in the directions normal to striker motion,

$$P_G - \rho_G a_G \, \Delta u_R = 0 - E_A \epsilon_T = \rho_A a_A \, \Delta u_T \tag{3.7}$$

where the reflected wave (u_R) is now traveling into the gel, and the transmitted wave (u_T) into the structure, and subscript A represents either acrylic or aluminum. It is expected that high pressure will generate outward motion in the structure and compressive stresses, which also requires the gel to be accelerated outward for the interfaces not to separate. This outward motion creates a tensile wave in the gel, reducing the pressure. Using ρ_A=1180 kg/m^3, E_A=8.6 GPa, and a_A=2700 m/s for acrylic, and the abovementioned values for aluminum, the interface velocities are 8 m/s and 2.3 m/s respectively. The associated pressure drops in the gel are 12 MPa and 3.5 MPa.

These computed values reflect only an idealized estimate of instantaneous response of the gel-structure interfaces to a sudden rise in pressure. Several factors will reduce the effect of these waves on the gel and the fixture.

First, the foregoing analysis assumed perfectly sharp wavefronts. However, the simulations show finite rise times of pressures and velocities in all components. As pressure in the gel adjacent to the striker rises over the course of 5 μs, small disturbances are generated in the face plates and spacers and propagate back into the gel, relieving some of the pressure. This lower pressure alters subsequent interactions of the striker and the gel, lowering the magnitude of the reflected waves sent through the striker. It takes 1.6 μs for a wave reflected from the face plate to propagate to the center of the gel sheet, significantly less than the rise time of the pressure signal, which gives adequate time for coupled interactions to occur. Additionally, the propagation of the wave profile downstream creates a continuous plane of disturbances along the edges of the gel bordering on the face plates and spacer bars. The wave profile could be described as a continuous sequence of sharp pulses of varying magnitudes, and the reflected disturbances created by each pulse interacts with every other, making it increasingly impractical to obtain an analytical solution for the whole system for later times.

The second factor that reduces the magnitude of the reflected waves is that because pressure acts uniformly in all directions, the waves arising a single, narrow pressure pulse do not propagate linearly into the gel or the structure, normal to the impact direction. Instead, they propagate radially, originating from a thin line at the intersection of the plane of a given wavefront and the neighboring fixture component. In waves that propagate cylindrically in this way, the pressure decreases as $r^{-1/2}$ at large distances (r) from the source [158, 159]. There is no readily apparent timescale or lengthscale in the problem that allows a “small” source size to be defined without some degree of arbitrariness; the rise time of 5 μs is a large portion of the time required for waves to reach the bubble location (6.4 μs), and clearly many wave interactions occur in the fixture in this time. Instead, as a pessimistic upper bound, a value of 0.1 mm is proposed; this is 5% of the half-thickness of the gel (2.4 mm) and 1% of the initial distance from striker to bubble location (nominally 9.6 mm). This assumption makes 1 mm justifiable as a “large distance” from the source. The pressure at 10 mm from the source will be 32% of pressure at 1 mm; if 12 and 3.5 MPa are used as pressure magnitudes at 1 mm of reflected waves from the acrylic faceplates and aluminum spacers respectively, the resulting disturbances at the bubble location come out to 3.8 and <1 MPa (at 13.5 mm, due to gel having larger width than thickness). Doubling these for two of each wave (one from each corner), results in 7.6 and <2 MPa. The first value has the potential to significantly change the pressure applied to the bubble, whereas the second value is quite small compared to predicted pressures in the fixture.

There is also potential for the waves transmitted into the face plates and spacer bars to reflect off the exterior free surfaces of the fixture and return to induce a pressure change. However, pressures at 50 mm and 38 mm are 14% and 16% of that at 1 mm respectively. Moreover, the difference in acoustic impedance (ρa) of the materials at the interface further lowers the pressure magnitude as it propagates into the gel, resulting in an extremely small disturbance relative to the peak pressures.

The role of the deformation of the face plates in relieving the pressure in the fixture is quite apparent in simulations and was discussed in the previous section. Corner waves from the spacers are visible as pressure fluctuations in a 3 MPa range in Figure 3.10(a). The waves are propagating outward from the corner. The most readily apparent wavefront is a compressive one, which could be expected to occur if wave interactions in the gel caused a pressure decrease in the gel, and the higher pressure in the structure at that time caused a deceleration of the interface to restore force and velocity equilibrium. The waves are easier to identify in the acceleration of the fluid (Figure 3.10(b)), but the magnitude is only on the order of 1 (m/s)/μs; given the small extent and residence time of these waves, they can only be expected to change the velocities by a few m/s out of peak velocities of 25-30 m/s. Velocity plots confirm that fluctuations due to these waves are not clearly visible (Figure 3.10(c) and (d)).

It can be concluded from this analytical investigation that the pressure state within the fixture is extremely complex, due to its origin as a distributed wave in the aluminum striker, and the eventual superposition of many wave reflections off fixture surfaces. The best way to obtain a pressure prediction that accounts for all these mechanisms is through numerical simulation or direct pressure measurement. However, the analytical approach was used to demonstrate that the dominant mechanisms in establishing the pressure state in the fixture are the striker velocity and impact into the gel, as well as the motion and deformation of the face plates; waves reflected from the spacer bars and wave reflections from the exterior free surfaces of the fixture are comparatively minor effects. This was found to be in agreement with simulation results. However, the minor reflected waves may be associated with pressure fluctuations as large as 3 MPa, which can be expected to generate refractive index changes on the order of 10^{-4} [147]. This magnitude of refractivity disturbance can potentially register on shadowgraph imaging, depending on the lengthscale of the disturbance.

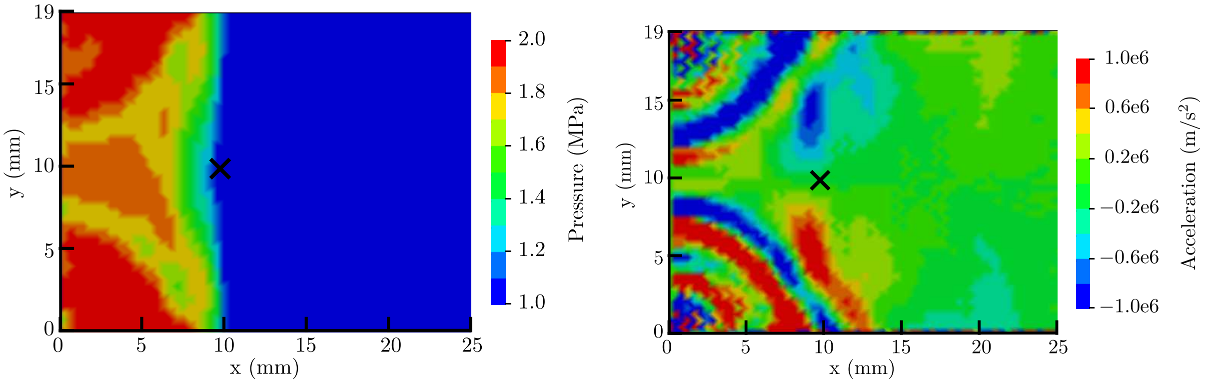

(a) Pressure.

(b) Acceleration.

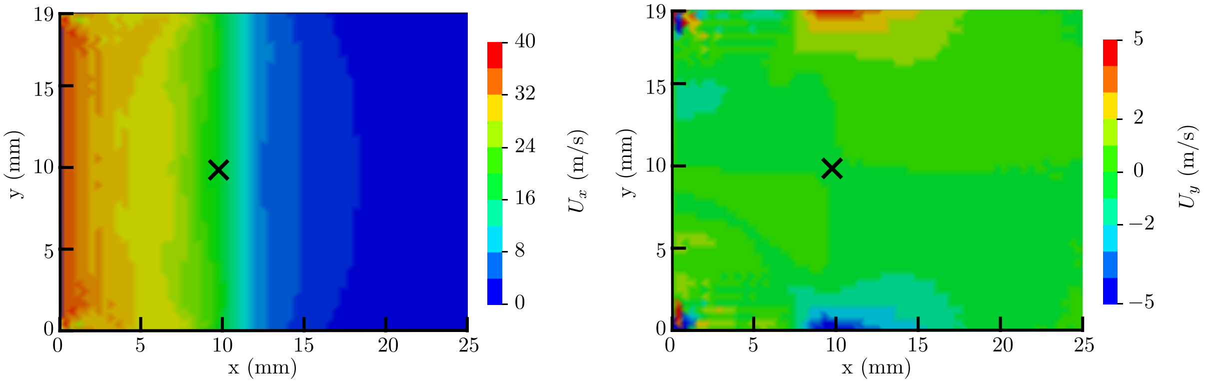

(c) Longitudinal velocity (x).

(d) Transverse velocity (y).

Figure 3.10: Contour plots of pressure, acceleration, and longitudinal and transverse velocity at 15 μs simulation time, from LS-DYNA modeling of the experimental fixture. × marks bubble location, although one was not included in these tests.

3.5 *In situ* Pressure Measurements

Although it was encouraging that simulations predicted tension zones precisely coincident with surface cavitation zones in the original fixture, actual pressure measurements were collected to further verify the validity of the simulated behaviors and note the degree of experimental deviation from prediction. Several pressure measurements for each geometry are presented in Figure 3.11, along with traces from the appropriate simulation for comparison (Section 3.3.1). The PCB 113A23 transducer face was 6 mm in diameter, which is quite large for this experiment and covers the entire region of interest. It was clear the transducer would introduce some averaging, but not whether certain locations on the face (e.g. center) would be effectively "weighted" relative to other locations. Therefore, the predicted pressure traces at 2.8 mm upstream and downstream of the bubble location are included for comparison alongside the central, 9.4 mm location. Theoretically, regardless of the distribution of transducer response, the curve should fall between these two traces.

This is not quite what happens, but on the whole the simulations offer a good prediction of average

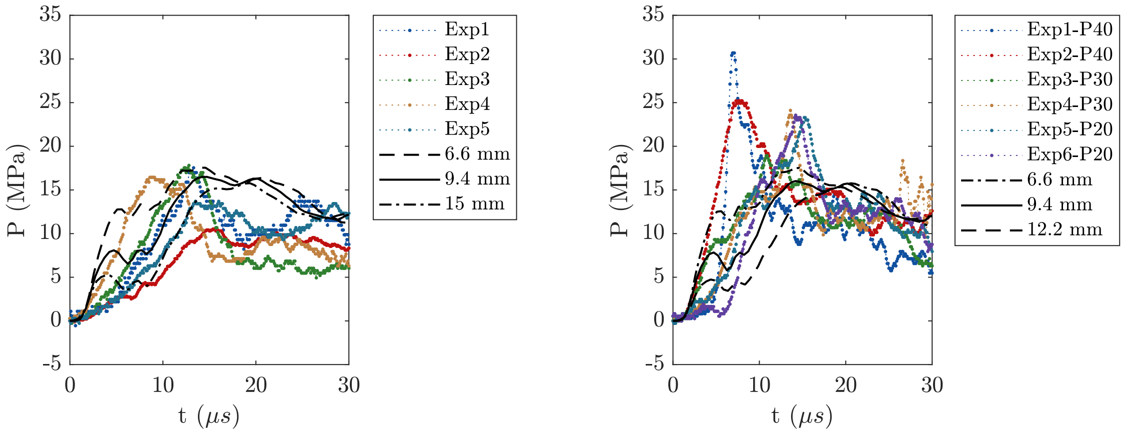

(a) No Boundaries.

(b) Downstream Boundary.

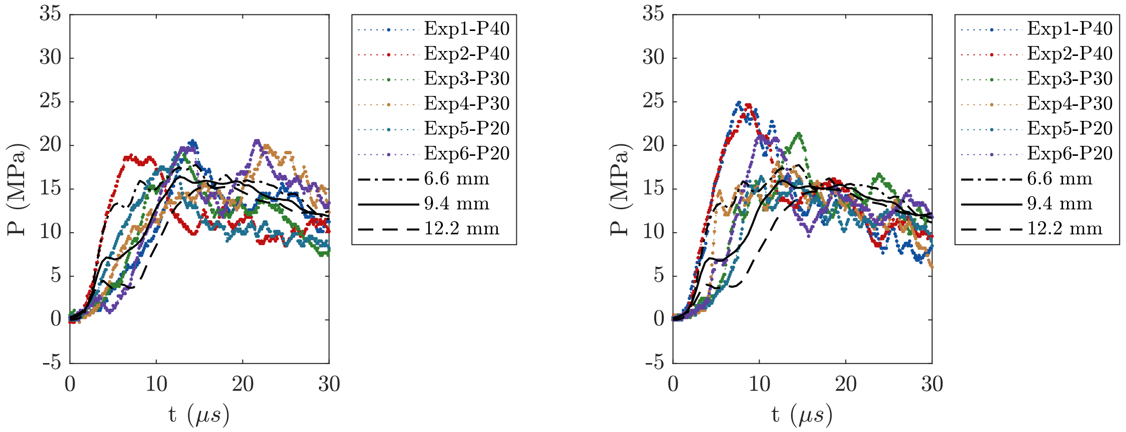

(c) Upstream Boundary.

(d) Two Boundaries.

Figure 3.11: Predicted and experimentally measured pressures for all four geometries of interest. Curves have been shifted in time to maximize overlap. Pressure in the sample with an aluminum boundary could not be measured experimentally without risk to equipment, and thus is not included.

pressure behavior. There are, as expected, more fluctuations in the experimental traces, and also variations in time of arrival. The signals have been shifted based on the start of pressure rise to make the curves easier to compare, but the time of arrival of a detectable pressure rise relative to the trigger signal actually fluctuates over a range of 15 μs. Even with the time-shift adjustment, the varying rise profiles and rise times result in peak pressure being reached at varying times. Almost none of the traces exhibit the small "bump" seen on the simulated pressure trace; it is not clear if this does not occur in experiment, or if it is averaged out by the size of the transducer.

The pressure traces vary slightly from geometry to geometry. In the no-boundary cases, the pressure reaches the predicted peak, but drops much faster to about half the predicted pressure (although in two of the tests (Exp1 and Exp5) it subsequently recovers to the predicted pressure levels, and in Exp2 it never achieves the predicted peak pressure, but remains around 10 MPa once that value is reached. The upstream boundary cases follow the predicted curves quite closely, with allowances for experimental fluctuations and noise. Just one (Exp3) exhibits a noticeably steeper rise, but is otherwise not dissimilar from the other traces. The downstream and two-boundary cases, which both feature the downstream boundary, exhibit a steeper rise to a peak pressures of 25–30 MPa rather than 15–20 MPa as predicted in simulation or observed in the no-boundary and upstream boundary geometries. This also contradicts acoustic expectations. Based on the properties in Section 2.3.1 and 2.3.2, the acoustic impedance (ρa) of agarose is 1.5×10^6 Pa·s/m, whereas that of PDMS is 1.1–1.2$\times 10^6$ Pa·s/m. The magnitude of a wave reflected at an impedance-mismatched boundary is given by:

$$R = \frac{Z_2 - Z_1}{Z_1 + Z_2} I \tag{3.8}$$

where I is the incident wave magnitude and Z is acoustic impedance. This would suggest that the reflected wave should be a rarefaction wave with 12–16% of the original magnitude, reducing the pressure, rather than a compression wave as indicated by the pressure rise. The observed increase in pressure is transient; the excessive level persists approximately 10 μs, after which time the pressure in the sample returns to predicted levels. One potential explanation is that in spite of efforts to lubricate the PDMS–PMMA interface, there is some sticking occurring at the fixture sidewall. This should not affect acoustic properties of the system, but would prevent the acceleration of particles at the boundary near the interface until the adhesive force is overcome. The boundary would locally (at the surface, where the pressure sensor was located) be acting more rigid by resisting deformation, or more dense by resisting acceleration. Once the pressure exceeds the strength of the bond, the PDMS accelerates and the pressure is relieved, returning the system to its predicted state. The fact that the 40:1 PDMS, which is observably softer and stickier on the surface exhibits the most pronounced pressure spikes gives credence to this theory, but it has not been tested in a quantitative way.

3.6 Conclusions

Computational modeling of the experimental fixture and the impact process allowed the loading state within the fixture to be intentionally designed. The state generated within the fixture by an impact differs from that expected in a two-dimensional system under ideally rigid confinement due to the deformation of the fixture and fluid-structure interaction between the sidewalls and the fluid within. The degree of coupling of these systems can be controlled by selection of fixture materials and geometric parameters. Once the loading in the fixture was well-understood, the model was used to predict the effect of more complex features, such as material boundaries and the air-filled bubble, subject to the limitations of the software. The predicted pressures generally agreed well with experimentally-determined traces, barring small oscillations and test-to-test variations in timing up to 15 μs.

The following chapter will investigate the significance of the fluctuations and variations seen in the pressure signal with regards to their measurable effect on the bubble collapse process, using theoretical relations available to describe bubble collapse. Subsequent chapters will present the experimental data collected, and relate the results to the computation model of air-filled bubble collapse discussed in this chapter, as well as the theoretical results.

CHAPTER 4

CYLINDRICAL BUBBLE COLLAPSE ANALYSIS

The modeling discussed in the previous chapter was very useful for understanding the loading conditions in the sample as well as obtaining a rough estimate of the effect of material inhomogeneities on the resulting state. The modeling process was able to resolve the complex interactions between system components and provide an accurate prediction. However, it was not the ideal tool for modeling the system interaction with the air-filled cavity due to resolution constraints. Moreover, the fixture geometry created a fairly complicated pressure waveform, which makes it difficult to discern the response of the bubble to any one specific feature of said waveform. The goal of this section is to investigate how the fluctuations in pressure affect the collapse process by using theoretical relations. Simple waveforms will be explored initially, followed by pressure profiles of increasing complexity, up to and including those recorded pressure measurements. While there are a number of linear analyses of shocks interacting with gas bubbles [106], there is not an analytical model for the asymmetric collapse of a spherical or cylindrical bubble under the influence of a traveling wave; therefore, only the problem of a symmetrical collapse will be explored, neglecting the additional complexity of spatial pressure gradients and asymmetric flowfields produced.

4.1 Problem Statement

The problem considered is an initially cylindrical bubble in two-dimensional geometry, with radius $R_o =$ 1 mm and filled with air at atmospheric pressure $P_o = 100$ kPa. It is surrounded by water of density $\rho_L = 1000$ kg/m^3. To simulate the shock wave, the pressure in the far-field varies as a function $P_L(t)$ for time $t > 0$. This model is appropriate for a wave-induced collapse if the wavefront width is significantly larger than the bubble size. Under the influence of the loading pressure difference $P_L(t) - P_o$, the fluid surrounding the bubble begins moving inward, establishing a flowfield $\boldsymbol{U}(r)$ and resulting in bubble interface motion $\dot{R}$. Schematics of the problem in its initial state and an arbitrary time during the collapse are presented in Figure 4.1

The nature of $P_L(t)$ is of interest as a variable in the investigation. A representative pressure trace measured experimentally, along with an LS-DYNA predicted trace for the matching condition, is presented in Figure 4.2. This trace exhibits: a rise to a peak, a short plateau, and a steep drop down to a longer plateau. The simulated pressure trace has a similar rise, but a more gradual fall. All these changes happen

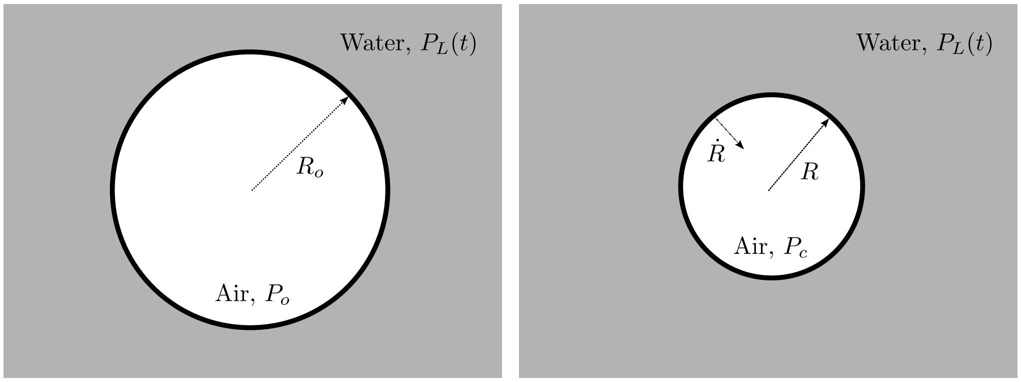

(a) Initial state of problem to be investigated theoretically.

(b) State of problem at intermediate state, during collapse.

Figure 4.1: Geometry of problem to be investigated theoretically.

on a comparable timescale to the bubble collapse (15 μs), and therefore have the potential to affect the process and its salient effects: the maximum velocities, minimum volume, and maximum pressure attained.

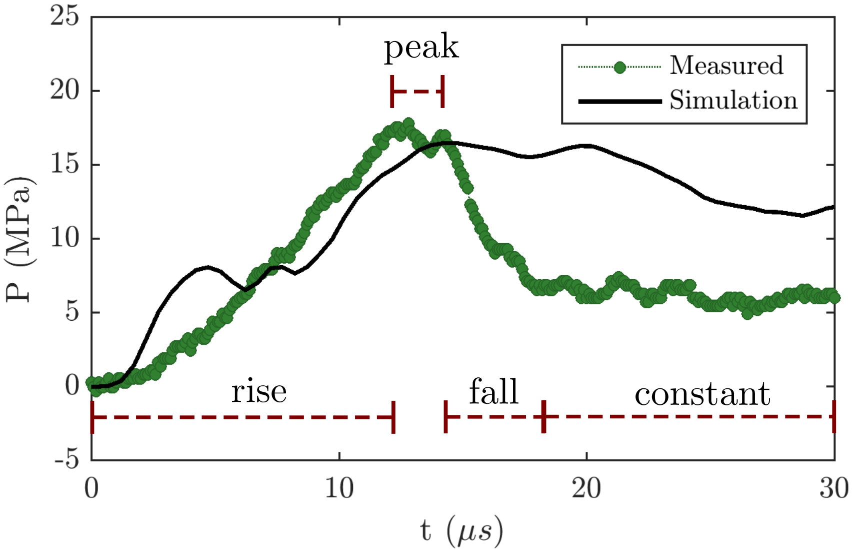

Figure 4.2: Representative measured and simulated pressure traces in agarose gel sample with no cavity. Regions of different characteristic pressure behaviors are annotated.

4.2 Review of Theory

As discussed in Section 1.7, although significantly more theoretical consideration has been given to the dynamics of spherical bubbles impacted by planar waves in an axisymmetric geometry (e.g. Brennen [24] and Plesset and Chapman [29]), some considerations have been given to cylindrical bubbles and voids (e.g.

by Epstein and Keller [160], Kedrinskii [97], Ilinskii et al. [96], Leighton et al. [25]). The applicability of the cylindrical geometry to underwater explosions, as well as bubbles confined between rigid plates, spurs continued interest.

Ilinskii et al. considered several models for bubble collapse and derived differential equations for $R(t)$ under constant applied pressure (P_L =constant for all $t > 0$) and compared the results obtained from each [96]. Their derivations did not depend on assuming a constant pressure, so these models can readily be extended to a time-variable pressure. The derivation of the two main expressions they investigated will be briefly reviewed here. One of the relations will then be used to investigate bubble response to a variety of pressure loading functions.

It is well established that an elevated far-field pressure on a bubble in a homogeneous environment initially creates only inward flow to the center of the bubble, i.e. radial flow U_r. Assuming potential flow of an incompressible fluid, the conservation of mass determines the velocity at all points in the liquid surrounding the bubble in terms of the bubble boundary dynamics:

$$U_r = \frac{R\dot{R}}{r}, \tag{4.1}$$

where r is the radial coordinate, R is the bubble radius, and $\dot{R}$ is the time rate of change of bubble radius. Ilinskii et al. use this flowfield to derive expressions for kinetic energy $\mathscr{E}_K$ and potential energy $\mathscr{E}_P$, and substitute these into Lagrange's equation for $\mathscr{E}_L = \mathscr{E}_K - \mathscr{E}_P$:

$$\frac{\partial}{\partial t}\left(\frac{\partial \mathscr{E}_L}{\partial \dot{R}}\right) - \frac{\partial \mathscr{E}_L}{\partial R} = 0 \tag{4.2}$$

The potential energy only appears in $\frac{d\mathscr{E}_P}{dR}$, and is determined by considering the work done on the cylindrical bubble of length h_z by the pressure difference due to a differential change in radius:

$$\frac{d\mathscr{E}_P}{dR} = -2\pi R h_z (P_g - P_L) \tag{4.3}$$

The kinetic energy is derived by integrating $\rho_L U_r^2$ throughout the flowfield, to obtain:

$$\mathscr{E}_K = \pi \rho_L h_z R^2 \dot{R}^2 \int_R^{R_M} \frac{dr}{r} \tag{4.4}$$

The integral is divergent as $R_M \to \infty$, resulting in an infinite kinetic energy, and Ilinskii et al. suggest it is reasonable to replace the upper integral limit with a finite, sufficiently large value of R_M in order to calculate the integral

$$\mathscr{E}_K = \pi \rho_L h_z R^2 \dot{R}^2 \ln\left(\frac{R_M}{R}\right) \tag{4.5}$$

Substituting Equations 4.3 and 4.5 back into Lagrange's equation, and using an adiabatic assumption to model pressure changes inside the bubble, the following expression is obtained:

$$\left(R\ddot{R} + \dot{R}^2\right) \ln \frac{R_M}{R} = \frac{P_g - P_L}{\rho_L} \quad \text{with} \quad P_g = \left(\frac{R_o}{R}\right)^{2\gamma} P_o, \tag{4.6}$$

where $R_o = R(0)$ is the initial radius.

This form is analogous to the Rayleigh-Plesset equation for spherical bubbles. To complete the model, Ilinskii et al. propose a value of $R_M = 10$ for large bubble oscillations (including collapse), and cite several experimental studies that exhibit good agreement with this model [95, 97, 98]. For small oscillations and acoustic radiation considerations, Ilinskii et al. indicate that a larger R_M is required.

The second approach reviewed by Ilinskii et al. relies upon a generalization of the Gilmore equation to an arbitrary number of dimensions, as derived by Kedrinskii [97]. The derivation relies on making the Kirkwood-Bethe approximation that the value $r^{\frac{\alpha}{2}}\left(h + \frac{U^2}{2}\right)$ is an invariant along characteristics of form $r - a_o t$, where α is 0, 1, or 2 for planar, cylindrical, and spherical cases respectively and a_o is sound speed in the surrounding liquid. In the cylindrical case, this only holds true for large distances and high frequencies, so this assumption is less accurate than for the planar or spherical cases, but nonetheless it produces useful results. The Gilmore-type equation is formulated in terms of enthalpies (h), but if values appropriate for an incompressible liquid are used, the resulting equation is,

$$\left(1 - \frac{\dot{R}}{a_o}\right) R\ddot{R} + \left(1 - \frac{\dot{R}}{3a_o}\right) \cdot \frac{3}{4}\dot{R}^2 = \left(1 + \frac{\dot{R}}{a_o} + 2\frac{R}{a_o}\frac{d}{dt}\right) \frac{P_g - P_L}{2\rho_L} \tag{4.7}$$

Like the counterpart Keller-Miksis equation for spherical bubbles, this result enables compressibility effects to be included in the collapse model. The results reflect the difficulty of accelerating the fluid as velocities approach a significant fraction of the fluid sound speed. Another way to utilize this equation, as demonstrated by Ilinskii et al., is to take its incompressible limit (i.e. $\dot{R}/a_o \to 0$). This results in:

$$R\ddot{R} + \frac{3}{4}\dot{R}^2 = \frac{P_g - P_L}{2\rho_L}. \tag{4.8}$$

Ilinskii et al. point out that when this is compared with the Rayleigh-Plesset type equation, it is clear they can be made equivalent if R_M/R is set to 2, and therefore $R_M = e^2 \approx 7.4$, further confirming that an R_M value of order 10 is reasonable. Kedrinskii suggested that the coefficient of the $\dot{R}^2$ term is a consequence of the Kirkwood-Bethe approximation and a value of 1 compares better with experimental work than $3/4$. Ilinskii et al. find this has minimal (5%) effect on the collapse time in the constant-pressure case they examine.

If the internal pressure is neglected, an analytical expression can be derived for the value of $\dot{R}$, which can be integrated to find a collapse time. The expression is analogous to the Rayleigh collapse time, scaled by a constant:

$$T_c = \Gamma R_o \sqrt{\frac{\rho_L}{P_L}} \tag{4.9}$$

The constant Γ is a function of R_M for the Rayleigh-Plesset type equation, equal to about 1.6 for $R_M = 10R_o$, and 1.49 for the Keller-Miksis type formulation and for $R_M = 7.0R_o$. These values provide useful scaling factors for interpreting modeling results.

4.3 Computational Approach

The preceding derivation yields a choice of three relations, the cylindrical analogues of the Rayleigh-Plesset type equation (4.6), the Keller-Miksis type equation (4.7), and the incompressible limit of the Keller-Miksis type equation (4.8). Ilinskii et al. present a comparison of the three in terms of the R vs $\dot{R}$ behavior of a cylindrical void ($P_g = 0$). The three models predict the same behavior for large radii and small interface velocities, but the Rayleigh-Plesset type equation begins to overpredict velocity at around $\dot{R} \geq 0.03a_o$, which is 45 m/s for water, and the incompressible Keller-Miksis type begins to overpredict interface velocity at $\dot{R} \geq 0.15a_o$ or about 225 m/s. For higher velocities, neither of these models is appropriate.

Modeling in LS-DYNA, as well as the experimental data (Chapters 5 and 6) show the development of velocities up to about 300 m/s in this study. This indicates that a compressible model is the optimal choice. However, convergence was difficult to attain with the compressible model for the conditions of interest, so the incompressible Keller-Miksis type equation was selected for further work. Considerations in making this choice include the following: first, the highest velocities observed in simulation and experiment develop as a result of the asymmetry of the collapse; the average velocity is much lower than 225 m/s. Second, the highest velocities in bubble collapse occur at the smallest bubble volumes, and at this point additional mechanisms associated with real gas effects can become significant [24]. The simple theoretical models do not reflect this and so are expected to lose predictive power at these conditions. Third, the small scale at which such conditions occur is not resolved in any of the experiments performed, which are limited to area ratios $A^* = A/A_o$ of about 0.05, and time intervals of 0.2 or 1 μs depending on the diagnostic used. Given these issues, the value of taking the theoretical prediction to this point is limited. Likewise, due to the complexities inherent in the last stages of collapse, the theoretical predictions are not used here to try to predict or explain rebound behavior.

The equation was solved using the ode15s solver in MATLAB®, using 10,000 points over the simulation time to resolve the smaller final radii, as a benchmark for the behavior of different cases rather than necessarily a prediction.

4.3.1 Applied Pressure Characterization

The pressure signal shown in Figure 4.2 (above) exhibits several characteristics: ramped pressure rise, ramped pressure drop, constant pressure. To determine what characteristics of these pressure traces have the greatest effects on the resulting collapse, the following idealized pressure loading functions $P_L(t)$ for $t > 0$ were considered:

1. $P_L(t) = P_{\max}$, for a range of $P_{\max}$ values.
2. $P_L(t) = \dfrac{P_{\max}}{t_w} t$ for $t < t_w$, then $P_{\max}$. A linear ramp with various rise times t_w.
3. $P_L(t) = P_{\max}$ for $t < t_w$ then P_o. A square pressure pulse with width t_w.
4. $P_L(t) = P_{\max} - \dfrac{P_{\max} - P_o}{t_w}$ for $t < t_w$, then P_o, a downward ramp.
5. Measured $P_L(t)$ traces.

4.4 Effect of Constant Loading Pressure

Figure 4.3(a) presents the results of a pressure sweep for a simple step-function loading wave (i.e. constant pressure). The loading pressure is given as a pressure ratio to the atmospheric pressure inside the bubble $P_o = 100$ kPa. Lower pressure ratios result in longer collapse times and larger final volume (proportional to area). A smaller pressure does not accelerate the fluid as quickly, and cannot compress a bubble as much as a larger pressure. What is potentially more interesting are the changes in the profile of the collapse: the lower pressures exhibit a distinct "S"-curve, whereas the higher pressure curves are concave at first and appear virtually linear at the end. To see these patterns more clearly, the traces can be put on the same timescale, $t^* = t/t_c$ where t_c is the estimated collapse time (Equation 4.9) and $A^* = A/A_o$. While pressure ratios above about 50 (5 MPa) result in essentially identical curves, the lower pressures do not and take longer to collapse with lower pressure. The reason is that the estimate for t_c by definition does not account for pressure within the bubble.

This effect of the gas pressure in the bubble can be quite clearly seen if Equation 4.8 is solved for $\ddot{R}$:

$$\ddot{R} = \frac{P_g}{2R\rho_L} - \frac{P_L}{2R\rho_L} - \frac{3}{4}\frac{\dot{R}^2}{R} \tag{4.10}$$

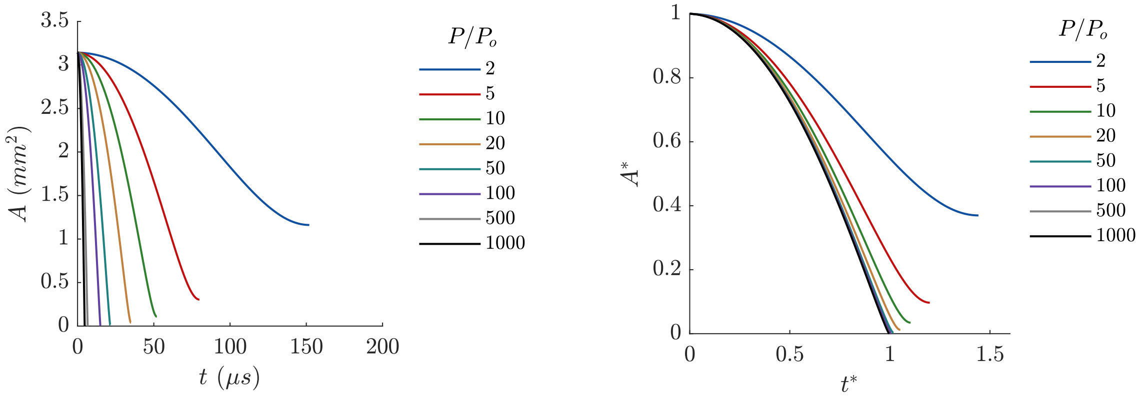

(a) Dimensional units.

(b) Nondimensional units.

Figure 4.3: Collapse of 1 mm radius bubble under a range of pressures.

The value of $\ddot{R}$ depends on the balance of these terms. The P_g term creates acceleration outward, whereas the P_L and $\dot{R}^2$ terms act inward. Figure 4.4 shows the relative magnitude of these terms for the collapse under a pressure ratio of 5. Initially, the P_L term is dominant and accelerates the bubble interface inward, increasing the $\dot{R}^2$ by virtue of both increasing $\dot{R}$ and decreasing R. At about the time that the $\dot{R}^2$ term becomes comparable to the P_L term, the P_g term, growing at an exponential rate, overtakes them both. This quickly turns the total acceleration outward, and the $\dot{R}^2$ term drops rapidly, until it reaches 0 and P_g accelerates it outward as part of the rebound process (which, for such a low pressure condition, might even be believable).

Figure 4.5 demonstrates how essentially the same process occurs for pressure ratios of 20 and 100, but with increasing severity and decreased time. In Figure 4.5(a), it is clear that the $\dot{R}^2$ term becomes dominant at $t^* = 0.8$, but the P_g term does not exceed P_L until about $t^* = 0.9$. Moreover, because the $\dot{R}^2$ term is dominant, the acceleration does not reverse until the P_g term exceeds the $\dot{R}^2$ term, between t^* of 0.95 and 0.975 in the inset (Figure 4.5(b)). Even so, this is visible as a slight upturn in the respective trace in Figure 4.3, toward the end of the collapse. For a pressure ratio of 100, the reversal of acceleration is no longer even clear on the full plot, as it has been pushed to after $t^* = 0.995$ as visible on the inset. As a result, the deceleration of the collapse is no longer visible on the area-time plot.

4.5 Effect of Linearly Increasing Pressure

Figure 4.6 shows a range of ramped pressure traces applied to a 1 mm bubble and the collapse profiles attained. For rise times t_w that constitute a small fraction of the collapse time, the collapse acts essentially like that under a step pressure change, as would be expected. As the rise time increases, the beginning of the collapse becomes more and more gradual and the collapse takes longer. However, unlike for very low

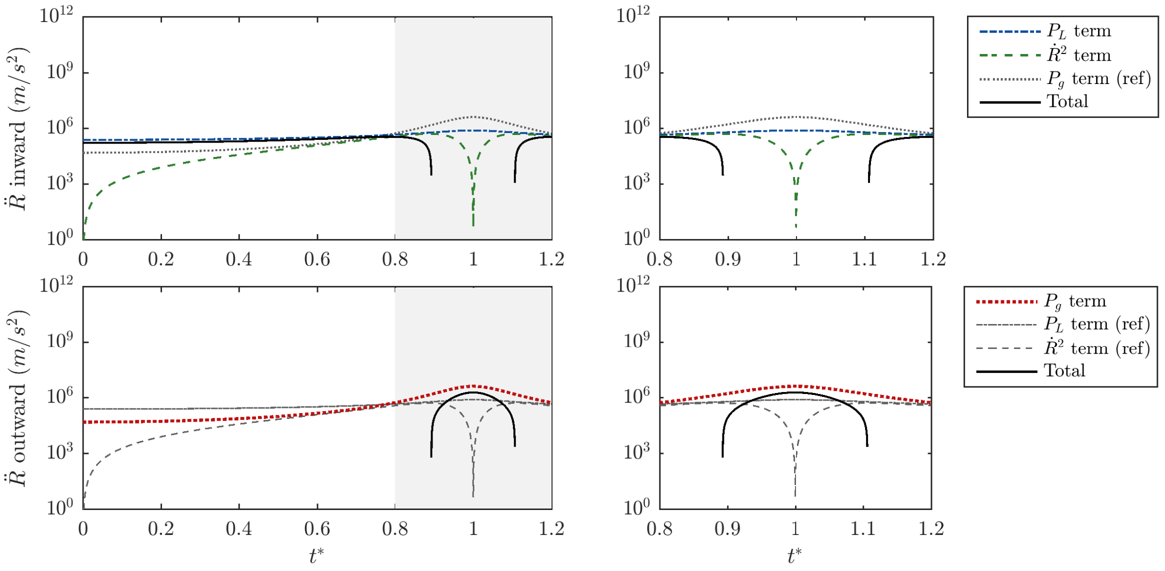

(a) Full collapse.

(b) Inset on end stage and early rebound.

Figure 4.4: Acceleration terms for collapse under pressure ratio of 5. Time is nondimensionalized by actual collapse time, $t^* = t/t_A$. Gray box indicates inset area. Gray lines are terms opposite in sign, for reference and comparison.

pressure ratios, the reduced collapse time does not appear to translate into a significantly less severe collapse (with lower minimum volume); in fact, all the traces appear to approach $A^* = 0$ at about the same slope.

Examining the behavior of the acceleration components largely confirms this and explains how it comes about. The plot of acceleration components for the trace with $t_w = t_c = 0.68t_c$ is shown in Figure 4.7. Upon comparison with Figure 4.5, the most distinct differences are before $t^* = 0.2$. Where a step pressure change induces essentially an instant change in acceleration, the acceleration in this case grows more gradually, as does the $\dot{R}^2$ term. However, by $t^* = 0.6$, the acceleration is reaching similar levels as seen in the step collapse, and from there the remaining behavior is very similar. The order of magnitude of peak accelerations and timing of the reversal, as seen in the inset, are comparable.

Although using a peak pressure based scaling for the time is informative, in many situations the ideal collapse time t_c is not known, and researchers have instead utilized the actual collapse time t_A to nondimensionalize their data. In Figure 4.8(a), the data are replotted using t/t_A for nondimensional time. In fact, in experimental work, collapse time must be determined by the crossing of some area or perhaps rate of change threshold, typically with a degree of noise involved, so a later starting point may be chosen. If the "start of collapse" is redefined as $A^* = 0.95$, and the new reference time $t_{0.95}$ used to scale the plots, the area-time curves approach a common curve (Figure 4.8(b)).

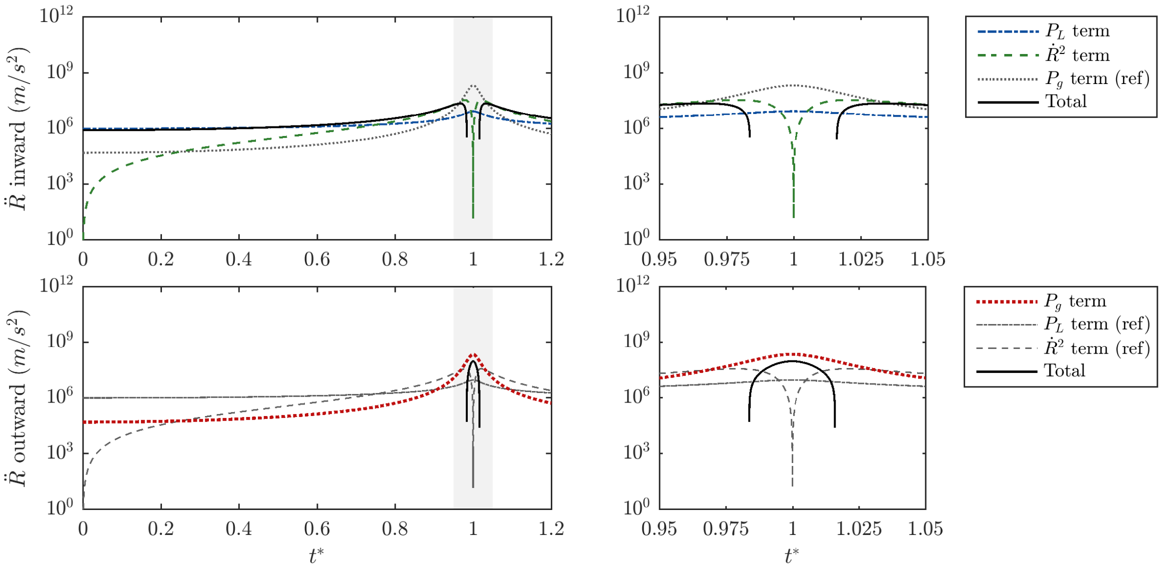

(a) PR=20, full collapse.

(b) PR=20, inset.

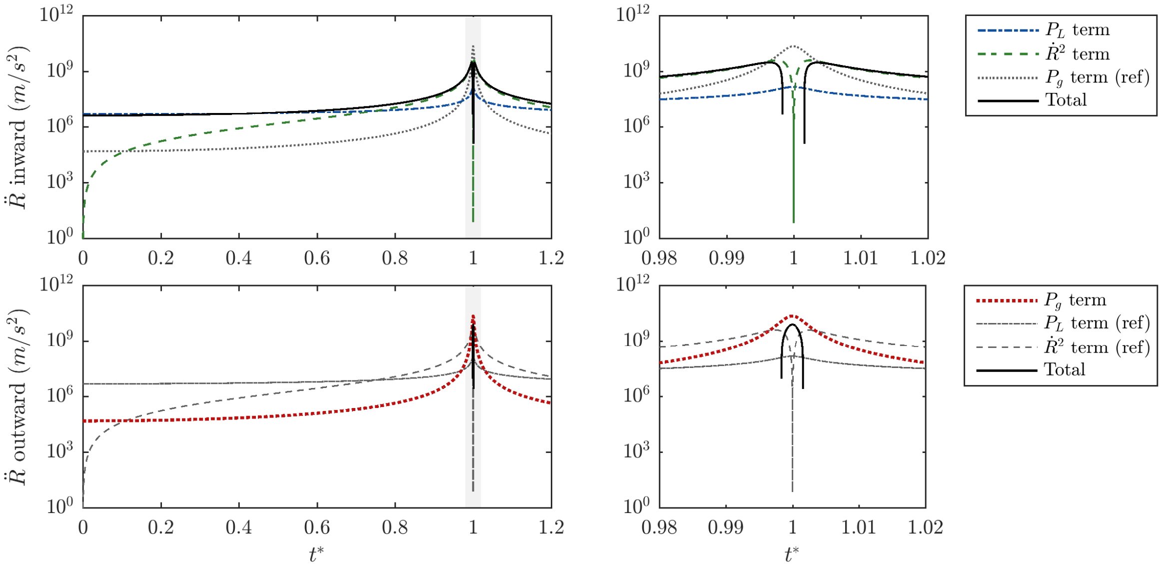

(c) PR=100, full collapse.

(d) PR=100, inset.

Figure 4.5: Acceleration terms for collapse under pressure ratios of 20 and 100. Time is nondimensionalized by actual collapse time, $t^* = t/t_A$. Gray box indicates inset area. Gray lines are terms opposite in sign, for reference and comparison.

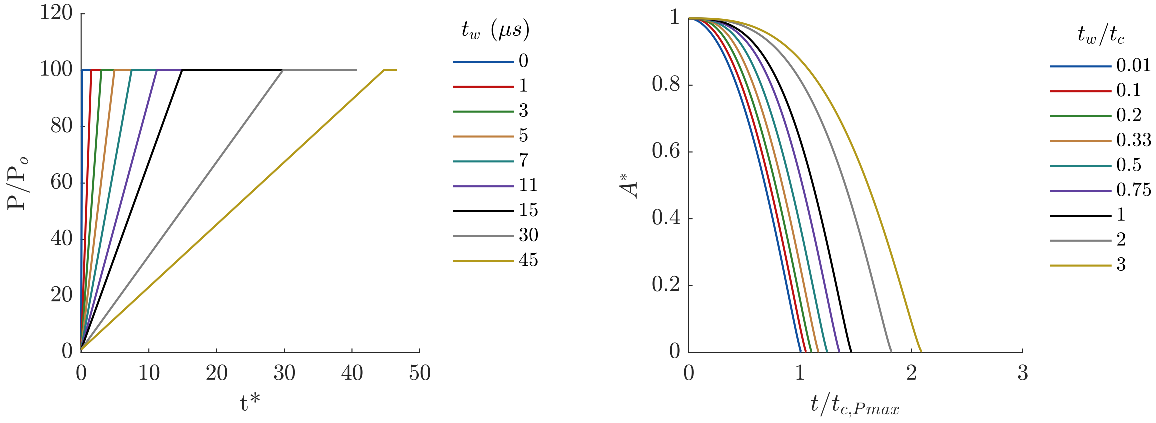

(a) Pressure traces for various rise times.

(b) Collapse in nondimensional units.

Figure 4.6: Loading pressure traces and collapse profiles for linearly ramped pressure rise with range of rise times. $PR_{\max} = 100$.

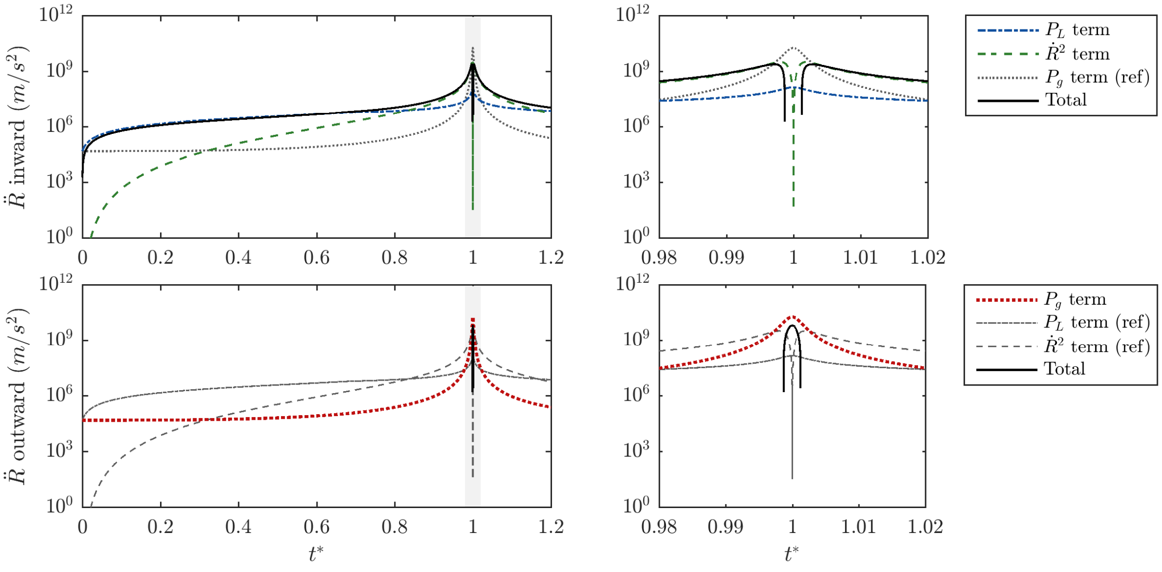

(a) Full collapse.

(b) Inset on end stage and early rebound.

Figure 4.7: Acceleration terms for collapse under pressure ratio of 100 with linear ramp of width $t_w = t_c$. Time is nondimensionalized by actual collapse time, $t^* = t/t_A$. Gray box indicates inset area. Gray lines are terms opposite in sign, for reference and comparison.

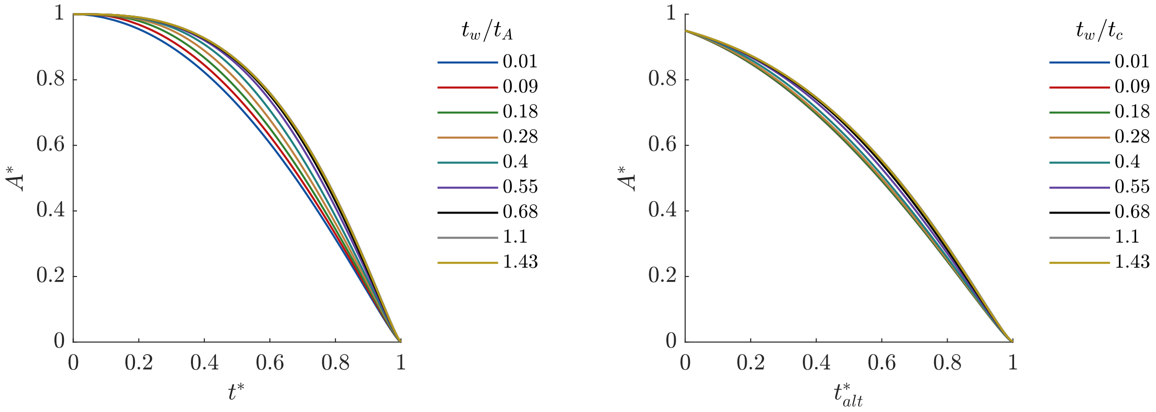

(a) Nondimensionalized by t_c.

(b) Nondimensionalized by $t_{0.95}$.

Figure 4.8: Comparison of time nondimensionalization that might be used on experimental data if t_c is not known. Collapse under linearly increasing pressure with range of rise times t_w.

4.6 Effect of Suddenly Decreasing Pressure

Before addressing the linear decrease in pressure (the "reverse" of the linear increase), a sudden pressure drop will be addressed. This amounts to applied pressure as a square wave pulse of width t_w.The applied pressure traces and the resulting collapse behavior for $P_{\max}/P_o = 100$, with $t^* = t/t_c$ are shown in Figure 4.9. Removing the pressure has an effect akin to using a much lower peak pressure in the constant pressure case: the collapse time and minimum volume both increase with decreasing pulse width t_w. The profile of the collapse is different. Where a lower pressure creates an "S" shaped curve, a briefly applied high pressure creates a "ski jump"—it quickly attains a particular $\dot{A}$, which after removal of pressure decreases in magnitude at an increasing rate up to the point of collapse.

The components of acceleration for this case, Figure 4.10, demonstrate this more clearly. In the initial stages, while pressure is applied, the acceleration terms behave the same as in Figure 4.5(c), under constant pressure. The $\dot{R}^2$ term grows as the interface accelerates. When the pressure is removed, the $\dot{R}^2$ term becomes dominant, and it is much greater than the P_g term. The collapse continues, driven by inertia alone, until P_g grows sufficiently to reverse the behavior at $t^* \approx 0.9$. Based on the traces in Figure 4.9(b), the collapse is affected minimally if pressure is removed after about halfway through the collapse process. The reason for this is apparent when considering the acceleration components. After $t^* \approx 0.5$, the $\dot{R}^2$ term is comparable in magnitude to the P_L term, so the total acceleration experienced does not change significantly (that is, by an order of magnitude), when the pressure is suddenly decreased, $P_L \to 0$. If $P_L \to 0$ even later, when the $\dot{R}^2$ term is dominant, the effect on the collapse is even less significant.

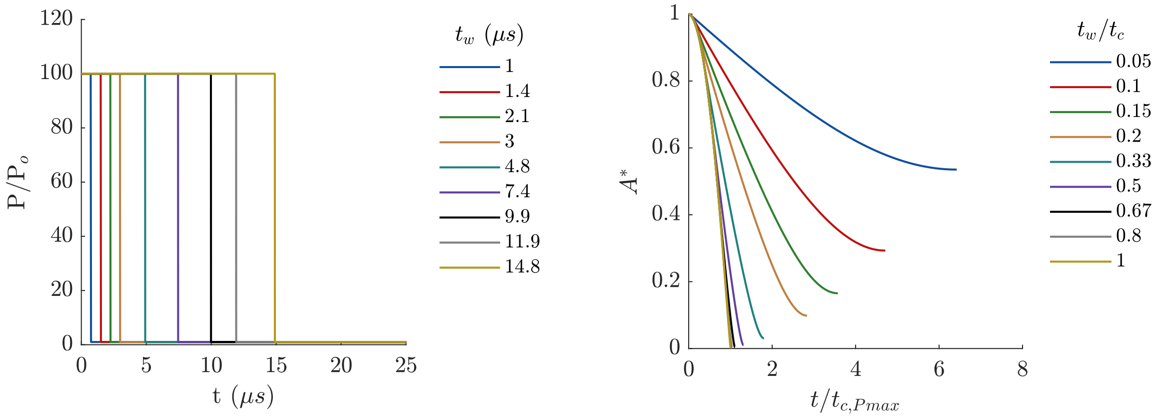

(a) Pressure traces for various rise times.

(b) Collapse in nondimensional units.

Figure 4.9: Loading pressure traces and collapse profiles for linearly ramped pressure rise with range of rise times. $P_{\max}/P_o = 100$

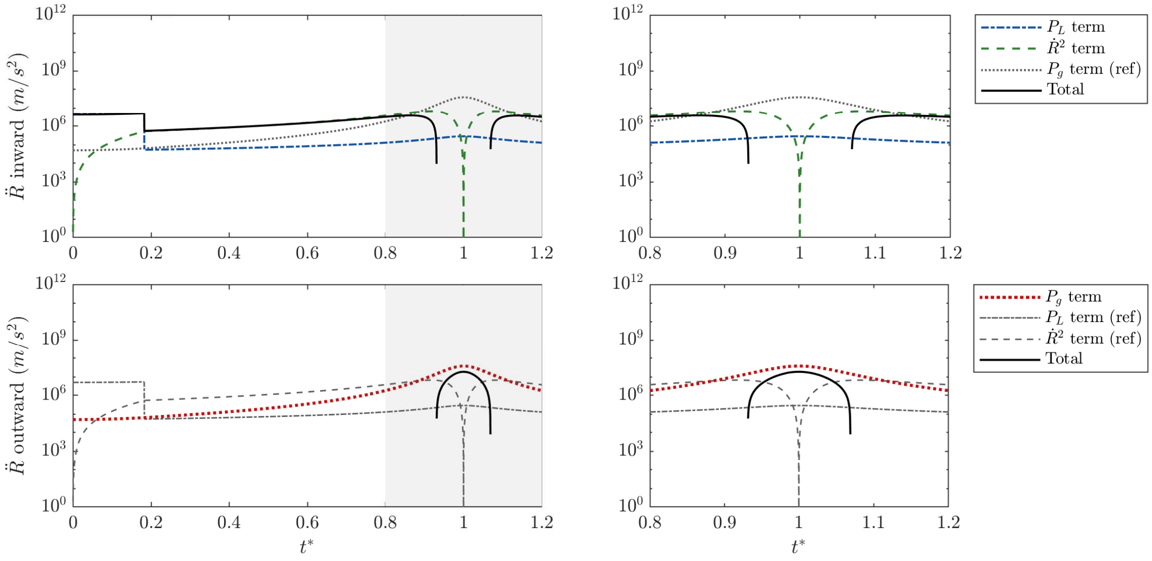

(a) Full collapse.

(b) Inset on end stage and early rebound.

Figure 4.10: Acceleration terms for collapse under square pulse with $P_{\max}/P_o$ of 100 and width $t_w = 0.33t_c$. Time is nondimensionalized by actual collapse time, $t^* = t/t_A$. Gray box indicates inset area. Gray lines are terms opposite in sign, for reference and comparison.

4.7 Linearly Decreasing Pressure

Figure 4.11 illustrates the applied linearly decreasing pressure loading and the bubble response. The pressure begins at $P_{\max}/P_o = 100$ at $t^* = 0$ and decreases over a fall time of t_w. The response of the bubble to a ramped pressure decrease is very similar to its response to a step decrease with a smaller t_w, approximately one-half for small pulse widths. The average pressure applied by a linearly decreasing pressure will be about one-half of that applied by a square wave with the same value of t_w. If changes in radius are small, this would translate into half the work done on the bubble, and half the energy imparted to the collapse. However, for large t_w, where the radius changes significantly during the pressure drop, the relative contribution of the first half and second half of the ramped wave to the kinetic energy of the system will be quite different, and average pressure will no longer accurately reflect the conditions of the collapse, but the behavior will reflect lower energy imparted to the bubble than the sudden pressure drop case for the same t_w.

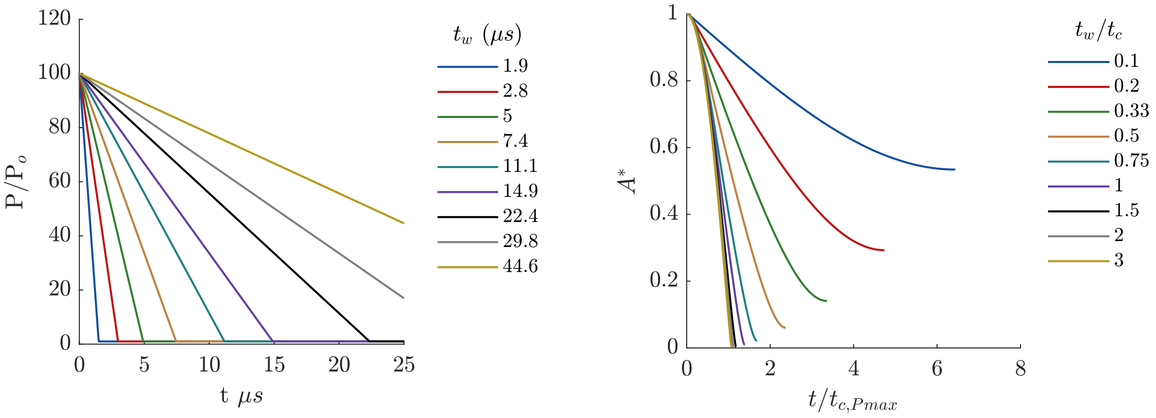

(a) Pressure traces for various rise times.

(b) Collapse in nondimensional units.

Figure 4.11: Loading pressure traces and collapse profiles for linearly ramped pressure rise with range of rise times. $P_{\max}/P_o = 100$

The acceleration components for the collapse of a bubble under a linearly decreasing pressure are presented in Figure 4.12, at the same t_w as in Figure 4.10 so that a direct comparison can be made, although due to the longer collapse time of the ramped case, the time coordinates are different. The decrease in pressure is apparent in the rapid dropoff of the P_L term in the ramped case. The $\dot{R}^2$ term never reaches the magnitude it does when constant pressure is applied for the entire duration, and P_g overtakes it much earlier in the collapse time, facilitating a gradual deceleration of collapse like the one seen for extremely low pressures.

4.8 Measured Pressures

The actual pressures presented in Section 3.5 can be applied to the differential equation as the P_L forcing function, and the behavior of the area of the bubble can be predicted. Figure 4.13 shows these predictions.

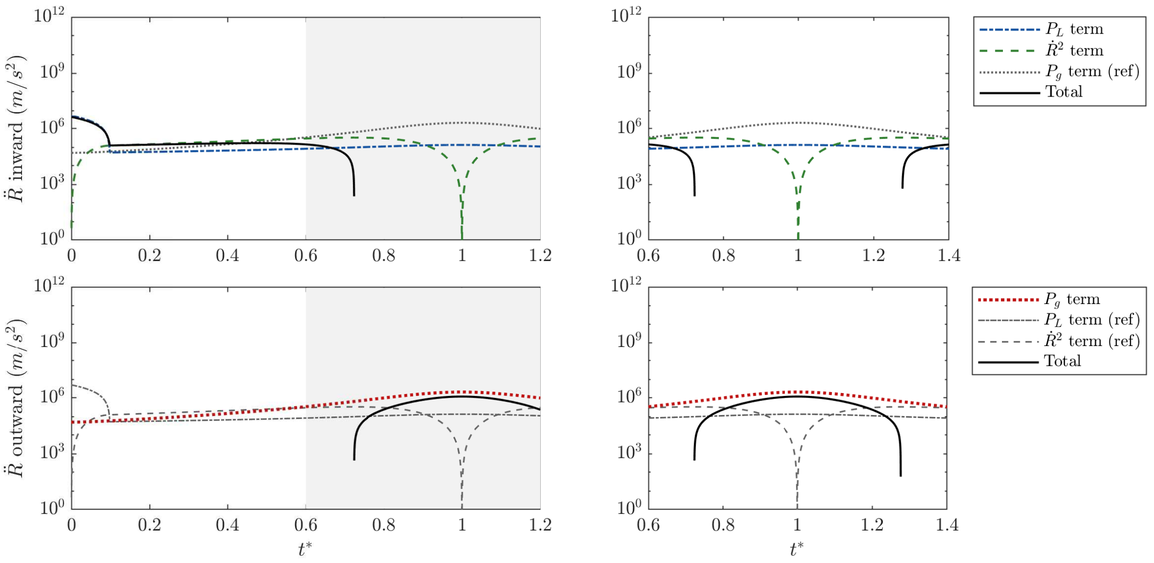

(a) Full collapse.

(b) Inset on end stage and early rebound.

Figure 4.12: Acceleration terms for collapse under square pulse with $P_{\max}/P_o$ of 100 and width $t_w = 0.33t_c$. Time is nondimensionalized by actual collapse time, $t^* = t/t_A$. Gray box indicates inset area. Gray lines are terms opposite in sign, for reference and comparison.

Although the peak pressure in some traces exceeds 20 MPa, the predicted collapse times fall in the range of 15–25 μs, which would be associated with constant pressures of 3.6–10 MPa per theoretical estimates. Because all pressure traces exhibit some finite rise time, the beginning of collapse is very gradual; in an experimental setting, a shorter collapse time might be found because area change would not be detectable for several microseconds. In fact, this is what is shown in Chapter 5; the collapse times and profiles found exhibit good agreement within this range. The decrease in the pressure loading occurs at times greater than one-half the collapse time, and decreases only to one-half the peak pressure. As a result, the effect of the pressure decrease is not readily apparent in the collapse behavior of the bubble. The predicted collapse times for these pressure traces appear to depend primarily on the properties of the initial pressure rise. The two tests where pressure rises in 10 μs or less have collapse times of less than 20 μs. Those where pressure rise takes ∼12—13 μs have collapse times of about 20 μs, and those where the rise time is 15 μs or more exhibit the longest collapse times of over 20 μs. The peak pressure of the tests with rise time longer than 15 μs is also lower than the tests with a rise time of less than 15 μs.

4.9 Conclusions

The process of cylindrical bubble collapse is shown to be sensitive to variations in the pressure loading temporal profile. If the collapse process for a given peak pressure applied for the entire duration of the

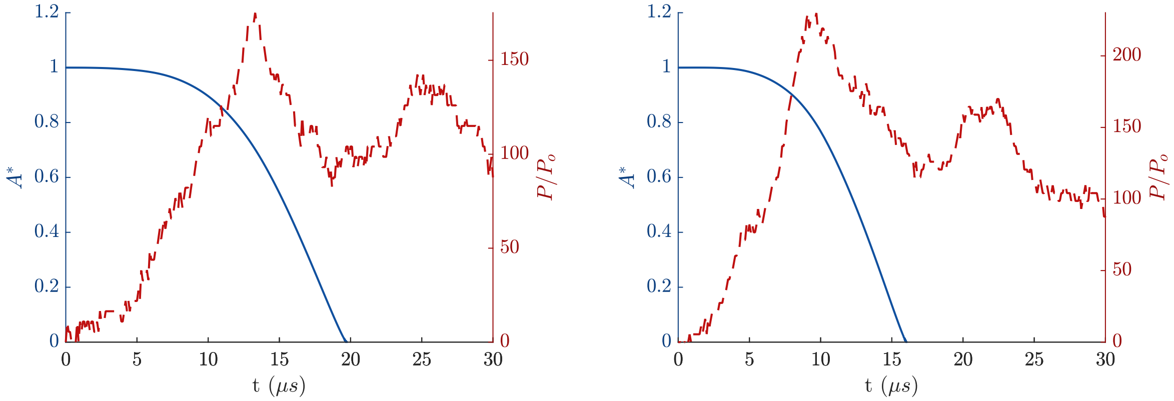

(a) Pressure Trace #1.

(b) Pressure Trace #2.

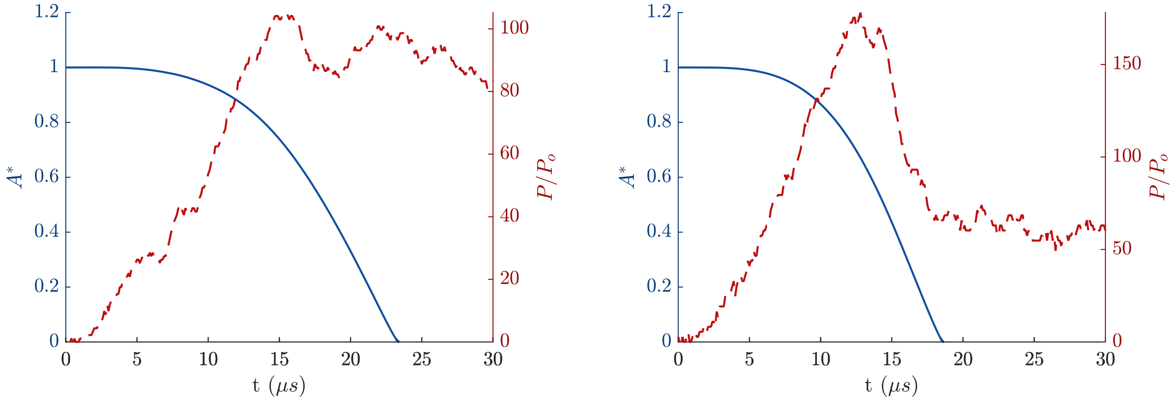

(c) Pressure Trace #3.

(d) Pressure Trace #4.

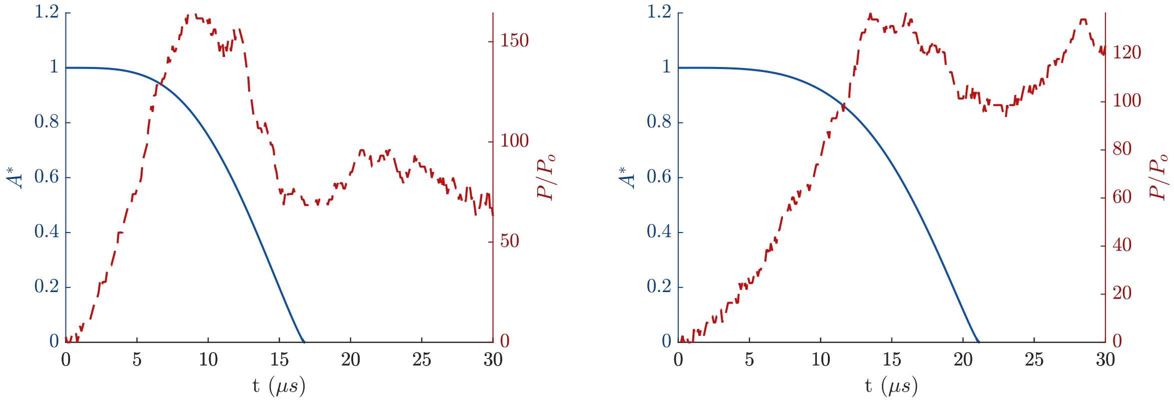

(e) Pressure Trace #5.

(f) Pressure Trace #6.

Figure 4.13: Predicted bubble area (in blue, solid; on left axis) under measured pressure loading (in red, dashed; on right axis). Rebound is not calculated.

collapse (P_L = constant = $P_{\max}$) is taken as a baseline behavior, applying a ramped profile that reaches $P_{\max}$ only at the end will extend the collapse time by virtue of the bubble collapse proceeding slower early in the collapse time; $\dot{R}$ will be low for small $t^* = t/t_c$. Late in the collapse time, $t^* \to 1$, $\dot{R}$ will increase to close to that of the baseline case, so the minimum volume and maximum pressure produced will be comparable to the baseline.

If the collapse begins with $P_L = P_{\max}$ and the pressure then decreases (either suddenly or gradually) before $t \approx 0.5t_c$, the collapse time will also be extended. In this case, $\dot{R}$ will be similar to that of the baseline case in early times, but when applied pressure is removed, no additional work will be done on the bubble, and it will not continue to accelerate as the baseline case does, so it will collapse slower than the baseline at the end of collapse. One result of this is that it will reach its minimum volume at a higher volume and lower pressure than the baseline case. The intensity of the collapse will be impacted.

If the collapse begins at $P_L = P_{\max}$ and pressure is only removed late in the collapse, after $t \approx 0.5t_c$, the change in the collapse time and collapse intensity will be minimal, because at late times the inertia term $\dot{R}^2$ dominates the differential equation, and a decrease in P_L does not significantly change the balance of terms in the equation.

The analysis in this chapter demonstrates that the response of a bubble to a pressure load cannot be predicted by peak pressure and bubble size alone; the time history of the pressure over the collapse time is important to predicting $R(t)$ and the actual collapse time t_A.

CHAPTER 5

ULTRA HIGH-SPEED SHADOWGRAPH VIDEO

Shadowgraph video of the collapse process recorded at 5 Mfps allowed collapse times of bubbles in various geometries to be measured and features of the collapse process to be identified. The formation of a re-entrant jet through the bubble center and the deformation of boundaries were features of particular interest as potential damage mechanisms. The area enclosed in the bubble was measured, and theoretical relations for symmetrical bubble collapse were used to predict the pressure acting on the bubble; the predictions agreed well with experimental measurements and computational predictions, suggesting that area change proceeds in the same way regardless of whether collapse is symmetrical or asymmetrical. A cross-section of the image stack through the centroid allowed the upstream boundary velocity to be estimated from the displacement; velocities in excess of 200 m/s were observed. This has the potential to produce pressures several times the applied pressure upon impact with the opposite interface.

5.1 Collapse Process and Features

Viewing the collapse in its entirety, particularly across a number of repeat tests, can help identify features of the collapse that may merit further study or quantification. 104 total videos were recorded across all conditions. Of these, 66 could be processed so that bubble outline was clear throughout the collapse (see Section 5.4, below). Snapshots from these 66 tests are presented in Appendix B, with only a few reproduced in this section as examples. The other 38 tests are not shown, but are included in statistics because the visual aberrations preventing the interior area from being properly resolved generally did not preclude other kinds of measurements.

Figure 5.1 shows the collapse of a single cylindrical, air-filled bubble in agarose gel; this is the simplest case of bubble collapse that was investigated and was considered a baseline for the behavior of other cases. The incident wave may be visible as intensity ripples at the bottom and top of the 0 μs frame, compared to the quiescent gel in the first frame (-30 μs). These ripples are likely caused by relatively large pressure gradients of short extent, caused by small amplitude pressure fluctuations over a short timescales and lengthscales, as suggested by pressure measurements described in Section 3.5. Under this interpretation, it becomes apparent that the leading edge of the pressure waveform has significantly passed the bubble, past the edge of the image, by the time detectable motion occurs. This suggests that pressure must rise to a sufficient

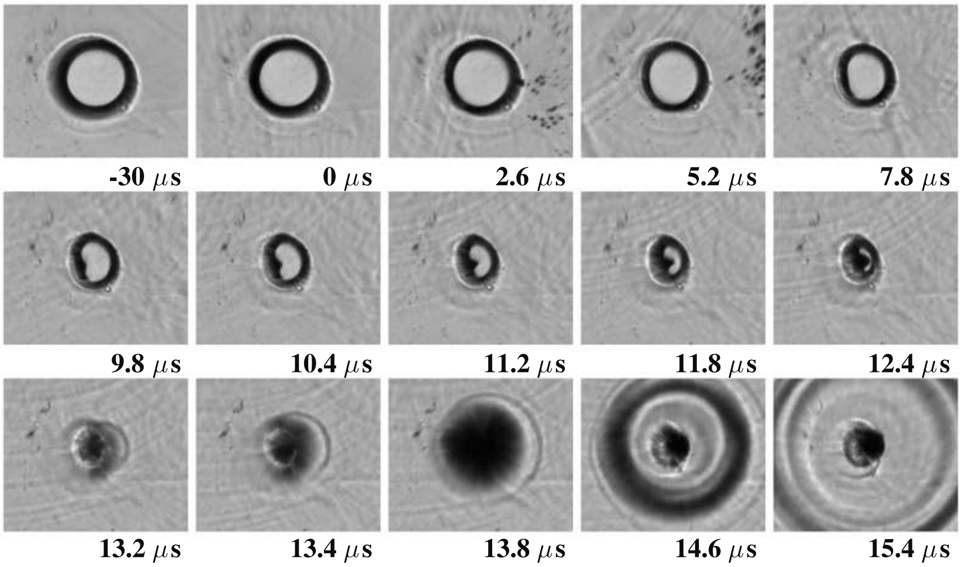

-30 μs **0 μs** **2.6 μs** **5.2 μs** **7.8 μs**

9.8 μs **10.4 μs** **11.2 μs** **11.8 μs** **12.4 μs**

13.2 μs **13.4 μs** **13.8 μs** **14.6 μs** **15.4 μs**

Figure 5.1: Collapse of a single cylindrical bubble in a homogeneous (agarose gel) environment. The frames are nonuniformly spaced in time, and cropped such that the bubble remains centered. The downstream bubble interface is stationary in the lab frame during collapse.

level, and/or persist for a sufficient amount of time, before observable bubble collapse begins.

At 2.6–5.2 μs, the upstream bubble interface is beginning to move and slightly flatten. Downstream, small black dots are observed. These are small cavitation bubbles on the surface of the gel due to a region of tension in the fluid, caused by fluid-structure interaction, described in Chapter 3. There is no indication that this effect has any influence on the bubble collapse process; all evidence suggests these cavitation bubbles are a surface effect taking place in a thin layer of water between the gel and PMMA sidewall. At 5.2 μs, a pattern of three dark lines is visible in the upper left quadrant of the image, seemingly emanating from the corner and just reaching the bubble between the upstream and topmost points on the interface. Although the clear intensity pattern suggests steep density gradients, it is important to recall here that the shadowgraph technique is very sensitive in water (Section 2.4) and that the highest estimate of the strength of waves reflected off the spacer bars yielded pressures of just a small fraction of the original wave (Section 3.4). There is no apparent acceleration of the impacted portion of the bubble interface after the arrival of this wave, which further confirms that in spite of its conspicuous appearance, this reflected wave is quite weak. Due to the relatively small thickness of the gel layer, waves reflected off the acrylic faceplates have a much greater effect on pressure state, but due to the orientation of the faceplates normal to the optical axis, these waves would appear as linear disturbances propagating longitudinally through the gel.

By 7.8 μs, the flattening of the upstream boundary is evident, and by 9.8 μs, a cusp begins to form which

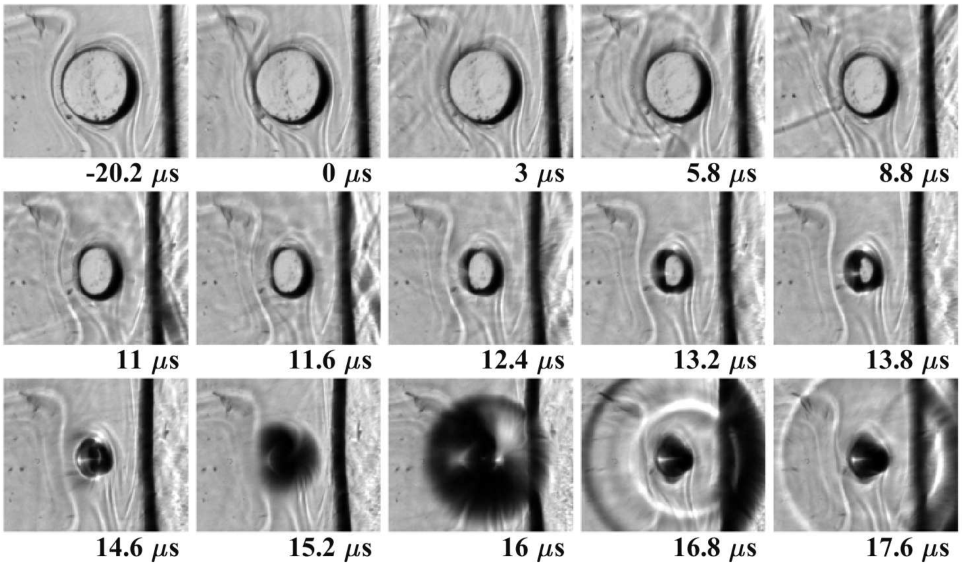

Figure 5.2: Collapse of a single cylindrical bubble near a downstream boundary with 20:1 PDMS. The frames are nonuniformly spaced in time, and cropped such that the bubble remains centered. The downstream bubble interface is stationary in the lab frame during collapse.

develops into a liquid jet across the bubble in the next 3 μs. The jet is about to impact the downstream interface at 12.4 μs. At 13.2 μs the bubble is at minimum volume and the collapse is complete. A wave is seen as a thin, dark line radiating from the apparent point of impact of the jet. During the next 0.6 μs, when the bubble is beginning its rebound, a circular region centered on the bubble darkens and the outer edge of the dark region expands. By 14.6 μs, the center clears again, and a multi-ring, expanding structure develops. While this phenomenon can be dubbed a “rebound wave” the physical mechanism that is actually generating these features is uncertain. This will be discussed in greater detail in Section 5.2.

Figure 5.2 shows the progression of the collapse for a bubble in agarose near a downstream boundary with 20:1 PDMS. The PDMS shows up as a lighter-colored material to the right of a black vertical line; agarose gel is the material surrounding the bubble. The collapse proceeds quite similarly to that of a bubble in homogeneous agarose: the incident wave is evident as slight intensity fluctuations from the second frame onwards (0 μs onwards), and although wavefronts appear to propagate at an angle in several frames, the bubble collapse does not appear asymmetrical, suggesting these are weak disturbances over short lengthscales, as discussed above. The bubble collapse takes a similar amount of time, and a rebound wave of similar characteristics is produced. The interaction of the incident and rebound waves with the boundary is, of course, new. The boundary exhibits increasing, slight curvature as the bubble collapses (0–14.6 μs), but the curvature appears completely rectified after the passage of the rebound wave (17.6 μs). This behavior is

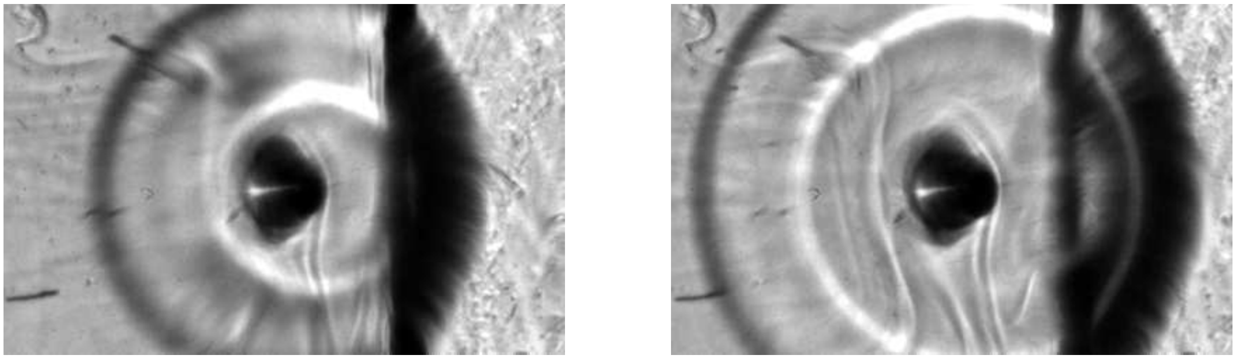
(a) 16.6 μs.

(b) 17.2 μs.

Figure 5.3: Asymmetry of rebound wave after collapse of bubble in agarose near boundary with 20:1 PDMS.

readily explained by the diffraction of the loading wave around the bubble: points along the boundary far from the bubble are accelerated, as they would be if no bubble was present, but the point on the boundary along the bubble centerline was shielded from the loading wave by the presence of the bubble, so it did not experience any acceleration until the rebound wave arrived. In between, a gradual transition between the two behaviors occurred. When the rebound wave propagates across the material boundary, it visibly changes speed, as evidenced by its increasing asymmetry as it continues to expand. Figure 5.3 shows two additional frames that have not been cropped in order to better demonstrate this. A faint reflected wave is also visible at 17.2 and 17.6 μs.

The most marked difference in the collapse in Figure 5.2 was that in spite of noticeable flattening of the upstream bubble interface observable from 11.0–12.4 μs, no jet is produced across the bubble, in contrast to the no-boundary case. This behavior was unexpected, as studies on bubble collapse near solid boundaries, as well as the more rigid gelatin and polyacrylamide boundaries, all demonstrated jetting toward the boundary, particularly when interacting with a wave traveling in the direction of the boundary [71, 75, 76, 85, 87, 88]. However, all these boundary materials had acoustic impedance (ρa value) greater than or equal to that of water (the fluid in all these studies). On the other hand, PDMS has an acoustic impedance of 70±3% that of water, suggesting that it may have an effect more similar to a free boundary than a rigid one (collapsing bubbles exhibit jetting away from a free boundary), if jet formation is driven purely by acoustic properties. The work of Brujan et al. and Kodama and Tomita suggests that strength and rigidity also play a role, but they do not define specific benchmarks [85, 88]. With these factors in mind, the absence of jetting may not be so unexpected after all.

Figure 5.4 shows the progression of the collapse for a bubble in agarose near a downstream boundary with 40:1 PDMS. The bubble in this case was slightly farther from the boundary (1.09 bubble diameters, compared to 1.03 for the collapse in Figure 5.2). The crack-like features on the upstream edge of the bubble are actually dust particles that contaminated the gel; aside from that small flaw, it is one of the best examples

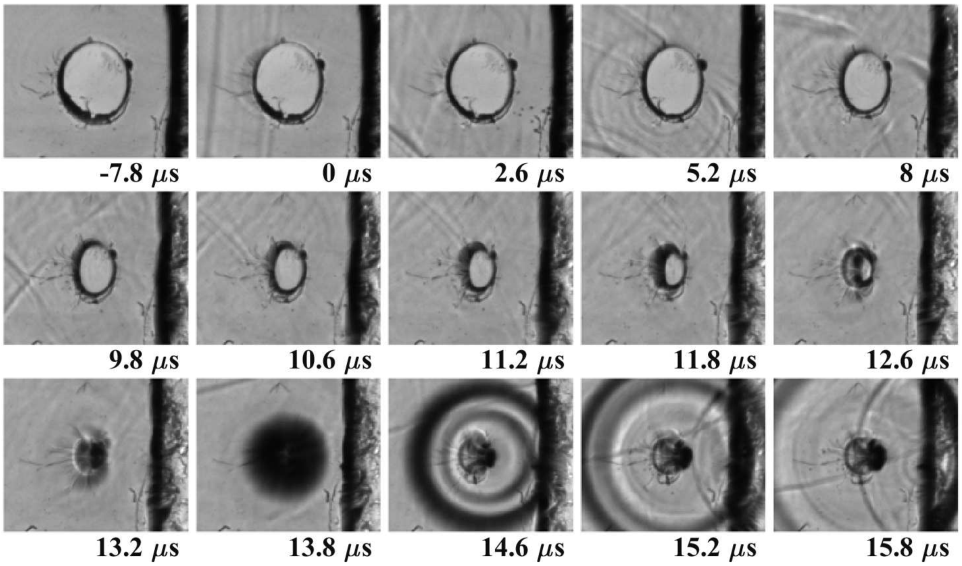

Figure 5.4: Collapse of a single cylindrical bubble near a downstream boundary with 40:1 PDMS. The frames are nonuniformly spaced in time, and cropped such that the bubble remains centered. The downstream bubble interface is stationary in the lab frame during collapse.

of collapse in this condition. Curvature of the boundary is not apparent in this case, perhaps because it is more irregular to begin with and curvature of the boundary is slight. Other than that, the collapse progresses similarly to the case with 20:1 PDMS, including upstream interface flattening from 10.6–12.6 μs, but no jet formation observed.

Figure 5.5 shows the progression of the collapse for a bubble in agarose near an upstream boundary with 20:1 PDMS. Initially, the boundary is 0.90 diameters upstream of the bubble center. In this test, a jet did form away from the boundary. This did not occur in all tests at this condition, but did in a few, as described in Section 5.3, below. The boundary deformation in this condition is much more extreme than in the downstream boundary case, and persists long after the collapse is complete, see Figure 5.6. The deformed portion of the boundary falls within a region where the fluid is accelerated first by the incident wave, then by a rarefaction wave reflected off the bubble interface. As a consequence, the upstream boundary closest to the bubble moves further downstream than the portion of the boundary only affected by the incident wave (the rarefaction wave weakens as it radiates outward until its effect is negligible).

Figure 5.7 shows the progression of the collapse for a bubble in agarose near an upstream boundary with 40:1 PDMS. Initially, the boundary is 1.0 diameter upstream of the bubble center. No jet forms in this collapse in spite of visible flattening of the upstream interface during the last 3 μs of the collapse, but the deformation of the boundary due to the rarefaction wave is nonetheless quite evident.

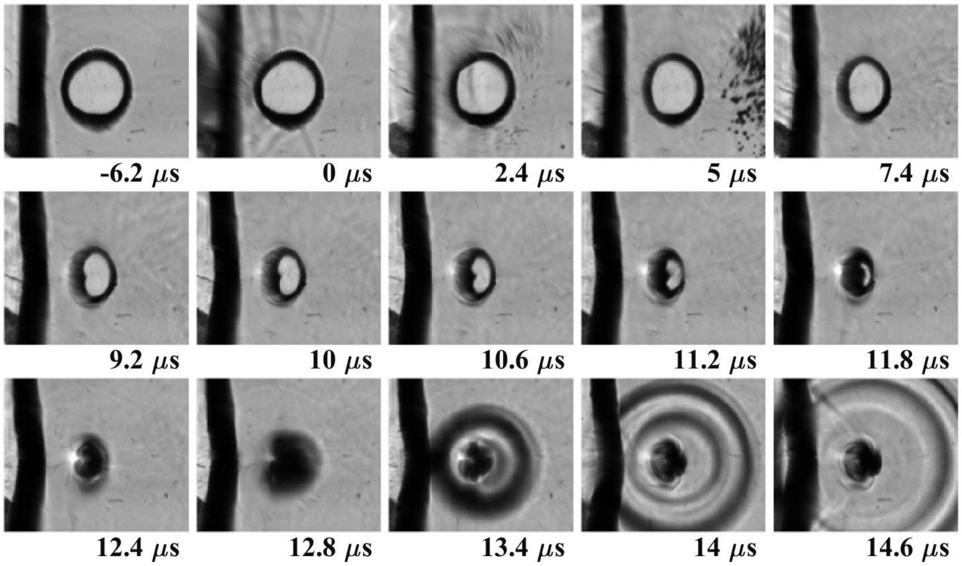

Figure 5.5: Collapse of a single cylindrical bubble near an upstream boundary with 20:1 PDMS. The frames are nonuniformly spaced in time, and cropped such that the bubble remains centered. The downstream bubble interface is stationary in the lab frame during collapse.

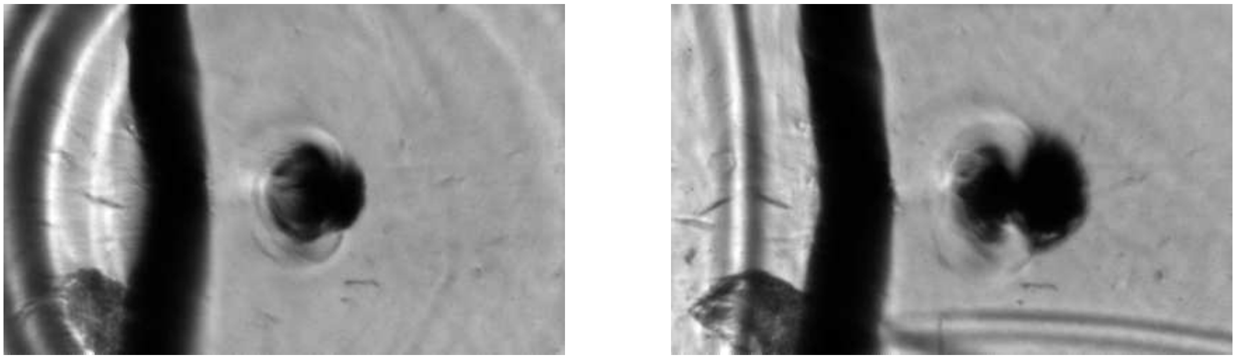

(a) 16.2 μs.

(b) 23.8 μs.

Figure 5.6: After collapse of bubble initially 0.9 diameters downstream of boundary with 20:1 PDMS, deformation in the boundary persists.

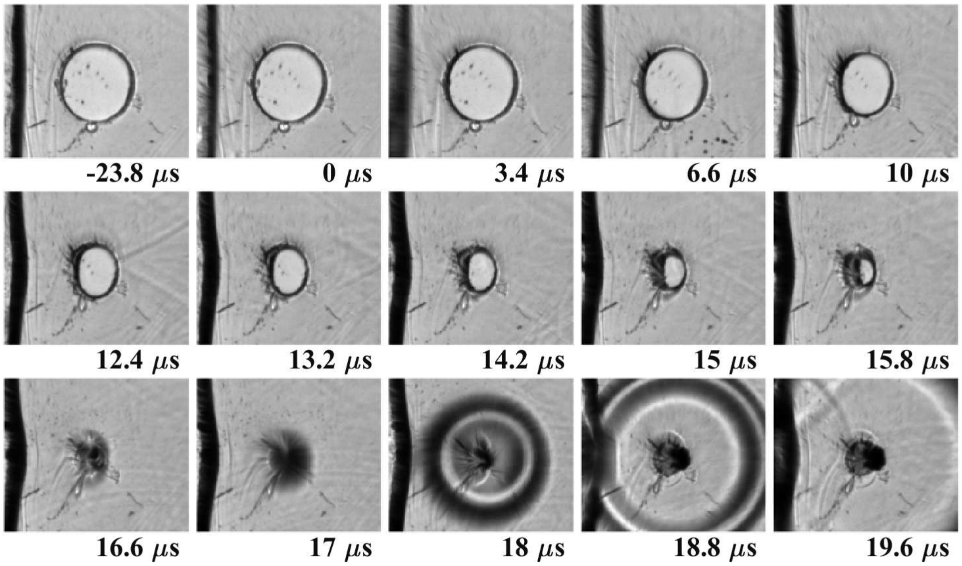

Figure 5.7: Collapse of a single cylindrical bubble near an upstream boundary with 40:1 PDMS. The frames are nonuniformly spaced in time, and cropped such that the bubble remains centered. The downstream bubble interface is stationary in the lab frame during collapse.

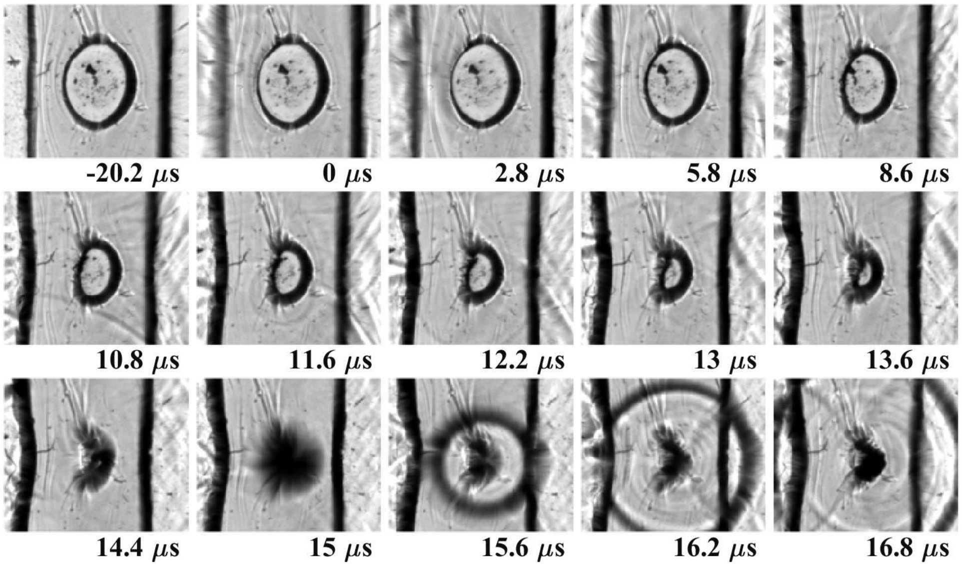

Figure 5.8: Collapse of a single cylindrical bubble between two boundaries with 20:1 PDMS. The frames are nonuniformly spaced in time, and cropped such that the bubble remains centered. The downstream bubble interface is stationary in the lab frame during collapse.

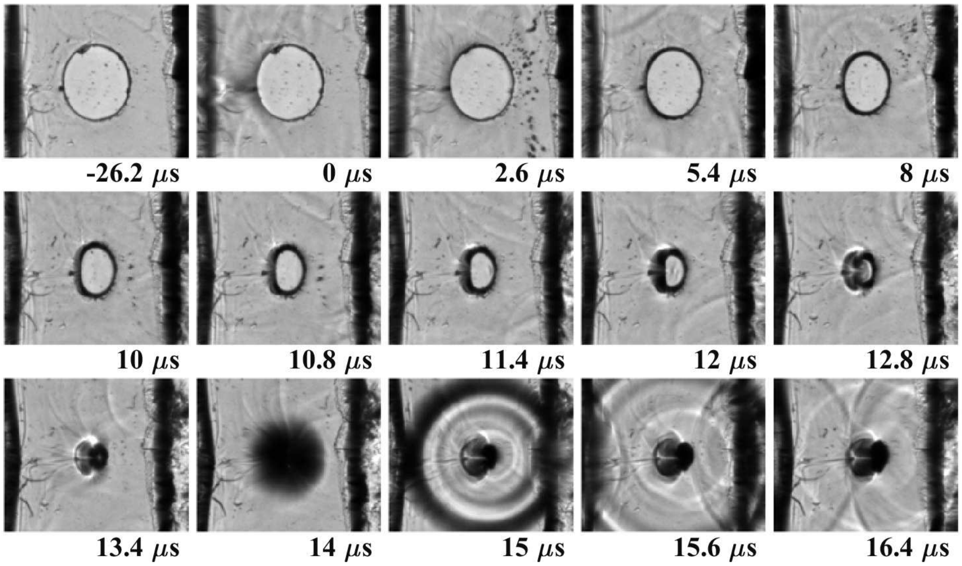

Figure 5.9: Collapse of a single cylindrical bubble between two boundaries with 40:1 PDMS. The frames are nonuniformly spaced in time, and cropped such that the bubble remains centered. The downstream bubble interface is stationary in the lab frame during collapse.

Figure 5.8 shows the progression of the collapse for a bubble in agarose between an upstream and a downstream boundary with 20:1 PDMS, a geometry intended to approximate a 2-dimensional version of a bubble in a small blood vessel. This sequence is presented to demonstrate the interaction of the bubble with both boundaries, which was particularly strong in this test due to the very narrow agarose channel width (1.7 diameters). The interaction of the bubble with both boundaries combines the effects of interactions with the upstream and downstream boundaries: the downstream boundary curves slightly as the bubble shields the center portion from the effect of the loading wave and delays its motion, and the center portion of the upstream boundary overtakes the edges as the incident wave reflects off the bubble interface as a rarefaction wave and accelerates nearby fluid into the bubble. The result, when viewed at the end of collapse (13–15 μs), is the formation of a “waist” on the channel, where the boundaries are displaced in toward the bubble on both sides. This “waist” is asymmetrical: the deformation on the upstream side clearly exceeds the deformation on the downstream side.

Unfortunately, although a very thin channel guarantees proximity between bubble and boundaries and yields well-pronounced boundary deformation, it also causes the oblong shape of the bubble (height-to-width ratio of 1.3). The slight pressure required to maintain good contact between agarose and PDMS on both sides flattens the bubble between the two boundaries. The oblong shape somewhat confounds direct comparison with more perfectly circular bubbles in other tests.

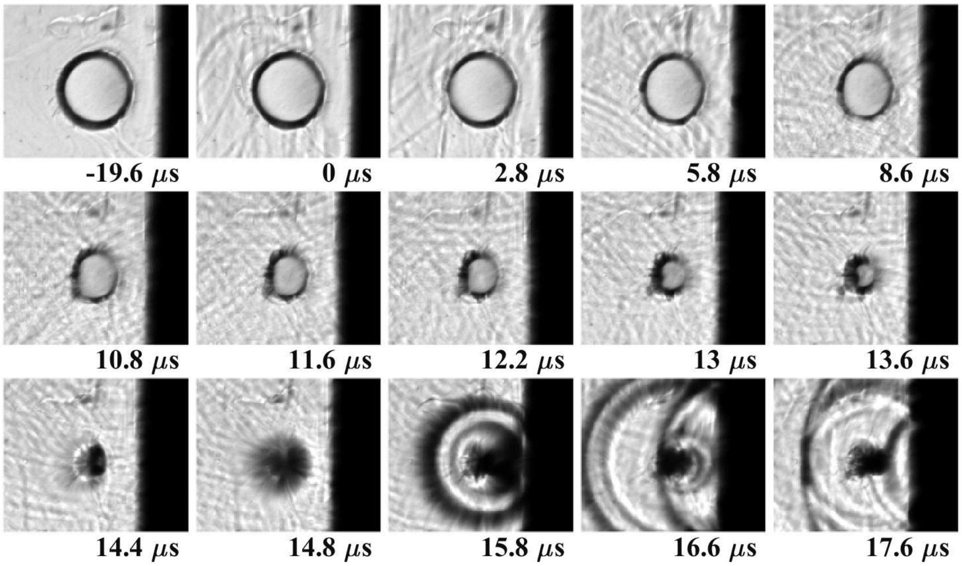

Figure 5.10: Collapse of a single cylindrical bubble near a downstream boundary with aluminum. The frames are nonuniformly spaced in time, and cropped such that the bubble remains centered. The downstream bubble interface is stationary in the lab frame during collapse.

Figure 5.9 shows the progression of the collapse for a bubble in agarose between two boundaries with 40:1 PDMS. The channel in this case is 2.4 bubble diameters wide, and the larger offset between bubble and boundaries led to a weaker interaction and less deformation in spite of the more compliant PDMS used, though some deformation of the upstream boundary is still apparent. The bubble is clearly much more circular initially than in the previous test shown (Figure 5.8), with a height-to-width ratio of 1.13. No jet is formed during this collapse, although the upstream boundary visibly flattens and the shape of the bubble is asymmetric.

For completeness, a series of tests with a downstream solid boundary (aluminum) were performed. An example of such a test is presented in Figure 5.10. In this case, a small jet forms between 13 and 13.6 μs, but in most such tests, if a jet formed it was so late in the collapse it could not be clearly discerned (see Section 5.3 for exact counts). This was unexpected, since even under uniform pressure loading, jets formed toward solid boundaries in similar studies [28, 71, 75].

5.2 Rebound Wave

There are a number of statements that can confidently be made about the rebound wave based on observations of the shadowgraph video data.

1. The wave originates at the end of collapse or beginning of rebound of the bubble.
2. The wave appears first as a dark circle, then as a series of concentric, alternating, dark and light circular bands in the image. This suggests a structure more complex than a simple shock. The circular bands narrow, the dark bands lighten, and the whole wave profile becomes thinner as the leading edge propagates outward.
3. Wave edges do not appear sharply defined during the first few microseconds of its propagation; they are characterized by an intensity gradient. This could indicate a characteristic length scale of the wave's structure, or be caused by its motion during the 100 ns exposure time.
4. In agarose, the wave propagates fairly symmetrically out from its origin.
5. The wave interacts with material boundaries. It slows significantly upon entering PDMS, breaking the symmetry it previously exhibited, and also emits a visible reflected wave in many of the tests observed. This reflected wave is faint, suggesting a weaker reflection. However, following bubble collapse near an aluminum boundary, the reflected rebound wave exhibits the same contrast as the incident rebound wave, consistent with wave reflection from a high acoustic impedance material. The transmitted wave, of course, cannot be observed in this case.

The velocity of the rebound wave can be estimated by tracking the position of the wavefront. Doing so requires making a somewhat arbitrary choice of what portion of the wave to track. Two methods were used: the first involved taking an averaged intensity profile from a narrow cross section of the image (30–50 px), then tracking the minimum corresponding to the outermost dark band of the wave, before applying a linear fit. 4 frames could be used to track the wave's vertical propagation, and 6 frames for horizontal, before the wave propagated outside the field of view. This method produced a velocity for each geometric extreme of the circular rebound wave: left, right, top, and bottom. These were then averaged.

The second method involved manually fitting an ellipse on the image to the interior of the first dark band, and measuring its area to calculate an equivalent radius. Figure 5.11 shows what this looks like for the test in Figure 5.1. The radius-time relation was then fit with a linear function. Although the placement of any individual point might have been less consistent, many more points were involved, allowing random errors to average out. Magnitudes of residuals were comparable between the two methods, suggesting they had similar validity. Residuals from both methods did not appear to have a functional dependence, indicating any attenuation of the leading edge of the wave either occurs very quickly before the first measurement point, or occurs over a much longer timescale than when the wave is in the field of view. The calculated velocities are presented in Table 5.1, along with several estimates of measurement error.

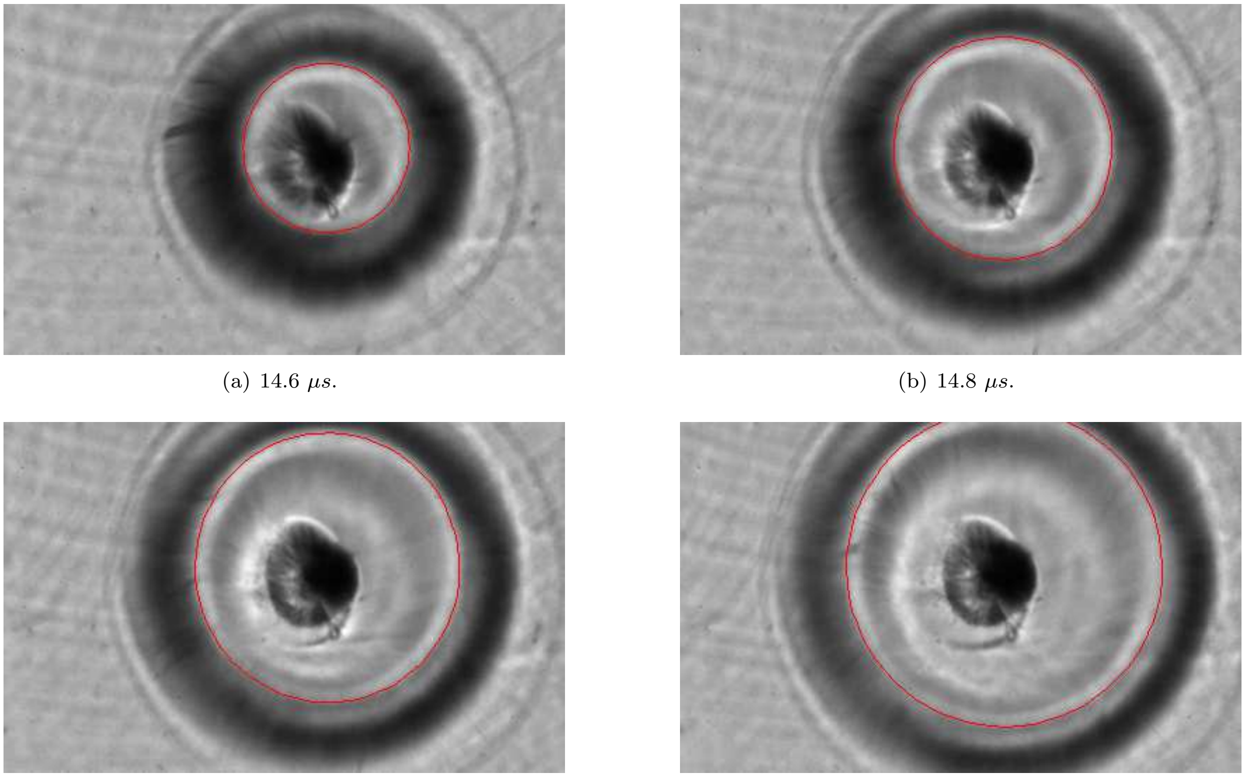

(a) 14.6 μs.

(b) 14.8 μs.

(c) 15.0 μs.

(d) 15.2 μs.

Figure 5.11: Propagation of rebound wave with fitted circles.

Table 5.1: Top half: rebound wave speed in agarose in m/s, obtained by tracking the left, right, top, and bottom extrema of the wave; also the average of these values, and the wave speed obtained by fitting a circle. Bottom half: standard deviation of wave speed across all tests (N=15, except N=10 for v_{cir}); average and maximum of standard error values calculated per Equation 5.1 for each line fit individually.

	v_L	v_R	v_T	v_B	v_{avg}	v_{cir}
Minimum	1520	1593	1566	1549	1601	1610
Maximum	1773	1769	1973	2116	1790	1816
Mean	1611	1642	1744	1764	1690	1693
σ	66	48	119	159	51	61
Mean SE	33	32	54	79	–	47
Maximum SE	57	61	92	235	–	110

Standard error for each of the linear fits was calculated from the relation [161]:

$$SE(v) = \sqrt{\frac{\sum(r - \hat{r})}{\sum(t - \bar{t})}} \tag{5.1}$$

where $\hat{r}$ indicates the radius predicted by the relation, and $\bar{t}$ indicates the average of included time values. These standard error values were computed for each test; the average and maximum (worst-case) values are presented. The standard deviation of all velocities of a particular kind was also calculated across all tests.

Virtually all calculated wave velocities fall in the range of 1500–2000 m/s, excluding the possibility the wave is propagating exclusively in the PMMA sidewalls (the longitudinal velocity of PMMA is about 2700 m/s, and the shear velocity is about 1400 m/s [162]). The fact that the wave clearly interacts with material boundaries between the plastic plates also supports this conclusion. Yet, it would be unjustified to immediately assume the wave is simply a representation of pressure and density changes in the gel components. FEA simulations showed significant, and rapid, deformation on the surface of the gel and PMMA. The dynamics that can occur here due to pressure in the fluid include: deflection of the gel and/or PMMA surface, delamination of the two surfaces, and the coupling of wave dynamics in the fixture and gel. Unfortunately, it is not possible to come to definitive conclusions about the conditions in the material around the wave without determining which of these mechanisms are taking place. Moreover, although it would seem all these behaviors would depend on the maximum pressure developed, the wave velocity does not correlate with the collapse time of the bubble, Figure 5.12. Collapse time was selected as a parameter characterizing collapse intensity.

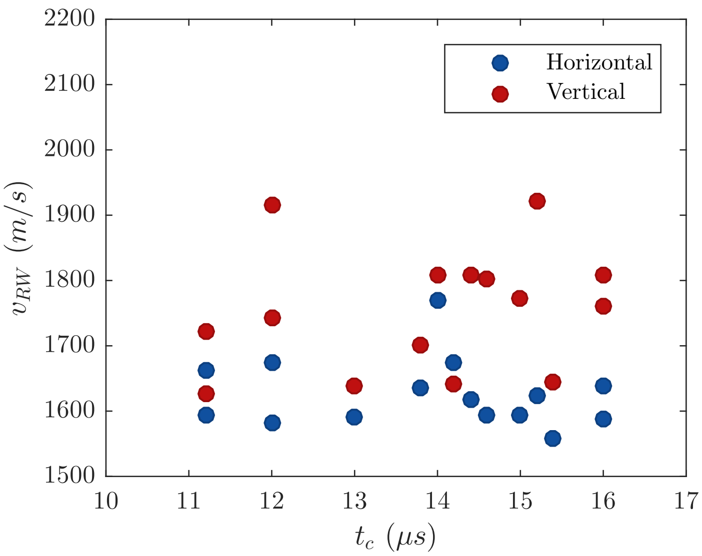

Figure 5.12: Wave speed determined from horizontal and vertical cross sections, variation with collapse time of respective test, showing no correlation. Wave speed measured from vertical cross section averages 8% higher than that measured from horizontal cross section.

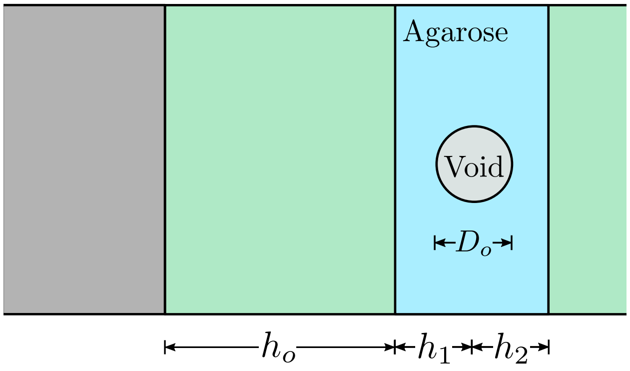

Figure 5.13: How geometric measurements of samples were defined. Not all measurements were possible for all tests, e.g. upstream boundary cases only had an h_1 parameter and the downstream boundary cases only had h_2.

5.3 Statistics

A number of properties were used to characterize each test. These included: geometric measurements, impact conditions, collapse times, and jetting behavior. A diagram illustrating the geometric measurements made is presented in Figure 5.13. A full test-by-test tabulation of these values is presented in Appendix C. Average values for each of the 11 test groups are summarized in Tables 5.2 and 5.3, below. Tests are grouped by geometry (the presence and location of a material boundary) and the material (other than agarose gel) involved. As shorthand, PDMS is simply indicated by P and then the proportion of base in the composition, e.g. P20 indicates PDMS mixed with a 20:1 base to hardener ratio.

Table 5.2: Summary of dimensions of samples for all tests, presented as "mean value (standard deviation)". The dimensions $D_{o,out}$–h_2 are measured from a pre-test photo (which included a calibration scale). D_o and H/W are measured from the first frame of the video.

Geometry	Mat'l	$D_{\mathrm{o,out}}$ (mm)	h_o (mm)	h_1 (mm)	h_2 (mm)	D_o (mm)	H/W
No Boundary	—	2.41 (0.12)	9.54 (0.53)	—	—	1.85 (0.13)	0.99 (0.06)
Upstream	P40	2.34 (0.13)	9.18 (0.48)	2.40 (0.32)	—	2.05 (0.10)	1.12 (0.09)
	P30	2.38 (0.09)	9.35 (0.44)	2.54 (0.29)	—	1.99 (0.10)	1.15 (0.11)
	P20	2.40 (0.18)	10.2 (0.73)	2.53 (0.36)	—	1.84 (0.22)	1.09 (0.09)
Downstream	P40	2.40 (0.08)	9.53 (0.55)	—	2.42 (0.20)	2.03 (0.08)	1.16 (0.10)
	P30	2.40 (0.06)	9.77 (0.28)	—	2.50 (0.18)	1.99 (0.11)	1.09 (0.06)
	P20	2.40 (0.09)	9.67 (0.40)	—	2.36 (0.36)	2.00 (0.14)	1.12 (0.08)
	Al	2.26 (0.08)	9.73 (0.30)	—	2.29 (0.06)	1.94 (0.10)	1.04 (0.07)
2 Boundary	P40	2.41 (0.07)	9.21 (0.47)	2.78 (0.23)	2.68 (0.10)	2.05 (0.05)	1.19 (0.08)
	P30	2.38 (0.12)	9.18 (0.50)	2.68 (0.39)	2.58 (0.32)	1.95 (0.18)	1.23 (0.13)
	P20	2.39 (0.10)	9.25 (0.29)	2.65 (0.20)	2.50 (0.37)	2.04 (0.05)	1.09 (0.06)
ALL		2.38 (0.12)	9.55 (0.56)	2.54 (0.32)	2.46 (0.30)	1.97 (0.15)	1.10 (0.10)

The dimensions of each sample are measured from a pre-shot photograph taken with the sample flat on a lab bench; however, the dimensions of the bubble are measured in three ways. First, the outline of the bubble can be identified in the pre-shot photo and the enclosed area measured to determine equivalent diameter. This measurement is consistent between samples and agrees well with the diameter of tubing used to make the bubble ($^3/_{32}$ in or 2.38 mm). The bubble can also be measured directly in the first frame of the shadowgraph video. However, the shadowgraph technique causes small imperfections of the cylindrical bubble edges (curvature, barreling, small bead of water) to show up as significant thickness of the bubble interface, as seen in the video snapshots in Section 5.1. Therefore, in the video the outside or the inside of this outline can be measured. While the outside generally correlates better with the measurement from the pre-shot photo, the inside ("see-through" area) is least subject to disturbances from passing waves and therefore most feasible to track reliably for area measurements (see Section 5.6, below). Therefore, the pre-shot measurement is identified as $D_{o,out}$ whereas the inside as simply D_o.

The measured dimensions show good consistency both within and between test groups, particularly in the $D_{o,out}$ and h_o parameters which only vary by about ±5%. These would translate into less than ±1 μs

variations in wave arrival and collapse time respectively (assuming both scale linearly with the dimensions involved). Variations in h_1 and h_2 approach ±15%, or a third of a millimeter in absolute terms, which may well be the practical limit of accuracy for these manufacturing techniques. The mean values are quite close to $D_{o,out}$, as was intended. The inner diameter of the bubbles averages 17% smaller than the outer, and varies similarly to $D_{o,out}$, which suggests the variation in D_o primarily reflects slight variations in bubble size, and is not significantly distorted by the visual effects that create the wide interface.

The aspect ratio varies more significantly, ranging from about 1 (the ideal) to over 1.3 in several cases, which represents a noticeable degree of oblateness (see Figure 5.8). This occurs because in many tests, light pressure must be applied to the sample to maintain good contact between agarose and PDMS layers, and the soft materials used deform easily. When the bubble is located close to the edge of the agarose piece, the thin section of agarose deforms more readily than the surrounding gel, causing the bubble to stretch in a direction parallel to the boundary. This phenomenon is concerning, as other studies have tied jet formation and collapse dynamics generally to local boundary curvature [33, 87, 88]. Given that average aspect ratio varies between groups, it will be important to consider as a factor driving collapse mechanics.

The pressure applied during sample assembly may also explain the slightly lower diameter measurement obtained near an aluminum boundary. Some pressure is always applied during assembly to avoid air gaps on the gel surface as well as establish contact between materials. The softer materials relax over the hour-long timeframe while the sample is being prepared, but aluminum provides rigid confinement and evidently enough pressure builds up in the fixture to compress the bubble by 0.1 mm (5% diameter or 10% volume). This would increase pressure by 30% which is not significant next to the >10 MPa pressure the bubble experiences in the experiment. The diameter variation is also still within the range of variation in the other tests, so the compression of the bubble in this case was not expected to have a significant effect on the results.

The characteristic properties of the impact and collapse are presented in Table 5.3. The average impact velocity across all tests is 25.9 m/s with a standard deviation of 0.4, or less than 2%. This translates into a pressure variation of at most 0.6 MPa in the maximum pressure that is typically in excess of 15 MPa (see Section 3.5). Such fluctuations are not expected to produce significant effects on any measured aspects of collapse.

In spite of the consistency of impact conditions, the time of initiation of collapse varies by as much as 7.5 μs. A small part of this may be explained by the dimensions of the geometry (<1 μs). Positioning of the sample is accurate to ±25 μm, which accounts for about 2 μs variation at most. Striker length, fixture sidewall thickness, and electronics response time showed excellent consistency, making those sources of timing error unlikely. The last, speculative, explanation under consideration is that small variations in thickness of the bar stock used for aluminum strikers and spacers affect the clamping force and subsequently the acceleration profile of the striker. This, in turn, would explain the observed test-to-test variations in pressure profile as well as collapse initiation time. However, no satisfactory way to test this theory has been

Table 5.3: Summary of impact and collapse time conditions for all tests, presented as "mean value (standard deviation)". Values in brackets indicate the number of tests in the group for which jetting behavior could not be clearly identified. ^{ss} indicates the collapse time exhibits a statistically significant difference from that observed for agarose, with 95% confidence. (Procedure from [161] was used to determine confidence interval for two samples with unknown, unequal variance.)

Geometry	Material	N	Jet : No Jet	v_I (m/s)	$t_{c,o}$ μs	$t_{c,f}$ (μs)	t_c (μs)
No Boundary		15	12:2 [1]	26.0 (0.4)	25.5 (5.0)	39.4 (5.9)	13.9 (1.6)
Upstream	P40	10	2:7 [1]	25.9 (0.2)	26.7 (7.6)	42.9 (8.4)	^{ss}16.2 (2.5)
	P30	13	3:7 [3]	25.6 (0.3)	24.3 (6.9)	37.8 (5.8)	13.5 (2.0)
	P20	10	5:2 [3]	25.7 (0.5)	28.7 (5.1)	42.2 (4.6)	13.5 (1.3)
Downstream	P40	8	1:4 [3]	25.7 (0.3)	18.2 (3.4)	32.4 (5.3)	14.2 (3.1)
	P30	11	4:7 [0]	26.0 (0.3)	19.9 (7.5)	36.3 (8.7)	^{ss}16.4 (2.2)
	P20	12	4:8 [0]	25.9 (0.3)	23.4 (6.2)	40.4 (6.5)	^{ss}17.0 (3.3)
	Al	8	2:1 [5]	26.2 (0.3)	30.5 (4.3)	46.3 (4.2)	^{ss}15.8 (1.9)
2 Boundary	P40	6	1:4 [1]	25.9 (0.2)	32.8 (5.7)	49.0 (7.2)	16.2 (3.7)
	P30	5	1:4 [0]	25.8 (0.3)	29.6 (5.0)	44.0 (5.5)	14.4 (3.2)
	P20	5	0:3 [2]	25.9 (0.2)	29.6 (6.2)	45.4 (5.4)	15.8 (2.9)

devised, and these variations remain unexplained.

The collapse time for each test group can very by as much as ±20%. This would be explained by a roughly ±40% effective pressure difference. Average pressures measured in the fixture ranged from 7-11 MPa, a ±22% fluctuation (which would explain a ±11% fluctuation in collapse time). This is actually roughly what is observed in the no boundary case. In the other 10 test groups, the presence of boundaries introduces other variables (h_1, h_2, H/W) that may play a role in the scatter of the collapse time data. However, since it is not yet clear exactly how compliant boundaries affect the collapse of bubbles, it is essentially impossible to estimate how much a 20% fluctuation in offset distance is expected to change that behavior.

The data collected for this study can start to answer what effect the compliant boundaries have on the collapse. Analysis followed a standard procedure for evaluating confidence intervals on the difference of two means with unknown variances [161]. A statistical test parameter T_o^* was introduced,

$$T_o^* = \frac{\mu_{XB} - \mu_{NB}}{\sqrt{\dfrac{\sigma_{XB}^2}{N_{XB}} + \dfrac{\sigma_{NB}^2}{N_{NB}}}} \tag{5.2}$$

where μ is the mean of the quantity of interest (in this case, t_c), σ is standard deviation of values in the sample, and N is number of tests in the sample. Subscript NB indicates the no boundary test group, whereas XB indicates an arbitrary boundary test group (e.g. UB20). This test parameter is expected to be distributed as Student's t-distribution [161] with the degrees of freedom (DOF) found by:

$$DOF = \frac{\left(\sigma_{XB}^2/N_{XB} + \sigma_{NB}^2/N_{NB}^2\right)}{\frac{\left(\sigma_{XB}^2/N_{XB}^2\right)}{N_{XB}-1} + \frac{\left(\sigma_{NB}^2/N_{NB}^2\right)}{N_{NB}-1}} \tag{5.3}$$

from these two values, a probability that the two means are equal can be found using tables or software to evaluate the t-distribution (Microsoft Excel was used [163]). The values of t_c marked with ^{ss} in Table 5.3 had a p-value of less than 0.05, indicating low probability that the values are equal (and therefore high probability they are not). However, the numbers of tests in each group are quite low for statistical analysis (particularly for the two boundary cases). A better approach may be to note that no clearly defined (or statistically significant) difference arises between tests with different PDMS compositions, and pool the tests of each geometry together (excluding the downstream aluminum boundary tests). In this case, the upstream and downstream groups have about 30 tests each, much more appropriate for statistical analysis. The upstream boundary pooled mean t_c=14.3 μs, giving p=0.37 of being distinct from the collapse time of agarose, and downstream boundary pooled mean t_c=16.0 μs, giving p<0.0002. The two boundary case, with only 16 total tests (still low for statistics), gives a mean t_c of 15.5 μs and p=0.15, indicating a possible difference in need of additional tests for verification.

All in all, the statistics on this data set support the conclusion that collapse time is reduced for bubbles 1.01±0.12 radii upstream of a compliant or rigid boundary, but not affected for bubbles 1.05±0.14 diameters downstream of a boundary. Different offset distances or material properties outside the range considered may well change whether a significant difference is observed. In fact, this may explain why the upstream-P40 case shows a statistically significant decrease in collapse time—the bubble is on average 0.14 mm (6%) closer to the boundary.

This data set does not show any significant correlation between aspect ratio, collapse time, and jet formation. To demonstrate, a plot is presented in Figure 5.14. Although it does appear that jetting does not occur for bubbles with aspect ratio above 1.2, it is important to note that all these cases occur in test conditions where jetting is observed in few tests overall.

5.4 Image Processing

5.4.1 Processing Algorithm

In evaluating the shadowgraph videos, two quantities of great interest were the evolution of the bubble area with time, and the evolution of bubble shape with time. These measurements could be used to in-

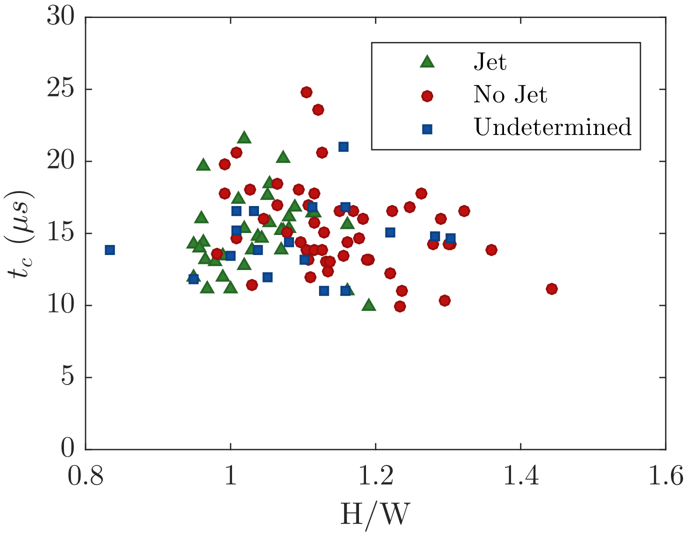

Figure 5.14: Effect of aspect ratio on collapse time and jetting behavior for all tests.

form the analysis of PIV data, predict maximum generated pressure (from jet velocity), compare results with theoretical predictions, and compare with the work of other researchers who had reported the same quantity [33, 36, 76]. Of course, acquiring this data required identifying the coordinates of every point on the bubble interface in each frame, a total of at least 5000 frames to process. As such, automated digital image processing was a necessity. The image needed to be binarized so that objects could be identified and analyzed with subroutines in MATLAB [164].

Ideally, a simple constant threshold would be sufficient to identify the dark outlines of the bubble and boundary. However, it should be apparent from images presented in Section 5.1 that identifying the boundary was not always so straightforward. Processing the images presented certain challenges, specifically:

- Physical contaminants such as dust and droplets would be binarized with the interface or boundary and distort its shape and the bubble size.
- Optical effects due to propagating waves (including the incident wave and the shock wave inside bubble) interfered with physical features, darkening or lightening them. With simple thresholding, this would cause a break in the bubble interface outline.
- There were variations in background intensity test-to-test and also within an image, due to the appearance of the incident wave and small physical contaminants.
- The bubble interface also varied in its appearance. Small off-axis shifts made one location on the interface appear thicker, and the location opposite, thinner. The apparent thickness varied in general from test-to-test, presumably based on small variations in manufacturing; curvature of the corner of the gel between the bubble and the surface would cause an interface to appear wider and darker. A

bead of water between the inside surface of the cylinder and the PMMA sidewall was observed to do the same (extreme examples of this were excluded from analysis, because the apparent shape and size of the bubble were distorted by the water).

- Passing fronts of the incident wave tended to introduce some local blur. While generally not a problem, interference between the wavefront and a very thin bubble interface lightened the color and blurred the intensity gradient around the interface, making it difficult to detect.

Given these challenges, it was necessary to apply judgment on a case-by-case basis to bring out the desirable features from each sequence. Consistency within each image sequence was valued above consistency between image sequences, since they exhibited so much variation to begin with. The general procedure for binarizing the images using ImageJ software [153] was as follows:

1. A Gaussian blur with radius 2 was applied to eliminate high-frequency content in the image, such as small dust or incident wave fronts.

2. An unsharp mask with radius 3 and mask of 0.75 was applied. This was found to help bring out edges and gradients, thus helping identify lighter portions of the bubble interface.

3. If the rest of the procedure was followed and a clear outline was not produced, a test was reprocessed with Gaussian blur and unsharp mask applied twice, sequentially. This further helped darken the outline and blur out undesirable image features.

4. In some particularly difficult tests, adjusting contrast to saturate the free-field and inside of the bubble helped the thresholding algorithm bring out the interface more effectively.

5. Local thresholding was applied using the Sauvola method with a radius of 30. This method adjusts the threshold value based on the mean and standard deviation of the local neighborhood of pixels and is described in more detail below.

6. Small particles were removed to clean up the appearance of the image, using the "Analyze Particles" tool.

7. In some cases, a few frames were adjusted manually to remove a stubborn droplet, speck, or bright spot, referencing the original image, to allow the image sequence to be used. This essentially amounted to manually identifying features, which has precedent in similar work [33]. This process was estimated to generate up to 5% error in a worst-case scenario (bubble down to 840 px, or 10% of its original area, a $^{\pi}/_{6}$ sweep of 8 px of the boundary reconstructed with an error of 3 px for the whole length).

The Sauvola local thresholding method compares the value of each pixel with a threshold value based on

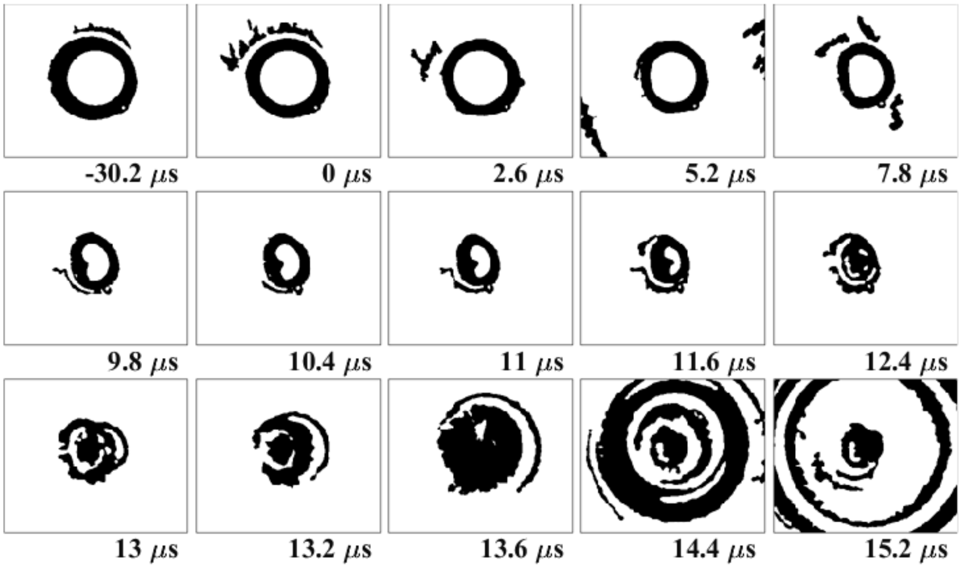

-30.2 μs
0 μs
2.6 μs
5.2 μs
7.8 μs
9.8 μs
10.4 μs
11 μs
11.6 μs
12.4 μs
13 μs
13.2 μs
13.6 μs
14.4 μs
15.2 μs

Figure 5.15: Binarized frames from the collapse in Figure 5.1.

properties of its neighborhood [165, 166]:

$$\text{threshold} = \mu_I \left(1 + k \left[\frac{\sigma_I}{q} - 1\right]\right) \tag{5.4}$$

where μ_I indicates mean and σ_I indicates standard deviation of image intensity in the local neighborhood of the pixel. The threshold thus ends up lowered to $1-k$ times the mean in areas where intensity variation is high (such as near the boundary) and increases toward the value of the local mean where the variation is low. The parameter q controls the degree of dependence on the standard deviation (note that both ImageJ and Sauvola refer to this parameter as r, but this convention is confusing in the context of this work). Some images were processed using k=0.15 and setting q to the standard deviation of the image; it was later found that k=0.3 and q=64 produced good results on more challenging images. Earlier images were not re-processed, since the features of interest were already well-identified.

An example of a sequence of binary images is shown for reference in Figure 5.15. Only the frames where the bubble interface encloses an area are used for quantitative data.

5.4.2 Sources of Uncertainty

One of the largest sources of uncertainty stems from the apparent thickness of the bubble interface in images. This can originate from a number of physical imperfections of the system, as imaged by the shadowgraph optics. One reason the interface can appear thicker is if the circular edges at the surface of the gel are rounded, or a small bead of water expressed from the hydrogel is present along the edge; curved surfaces from either cause will deflect light rays, creating a dark zone. Another reason is nonuniformity of the bubble cross-section in the thickness direction (along the optical axis). In some cases, the cylindrical bubble was cast in the gel at a slight angle, and the tilt of the edges relative to the optical axis created additional apparent interface thickness, predominantly in the direction of inclination. In other cases, uniform broadening of the interface was possible due to outward or inward curvature of the walls of the cylinder; this could occur due to loads applied in the assembly process. Instead of a cylinder, with the volume proportional to the see-through area, the bubble would then be shaped like a barrel (wider in the center plane) or have a waist (narrowing at the center plane), and the actual volume would be proportional to an area between those defined by the inner and outer outlines.

The bubble outline in initial video frames averages 11±5 pixels in thickness, which accounts for 18±8% of the bubble's radius. The annulus defined by the outer and inner outlines of such an average boundary accounts for 34±16% of the area within the outer boundary. The inner outline was selected for identifying the bubble cross-section for two primary reasons: it is much more consistent as a measurement, due to suffering less optical distortion from passing wavefronts and surface cavitation bubbles, and it clearly shows the development and propagation of the transverse jet, when one occurs. As a consequence of this choice, the area measurement is a lower bound of bubble cross-sectional area; the outer outline, when it can be discerned, defines an upper bound. The bubble outline thickness remains constant during the collapse process, or decreases by a small amount after the arrival of the wave; the outer outline does not remain stationary or move significantly slower than the inner. Tests with extreme apparent thickness of the interface (annulus comprising >40% of bubble area), were not used for area data due to the more pronounced differences in behavior between inner and outer outlines. Many tests with extremely thin bubble interface appearance also had to be excluded, as very thin interfaces did not provide sufficient contrast to be identifiable along the entire perimeter. Interaction with intensity fluctuations due to passing wavefronts exacerbated this effect.

One of the main reasons to study the initially-cylindrical bubble rather than the initially-spherical bubble is to maximize the visibility of features inside the bubble and minimize distortions. However, it was known from numerical modeling (Chapter 3) that the acrylic sidewalls deformed as much as 0.1 mm along the optical axis. The curvature of the inner surface of the sidewall in this way would act as an optical lens; therefore, it was important to consider how this might distort the final image.

The deformation of the surface was modeled as a spherical cap with a height of 0.1 mm and a diameter of 20 mm; this requires a constant radius of curvature of 502.6 mm. Using the small angle approximation,

$\sin\alpha = \alpha$ for small angles α, the angle of the surface is then given by $r_p/503$ where r_p is the distance from the center of the spherical cap to the point in question, in mm. The maximum angle of interest is therefore 10/500 radians, or 1.14°.

The propagation of light rays through both surfaces of the acrylic sidewall was modeled by Snell's law [167],

$$n_1 \sin\alpha_1 = n_2 \sin\alpha_2 \tag{5.5}$$

where α is the angle of the light ray to the surface normal and n is the index of refraction in the material indexed by the subscript. The indices of refraction for gel(water), acrylic, and air were taken as 1.333, 1.489, and 1.00029 respectively [146, 147, 168]. Light rays initially entering along the optical axis of the system will be deflected away from the centerline (of the spherical cap) by $0.00021r_p$ radians/mm within in the acrylic plate, and by $0.00031r_p$ radians/mm upon entering air.

During the 25.4 mm it travels through the acrylic faceplates, the light ray is deflected 0.06 mm at the maximum r_p value of 10 mm. This is about 2.5 pixels on the typical video frame. However, this figure is relative to an undisturbed light ray, but if the face plate over the bubble is deformed, the entire bubble image will be affected by the disturbance. Across the 2.5 mm bubble diameter, the difference in light deflection can be expected to be a quarter of the maximum value, or less than 1 pixel.

After propagating through the acrylic plate, the light ray leaves the outer surface at an angle of $0.00031r_p$ radians/mm. Along this trajectory, the rays would appear to converge to a point 1/0.00031 mm, or 3.23 m, behind the surface of the fixture. Effectively, the plastic plate with a deformed inner surface is acting as a diverging lens with very long focal length. Inserting an additional lens into the focusing optics on the far side of the shadowgraph setup could potentially defocus the image. However, adding a lens with such large focal length just 2.4 mm from the object plane (the center plane in the gel), without changing the locations of the other optics, only changes the location of the final image plane by 0.004 mm out of 1250 mm, as determined with simple geometric optics. This degree of defocusing would not be observable in the final image, and is quite certainly below the precision in focusing the undisturbed system.

The optical disturbance caused by the deformation of the fixture is, therefore, not of significant concern with regards to uncertainty in the data. Deviation of the physical system from the assumed cylindrical geometry plays a much greater role in the uncertainty of area measurements from video images.

5.5 Thermal Effects

One of the mechanisms of damage associated with cavitation is the high temperatures that can be generated by the compression within the rapidly collapsing bubble. Under the right conditions of bubble size and applied pressure, temperatures can become sufficiently high that the gas in the bubble emits light, a phenomenon known as sonoluminescence [33]. The heating has also been implicated in the initiation of detonation in energetic materials [30]. Although thermal effects specifically were not the primary objective of this experiment, and no specialized techniques were used to attain temperature or heat transfer data, some benchmarks for the thermal effects involved can still be deduced.

Isentropic compression is frequently used to model the temperature rise within the bubble [33]. This is not applicable for very strong shocks, as demonstrated through numerical simulation by Ball et al., because repeated shock processing of the gas within the bubble can significantly increase the temperatures attained [36]. Conversely, Hickling demonstrated through an analytical formulation (and a finite-difference numerical solution) that in very small bubbles filled with non-condensable gas, the presence of extreme temperature gradients makes heat transfer significant and decreases the temperatures developed substantially below the adiabatic estimate [169]. In all cases, heating of the ambient fluid (water) is largely ignored, due to its relatively high value of thermal diffusivity compared to the gas, a difference driven primarily by the much lower density of the gas, and thus applicable to most solid substances. Hickling's analysis includes the case of a 1 mm nitrogen bubble in water, collapsing under a pressure ratio of 40. He finds that in this case an adiabatic model of gas heating is appropriate up to a radius of $0.3R_o$, which would correspond to 2.7% of the initial volume [169]. It is straightforward to show that the properties of air are sufficiently similar that this result holds for air as well, even for a higher pressure ratio of 150.

On this basis, the isentropic compression model is assumed adequate for modeling the temperature rise in the bubble during the experiment [36]:

$$\frac{T}{T_o} = \left(\frac{V}{V_o}\right)^{1-\gamma} \tag{5.6}$$

Here, T and V represent gas temperature and volume respectively, subscript o indicates the initial state, and γ is the specific heat ratio (1.4 for air).

The volume ratio can be estimated from the minimum observed bubble area. Treating the cylinder of this cross-sectional area as an upper bound on the smallest volume can give a minimum temperature the gas is expected to reach. The smallest observed areas range from 5–20% of the original bubble area; the same ratio is applicable to cylinder volumes. The 5% value yields a temperature of 970 K (for $T_o = 293$K). However, the pressure ratio predicted by the same volume fraction is only 66.3 (or a pressure of 6.7 MPa). In many cases, the applied pressure ratio is expected to be over 100 at the end of collapse (or even over 150, see Section 4.8), and to arrest the collapse of the bubble, the pressure inside must rise higher than the external pressure. Taking a conservative estimate of 15 MPa as the pressure developed inside the bubble yields a volume ratio of only 2.8%, and a temperature of 1230 K. This is a more realistic lower bound for the temperature developed.

An upper bound is much more difficult to determine. The collapse processes studied by Ball et al. and Bourne and Field are in many ways analogous, using the same materials, initial conditions, and order-of-magnitude length scales, but applying a higher pressure loading [33, 36, 170]. Analyses that consider the shock-heating effects in this problem find temperatures in excess of 6000 K inside the bubble during the times where luminescence is observed, when bubble volume is less than 10% of the original volume [36, 170]. In the current experiment, luminescence is not observed, suggesting that temperatures remain below this level.

Obtaining more precise values of peak pressure and temperature, as well as minimum volume, may not be possible from available data. The high values of $\dot{R}$ and volume rate of change at the end of collapse lead to a rapid rise in pressure that arrests and reverses the bubble collapse into a rebound. Based on the observed bubble areas and the theoretical modeling of the collapse process (Chapter 4), it's expected this reversal occurs very quickly, between video frames. This would indicate that any temperatures in excess of 1000 K and pressures in excess of 7 MPa persist for less than 0.2 μs. The analysis of Hickling suggests that the elevated temperatures do not propagate into surrounding solid materials due to the difference in thermal diffusivity, and therefore do not play a significant role in damage mechanisms.

Using the theoretical relations to predict the end of collapse and early rebound conditions more accurately was also not a viable option. The early rebound behavior observed in videos is much slower than the late collapse process (rather than symmetrical as theoretical relations would predict), which suggests that energy dissipation mechanisms that are neglected in the theoretical relations do become significant under the intense conditions at the very end of collapse. This might include processes such as viscosity, compressibility, radiation, and chemical reaction, and the high temperatures, pressures, pressure gradients, strains, and strain rates expected may all contribute to the loss of energy. However, the relative contributions of these mechanisms are not well understood, and therefore could not be accurately modeled.

5.6 Area Data and Pressure Estimates

5.6.1 Computation of a Pressure Estimate

The area time histories obtained from the process detailed above are in most cases quite smooth (See Appendices D and E. However, even the smoothest experimental data often produces extremely noisy derivatives. In order to acquire the derivatives of the data, a Savitzky-Golay smoothing filter was applied. In principle, this filter is a hybrid between a running average and a polynomial fit. A polynomial fit (typically of degree 3 or less) is applied to a local window, and the expected value of the central point is determined from this fit; however, this is performed with a computationally efficient algorithm [171]. The method has two advantages: it does not time-shift signal peaks, and it calculates the derivatives of the data as part of the smoothing process.

The goal of calculating the derivatives is to use them with the theoretical relations introduced in Chapter 4 to calculate an estimate for the pressure variation experienced by the bubble. Of course, these relations were developed for symmetrical bubble collapse and are in terms of radius, so they need to be converted to area. First, it is necessary to find the time derivatives of area in terms of radius:

$$A = \pi R^2 \tag{5.7}$$

$$\frac{dA}{dt} = 2\pi R \frac{dR}{dt} \tag{5.8}$$

$$\frac{d^2A}{dt^2} = 2\pi \left(\frac{dR}{dt}\right)^2 + 2\pi R \frac{d^2R}{dt^2} \tag{5.9}$$

These relations are then solved for the derivatives of R:

$$R = \sqrt{\frac{A}{\pi}} \tag{5.10}$$

$$\frac{dR}{dt} = \frac{1}{2\pi R}\frac{dA}{dt} = \frac{1}{\sqrt{4\pi A}}\frac{dA}{dt} \tag{5.11}$$

$$\frac{d^2R}{dt^2} = \frac{1}{\sqrt{4\pi A}}\frac{d^2A}{dt^2} - \frac{1}{4\pi A}\left(\frac{dA}{dt}\right)^2 \tag{5.12}$$

These can then be substituted into Equation 4.8, from [96], to obtain:

$$\frac{\ddot{A}}{\pi} - \frac{\dot{A}^2}{8\pi A} = \frac{P_g - P_L}{\rho_L} \tag{5.13}$$

Solving for P_L, which is to be estimated, and substituting the adiabatic relation for P_g

$$P_{est} = P_L = -\rho_L \frac{\ddot{A}}{\pi} + \rho_L \frac{\dot{A}^2}{8\pi A} + \left(\frac{A_o}{A}\right)^{2\gamma} \tag{5.14}$$

where the overdot indicates a time derivative.

The measured $A(t)$, $\dot{A}$, $\ddot{A}$, and the calculated pressure estimate (P_{est}) for one test are shown in Figure 5.16. Additional plots of these values are provided in Appendix D.

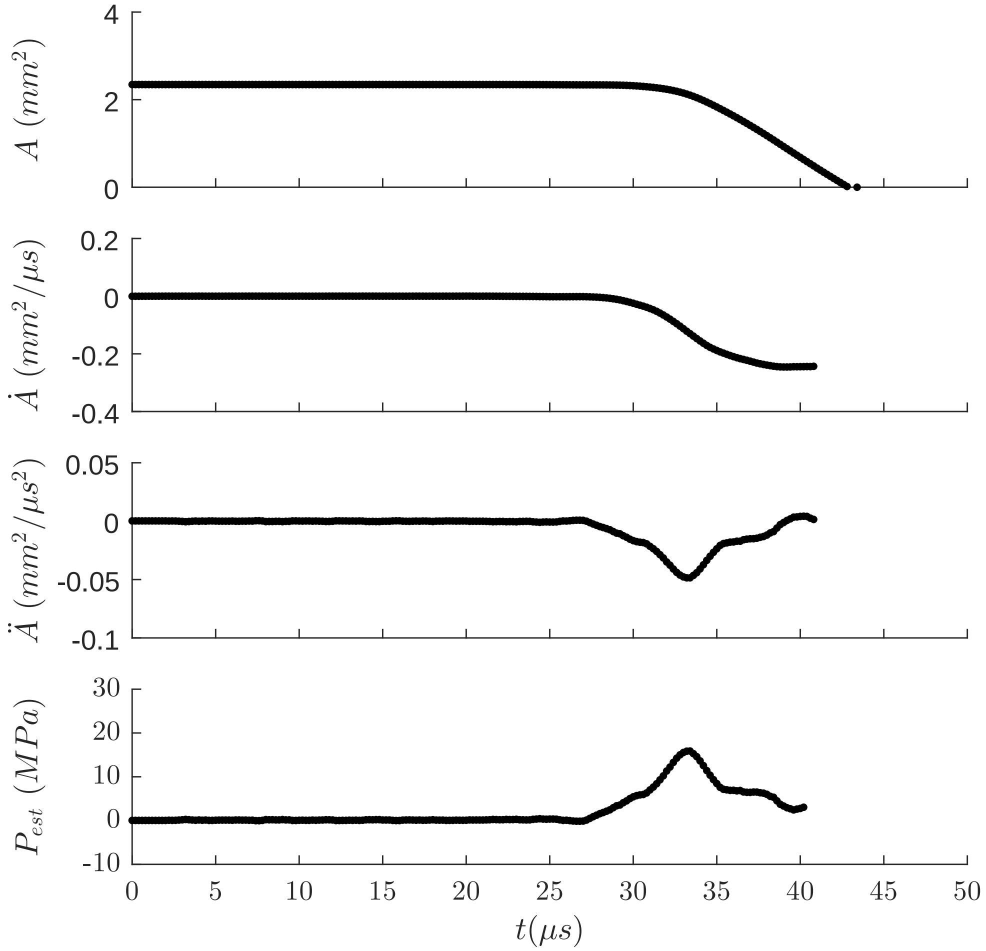

Figure 5.16: Area with time, its first two derivatives as calculated by Savitzky-Golay filter, and calculated estimate of loading pressure, for test in Figure 5.1.

5.6.2 Savitzky-Golay Filter Parameters

The window size for the Savitzky-Golay filter was determined by examining the behavior of $\dot{A}$ and P_{est} with changing filter windows for five arbitrarily selected tests. It was clear that a window of 5 points was quite small for this type of filter, whereas a window of 51 was likely excessive, as it would occupy almost the full collapse time in some cases. The peak values of P_{est} and $\dot{A}$ were investigated first, with the expectation that as window size increased, the peak value would exhibit a plateau across optimal filter values. While an initial steep drop occurred, the peak value of P_{est} varied roughly as an inverse function ($1/x$), with continuously decreasing value and slope. A window size determined based on this variation would be an arbitrary threshold.

The peak of $\dot{A}$ behaved closer to the expected trend. The initial steep drop in magnitude was followed by a fairly sharp transition to a linear region with a low slope (in some tests close to zero, but not always).

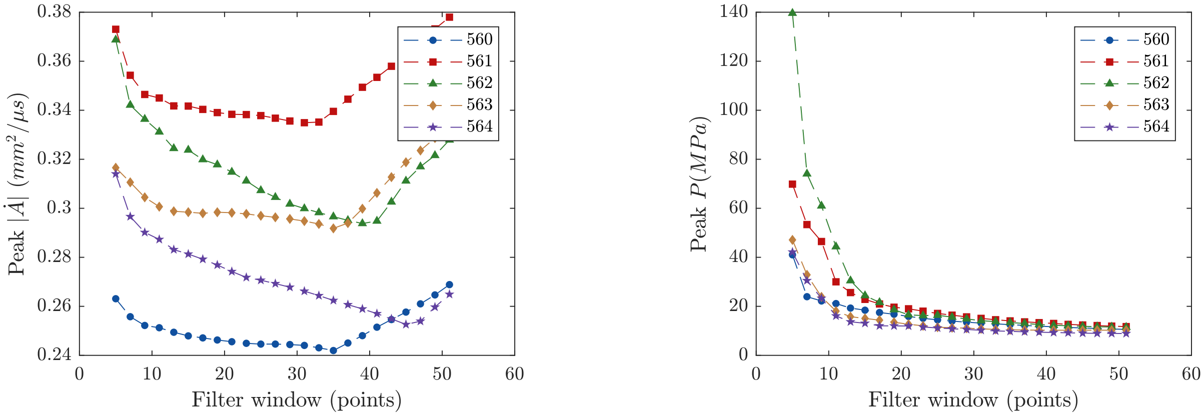

(a) Peak $\dot{A}$

(b) Peak P_{est}

Figure 5.17: Peak values of $\dot{A}$ and P_{est} with filter window size.

For large window sizes, the peak value trended upward again. Observing the behavior of the actual filtered signals, it became clear the treatment of the end of the signal results in a linear prediction of $\dot{A}$ for the last half-window of points. If half the window width requires more points than there are between the peak and the end of the data set, the data does not "dip" again after the peak, but continues increasing, and the maximum value of $|\dot{A}|$ exceeds the peak predictions of less-smoothed data. Clearly, windows that exhibit this (larger than 31–33 points) are too large to use on this dataset. However, this still leaves a wide range of choices, from about 9–11 points on the low end, to choose as a filter width, and this presents a fairly large variation in corresponding peak P_{est} values (14–74 MPa).

To further inform the choice of filter window size, the oscillations in the $\dot{A}$ signal were investigated. Since some variation with time is expected, the signal derivative obtained with a 50 point window was used as an "expected value," rather than using a mean value. This signal is subtracted from that obtained by using a different window, then the differences are squared and summed for a metric loosely described as "variance" of the signal for that window size. Though this metric also does not produce a clear plateau, it did have gradual changes in slope and an inflection point within the 9-33 point range. For greater clarity, the derivative of this value with respect to window size is shown, and was used to help identify the inflection point. The minimum of this derivative varies somewhat between tests, but in a much narrower range of 17–23 points. 21 points was selected as the filter width to use on all tests, close to the minimum for all five tests investigated. The value of P_{est} varies at most by about 30% as window size decreases from 17 to 25 points, so P_{est} data should be interpreted in light of this $\pm 15\%$ accuracy.

The order of the Savitzky-Golay filter can be varied, but typically a 2nd or 3rd order is sufficient (quadratic or cubic functions used for local fitting). Since the area data was not observed or expected to have inflection points that would require a cubic to locally describe, the 2nd order method was used.

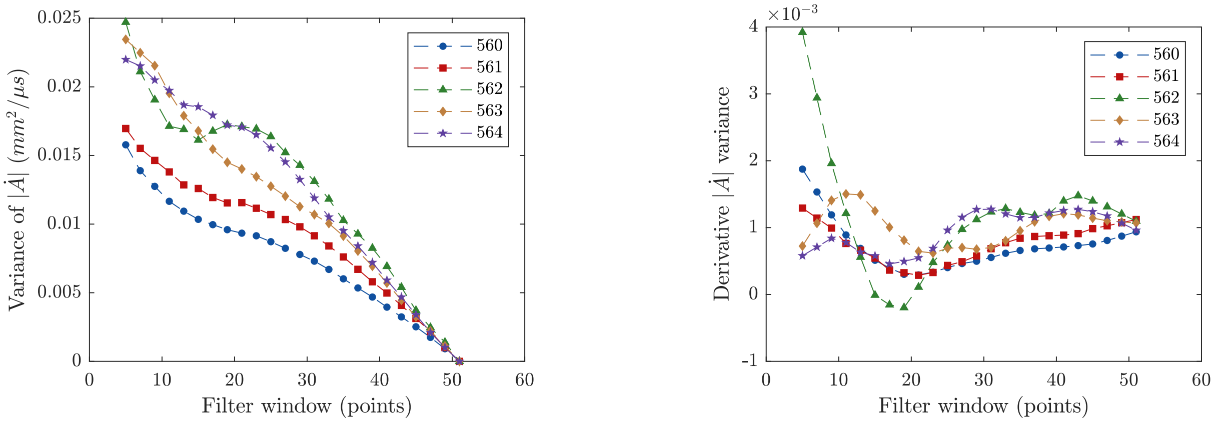

(a) Variance of $\dot{A}$.

(b) Derivative of variance of $\dot{A}$ with window size.

Figure 5.18: Finding inflection points in variance of $\dot{A}$ versus window size, as a metric for optimizing filter.

5.6.3 Collapse and Estimated Pressure, Comparison to Theory

Computing an estimated pressure is useful for two reasons. First, by comparing to the pressure predicted by FEA simulations and measured directly (Section 3.5), the consistency of the experiment and validity of relating loading pressure to area change of the bubble can be confirmed. On the other hand, a large, consistent discrepancy between the pressure estimated from bubble behavior would indicate the presence of a mechanism that is not accounted for in the way the area-pressure relationship is being modeled, for example, an effect of material strength.

Second, having this pressure estimate allows an informed comparison with the collapse of a bubble under different loading conditions. This completes one of the major goals of this study, furthering an understanding of how dynamic pressure loading affects bubble collapse. In this section, the nondimensional area-time collapse profile from experimental data is plotted alongside the pressure profile estimated using Equation 5.14. Area-time traces are also calculated for two simple pressure functions: a step pressure increase, and increase in the form of a linear ramp in time. The ramp profile is calculated so it has a rise time equal to the rise time of the experimental pressure from the start of collapse to the maximum P_{est}. The maximum pressures attained by the step and ramp pressure profiles were selected to match the collapse time of the experimental data. The three pressure profiles are shown just below each plot of the three area profiles in Figures 5.19–5.22. The full set of these plots for all tests that exhibited distinguishable "see-through" bubble area can be found in Appendix E.

It is important when interpreting these plots to be mindful that the "estimated experimental pressure" is not a measurement, but a value inferred from the area change and its derivatives. This depends on reliable area measurements and reasonably accurate derivatives. The small uncertainties in area determination become proportionally more significant for small areas, and the Savitzky-Golay algorithm cannot be applied close to the end of the data set. Of course, calculating the pressure also requires assuming Equation 5.13

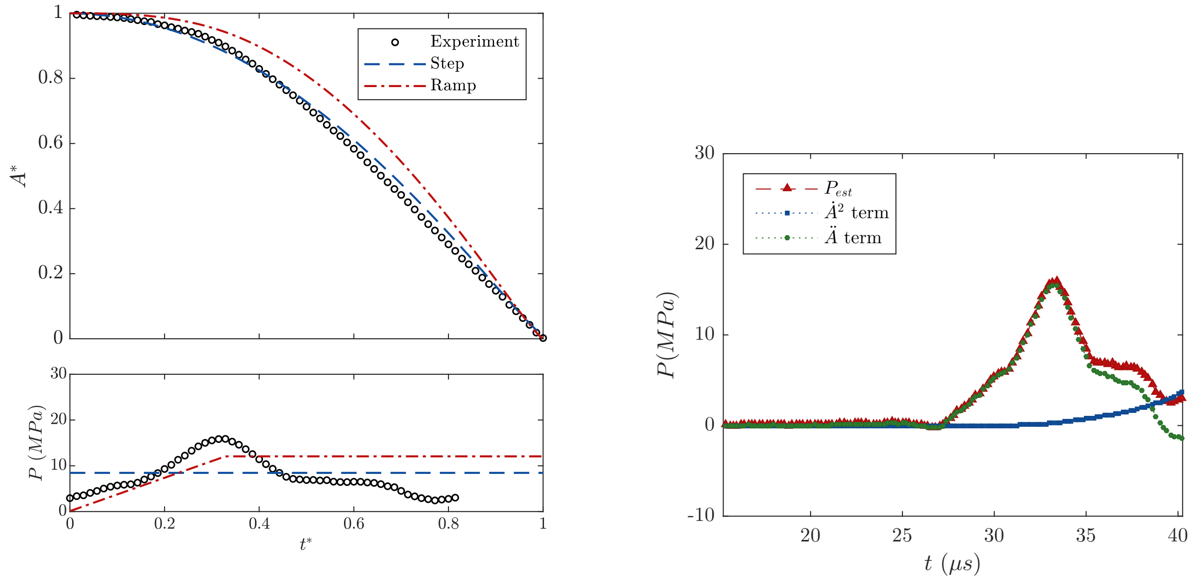

(a) Nondimensional area profile and estimated pressure profile, accompanied by theoretical predictions for collapse under step and linear ramp pressure loading, as shown. Pressures for comparison selected to match bubble collapse time.

(b) Magnitudes of constituent terms of P_{est} in Equation 5.13 dependent in $\dot{A}$ and $\ddot{A}$ and resultant pressure estimate.

Figure 5.19: Predicted pressure behavior of bubble in the absence of nearby boundary (corresponding to Figure 5.1).

holds; this is also the case for the theoretical profiles, but those start with an idealized pressure behavior rather than area as the known quantity.

Figure 5.19(a) shows the nondimensional collapse profile of a bubble in the absence of a boundary, obtained from the test in Figure 5.1. While it appears to follow the profile of the step function-induced collapse quite closely, there are some variations, which can all be explained by observable differences in the pressure waveforms. The estimated experimental pressure starts higher than the ramped profile pressure, but lower than the step pressure increase. Accordingly, until about t^*=0.2, the collapse accelerates faster than under ramped loading, but somewhat slower than the step loading, and the area remains between the two theoretical curves. At approximately t^*=0.2, the estimated experimental pressure rises above both the step and ramp pressures, and the experimental area decreases more rapidly than the others, dipping below the step collapse area profile. After this, experimental pressure decreases to less than the ramped and step pressures, which allows all three collapse processes to reach $A^* = 0$ at $t^* = 1$. Particularly notable is that the higher pressure of the ramped profile from $t^* = 0.4$ to $t^* = 1$ causes curvature, and therefore acceleration, of its A^* profile relative to the two lower pressures. This behavior has a significant implication: in spite of its slower start, the ramped collapse exhibits the highest area rate of change ($\dot{A}$) at the end stages of collapse, signifying more kinetic energy present in the system and a higher pressure built up inside the bubble to decelerate and reverse the flow. Although the estimated experimental pressure reaches the highest peak pressure, it also

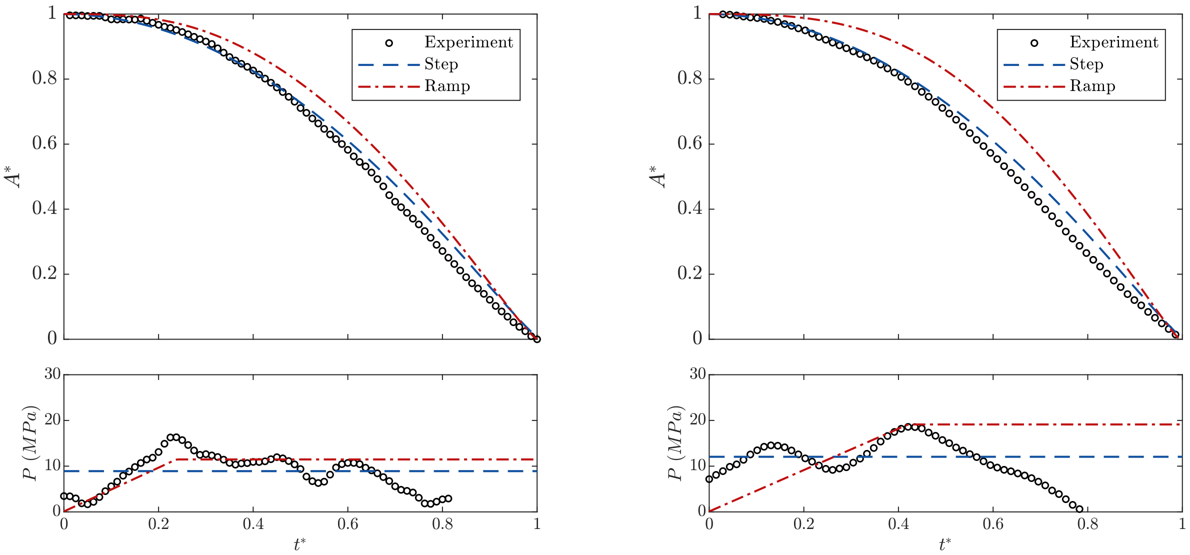

(a) 20:1 PDMS (corresponding to Figure 5.2)

(b) 40:1 PDMS (corresponding to Figure 5.4)

Figure 5.20: Two examples of nondimensional area profile and estimated pressure profile corresponding to collapse of bubble near a downstream boundary with PDMS. Accompanied by theoretical predictions for area profile of collapse under step and linear ramp pressure loading, as shown. Pressures for comparison selected to match bubble collapse time.

exhibits the lowest $\dot{A}$ of the three cases at the end of collapse, indicating less intense behavior.

Figure 5.19(b) shows the constituent terms of P_{est} to demonstrate their relative magnitudes. The pressure of gas within the bubble (P_g) was considered in calculations, but was omitted from the plot for clarity, as it grows slowly and does not dominate behavior until the area is too small to determine its derivatives accurately ($A^* < 0.2$). Until t=35 μs, which corresponds to about t^*=0.4, P_{est} trends closely with the magnitude of $\dfrac{\rho \ddot{A}}{\pi}$. The $\dot{A}^2$ term is actually $\dfrac{\rho \dot{A}^2}{8\pi A}$, and it is the $1/A$ behavior that causes the term to grow after t=35 μs until it dominates the predicted pressure, even though $\dot{A}$ becomes virtually constant by this time (see Figure 5.16). In fact, the near constant behavior of $\dot{A}$ can be explained by the dominance of this term in the equation: if it is equal to the complete pressure term $(P_g - P_{\text{est}})$, $\ddot{A}$ must be zero, indicating $\dot{A}$ is not changing.

Figure 5.20 shows the area and estimated pressure behavior of two tests in which bubbles collapse near a downstream boundary with PDMS, with two different compositions. Both tests exhibit two features common to other tests involving downstream boundaries (see Appendix E). First, the estimated pressure is higher, earlier in the collapse, and persists for a significant portion of the collapse. Either bubble motion does not start until pressure rises to a particular level, or the pressure rises rapidly just before or just after the start of collapse was detected. The higher loading pressure causes the area trace to consistently fall below both theoretical traces for half of the collapse (by time). The second notable feature is that in most of the tests performed, the experimental area trace exhibits a deceleration region during the last fifth of the collapse ($0.8 < t^* < 1.0$). Although the derivatives cannot be reliably calculated in this region to infer a pressure trace, the behavior requires that P_g can overcome the effects of both applied pressure and the $\dot{A}^2$ term to generate outward acceleration of the fluid.

This region of deceleration lowers $\dot{A}$ further compared to the two theoretical traces, which has the same effect on conditions generated by collapse as in the no-boundary case. In spite of more rapid collapse progression initially, the area trace has a lower slope at the end of the collapse compared to both theoretical traces, indicating less severe collapse than those would predict (less kinetic energy in the system, lower maximum pressure when deceleration is achieved). The question that arises is how does the presence of the boundary cause the higher acceleration in the beginning and deceleration at the end of the collapse?

Pressure measurements indicate that in samples with a downstream boundary (or two boundaries) pressure initially rises to higher values than the no-boundary and upstream-boundary samples, reaching maxima between 20–30 MPa consistently, rather than 15–20 MPa. The average pressure is not significantly affected as a result, but the change in distribution would certainly lead to greater acceleration occurring early in the collapse, and the remainder of the collapse proceeding primarily on inertia. This, in turn, would lead to a gradual transition to outward acceleration (positive $\ddot{A}$ and deceleration of collapse) with the growth of the $\dot{A}^2$ term as A^{-1} and the P_g term as $A^{-2.8}$. As discussed in Section 3.5, it should be noted that a higher initial loading pressure is the opposite of the expected behavior near a boundary with lower acoustic impedance. The bubble should be expected to respond to the loading condition that it experiences, as it does in this case. If the presence of the boundary actually lowers the pressure rather than raises it, more gradual acceleration early in the collapse process would be expected.

The boundary can potentially have a different type of effect on the collapse process: the strength and resistance to shear introduced by the viscoelastic PDMS compared to the relatively weak agarose gel can alter the deformation and flowfield that forms in response to the loading condition. The estimated pressures in the downstream boundary tests do not, in general, reach the same magnitudes as the measured pressures, which suggests either a cause of error in measurement, or that another process is resisting the development of the collapse flowfield around the bubble. Since the flowrates and displacements are largest at the end of collapse, it seems reasonable to expect the effect of material strength would be greatest then, and explain the deceleration of collapse observed in many more of the tests that feature boundaries, than ones that do not.

Cases of the collapse of a bubble near an upstream boundary, two of which are shown in Figure 5.21, do not exhibit a distinguishing behavior early in collapse; there are test-to-test variations toward both higher and lower accelerations and inferred pressures in the dataset. The collapse in general stays below ("ahead of") the collapse under ramped profile loading, but can end up on either side of the step loading trace; this behavior is not very different from that in the absence of a boundary. However, many more of the tests exhibit deceleration toward the end of collapse, similarly to the downstream boundary cases. This

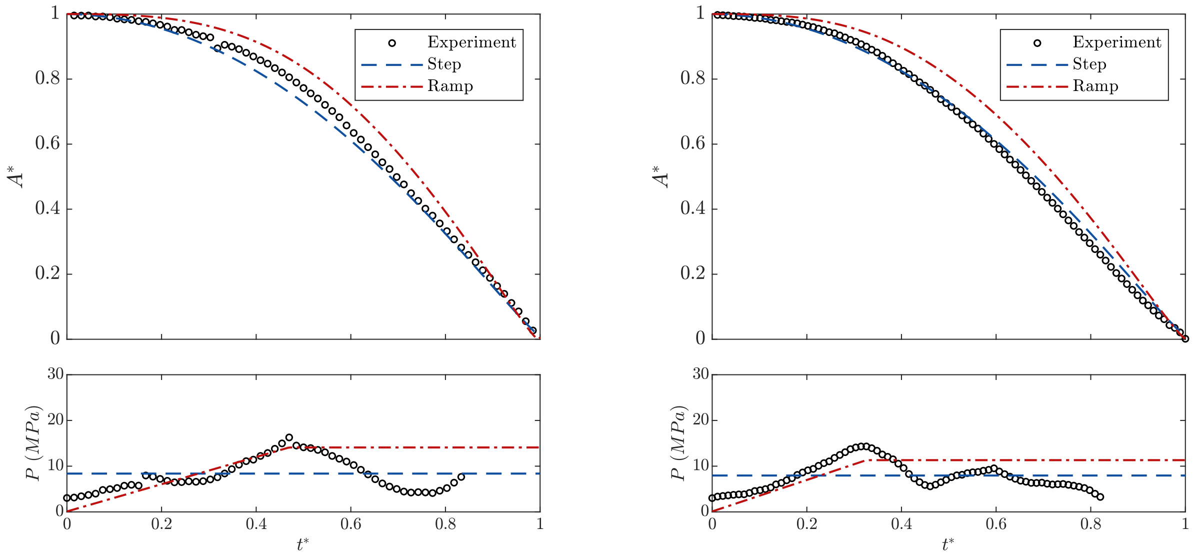

(a) 20:1 PDMS (corresponding to Figure 5.5)

(b) 40:1 PDMS (corresponding to Figure 5.7)

Figure 5.21: Two examples of nondimensional area profile and estimated pressure profile corresponding to collapse of bubble near an upstream boundary with PDMS. Accompanied by theoretical predictions for area profile of collapse under step and linear ramp pressure loading, as shown. Pressures for comparison selected to match bubble collapse time.

supports the reasoning that strength may be affecting the collapse at this time, since the discontinuity in properties on either side of the bubble would be expected to generate resistance to motion if the boundary was close enough. In fact, since larger displacements and velocities develop on the upstream side, the effects of strength should be more evident in cases with an upstream boundary.

The measured pressures in samples with upstream boundaries were consistently observed to reach 20 MPa, whereas samples with no boundaries only showed maximum pressures of about 15 MPa. This distinction is not apparent in estimated pressure traces, which range from near-constant traces around 10 MPa to peaks around 20 MPa, regardless of geometry and material composition of the sample. Both results contradict the expected behavior of a 15% reduction in wave amplitude due to the impedance discontinuity at the boundary and partial reflection of the incident wave. It seems apparent that just like the case near the downstream boundary, the bubble responds to any pressure state that develops, possibly modified by the effect of material strength.

When the bubble is located between two material boundaries, as in the two cases shown in Figure 5.22, the features observed are quite similar to those in the downstream boundary cases. Since the upstream boundary was found to introduce little change to the collapse profile, it stands to reason that the changes introduced by the downstream boundary would be more evident. The collapse is only detected when the pressure is already quite high in several cases, the collapse proceeds “ahead of” the step-function induced

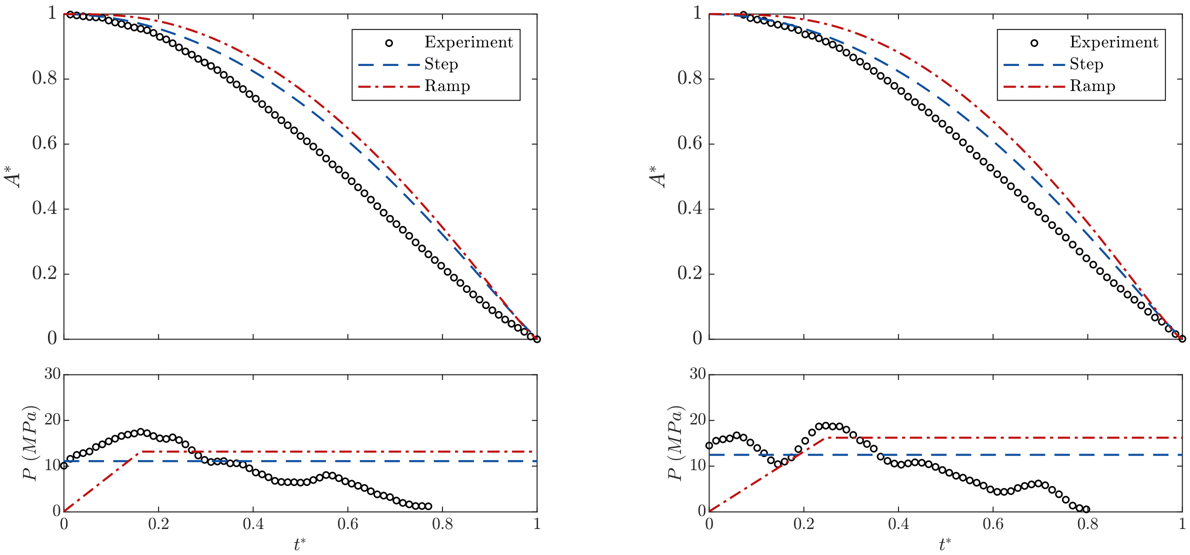

(a) 20:1 PDMS (corresponding to Figure 5.8)

(b) 40:1 PDMS (corresponding to Figure 5.9)

Figure 5.22: Two examples of nondimensional area profile and estimated pressure profile corresponding to collapse of a single cylindrical bubble between two boundaries with PDMS. Accompanied by theoretical predictions for area profile of collapse under step and linear ramp pressure loading, as shown. Pressures for comparison selected to match bubble collapse time.

collapse for much of the process, and deceleration is quite evident during the second half of most tests. This may be more pronounced due to the double effect of both boundaries.

Figure 5.23 shows the behavior of a bubble collapsing near an aluminum boundary. The expected pressure behavior near a solid boundary (such as aluminum used here) is for a doubling of the pressure to occur due to a strong wave reflection. Pressure measurements could not be done in this geometry due to risk of damage to the sensor upon impact with the aluminum behind the boundary, but higher pressures were not observed in estimated pressure traces. It is possible the presence of the bubble and diffraction of the incident wave around it resulted in a nonuniform pressure distribution around the bubble, wherein regions of higher pressure are balanced by regions of low pressure (e.g. downstream of the bubble), resulting in an average pressures peaking at 10-20 MPa, roughly the same as in the no-boundary cases. It is also likely the resistance of the aluminum to deformation is altering the flowfield and slowing the collapse, which then yields a lower estimated pressure.

The area of bubble collapse near an aluminum boundary tends to proceed with the area staying between the two theoretical traces, as it does in most of the tests performed. As discussed previously, this indicates the generation of more extreme conditions at the end of collapse, based on the value of $\dot{A}$.

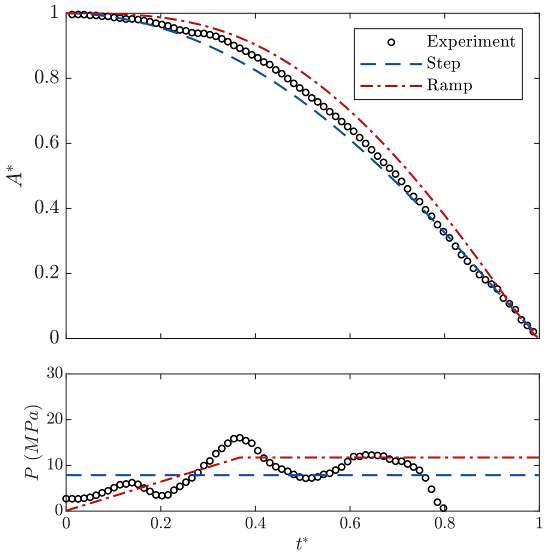

Figure 5.23: An example of nondimensional area profile and estimated pressure profile corresponding to collapse of bubble near a downstream boundary with aluminum. Accompanied by theoretical predictions for area profile of collapse under step and linear ramp pressure loading, as shown. Pressures for comparison selected to match bubble collapse time.

5.6.4 Discussion

Although there has been much study of bubble and cylindrical bubble collapse in numerous environments and geometries, to the best of the author's knowledge there has not been extensive investigation of how variation of pressure with time may affect collapse behavior. Chapter 4 developed the theory for a symmetrical bubble collapse under variable pressure and explored the effect of some simple pressure functions on the area-time relationship, as well as predicting the effect of the measured pressures. In this section, the reverse approach was used, backing out the expected pressure based on area change, and considering what kinds of deviations of the area-time curve from expected behaviors can be explained by pressure fluctuations.

Small fluctuations around the area-time curve may have little practical meaning, but sustained differences in pressure translate into acceleration and kinetic energy of the system, and higher P_g at smaller minimum volume at the end of the collapse process. Whether a bubble experiences a period of elevated pressure early or late in its collapse affects the acceleration that pressure produces on the bubble, and a higher $\dot{A}$ in mid-collapse caused by early acceleration can actually contribute to deceleration once the pressure drops, based on its contribution to Equation 5.14. Increasing the pressure continuously during collapse, as opposed to keeping it steady, produces a larger $\dot{A}$ at the end, in the same collapse time.

Due to the variations in pressure loading and the resistance of material boundaries, the complete set of tests sweeps out a range of paths on the nondimensional area-time plot. The eight example tests used in this chapter are shown in Figure 5.24. It may at first appear that the main difference is the choice of

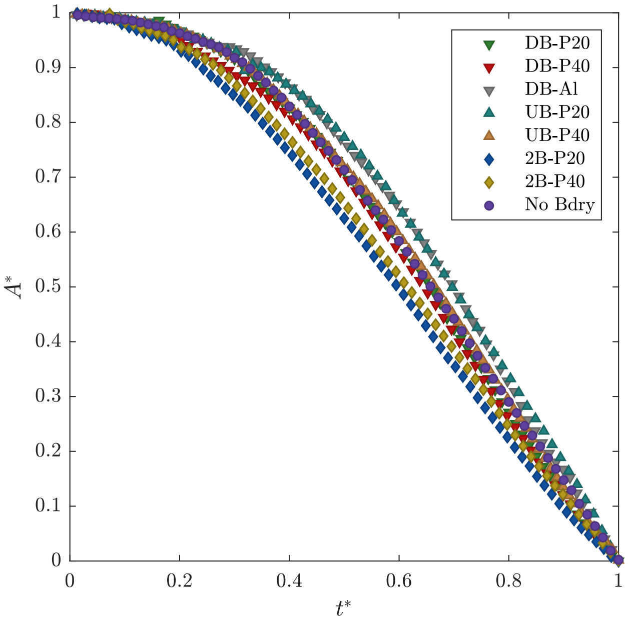

Figure 5.24: Comparison of nondimensional area-time traces of bubble collapse tests featured throughout this chapter. UB: upstream boundary, DB: downstream boundary, 2B: two boundary. PXX: PDMS with base:hardener ratio XX:1, Al: Aluminum.

collapse time, that if the tests were shifted and stretched slightly on the time axis, they would overlap. This impression is erroneous, as the curvature of each trace varies continuously; a better match might be obtained with a time-shift, but some variation would remain, as was demonstrated in Section 4.5. It is more accurate to define a consistent metric that will identify the first signs of motion of the bubble as well as possible, but not be triggered by signal noise during the preceeding steady-state period. The selected metric was $-\dot{A}$ exceeding 3% of its maximum value.

Other researchers have used other metrics. In some earlier studies (e.g. [33]), the temporal resolution was so low, few frames were obtained during the collapse, and the first frame exhibited significant area reduction. Swantek used the motion of a point on the upstream boundary [5]. Computational studies generally use the arrival of the wave as the metric [36]. The area-time traces of these studies are presented in Figure 5.25. It is important to note these data span a large scale of pressures: the computational study by Ball used a 1.9 GPa shock; the experiments of Bourne and Field used a 300 MPa shock; and Swantek reported about 42 MPa based on particle velocities, but did not account for the dissipative effects of the flexure of the fixture (see Chapter 3). As such, the final slopes of the traces should not be compared as a measure of collapse severity against each other.

All the area-time data stay fairly close to the linear relationship initially proposed by Bourne and Field to describe their sparse data [33]. Simulations of one of their test conditions by Ball et al. showed the acceleration and deceleration regions at the beginning and end of the collapse, which are quite small. It is

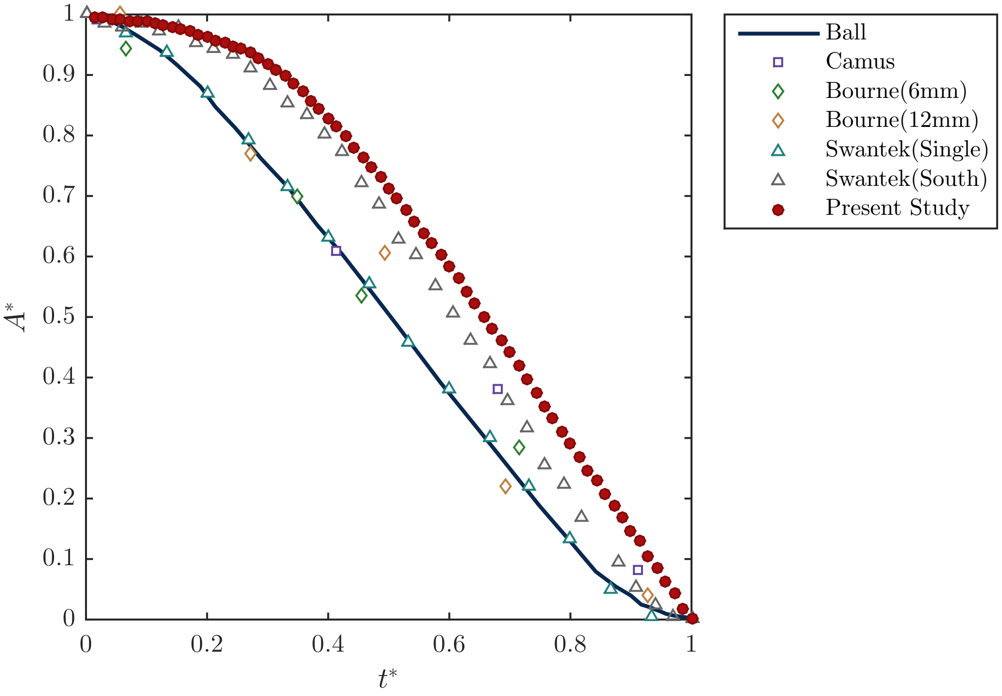

Figure 5.25: Comparison of nondimensional area-time traces of a no-boundary bubble collapse case with data for shock-induced collapse from [33, 34, 36] and stress-wave collapse from [5]

.

possible the sudden rise in pressure or the jump in velocity across a strong shock front contributes to the rapid acceleration of the collapse. The results of Swantek and Austin follow the simulation results of Ball et al. quite well, in spite of the lower pressure loading. However, the bubble was within 1-2 mm of the striker plate in this study, and would have experienced a very sharp pressure rise and velocity gradient. When they investigated the behavior of a diamond-shaped array of bubbles, the "south" bubble was located about 2 mm further downstream, and between the dynamics of the fixture (see Chapter 3), and the diffraction of the wave around the "west" bubble (farthest upstream), the pressure condition would have changed. The south bubble exhibits a similarly slow start to the no-boundary case in this experiment, but exhibits more consistent acceleration and gets ahead in the collapse process, before decelerating near the end.

5.7 Centerline Velocity

Although the enclosed bubble area was a much more informative parameter, it bears mentioning that the behavior along the centerline of the bubble could be extracted from the video in a very straightforward way. ImageJ software includes a tool for taking cross-sections of an image stack through any given point [153]. When applied through the centroid, the output is essentially a plot of upstream and downstream bubble interface positions with time. This image can be binarized and the coordinates of the interfaces can be measured to determine interface displacement along the centerline at any given time. A Savitzky-Golay filter (see Section 5.6) can also be applied to this data set to estimate interface velocities. The downstream interface hardly moves, but the upstream interface exhibits high velocities. Measuring them in this way allows them to be compared with the centerline velocities obtained from the model in LS-DYNA (Section 3.3.2, and the velocities that will be obtained from PSV (Chapter 6). Figure 5.26 shows the velocity-time traces for four such computations, found with a 2nd order Savitzky-Golay filter with a window of 13. This means that velocity for about the last 1.6–1.8 μs cannot be acquired due to end treatment by the filter. All four tests show that interface velocity upstream of the bubble reaches at least 200 m/s, possibly higher, since most of the tests demonstrate a high rate of change at the end. Liquid traveling with those speeds is capable of generating pressures in the hundreds of megapascals if it impacts the downstream interface before it is decelerated.

5.8 Conclusions

5 million frame per second data on the bubble collapse allowed collapse times to be measured for 10–15 tests of each geometry. Average collapse times and the variation of collapse times were quantified, along with geometric properties of the samples. Geometric properties and impact velocity generally showed good repeatability, but the collapse times varied quite significantly. Much of the variation in collapse time within test groups can be explained by variations in pressure profile by considering average pressure. Jet formation occurs in most tests of the no-boundary case, but fewer than half of upstream and downstream boundary cases, and very few two-boundary cases. Upstream bubble interface velocity in all cases achieves comparable values in excess of 200 m/s. These velocities can generate pressures of 75 MPa upon impact with the opposite liquid interface, but with 1.6–1.8 μs at the end of the collapse unaccounted for, the boundary could still accelerate or decelerate before impact. Once the collapse occurs, a wave is seen propagating radially outward, but measurement of the wave properties did not elucidate its physical nature.

The area enclosed in the bubble could be measured in each frame of the good quality collapse videos (for 66 out of 104 total videos). The resulting area histories showed small deviations from predicted collapse at constant pressure. The differential equations for the symmetric collapse of a cylindrical bubble were solved for the pressure, and the pressure was estimated using derivatives of the measured area curves. The derivatives were computed by a Savitzky-Golay filter algorithm with a window of 21 points. The agreement between peak values of estimated pressure and the experimentally measured pressure traces is quite good for most cases.

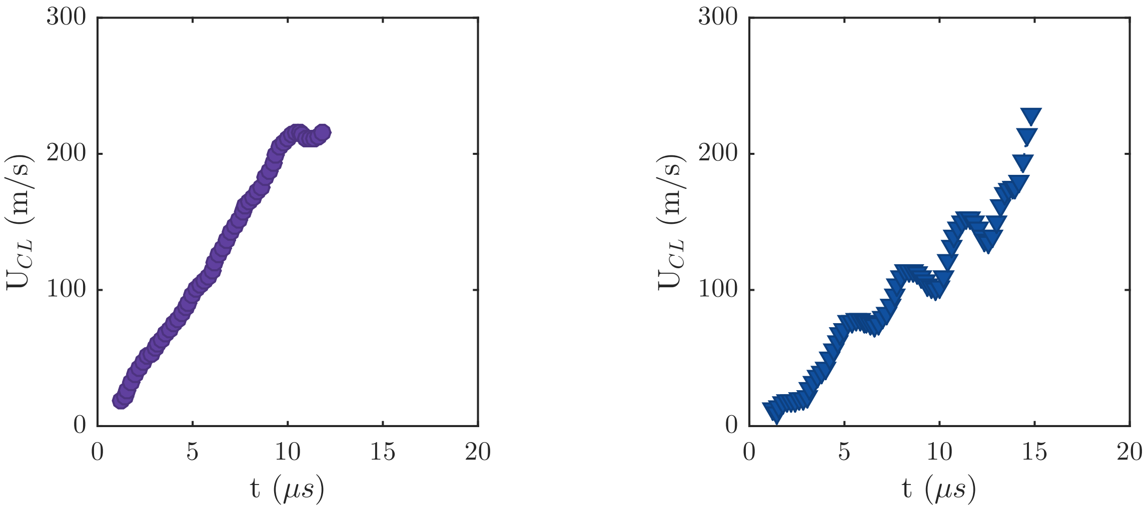

(a) No boundary.

(b) Downstream boundary.

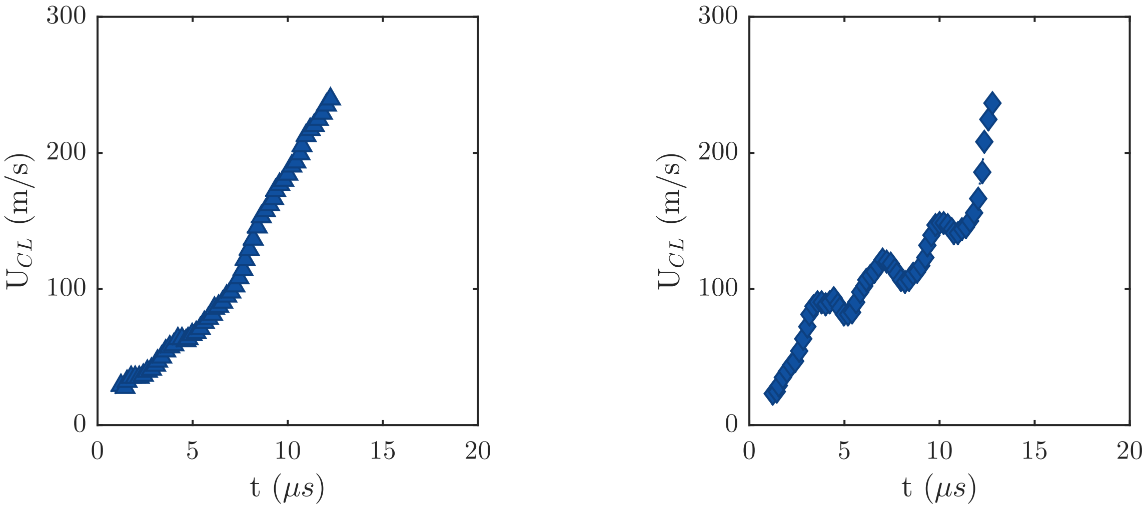

(c) Upstream boundary.

(d) Two boundaries.

Figure 5.26: Some examples of upstream velocity traces obtained from centerline cross-section views, using a SavitzkyGolay filter with window size 13 to differentiate the interface position. All cases with boundaries are 20:1 PDMS. The tests correspond to the ones used in previous sections.

CHAPTER 6

PARTICLE SHADOW VELOCIMETRY

One of the advantages of performing the study in a two-dimensional geometry was the ability to get high-resolution velocity vector data for the entire flowfield at select moments during the collapse process. Particle shadow velocimetry (PSV) is essentially a subtype of particle image velocimetry (PIV), the key difference being that shadows of seeding particles are imaged by backlighting the sample, rather the more typical imaging of scattered laser light off particles. Details of implementation and the advantages over traditional PIV are discussed in Section 2.5. The flowfield data obtained were analyzed for patterns, in search of explanation for the differences in the character of collapse between different boundary geometries. A model capable of describing the flowfield with the fitting of a few parameters was derived, and the variation of these parameters during the process of collapse is discussed. The model also provides an effective way of smoothing the data so that derivative quantities, such as shear rate and vorticity, can be investigated.

6.1 Flowfield Development

In this section, selected flowfields from collapse in 8 of the 11 test groups are presented and the features of these flowfields, discussed. A full collection of PSV data is included in Appendix F, which includes all tests involving 30:1 PDMS, as well as additional frames for the test conditions that are presented here.

In each flowfield sequence, each image is from a separate collapse event, due to limitations of imaging technologies available. Due to this and the time jitter present in the experiment, the flowfields in each sequence are arranged by area ratio, $A^* = A/A_o$ as a time-surrogate variable. The bubble area can be well-resolved in all raw PSV images, and initial area is obtained from a pre-shot reference image. It is well-established that area decreases monotonically with time during the collapse process, so using area as a time surrogate was effective for ordering tests correctly. In order to extend this ordering to flowfields at the very end or just after the end of collapse, the centroid of the bubble (x_c) was tracked as a secondary time-surrogate. After collapse, the bubble presents as a dark spot convecting downstream as it rebounds; the centroid of this feature was used when an interior bubble area could not be discerned. With regards to notation, it should also be noted that only every 4^{th} or 5^{th} vector is plotted on the flowfields, for clarity. The actual resolution of obtained flowfields is 10–14 vectors per millimeter.

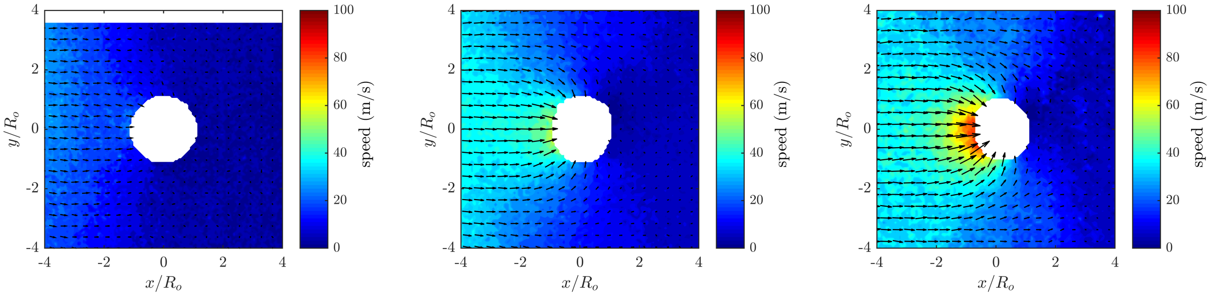

(a) A^*=1, x_c^*=0.02.

(b) A^*=0.89, x_c^*=0.09.

(c) A^*=0.74, x_c^*=0.24.

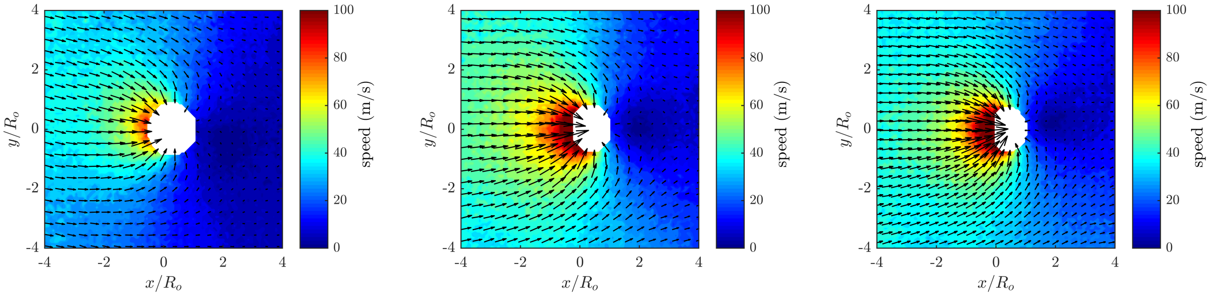

(d) A^*=0.56, x_c^*=0.32.

(e) A^*=0.39, x_c^*=0.48.

(f) A^*=0.29, x_c^*=0.53.

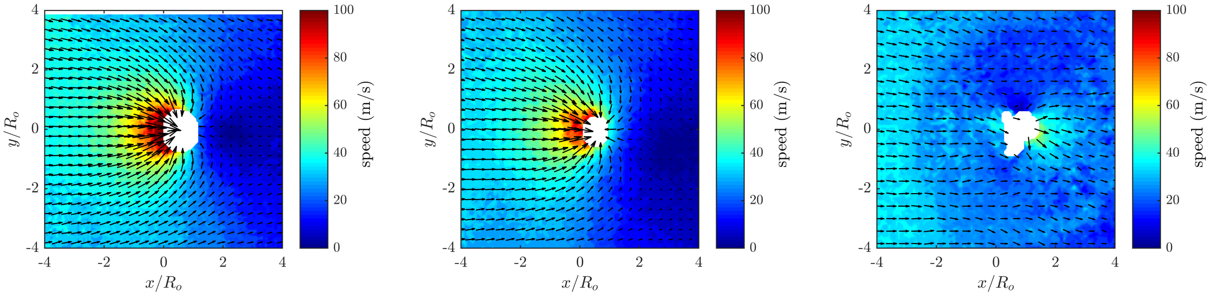

(g) A^*=0.15, x_c^*=0.69.

(h) A^*=0.06, x_c^*=0.79.

(i) A^*=0, x_c^*=1.04.

Figure 6.1: PSV of flowfield during collapse of a cylindrical bubble far from any material boundaries. Area ratio $A^*{=}{}^{A}\!/_{A_o}$ and centroid displacement $x_c^*{=}{}^{x_c}\!/_{R_o}$ of the bubble are indicated.

6.1.1 No Boundary Case

Nine select recorded flowfields around a collapsing bubble in the absence boundaries are presented in Figure 6.1. The flowfields demonstrate the diffraction of the incident wave around the bubble, resulting in a shielded region of extremely low velocity downstream, and a region directly upstream of the bubble that is accelerated relative to flow far from the bubble, which is apparent as early as A^* of 0.9. That the bubble is inducing a flow component in the transverse direction, deflecting the flow toward its center, is also apparent at this time.

The flow directly upstream of the bubble exceeds 100 m/s by the time A^* is 0.4, as predicted in the computationally modeled flow discussed in Section 3.3.2. The deflection of flow into the bubble is also evident throughout the flow by this time, particularly just above and below the bubble, where flow vectors are essentially vertical. Some flow directed upstream ($U_x < 0$) begins to arise on the downstream bubble interface around this time.

By the end of collapse, $A^* = 0.06$, the flow upstream appears to be decelerating; however it is probable this is a deceptive effect of the diagnostic; analysis of boundary motion along the centerline in shadowgraph videos estimates boundary velocities over 250 m/s (Chapter 5). In PSV images recorded very close to the end of collapse, the high velocities near the bubble interface result in particle smearing that interferes with the correlation algorithm. Moreover, the spatial averaging causes the method to underpredict velocities where a large velocity gradient exists across the correlation region.

The final frame in Figure 6.1 occurs just after the end of collapse. Just downstream of the bubble, where impact of the re-entrant jet would have occurred, a region of fluid is accelerated relative to surrounding flow. Additionally, the rebound wave is visible as a round region of predominantly ∼20 m/s flow, propagating outward into the ∼35 m/s flow upstream of the bubble. Above and below the bubble ($y = \pm 2$ mm, the flow processed by this wave that was oriented in toward the bubble center at $A^* = 0.15$ and 0.06 is now moving entirely horizontally (in the x-direction). It appears that propagation of the wave slows the higher-speed flow upstream of the bubble and accelerates the flow downstream, restoring both to the mean flow conditions at that longitudinal location, while also negating most transverse components of velocity that were induced by the bubble collapse. A small region of apparent flow disturbance remains in the immediate vicinity of the bubble ($r \lesssim R_o$); the reason this persists is not immediately clear.

6.1.2 Downstream Boundary Cases

Figure 6.2 presents 6 flowfields from the collapse of a bubble near an aluminum boundary, downstream. The white space from $^x/_{R_o} = 2$ to 4 represents the aluminum region, where vectors could not be acquired due to the opacity of aluminum. Many of the same features are developed in this collapse process, compared to the no-boundary case, such as the diffraction of the incident wave around the bubble, the development of high velocity flow immediately upstream, and shielding of the downstream region. The most notable difference is that the horizontal component of the flow adjacent to the aluminum boundary vanishes by $A^* = 0.6$. This is to be expected, as videos showed the aluminum boundary not moving for the duration of the collapse. The fluid flow farther from the boundary, $^x/_{R_o} < 0$, does not appear to be significantly affected by the boundary presence at these times.

Flowfields from bubble collapse near downstream boundaries with PDMS are presented in Figures 6.3 and 6.4, for 20:1 and 40:1 PDMS respectively. Because PDMS is transparent and cast in the lab, it can be impregnated with particles and flow velocities measured both upstream of the boundary (in agarose, left) and downstream (in PDMS, right). The white line of absent vectors around $^x/_{R_o} \approx 2$ represents the position of the boundary, across which vectors cannot be reliably determined. The main difference from the

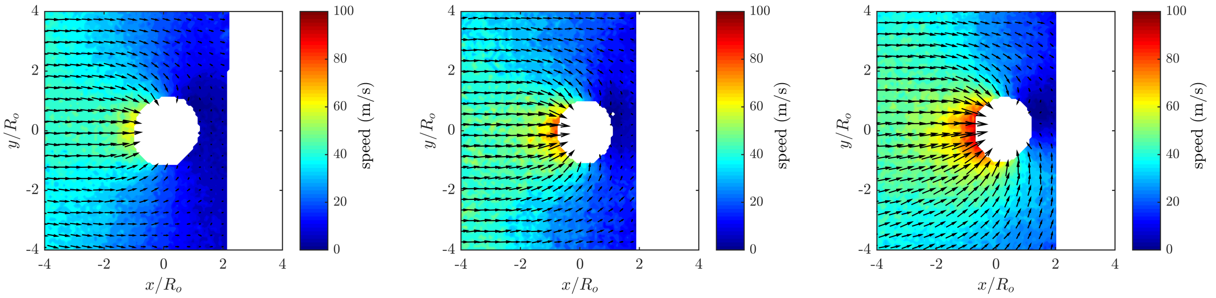

(a) A^*=0.89, x_c^*=0.11.   (b) A^*=0.7, x_c^*=0.23.   (c) A^*=0.6, x_c^*=0.33.

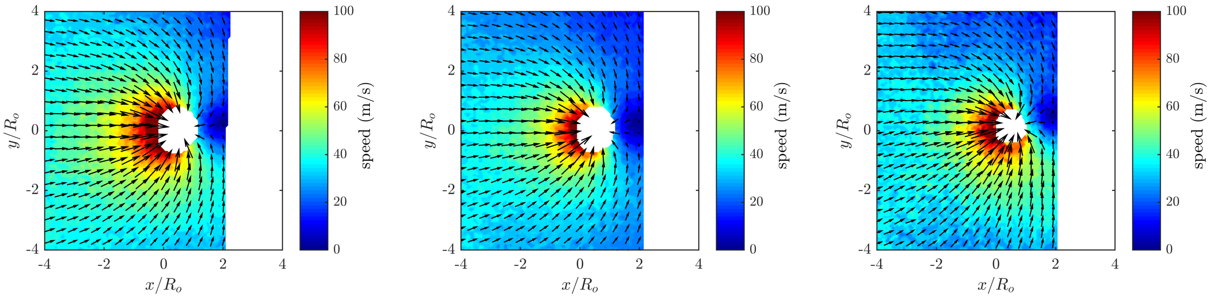

(d) A^*=0.21, x_c^*=0.56.   (e) A^*=0.14, x_c^*=0.53.   (f) A^*=0.04, x_c^*=0.75.

Figure 6.2: PSV of flowfield during collapse of a cylindrical bubble near a downstream boundary with aluminum. Area ratio $A^*={}^{A}/_{A_o}$ and centroid displacement $x_c^*={}^{x_c}/_{R_o}$ of the bubble are indicated.

aluminum boundary is that a horizontal component of velocity persists across the boundary, particularly far from the bubble. Near the bubble and along the boundary, the flow does appear almost vertical, but the same effect is present in Figure 6.1. Therefore, it appears to be a feature of the bubble collapse flow generally, rather than an effect of the boundary.

Some deformation of the boundary is apparent in later frames of the collapse, particularly in Figure 6.4. The boundary develops some curvature, with the point on the centerline closest to the bubble, and the parts near the edges farther downstream. This boundary deformation effect is far more pronounced in the softer 40:1 PDMS than in the 20:1 PDMS. There are two possible ways of explaining this. The first is that the portion of the boundary downstream of the bubble is shielded from the effect of the incident wave, so it is left behind as the flow on the edges develops and convects the boundary downstream. The other is to consider the entire system convecting downstream due to the incident wave, but the bubble inducing a flow toward its center, such that downstream both flows cancel out, and no boundary motion occurs.

The last frame in each of the sequences in Figures 6.3 and 6.4 is taken just after the collapse is complete, and both capture the behavior of the rebound wave. In Figure 6.3, it is apparent as a circular arc of lower-velocity (∼20 m/s) flow, propagating into higher velocity (∼40 m/s) flow upstream. Downstream, the circular outline of a region of ∼25–30 m/s flow is faintly visible against surrounding ∼15–20 m/s flow. Just upstream and downstream of the bubble, the remnants of the high velocity flow and the flow accelerated

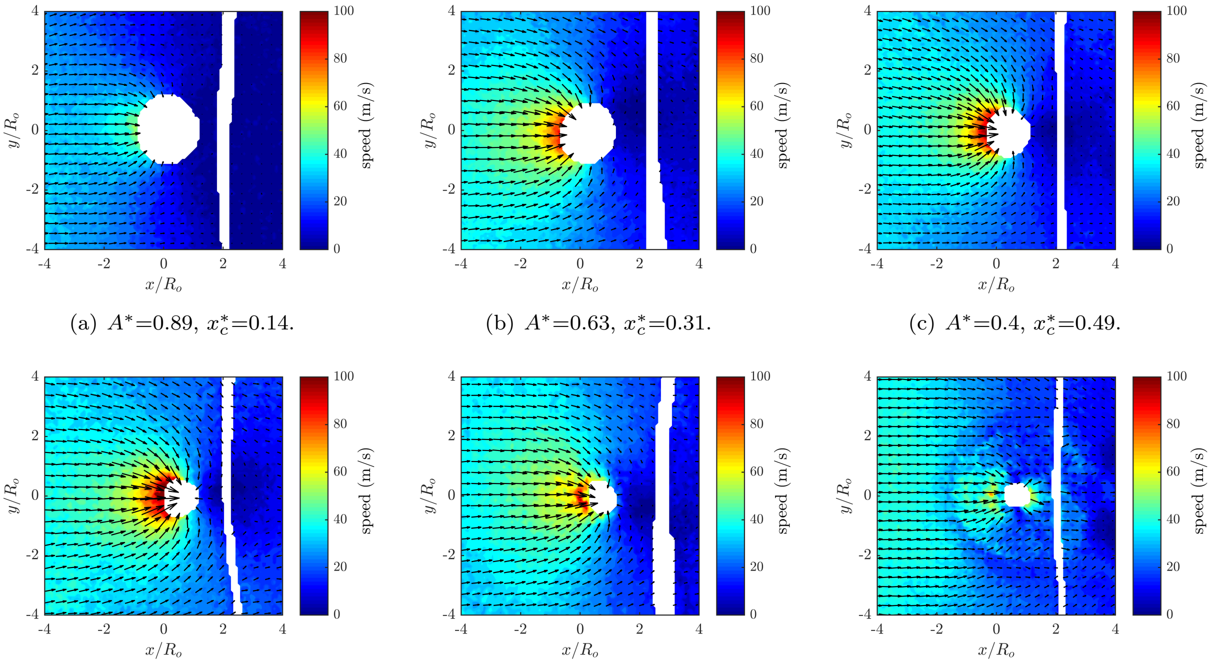

(a) A^*=0.89, x_c^*=0.14.

(b) A^*=0.63, x_c^*=0.31.

(c) A^*=0.4, x_c^*=0.49.

(d) A^*=0.10, x_c^*=0.67.

(e) A^*=0.01, x_c^*=0.86.

(f) A^*=0, x_c^*=0.90.

Figure 6.3: PSV of flowfield during collapse of a cylindrical bubble near a downstream boundary with 20:1 PDMS. Area ratio $A^*= {}^{A}\!/_{A_o}$ and centroid displacement $x_c^*= {}^{x_c}\!/_{R_o}$ of the bubble are indicated.

by impact are visible within the outgoing rebound wave. In Figure 6.4, the presence of the rebound wave is more apparent downstream of the bubble and boundary, as a circular arc of ∼40 m/s flow surrounded by ∼20 m/s flow in the PDMS. Faint circular outlines can also be made out in variations of flow speed upstream of the bubble, but the wave appears to be more disperse in this case. It also appears to have traveled further; this is understandable given the disparity in wave speeds in the two materials. Elevated flow velocity upstream and downstream of the bubble is still apparent.

6.1.3 Upstream Boundary Cases

Figures 6.5 and 6.6 present the flowfields measured during the collapse of a bubble near an upstream boundary with 20:1 and 40:1 PDMS, respectively. There are two notable features in these flowfields. The first is truly how little the presence of the upstream boundary changes the flowfield. There is no evidence of reflections, or large changes in the magnitude or direction of the velocity, globally or locally. Flow accelerates to over 100 m/s upstream of the bubble and the magnitudes of the velocities decrease smoothly if tracing them upstream, even across the boundary. The second feature of note is the deformation of the boundary, which is slightly more extreme and significantly more localized just upstream of the bubble than in the downstream boundary case. It is most evident in Figure 6.5(e) and Figure 6.6(f). The reason for this is apparent in the flowfield. A steep velocity gradient is sustained just behind the bubble for much of the collapse process, with

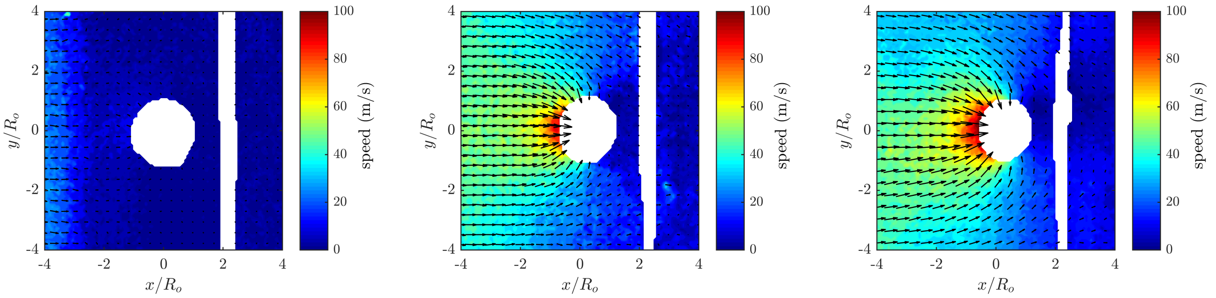

(a) A^*=1, x_c^*=0.03. (b) A^*=0.67, x_c^*=0.25. (c) A^*=0.59, x_c^*=0.32.

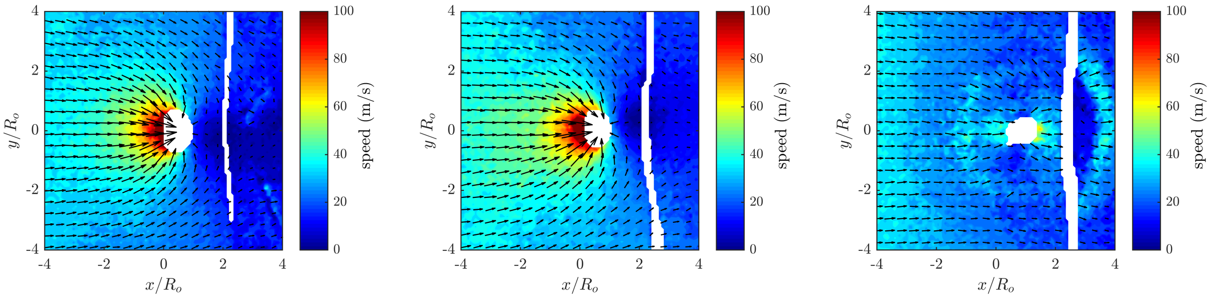

(d) A^*=0.21, x_c^*=0.58. (e) A^*=0.07, x_c^*=0.69. (f) A^*=0, x_c^*=0.98.

Figure 6.4: PSV of flowfield during collapse of a cylindrical bubble near a downstream boundary with 40:1 PDMS. Area ratio $A^*={}^{A}\!/_{A_o}$ and centroid displacement $x_c^*={}^{x_c}\!/_{R_o}$ of the bubble are indicated.

the flow directly behind the bubble exhibiting significantly higher velocity than flow far from the bubble. This sustained velocity difference would, over the course of the collapse, convect the boundary significantly further downstream, producing the observed deformation. The velocity differences are much greater, and the velocity gradients much sharper, than are experienced downstream, which produces much more pronounced deformation.

The last frame of Figure 6.5 offers one of the best snapshots of the effect of the rebound wave on the flow. Along a clear-cut line, the flow ahead of the bubble centroid is accelerated in the $+x$ direction, while the flow upstream of the bubble is decelerated. The region of higher velocity (∼40 m/s, shaped like a sideways T in this shot) is reflective of the pre-existing state of elevated velocity in the region caused by the acceleration of the flow upstream of the bubble during collapse. On the upstream side, the leading edge of the rebound shock is visible, and its structure is apparent. It is composed of two consecutive shock fronts. The first accelerates the flow radially outward, in this particular case enough to arrest flow directly upstream of the bubble. The second front accelerates the flow inward by a smaller amount, resulting in longitudinally-oriented ($+x$ direction) flow at moderate velocities (generally <40 m/s). Downstream, the wave propagates faster, so the leading edge is no longer in the field of view, but the effect should be opposite: the first front accelerates the flow outward (by ∼50 m/s in this case); the second decelerates it to more moderate velocities (and redirects it along the horizontal). The second front transition is just visible at the corners of the flowfield, and it

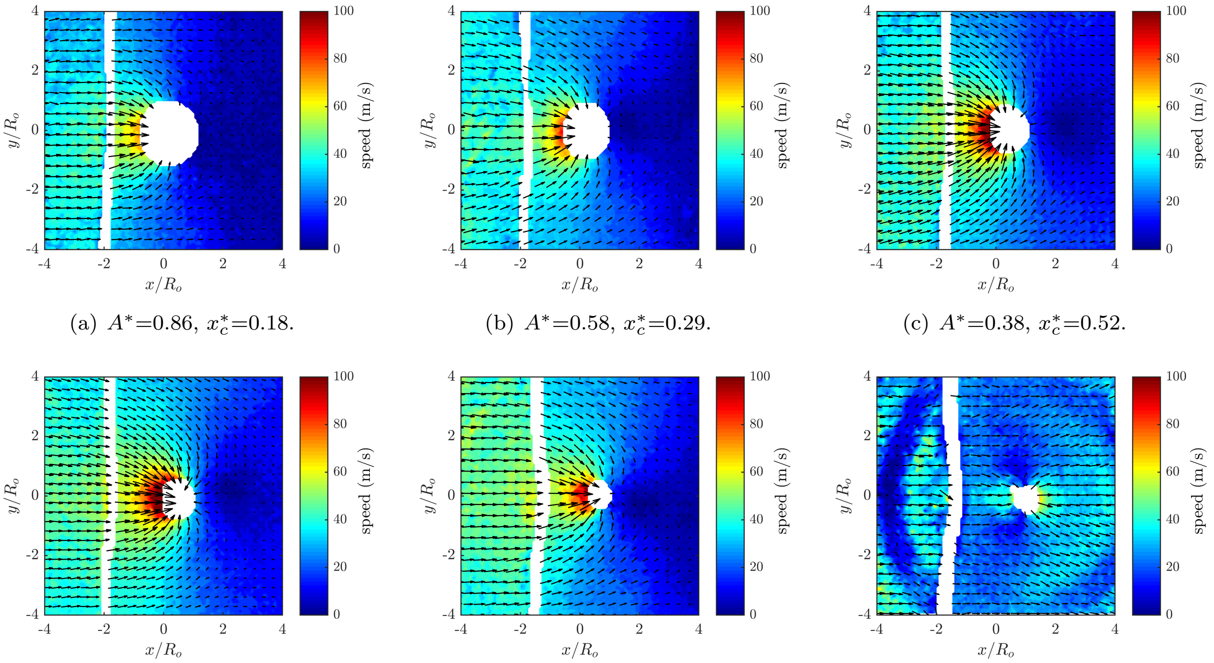

(a) A^*=0.86, x_c^*=0.18.

(b) A^*=0.58, x_c^*=0.29.

(c) A^*=0.38, x_c^*=0.52.

(d) A^*=0.19, x_c^*=0.60.

(e) A^*=0.03, x_c^*=0.83.

(f) A^*=0, x_c^*=1.17.

Figure 6.5: PSV of flowfield during collapse of a cylindrical bubble near an upstream boundary with 20:1 PDMS. Area ratio $A^*={}^{A}/_{A_o}$ and centroid displacement $x_c^*={}^{x_c}/_{R_o}$ of the bubble are indicated.

appears a third wavefront then accelerates the flow from ∼20 m/s to ∼35–40 m/s and gives it an outward radial component. This wavefront is not yet evident in the flow upstream of the boundary.

The rebound wave is evident in Figure 6.6(f), but not nearly as distinct as in the previous figure. This begs the question of why the appearance of the rebound is so variable between different shots, even when the size of the affected region (and thus, presumably, time after collapse) is quite similar. It can be surmised from the variation in collapse times, as well as the form of area-time traces observed in shadowgraph video (Chapter 5) that there is variation in the intensity of the collapse. This, in turn, is expected to affect the intensity of the rebound; a weaker shock will produce smaller velocity changes that are less obvious on the flowfield plot.

6.1.4 Two Boundary Cases

The flowfields for the last group of tests, featuring two boundaries with 20:1 and 40:1 PDMS are presented in Figures 6.7 and 6.8. Again, there does not appear any obvious effect on the flowfield from the presence of the boundaries. The effects of the boundaries appear to combine in straightforward superposition. The deformation of both boundaries is observed, following the behavior of the flowfield and velocity gradients in the same way as the single boundary cases. The combined deformation forms a local narrowing in the agarose channel, a “waist” or an hourglass shape, reminiscent of the deformations observed by Chen et

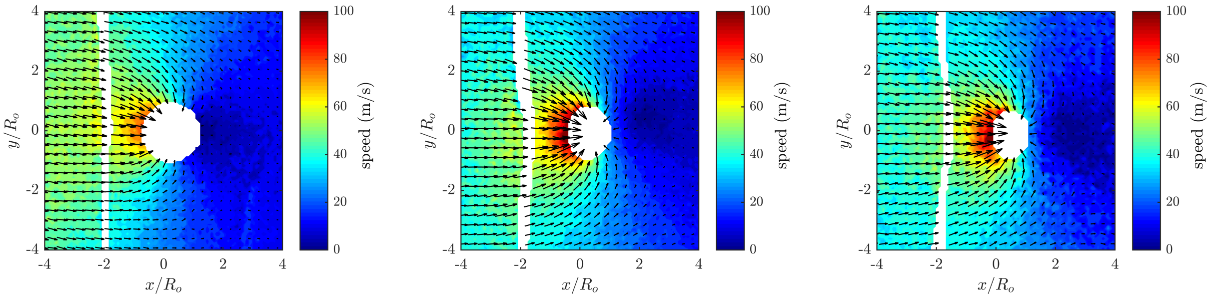

(a) A^*=0.65, x_c^*=0.32.

(b) A^*=0.38, x_c^*=0.40.

(c) A^*=0.21, x_c^*=0.54.

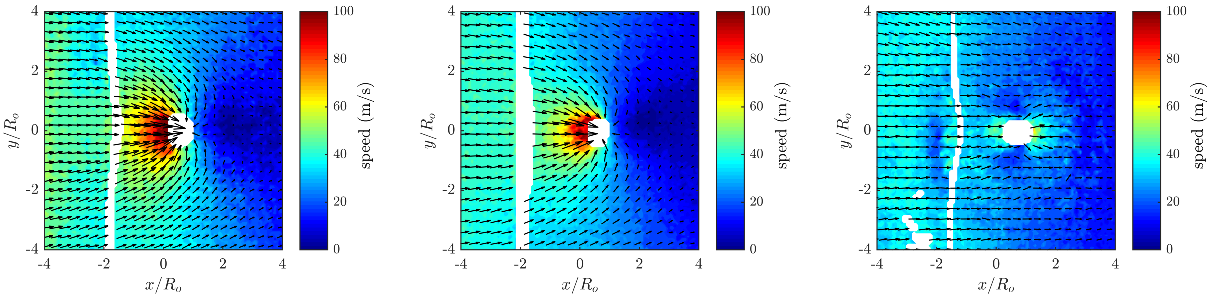

(d) A^*=0.06, x_c^*=0.75.

(e) A^*=0.04, x_c^*=0.83.

(f) A^*=0, x_c^*=0.99.

Figure 6.6: PSV of flowfield during collapse of a cylindrical bubble near an upstream boundary with 40:1 PDMS. Area ratio $A^*={}^{A}/_{A_o}$ and centroid displacement $x_c^*={}^{x_c}/_{R_o}$ of the bubble are indicated.

al. [81] and by Coralic and Colonius [83]. These deformations appear to persist even after the rebound wave has passed.

Figures 6.7(e) and (f) present two post-collapse flowfields showing the rebound wave. The first of these is one of the earliest post-collapse shots, and the leading edge of the rebound wave is visible just barely crossing the boundary into PDMS on both sides, accelerating the flow downstream of the bubble while decelerating the flow upstream. Its outline is also visible, more faintly, in the agarose. Directly above and below the bubble, the existing flow and the flow induced by the bubble add at 90°, which results in the wave having the smallest effect on the flow speed in these locations, making it less clearly visible on the contour plot. In the next image, the wave has propagated further into the PDMS in both directions, and exhibits similar properties to the flowfield in Figure 6.5(f). However, this shot is timed just slightly earlier so that the leading edge of the downstream-traveling wave is still visible. A band of ∼45–50 m/s flow is observed as predicted. A blue region indicates the arrival of a second wavefront, which is just beginning to form behind this band. On the upstream side, only the first front is visible, decelerating the flow from ∼45–50 m/s to almost 0. The post-collapse flowfield in Figure 6.8 features lower velocities, but presents a clear picture of the wave structure overall. All three wavefronts and their velocity transitions between ∼40 m/s and ∼20 m/s are apparent downstream of the bubble, and two wavefronts upstream of the bubble entering the PDMS.

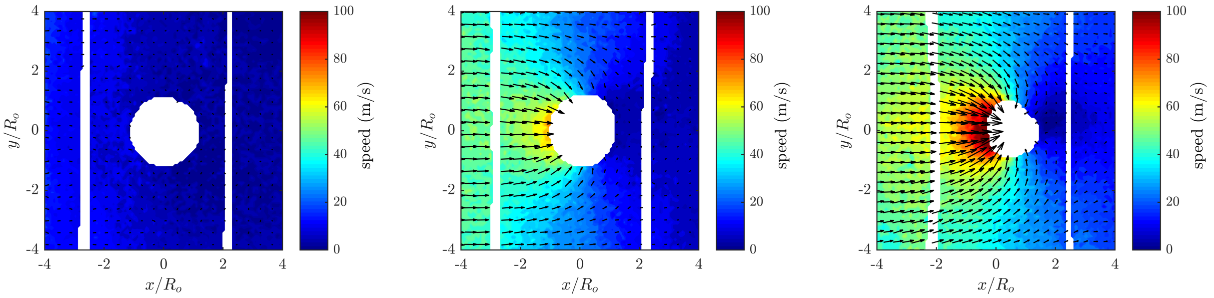

(a) A^*=1.01, x_c^*=0. (b) A^*=0.89, x_c^*=0.10. (c) A^*=0.4, x_c^*=0.50.

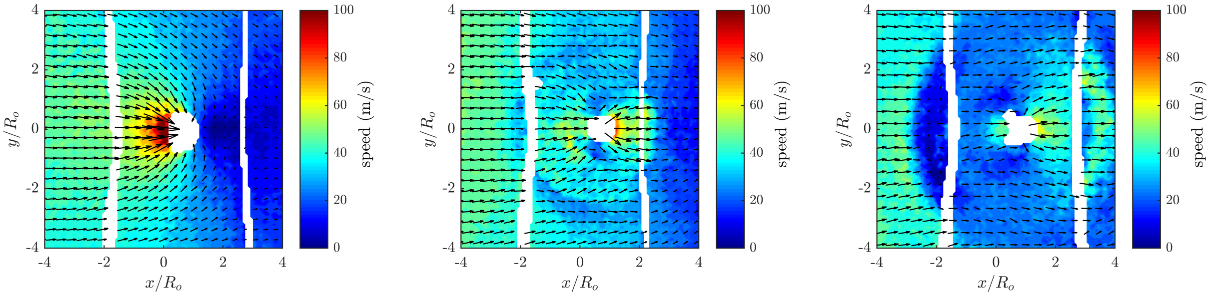

(d) A^*=0.05, x_c^*=0.71. (e) A^*=0, x_c^*=0.82. (f) A^*=0, x_c^*=0.91.

Figure 6.7: PSV of flowfield during collapse of a cylindrical bubble between two boundaries with 20:1 PDMS. Area ratio $A^*={}^{A}/_{A_o}$ and centroid displacement $x_c^*={}^{x_c}/_{R_o}$ of the bubble are indicated.

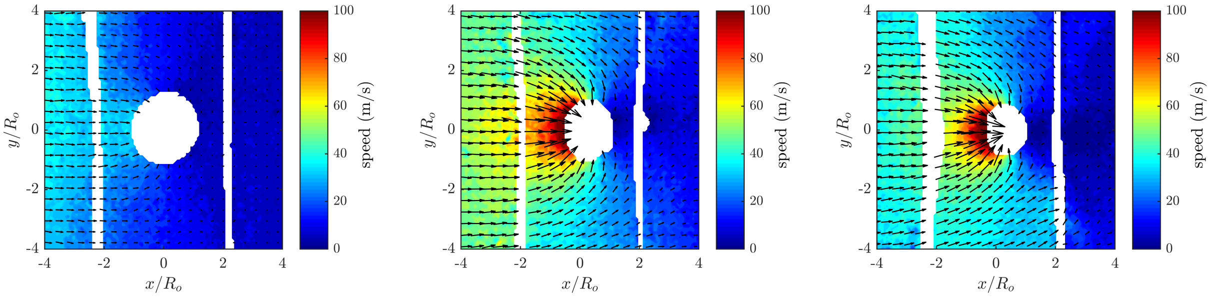

(a) A^*=0.94, x_c^*=0.06. (b) A^*=0.54, x_c^*=0.35. (c) A^*=0.40, x_c^*=0.47.

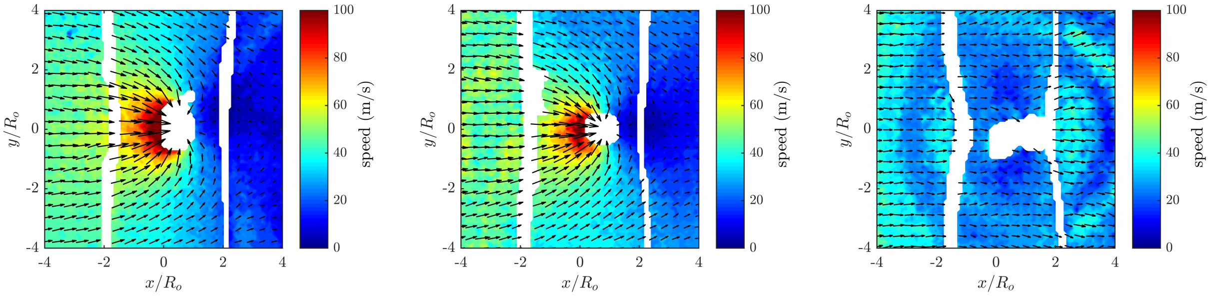

(d) A^*=0.26, x_c^*=0.58. (e) A^*=0.02, x_c^*=0.92. (f) A^*=0, x_c^*=1.26.

Figure 6.8: PSV of flowfield during collapse of a cylindrical bubble between two boundaries with 40:1 PDMS. Area ratio $A^*={}^{A}/_{A_o}$ and centroid displacement $x_c^*={}^{x_c}/_{R_o}$ of the bubble are indicated.

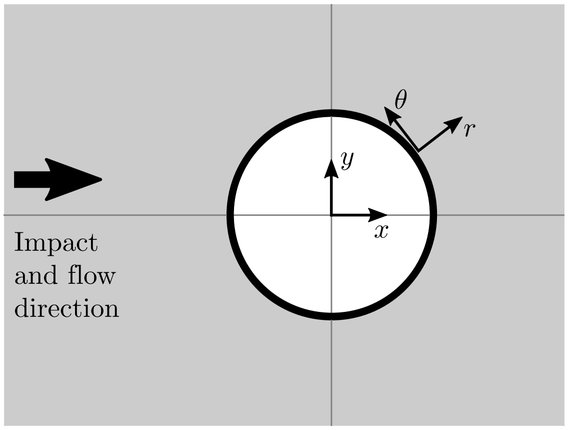

Figure 6.9: Coordinate systems on which flowfields are defined, and discussed.

6.2 Flow Decomposition

As should be clear from the preceding discussion, it is difficult to make comparisons based on just the raw flowfield data, particularly when test-to-test variation in the experiment is taken into account. However, there are observable differences in the type of collapse, which suggests that differences do exist, even if they are subtle. To reveal these subtle differences, aspects of the flow that can be explained by known physics are removed by subtraction, to investigate what remains. Effectively, linearity and superposition of flows is being assumed, without much up-front justification. The two coordinate systems used to define the flows are illustrated in Figure 6.9.

As a first step, the flow caused by the incident wave is identified. The best way to do this given experimental limitations was to use the known fact established by prior research [5, 71] that collapsing bubbles have a limited region of influence on their surroundings. General agreement is that more than 1–2 diameters away from the bubble edge, the flow is minimally influenced by the bubble collapse. The PSV images collected are 4–5 bubble diameters wide, so flow at the edges is assumed to be a good estimate for the flow induced by the incident wave in the free-stream, unaffected by the bubble. The top and bottom 3 rows of each data set were averaged in the transverse direction (spanning 64 pixels in the image, or 0.33 ± 0.05 mm), creating a longitudinal profile of particle velocity for each data set. Averaging, of course, helps smooth out any small fluctuations in the data. The result of this process is shown in Figure 6.10(b). This profile is then subtracted from each row of vectors in the raw data, Figure 6.10(a), to yield the result in Figure 6.10(c). This will be referred to as the bubble-induced flow, as the component of the flow that would not occur if the bubble was absent. It should be noted that separating these flows does not necessarily indicate they are not coupled. It is likely the flow in Figure 6.10(c) could not be produced without also producing the free-stream flow that was subtracted.

The flow in Figure 6.10(c) clearly has a strong radial component that decays with distance. It brings to mind the flowfield for the symmetrical collapse of a bubble, which in turn is of similar form to the equation

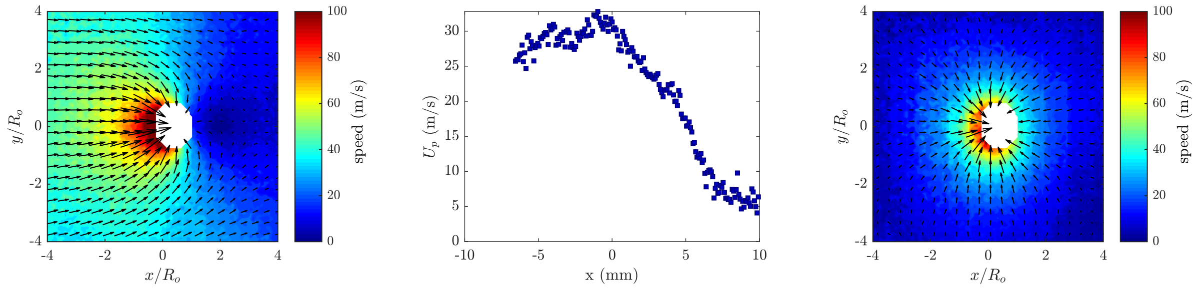

(a) Raw data. (b) 1-D wave profile. (c) Bubble-induced flow.

Figure 6.10: First step in flow field deconstruction: subtract free-stream flow. A test with no boundary, A^{*}=0.39, x_c^{*}=0.48.

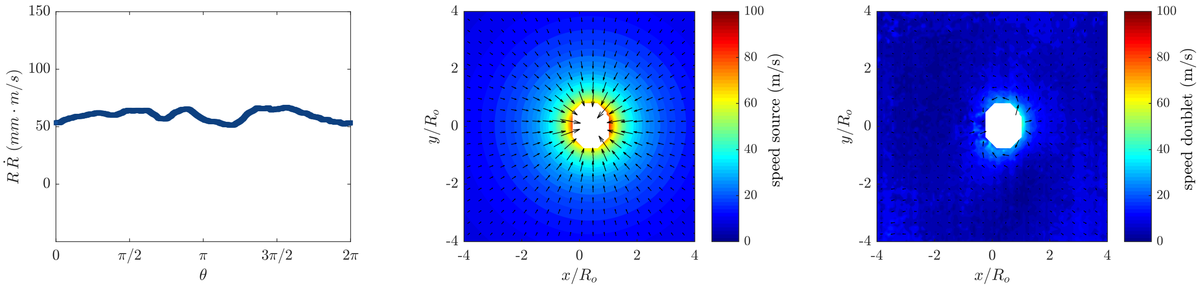

(a) Estimated source strength $Q = R\dot{R}$ at bubble boundary. (b) Source flow. (c) Bubble-induced flow with source subtracted).

Figure 6.11: Second step in flow field deconstruction: compute and subtract symmetrical source flow. Source magnitude shown in convention with $\dot{R}$ positive inward for bubble collapse flows. A test with no boundary, A^{*}=0.39, x_c^{*}=0.48.

for a source flow in potential flow:

$$U_r = \frac{R\dot{R}}{r} = \frac{Q}{r} \tag{6.1}$$

where r is the radial coordinate, R is the bubble radius, overdot indicates rate of change, and Q is a source strength parameter. At first, it was suspected that the source has a strength that is variable with azimuthal coordinate, $Q(\theta)$. This can be tested by obtaining the bubble interface coordinates from the raw images of both PSV frames, converting them to a polar coordinate system with the origin at the bubble centroid, averaging the coordinates to get R and subtracting them to obtain a ΔR, which when divided by the interframe time of 1 μs provides the interface velocity $\dot{R}$. However, when $R\dot{R}$ is plotted against θ as in Figure 6.11(a), no systematic variation emerges, only the random fluctuations of noise. It appears that the higher velocity on the upstream interface are compensated by greater proximity to the centroid, keeping the total $R\dot{R}$ term constant. Therefore, instead of assigning a $Q(\theta)$, an average Q is determined, and a uniform source flow toward the centroid, as in Figure 6.11(b) is subtracted from the bubble-induced flowfield, to produce the flow in Figure 6.11(c).

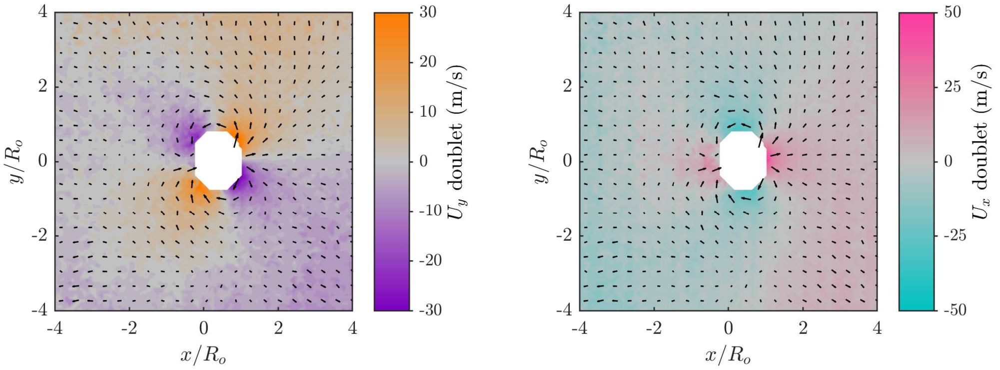

(a) Doublet flow, V (y-direction).

(b) Doublet flow, U (x-direction).

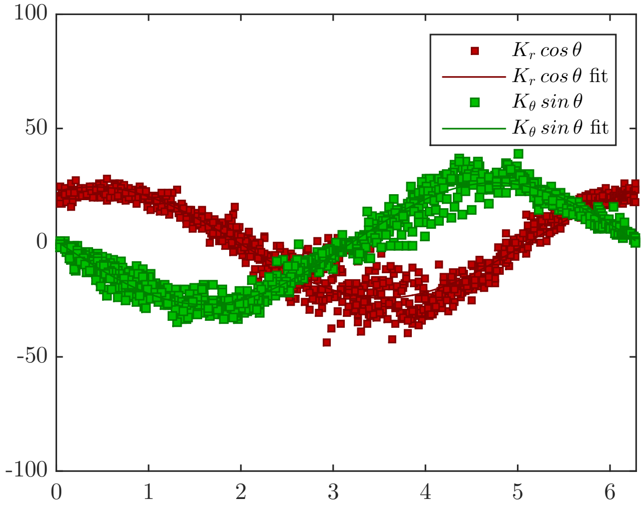

(c) Fitting to determine strength (K).

Figure 6.12: Doublet flow fitting for a test with no boundary, A^*=0.39, x_c^*=0.48.

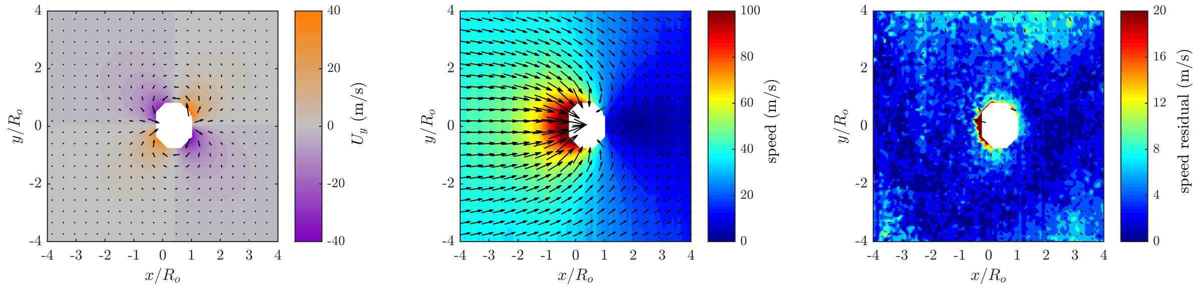

(a) Modeled doublet flow.

(b) Complete model flow, comprised of: wave+source+doublet.

(c) Residuals: difference between data and model.

Figure 6.13: Last step in flow field deconstruction: subtract doublet flow. Complete model flow also shown. A test with no boundary, A^*=0.39, x_c^*=0.48.

The flow in Figure 6.11(c) may be difficult to identify on sight, but its nature becomes much clearer when contours of U_y and U_x are plotted instead of speed (i.e. total velocity magnitude), as in Figures 6.12(a) and 6.12(b). There is a clear pattern to the remaining flow, and it is that of a potential flow doublet, described by:

$$U_r = \frac{K\, cos\theta}{r^2} \tag{6.2}$$

$$U_\theta = \frac{K\, sin\theta}{r^2} \tag{6.3}$$

where K is the doublet strength. To further demonstrate the doublet character of this flow, r^2U_θ and r^2U_r are plotted for a set of points with $r < 1.25R_o$, and then a least squares fit algorithm is used to fit $K\, cos(\theta+a)+b$ and $K\, cos(\theta+c)+d$ respectively to these sets of points. The values a,b,c, and d are arbitrary constants to allow for shifts due to an off-axis incident wave and subsequent flow and improve determination of the strength K that is of greatest interest. The result of the fit is shown in Figure 6.12(c), and it presents an excellent representation of both velocity components.

The modeled doublet flow is presented in Figure 6.13(a). When this is subtracted from the flow in Figure 6.11(c), the result is as shown in Figure 6.13(c). Note the change in colorbar scale. The remaining values are very low across most of the flowfield ($\lesssim$7 m/s), and do not have a readily apparent functional form. There are a few locations where error is higher. Along the top and bottom edges of the flowfield ($^{y}/_{R_o} = \pm 4$), the somewhat higher residual may reflect slightly off-axis propagation of the incident wave. There is also very high absolute residual along the interface of the bubble itself, exceeding 20 m/s. In relative terms, this is not so large, as this is the region where velocity can exceed 100 m/s. The larger error can also be explained by the large velocity gradients and tendency for PIV processing to introduce spatial averaging to the data.

The other way to obtain the residual flowfield is starting with the raw data and subtracting a complete model flowfield comprised of all three flows discussed (that due to the incident wave, the symmetrical source, and the doublet). This complete flowfield is shown in Figure 6.13(b). Mathematically, this model can be represented as follows:

$$\boldsymbol{U} = U_p \boldsymbol{e_x} - \frac{Q}{r}\boldsymbol{e_r} + \left(\frac{K\,cos\,\theta}{r^2}\boldsymbol{e_r} + \frac{K\,sin\,\theta}{r^2}\boldsymbol{e_\theta}\right) + \boldsymbol{U}_{\text{res}} \tag{6.4}$$

Here, bolded variables represent vectors, and $\boldsymbol{e}$ represents a unit vector in the subscripted dimension. The first term, U_p represents the flow caused by the incident wave. The second should be recognizable as the equation of a source from Equation 6.1. The third and fourth are the two components of the doublet flow, Equation 6.2. The final term captures any higher order terms that could not be discerned in the data, effects of asymmetry and off-axis flow, noise, and any other reason for deviation from the model.

Now that the whole model is defined, it becomes apparent the method for fitting it was suboptimal, with two issues of greatest concern. First, at the flowfield edges the source flow can still have $^1/_4$ of the magnitude it does at $R = R_o$. This can noticeably distort the measurement of U_p, given that values of Q as large as 60 mm·m/s have been found. Near $x = 0$ the effect would be negligible, but somewhat upstream and downstream, $\boldsymbol{e_r}$ attains a significant component in $\boldsymbol{e_x}$. The second concern is that there are a number of uncertainties in the determination of Q by using boundary motion; although the PSV images were much higher-resolution, some of the same issues of determining bubble area in shadowgraph videos applied: the presence of dust, droplets, shadows, or smudges could cause the appearance of a jump in velocity or an artificially low radius and throw off the estimate of Q. Any errors in the value of Q would also propagate to fitting $K\,cos\theta$, resulting in different K values from fitting to the two velocity components.

To resolve these issues, a slightly more involved process was ultimately followed:

1. Begin with raw vector data ($\boldsymbol{U}$) and bubble boundary outlines at both PSV exposures.
2. Use bubble boundary outlines to calculate $Q_{\text{est}} = R\dot{R}$ for all θ, then average these values to estimate source flow strength and calculate an estimated source flow ($\boldsymbol{U}_{\text{s,est}}$).
3. Subtract estimated source flow from raw data ($\boldsymbol{U} - \boldsymbol{U}_{\text{s,est}}$). Calculate particle velocity due to the incident wave based on this resulting flowfield ($\boldsymbol{U_p}$).
4. Subtract wave profile from raw data to get bubble-induced flow ($\boldsymbol{U} - \boldsymbol{U_p} = \boldsymbol{U_b}$).
5. Convert resulting flowfield to radial coordinates, with particular interest in azimuthal coordinate $\boldsymbol{U_b}\cdot\boldsymbol{e_\theta}$.
6. Use vectors within a small region around the bubble to fit strength of doublet flow, using $K\,sin\theta = \boldsymbol{U_b} \cdot \boldsymbol{e_\theta}\, r^2$. The "small region" is defined below the list.

7. Use the calculated strength to calculate model doublet flow ($\boldsymbol{U_d}$) and subtract it from the bubble-induced flowfield ($\boldsymbol{U_b}$).

8. What should remain is the source flow ($\boldsymbol{U_S}$) and residuals ($\boldsymbol{U}_{\text{res}}$), which include higher order terms not evident from these data, and experimental error.

9. Re-evaluate source strength Q based on the flowfield instead of boundary motion, then recalculate source flowfield ($\boldsymbol{U_S} = \frac{Q}{r}\boldsymbol{e_r}$). Q was obtained from the flow averaging $(\boldsymbol{U_S} + \boldsymbol{U}_{\text{res}}) \cdot \boldsymbol{e_r} r$ of vectors within a small region around bubble.

10. Now, all components ($\boldsymbol{U_p}$, $\boldsymbol{U_d}$, $\boldsymbol{U_S}$) have been determined, as have the source and doublet strength parameters Q and K.

The "small region" used for fitting K and averaging Q around the bubble was defined as an annulus with area $0.5\,A_o$. Defining it this way maintained the same order of magnitude of points in the fit regardless of the area ratio of the bubble in that test. 400–700 points were included in each fit, varying with A_o and image scale. Since flow right at the bubble interface may violate assumptions that apply elsewhere in the flowfield, and those data had higher uncertainty due to large velocity gradients, the region was excluded from the fit by defining the inner radius of the annulus as $1.1\,R_{\max}$ (where $R_{\max}$ is the largest value of $R(\theta)$). The outer radius was computed from $R_{\text{out}}^2 = 0.5R_o^2 + R_{\text{in}}^2$.

This model was applied to all the flow geometries. The expectation was that for flows with boundaries one of two things would occur: either an observable difference in parameters would be observed, or a pattern of deviation from the model would occur, suggesting that an underlying assumption of the model has been violated. The parameters thus determined across all the tests are tabulated in Appendix H, and plots of U_p, $R\dot{R}$, and the fitting of K_θ are provided in Appendix G. 80% of tests with A^* between 0.1 and 0.9 had an R^2 value of 0.7 or greater for the fitting of K_θ. The average residual values range from 1.7 to 8.3 m/s with an average of 4.6 m/s, which constitutes 2–13% of the maximum velocity (average of 4.6%), and 10–56% of the average velocity (average of 23%), with higher error being associated with higher area ratios and slower flows. These average residual values are elevated by not adjusting the model for off-axis wave propagation in the data, and deviations from the model by some flows with boundaries. If an adjustment was introduced for the first, and the second group were excluded, even better fit quality would be expected.

6.3 Modeled Flows and Residuals

Select examples of modeled flows and residuals will be presented in this section, but a complete set of data, models, and residuals is provided in Appendix F. The examples were selected from the sets in Section 6.1 to show well-developed flows and span a good range of area ratios for each condition. Each image presented here will be accompanied by its area ratio A^*, for reference, as well as its mean absolute residual (MAR) value to describe the quality of the fit. This is simply the average of all the residual values in the dataset. Incidentally, the noise threshold of the PIV system is about 5 m/s, as determined by running the analysis on a stationary object, and by analyzing an image pair with known particle displacement (see Section 2.5). It is telling that the average residual for all tests is also around this value.

Figure 6.14 presents modeled flows and residuals for 6 of the 9 tests presented in Figure 6.1. Most of the MAR values are at or below the noise threshold, suggesting the agreement is quite good. The flowfield in Figure 6.14(b) has elevated residual values and a pattern to the error. Based on the direction of the residual vectors, it appears there was a problem in the confinement of gel by the spacer bars, allowing the gel to flow outwards along the edges. This was difficult to identify in the raw data, because the outward flow was compensated by inward flow from the bubble collapse, leaving inconspicuous horizontal vectors. In spite of this apparent issue, the fit is good in the vicinity of the bubble.

The residuals in Figure 6.14(c) also deserve some comment. Although the average value is not particularly high, there are clearly zones of elevated residuals. If the model is cross-referenced with the original data plot, it becomes clear that this was a case of slightly off-axis wave propagation. The diagonal pattern of the error is characteristic of this issue. This can certainly be accounted for in future implementations of the modeling process.

The remaining images in Figure 6.14 have elevated residuals only around the bubble interface, co-located with the higher velocities and velocity gradients experienced by the flow. How this can generate higher residuals was discussed in Section 6.2.

Modeled flows and residuals for the collapse of a bubble near a downstream aluminum boundary are shown in Figure 6.15. Although the fit is good in the first frame, where the bubble collapse has hardly begun, the fit deteriorates in the immediate vicinity of the bubble as the collapse progresses, particularly just upstream of the bubble, and between the bubble and the boundary. This is the kind of deviation from the model that was expected to occur, if the introduction of boundaries constituted sufficient change to system parameters.

For the case of the aluminum boundary, it may be helpful to consider that the collapse of bubbles near solid boundaries under constant pressure loading has been modeled using the method of images, with a potential source centered on the bubble, and another reflected across the solid surface [90, 93]. It would stand to reason that the same reasoning would applies to this incompressible model. However, because the reflection of the wave off the boundary, and effect on U_p, is already accounted for by the measurement of U_p, and the flow speed associated with the doublet drops off rapidly as $^1/_{r^2}$ from its origin, the dominant cause of error of the model is likely the absence of an image source, specifically.

When the rigid aluminum boundary is replaced with a more compliant one of 20:1 PDMS, the large region of error between the bubble and the boundary does not appear. A smaller region just upstream of the bubble does exhibit elevated residuals in Figure 6.3(c); this occurs for smaller area ratios in a number of tests in the downstream and two-boundary groups, following the same pattern, which may indicate a deviation from the model due to the presence of the boundary.

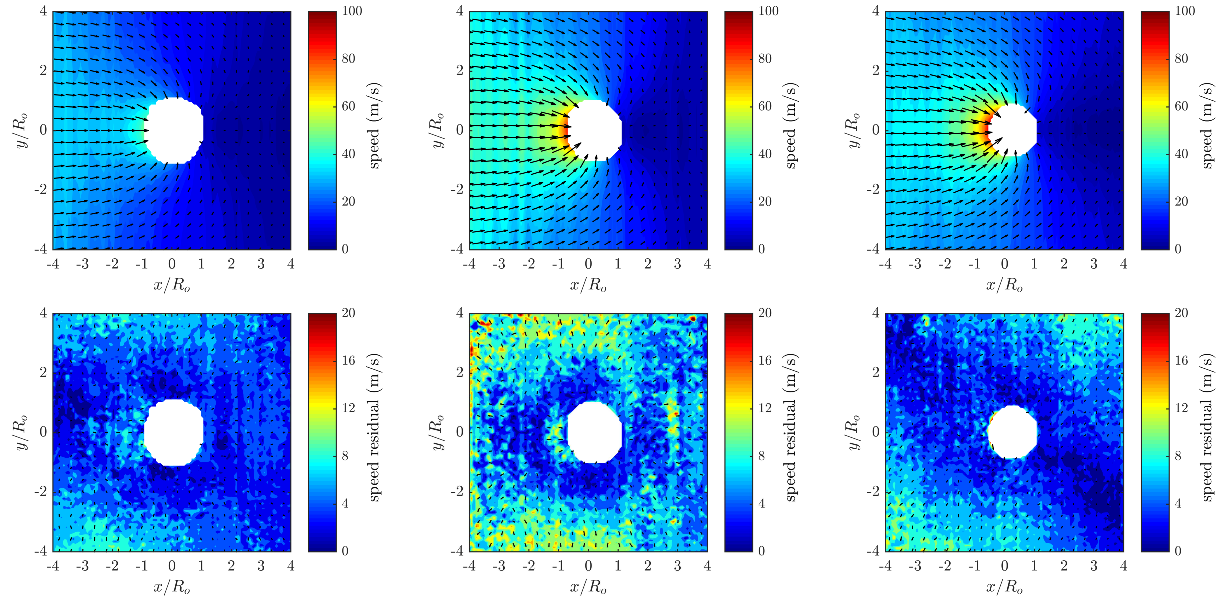

(a) A^*=0.89, MAR=4.7 m/s.

(b) A^*=0.74, MAR=7.3 m/s.

(c) A^*=0.56, MAR=5.1 m/s.

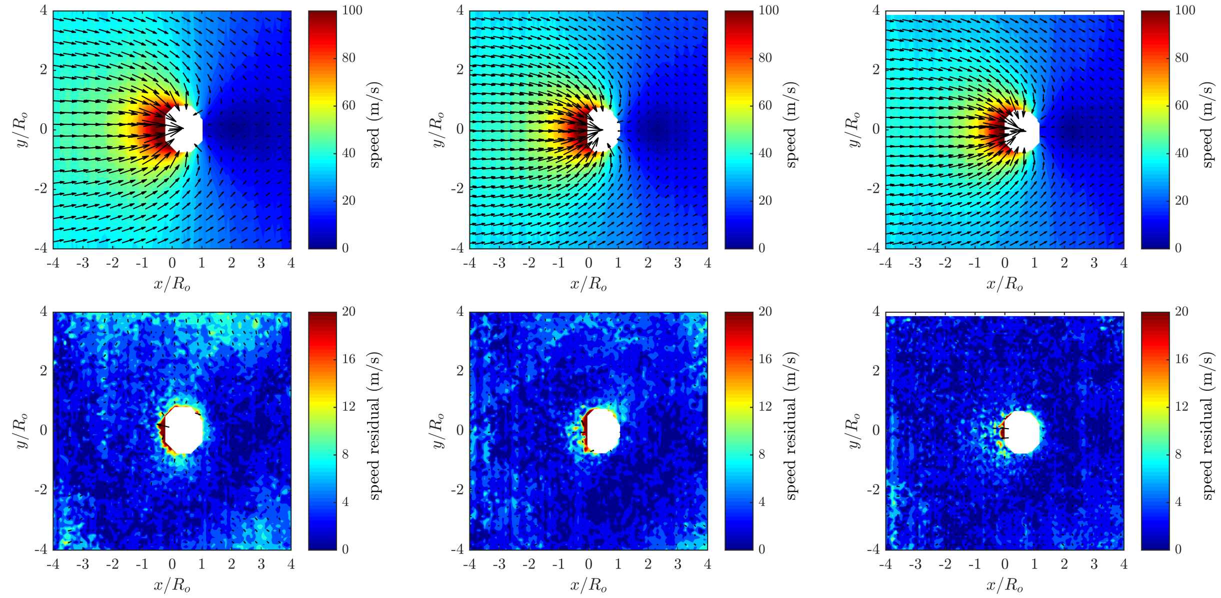

(d) A^*=0.39, MAR=4.4 m/s.

(e) A^*=0.29, MAR=3.7 m/s.

(f) A^*=0.15, MAR=2.9 m/s.

Figure 6.14: Model flowfield and residuals for selected data in Figure 6.1. Area ratio $A^*={}^{A}/_{A_o}$ and centroid displacement $x_c^*={}^{x_c}/_{R_o}$ of the bubble are indicated.

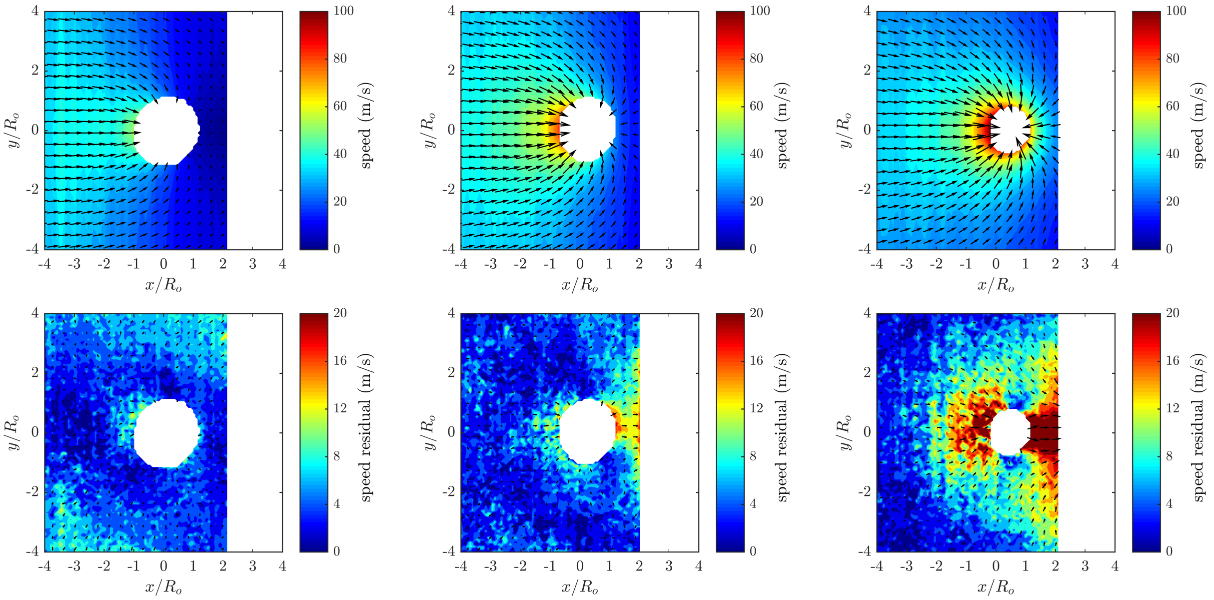

(a) A^*=0.89, MAR=5.1 m/s.

(b) A^*=0.6, MAR=4.8 m/s.

(c) A^*=0.21, MAR=7.4 m/s.

Figure 6.15: Model flowfield and residuals for collapse of a cylindrical bubble near a downstream boundary with aluminum. Area ratio $A^*={}^{A}/_{A_o}$ and centroid displacement $x_c^*={}^{x_c}/_{R_o}$ of the bubble are indicated.

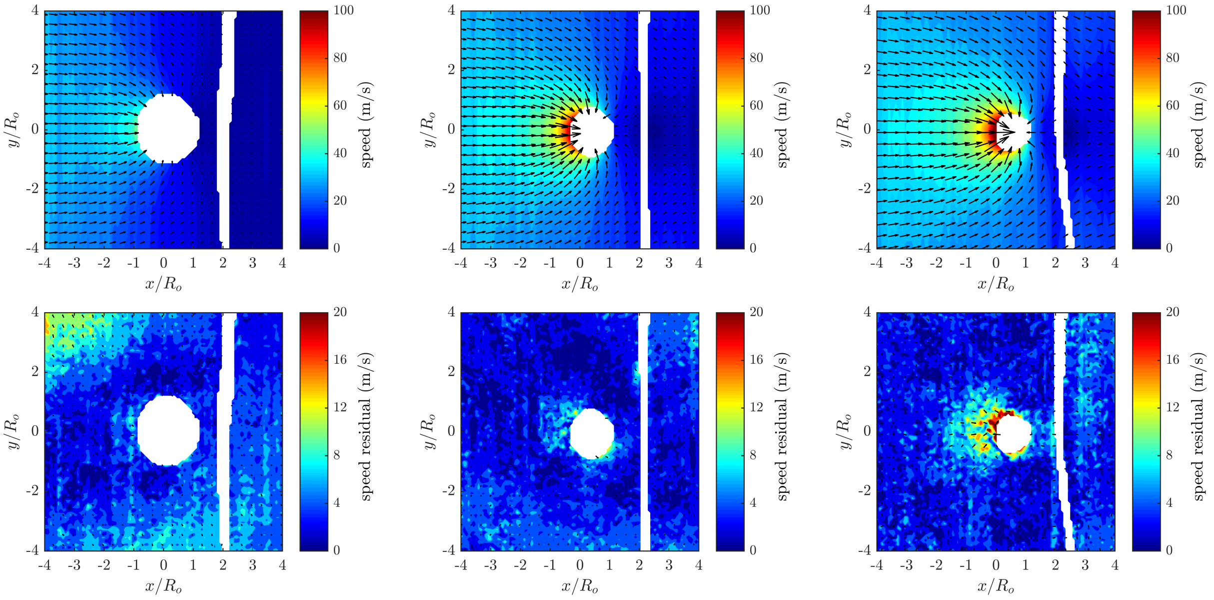

(a) A^*=0.89, MAR=4.6 m/s.

(b) A^*=0.4, MAR=3.7 m/s.

(c) A^*=0.10, MAR=3.9 m/s.

Figure 6.16: Model flowfield and residuals for collapse of a cylindrical bubble near a downstream boundary with 20:1 PDMS. Area ratio $A^*={}^{A}/_{A_o}$ and centroid displacement $x_c^*={}^{x_c}/_{R_o}$ of the bubble are indicated.

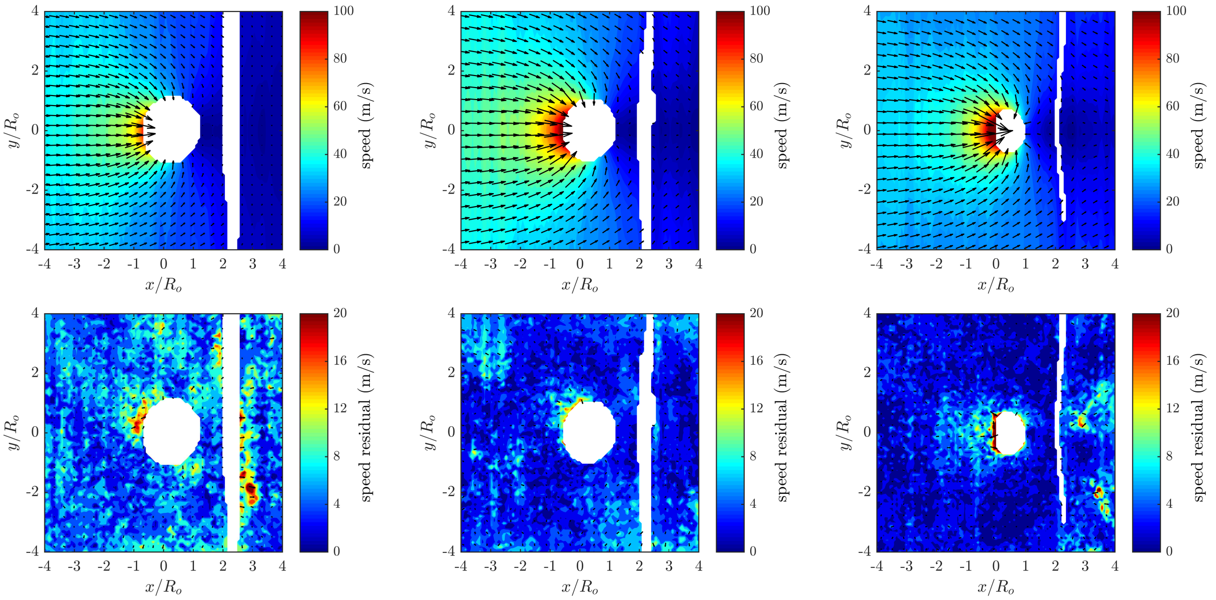

(a) A^*=0.67, MAR=5.5 m/s. (b) A^*=0.59, MAR=4.3 m/s. (c) A^*=0.21, MAR=3.3 m/s.

Figure 6.17: Model flowfield and residuals for collapse of a cylindrical bubble near a downstream boundary with 40:1 PDMS. Area ratio $A^*={}^{A}\!/_{A_o}$ and centroid displacement $x_c^*={}^{x_c}\!/_{R_o}$ of the bubble are indicated.

When 20:1 PDMS is replaced with 40:1 PDMS (Figure 6.17), the region of elevated residuals upstream of the bubble becomes very faint, but is still present. It also appears in other tests at this condition with low area ratio, more faintly than the 20:1 PDMS and 30:1 PDMS cases. The high-residual regions in Figure 6.17(a) appear quite random, and are likely due to small disturbances to the PSV due to scratches, smudges, or dust that were not apparent in the original flowfield.

The cases of collapse near an upstream boundary, shown in Figures 6.18 and 6.19, agree with the model very well, with only some moderate-level experimental noise, and the high residual right at the bubble interface for the smallest area-ratio shots.

The two boundary case with 20:1 PDMS (Figure 6.20) exhibits a much fainter region of elevated residuals than did the downstream boundary case, and in the 40:1 PDMS two-boundary case, the error in all cases with small area ratios appears symmetric or random, due to experimental flaw (such as the one in Figure 6.21(b)).

It is apparent from the modeled flows and residuals showcased in this section as well as the complete set in Appendix F that the model fits the data in most cases down to the threshold of experimental error. Deviation from the model was clearly observed for the case of bubble collapse near a downstream aluminum boundary, but was not quite so apparent for the cases involving PDMS boundaries. The differences between the flows that facilitate the formation of re-entrant jets in the case of agarose, but far less frequently or not at all in the other geometries will need to be sought in the evolution of the model parameters themselves.

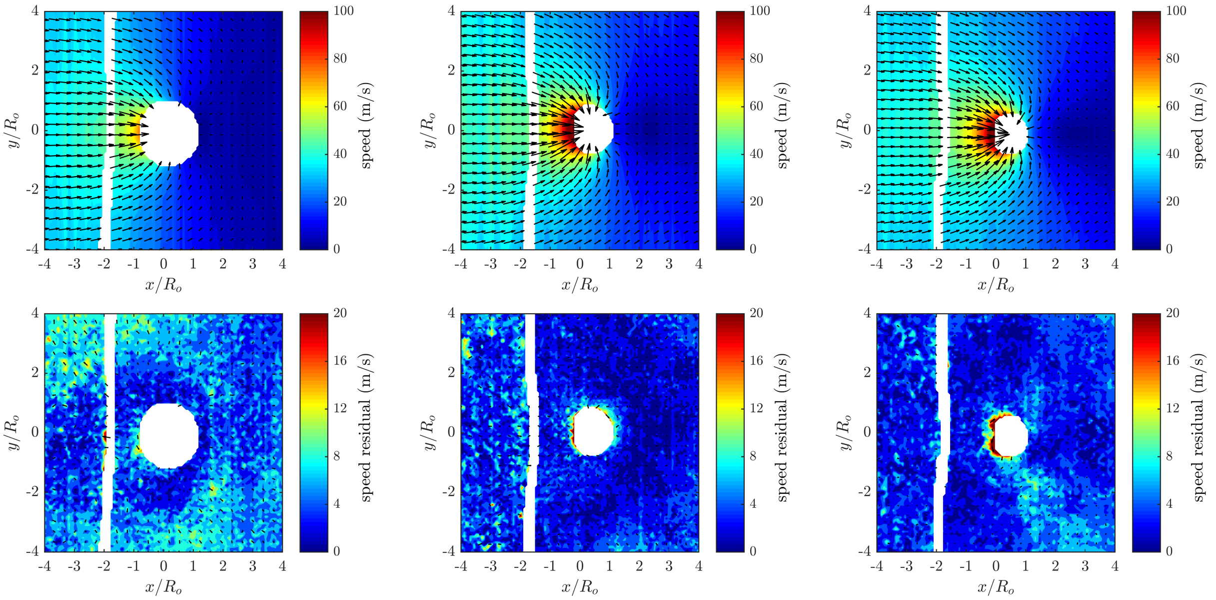

(a) A^*=0.86, MAR=5.5 m/s.

(b) A^*=0.38, MAR=3.8 m/s.

(c) A^*=0.19, MAR=4.3 m/s.

Figure 6.18: Model flowfield and residuals for collapse of a cylindrical bubble near an upstream boundary with 20:1 PDMS. Area ratio $A^*={}^{A}/_{A_o}$ and centroid displacement $x^*_c={}^{x_c}/_{R_o}$ of the bubble are indicated.

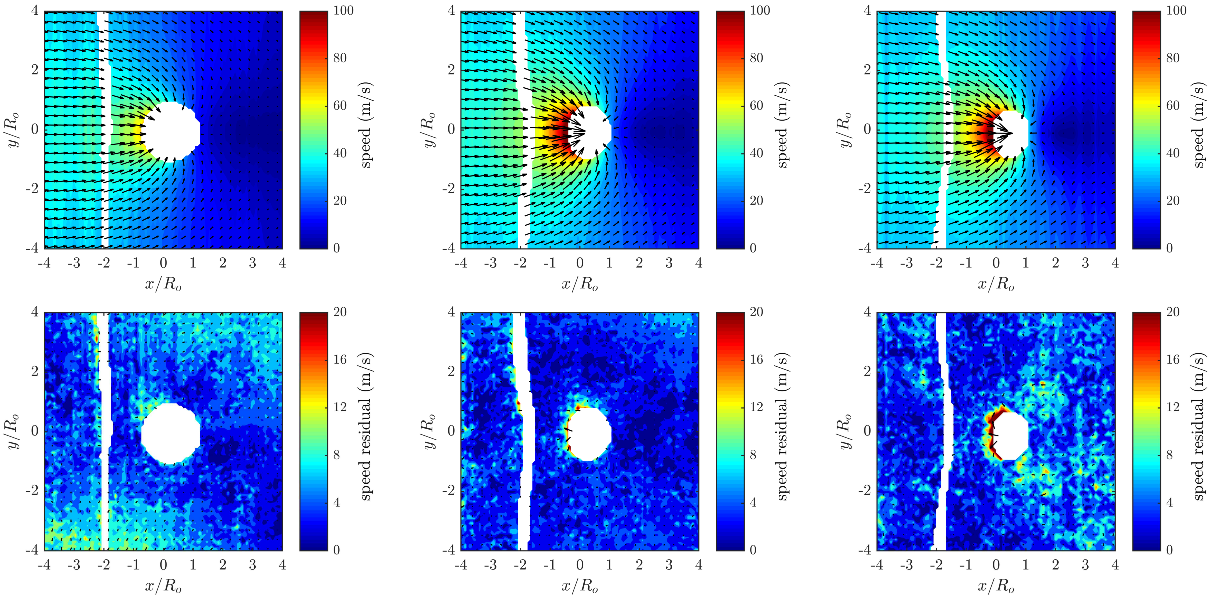

(a) A^*=0.65, MAR=5.4 m/s.

(b) A^*=0.38, MAR=4.0 m/s.

(c) A^*=0.21, MAR=4.7 m/s.

Figure 6.19: Model flowfield and residuals for collapse of a cylindrical bubble near an upstream boundary with 40:1 PDMS. Area ratio $A^*={}^{A}/_{A_o}$ and centroid displacement $x^*_c={}^{x_c}/_{R_o}$ of the bubble are indicated.

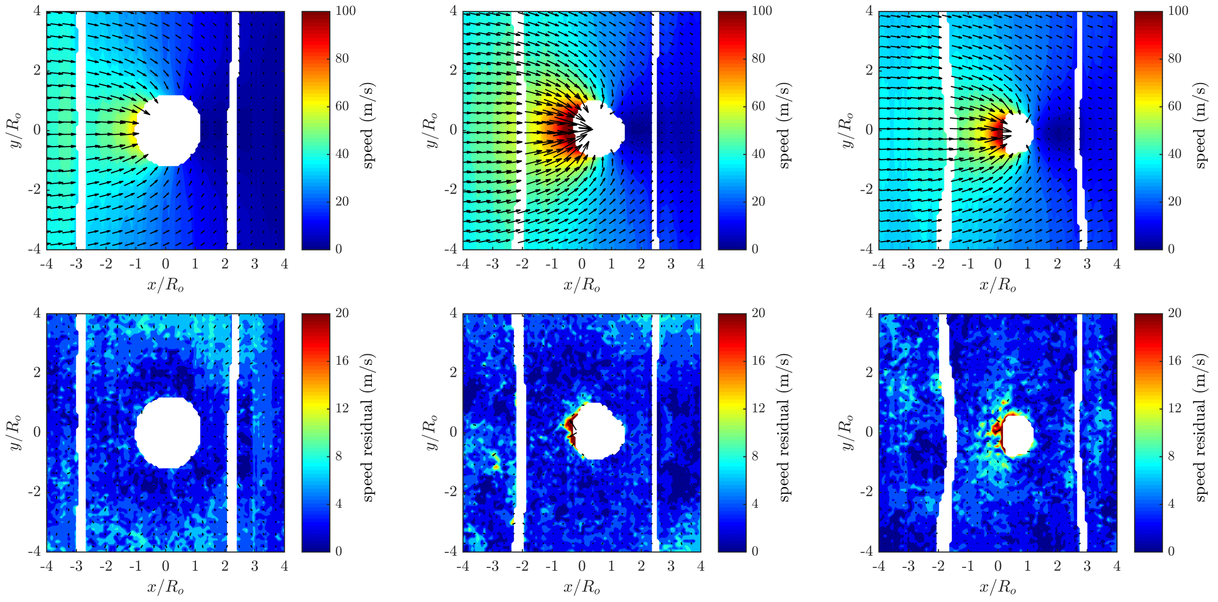

(a) A^*=0.89, MAR=4.1 m/s. (b) A^*=0.4, MAR=4.5 m/s. (c) A^*=0.05, MAR=3.9 m/s.

Figure 6.20: Model flowfield and residuals for collapse of a cylindrical bubble between two boundaries with 20:1 PDMS. Area ratio $A^*={}^{A}/_{A_o}$ and centroid displacement $x_c^*={}^{x_c}/_{R_o}$ of the bubble are indicated.

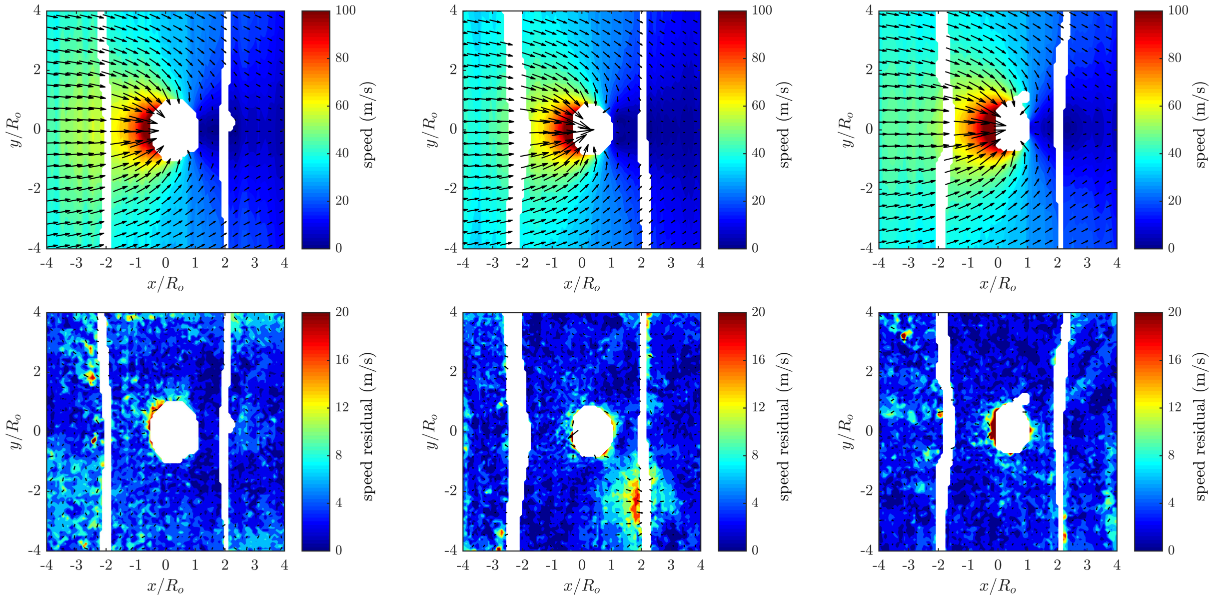

(a) A^*=0.54, MAR=4.4 m/s. (b) A^*=0.40, MAR=4.0 m/s. (c) A^*=0.26, MAR=3.9 m/s.

Figure 6.21: Model flowfield and residuals for collapse of a cylindrical bubble between two boundaries with 40:1 PDMS. Area ratio $A^*={}^{A}/_{A_o}$ and centroid displacement $x_c^*={}^{x_c}/_{R_o}$ of the bubble are indicated.

6.4 Evaluation of Flow Regime and Applicability of the Potential Flow Model

It should be apparent from the previous section and associated appendices that a potential flow model with time-variant strength parameters can represent the data at multiple time points throughout the collapse process to experimental accuracy. This section will focus on examining the regime of the fluid flow in the experiment as well as the assumptions included in the proposed model, and the extent of its applicability. First, a thorough dimensional analysis of all the parameters of this problem will be used to elucidate the role of various physical mechanisms, and subsequently, the time-dependence of the problem will be explored. As a result, it will become clear that applied pressure and fluid inertia dominate this problem, whereas viscosity, compressibility, surface tension, gravitational forces, and heat transfer all have minimal effects on the flow.

6.4.1 Dimensional Analysis: Problem Summary

Although the problem of bubble collapse overall is complex, the geometry in two dimensions (cylindrical coordinates) can be described by only the initial size of the bubble, R_o. This is also true of an initially spherical bubble, but that is not the problem under investigation. A number of studies have investigated the collapse of bubbles of different cross-sectional shapes, such that $R_o = R_o(\theta)$ and it is clear this initial shape influences the flow that develops [33, 172]. However, it is not clear to what extent, if any, the results of this study are applicable to such a geometry; therefore, no attempt will be made to quantify bubble shape in the dimensional analysis.

A number of material properties can have an effect on the collapse process, including the viscosity (μ), density (ρ), and sound speed (a), of both the bubble (b) and ambient (a) fluids. Surface tension (S) and thermal effects (dependent on any or all of: conductivity, k, specific heat, C_p, and initial temperature T_o) could also potentially become significant under certain conditions, for example if the bubble is very small, or at the end of an intense collapse process. In the case of a viscoelastic ambient environment, the elastic aspect of the material response must also be considered. There are many models of varying complexity that represent viscoelastic behavior, but a simple viscoelastic fluid might be represented as having an elastic modulus (E) as well as a viscosity parameter. Thus, the material properties contribute an additional 6 variables to the problem in the case of a Newtonian ambient fluid, or 7 in the case of a viscoelastic ambient fluid, and potentially 6 additional variables in cases where surface tension and thermal effects must be considered.

The loading condition is the most complex aspect of the problem to define. The simplest case is that of an instantaneous change in pressure in the far field, i.e. several diameters from the bubble in the ambient fluid. This creates a differential between the interior of the bubble and the far-field, $\Delta P_b = P_\infty - P_o$. However, this simplified scenario is expected to result in symmetrical bubble collapse as investigated in Chapter 4. To create asymmetrical collapse, asymmetrical confinement such as a material boundary must be present (see Sections 1.5 and 1.6), or a pressure imbalance must be created, for example, by a moving wave. A shock wave would be associated with not only a pressure change across the wave of ΔP_w, but also with a shock velocity U_s. This introduces a timescale $t_w = R_o/U_s$ during which a pressure imbalance persists across the bubble; that is, the bubble experiences a nonuniform pressure loading $P(\theta)$ around its perimeter. The propagating wave also accelerates the fluid behind the wavefront, far from the bubble, to a free-stream velocity U_∞. This velocity is dependent on the equation of state of the ambient substance.

If the propagating wave also has a finite lengthscale L_w over which the pressure rises, the duration of pressure imbalance becomes approximately $t_w = (R_o + L_w)/U_s$, which allows the duration of pressure imbalance on the bubble to be independent of R_o/U_s. Such a model is representative of the loading wave in the experiment, where the flow is primarily two-dimensional, but the pressure is continually affected by the flexure of the structure (see Section 3.4). In a two-dimensional representation of this system, U_∞ no longer appears to correspond to P_w per the equation of state, due to the deformation of the fixture relieving pressure in the gel layer. Accounting for this mechanism by assigning both U_∞ and P_w to the two-dimensional system allows the fluid system to be analyzed without modeling the dynamics of the structure in detail.

Following the reasoning in the previous three paragraphs, the following quantities are required to model the loading wave: ΔP_w, U_s, L_w, U_∞. Fewer quantities can be used to model simpler loading scenarios, e.g. if $L_w = 0$. Gravitational loading can also be included (g). Although not expected to be significant in this case, the hydrostatic gradient can become significant for large bubble dynamics (as in underwater explosion problems [97]) or in bubbles experiencing no additional loading [104, 105].

The result of the bubble collapse interaction can be described by the time- and spatially-variant velocity ($\mathbf{U}$), pressure (P), and temperature (T) fields. Strain (ϵ) and bubble morphology ($R(\theta, t)$) may be substituted for velocity if they are the focus of particular studies, but these quantities would be dependent on the velocity field over time, and thus would not qualify as independent outputs of the system. The velocity, pressure, and temperature results will be coupled through the conservation of mass, momentum, and energy (the Navier-Stokes equations), but collectively they define the state of the system during the collapse process. These three output functions are a function of as many as 19 total variables: R_o to describe the initial geometry, up to 12 material properties, 4 values describing the loading wave, and g. Per the Buckingham Pi theorem, the problem can instead be modeled with up to 15 dimensionless groups. These dimensionless groups can be used to highlight the relative importance of various physical mechanisms in the problem, to justify neglecting those of limited importance in order to simplify analysis.

Of the 19 variables (plus three spatial coordinates), 4 must be selected to nondimensionalize the rest. A reasonable set that contains all the physical dimensions includes: the initial radius (R_o), the initial ambient density (ρ_a), the ambient sound speed (a_a), and the initial temperature (T_o).

6.4.2 Geometry and Loading Wave Parameters

The problem includes two characteristic velocities: the shock velocity (U_s) and the free-stream velocity (U_∞). The two are related through mechanics of the system; defining them separately captures the effect of the fixture mechanics on the fluid. In some systems, the variables may be more simply related, e.g. directly through the shock Hugoniot, without influence from additional mechanics; in this case only one may be necessary to quantify the fluid state. A third reference velocity is useful to define for scaling considerations, an average collapse velocity $U_c = R_o/t_c$. The collapse time t_c can be estimated based on the applied pressure and density from $t_c = 1.5R_o\sqrt{\rho_a/\Delta P_w}$, as discussed in Chapter 4. Neglecting the coefficient of 1.5 as largely irrelevant for the scaling analysis, this velocity can also be expressed as $U_c = \sqrt{\Delta P_w/\rho_a}$.

The first three nondimensional groups to consider are the reference velocities above, scaled by the sound speed:

$$\Pi_1 = M_s = \frac{U_s}{a_a} \tag{6.5}$$

$$\Pi_2 = M_\infty = \frac{U_\infty}{a_a} \tag{6.6}$$

$$\Pi_3 = M_c = \frac{U_c}{a_a} \tag{6.7}$$

These values represent the role of compressibility of the ambient fluid during the collapse process. The free-stream flow velocity is around 40 m/s, yielding a flow Mach number (M_∞) is about 0.03, far below the M=0.3 threshold typically used as the lower bound of compressible flow [173]. The collapse velocity U_c is between 60 and 120 m/s for R_o =1.2 mm and collapse times between 10 and 20 μs. This is yields M_c <0.1, although the actual velocity of the bubble boundary increases exponentially during much of the collapse, so the actual value of $\dot{R}$ may significantly exceed U_c near the end of the collapse. If $\dot{R}(t)$ is known, it can be used instead of U_c to determine at what time in the collapse the compressibility of the ambient fluid becomes significant. In contrast to the present experiments, the 1.9 GPa shocks used by Bourne and Field, and later Ball et al. [33, 36] yield U_c =1378 m/s (M_c =0.92), indicating that compressibility is important throughout most of the collapse process.

For a fourth nondimensional group, the lengthscale of the wave (L_w) should be considered. It is tempting to simply use the reference length R_o, but it should also be determined whether this is meaningful. The bubble responds to pressure changes in the far-field which occur at a given time, $P_\infty(\theta) - P_o$. If the wave has not yet arrived and P_∞ is uniformly P_o, the bubble will remain stationary. If the wave has fully passed, the bubble will experience a uniform pressure environment (P_∞) and respond accordingly. If a shock wave has traversed half the bubble, then half the bubble will experience elevated pressure (and thus acceleration) while the other half remains stationary, and a small region near the sharp wave front experiences a complex loading and acceleration scenario. If the wavefront is no longer sharp, but spans a significant portion of the bubble, it places the bubble under moderately elevated pressure and a pressure gradient. However, this loading condition will only last as long as the wavefront remains over the bubble. Therefore, a wave passage timescale is proposed, for the time a pressure imbalance persists over the bubble:

$$t_w = \frac{R_o + L_w}{U_s} \tag{6.8}$$

and a nondimensional scaling with collapse time logically follows, so as to indicate what portion of the collapse would be affected by the pressure imbalance:

$$\Pi_4 = \frac{t_w}{t_c} = \frac{(R_o + L_w)/U_s}{R_o\sqrt{\rho/\Delta P_w}} = \left(1 + \frac{L_w}{R_o}\right)\frac{U_c}{U_s}. \tag{6.9}$$

While the ratio of timescales is expected to be relevant for all conditions, the exact form of the right-hand side of the equation is dependent on reasonable estimates for the collapse time. The estimate $t_c = 1.5R_o\sqrt{\rho/\Delta P_w}$ is derived from relations for symmetrical bubble collapse (see Chapter 4). It will apply only as long as the area change of the bubble is primarily dependent on a radially symmetric flow; note that this does not preclude bubble deformation into an asymmetrical shape through the presence of other flow components such as the doublet flow.

This estimate for t_c may underpredict collapse time at shock pressures above about 350 MPa, as M_c exceeds the threshold value of 0.3, and compressibility begins to play a significant role. Compressibility effects will decrease the velocities that develop, and therefore increase collapse time above the estimate [96]. However, above the same pressure threshold, the velocity difference across the bubble caused by the loading wave can compress the bubble in the longitudinal direction by over 10%, accelerating the collapse process. Assuming $t_w < t_c$, the contribution of this mechanism to the bubble collapse can be estimated using the following:

$$\frac{\Delta W}{W_o} = \frac{U_p t_w}{2R_o} = \frac{U_p}{2U_s} \tag{6.10}$$

$$\Delta P = \rho_a U_s U_p \tag{6.11}$$

$$U_s = 1500\text{m/s} + 2U_p \quad \text{for gel} \tag{6.12}$$

where W indicates bubble width at the centerline. The change in width due to difference in U_p across the bubble comes to less than 1% for pressures under 23 MPa, and less than 10% for pressures under 350 MPa. Quantifying the effect of liquid compressibility is much more complicated, but it is evident that as U_c decreases below $\sqrt{\Delta P_w/\rho}$ the symmetric flow will contribute less than predicted to the collapse and the imbalance in U_p across the bubble will have a more pronounced effect. However, it is not apparent which effect will dominate, and thus whether collapse time will increase or decrease overall, or how it will scale with increasing Mach number. At lower pressures, even if the wave is distributed over L_w and persists for the entire collapse time, the velocity difference does not contribute significantly to the collapse, so the scaling proposed for Π_4 is expected to apply (Equation 6.9). The entire expression scales as $\sqrt{(M_s-1)/M_s}$, which for Mach numbers close to 1 behaves as $\sqrt{M_s-1}$. For large Mach numbers, as previously discussed, the scaling of t_c and therefore the expression as a whole may change.

The foregoing discussion primarily focused on the effect of compressibility on bubble collapse time. The role of compressibility in the development of the flowfield around the collapsing bubble will be discussed in greater detail in Section 6.4.6.

6.4.3 Ambient Fluid Property Parameters

The next four nondimensional groups are intended to evaluate contributions of the viscosity (μ_a), surface tension (S_a), gravitational acceleration (g), and elasticity (E) to the collapse process.

The role of viscosity can be deduced from a Reynolds number,

$$\Pi_5 = Re = \frac{\rho_a U_c R_o}{\mu_a}. \tag{6.13}$$

This can also be rewritten using the pressure-based expression for U_c, in which case it matches a Reynolds number proposed by Khasainov for void collapse processes [174]:

$$Re = \frac{R_o\sqrt{\rho_a \Delta P_w}}{\mu_a}. \tag{6.14}$$

The choice of which one to use will depend on the availability or relative certainty of the pressure loading condition or the collapse time in any particular situation. Using $R_o = 1.2$ mm, $U_c = 100$ m/s, $\rho_a = 1000$ kg/m^3, and $\mu_a = 8\times10^{-3}$ Pa·s for agarose gel yields a Reynolds number of 15,000. This puts the collapse process firmly in the hydrodynamic regime, where pressure and inertial forces dominate over viscous forces. The Reynolds number could be justifiably considered "high" for bubble radii up to 100 times smaller, or tens of micrometers in radius in the same conditions, but a wider range of bubble sizes if higher pressure loading wave or a lower-viscosity medium (more similar to water) were considered.

The Froude number demonstrates the contribution of gravity relative to inertial forces [175]:

$$\Pi_6 = Fr = \frac{U_c}{\sqrt{gR_o}}. \tag{6.15}$$

The role of gravity proves to be minimal; with the denominator value coming to only 0.1 m/s, the Froude number of this flow is on the order of 1000. Even significantly lower pressures and thus collapse velocities are sufficient to exceed the effect of the gravitational gradient; for example $\Delta P_w = 1$ kPa will result in $U_c = 1$ m/s and $Fr = 10$.

The Weber number compares the magnitudes of inertial effects to surface tension [175]:

$$\Pi_7 = We = \frac{\rho U_c^2 R_o}{S_a}. \tag{6.16}$$

For agarose gel, the surface tension is very similar to that of water, at 0.06 N/m [176], yielding a Weber number of 12,000. For otherwise identical conditions, a bubble would require a radius on the order of 0.1 μm for the surface tension to have comparable magnitude. For higher-pressure loading, this would decrease further.

It is not readily apparent how to reasonably include elasticity (E_a) in a dimensionless group in the context of a fluid flow; however, viscoelasticity can readily be approached from a more general continuum mechanics perspective [177]. In this context, the momentum balance on a material element is expressed as:

$$\nabla_x \cdot \boldsymbol{\sigma} + \rho \boldsymbol{b} = \rho \frac{D\boldsymbol{u}}{Dt} \tag{6.17}$$

where $\boldsymbol{\sigma}$ is the (total) stress tensor, $\boldsymbol{b}$ is the total body force, $\boldsymbol{u}$ is the velocity vector of the material element, and the D/Dt operator indicates a material derivative. It should be apparent that both viscosity and elasticity enter this balance through the stress tensor $\boldsymbol{\sigma}$, but whereas viscosity μ relates stress to strain rate ($\sigma = \mu\dot{\epsilon}$, for a Newtonian fluid), the elastic modulus relates stress to strain ($\sigma = E\epsilon$, for a Hookean solid).

With this in mind, it would be reasonable to seek a way to compare elastic stresses with inertial forces in the flow, which requires finding a representative strain ϵ. Strain rate for simple shear in a continuum system is the gradient of the velocity field, so it is expected to scale as the characteristic velocity over the characteristic length scale of the system, or U_c/R_o. To get the strain developed in the system, this must be multiplied by a characteristic time, such as t_c. This gives $U_c/(R/t_c) = U_c/U_c = 1$. This suggests that the elastic modulus can be compared directly to dynamic pressure, ρU_c^2, or applied pressure ΔP_w (based on the definition of U_c):

$$\Pi_8 = \frac{\rho U_c^2}{E_a} = \frac{\Delta P_w}{E_a}. \tag{6.18}$$

This expression can also be thought of as a Reynolds number analog for elastic forces, given that the dimensions of E_a match the dimensions of μ_a/t_c, and $\rho U_c^2 = \rho_a U_c R_o/t_c$.

For agarose, $E_a = 38$ kPa, so Π_8 is on the order of 250; this is sufficiently high that pressure forces are expected to dominate the flow. The stiffest composition of PDMS used has an elastic modulus of 0.75 MPa, which would make the ratio approximately 13. It is possible that in this condition, the elasticity has a discernible effect on the flow. However, since the PDMS does not contain the bubble, but rather is located about one radius away from the bubble interface, the effect of higher material stiffness on bubble dynamics is indirect. At those distances, it will experience lower velocities and strain rates than material close to the bubble, and respond with lower stresses.

6.4.4 Bubble Contents Parameters

The preceding eight expressions are sufficient to describe the flow regime of the ambient fluid, if thermal effects and flow within the bubble do not have a strong effect on the flow of ambient fluid. However, these additional effects can be important in some systems. For example, the dynamics within the bubble are very important in the studies of gas inhomogeneities by Sturtevant, Quirk and Karni, and others [35, 99, 103].

To evaluate whether viscosity of the fluid in the bubble is relevant, a Reynolds number can be calculated using either Equation 6.13 or Equation 6.14, using μ_b and ρ_b instead of μ_a and ρ_a:

$$\Pi_9 = Re_b = \frac{\rho_b U_c R_o}{\mu_b}. \tag{6.19}$$

For air at standard conditions, $\rho_b = 1.20$ kg/m^3 and $\mu = 1.82{\times}10^-5$Pa·s, which gives $Re = 7900$, indicating viscosity is not a major factor in the dynamics within the air cavity, either.

The density jump across the interface may be useful to consider as the Atwood number, which is used in analyzing the development of a Richtmeyer-Meshkov instability along the interface [35]:

$$\Pi_{10} = A = \frac{\rho_a - \rho_b}{\rho_a + \rho_b}. \tag{6.20}$$

For a gas bubble in liquid this would be very close to 1, and the interface can be treated as a free surface.

For gases with closely matched densities, the value would approach 0. If the bubble was of higher density, as can occur in a two gas system, the Atwood number can become negative.

The compressibility within the bubble can be considered one of two ways. First, through comparing the collapse velocity to the sound speed in the gas, essentially getting a Mach number for the gas at the bubble interface:

$$\Pi_{11} = \frac{U_c}{a_b}. \tag{6.21}$$

In this experiment, this value comes to about 0.3, indicating that compressibility will have a much greater effect on the dynamics of the air in the bubble than on the dynamics of the ambient water. This is to be expected; the reduction in size inherent to the collapse of a bubble requires the gas within to be compressed! As in Equation 6.7, the value of $\dot{R}(t)$ can be substituted for U_c to determine if compressibility is playing a large part in the overall system mechanics at particular times.

An alternative way to introduce the gas sound speed to the system is to consider the ratio of acoustic impedance (ρa) values of the two fluids. This is particularly relevant if the response of the ambient fluid is of greater interest than the dynamics within the bubble:

$$\text{Alternate } \Pi_{11} = \frac{\rho_b a_b}{\rho_a a_a} \tag{6.22}$$

If this value is close to zero, as in the current experiment, the interface will behave as a free surface. It will reflect any incoming velocity disturbance (u_a) with opposite sense (e.g. a compression wave as a tension wave) but comparable magnitude, and as a result the particle velocity behind the shock along the centerline of the bubble will be doubled. The transmitted wave must then cause a velocity disturbance of double the incoming wave, to equalize velocities on either side of the interface. The associated pressure change in both fluids is given by $\Delta P = \rho u_s \Delta u_p$ (where u_s is shock velocity and u_p is fluid particle velocity). The pressures in both materials must also equalize after the passage of the wave, but while pressure in the gas bubble will rise slightly due to Δu_p, the pressure in the liquid will decrease to almost zero after the passage of the rarefaction wave, i.e. the pressure change in the liquid will be much larger in magnitude, primarily due to its much higher density.

If the value of this alternate Π_{11} is on the order of 1, as for some gas-in-gas bubbles, a velocity disturbance of approximately the same magnitude as the incident disturbance will be transmitted into the bubble; pressure magnitudes will also be approximately equal. A reflected wave may be weak (if the ratio is very close to 1) or comparable in magnitude (e.g. if the ratio is around 0.5, or 2). Finally, if Π_{11} is high, the interface will reflect disturbances increasingly like a rigid surface (same sense and magnitude), and arrest the flow upstream of the bubble. Only a small velocity disturbance will propagate into the high-impedance "bubble" (likely a liquid drop or solid inclusion, given such an impedance ratio), though the associated pressure change will equal twice that of the reflected wave, to equalize pressures on the boundary.

It should be noted that for a gas bubble in a liquid, the last situation describes the propagation of the wave from the bubble back into the ambient liquid once it has traversed the bubble diameter. For an air-water interface, the wave would create a velocity change of 4×10^{-4} times the original velocity jump (u_a); the associated pressure jump would also remain several orders of magnitude lower than that of the original incident wave.

6.4.5 Thermal Property Parameters

The nondimensional groups Π_9–Π_{11} account for the effects of the mechanical properties of the fluid in the bubble. However, the thermal properties of both ambient and bubble fluids have not yet been considered. The analysis of Hickling is used to guide discussion of these effects [169].

For a bubble of inert, non-condensing gas in an ambient medium, the heat transfer behavior will largely be described by the initial temperature of the system T_o and, for each material, the conductivity k and specific heat capacity (either at constant pressure C_p, or at constant volume, C_v). The nondimensional specific heat ratio (γ) of each fluid can be used to convert between C_p and C_v as needed. If the only relevant mechanism in one of the materials is thermal diffusion, the two constants for that material can be combined into one property, the thermal diffusivity, $\alpha = k/(\rho C_p)$.

Hickling discusses how the relative specific heats and the ratio of thermal diffusivity coefficients provides a good metric for whether a thermal disturbance in the bubble will propagate into the ambient fluid [169].

$$\Pi_{12} = \frac{C_{p,a}}{C_{p,b}} \tag{6.23}$$

$$\Pi_{13} = \frac{\alpha_a}{\alpha_b} = \frac{k_a/(\rho_a C_{p,a})}{k_b/(\rho_b C_{p,b})} \tag{6.24}$$

For a gas bubble in a liquid, the disparity in density far outweighs the disparity in k/C_p, giving the gas a significantly higher α. Although the liquid may absorb some heat from the gas, its higher heat capacity limits the temperature rise, and its lower diffusivity limits the extent of heat conduction; the liquid temperature at the boundary is thus expected to remain very close to T_o for most of the collapse process. Note that this does not preclude heating or thermal damage of the ambient fluid or tissue through other mechanisms (e.g. ultrasound excitation [48]), it is only the potential of the bubble collapse process to cause significant ambient fluid heating that was considered.

On the other hand, the temperature in the gas can rise dramatically, but the properties of the gas and the geometry of the problem determine whether the temperature rise can be treated as adiabatic, or if the heat loss to the surrounding liquid and the temperature distribution within the bubble must be considered. From the energy balance equation for the bubble collapse, Hickling derives three nondimensional quantities that must be compared to make this determination. The first of these is nondimensional pressure, $P/(\rho a^2)$; note that this is the square of Π_3, if it is expressed with $U_c = \sqrt{\Delta P_w/\rho_a}$.

Hickling's second nondimensional group is an expression for $C_{v,b}$:

$$\Pi_{14} = \frac{C_{v,b}T_o}{a_b^2}. \tag{6.25}$$

This is the coefficient to $\frac{\partial T}{\partial t}$, i.e. it represents the change in bubble temperature over time. Hickling's third term is an expression for k_b:

$$\Pi_{15} = \frac{k_b T_o}{R_o \rho_b a_b^3}, \tag{6.26}$$

where ρ_b refers to the initial density of the gas in the bubble, rather than a time-dependent value, consistent with the rest of this section. This term is the coefficient to a term analogous to $\frac{\partial^2 T}{\partial r^2}$, representing the conduction of heat through the gas. The resulting behavior, demonstrated by Hickling, is that for particularly small bubbles, or when the bubble gas has particularly high conductivity (for example helium or hydrogen), the bubble can experience significantly reduced temperatures. However, for 1 mm scale bubbles of nitrogen (or air), the conductivity term becomes negligible for pressures as low as 3 atm (0.3 MPa) studied by Hickling, and certainly for the higher pressures studied here. The temperature of the bubble contents can then be modeled through adiabatic relations, as in Section 5.5.

6.4.6 Potential Flow: Requirements and Limitations

Clearly, the problem of asymmetric bubble collapse can be very complex and dependent on numerous parameters. However, when the effects of various physical mechanisms are compared in non-dimensional terms, it becomes apparent that for this study pressure forces and fluid inertia are dominant and other mechanisms can be neglected. Behavior in the same mechanical regime is expected for bubbles on the order of 1–10 μm in size under pressures of tens or hundreds of megapascals, as expected in biological environments (see Chapter 1). Thermal effects and the dynamics within the bubble are negligible in their impact on the ambient fluid in this range of parameters.

Where applicable, previously cited studies were referenced to give context to the present investigation and highlight the wide range of conditions in which bubble dynamics have attracted research interest. However, certain mechanisms were neglected altogether, such as heat generation, which occurs in underwater explosions, and condensation, which drastically changes thermal behavior of vapor bubbles near the end of collapse (as mentioned in Chapter 1). These cases involve additional physical mechanisms that cannot be reasonably applied to inert, non-condensing gas; therefore, quantitative analysis of these mechanisms was deemed irrelevant to the work at hand and was not included.

It remains to be demonstrated under what range of conditions it is valid to model the flowfield in question as a potential flow. In general, there are two requirements for representing a flowfield using a potential function: the flow must be inviscid and irrotational [159, 178, 179]. The first requirement is satisfied by a sufficiently high Reynolds number, as was computed in Equation 6.13, above. If viscosity, a dissipation mechanism, played a strong role in the flow, it would violate the assumption that flow is isentropic, which is used in deriving the potential flow relations.

The second requirement, that the flow is irrotational, is required to justify expressing velocity as the gradient of a potential function, $\mathbf{u} = \nabla\phi$ [175, 178]. It is a vector identity that the curl of the divergence of a scalar quantity will be zero: $\nabla \times \nabla\phi = 0$. If vorticity, $\omega = \nabla \times \mathbf{u}$, is also zero, the two expressions can be equated, and the potential function can be defined. The flow in the bubble collapse problem is irrotational outside the bubble, where a potential flow solution would be applied, and this can be explained as follows. The initial state of the fluid is quiescent, and therefore inherently irrotational. The one-dimensional flow introduced by the loading wave is also irrotational. As explained in Section 1.8, most terms in the vorticity equation can be neglected in a flow that is not highly viscous or highly compressible. The main mechanism of vorticity generation in this flow condition is then baroclinic vorticity, which arises due to the misalignment of the density and pressure gradients [106]. The only location where this occurs is along the bubble interface. The bubble interface is the edge of the domain where the potential flow model is used; everywhere else within the domain, the flow would remain irrotational, as is required.

Expressing the velocity in terms of the potential function, the following equation can be derived by multiplying the momentum balance equation with velocity, and using the compressible Bernoulli equation [179]:

$$\frac{\partial^2\phi}{\partial t^2} + \frac{\partial}{\partial t}\left(\nabla\phi\right)^2 + \frac{1}{2}\nabla\cdot\nabla\left(\nabla\phi\right)^2 - a^2\nabla^2\phi = 0. \tag{6.27}$$

For small velocity disturbances, the equation can be linearized by neglecting $(\nabla\phi)^2$ terms (i.e. u^2 terms). This simplifies the relation to the wave equation,

$$\frac{\partial^2\phi}{\partial t^2} = a^2\nabla^2\phi. \tag{6.28}$$

If $u \ll a$, then the wave speed a can be treated as constant (not a function of u), and the differential equation is linear, in which case the solutions exhibit useful qualities, such as superposition. The equation then describes acoustic waves, wherein small disturbances in the flow propagate outwards at a fixed velocity.

In the case of bubble collapse, the disturbances originate from the acceleration of the bubble interface inward.

In cylindrical coordinates, the equations for the potential of an acoustic source flow (or a sink flow, if its strength is negative) are derived by considering an infinite line of point sources emitting spherically-uniform disturbances. Whitham performs the derivation and gives the following expressions for potential and velocity [159]:

$$\phi = -\frac{1}{2\pi} \int_{-\infty}^{t-r/a} \frac{q(\eta)\; d\eta}{\sqrt{(t-\eta)^2 - (r/a)^2}} \tag{6.29}$$

$$u_r = \frac{\partial \phi}{\partial r} = \frac{1}{2\pi} \int_{-\infty}^{t-r/a} \frac{t-\eta}{r} \frac{\dfrac{dq}{d\eta}\, d\eta}{\sqrt{(t-\eta)^2 - (r/a)^2}} \tag{6.30}$$

where the function q is defined as the volume flux per unit length at the source, and in the case of void collapse it is equal to $\dot{A}$. The integration variable $\eta = t - L/a$, with $L = \sqrt{r^2 + z^2}$, is the delayed propagation time between each point on the line source and a point of interest in the plane of the flow [159]. The integral represents collecting the contributions from each point source along the line to the flow at each point in the flowfield; put another way, the integral is evaluated at a fixed time and location (t and r), and η varies only due variation in z, the coordinate along the line source, which is normal to the plane of the flow.

This relation can be evaluated for simple functions of $q(\eta)$, such as step function (i.e. constant after η =0), linear, and quadratic behaviors. It is perhaps easiest to use Equation 6.30 and work with the derivatives of each function: a delta function, a constant, and a linear function respectively:

$$\text{For } q(\eta) = Q\,H(0): \qquad u_r = \frac{1}{2\pi} \int_{0}^{t-r/a} \frac{t-\eta}{r} \frac{Q\,\delta(0)\; d\eta}{\sqrt{(t-\eta)^2 - (r/a)^2}} \tag{6.31}$$

$$\text{For } q(\eta) = Q'\;\eta: \qquad u_r = \frac{1}{2\pi} \int_{0}^{t-r/a} \frac{t-\eta}{r} \frac{Q'\; d\eta}{\sqrt{(t-\eta)^2 - (r/a)^2}} \tag{6.32}$$

$$\text{For } q(\eta) = \frac{Q''}{2}\,\eta^2: \qquad u_r = \frac{1}{2\pi} \int_{0}^{t-r/a} \frac{t-\eta}{r} \frac{Q''\,\eta\; d\eta}{\sqrt{(t-\eta)^2 - (r/a)^2}} \tag{6.33}$$

where Q, Q', and Q'' represent the constant values of the function $q(t)$, its first derivative, or its second derivative respectively for the three functions under consideration. $H(t)$ is the Heaviside step function and $\delta(t)$ is the Dirac delta. An alternate way to compute the response to the step function is to solve for the potential function ϕ with $q(\eta) = Q\,H(0)$, then take a derivative with r. This will yield the same result.

The following expressions for u_r are obtained by evaluating the integrals. $\tilde{r} = r/at$ is used to normalize the result by the location of the wavefront (at):

$$\text{For } q(\eta) = Q\,H(0): \qquad u_r = \frac{Q}{2\pi r}\left[1-\left(\frac{r}{at}\right)^2\right]^{-1/2} = \frac{q(t)}{2\pi at}\,\frac{1}{\tilde{r}}\left(1-\tilde{r}^2\right)^{-1/2} \tag{6.34}$$

$$\text{For } q(\eta) = Q'\eta: \qquad u_r = \frac{Q'}{2\pi a}\left[\left(\frac{at}{r}\right)^2-1\right]^{1/2} = \frac{q(t)}{2\pi at}\left(\frac{1}{\tilde{r}^2}-1\right)^{1/2} \tag{6.35}$$

$$\begin{aligned} \text{For } q(\eta) = \frac{Q''}{2}\eta^2: \qquad u_r &= \frac{Q''t}{4\pi a}\left[\left(\left[\frac{at}{r}\right]^2-1\right)^{1/2}+\frac{r}{at}\cosh^{-1}\left(\frac{at}{r}\right)\right] \\ &= \frac{q(t)}{2\pi at}\left[\left(\frac{1}{\tilde{r}^2}-1\right)^{1/2}+\tilde{r}\cosh^{-1}\left(\frac{1}{\tilde{r}}\right)\right]. \end{aligned} \tag{6.36}$$

It is apparent that the expression has two factors: $\tilde{q} = q(t)/2\pi at$, which has dimensions of velocity and scales the flow to the correct magnitude for a given time, and a function of $\tilde{r}$, which depends on the form of $q(\eta)$ and will be denoted $\tilde{u}_r$. The $1/at$ dependence of the first factor ($\tilde{q}$) is a result of normalizing the second factor ($\tilde{u}_r$). It should also be noted that in Equation 6.34, the term $\left(1-\tilde{r}^2\right)^{-1/2}$ vanishes for large values of t, simplifying the expression to the familiar form of steady two-dimensional potential source flow, $u_r = Q/2\pi r$. The inverse square root term is associated with the instantaneous startup of the source, and is therefore somewhat aphysical; any real startup process will be continuous, and as a result generate a finite disturbance.

In fitting the potential flow model to the PIV data, the incompressible relation $u_r = q(t)/2\pi r$ was used to describe the flow rather than any of the above expressions. An incompressible flow is expected to respond instantaneously to any changes or disturbances, as if it had infinite sound speed; in real flows, this implies a long observation time compared to the time required for a signal to propagate across the region of interest. This is not evident in the system under investigation, which exhibits numerous indicators that wave propagation was an important part of the dynamics of the system. For example, the timescale of wave propagation to the outer edge of the field of view was on the order of 2–3 μs, which constitutes a significant proportion of a 15 μs collapse time.

To demonstrate why use of an incompressible approximation does not cause a problem, the three functions of $\tilde{r}$ are plotted in Figure 6.22(a)–(c), along with a $1/\tilde{r}$ relationship representing the incompressible model. Figures 6.22(d)–(f) show the percent difference between the acoustic and incompressible functions of $\tilde{r}$ for each case.

The step function case exhibits rapid growth near the wavefront ($\tilde{r} = 1$), trending toward infinity. This arises from the inverse square root term becoming dominant at values of $\tilde{r}$ close to 1, and as mentioned previously, this anomaly is due to the aphysical nature of a truly impulsive initialization of the source. For both continuous forms of $q(\eta)$, $\tilde{u}_r$ trends toward 0 at the wavefront, as would be intuitively expected for

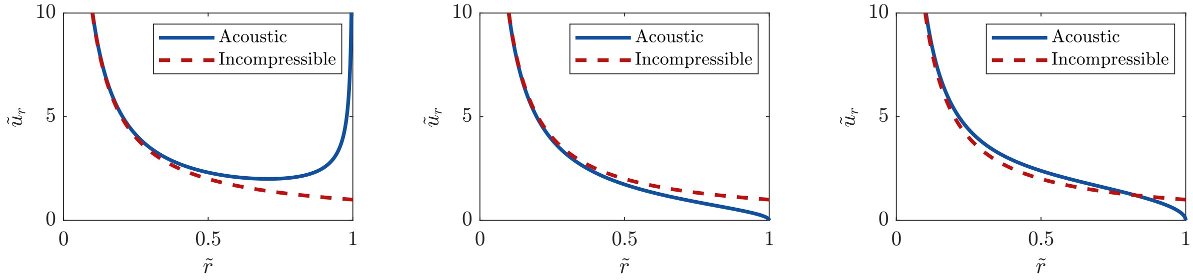

(a) $\tilde{U_r}$ for $q(\eta) = Q \cdot H(0)$. (b) $\tilde{U_r}$ for $q(\eta) = Q'\eta$:. (c) $\tilde{U_r}$ for $q(\eta) = \frac{Q''}{2}\eta^2$.

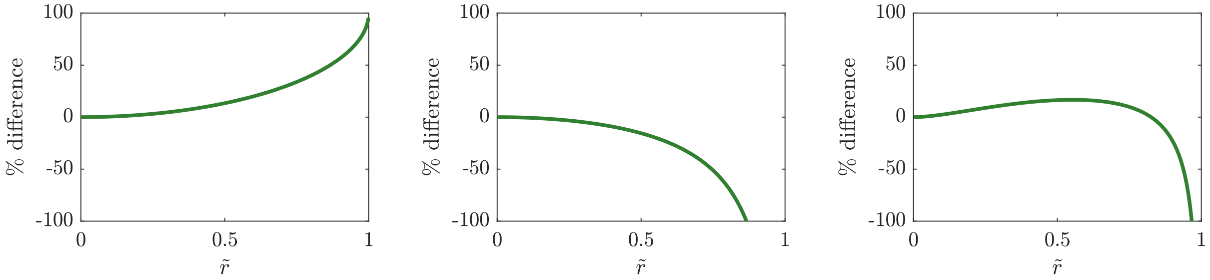

(d) $\tilde{U_r} - 1/\tilde{r}$, step function. (e) $\tilde{U_r} - 1/\tilde{r}$, linear function. (f) $\tilde{U_r} - 1/\tilde{r}$, quadratic function.

Figure 6.22: Normalized velocity distribution $\tilde{u_r}(\tilde{r})$ for various functional forms of source strength $q(\eta)$. $\tilde{u_r}$ is velocity normalized by $q(t)/2\pi at$, $\tilde{r}$ is radius normalized by at, the wavefront location.

such a wave. Since the reference value approaches 0, the percent difference values grow rapidly near the wavefront; however, the absolute differences remain bounded such that $\Delta\tilde{u}_r \leq 1$. Whether this value is significant to the overall flowfield depends on the size of the bubble radius compared with wavefront location ($\tilde{R}$), and therefore what the peak and average velocities are in the region of interest.

To more precisely evaluate the effect of such a discrepancy on the fitting of the data, an expression for $q(t) = \dot{A}(t)$ is required. Based on the data presented in Figure 5.19 (Section 5.6) and Appendix D, the following expression is proposed:

$$q(t) = \dot{A}(t) = \begin{cases} -\frac{m}{2}t^2 & \text{for } 0 < t < \frac{t_c}{2} \\ -\frac{m}{2}t^2 + m\left(t - \frac{t_c}{2}\right)^2 & \text{for } \frac{t_c}{2} < t < t_c \end{cases} \tag{6.37}$$

$$\frac{dq}{dt} = \ddot{A}(t) = \begin{cases} -mt & \text{for } 0 < t < \frac{t_c}{2} \\ -mt + 2m\left(t - \frac{t_c}{2}\right) & \text{for } \frac{t_c}{2} < t < t_c \end{cases} \tag{6.38}$$

where $m = 2\ddot{A}_{max}/t_c$, the slope of the $\ddot{A}$ function. The derivative of q is of importance here because it is found in the integrand of Equation 6.30 for u_r. This value comes out to about 0.007 $\text{mm}^2/\mu\text{s}^3$ for reasonable estimates of $\ddot{A}_{\max} = 0.05$ mm$^2/\mu$s^2 and $t_c = 15$ μs from the data. This piecewise-linear definition for $\ddot{A}(t)$ may be the simplest way to model the data such that $\dot{A}(t)$ and $\ddot{A}(t)$ are both continuous. There are many higher-order ways to represent the data, but this should capture the magnitude and timescale of variation in $q(t)$ so that reasonable estimates can be made of differences between the acoustic and incompressible models.

For times $t_c/2 < t < t_c$, the potential and velocity can be viewed as the sum of two potential functions: a sink that initiates at $t = 0$, represented by the first term, and a source that initiates at $t = t_c/2$, represented by the second term. However, the incompressible estimate itself does not exhibit superposition, because when two component flows with a difference in initiation time are involved, the sum of the strengths of these flows may not be representative of the best fit to the entire flowfield. For example, at the end of collapse the sum of strengths is 0, but it is apparent the flow will not be 0 everywhere at this time. Therefore, to evaluate the performance of an incompressible model, a least squares fit of $u_r = Q/2\pi r$ was used to find a best-fit total strength Q. This is consistent with how the incompressible model was fitted to the experimental data.

Figure 6.23 shows the velocity profile developed due to the source strength function defined in Equation 6.37, as well as the discrepancy resulting from assuming and fitting an incompressible model, for four key times spanning the beginning, middle, and end of the collapse process. The first two times of interest are selected to fall within the first half of the piecewise definition of $q(t)$, when it consists only of the sink component: $t = 2$ μs, when the wavefront location is at the edge of the field of view, or $R + at = 4$ mm (assuming R=1 mm), and at $t = t_c/2 = 7.5$ μs where the value of $q(t)$ reaches a maximum. The velocity profiles for these cases are the same as in Figure 6.22(c), scaled by $\tilde{q}$.

At $t = 7.5$ μs, the second component, a source, initiates and creates a second outgoing wave partially overlapping with the first, causing the velocity profile to begin to diverge from that in Figure 6.22(c). The strength subsequently grows until it fully counteracts the sink component at the end of collapse (t_c). The next two times evaluated for Figure 6.23 are $t = 9.5$ μs, when the leading edge of the disturbance from the source component reaches the edge of the field of view (4 mm), and $t = t_c = 15$ μs, just before the end of collapse. Since the collapse arrests at finite volume, $R = 0.2$ mm ($A^* = 0.04$) was used as the bubble interface location here, which yields velocities of around 300 m/s at the interface, equal to those measured in the last frames of shadowgraph videos.

It should be apparent from Figure 6.23 that within the 4 mm field of view, the discrepancy between the acoustic and incompressible model stays below about 3 m/s for all times. Such a discrepancy would be below the 5 m/s resolution of the PIV system and therefore could not be detected in the flowfield data. Note that the magnitude and form of $q(t)$ used to estimate the acoustic-incompressible discrepancy was based on area measurements from shadowgraph video, which allow a more accurate estimate of $q(t)$ than the PIV velocity measurements. The discrepancy values should not be interpreted as an error measurement. They represent the difference between the velocities computed by two different theoretical models from an idealized input function. However, since the input function parameters are representative of measured bubble behavior, this analysis should adequately capture the magnitude of difference between models and therefore explain why

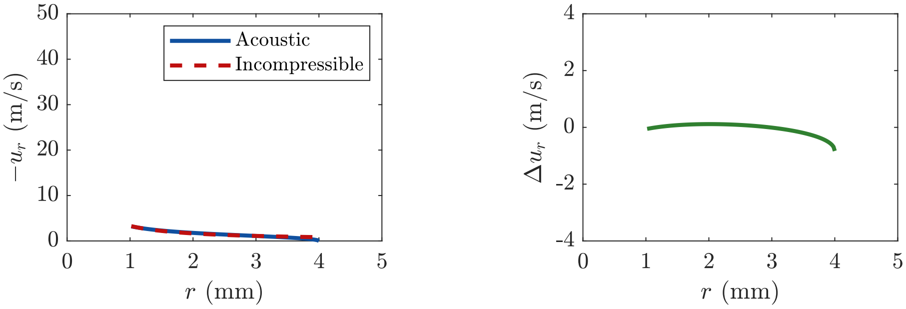

(a) $t = 2$ μs. $\tilde{q}_1 = -0.74$ m/s. $\tilde{q}_2 = 0$ m/s.

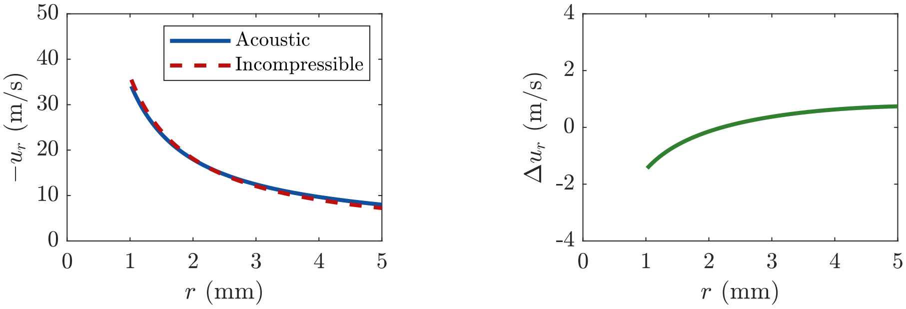

(b) $t = 7.5$ μs. $\tilde{q}_1 = -2.8$ m/s. $\tilde{q}_2 = 0$ m/s.

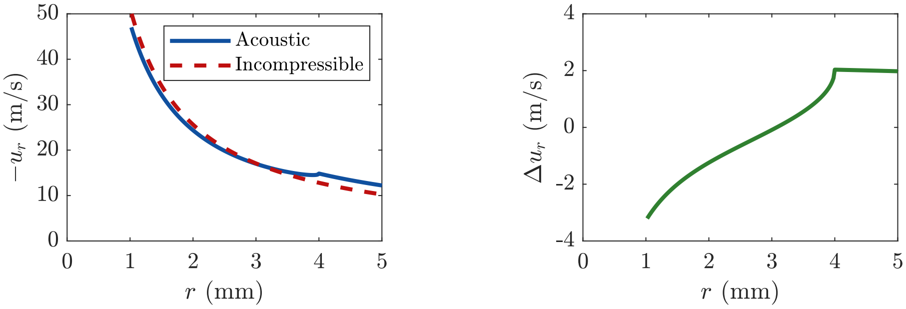

(c) $t = 9.5$ μs. $\tilde{q}_1 = -3.5$ m/s. $\tilde{q}_2 = 1.5$ m/s.

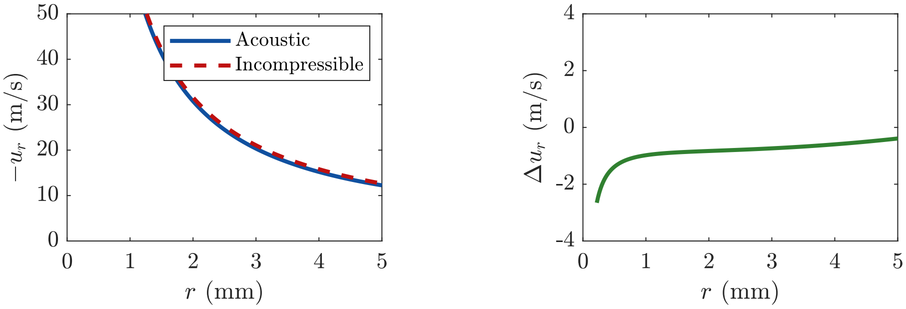

(d) $t = 15$ μs. $\tilde{q}_1 = -5.6$ m/s. $\tilde{q}_2 = 5.6$ m/s.

Figure 6.23: Velocity distribution $u_r(r)$ for source strength defined by Equation 6.37, and discrepancy Δu_r from assuming incompressible model $u_r = Q/2\pi r$ for field of view comparable to experiment. Velocities are in m/s. q_1 is strength of sink term, q_2 is strength of source term, and $\tilde{q} = q/2\pi a t$.

the incompressible model was adequate to fit the PIV data in spite of clear evidence of wave phenomena in the flow.

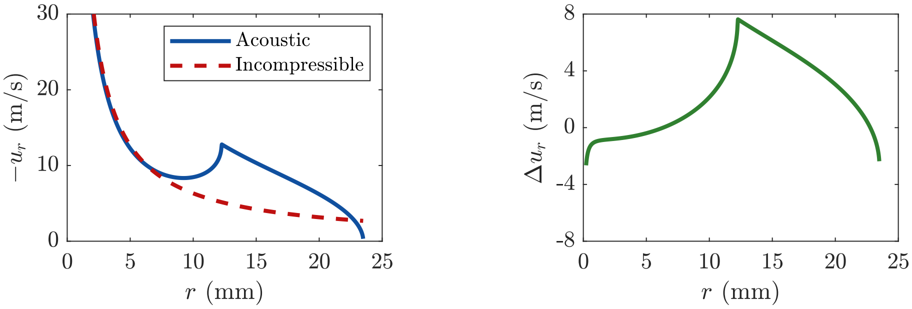

Figure 6.24: Velocity distribution $u_r(r)$ for source strength defined by Equation 6.37, and discrepancy Δu_r from assuming incompressible model $u_r = Q/2\pi r$ for 25 mm field of view at $t = 15$ μs. Sink term strength $\tilde{q}_1 = -5.6$ m/s. Source term strength $\tilde{q}_2 = 5.6$ m/s. Velocities are in m/s.

If a wider region of interest is considered, such that the wavefront can be tracked throughout the collapse process, the discrepancy between models at the end of collapse rises to almost 8 m/s at a radius of about 12 mm as shown in Figure 6.24. This is the location of the wavefront produced by the initiation of the source flow at $t =$7.5 μs, and also the inflection point in the $q(t)$ function. In fact, the wavefronts of both the sink and the source components are associated with higher discrepancy values at any given time, though for earlier times the absolute magnitude of these disturbances remains quite low due to lower values of $\tilde{q}$. It is difficult to make a general statement regarding the discrepancy produced between a fitted incompressible model and the acoustic model. The fit depends significantly on the number and range of points used. For example, if the points from $r =$0.2 mm to $r =$1 mm are eliminated from the fit at the end of collapse, the velocity predicted at the interface by the fitted model exceeds that specified by the acoustic model by 17 m/s or 5.6%, whereas normally the discrepancy here is <3 m/s or <1%. Since it was not possible to get accurate velocity data from PIV right up to the bubble interface, this may partially explain the larger errors observed adjacent to the bubble at later times in the collapse.

The incompressible model offers a reasonable fit for most of the collapse process in the case of the experiment because the acoustic source (or sink) behavior changes gradually compared to wave propagation across the region of interest (the field of view). Since the discrepancies between the two models and within the field of view are low compared to the other velocities developed, the behavior appears quasi-steady. At the end of the collapse process, the bubble interface undergoes rapid deceleration followed by outward acceleration due to the rise of pressure within the bubble (rebound). In the acoustic model, this would be represented by a short-duration, large-amplitude fluctuation in $dq/dt = \ddot{A}(t)$. The dramatic variation in the source strength in time translates to dramatic variation in the potential and flowfield velocity in space, given the near-constant velocity of signal propagation. It is clear from observations of the rebound wave in both video (Section 5.2) and PIV (Section 6.1) that in this case propagation of the wave according to the acoustic model is quite important, and the incompressible model is not adequate. Whether such phenomena are significant in a system for a particular field of view and observation time must be considered on a case-by-case basis. It is expected that even if the incompressible approximation cannot be made, the potential flow model can be applied using the appropriate acoustic potential functions and associated velocity distributions, so long as the flow regime remains acoustic.

6.5 Differential Quantities

The potential flow model of bubble collapse flow, as it has been addressed thus far, is primarily descriptive; the temporal variation of the strength parameters has not yet been given a quantitative basis. This will be addressed in Section 6.6, below. However, there are certain benefits to even a descriptive model; one such benefit is that unlike the noisy, original data, the modeled data is smooth and differentiable. This allows properties that rely on the derivative of the flowfield, such as shear rate ($\dot{\epsilon}$), to be examined:

$$\dot{\epsilon} = \frac{dU_y}{dx} + \frac{dU_x}{dy} \tag{6.39}$$

The shear rate in the flowfield for the collapse of a bubble in the absence of material boundaries is presented in Figure 6.25. The shear distribution does not change significantly in tests with boundaries, so those have been omitted. The higher values of shear develop within the initial radius of the bubble. It is interesting to note that these areas develop in one location on the bubble and do not migrate; material that is located sufficiently near the bubble to begin with will experience high shear rates for a significant portion of the collapse. Whether those shear rates can cause damage will certainly depend on the material properties of all materials involved. It is beyond the scope of this work to do a full survey on biological tissues to determine the potential for damage. Moreover, the geometry of bubbles in clinical applications will certainly be different from those here. However, it is reasonable to consider some benchmarks for interpreting the shear stresses observed.

The maximum regions in the plots below experience shear rates of more than $100\times10^3\ s^{-1}$ or 0.1 μs^{-1} for at least half the collapse time; these values must be multiplied with the material viscosity to obtain a shear stress. The viscosity of water is 8.9×10^{-4} Pa·s [175]. The viscosity of 1% agarose has been reported as 70 Pa·s [121]; however, this is measured at only 0.05 Hz; this is a poor estimate for this experiment, because agarose behavior is very rate-dependent and the experiment is occurring at roughly 10^5 Hz. For an alternate approach, the value of the elastic modulus can be used along with the so-called "phase angle" of the material, δ. This value characterizes the ratio of loss modulus to storage modulus of a viscoelastic material, as $\delta = G''/G'$; the dynamic viscosity is related to the loss modulus as $G'' = \mu\omega$ and the storage

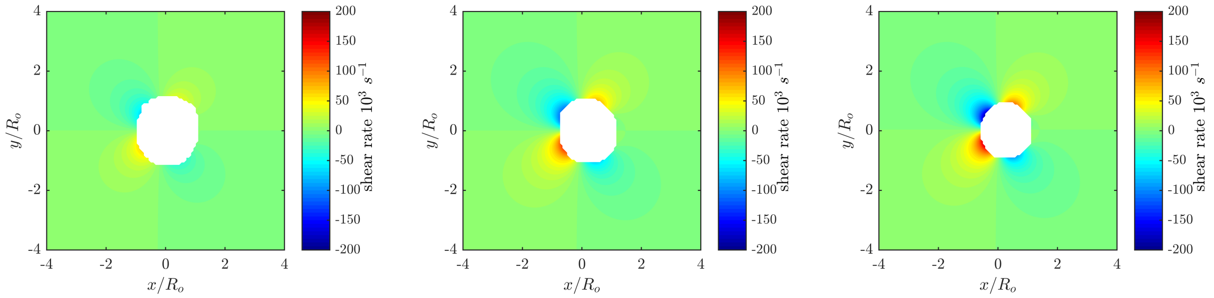

(a) A^*=0.89, x_c^*=0.09. (b) A^*=0.74, x_c^*=0.24. (c) A^*=0.56, x_c^*=0.32.

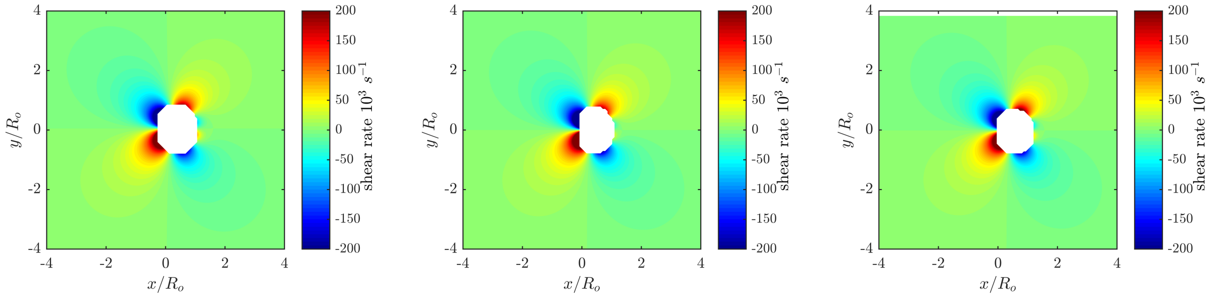

(d) A^*=0.39, x_c^*=0.48. (e) A^*=0.29, x_c^*=0.53. (f) A^*=0.15, x_c^*=0.69.

Figure 6.25: Shear rate in fluid around a collapsing cylindrical bubble far from any material boundaries. Area ratio $A^*={}^{A}/_{A_o}$ and centroid displacement $x_c^*={}^{x_c}/_{R_o}$ of the bubble are indicated.

modulus is effectively the shear modulus [180]. Barrangou et al. report δ for agarose across a range of strain rates [181]. For 2.5% w/w agarose, δ plateaus at 3.8±1° for frequencies above 1Hz. Using $E = 3G'$ for an incompressible material, $E = 38$kPa for agarose, and $\omega = 2\pi \cdot (15\mu\text{s})^{-1} = 4{\times}10^5$, the more reasonable value for agarose viscosity in this application is 0.03 Pa·s. The viscosities of liver and muscle tissue are reported as ranging from 0.013–0.016 Pa·s [116].

Multiplying these possible viscosities with the shear rate gives the shear stress experienced in the fluid: 89 Pa for water, 3 kPa for agarose, and 1.5 kPa in tissue. Values in the hundreds of Pascals are reported as being damaging to living cells [182, 183]. Based on these values, the potential for shear stresses upstream of a collapsing bubble to damage cells in a biological environment should be considered.

The model was not applied to flows after the collapse was complete, because the location and profile of the rebound wave could not be well-predicted. As a result, shear rates could not be calculated for those flowfields. However, it is apparent from the flowfields themselves that velocity gradients are moderate after collapse, and therefore so is shear. All evidence points to large pressures generated at the point of jet impact or the start of rebound, but the effect is so localized in both space and time that it did not register in the PIV experiments, whereas the shear upstream of the bubble is persistent, on the order of the collapse time.

6.6 Parameter Evolution

For all the merits of a descriptive model for evaluating experimental data sets, a predictive model would have significantly more value. To achieve this goal, it is necessary to understand what is driving each of the terms, and how they evolve during the bubble collapse process.

The first term, wave-induced flow ($\boldsymbol{U_p}$), was measured at the edge of the flowfield where the effect of the bubble was minimal. This flow is treated as determined by external factors and not directly affected by the presence of the bubble; in the case of this experiment, the external factors are a combination of the pressure loading and fixture deformation, but in a two-dimensional system it should be possible to compute this flow from only the pressure and the fluid properties. In an alternative experimental system, it may be independently measurable, or possible to estimate.

The second term, the source $\left(\frac{Q}{r}\right)$, is the primary mechanism for area change of the bubble. The doublet flow cannot change the bubble area by definition; it is composed of two sources of equal but opposite strength, producing a flow with symmetric flows in and out of the origin. It might be argued that a velocity differential due to the incident wave would compress the bubble in the horizontal direction, but the average velocity gradient measured in the incident wave across the bubble location is only 2.54 m/s per mm. At this rate it would take over 400 μs to close the 2.4 mm bubble diameter, whereas the actual collapse time is about 15 μs. Collapse times in the appropriate range were estimated by assuming symmetrical collapse and using the experimentally measured pressure traces (Section 4.8. Similarly, disregarding the deformation and considering only the area change of the bubble, as if it were symmetrical, allowed believable pressure traces to be determined from area data obtained from shadowgraph video (Section 5.6). This suggests that Q is dependent on the applied pressure, following the relations that describe symmetrical bubble collapse. To test this hypothesis, values of Q determined from PIV are presented in Figure 6.26 along with theoretically computed $R\dot{R}$ from both a measured pressure trace and a theoretical constant pressure $P_{\text{step}} = \left(\frac{1.49\rho_L R_o}{t_c}\right)^2$. In this plot, $1 - A^*$ was used as a time-surrogate variable to put the progression in familiar left-to-right orientation.

The agreement is not absolute, but sufficient to strongly support the hypothesis. Each data point was acquired from a different test, which introduces significant scatter due to test-to-test variations in impact. Test-to-test variation was also observed in measured pressure profiles in Section 3.5 and as variations in collapse time in the shadowgraph data (Chapter 5). The theoretical curves shown on the plots can in a sense be treated as bounds on the expected behavior of Q. The constant pressure condition creates a lower bound for behavior. All measured pressures exhibited a peak at early times far above the theoretical constant pressure; this peak results in steeper growth of Q expected under all measured pressures compared to the growth of Q under constant pressure. A curve that predicted the steepest growth and the highest Q values was selected to demonstrate the upper bound on the expected behavior. The other predictions of Q behavior based on measured pressures fell between the constant line and this highest line so they were omitted for

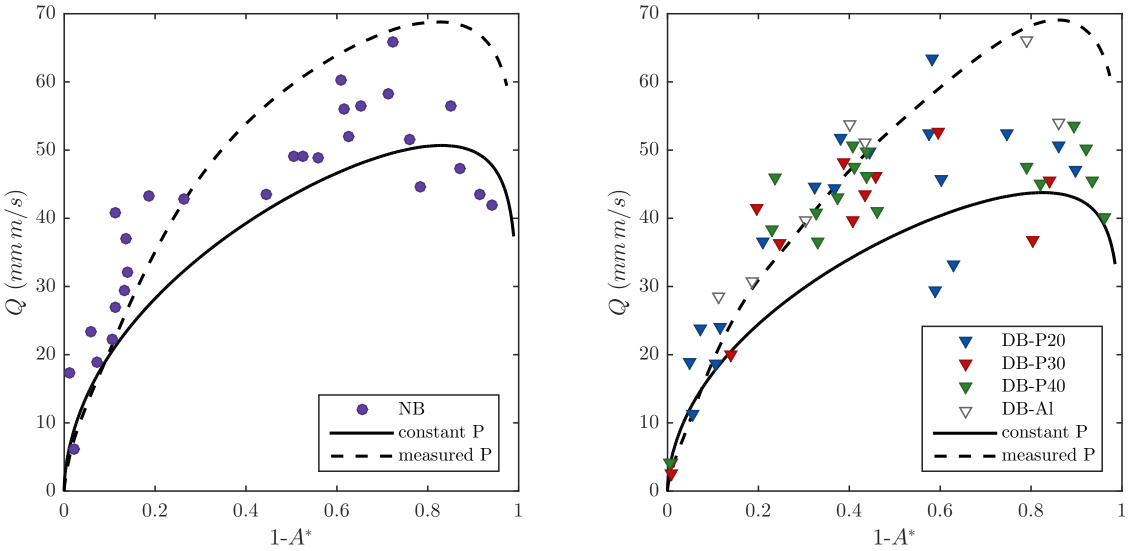

(a) No Boundary.

(b) Downstream Boundary.

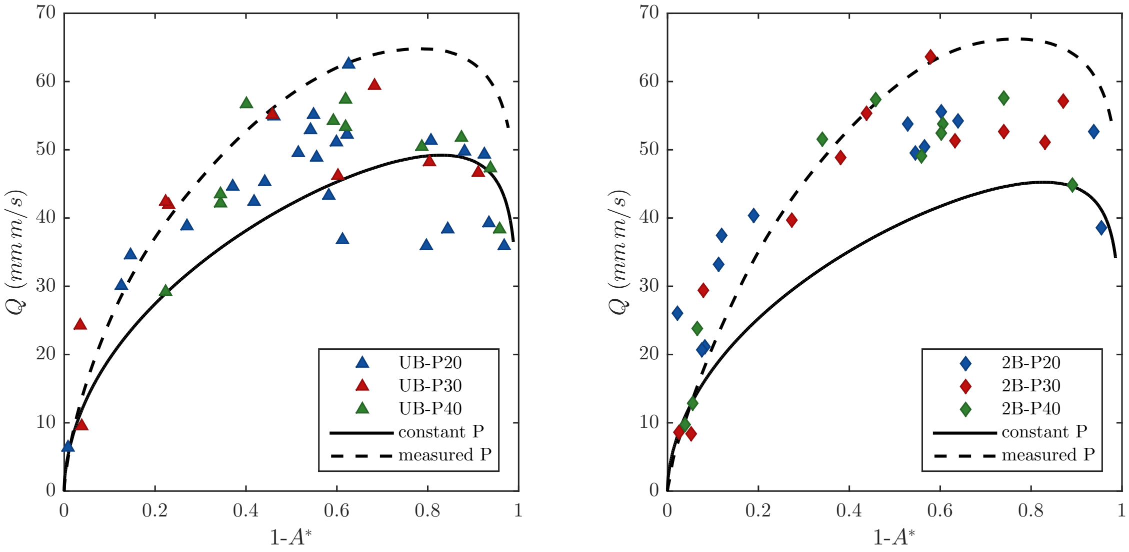

(c) Upstream Boundary.

(d) Two Boundary.

Figure 6.26: Evolution of source strength during collapse, from test PSV data. The theoretical curves at constant pressure assume average collapse time and represent a lower bound for expected Q values. Actual pressure histories exhibit a peak at early times, which is expected to drive steeper rise in Q. The theoretical curves using measured pressure (from Section 3.5) were selected to demonstrate the steeper rise and to provide an upper bound on expected Q values.

clarity.

There is also the possibility of a shift in A/A_o on these plots. The see-through area used as an area measurement throughout this study is a lower bound; the edge effects visible as the "bubble interface" cause the inner and outer radii to differ by about 18%. These interface effects can obscure some of the initial area motion, so by the time $A/A_o < 1$ is detected, the behavior of the flowfield reflects a lower area ratio. Assuming the actual radius is halfway between the two measured values, so the area difference is 15%, and the bubble collapses through one half of that before the inner radius begins to decrease, an estimate of 7–8% can be made for the error in $1 - A/A_o$. At the end of collapse, it is more difficult to give a quantitative estimate, but zero area is certainly detected while the bubble remains at a finite volume; per shadowgraph data, typically 1–3 frames or 0.2–0.6 μs before the rebound shock commences.

While the origins of the first two terms were fairly intuitive, but the doublet poses a more difficult question. What aspect of the flow is it related to, and what parameters of the system are responsible for its strength? To help discern this, plots of the flowfield resulting from the wave-induced flow and doublet alone, as well as the source and doublet alone are presented in Figure 6.27. These flowfields demonstrate how the doublet interacts with the other constituent flows. In the first case, the flow is deflected toward the centerline in the vicinity of the bubble. As a result, the flow directly upstream and downstream accelerates, whereas the flow on the top and bottom of the bubble decelerates. As this disparity persists over the timeframe of the collapse, it is not difficult to imagine how the bubble outline would become deformed, the boundary moving faster along the centerline than the top and bottom are, and stretching the bubble into a "D" shape and then a kidney shape. In the second case, removing the wave-induced flow $U_p(x)$, the presence of the doublet introduces asymmetry to the source flow, accelerating the upstream portion while decelerating the downstream flow. Again, it is apparent that the faster flow on portions of the bubble boundary would result in changes in bubble shape as the size of the bubble changes due to the source flow. These observations demonstrate how the doublet component is responsible for bubble deformation. This would also make it the component primarily responsible for the formation of the re-entrant jet.

Association of the doublet with bubble deformation suggests that it has ties to vorticity generation in the system. The distribution of vorticity generated at the surface of a gas bubble in a gas has been implicated in the deformation of the bubble interface and the eventual conversion of the bubble into a pair of counter-rotating line vortices as regions of elevated vorticity "roll up" regions of lower vorticity [35, 99, 103]. Similar behavior was observed in air bubbles in water, accelerated by gravitational gradients [104], and counter-rotating vortices have been observed after the shock-induced collapse of bubbles in water [33, 36]. In the bubble collapse system under investigation, the truncation of the potential (irrotational) flowfield at the bubble interface introduces a steep velocity gradient, which introduces vorticity into the flow at the

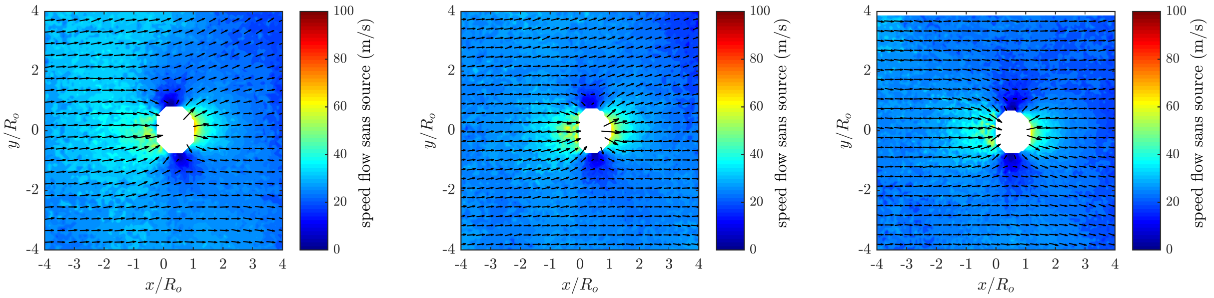

(a) A^*=0.39, x_c^*=0.48.
(b) A^*=0.29, x_c^*=0.53.
(c) A^*=0.15, x_c^*=0.69.

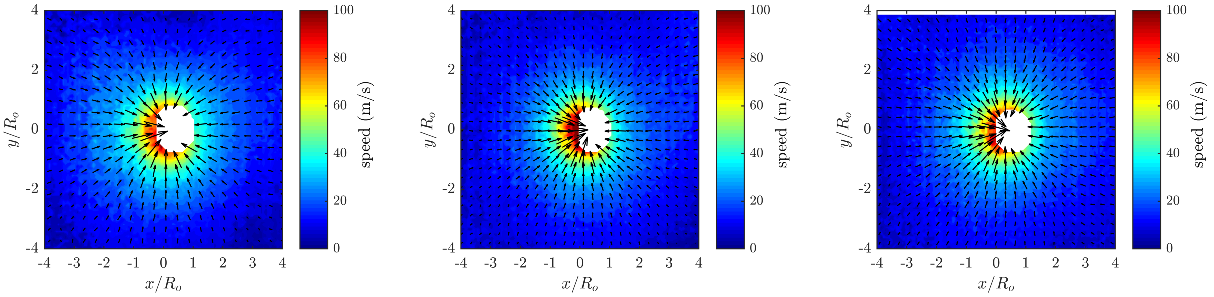

(d) A^*=0.39, x_c^*=0.48.
(e) A^*=0.29, x_c^*=0.53.
(f) A^*=0.15, x_c^*=0.69.

Figure 6.27: Top (a,b,c): Data with source flow subtracted, leaving wave-induced flow ($\boldsymbol{U}_p$) and doublet flow. Bottom (d,e,f): Data with wave-induced flow ($\boldsymbol{U}_p$) subtracted, leaving source and doublet flow. Case of collapse with no boundary present. Area ratio $A^*={}^{A}\!/_{A_o}$ and centroid displacement $x_c^*={}^{x_c}\!/_{R_o}$ of the bubble are indicated.

boundary. In cylindrical coordinates, vorticity is expressed as:

$$\omega = \bigtriangledown \times \boldsymbol{u} = \left(\frac{du_\theta}{dr} + \frac{1}{r}\frac{du_r}{d\theta}\right)\boldsymbol{e_z}. \tag{6.40}$$

At the boundary, $\frac{du_\theta}{dr}$ is high as the flow changes from the velocities determined by potential flow to very low velocities inside the bubble over a very small distance. The actual magnitude of the vorticity depends on this lengthscale, which cannot be determined from the experiment, but the form of $u_\theta(R,\theta)$ can offer insights into its distribution.

In the PIV data at later times, there is evidence of counter-rotating vortices in the flow after jet impact. This presents a possible motivation for the development of the doublet flow specifically, rather than vorticity generally. Although the doublet is typically conceptualized a source and a sink of equal strength brought infinitesimally closer together, it can also be derived from a flow involving two closely-spaced counter-rotating vortices [184]. In both cases, the doublet flow results from taking the limit as the spacing of the two constituent flows is reduced toward 0. That the flow around a bubble in the process of collapse includes a doublet component suggests the counter-rotating vortices develop early during the acceleration of the bubble in a pressure gradient, but then the centers diverge and create separate vortices once the transverse jet impact occurs. Since vorticity is no longer generated once the wavefront passes, the total vorticity in the flow should remain constant; therefore, the validity of this argument for the origins of the doublet in the flow can be evaluated by comparing either doublet strength, or the circulation around half the bubble, to previously established relations for the strength and spacing of the vortices produced.

The problem of a shock passing over a bubble of lighter gas was discussed in Section 1.8. Vorticity flux can be characterized by the circulation Γ around a closed contour of interest [106]; this can be calculated for the doublet flow around the top half of the bubble:

$$\Gamma = \oint_C \boldsymbol{U_d} \cdot \boldsymbol{e_\theta} ds = \int_0^\pi \frac{K\, sin\theta}{r^2} r d\theta = \frac{2K}{R} \tag{6.41}$$

if the asymmetry of the bubble is neglected and the surface modeled as a semicircle with $r = R$.

Yang, Kubota, and Zukoski present a model for the vorticity deposited on a bubble boundary by a passing shock as [99]:

$$\Gamma = \frac{2R_o}{u_s} \frac{\Delta P}{\rho_o} \tag{6.42}$$

where u_s is shock speed. For the problem of cylindrical bubble collapse in water, $\rho_o = \rho_L$, $u_s = a$ for a weak shock, and ΔP is on the order of $\rho_L a U_p$. Therefore the expression simplifies to:

$$\Gamma = 2R_o U_p \tag{6.43}$$

Equating the two expressions and rearranging, it is expected that:

$$K = RR_o U_p. \tag{6.44}$$

Although some liberties were taken with the definition of ΔP and R, this should be correct to order of magnitude. In fact, when it is used to nondimensionalize K, as in Figure 6.28, all the values fall quite close to 1. However, a definite linear trend emerges. Oddly enough, if K is scaled by $U_{p(x=0)}$ and $\sqrt{R}$, the resulting parameter remains around 1 during the entire collapse process (see Figure 6.29). However, the dimensions of this parameter are length$^{3/2}$. This, and the linear trend in K/URR_o suggest that some mechanism is being neglected. One possibility is that either bubble deformation or pressure relief through the fixture play a significant role, and therefore more careful treatment of ΔP and $R(\theta)$ will yield better agreement. Another possibility is that the deposition of vorticity depends on the specifics of the wave-bubble interaction near the bubble surface, as suggested by Quirk and Karni [103], and cannot be fully captured by the macroscopic wave and bubble properties. In both cases, obtaining a more accurate estimate of vorticity deposition would require significantly more computational power.

6.7 Conclusions

A model is derived in this section that accurately describes the behavior of the majority of the flowfields obtained via particle shadow velocimetry measurements. The model consists of three parts: the free-stream flow of the fluid in the absence of the bubble, a source flow which captures the symmetrical collapse of the bubble under the applied pressure, and a doublet flow that is primarily responsible for the bubble deformation. The doublet magnitude scales well with the parameter U_pRR_o derived by considering vorticity deposition on the curved bubble surface by a linear wavefront. However, a transient component remains throughout the collapse, suggesting that the transient behavior of some of the system parameters has not been adequately represented in the model.

Even though the predictive capability of the model requires refinement, its descriptive capabilities can be valuable. First, it provides a way to describe the flowfields developed in bubble collapse in just a few values, and therefore to easily compare the state of two flows. Secondly, the model can be applied to look for large errors where additional mechanisms are relevant and need to be considered, as was seen near the aluminum boundary. Finally, it can be used to estimate derivatives of the flowfields if necessary.

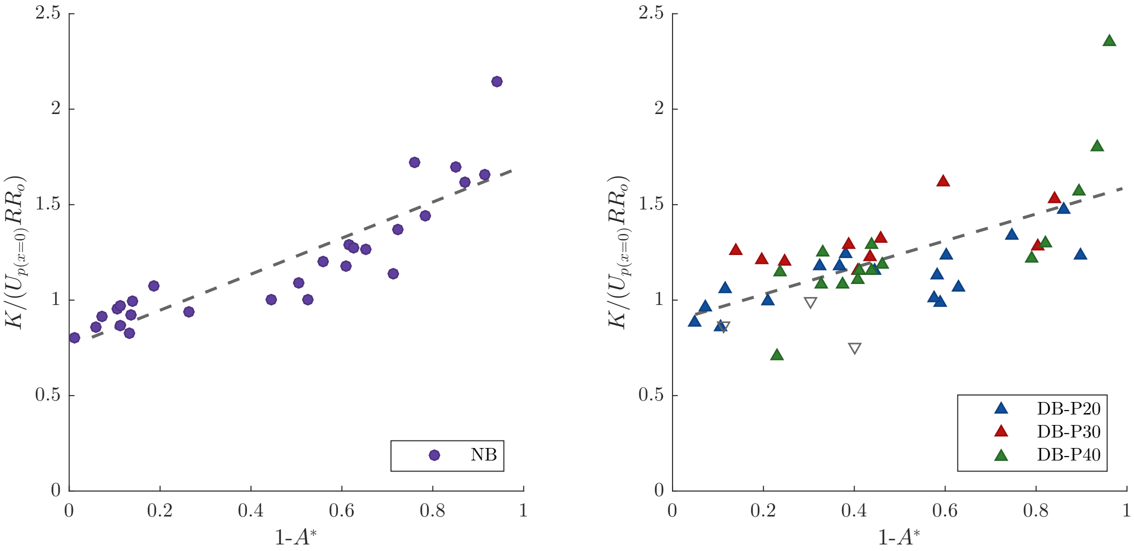

(a) No Boundary.

(b) Downstream Boundary.

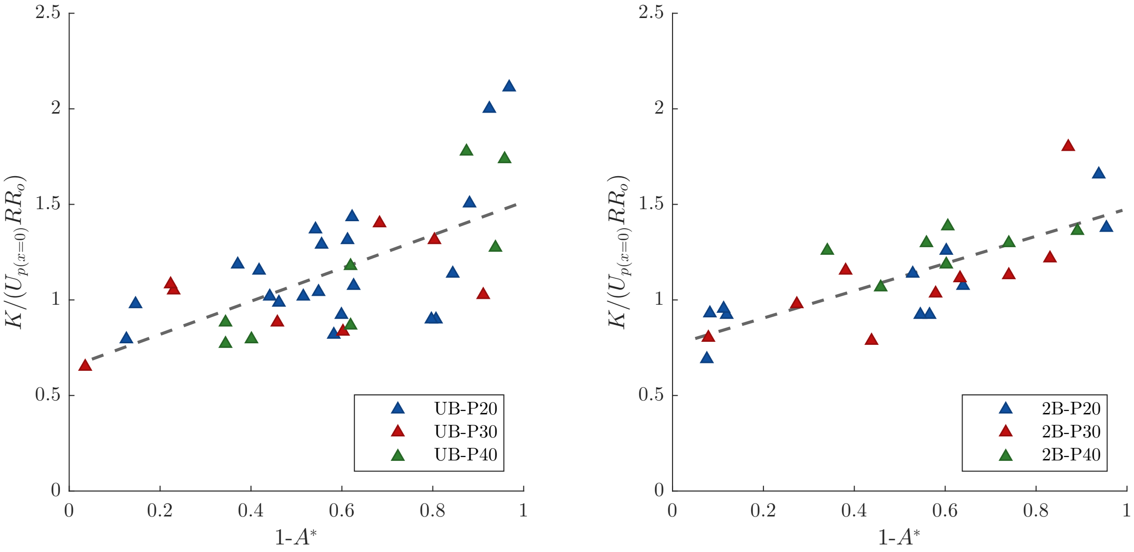

(c) Upstream Boundary.

(d) Two Boundary.

Figure 6.28: Doublet strength nondimensionalized by $U_p(x=0)$ and RR_o.

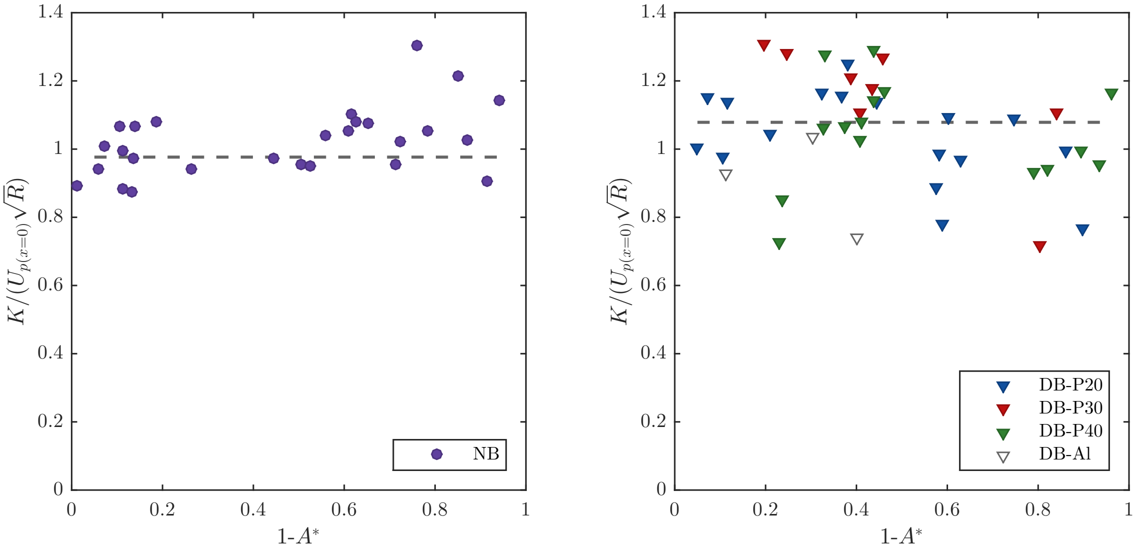

(a) No Boundary.

(b) Downstream Boundary.

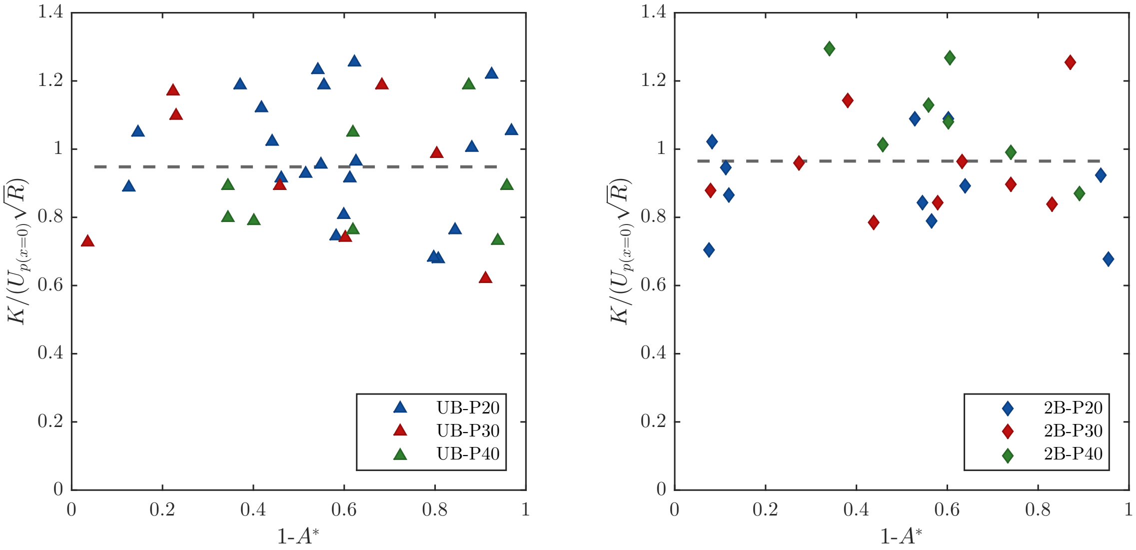

(c) Upstream Boundary.

(d) Two Boundary.

Figure 6.29: Doublet strength nondimensionalized by $U_p(x=0)$ and $\sqrt{R}$.

CONCLUSIONS

The collapse of bubbles is a phenomenon relevant to a wide range of industrial and medical applications. Initially researched with the goal of avoiding and suppressing cavitation in hydraulic turbomachinery, it was later found to be instrumental to lowering the detonation threshold of energetic materials, and one of the mechanisms responsible for the effectiveness of extracorporeal shock wave lithotripsy for the comminution of large kidney stones, as an alternative to a risky surgery. The success of the method has led to an interest in developing other non-invasive medical techniques that utilize shock waves or ultrasound waves of varying intensities to damage tissues therapeutically. The development of such systems requires an understanding of the interaction between bubbles, waves of various amplitudes and profiles, and heterogeneous compliant tissues as would be found in an anatomical setting. Hard data on bubble behavior in these conditions are lacking, in spite of extensive prior study on the collapse of bubbles under constant pressures and strong shock waves, in homogeneous environments and near rigid boundaries.

An experimental fixture was designed to create the desired loading conditions for the experiment, actuated by a single-stage compressed-air gas gun. The fixture was based on that used in previous work, and consisted of acrylic plates confining a layer of hydrogel pre-populated with a cylindrical, air-filled bubble. To accommodate the addition of compliant boundaries to the geometry, the region of interest in the experiment had to be shifted downstream, which moved it into a zone of the fixture that experienced tension due to a tensile precursor wave generated through fluid-structure interaction. By modeling the system in a finite element analysis package, the pressure state generated in the fixture was investigated and the geometric parameters of the fixture changed to eliminate tensile loading in the region of interest and achieve pressure rising to the tens of megapascals on a timescale comparable with the collapse of the bubble. Harnessing the flexural characteristics of the fixture was instrumental to obtaining the pressure profile desired, but the fluid-structure interaction resulted in a mismatch between the pressure conditions and the velocities achieved in the flow compared to an ideal two-dimensional system. The process of fixture design could potentially be applied to create high-speed loading environments with different desired properties for the loading condition.

The pressure state predicted by numerical modeling was verified by experimental measurement using dynamic pressure transducers. Multiple behaviors were observed in the pressure traces measured, including pressure rises over varying time scales, plateaus, and pressure drops. To better understand and be able to recognize the relationship between the pressure trace and resulting bubble behavior, the response of the bubble to each of these simple waveforms was modeled using a theoretical relation analogous to the Keller-Miksis equation for spherical bubbles. Larger pressure magnitude, unsurprisingly, correlates with shorter collapse time and more intense collapse, as evaluated by minimum volume reached and maximum accelerations experienced by the bubble interface. Increasingly gradual pressure growth is associated with lengthening collapse time compared to this estimate, without a significant decrease in collapse intensity. The bubble is quite sensitive to a large pressure drop if it occurs early in the collapse; the collapse time becomes significantly longer and the intensity decreases. However, about halfway through the collapse time, the effect becomes quite small. This sensitivity to timing is explained by considering the energy balance in the system between potential energy (determined by pressure difference and bubble size), and kinetic energy of all the flowing fluid. The collapse of the bubble was also theoretically modeled based on the measured pressure traces. The predicted area behavior exhibited effects associated with its rise time, but not with the drop in pressure, which happened late in the collapse. The slower startup of collapse due to the pressure rise time increased the collapse time to the collapse time expected at half the peak pressure, or less. These predicted collapse times agreed well with collapse times found in later experiments, validating the approach of using theoretical relations for symmetrical collapse to estimate collapse time, even if collapse is asymmetrical. The analysis also highlights the pitfalls of attempting to classify bubble collapse by peak pressure or collapse time alone; some pressure history information is required to draw conclusions about collapse intensity.

Experimentally, the collapse was observed by recording it in shadowgraph video at 5 million frames per second. Videos showed deformation of the bubble interface, and in some cases the formation of a re-entrant jet. Jets occurred in virtually all cases of collapse in homogeneous agarose gel. When boundaries with PDMS were introduced, the occurrence of jetting was reduced, but not eliminated. Three geometries of PDMS boundaries were investigated, the upstream, downstream, and two-boundary geometries. Jet formation was least likely to be observed in the two-boundary geometry. Collapse times measured from the videos showed a 15% statistically significant increase in the collapse time for the case of a downstream boundary compared to no boundary, whereas the upstream boundary did not show a statistically significant change in collapse time. However, the upstream boundary exhibited more distinct deformation during the collapse process, suggesting there is risk of damage potential for sensitive soft tissues in this area.

Measurements of area visible through the bubble were made for about 60% of the tests; the other 40% of the tests exhibited some degree of optical contamination that made it impossible to discern the bubble outline. The ratio of area to initial area was tracked for the entirety of the collapse and the profile compared against theoretical area profiles for a collapse under constant loading and linear ramp loading. The experimental data generally stayed quite close to the predicted traces, such that any deviations could be explained by known features of the measured pressure behavior and the theoretical ideas explored previously. The area behavior was smoothed and differentiated twice by a Savitzky-Golay filter algorithm in order to calculate estimated pressures based on area behavior. The estimated pressures were comparable in magnitude and profile to those measured experimentally. The agreement between the experimental data from clearly asymmetric collapse processes and the theoretical predictions made under the assumption of symmetry suggest the area change of the collapsing bubble is a distinct mechanism from the deformation, at least under the relatively low-pressure conditions studied here.

A rebound wave was detected on the shadowgraph after collapse was complete. This phenomenon appeared just as collapse ended and traveled outward in a circular fashion. Measurements overwhelmingly reported that its radial wavespeed was in excess of the 1500 m/s expected in agarose, typically 1650-1750±50 m/s in a given shot. The wave reflected off material boundaries within the sample, and transmitted into the PDMS while also slowing down in accordance with its lower sound speed. It always propagated slower than the sound speed of the sidewall material. The exact nature of the wave is unclear, including what physical phenomenon creates the optical effect (e.g. density difference or surface curvature) and whether it can be related to the state of the fluid in its vicinity, or at its origin.

The key part of this study was the collection of flowfield vector data for the three geometries with PDMS boundaries as well as the cases of no boundary, and a rigid boundary (aluminum). Only the aluminum boundary showed distinctive behavior that could be identifiable with the naked eye, namely the complete elimination of the normal flow component close to the boundary. In searching for a way to quantify the subtle differences between the other flowfields, a simple theoretical model for the flow around a collapsing bubble was developed. The model represented the flow with residuals that amounted, on average, to 5% of the maximum flow speeds detected and 23% of the average flow speeds detected, and exhibited variation that appeared random rather than systematic. The average residuals were also generally at or below the 5 m/s noise threshold of the PIV system used. The flowfield that develops around a cylindrical bubble collapsing under the effect of a traveling, distributed wave can be modeled as the superposition of three simple theoretical flowfields. It is the combination of the flow produced by the loading condition in the free-field away from the bubble ($\boldsymbol{U_p}$), a symmetrical source flow of negative strength $-Q$ ($\boldsymbol{U_s}$), and a doublet flow of strength K ($\boldsymbol{U_d}$). The doublet strength is opposite in sense than appears in the classic potential flow example of uniform flow over a cylinder; combined with $\boldsymbol{U_p}$, it doubles the flow directly upstream and downstream of the bubble. The addition of the symmetric source term on top of this results in an overall asymmetric flowfield developing very high velocities upstream of the bubble and very low ones downstream.

The three components can be interpreted as representing different aspects of the fluid motion. The source term represents motion of the fluid in the radial direction from the bubble center, and in the absence of the other flows, would create a symmetric collapse. The free-field flow $\boldsymbol{U_p}$ primarily provides convection of the bubble downstream, although combined with the other flowfields this amounts to the downstream interface remaining primarily stationary. When these flows are combined, the expected result is a symmetrically collapsing bubble with the centroid translating downstream as collapse proceeds. It is the third component, the doublet, that primarily represents the deformation that occurs to the bubble and may be related to the generation of vorticity at the bubble interface. The parameters of the model can be calculated from an experimentally acquired flowfield to smooth the flowfield and allow differential properties like shear rate to be calculated. However, they would be much more useful if their evolution could be predicted based on known aspects of the system loading condition. The free-field flow can generally be measured in a system in the absence of a bubble, or predicted from a known loading condition. The source strength correlates well with behavior predicted for symmetrical collapse under the applied pressure; if the pressure history and bubble size are known, the source behavior can be calculated. The doublet correlates well with the free-stream velocity at the bubble location, and oddly enough with the square root of the radius. Its strength can be estimated to within a factor about two by considering the circulation deposited on the bubble surface by the passing pressure gradient, but this scaling retains some functional dependence on bubble area ratio. Additional study is required to further elucidate the mechanisms driving the evolution of the doublet during the collapse. The model is expected to be applicable for loads that qualify as acoustic disturbances, and has a spatial range limited by bubble interface dynamics, the material sound speed, and acceptable margins of error. Despite these limitations, this work has made significant steps in developing a theoretical model for the collapse of a bubble under the effect of a traveling wave and the origins of asymmetry and jet formation in this context, which differ markedly from the origins of asymmetry for the case of bubble collapse near a rigid wall.

The model provided good fit not only to the case of bubble collapse in a homogeneous environment, but also generally for the collapse of the bubble near compliant boundaries. The presence of an aluminum boundary caused clear deviation from model predictions, and a drop in the strength of the doublet flow fitted to data. The presence of compliant boundaries did not produce either significant deviation from model behavior or a notable change in any strength parameters relative to predicted values, particularly of the doublet. The cause of the suppression of jet formation observed in flows featuring compliant boundaries remains an open question.

FUTURE WORK

The applicability of the proposed flow model has been established for the specific geometry and loading condition used, and contextualized using analytical relations and order-of-magnitude estimates. However, the extent to which it can be generalized has yet to be tested. This could be done by performing experiments over a wider range of conditions, but it would likely be more resource-effective to leverage finite-volume computational methods specialized for simulating bubble behavior with interface tracking and remeshing capabilities. Examining the fit for a wide range of conditions would elucidate the extent to which the dimensional analysis estimates were accurate, and whether utilizing delayed time can widen the spatial applicability of the model for high-amplitude acoustic applications. Limitations on the properties of the fluid or viscoelastic medium are also of interest, particularly since an understanding when viscous and elastic stresses become significant in shaping the flowfield could help fine-tune treatment algorithms to suppress or intensify cavitation, as needed. Greater understanding of the interaction between properties of the medium and bubble collapse flowfield may elucidate why the suppression of jet formation was observed in collapse near PDMS boundaries when no specific differences in the flowfields could be discerned.

Computational modeling of a wider range of systems would also be useful for determining the driving causes of the doublet flow component and its expected evolution with time. There is a possibility that the evolution of the doublet is related to a time-derivative property, or another property that could not be measured satisfactorily in the experiment. A lack of understanding of the origins and evolution of the doublet in the system is one of the big obstacles to applying this theory in a predictive way.

To facilitate comparison with computational studies, this experiment could be repeated with improvements and changes. First, to generate a better approximation of truly two-dimensional flow, the structure should be made stiffer to prevent deformation and flexure. Aluminum could be used, since it was shown for the spacer bars that waves reflected off the aluminum have far less impact on the pressure state in the gel than those reflecting off the acrylic sidewalls. Small plastic or glass windows would allow optical access without significantly changing the dynamics of the fixture. Second, a tool is required to characterize the motion of the striker plate for each test; data for the piston acceleration and velocity would be much more reliable for locating experiments in time than the impact sensor currently used. It would also provide information on the profile of the disturbance generated in any particular test. Third, since observations of wave phenomena gathered through shadowgraph imaging proved of limited value, video could be taken with diffuse illumination rather than collimated light. This may allow the bubble interface to be more clearly resolved and minimize the visual effect of droplets and surface bubbles in the sample. It would also permit experiments on three-dimensional bubbles (with appropriate modifications to the fixture). This would allow the extensibility of the model to three dimensions to be evaluated. In principle, three-dimensional analogues of the flows used in the model exist, but verification is required to determine if the combination of them describes the bubble collapse flowfield, and under what range of conditions. Finally, modifying the diagnostics to increase magnification so that the final stages of collapse can be captured in good resolution would provide experimental data in a rarely-accessed portion of the collapse process. This would be very difficult to do with cylindrical bubbles, since it is suspected that pressure gradients introduce three-dimensional effects to the bubble dynamics at the end of collapse; however, it could potentially be performed with spherical bubbles.

For purposes of comparison to theory, or to two-dimensional or axisymmetric studies, good confinement and a simple loading condition are desirable features. However, in real systems bubble collapse may occur under more complex conditions, such as flows with shearing (particularly in turbomachinery), or flows with sharp pressure gradients leaving half the bubble in tension and half in compression. In fact, this is what occurred in some of the preliminary tests in this project, but could not be well-understood at the time. With the new theoretical tools developed in this work, bubble collapse in more challenging environments can be approached. The design process for the experimental fixture can be useful in developing environments that generate controlled loading with the desired parameters.

Another aspect of real-world applications of bubble collapse is that typically clouds of bubbles arise in the systems of interest, and the interactions of flows around multiple bubbles become relevant. Since the flow model consisted of a superposition of flows, there is reason to expect that flows for multiple bubbles in close proximity can be superimposed. However, the constituent bubbles in multiple-bubble systems can exhibit different collapse times, so an additional model for post-collapse behavior, including rebound wave generation, would need to be developed before this method would be useful for understanding the interactions of bubbles in bubble clouds. This, in turn, would facilitate continued development of cavitation-based, non-invasive ablation techniques that are safe and effective for medical and industrial applications.

REFERENCES

[1] Kornfeld, M. and Suvorov, L., "On the Destructive Action of Cavitation," *Journal of Applied Physics*, 1944.

[2] Plesset, M. and Ellis, A., "On the mechanism of cavitation damage," Tech. rep., Office of Naval Research, 1954.

[3] Hammitt, F., "Observations on Cavitation Damage in a Flowing System," *Journal of Basic Engineering*, 1963.

[4] Bowden, F. and Yoffe, A., *Initiation and growth of explosion in liquids and solids*, University Press, 1983.

[5] Swantek, A. and Austin, J., "Collapse of void arrays under stress wave loading," *Journal of Fluid Mechanics*, Vol. 649, 2010, pp. 399–427.

[6] Falvey, H., "Cavitation in Chutes and Spillways," Tech. rep., United States Department of the Interior, Denver, CO, April 1990.

[7] Frizell, K., Renna, F., and Matos, J., "Cavitation potential of flow on stepped spillways," *Journal of Hydraulic Engineering*, Vol. 139, June 2013, pp. 630–636.

[8] Evan, A. P., Willis, L. R., Lingeman, J. E., and McAteer, J. A., "Renal Trauma and the Risk of Long-Term Complications in Shock Wave Lithotripsy," *Nephron*, 1008.

[9] Zhong, P., "Shock Wave Lithotripsy," *Bubble Dynamics and Shock Waves*, edited by C. F. Delale, Vol. 8 of *Shock Wave Science and Technology Reference Library*, Springer Berlin Heidelberg, 2013, pp. 291–338.

[10] Zhu, S., Cocks, F., Preminger, G., and Zhong, P., "The role of stress waves and cavitation in stone comminution in shock wave lithotripsy," *Ultrasound in Medicine and Biology*, 2002.

[11] El Sayed, T., Mota, A., Fraternali, F., and Ortiz, M., "Biomechanics of traumatic brain injury," *Computational Methods in Applied Mechanical Engineering*, Vol. 197, 2008, pp. 4692–4701.

[12] Hsu, A., Hardy, B., Eliasson, V., Bernstein, Z., Campos, D., Scheu, K., and Graves, T., "Non-penetrative blast-induced traumatic brain injury visualization of representative human skull and brain response to shock and blast loading," *41st AIAA Fluid Dynamics Conference and Exhibit*, American Institute of Aeronautics and Astronautics, Honolulu, HI, June 2011.

[13] Goeller, J., Wardlaw, A., Treichler, D., O'Bruba, J., and Weiss, G., "Investigation of cavitation as a possible damage mechanism in blast-induced traumatic brain injury," *Journal of Neurotrauma*, Vol. 29, July 2012, pp. 1970–1981.

[14] Crawford, A., "A practical introduction to ultrasonic cleaning," *Ultrasonics*, Vol. 1, 1963, pp. 65–69.

[15] Niemczewski, B., "Observations of water cavitation intensity under practical ultrasonic cleaning conditions," *Ultrasonics Sonochemistry*, Vol. 14, 2007, pp. 13–18.

[16] Ortiz, M. and Heyden, S., "Targeting cancer cells selectively via resonant harmonic excitation," 2017.

[17] Xu, Z., Ludomirsky, A., Eun, L., Hall, T., Tran, B., Fowlkes, J., and Cain, C., "Controlled Ultrasound Tissue Erosion," *IEEE Transactions on Ultrasonics, Ferroelectrics, and Frequency Control*, 2004.

[18] Xu, Z., Fowlkes, J., Rothman, E., Levin, A., and Cain, C., "Controlled ultrasound tissue erosion: The role of dynamic interaction between insonation and microbubble activity," *Journal of the Acoustical Society of America*, 2005.

[19] Petrovsek, M. and Dular, M., "Simultaneous observation of cavitation structures and cavitation erosion," *Wear*, 2013.

[20] Kim, S., Jang, S., and Park, J., "An investigation on the optimum corrosion protection potential for minimization of cavitation damage using the potentiostatic method in seawater," *Microscopy and Microanalysis*, 2013.

[21] Garcia, G., Lopez-Rios, V., Espinosa, A., Abenojar, J., Velasco, F., and Toro, A., "Cavitation resistance of epoxy-based multilayer coatings: Surface damage and crack growth kinetics during the incubation stage," *Wear*, 2014.

[22] Reynolds, O., "Experiments showing the boiling of water in an open tube at ordinary temperatures." *Report of the British Association for the Advancement of Science*, 1894, pp. 564.

[23] Lord Rayleigh, O. F., "On the Pressure developed in a Liquid during the Collapse of a Spherical Cavity," *Philosophical Magazine*, Vol. 6, April 1917, pp. 94–98.

[24] Brennen, C., *Cavitation and Bubble Dynamics*, Oxford University Press, New York, New York, 1995.

[25] Leighton, T., "The inertial terms in equations of motion for bubbles in tubular vessels or between plates," *Journal of the Acoustical Society of America*, Vol. 130, No. 5, 2011, pp. 3333–3338.

[26] Cook, S., "Erosion by Water-Hammer," *Proceedings of the Royal Society of London Series A*, Vol. 119, No. 783, 1928, pp. 481–488.

[27] Naude, C. and Ellis, A., "On the mechanism of cavitation damage by nonhemispherical cavities collapsing in contact with a solid boundary," *Journal of Basic Engineering*, Vol. 83, No. 4, December 1961, pp. 648–656.

[28] Benjamin, T. and Ellis, A., "The colapse of cavitation bubbles and the pressures thereby produced against solid boundaries," *Transactions of the Royal Society of London, Series A*, Vol. 260, No. 1110, July 1966, pp. 221–240.

[29] Plesset, M. and Chapman, R., "Collapse of an initially spherical vapour cavity in the neighbourhood of a solid boundary," *Journal of Fluid Mechanics*, Vol. 47, 1971, pp. 283–290.

[30] Chaudhri, M. and Field, J., "The role of rapidly compressed gas pockets in the initiation of condensed explosives," *Proceedings of the Royal Society of London, Series A*, Vol. 340, 1974, pp. 113–128.

[31] Dear, J., J.E., F., and Walton, A., "Gas compression and jet formation in cavities collapsed by a shock wave," *Nature*, 1988.

[32] Dear, J. and Field, J., "A study of the collapse of arrays of cavities," *Journal of Fluid Mechanics*, 1988.

[33] Bourne, N. and Field, J., "Shock-induced collapse of single cavities in liquids," *Journal of Fluid Mechanics*, 1992.

[34] Camus, J., *High-speed flow in impact and its effect on solid surfaces*, Ph.D. thesis, University of Cambridge, 1971.

[35] Haas, J. and Sturtevant, B., "Interaction of weak shock waves with cylindrical and spherical gas inhomogeneities," *Journal of Fluid Mechanics*, 1987.

[36] Ball, G., Howell, B., Leighton, T., and Schofield, M., "Shock-induced collapse of a cylindrical cavity in water, a free-Lagrange simulation," *Shock Waves*, 2000.

[37] Bourne, N. and J.E., F., "Bubble collapse and the initiation of explosion," *Proceedings of the Royal Society of London A*, Vol. 435, No. 1894, 1991, pp. 423–435.

[38] Chaussy, C., "Extracorporeally induced destruction of kidney stones by shock waves," *The Lancet*, Dec 1980, pp. 1265–1268.

[39] Mulley, A., "Shock Wave Lithotripsy: Assessing a Slam-Bang Technology," *New England Journal of Medicine*, Vol. 314, No. 13, 1986, pp. 845–847.

[40] Shao, Y., Connors, B., Evan, A., Willis, L., Lifshitz, D., and Lingeman, J., "Morphological Changes Induced in the Pig Kidney by Extracorporeal Shock Wave Lithotripsy: Nephron Injury," *The Anatomical Record Part A*, 2003.

[41] Coleman, A. and J.E., S., "A survey of the acoustic output of commercial extracorporeal shock wave lithotripters," *Ultrasound in Medicine and Biology*, Vol. 15, No. 3, 1989, pp. 213–227.

[42] Crum, L., "Cavitation microjets as a contributory mechanism for renal calculi disintegration in ESWL," *Journal of Urology*, Vol. 140, No. 6, 1988, pp. 1587–1590.

[43] Coleman, A. and J.E., S., "A review of the physical properties and biological effects of the high amplitude acoustic fields used in extracorporeal lithotripsy," *Ultrasonics*, Vol. 31, No. 2, 1993, pp. 75–89.

[44] Lifshitz, D., Williams, J., Sturtevant, B., Connors, B., Evan, A., and McAteer, J., "Quantitation of shock wave cavitation damage *in vitro*," *Ultrasound in Medicine and Biology*, Vol. 23, No. 3, 1997, pp. 461–471.

[45] Bailey, M., Pischalnikov, Y., Sapozhnikov, O., Cleveland, R., McAteer, J., Miller, N., Pischalniklva, I., Connors, B., Crum, L., and Evan, A., "Cavitation detection during shock-wave lithotripsy," *Ultrasound in Medicine and Biology*, Vol. 31, No. 9, 2005, pp. 1245–1256.

[46] Bailey, M., A.P, E., O.A., S., R.O., C., and Colonius, T., "Cavitation in shock wave lithotripsy," *Journal of the Acoustical Society of America*, Vol. 114, No. 4, October 2003.

[47] Evan, A., Willis, L., McAteer, J., Bailey, M., Connors, B., Shao, Y., Lingeman, J., Williams, J., Fineberg, N., and Crum, L., "Kidney damage and renal functional changes minimized by waveform control that suppresses cavitation in shock wave lithotripsy," *Journal of Urology*, Vol. 168, October 2002, pp. 1556–1562.

[48] Ghorbani, M., Oral, O., Ekici, S., Gozuacik, D., and Kosar, A., "Review on lithotripsy and cavitation in urinary stone therapy," *IEEE Reviews in Biomedical Engineering*, Vol. 9, 2016, pp. 264–283.

[49] Sauerbruch, T. and Paumgartner, G., "Gallbladder stones: management," *The Lancet*, Vol. 338, November 1991, pp. 1121–1124.

[50] Paumgartner, G. and Sauter, G., "Extracorporeal shock wave lithotripsy of gallstones: 20th anniversary of the first treatment," *European Journal of Gastroenterology and Hepatology*, Vol. 17, No. 5, 2005, pp. 525–527.

[51] Wang, C., "Extracorporeal shockwave therapy in musculoskeletal disorders," *Journal of Ortopaedic Surgery and Research*, Vol. 7, No. 11, 2012.

[52] Cirovic, S., Gould, D., Park, D., and M.C., S., "Cadaveric experiments to evaluate pressure wave generated by radial shockwave treatment of plantar fasciitis," *Foot and Ankle Surgery*, Vol. 23, 2017, pp. 285–289.

[53] *Ultrasound*, chap. Applications of ultrasound in medicine–comparison with other modalities, Advances in Applications, Biological Effects, and Dosimetry of Ultrasound, Springer, 1987.

[54] Qin, S., Caskey, C., and Ferrara, K., "Ultrasound contrast microbubbles in imaging and therapy: physical principles and engineering," *Physics in Medicine and Biology*, Vol. 54, 2009, pp. R27–R57.

[55] Hernot, S. and Klibanov, A., "Microbubbles in ultrasound-triggered drug and gene delivery," *Advanced Drug Delivery Reviews*, Vol. 60, 2008, pp. 1153–1166.

[56] Clayman, R., "From knife to needle to nothing: the waning of the wound," *Brazilian Journal of Urology*, Vol. 27, No. 3, 2001, pp. 209–214.

[57] Tran, B., Seo, J., Hall, T., Fowlkes, J., and Cain, C., "Microbubble-enchanced cavitation for noninvasive ultrasound surgery," *IEEE Transactions on Ultrasonics, Ferroelectrics, and Frequency Control*, Vol. 50, No. 10, October 2003, pp. 1296–1304.

[58] Ding, Z. and Gracewski, S., "The behaviour of a gas cavity impacted by a weak or strong shock wave," *Journal of Fluid Mechanics*, Vol. 309, 1996, pp. 183–209.

[59] Cleveland, R., Lifshitz, D., Connors, B., Evan, A., Willis, L., and Crum, L., "*In vivo* pressure measurements of lithotripsy shock waves in pigs," *Ultrasound in Medicine and Biology*, Vol. 24, No. 2, 1998, pp. 293–306.

[60] Delius, M., "Minimal static excess pressure minimises the effect of extracorporeal shock waves on cells and reduces it on gallstones," *Ultrasound in Medicine and Biology*, Vol. 23, No. 4, 1997, pp. 661–617.

[61] Williams, J., Woodward, J., Stonehill, M., Evan, A., and McAteer, J., "Cell damage by lithotripter shock waves at high pressure to preclude cavitation," *Ultrasound in Medicine and Biology*, Vol. 25, No. 9, 1999, pp. 1445–1449.

[62] Cathignol, D., Tavakkoli, J., Birer, A., and Arefiev, A., "Comparison between the effects of cavitation induced by two different pressure-time shock waveform pulses," *IEEE Transactions on Ultrasonics, Ferroelectrics, and Frequency Control*, Vol. 45, No. 3, May 1998, pp. 788–799.

[63] Bailey, M., Blackstock, D., Cleveland, R., and L.A., C., "Comparison of electrohydraulic lithotripters with rigid and pressure-release ellipsoidal reflectors I. Acoustic fields," *Journal of the Acoustical Society of America*, Vol. 104, No. 4, October 1998, pp. 2517–2524.

[64] Holmer, N., Almquist, L., Hertz, T., Holm, A., Lindstedt, E., Persson, H., and Hertz, C., "On the mechanism of kidney stone disintegration by acoustic shock waves," *Ultrasound in Medicine and Biology*, Vol. 17, No. 5, 1991, pp. 479–489.

[65] Zhong, P. and Zhou, Y., "Suppression of large intraluminal bubble expansion in shock wave lithotripsy with compromising stone comminution: methodology and in vitro experiments," *Journal of the Acoustical Society of America*, Vol. 110, No. 6, December 2001, pp. 3283–3291.

[66] Sokolov, D., Bailey, M., and Crum, L., "Dual-pulse lithotripter accelerates stone fragmentation and reduces cell lysis *in vitro*," *Ultrasound in Medicine and Biology*, Vol. 29, No. 7, 2003, pp. 1045–1052.

[67] Loske, A., Prieto, F., Fernandez, F., and van Cauwelaert, J., "Tandem shock wave cavitation enchancement for extracorporeal lithotripsy," *Physics in Medicine and Biology*, Vol. 47, No. 3945-3957, 2002.

[68] Lukes, P., Sunka, P., Hoffer, P., Stelmashuk, V., Pouchkova, P., Zadinova, M., Zeman, J., Dibdiak, L., Kolarova, H., Tomankova, K., Binder, S., and Benes, J., "Focused tandem shock waves in water and their potential application in cancer treatment," *Shock Waves*, Vol. 24, 2014, pp. 51–57.

[69] Tomita, Y. and Shima, A., "The effects of heat transfer on the behavior of a bubble and the impulse pressur ein a viscous compressible liquid," *ZAMM–Journal of Applied Mathematics and Mechanics*, Vol. 59, 1979, pp. 297–306.

[70] Tomita, Y., Shima, A., and Takahashi, K., "The collapse of a gas bubble attached to a solid wall by a shock wave and the induced impact pressure," *Journal of Fluids Engineering*, Vol. 105, 1983, pp. 341–347.

[71] Shima, A., Tomita, Y., and Takahashi, K., "The collapse of a gas bubble near a solid wall by a shock wave and the induced impulsive pressure," *Proceedings of the Institution of Mechanical Engineers, Part C: Journal of Mechanical Engineering Science*, 1984, pp. 81–86.

[72] Tomita, Y. and Shima, A., "Mechanisms of impulsive pressure generation and damage pit formation by bubble collapse," *Journal of Fluid Mechanics*, Vol. 169, 1986, pp. 535–564.

[73] Shima, A., Tomita, Y., and Ohno, T., "Temperature effects on single bubble collapse and induced impulsive pressure," *Journal of Fluids Engineering*, Vol. 110, June 1988, pp. 194–199.

[74] Shima, A., Takayama, K., Tomita, Y., and Miura, N., "An experimental study on effects of a solid wall on the motion of bubbles and shock waves in bubble collapse," *Acustica*, Vol. 48, 1981, pp. 293–301.

[75] Philipp, A. and Lauterborn, W., "Cavitation erosion by single laser-produced bubbles," *Journal of Fluid Mechanics*, Vol. 361, 1998, pp. 75–116.

[76] Johnsen, E. and Colonius, T., "Shock-induced collapse of a gas bubble in shockwave lithotripsy," *Journal of the Acoustical Society of America*, 2008.

[77] Coleman, A., Choi, M., Saunders, J., and Leighton, T., "Acoustic emission and sonoluminescence due to cavitation at the beam focus of an electrohydraulic shock wave lithotripter," *Ultrasound in Medicine and Biology*, Vol. 18, No. 3, 1992, pp. 267–281.

[78] Philipp, A., Delius, M., Scheffczyk, C., Vogel, A., and Lauterborn, W., "Interaction of lithotripter-generated shock waves with air bubbles," *Journal of the Acoustical Society of America*, Vol. 93, No. 5, 1993, pp. 2496–2509.

[79] Ohl, C. and Ikink, R., "Shock-wave-induced jetting of micron-size bubbles," *Physical Review Letters*, Vol. 90, No. 21, May 2003.

[80] Johnsen, E. and Colonius, T., "Numerical simulations of non-spherical bubble collapse," *Journal of Fluid Mechanics*, 2009.

[81] Chen, H., Brayman, A. A., Matula, T. J., and Evan, A., "Vascular damage by ultrasound-activated microbubble induced vessel invagination," *Ultrasonics Symposium (IUS), 2010 IEEE*, 2010, pp. 678–681.

[82] Chen, H., Brayman, A. A., Kreider, W., Bailey, M. R., and Matula, T. J., "Observations of translation and jetting of ultrasound-activated microbubbles in mesenteric microvessels," *Ultrasound in Medicine and Biology*, 2011.

[83] Coralic, V. and Colonius, T., "Shock induced collapse of a bubble inside a deformable vessel," *European Journal of Mechanics B/Fluids*, Vol. 40, 2013, pp. 64–74.

[84] Kodama, T. and Takayama, K., "Dynamic behavior of bubbles during extracorporeal shock-wave lithotripsy," *Ultrasound in Medicine and Biology*, 1998.

[85] Kodama, T. and Tomita, Y., "Cavitation bubble behavior and bubble-shock wave interaction near a gelatin surface as a study of in vivo bubble dynamics," *Applied Physics B*, 2000.

[86] Freund, J., Shukla, R., and Evan, A., "Shock-induced bubble jetting into a viscous fluid with application to tissue injury in shock-wave lithotripsy," *Journal of the Acoustical Society of America*, 2009.

[87] Brujan, E.-A., Nahen, K., Schmidt, P., and Vogel, A., "Dynamics of laser-induced cavitation bubbles near an elastic boundary," *Journal of Fluid Mechanics*, 2000.

[88] Brujan, E.-A., Nahen, K., Schmidt, P., and Vogel, A., "Dynamics of laser-induced cavitation bubbles near elastic boundaries: influence of the elastic modulus," *Journal of Fluid Mechanics*, 2000.

[89] Sankin, G. and Zhong, P., "Interaction between shock wave and single inertial bubbles near an elastic boundary," *Physical Review E*, 2006.

[90] Wang, Q., "Multi-oscillations of a bubble in a compressible liquid near a rigid boundary," *Journal of Fluid Mechanics*, Vol. 745, 2014, pp. 509–536.

[91] Gilmore, F., "The growth or collapse of a spherical bubble in a viscous compressible liquid," Tech. Rep. 26-4, Office of Naval Research, Pasadena, CA, April 1952.

[92] Keller, J. and Miksis, M., "Bubble oscillations of large amplitude," *Journal of the Acoustical Society of America*, Vol. 68, No. 2, August 1980, pp. 628–633.

[93] Prosperetti, A. and Lezzi, A., "Bubble dynamics in a compressible liquid Part 1 First-order theory," *Journal of Fluid Mechanics*, Vol. 168, 1986, pp. 457–478.

[94] Lauterborn, W. and Ohl, C., "Cavitation bubble dynamics," *Ultrasonics Sonochemistry*, Vol. 4, No. 2, April 1997, pp. 65–75.

[95] Quinto-Su, P. and Ohl, C., "Interaction between two laser-induced cavitation bubbles in a quasi-two-dimensional geometry," *Journal of Fluid Mechanics*, Vol. 633, 2009, pp. 425–435.

[96] Ilinskii, Y., Zabolotksaya, E., Hay, T., and Hamilton, M., "Models of Cylindrical Bubble Pulsation," *Journal of the Acoustical Society of America*, Vol. 132, No. 3, 2012, pp. 1346–1357.

[97] *Hydrodynamics of Explosion*, Springer, 2005.

[98] Zwaan, E., Le Gac, S., Tsuji, K., and Ohl, C., "Controlled Cavitation in Microfluidic Systems," *Physical Review Letters*, Vol. 98, No. 25, June 2007.

[99] Yang, J., Kubota, T., and Zukoski, E., "A model for characterization of a vortex pair formed by shock passage over a light-gas inhomogeneity." *Journal of Fluid Mechanics*, Vol. 258, 1994, pp. 217–244.

[100] Rudinger, G. and Somers, L., "Behaviour of small regions of different gases carried in accelerated gas flows," *Journal of Fluid Mechanics*, Vol. 7, No. 2, 1960, pp. 161–176.

[101] Jacobs, J., "Shock-induced mixing of a light-gas cylinder," *Journal of Fluid Mechanics*, Vol. 234, 1992, pp. 629–649.

[102] Samtaney, R. and Zabusky, N., "Circulation deposition on shock-accelerated planar and curved density-stratified interfaces: models and scaling laws," *Journal of Fluid Mechanics*, Vol. 269, 1994, pp. 45–78.

[103] Quirk, J. and Karni, S., "On the dynamics of shock-bubble interaction," *Journal of Fluid Mechanics*, Vol. 318, 1996, pp. 129–163.

[104] Walters, J. and Davidson, J., "The initial motion of a gas bubble formed in an inviscid liquid. Part 1. The two-dimensional bubble." *Journal of Fluid Mechanics*, Vol. 12, No. 3, 1962, pp. 408–416.

[105] Walters, J. and Davidson, J., "The initial motion of a gas bubble formed in an inviscid liquid. Part 2. The three-dimensional bubble and the toroidal bubble." *Journal of Fluid Mechanics*, Vol. 17, No. 3, 1963, pp. 321–336.

[106] Ranjan, D., Oakley, J., and Bonazza, R., "Shock-bubble interactions," *Annual Review of Fluid Mechanics*, Vol. 43, 2011, pp. 117–140.

[107] Sturdivan, L., "A mathematical model of penetration of chunky projectiles in a gelatin tissue simulant." Tech. Rep. ARCSL-TR-78055, Army Armament Research and Development Command, Aberdeen, MD, December 1978.

[108] Hollerman, J., Fackler, M., Coldwell, D., and Ben-Menachem, Y., "Gunshot wounds: 1. Bullets, Ballistics and Mechanisms of Injury," *American Journal of Roentgenology*, Vol. 155, October 1990, pp. 685–690.

[109] Ahearne, M., Yang, Y., El Haj, A., Then, K., and Liu, K., "Characterizing the viscoelastic properties of thin hydrogel-based constructs for tissuse engineering applications," *Journal of the Royal Society Interface*, Vol. 2, 2005, pp. 455–463.

[110] Mercey, E., Obeid, P., Glaise, D., Calvo-Munoz, M., Guguen-Guillouzo, C., and Foque, B., "The application of 3D micropatterning of agarose substrate for cell culture and *in situ* comet assays," *Biomaterials*, Vol. 31, 2010, pp. 3156–3165.

[111] Lotters, J., Olthius, W., Veltink, P., and Bergveld, P., "The mechanical properties of the rubber elastic polymer polydimethylsiloxane for sensor applications." *Journal of Micromechanics and Microengineering*, Vol. 7, No. 3, 1997, pp. 145–147.

[112] Alley, M., Schimizze, B., and Son, S., "Experimental modeling of explosive blast-related traumatic brain injuries." *NeuroImage*, Vol. 54, 2011, pp. S45–S54.

[113] G.J., A.-T., P.J., H., Sheldon, R., Stennet, C., Hameed, A., and Wilgeroth, J., "The high strain-rate behaviour of selected tissue analogues," *Journal of the Mechanical Behavior of Biomedical Materials*, Vol. 33, 2014, pp. 124–135.

[114] Trofin, L. and P.R., L., "Controlled geometry fabrication of polydimethylsiloxane nanofibers for biomimetics." *Journal of Applied Polymer Science*, Vol. 105, No. 5, September 2007, pp. 2549–2552.

[115] Sadaf, H., Ramesh, K., Lennon, A., Merkle, A., and J.C., R., "Mechanical properties of soft human tissues under dynamic loading," *Journal of Biomechanics*, 2007.

[116] Madsen, E., Sathoff, H., and Zagzebski, J., "Ultrasonic shear wave properties of soft tissues and tissuelike materials," *Journal of Acoustical Society of America*, Vol. 74, No. 5, 1983, pp. 1346–1355.

[117] Goss, S., Johnston, R., and Dunn, F., "Comprehensive compilation of empirical ultrasonic properties of mammalian tissues." *Journal of the Acoustical Society of America*, Vol. 64, No. 2, August 1978, pp. 423–457.

[118] Normand, V., Lootens, D., Amici, E., Plucknett, K., and Aymard, P., "New insight into agarose gel mechanical properties," *Miomacromolecules*, Vol. 1, 2000, pp. 730–738.

[119] Parker, M., *A study of shock induced pore collapse using high speed photography and particle image velocimetry*, Master's thesis, University of Illinois, 2007.

[120] Nagayama, K., Mori, Y., Motegi, Y., and Nakahara, M., "Shock Hugoniot for biological materials," *Shock Waves*, Vol. 15, 2006, pp. 267–275.

[121] Moritaka, H., Nishinari, K., Horiuchi, H., and Watase, M., "Rheological properties of aqueous agarose-gelatin gels," *Journal of Texture Studies*, Vol. 11, 1980, pp. 257–270.

[122] *Polymer Data Handbook*, chap. Poly(dimethylsiloxane), Oxford University Press, 1999, pp. 411–435.

[123] Weissler, A., "Ultrasonic investigation of molecular properties of liquids. III. Linear polymethylsiloxanes." *Journal of the American Chemical Society*, Vol. 71, Jan 1949, pp. 93–95.

[124] Gottlieb, M., Macosko, C., and Lepsch, T., "Stress-strain behavior of randomly crosslinked polydimethylsiloxane networks," *Journal of Polymer Science*, Vol. 19, 1981, pp. 1603–1617.

[125] Millett, J., Whiteman, G., Stirk, S., and N.K., B., "The shock induced shear strength in a silastomer," *Proceedings of the SEM Annual Conference*, Society for Experimental Mechanics, Inc., Albuquerque, NM, June 2009.

[126] Mata, A., Fleischman, A., and Roy, S., "Characterization of polydimethylsiloxane (PDMS) properties for biomedical micro/nanosystems," *Biomedical Microdevices*, Vol. 7, No. 4, 2005, pp. 281–293.

[127] Company, D. C., "Sylgard 184 Silicone Elastomer," Technical Data Sheet, Form No. 11-3184-01C.

[128] Wang, Z., *Polydimethylsiloxane mechanical properties measured by macroscopic compression and nanoindentation techniques*, Master's thesis, University of South Florida, 2011.

[129] Khanafer, K., Duprey, A., Schlicht, M., and Berguer, R., "Effects of strain rate, mixing ratio, and stress-strain definition on the mechanical behavior of the polydimethylsiloxane (PDMS) material as related to its biological applications," *Biomedical Microdevices*, Vol. 11, 2009, pp. 503–508.

[130] "Sylgard 184 Elastomer Kit," Dow Corning Corporation Material Safety Data Sheet, May 2010.

[131] Tsou, J., Liu, J., Barakat, A., and Insana, M., "Role of ultrasonic shear rate estimation errors in assessing inflammatory response and vascular risk," *Ultrasound in Medicine and Biology*, Vol. 34, No. 6, 2008, pp. 963–972.

[132] Hooper, J., Bedrov, D., Smith, G., Hanson, B., Borodin, O., Dattelbaum, D., and Kober, E., "A molecular dynamics simulation study of the pressure-volume-temperature behavior of polymers under high pressure," *Journal of Chemical Physics*, Vol. 130, 2009.

[133] J.C.F., M., Whiteman, G., Stirk, S., and Bourne, N., "Shear strength measurements in a shock loaded commercial silastomer," *Journal of Physics D: Applied Physics*, Vol. 44, 2011.

[134] Johnston, I., McCluskey, D., C.K.L., T., and Tracey, M., "Mechanical characterization of bulk Sylgard 184 for microfluidics and microengineering," *Journal of Micromechanics and Microengineering*, Vol. 24, 2014.

[135] Carillo, F., Gupta, S., Balooch, M., Marshall, S., Marshall, G., Pruitt, L., and Puttlitz, C., "Nanoindentation of polydimethylsiloxane elastomers: Effect of crosslinking, work of adhesion, and fluid environment on elastic modulus," *Journal of Materials Research*, Vol. 20, No. 10, October 2005, pp. 2820–2830.

[136] Schneider, F., Fellner, T., Wilde, J., and Wallrabe, U., "Mechanical properties of silicones for MEMS," *Journal of Micromechanics and Microengineering*, Vol. 18, 2008.

[137] Dattelbaum, D., Jensen, J., Schwendt, A., Kober, E., Lewis, M., and Menikoff, R., "A novel method for static equation-of state-development: Equation of state of a cross-linked poly(dimethylsiloxane) (PDMS) network to 10 GPa," *Journal of Chemical Physics*, Vol. 122, 2005.

[138] Winter, R., Whiteman, G., Haining, G., Salisbury, D., and Tsembelis, K., "Measurement of equation of state of silicone elastomer," *Shock Compression of Condensed Matter—2003*, edited by M. Furnish, Y. Gupta, and J. Forbes, Vol. 706 of *AIP Conference Proceedings*, American Institute of Physics, American Institute of Physics, 2004, pp. 679–682.

[139] Dowell, F., "A simple EOS for the silicone rubber Sylgard 184," Tech. Rep. LA-10164-MS, Los Alamos National Laboratory, Los Alamos, NM, August 1984.

[140] *LASL Shock Hugoniot Data*, chap. Sylgard, University of California Press, 1980, p. 452.

[141] Ahmed, S. and Jones, F., "A review of particulate reinforcement theories for polymer composites," *Journal of Materials Science*, Vol. 25, 1990, pp. 4933–4942.

[142] Guth, E., “Theory of filler reinforcement,” *Journal of Applied Physics*, Vol. 16, January 1945, pp. 20–25.

[143] Atkinson, C. and Kytomaa, H., “Acoustic wave speed and attenuation in suspensions.” *International Journal of Multiphase Flow*, Vol. 18, No. 4, 1992, pp. 577–592.

[144] Makishima, A. and Mackenzie, J., “Calculation of bulk modulus, shear modulus, and poisson’s ratio of glass,” *Journal of Non-Crystalline Solids*, Vol. 17, 1975, pp. 147–157.

[145] Zimmerman, R., “Elastic moduli of a solid containing spherical inclusions.” *Mechanics of Materials*, Vol. 12, 1991, pp. 17–24.

[146] *Schlieren and Shadowgraph Imaging*, Experimental Fluid Mechanics, Springer-Verlag Berlin Heidelberg GmbH, 2001.

[147] Harvey, A., Gallagher, J., and Levelt Sengers, J., “Revised formulation for the refractive index of water and steam as a function of wavelength, temperature, and density.” *Journal of Physical and Chemical Reference Data*, Vol. 27, No. 4, 1998, pp. 761–774.

[148] Schiebener, P., Straub, J., J.M.H., L. S., and Gallagher, J., “Refractive index of water and steam as a function of wavelength, temperature, and density,” *Journal of Physical and Chemical Reference Data*, 1990.

[149] *Particle Image Velocimetry*, Springer, 1998.

[150] Nogueira, J., Lecuona, A., and Rodriguez, P., “Identification of a new source of peak locking, analysis and its removal in conventional and super-resolution PIV techniques,” *Experiments in Fluids*, Vol. 30, 2001, pp. 309–316.

[151] Ochoa, H., “Optimizing Particle Image Velocimetry Setup for The Study of Void Collapse,” Tech. rep., California Institute of Technology, Office of Student-Faculty Programs, 2016.

[152] Nobach, H. and Bodenschatz, E., “Limitations of accuracy in PIV due to individual variations of particle image intensities.” *Experiments in Fluids*, Vol. 47, 2009, pp. 27–38.

[153] Rasband, W., “ImageJ,” 1997-2018.

[154] Swantek, A., *An Experimental Investigation of Hydrodynamic Void Collapse Under Stress Wave Loading in Detonation Initiation*, Master’s thesis, University of Illinois at Urbana-Champaign, 2009.

[155] Livermore Software Technology Corporation, “LS-DYNA,” 2016.

[156] Matweb LLC, “Overview of materials for Acrylic, Cast,” 2018.

[157] Tijsseling, A., “Fluid-structure interaction in liquid-filled pipe systems: a review,” *Journal of Fluids and Structures*, Vol. 10, 1996, pp. 109–146.

[158] Graff, K., *Wave Motion in Elastic Solids*, Dover Publications Inc., New York, 1991.

[159] Whitham, G., *Linear and Nonlinear Waves*, John Wiley and Sons, 1974.

[160] Epstein, D. and Keller, J., “Expansion and contraction of planar, cylindrical, and spherical underwater gas bubbles,” *Journal of the Acoustical Society of America*, Vol. 52, No. 3, 1971, pp. 975–980.

[161] *Applied Statistics and Probability for Engineers*, John Wiley and Sons, 4th ed., 2007.

[162] Christman, D., “Dynamic properties of Poly(methylmethacrylate) (PMMA) (Plexiglas),” Tech. rep., General Motors Corporation, Warren, MI, March 1972.

[163] Microsoft Corporation, “Microsoft Excel,” 2012-2018.

[164] Mathworks Corporation, "MATLAB," 1994-2018.

[165] Landini, G., "Auto Local Threshold," 2017.

[166] Sauvola, J. and Pietikainen, M., "Adaptive document image binarization," *Pattern Recognition*, Vol. 33, 2000, pp. 225–236.

[167] Young, H. and Freedman, R., *University Physics with Modern Physics*, Addison-Wesley, 10th ed., 2000.

[168] Kasarova, S., Sultanova, N., Ivanov, C., and Nikolov, I., "Analysis of the dispersion of optical plastic materials." *Optical Materials*, Vol. 29, No. 11, 2007, pp. 1481–1490.

[169] Hickling, R., "Effects of thermal conduction in sonoluminescence," *Journal of the Acoustical Society of America*, Vol. 35, No. 7, July 1963, pp. 967–974.

[170] Bourne, N. and Milne, A., "The temperature of a shock-collapsed cavity." *Proceedings of the Royal Society of London A*, Vol. 459, 2003, pp. 1851–1861.

[171] Savitzky, A. and Golay, M., "Smoothing and differentiation of data by simplified least squares procedures," *Analytical Chemistry*, Vol. 36, No. 8, July 1964, pp. 1627–1639.

[172] Rai, N. and Udaykumar, H., "Three-dimensional simulations of void collapse in energetic materials," *Physical Review of Fluids*, Vol. 3, No. 3, 2018, pp. 033201.

[173] Zucker, R. and Biblarz, O., *Fundamentals of Gas Dynamics*, John Wiley and Sons, 2002.

[174] Khasainov, B., Borisov, A., B.S., E., and Korotkov, A., "Two-phase visco-plastic model of shock initiation of detonation in high density pressed explosives," *7th Symposium (International) on Detonation*, Annapolis, MD, pp. 435–447.

[175] Munson, B., Young, D., and Okiishi, T., *Fundamentals of Fluid Mechanics*, John Wiley and Sons, 5th ed., 2006.

[176] Yoshitake, Y., Mitani, S., Sakai, K., and Takagi, K., "Surface tension and elasticity of gel studied with laser-induced surface-deformation spectroscopy," *Physical Review E*, Vol. 78, Oct 2008, pp. 041405.

[177] Dill, E., *Continuum Mechanics*, CRC Press, 2007.

[178] Liepmann, H. and Roshko, A., *Elements of Gasdynamics*, Dover Publications, 1957, 1985.

[179] Thompson, P., *Compressible Fluid Dynamics*, McGraw-Hill, 1972.

[180] Bird, R. B., Armstrong, R., and Hassager, O., *Dynamics of Polymeric Fluids*, Vol. 1, John Wiley and Sons, 2nd ed., 1987.

[181] "Textural properties of agarose gels. I. Rheological and fracture properties," *Food Hydrocolloids*, Vol. 20, No. 2, 2006, pp. 184–195.

[182] VanBavel, E., "Effects of shear stress on endothelial cells: possible relevance for ultrasound applications," *Progress in Biophysics and Molecular Biology*, Vol. 93, 2007, pp. 374–383.

[183] Leverett, L., Hellums, J., Alfrey, C., and Lynch, E., "Red blood cell damage by shear stress," *Biophysical Journal*, Vol. 12, 1972, pp. 257–272.

[184] Bernard, P., *Fluid Dynamics*, chap. 6. Doublets and Their Applications, Cambridge University Press, 1st ed., 2015, pp. 57–64.

APPENDIX A

GAS GUN DRAWINGS

The following pages include the CAD drawings for the single-stage compressed air gas gun built for this study. The drawings have been scaled by 85% for inclusion in the document.

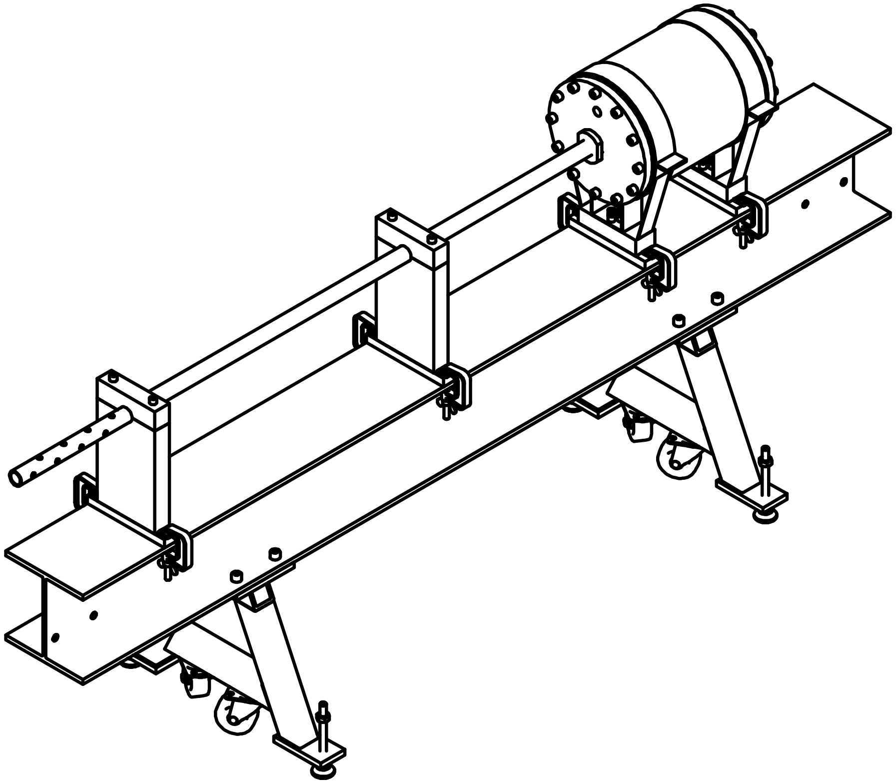

UNLESS OTHERWISE SPECIFIED	
TOLERANCES	
Format	Tol
.X	.1
.XX	.01

DRAWN Galina Shpuntova	2/11/2011	University of Illinois-Aerospace Engineering
CHECKED		
QA		TITLE
MFG		
APPROVED		Gas Gun
		SIZE A · DWG NO Complete_Drawings · REV 1
		SCALE · SHEET 1 OF 25

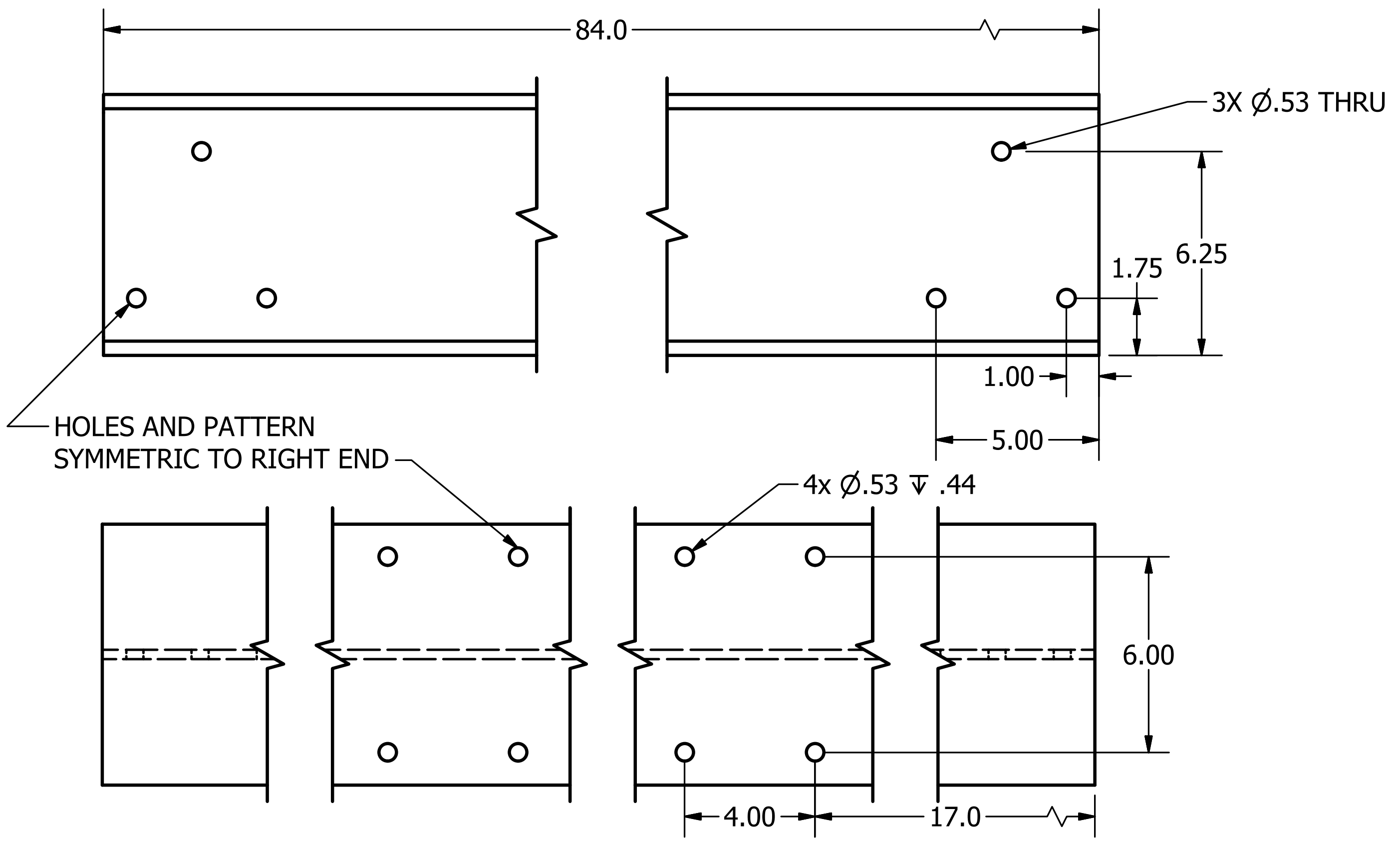

DRAWN Galina Shpuntova	2/11/2011	University of Illinois-Aerospace Engineering		
CHECKED				
QA		TITLE		
MFG				
APPROVED		Gas Gun		
MATERIAL W8x31 Steel I-Beam				
QUANTITY 1		SIZE A	DWG NO Complete_Drawings	REV 1
		SCALE 1:5		SHEET 2 OF 25

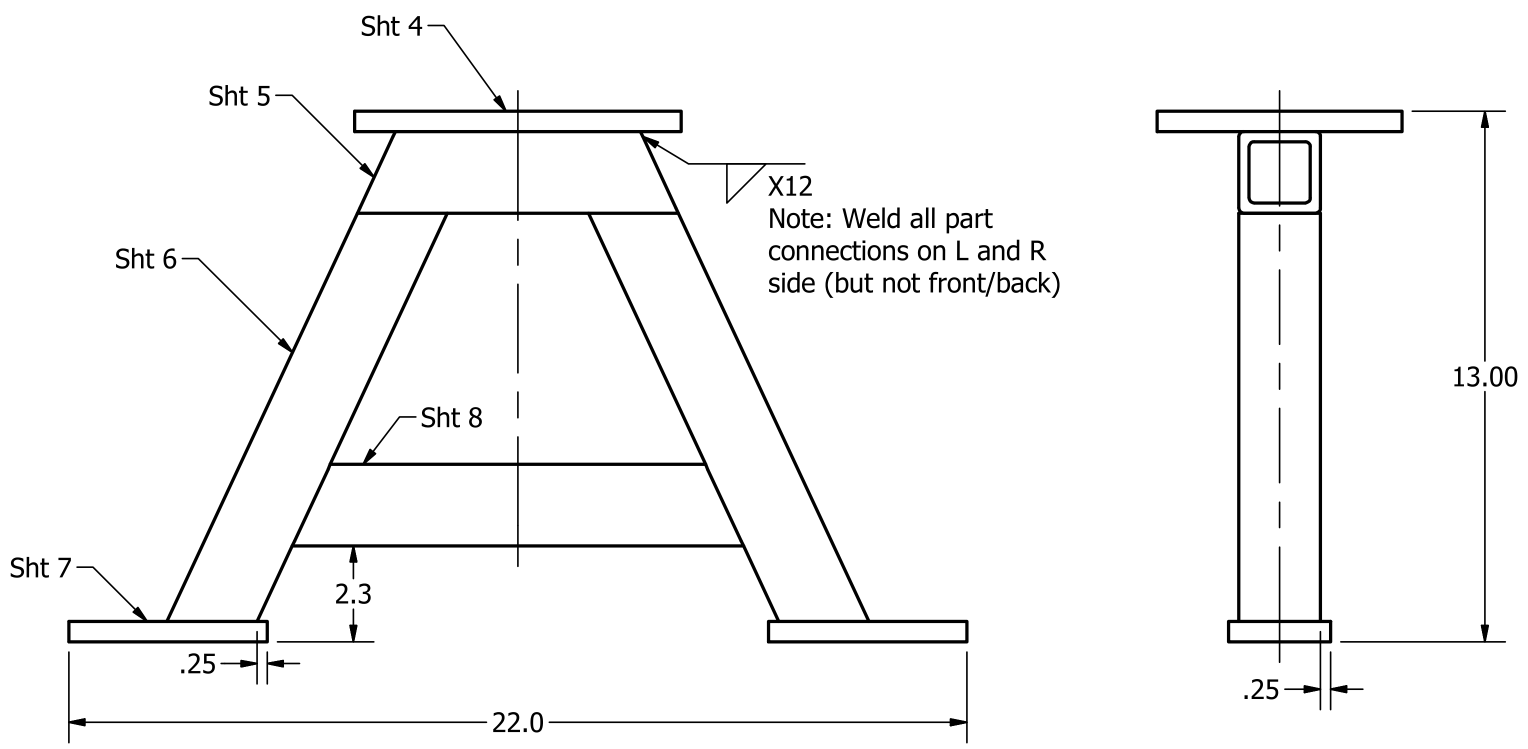

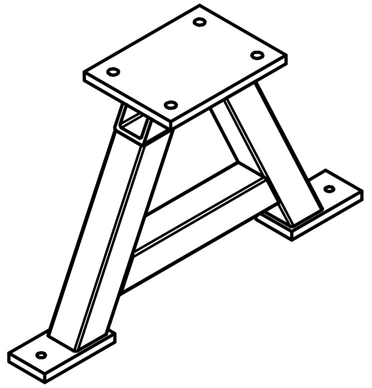

DRAWN Galina Shpuntova	2/11/2011	University of Illinois-Aerospace Engineering		
CHECKED		TITLE Gas Gun		
QA				
MFG				
APPROVED				
MATERIAL Steel		SIZE A	DWG NO Complete_Drawings	REV 1
QUANTITY 2		SCALE 1:4		SHEET 3 OF 25

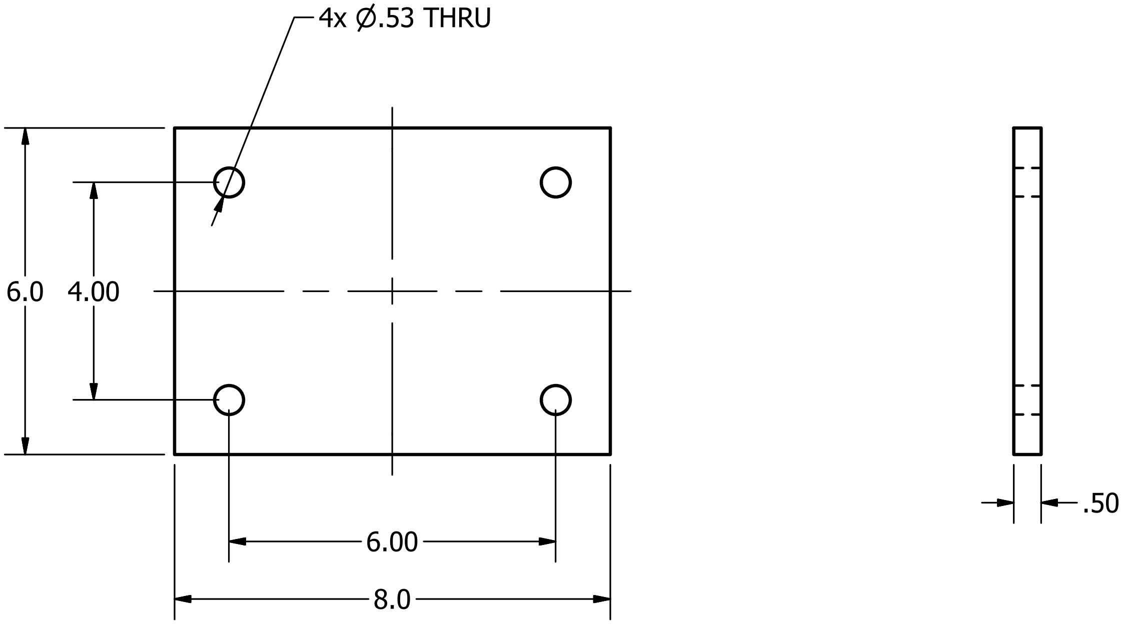

DRAWN Galina Shpuntova	2/11/2011	University of Illinois-Aerospace Engineering
CHECKED		TITLE Gas Gun
QA		
MFG		
APPROVED		
MATERIAL Steel		SIZE A
QUANTITY 2		DWG NO Complete_Drawings
		REV 1
		SCALE 1:3
		SHEET 4 OF 25

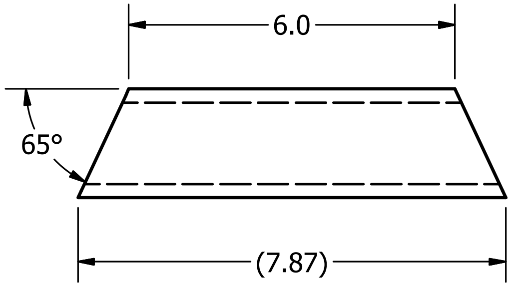

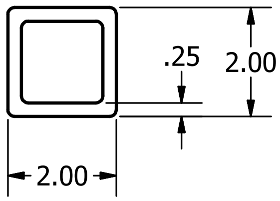

DRAWN Galina Shpuntova	2/11/2011	University of Illinois-Aerospace Engineering			
CHECKED					
QA		TITLE			
MFG		Gas Gun			
APPROVED					
MATERIAL 2x2 Steel Box Beam		SIZE A		DWG NO Complete_Drawings	REV 1
QUANTITY 2					
		SCALE 1:3		SHEET 5 OF 25	

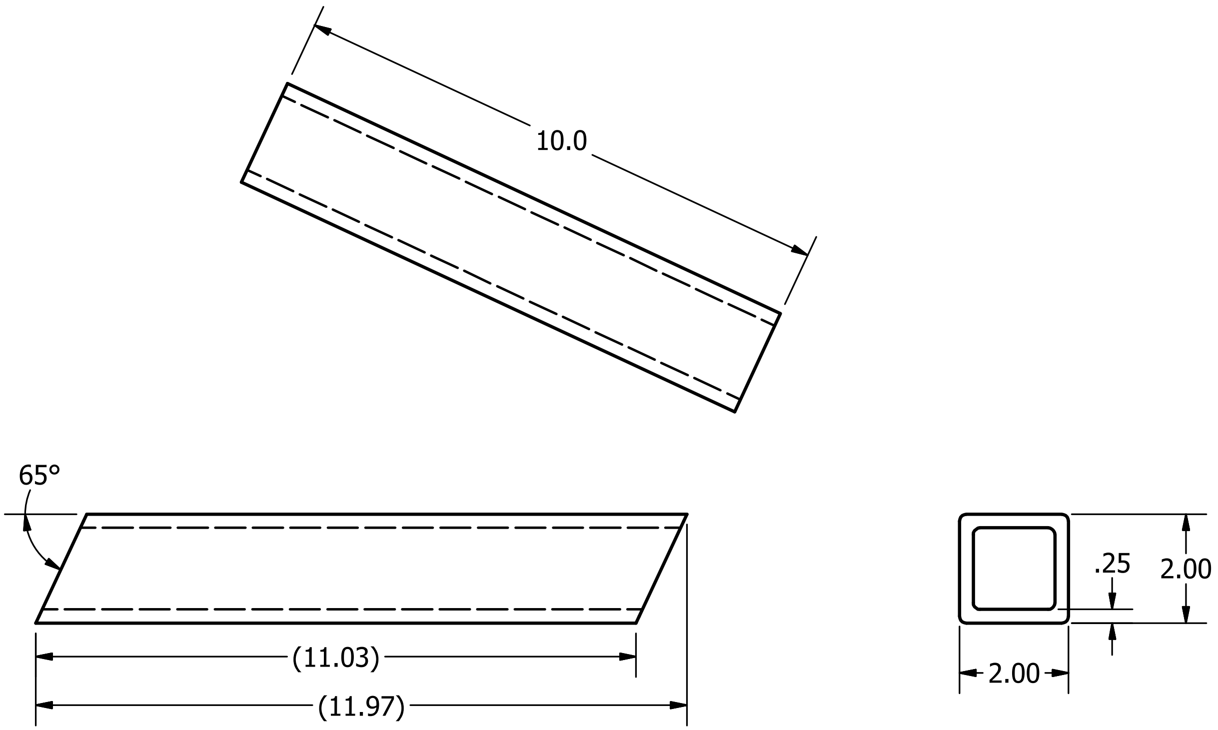

DRAWN Galina Shpuntova	2/11/2011	University of Illinois-Aerospace Engineering
CHECKED		TITLE Gas Gun
QA		
MFG		
APPROVED		
MATERIAL 2x2 Steel Box Beam		SIZE A · DWG NO Complete_Drawings · REV 1
QUANTITY 4		SCALE 1:3 · SHEET 6 OF 25

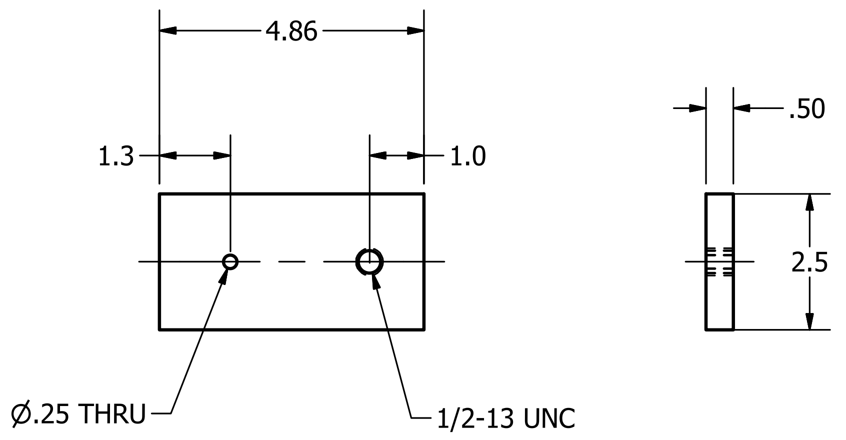

DRAWN Galina Shpuntova	2/11/2011	University of Illinois-Aerospace Engineering			
CHECKED					
QA		TITLE Gas Gun			
MFG					
APPROVED					
MATERIAL Steel		SIZE A		DWG NO Complete_Drawings	REV 1
QUANTITY 4					
		SCALE 1:3		SHEET 7 OF 25	

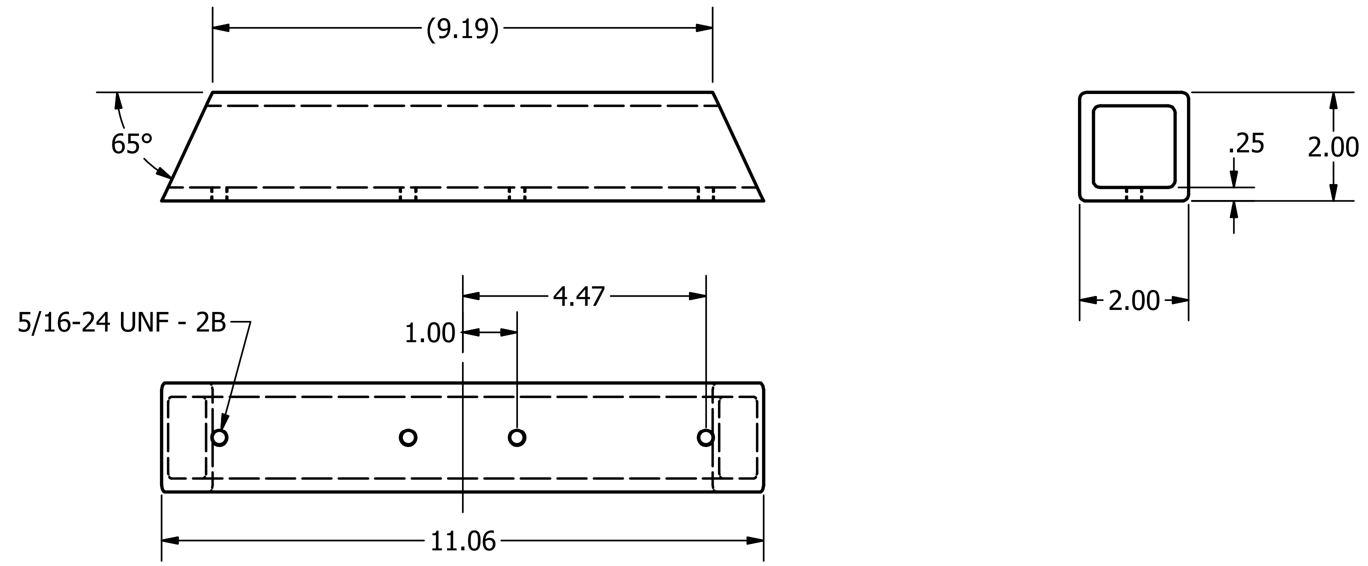

DRAWN Galina Shpuntova	2/11/2011	University of Illinois-Aerospace Engineering	
CHECKED			
QA		TITLE	
MFG			
APPROVED		Gas Gun	
MATERIAL 2x2 Steel Box Beam		SIZE A	DWG NO Complete_Drawings REV 1
QUANTITY 6			
		SCALE 1:3	SHEET 8 OF 25

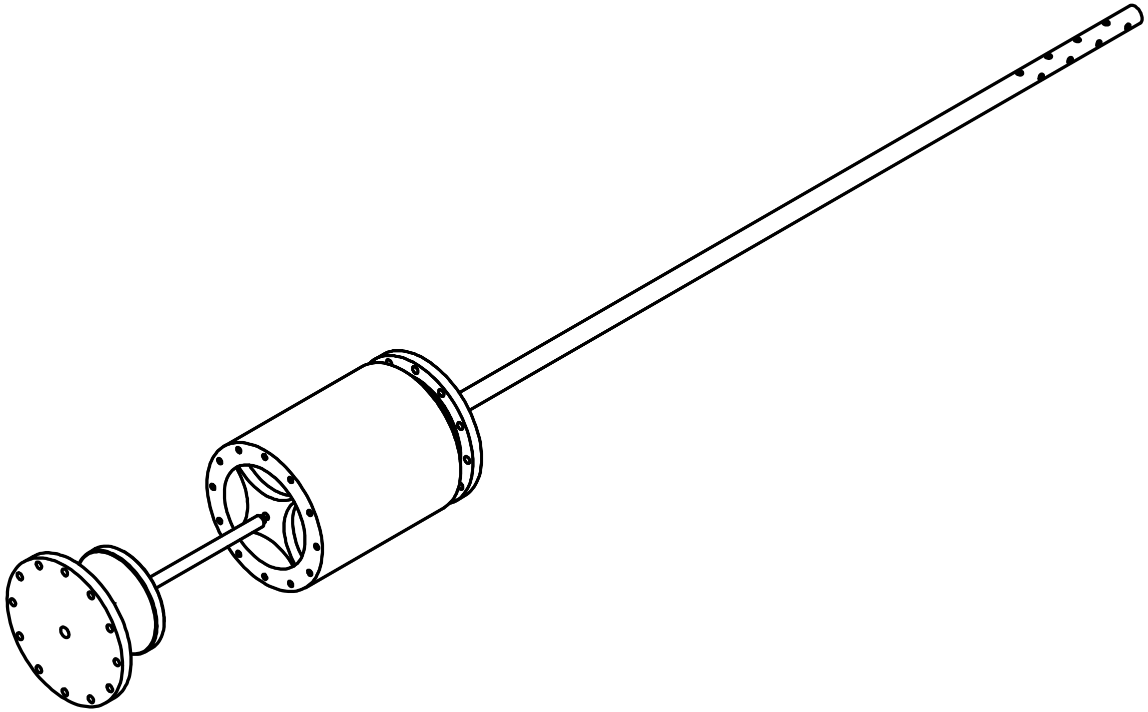

DRAWN Galina Shpuntova	2/11/2011	University of Illinois-Aerospace Engineering				
CHECKED						
QA		TITLE				
MFG		Gas Gun				
APPROVED						
MATERIAL Steel Lexan						
QUANTITY 1		SIZE A		DWG NO Complete_Drawings		REV 1
		SCALE 1:10			SHEET 9 OF 25	

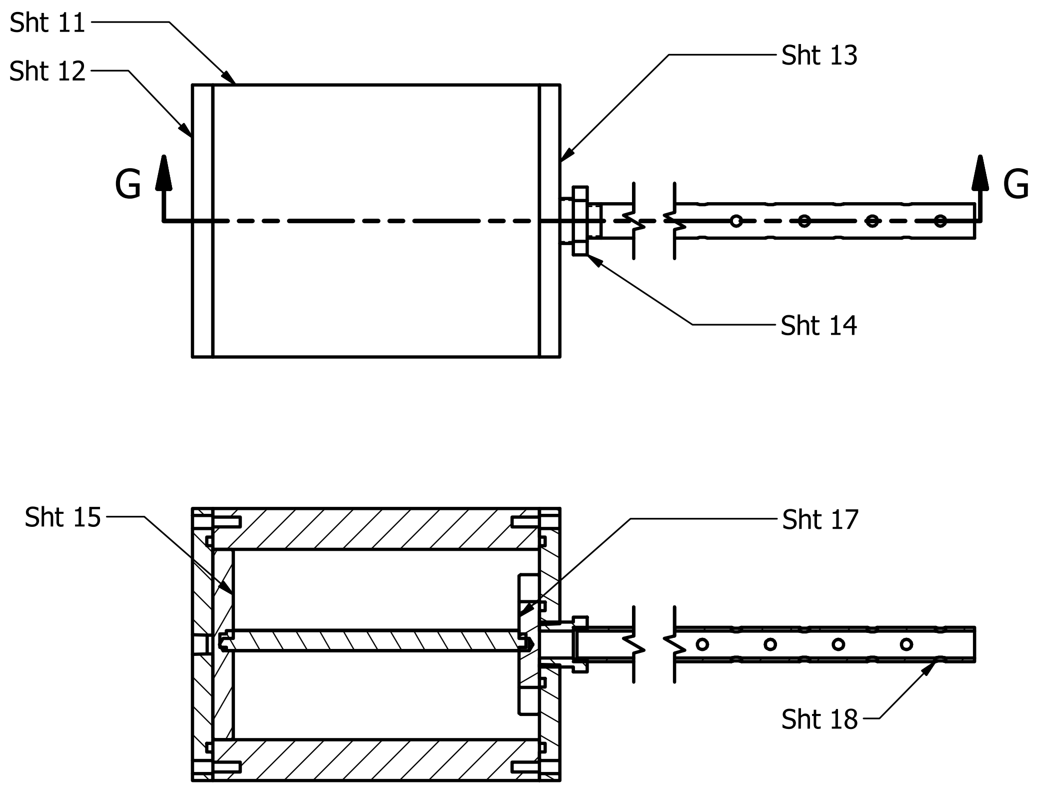

SECTION G-G
SCALE 1 / 6

DRAWN Galina Shpuntova	2/11/2011	University of Illinois-Aerospace Engineering			
CHECKED					
QA		TITLE Gas Gun			
MFG					
APPROVED					
		SIZE A		DWG NO Complete_Drawings	REV 1
		SCALE 1:6		SHEET 10 OF 25	

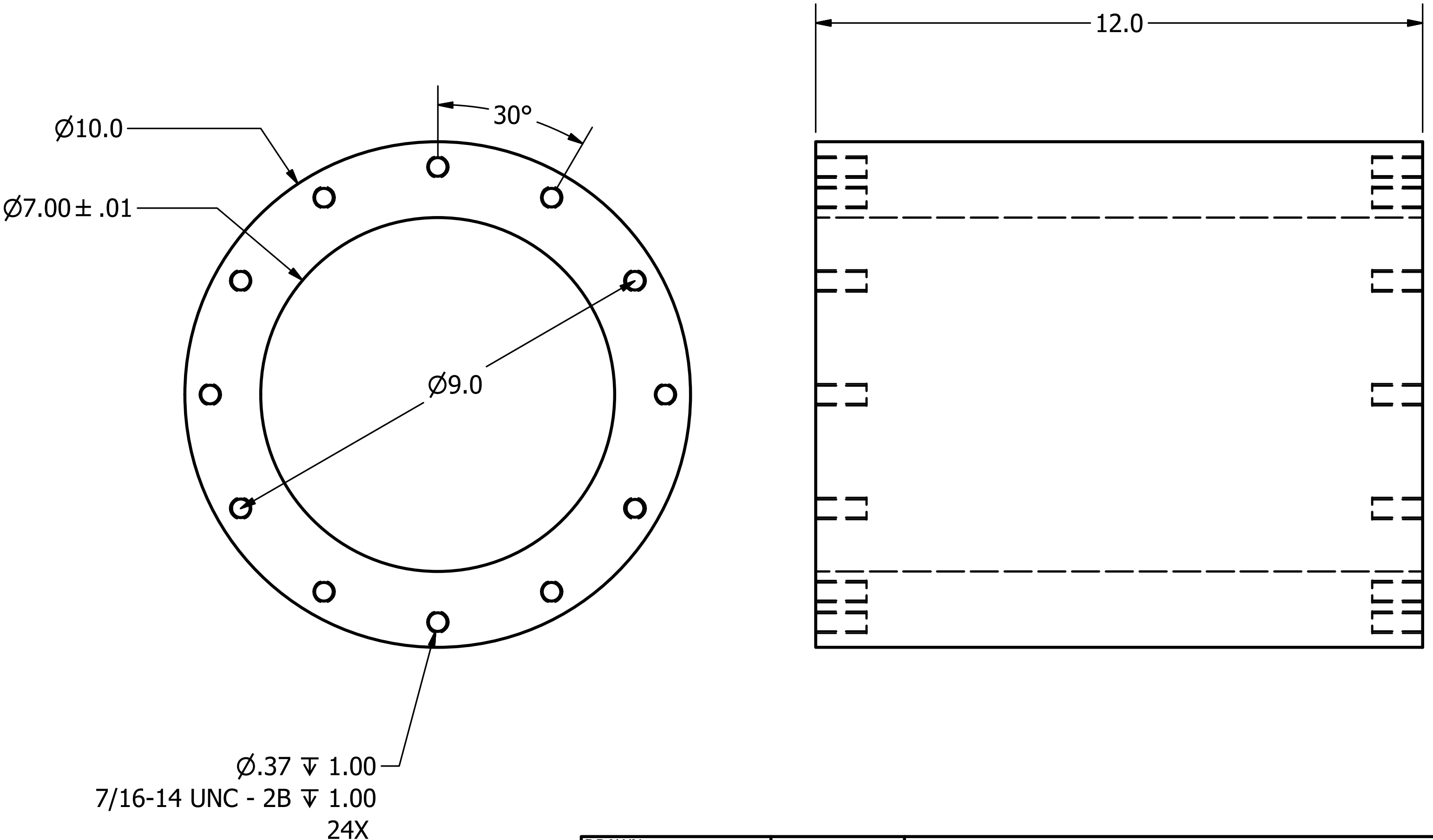

Note: 24 total holes to be drilled, 12 each on front and back ends of cylinder.

DRAWN Galina Shpuntova	2/11/2011	University of Illinois-Aerospace Engineering	
CHECKED			
QA		TITLE Gas Gun	
MFG			
APPROVED			
MATERIAL Honed Steel Tubing 7x10	Will be provided	SIZE A	DWG NO Complete_Drawings
QUANTITY 1			REV 1
		SCALE 1:3	SHEET 11 OF 25

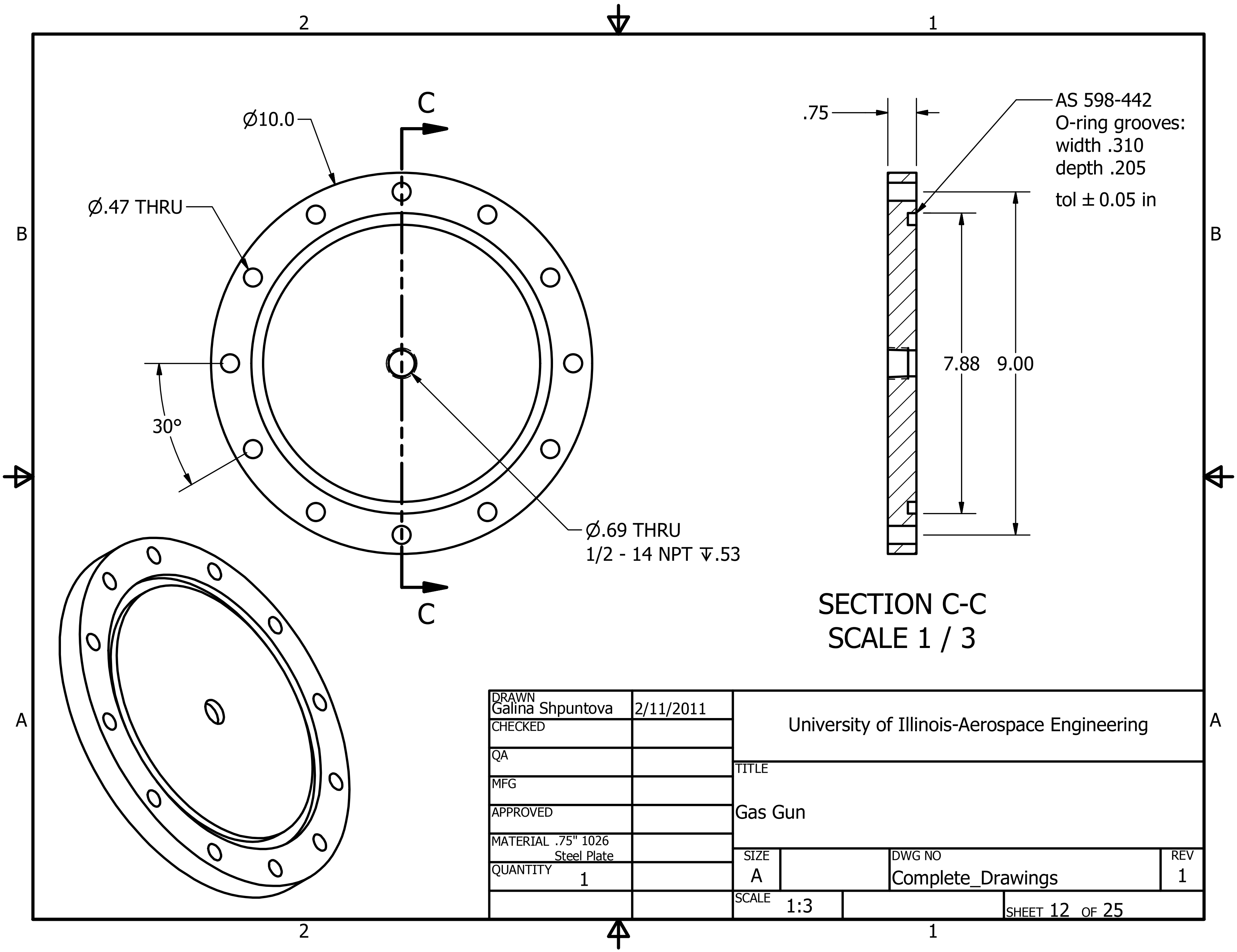

SECTION C-C
SCALE 1 / 3

DRAWN Galina Shpuntova	2/11/2011	University of Illinois-Aerospace Engineering
CHECKED		
QA		TITLE
MFG		Gas Gun
APPROVED		
MATERIAL .75" 1026 Steel Plate		SIZE A · DWG NO Complete_Drawings · REV 1
QUANTITY 1		
		SCALE 1:3 · SHEET 12 OF 25

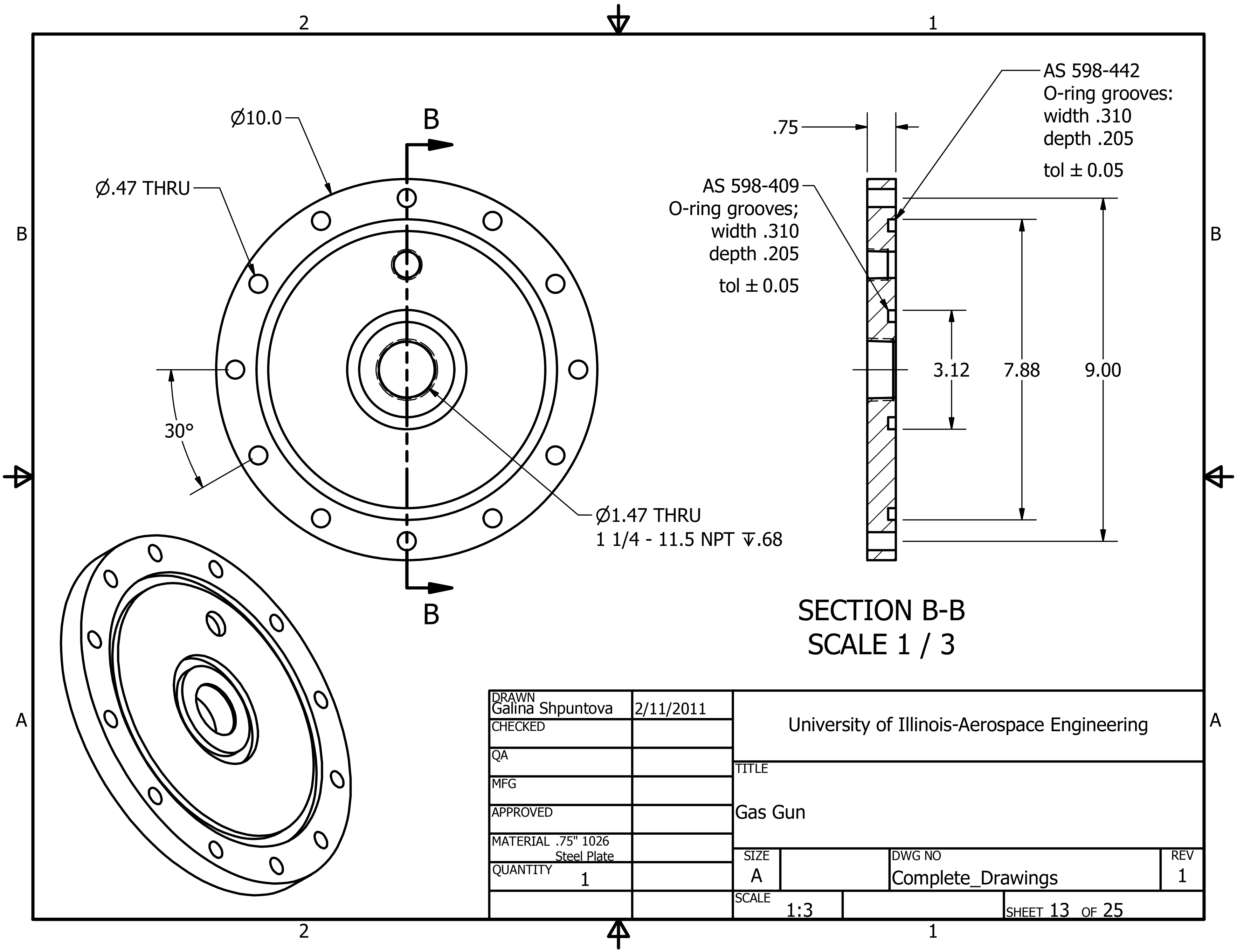

SECTION B-B
SCALE 1 / 3

DRAWN Galina Shpuntova	2/11/2011	University of Illinois-Aerospace Engineering			
CHECKED					
QA		TITLE			
MFG		Gas Gun			
APPROVED					
MATERIAL .75" 1026 Steel Plate					
QUANTITY 1		SIZE A		DWG NO Complete_Drawings	REV 1
		SCALE 1:3		SHEET 13 OF 25	

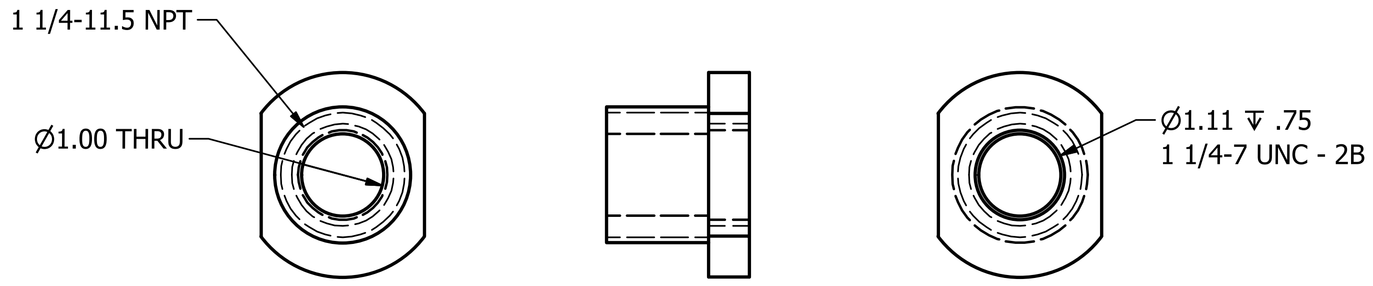

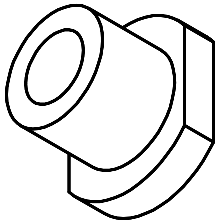

Note: This part was included because it was impossible to put NPT thread on the barrel (Sht 18) when the mating piece (Front cover, Sht 13) was already made. If the cover is remanufactured with straight threads to match the barrel, this piece can be eliminated.

DRAWN Galina Shpuntova	2/11/2011	University of Illinois-Aerospace Engineering
CHECKED		
QA		TITLE Gas Gun
MFG		
APPROVED		
MATERIAL Aluminum		SIZE A
QUANTITY		DWG NO Complete_Drawings
		REV 1
		SCALE
		SHEET 14 OF 25

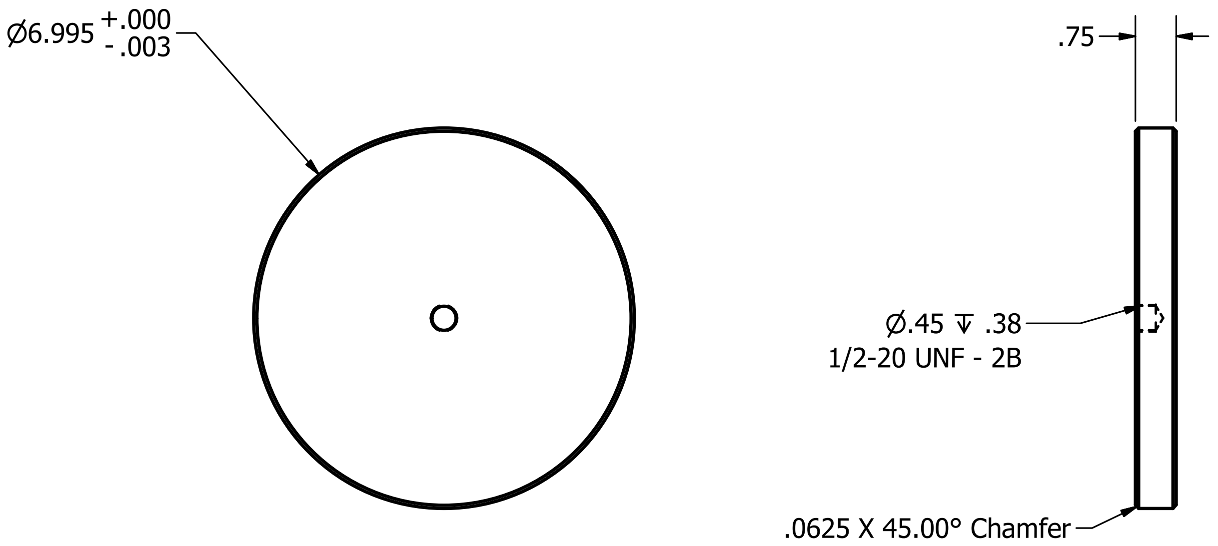

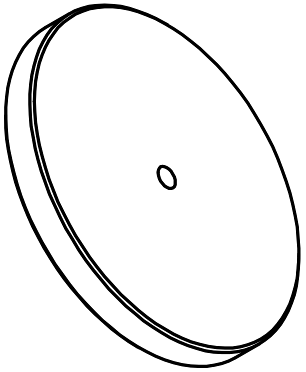

Note: It is very important to have a tight clearance fit on this piece relative to the cylinder (Sht 12). The clearance determines the gas flow around the piston, which affects the pressure across the piston, which affects the movement of the piston on which the mechanism depends. The piston won't move if it is wedged in too tightly (too little clearance, high friction), or if pressure equalizes across it quickly (too much clearance, allows high gas flow). Correct fit is possible, but difficult, to push in by hand.

DRAWN Galina Shpuntova	2/11/2011	University of Illinois-Aerospace Engineering		
CHECKED				
QA		TITLE		
MFG		Gas Gun		
APPROVED				
MATERIAL .75" Lexan Sheet				
QUANTITY 1		SIZE A	DWG NO Complete_Drawings	REV 1
		SCALE 1:3		SHEET 15 OF 25

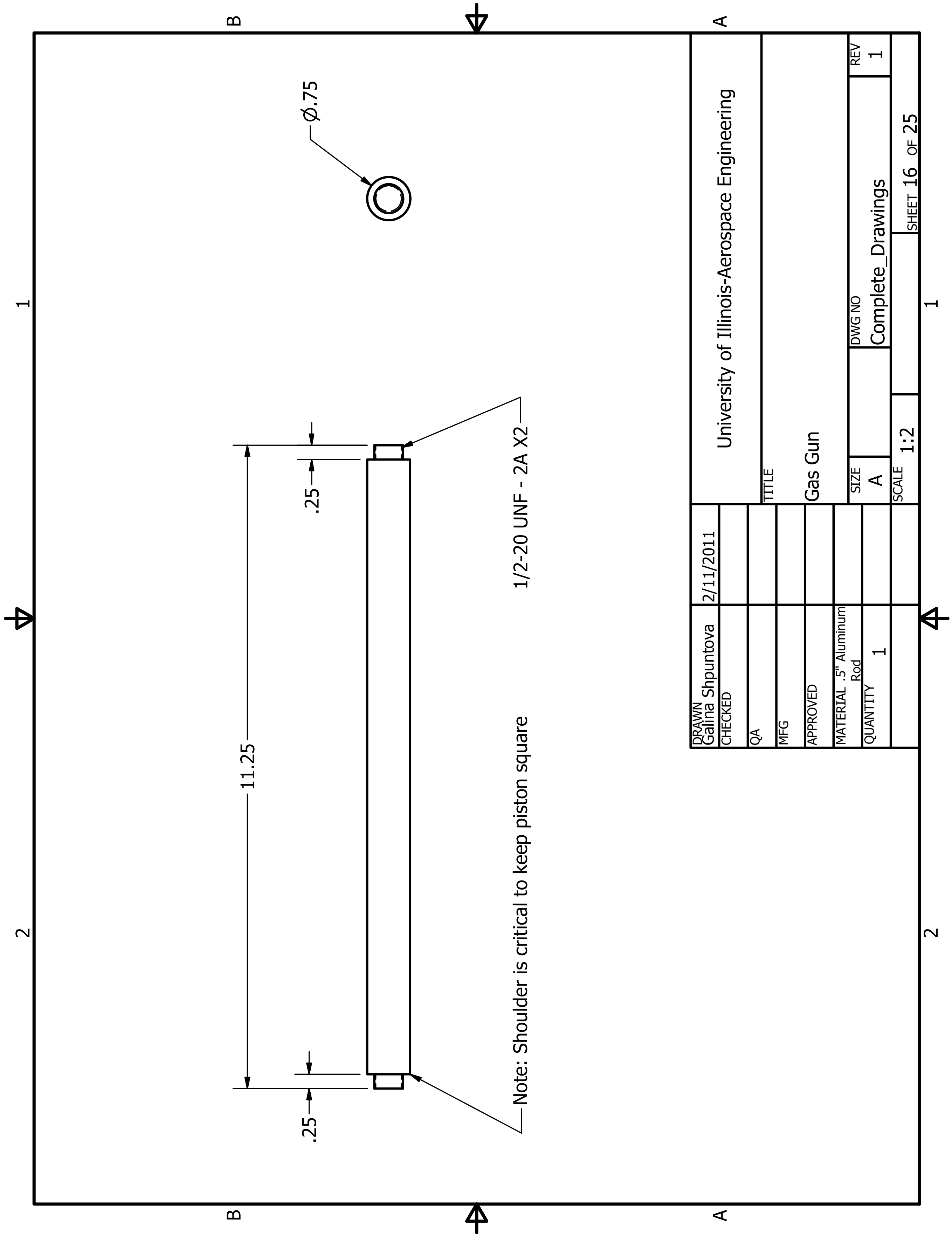

University of Illinois-Aerospace Engineering

DRAWN Galina Shpuntova 2/11/2011
CHECKED
QA
MFG
APPROVED
MATERIAL .5" Aluminum Rod
QUANTITY 1

TITLE Gas Gun

SIZE A
DWG NO Complete_Drawings
REV 1
SCALE 1:2
SHEET 16 OF 25

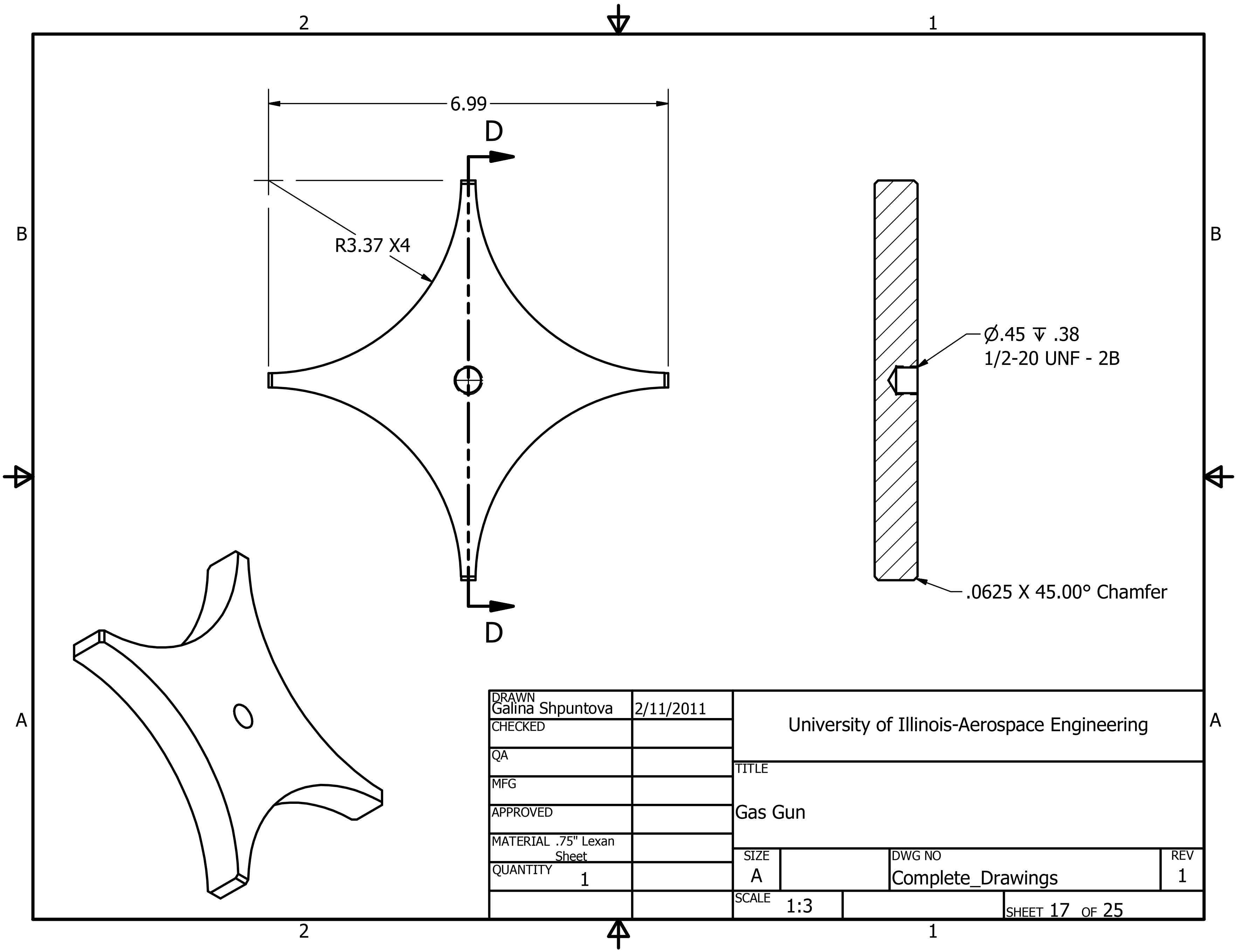

DRAWN Galina Shpuntova	2/11/2011	University of Illinois-Aerospace Engineering	
CHECKED			
QA		TITLE	
MFG			
APPROVED		Gas Gun	
MATERIAL .75" Lexan Sheet		SIZE A	DWG NO Complete_Drawings	REV 1
QUANTITY 1			
		SCALE 1:3	SHEET 17 OF 25

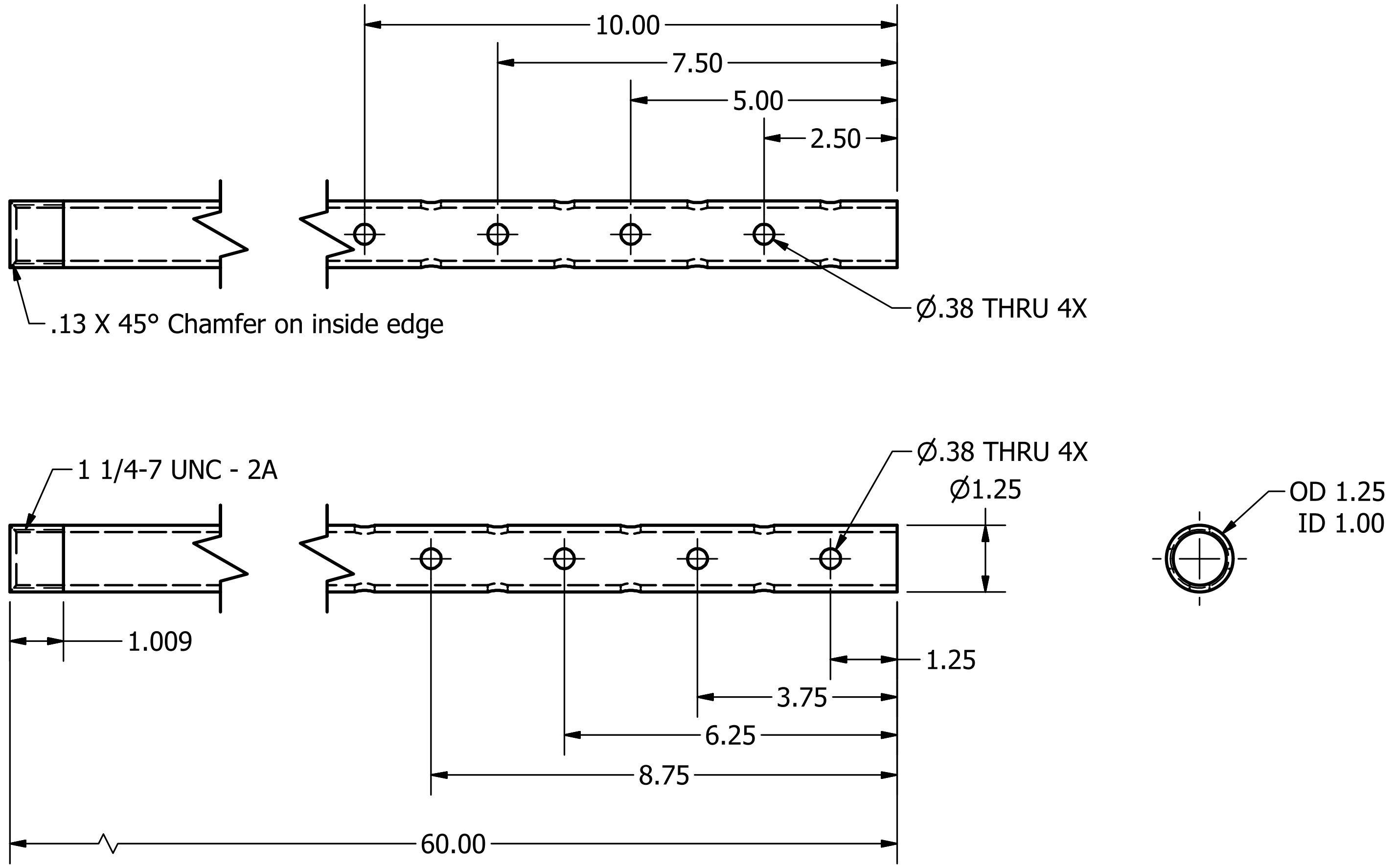

DRAWN Galina Shpuntova	2/11/2011	University of Illinois-Aerospace Engineering
CHECKED		
QA		TITLE
MFG		
APPROVED		Gas Gun
MATERIAL Honed Steel Tubing 1x1.25	Will be provided	
QUANTITY 1		SIZE A · DWG NO Complete_Drawings · REV 1
		SCALE 1:3 · SHEET 18 OF 25

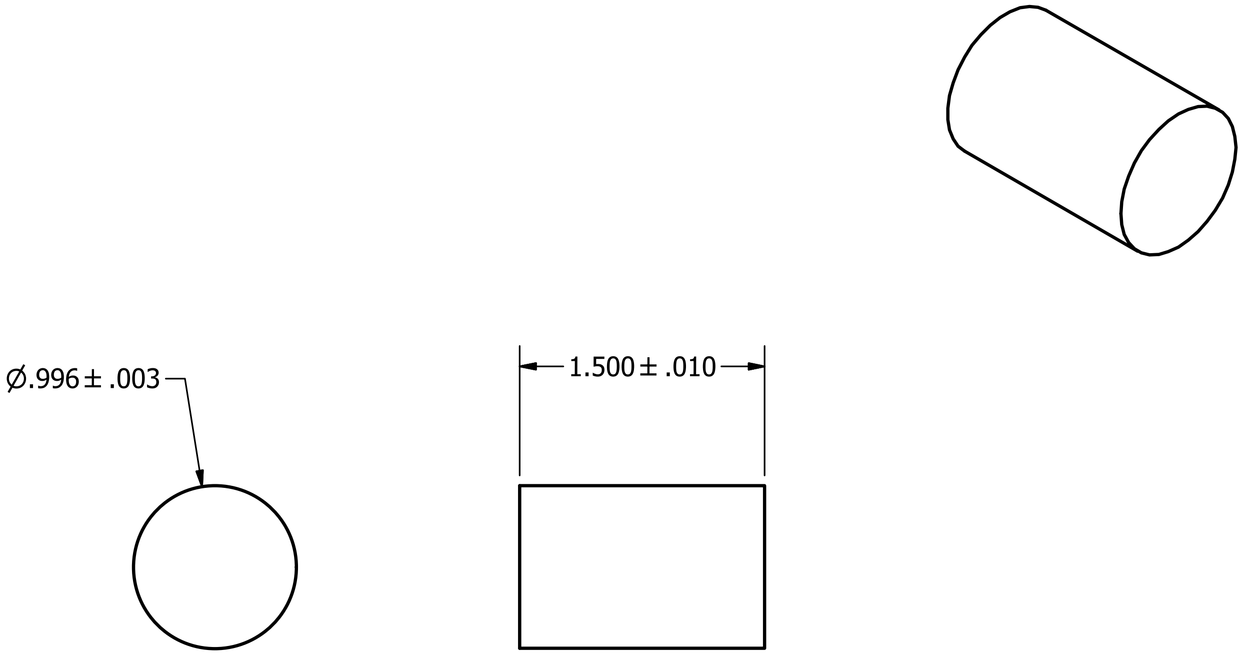

Note: Slug should fit snugly but still slide easily in the barrel (Sht 18). Loose slug will waste energy through gas leakage; tight slug will lose energy to friction.

DRAWN Galina Shpuntova	2/11/2011	University of Illinois-Aerospace Engineering
CHECKED		TITLE Gas Gun
QA		
MFG		
APPROVED		
MATERIAL Maraging Stl e.g. 18Ni300		SIZE A · DWG NO Complete_Drawings · REV 1
QUANTITY 1		
		SCALE · SHEET 19 OF 25

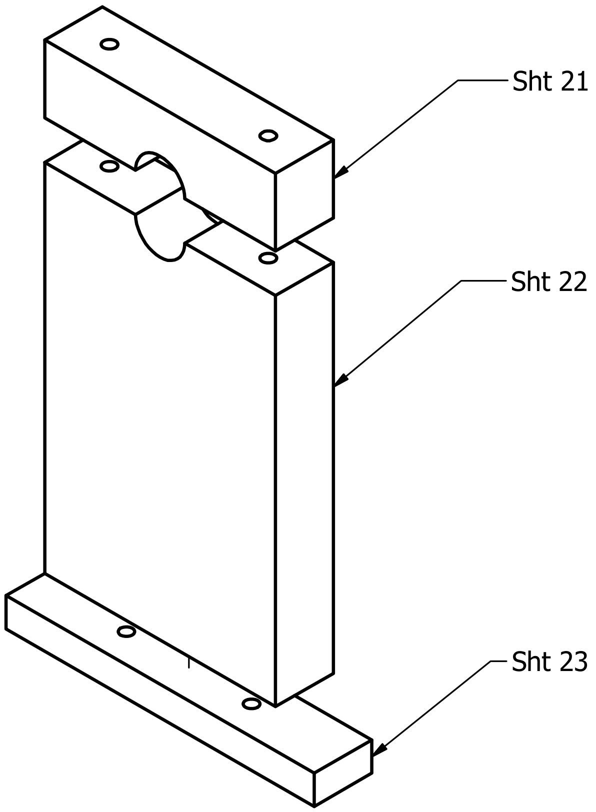

TOLERANCES	
Format	Tol
.X	.125
.XX	.0625
.XXX	.03125

DRAWN Galina Shpuntova	2/11/2011	University of Illinois-Aerospace Engineering
CHECKED		
QA		TITLE Gas Gun
MFG		
APPROVED		
MATERIAL Aluminum		
QUANTITY 2		SIZE A
		SCALE 1:3

DWG NO Complete_Drawings

REV 1

SHEET 20 OF 25

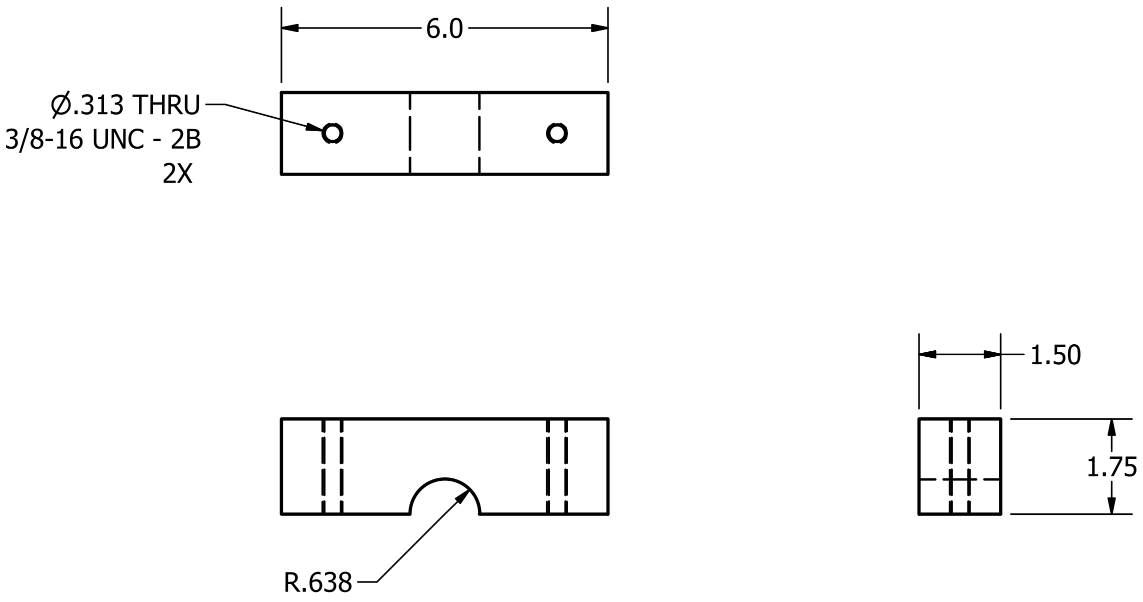

Note: The R= .638 hole is made to
comfortably fit the existing barrel stock.

DRAWN Galina Shpuntova	2/11/2011	University of Illinois-Aerospace Engineering
CHECKED		
QA		TITLE
MFG		Gas Gun
APPROVED		
MATERIAL Aluminum		SIZE A · DWG NO Complete_Drawings · REV 1
QUANTITY 1		
		SCALE 1:3 · SHEET 21 OF 25

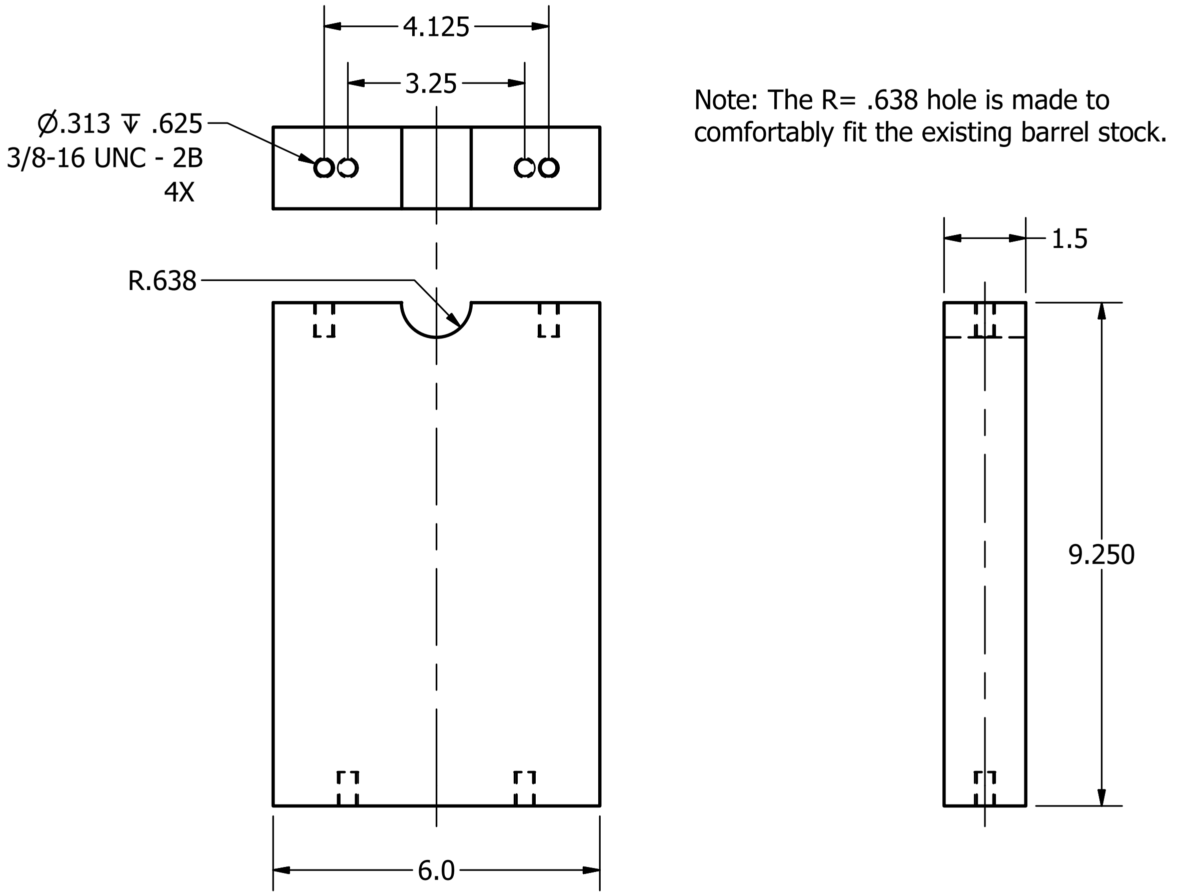

Note: The R= .638 hole is made to
comfortably fit the existing barrel stock.

DRAWN Galina Shpuntova	2/11/2011	University of Illinois-Aerospace Engineering			
CHECKED					
QA		TITLE			
MFG					
APPROVED		Gas Gun			
MATERIAL Aluminum					
QUANTITY 1		SIZE A		DWG NO Complete_Drawings	REV 1
		SCALE 1:3		SHEET 22 OF 25	

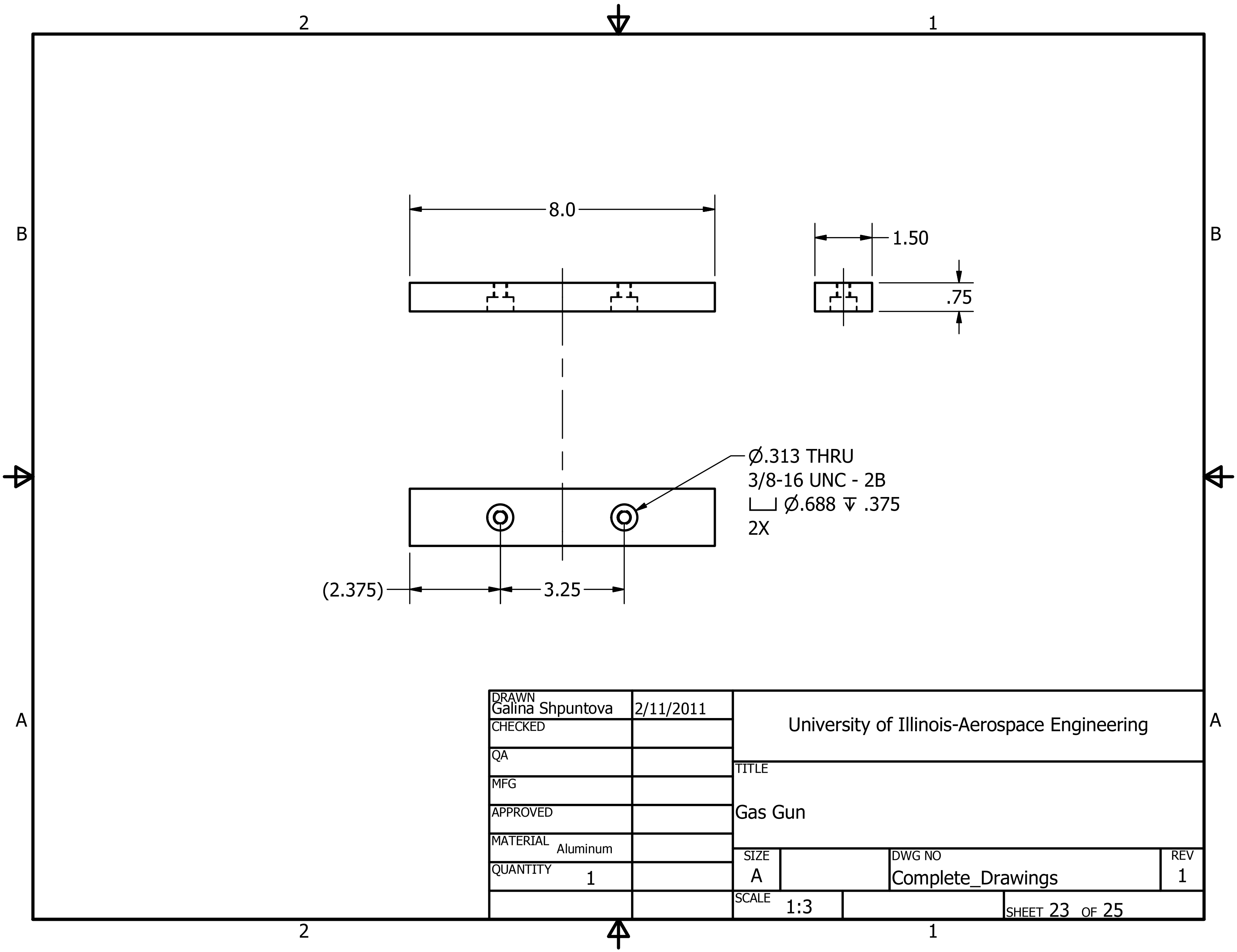

DRAWN Galina Shpuntova	2/11/2011	University of Illinois-Aerospace Engineering	
CHECKED		TITLE Gas Gun	
QA			
MFG			
APPROVED			
MATERIAL Aluminum		SIZE A	DWG NO Complete_Drawings REV 1
QUANTITY 1		SCALE 1:3	SHEET 23 OF 25

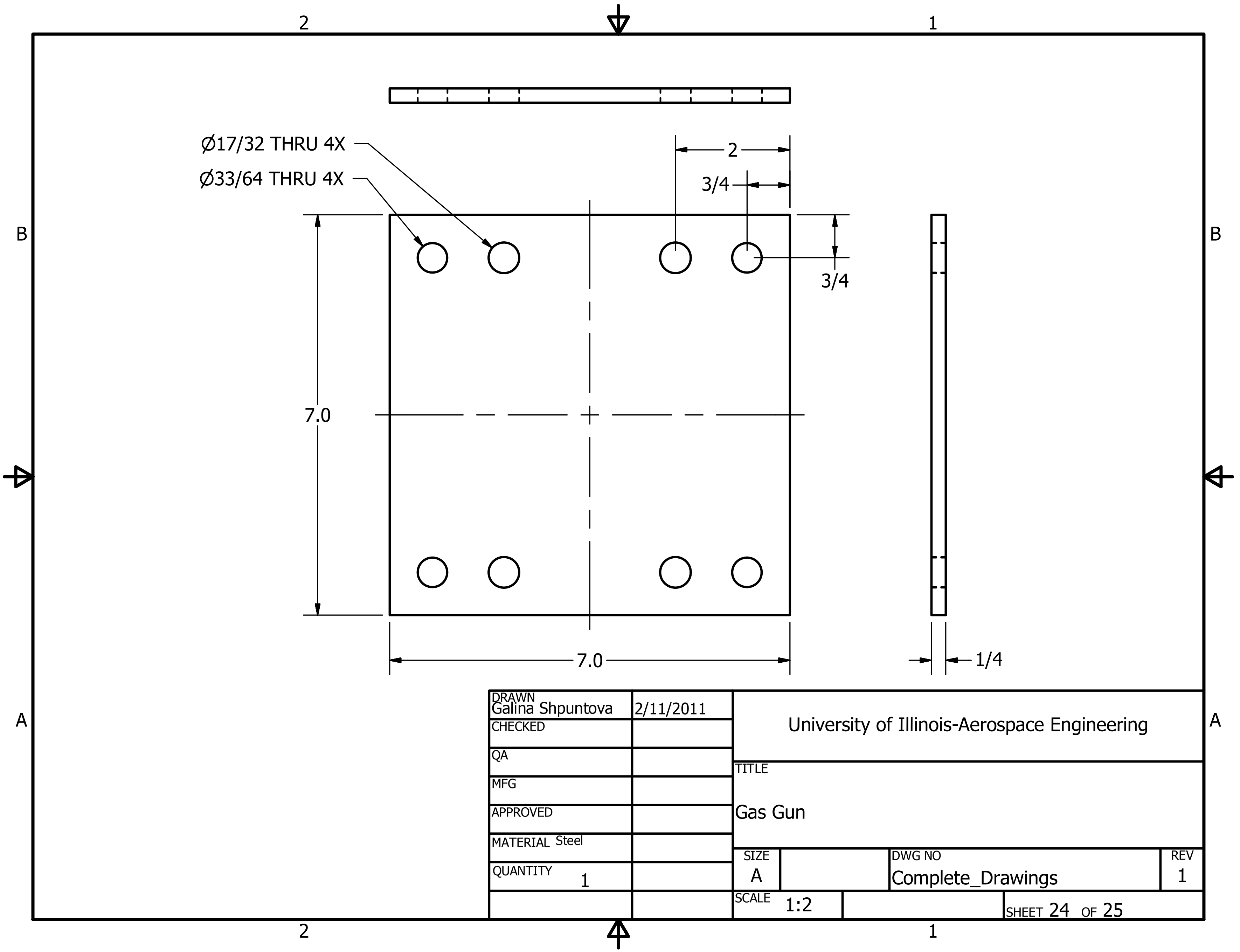

DRAWN Galina Shpuntova	2/11/2011	University of Illinois-Aerospace Engineering	
CHECKED			
QA		TITLE	
MFG		Gas Gun	
APPROVED			
MATERIAL Steel		SIZE A	DWG NO Complete_Drawings
QUANTITY 1		REV 1	
		SCALE 1:2	SHEET 24 OF 25

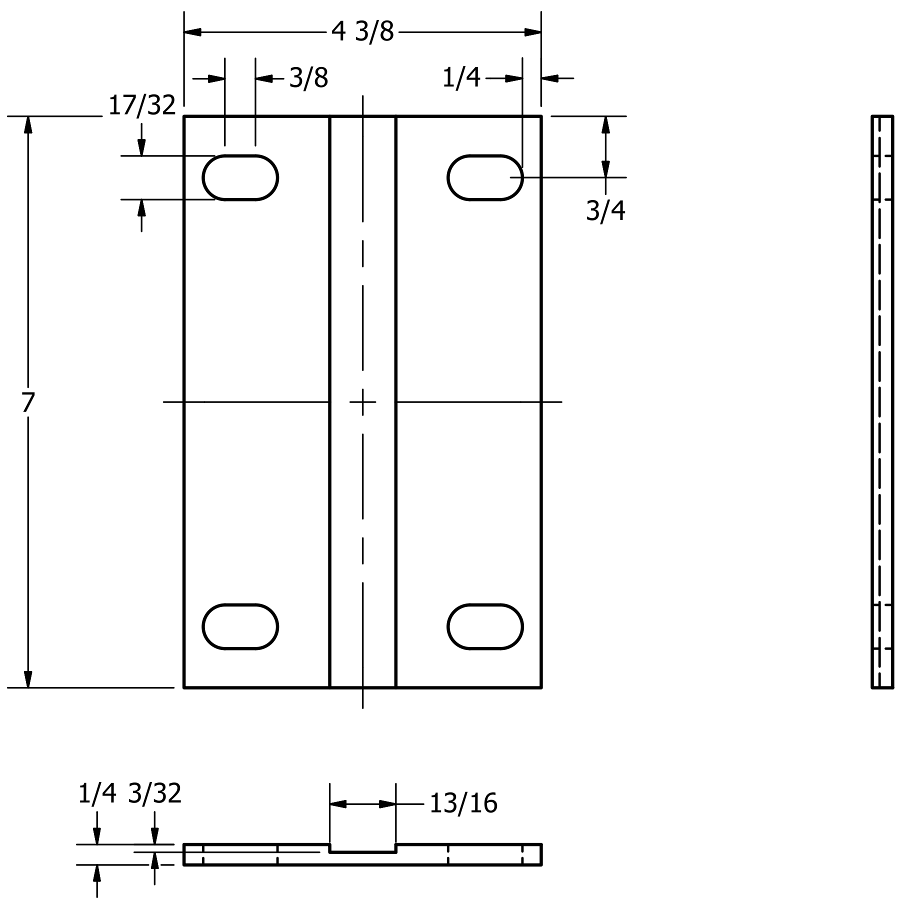

DRAWN Galina Shpuntova	2/11/2011	University of Illinois-Aerospace Engineering
CHECKED		TITLE Gas Gun
QA		
MFG		
APPROVED		
MATERIAL Steel		SIZE A · DWG NO Complete_Drawings · REV 1
QUANTITY 1		SCALE 1:2 · SHEET 25 OF 25

APPENDIX B

COMPLETE SHADOWGRAPH IMAGES

B.1 No Boundary

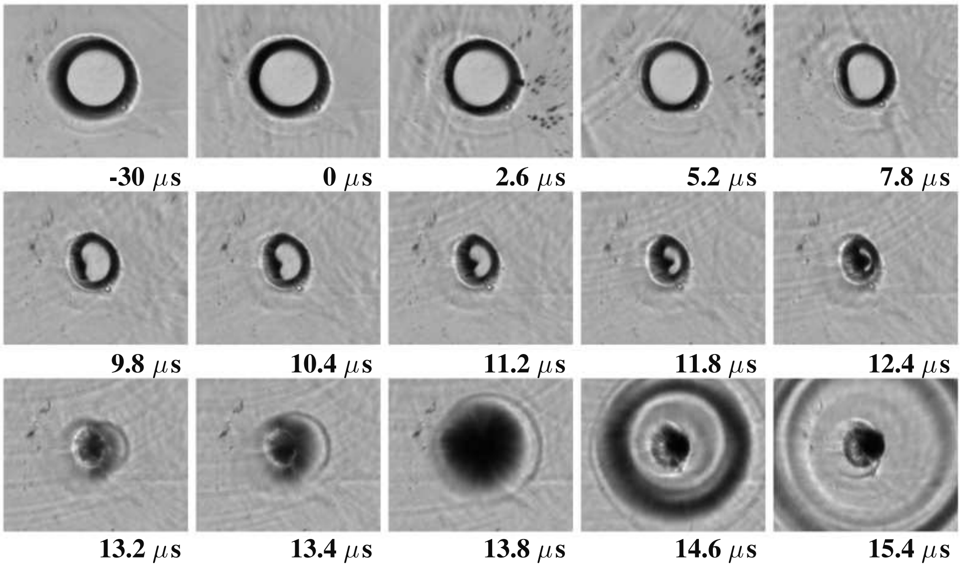

Figure B.1: Test #560.

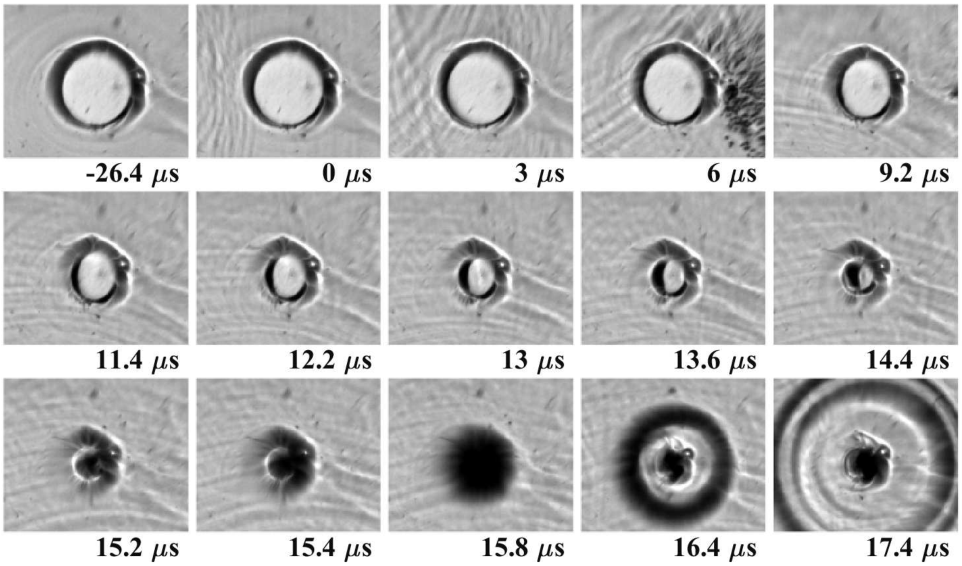

Figure B.2: Test #561.

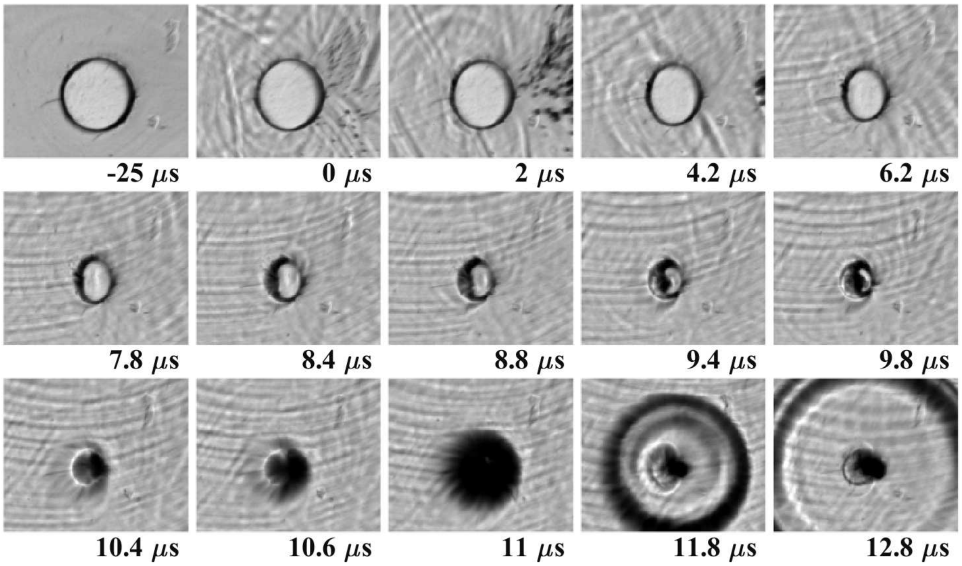

Figure B.3: Test #562.

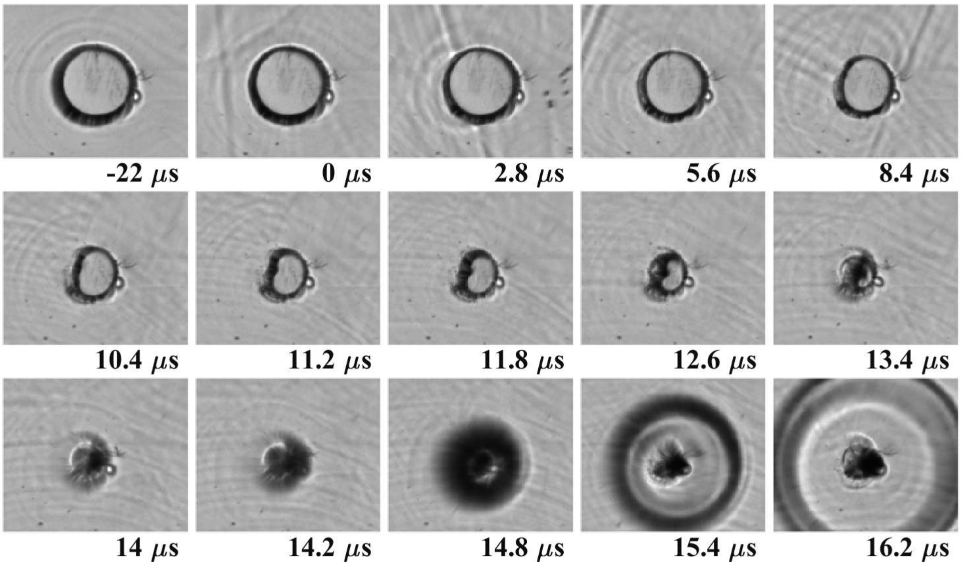

Figure B.4: Test #563.

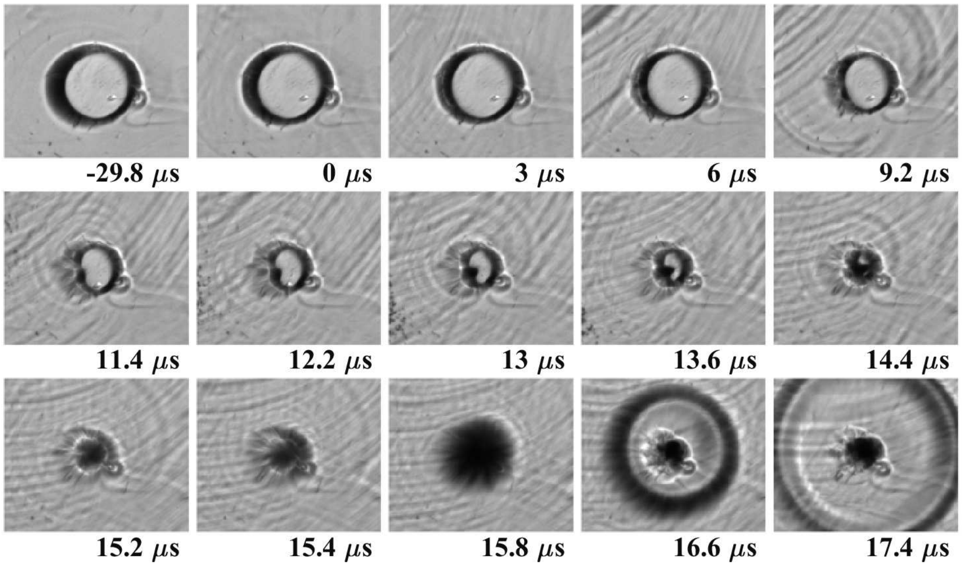

Figure B.5: Test #564.

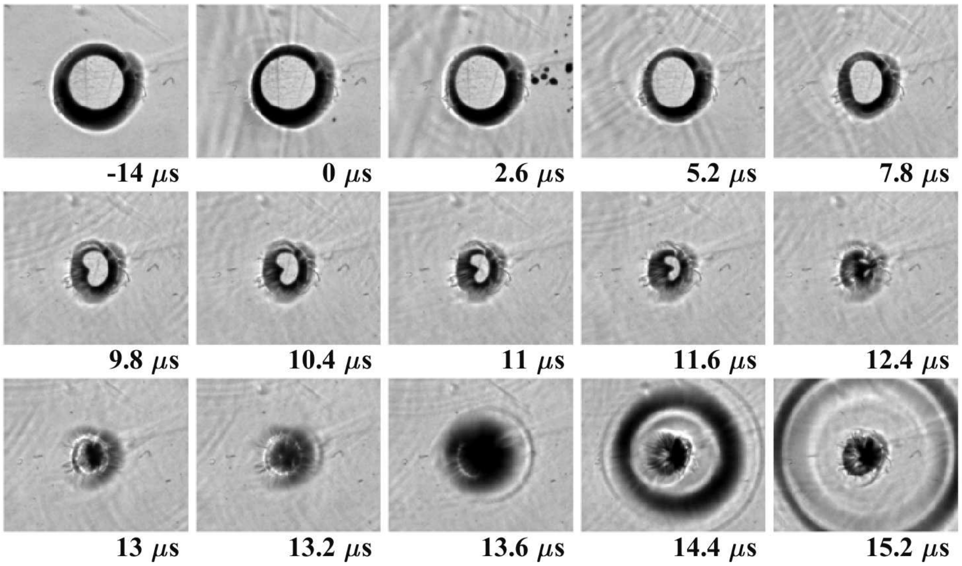

Figure B.6: Test #626.

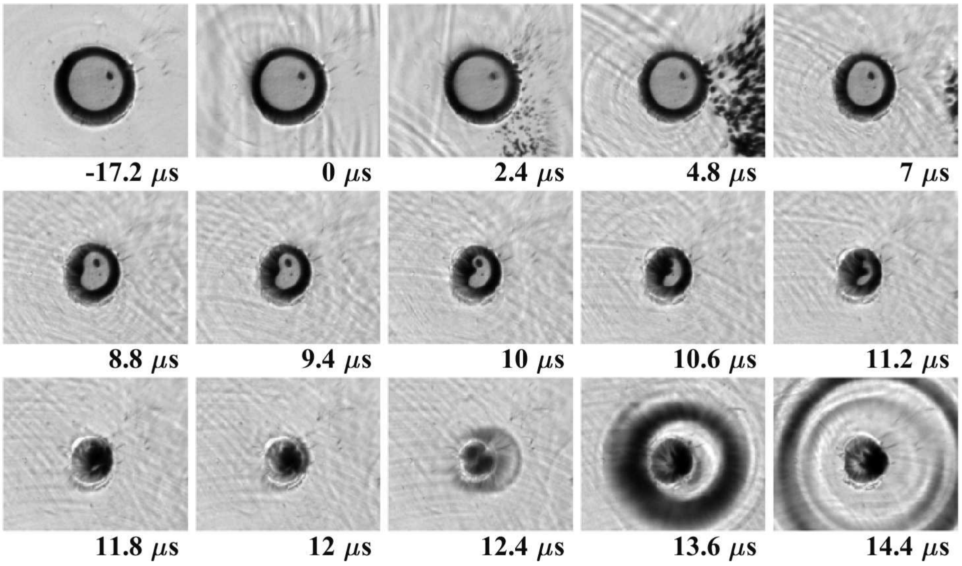

Figure B.7: Test #627.

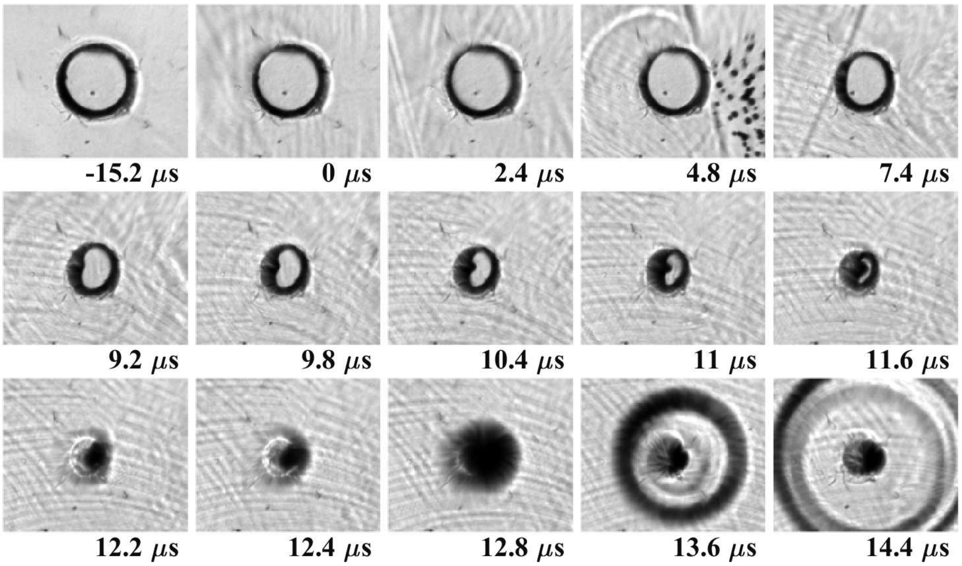

Figure B.8: Test #629.

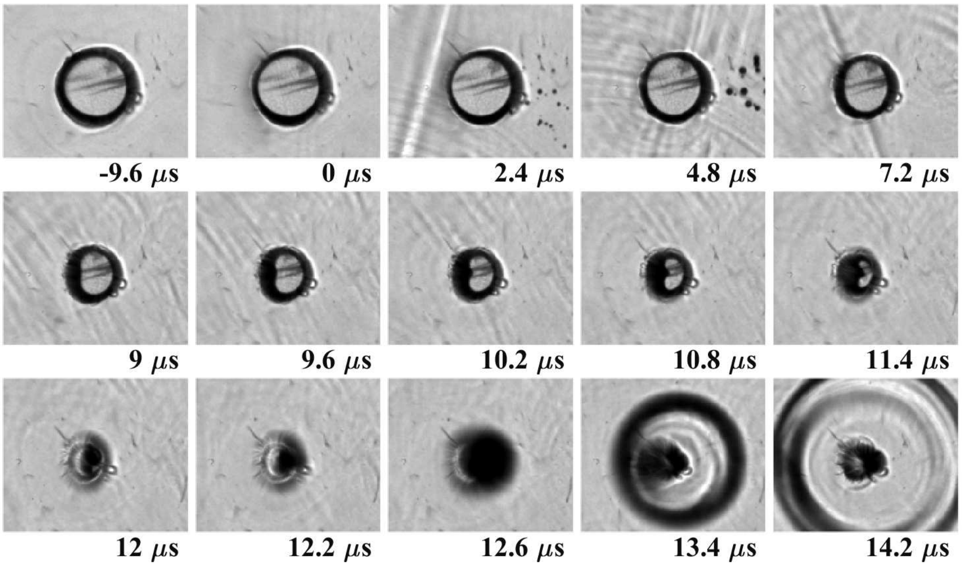

Figure B.9: Test #630.

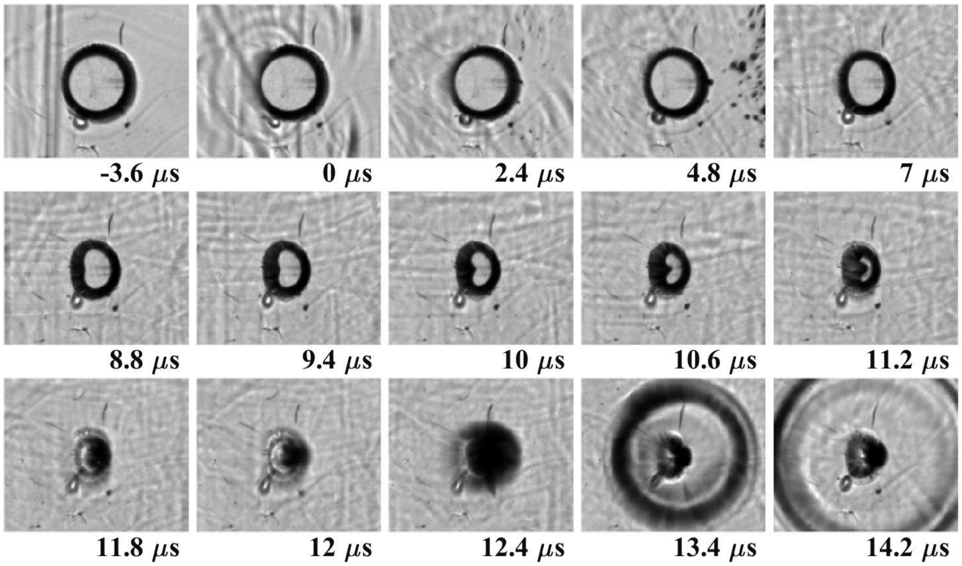

Figure B.10: Test #631.

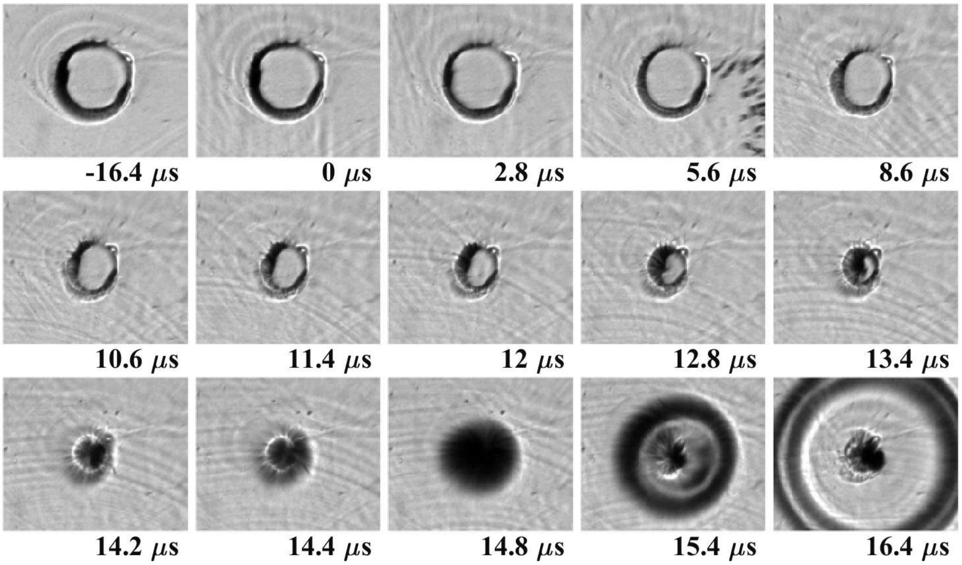

Figure B.11: Test #664.

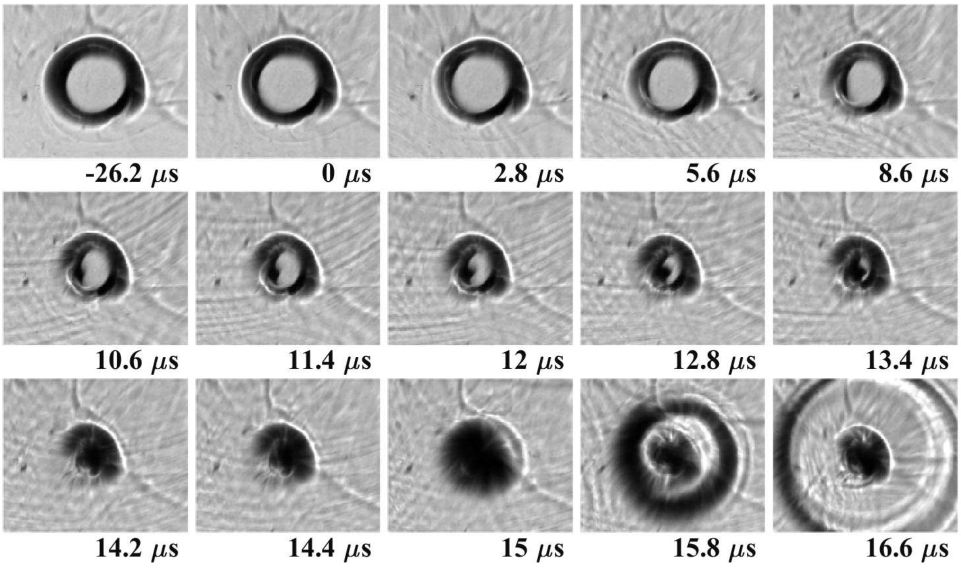

-26.2 μs
0 μs
2.8 μs
5.6 μs
8.6 μs
10.6 μs
11.4 μs
12 μs
12.8 μs
13.4 μs
14.2 μs
14.4 μs
15 μs
15.8 μs
16.6 μs

Figure B.12: Test #665.

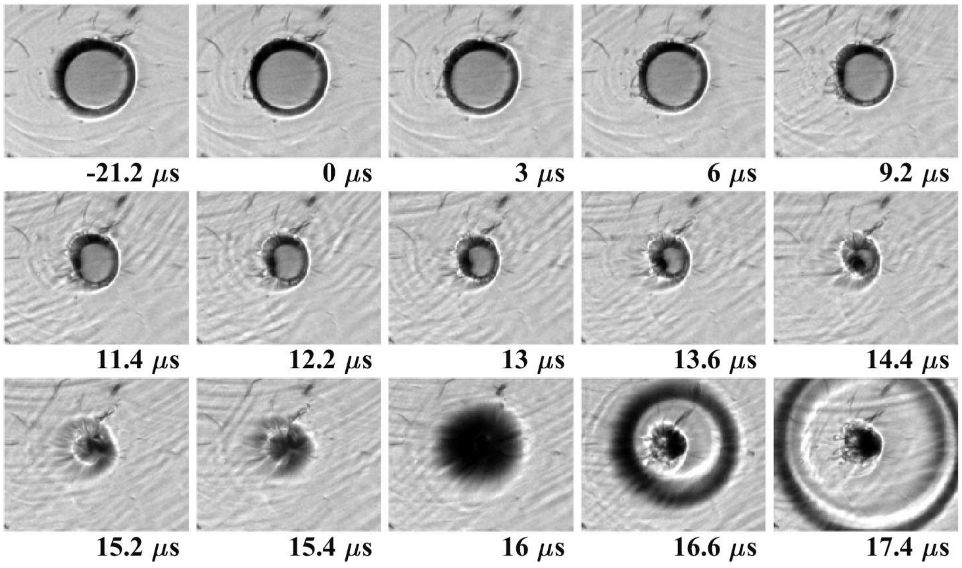

-21.2 μs
0 μs
3 μs
6 μs
9.2 μs
11.4 μs
12.2 μs
13 μs
13.6 μs
14.4 μs
15.2 μs
15.4 μs
16 μs
16.6 μs
17.4 μs

Figure B.13: Test #666.

B.2 Downstream Boundary

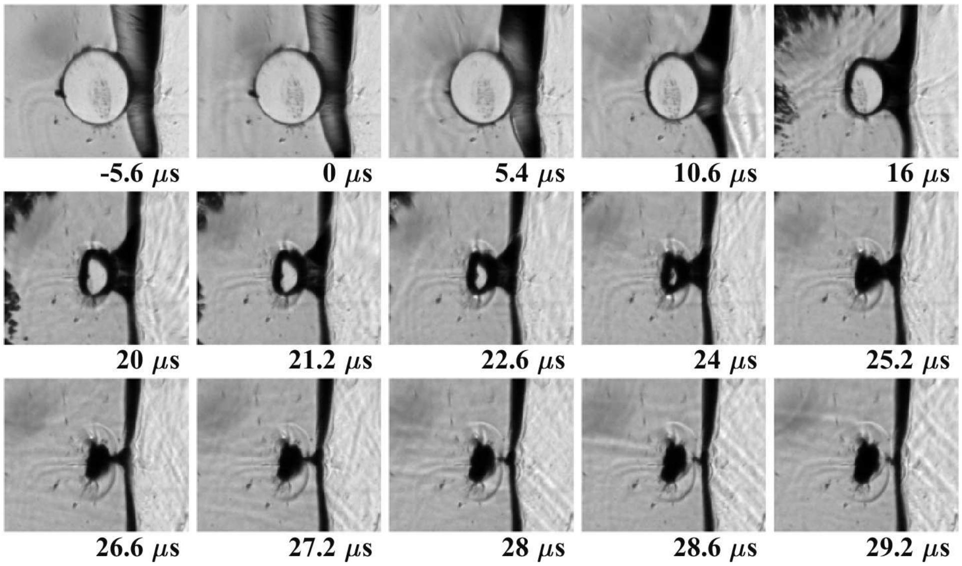

Figure B.14: Test #594. 1:20 PDMS.

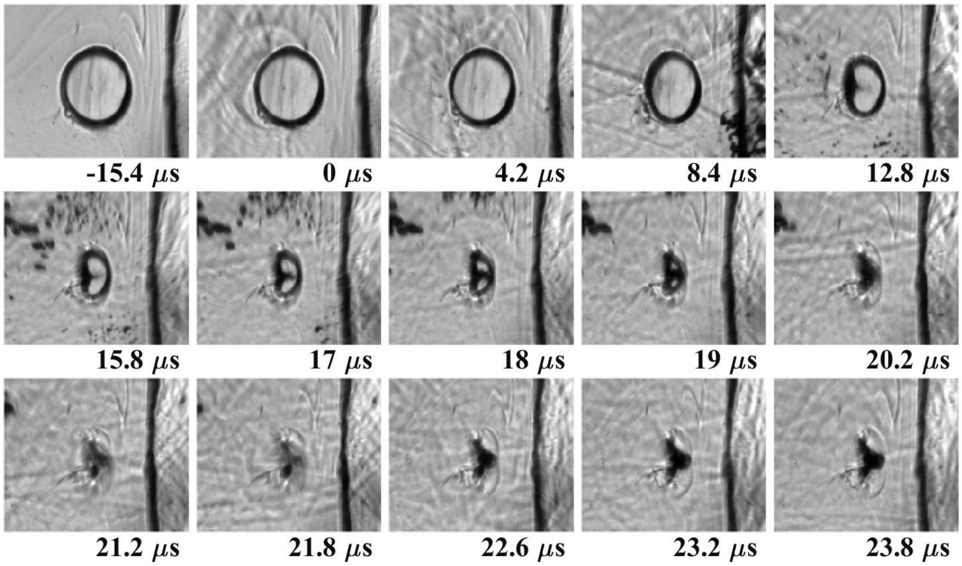

Figure B.15: Test #601. 1:20 PDMS.

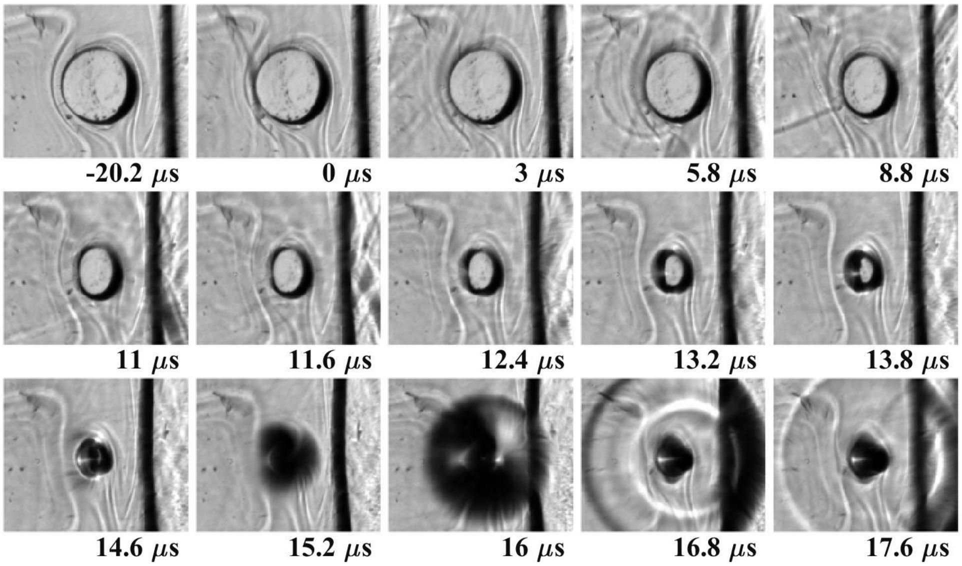

Figure B.16: Test #639. 1:20 PDMS.

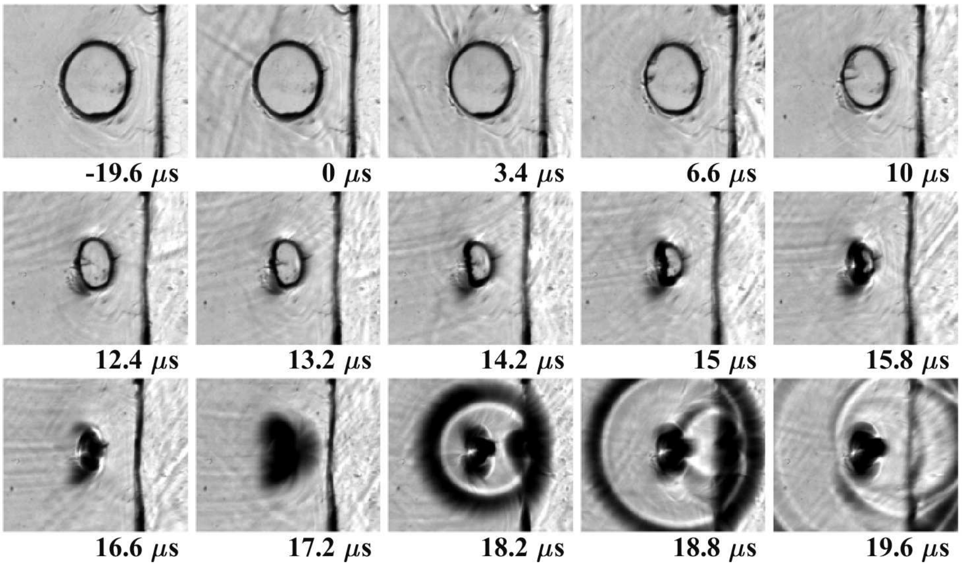

Figure B.17: Test #640. 1:20 PDMS.

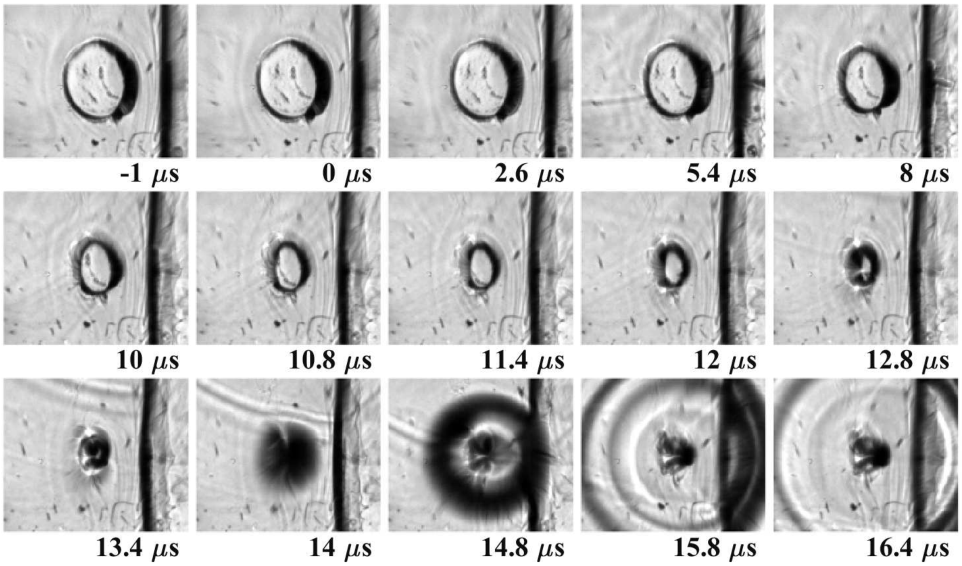

Figure B.18: Test #645. 1:20 PDMS.

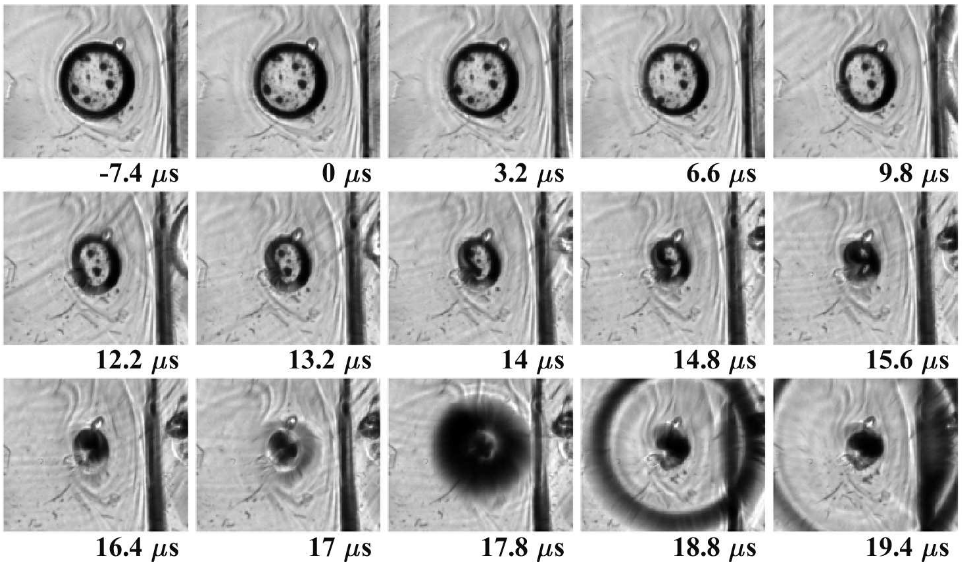

Figure B.19: Test #646. 1:20 PDMS.

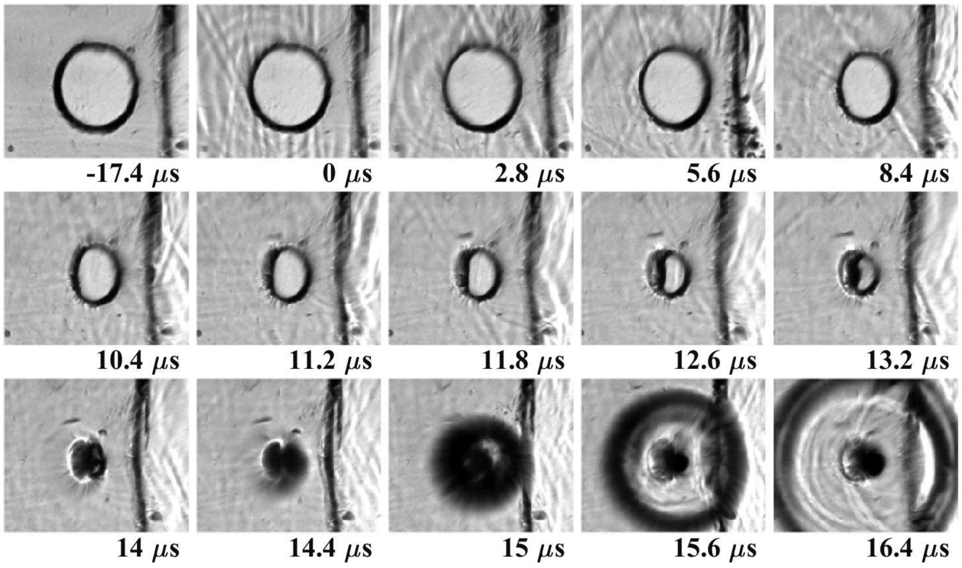

Figure B.20: Test #670. 1:20 PDMS.

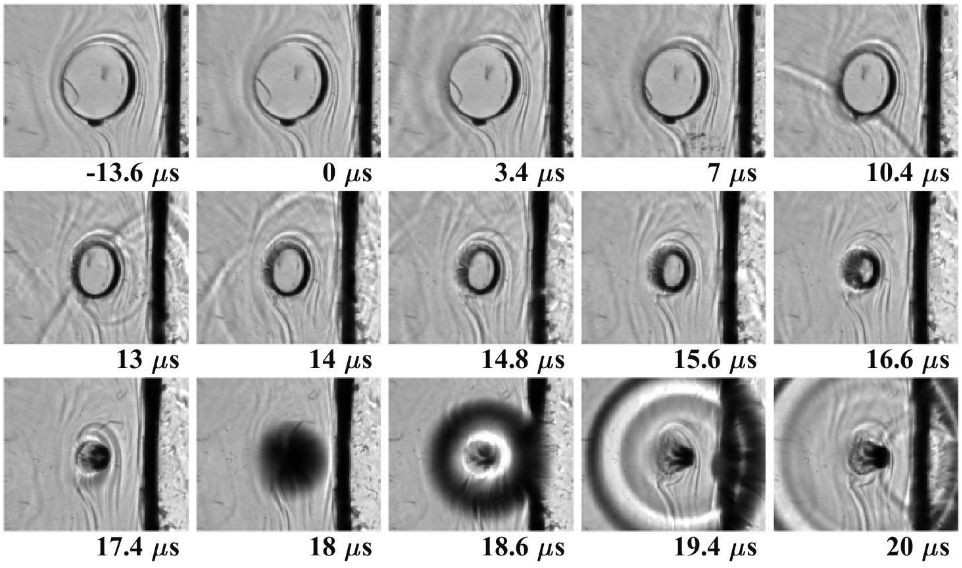

Figure B.21: Test #638. 1:30 PDMS.

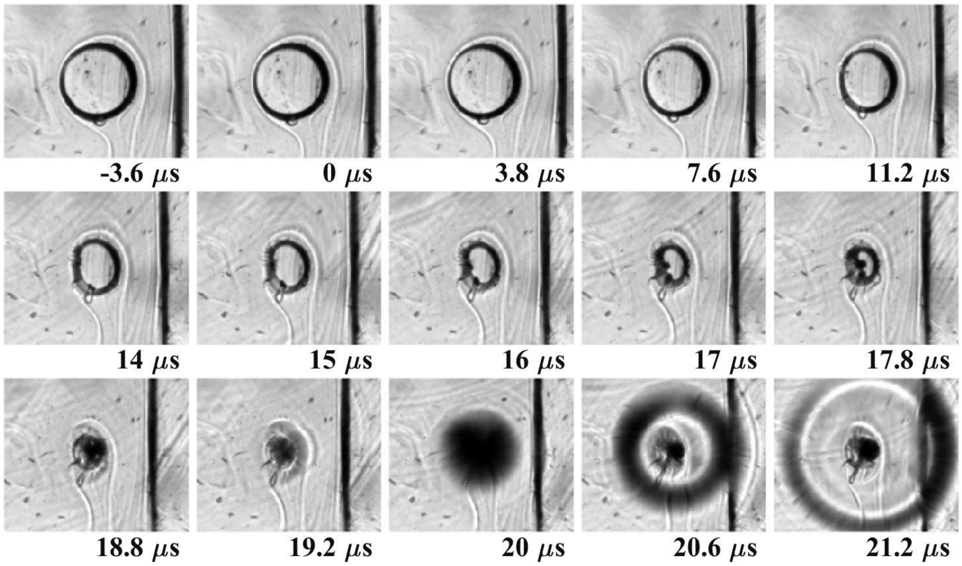

Figure B.22: Test #647. 1:30 PDMS.

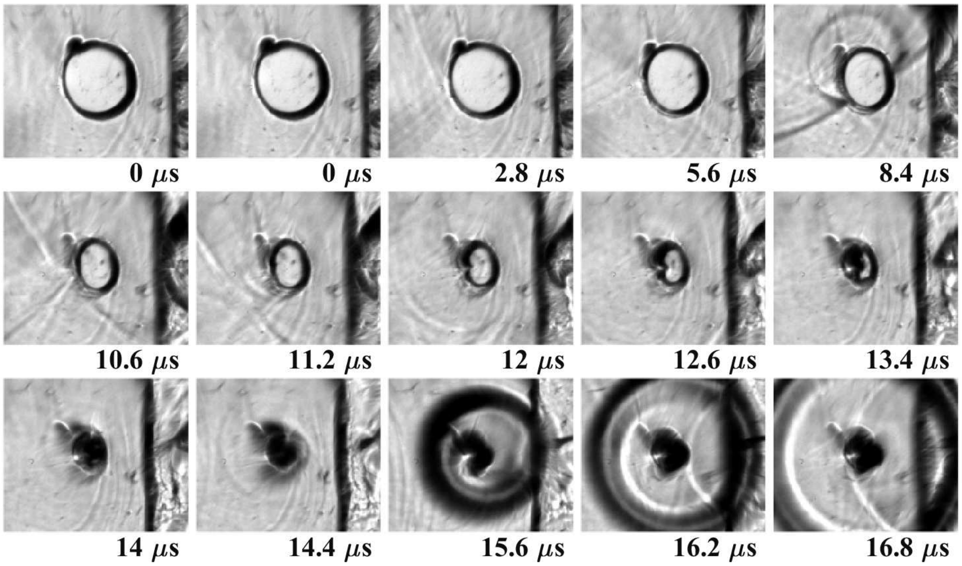

Figure B.23: Test #648. 1:30 PDMS.

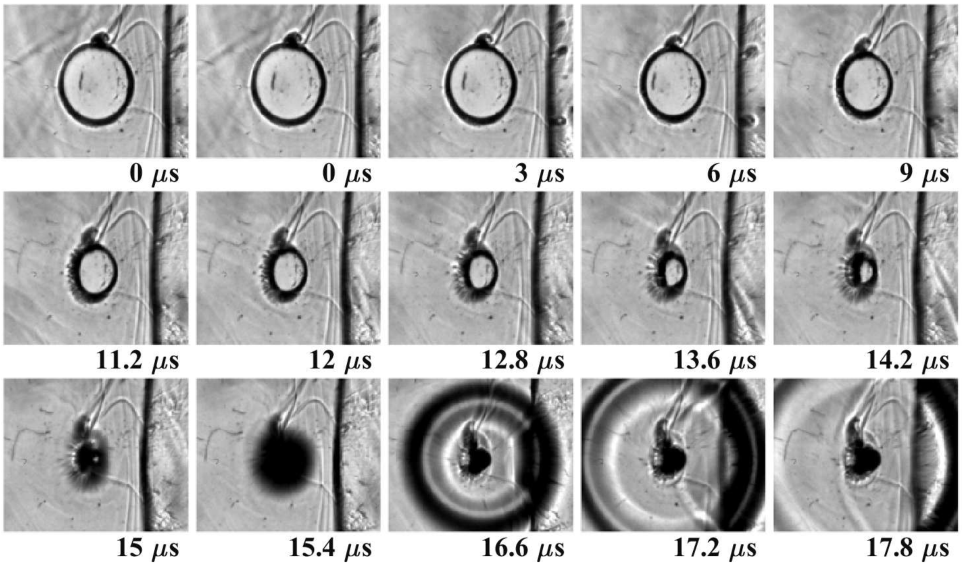

Figure B.24: Test #649. 1:30 PDMS.

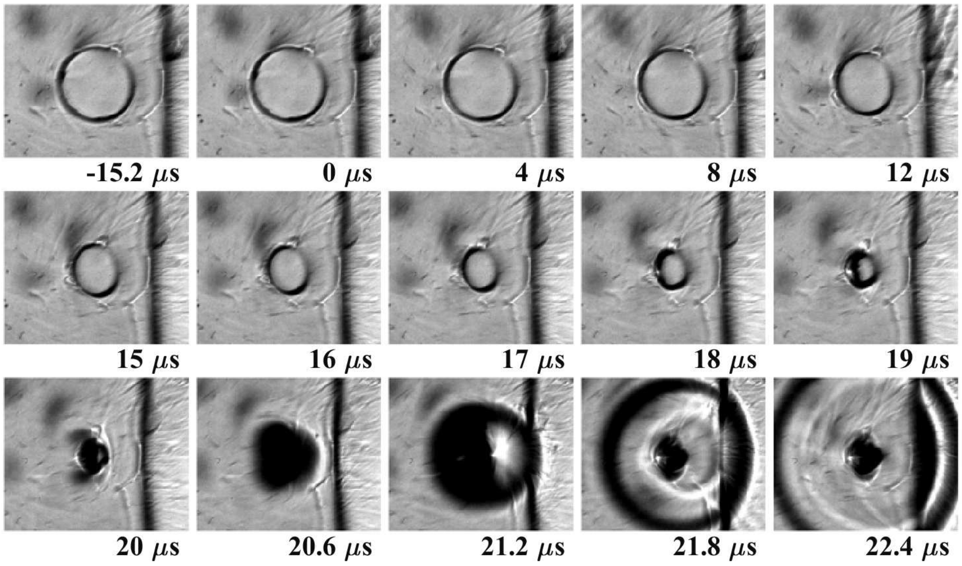

Figure B.25: Test #672. 1:30 PDMS.

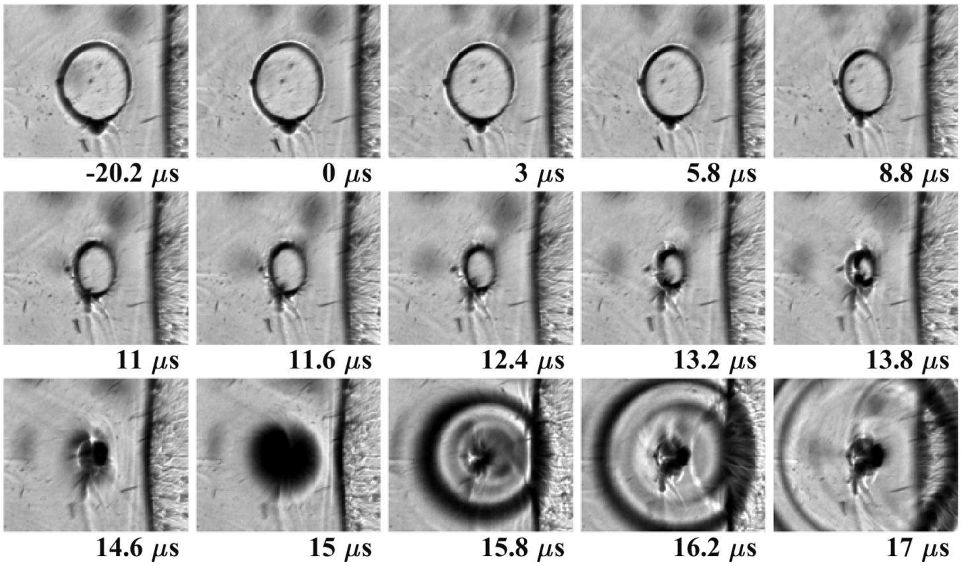

Figure B.26: Test #673. 1:30 PDMS.

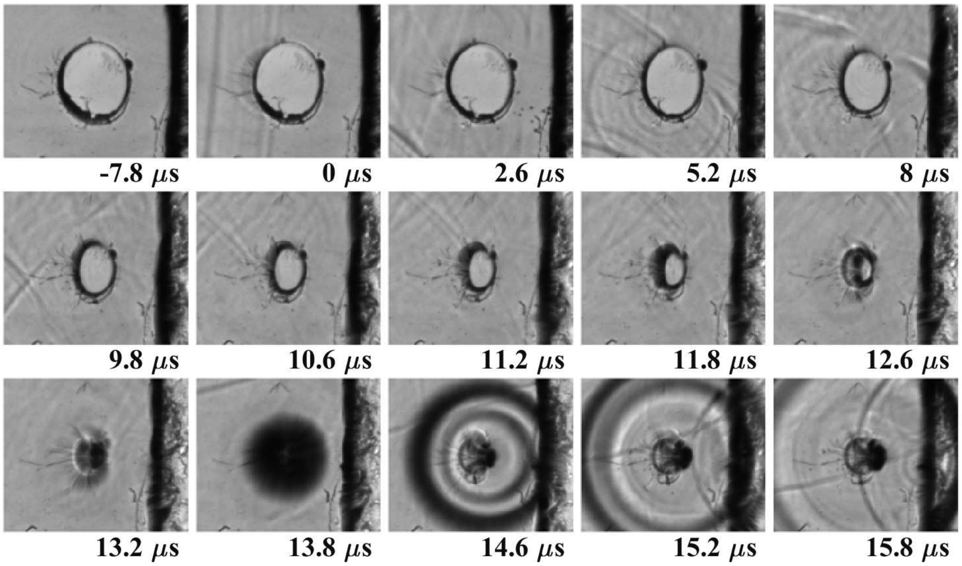

Figure B.27: Test #589. 1:40 PDMS.

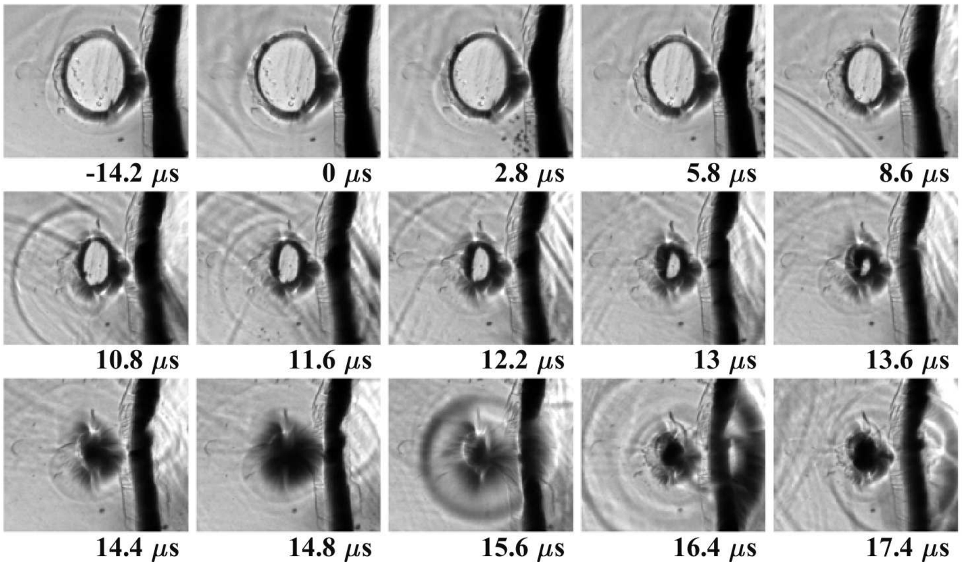

Figure B.28: Test #596. 1:40 PDMS.

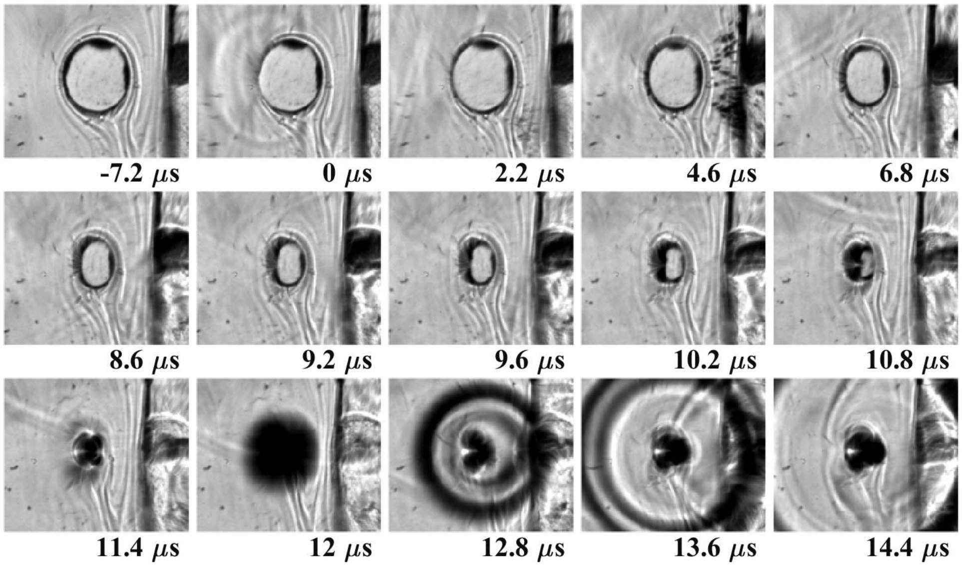

Figure B.29: Test #650. 1:40 PDMS.

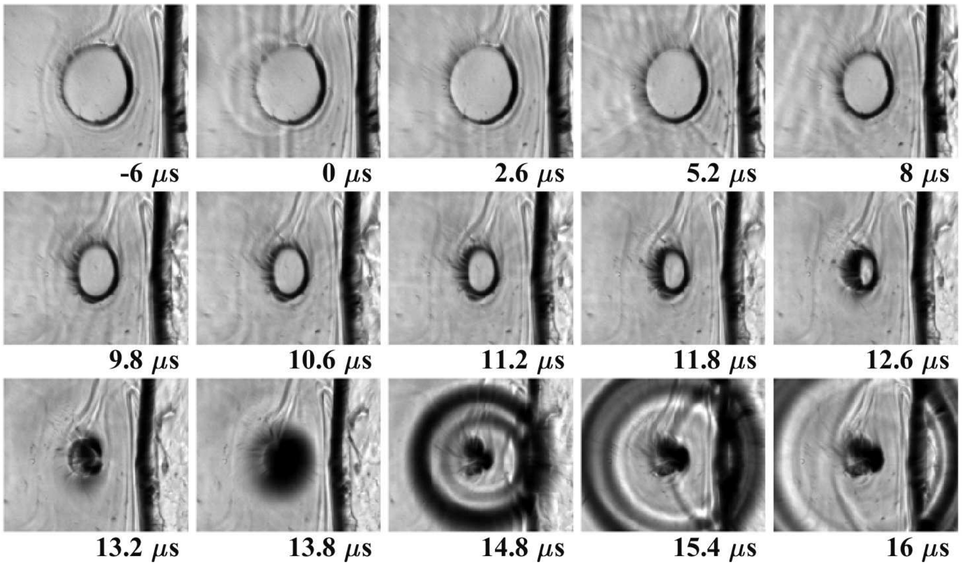

Figure B.30: Test #651. 1:40 PDMS.

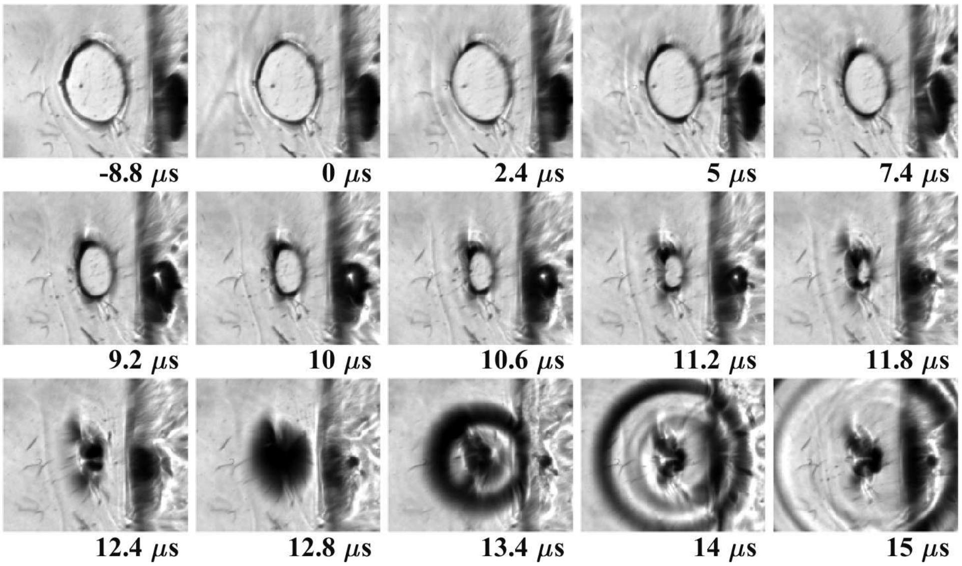

Figure B.31: Test #652. 1:40 PDMS.

B.3 Upstream Boundary

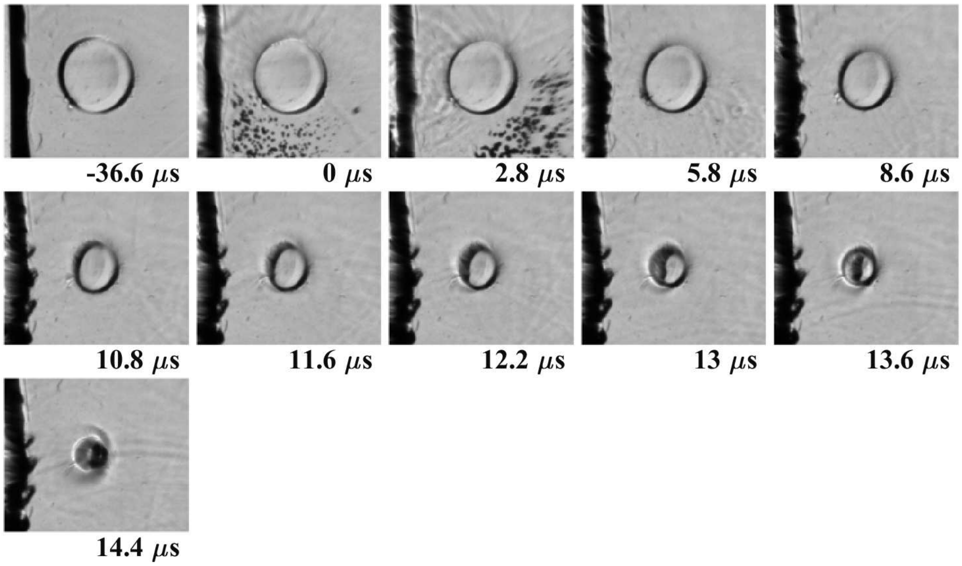

Figure B.32: Test #567. 1:20 PDMS.

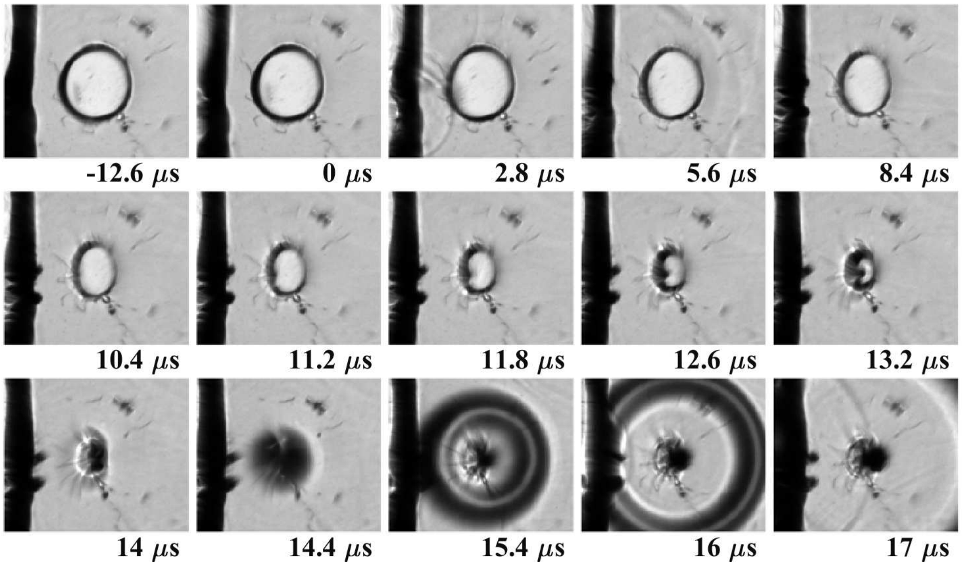

Figure B.33: Test #569. 1:20 PDMS.

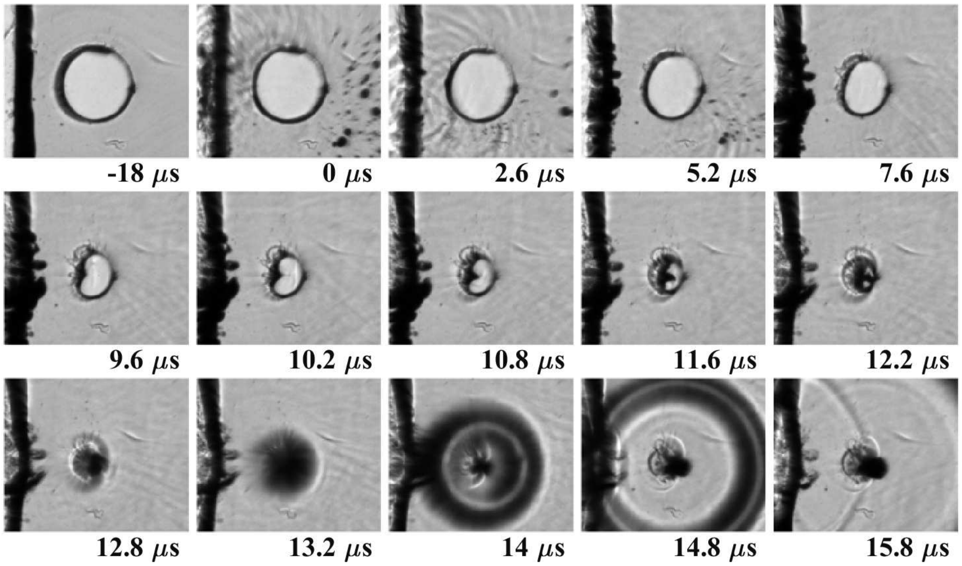

Figure B.34: Test #570. 1:20 PDMS.

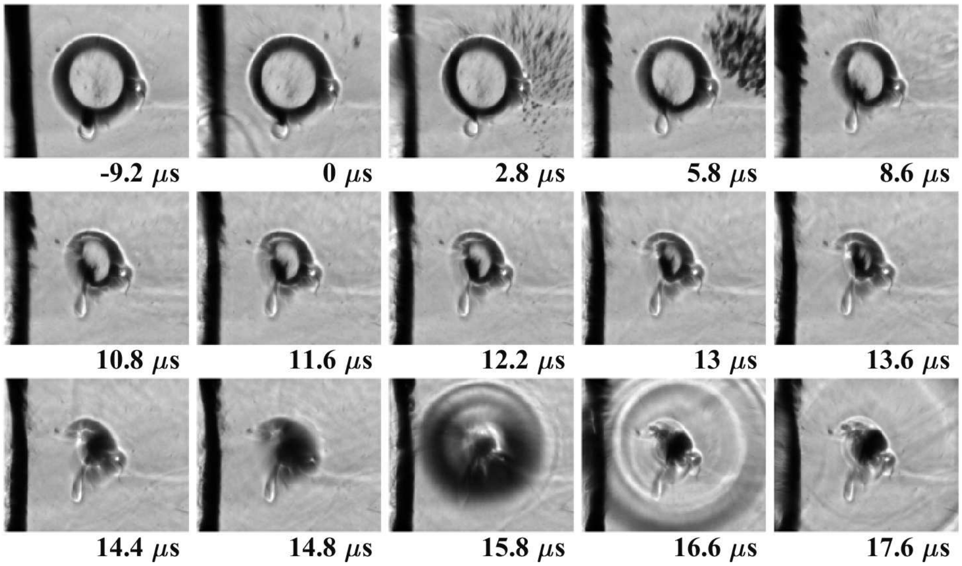

Figure B.35: Test #572. 1:20 PDMS.

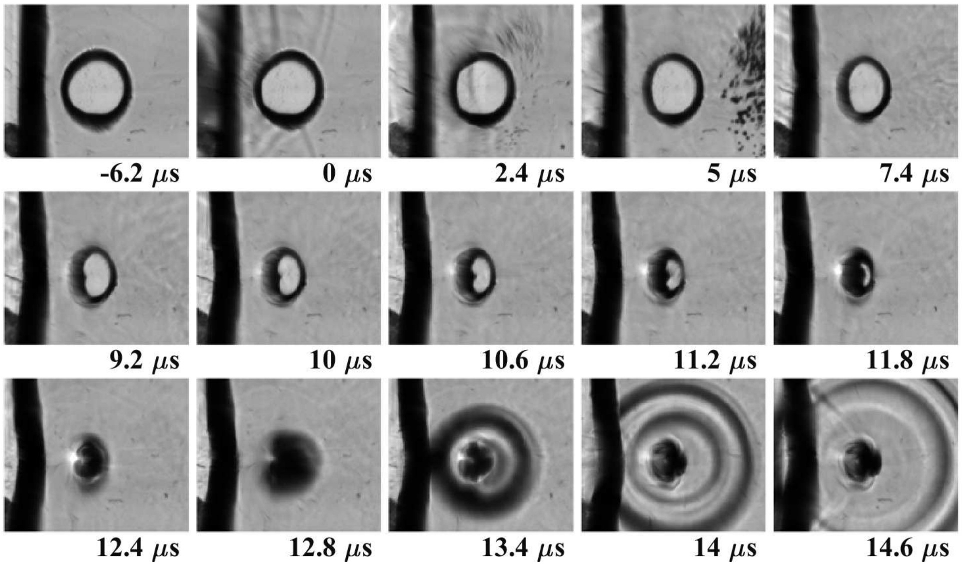

-6.2 μs 0 μs 2.4 μs 5 μs 7.4 μs

9.2 μs 10 μs 10.6 μs 11.2 μs 11.8 μs

12.4 μs 12.8 μs 13.4 μs 14 μs 14.6 μs

Figure B.36: Test #573. 1:20 PDMS.

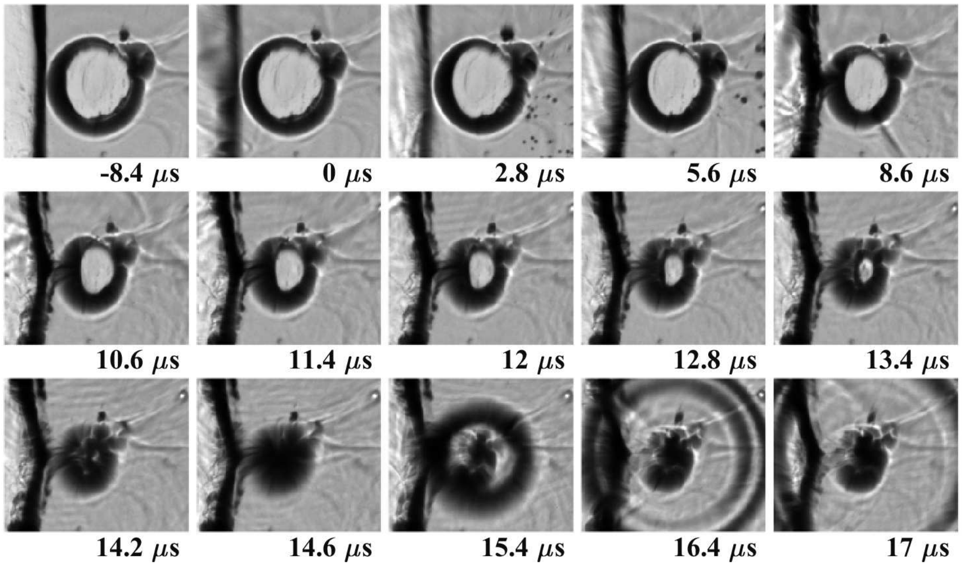

-8.4 μs 0 μs 2.8 μs 5.6 μs 8.6 μs

10.6 μs 11.4 μs 12 μs 12.8 μs 13.4 μs

14.2 μs 14.6 μs 15.4 μs 16.4 μs 17 μs

Figure B.37: Test #580. 1:30 PDMS.

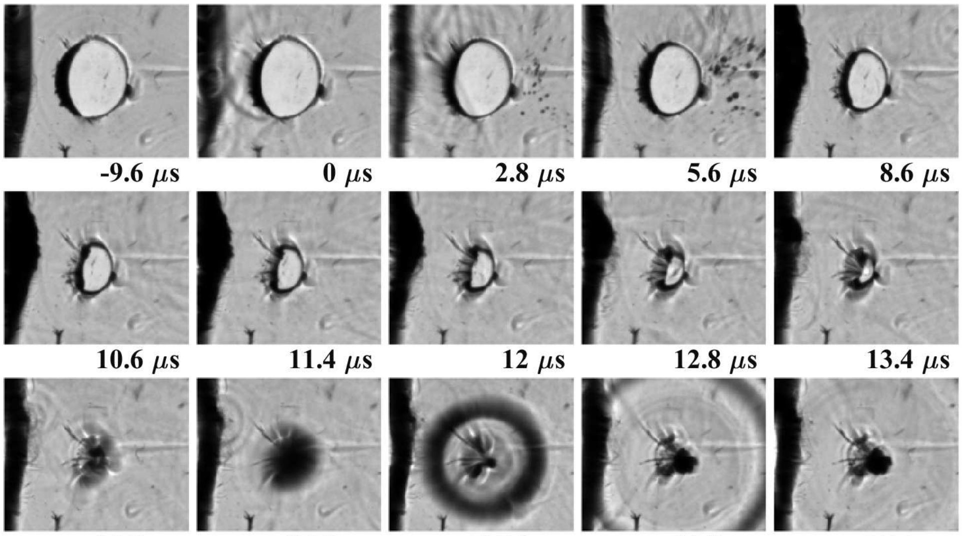

-9.6 μs 0 μs 2.8 μs 5.6 μs 8.6 μs

10.6 μs 11.4 μs 12 μs 12.8 μs 13.4 μs

14.2 μs 14.6 μs 15.4 μs 16.8 μs 17.4 μs

Figure B.38: Test #585. 1:30 PDMS.

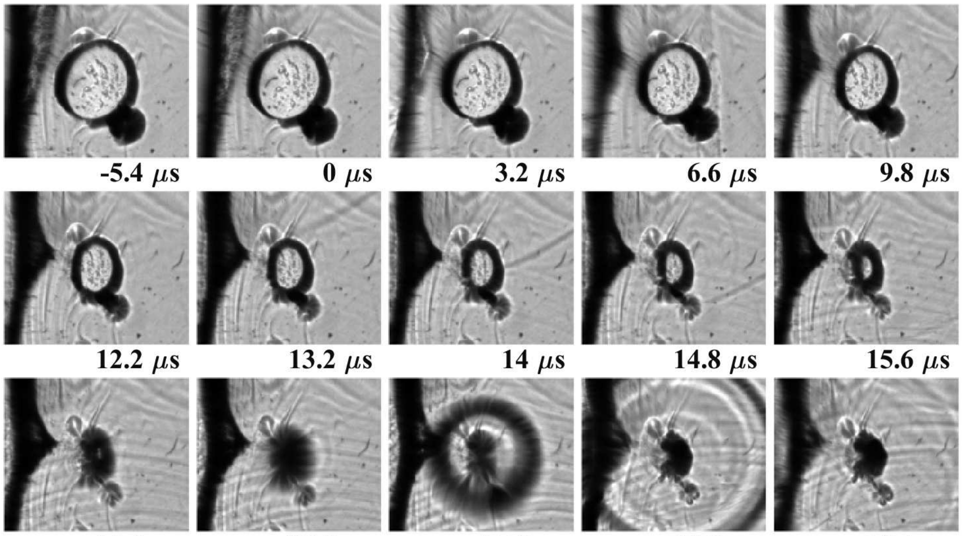

-5.4 μs 0 μs 3.2 μs 6.6 μs 9.8 μs

12.2 μs 13.2 μs 14 μs 14.8 μs 15.6 μs

16.4 μs 16.8 μs 17.6 μs 18.6 μs 19.4 μs

Figure B.39: Test #593. 1:30 PDMS.

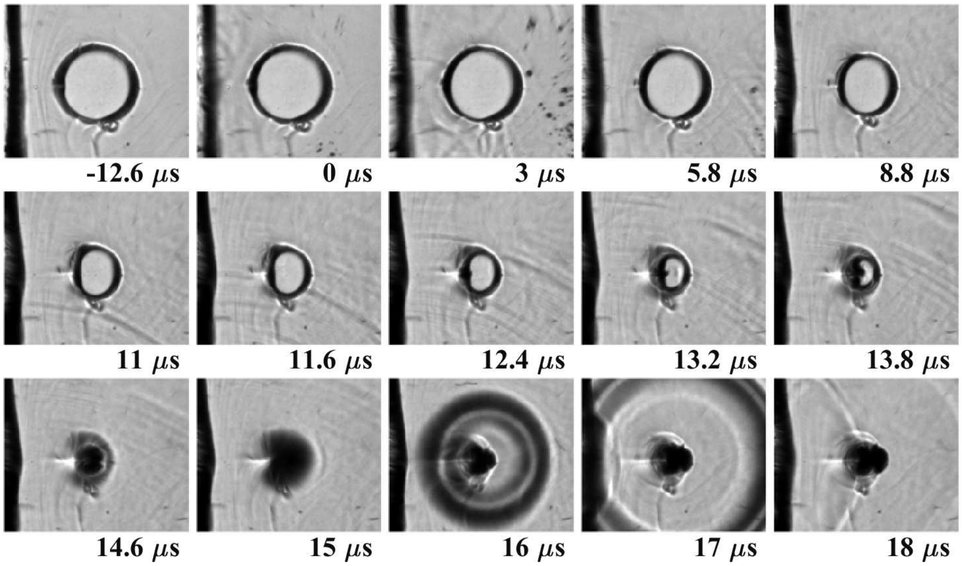

Figure B.40: Test #623. 1:30 PDMS.

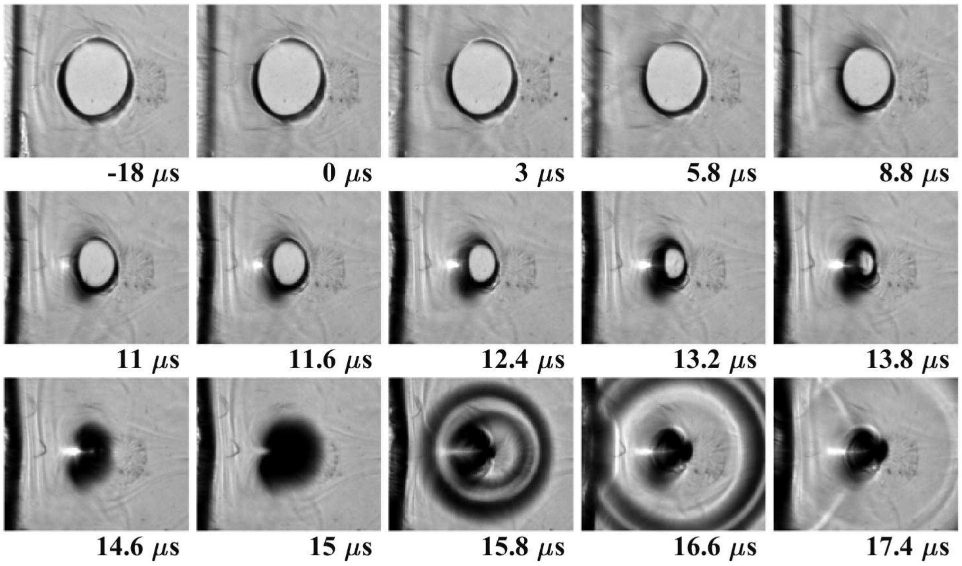

Figure B.41: Test #624. 1:30 PDMS.

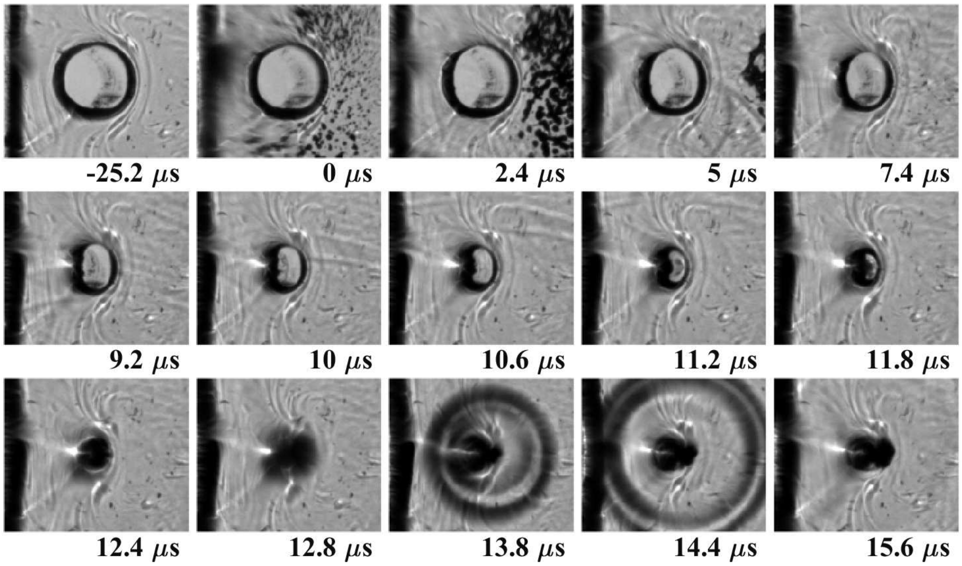

Figure B.42: Test #636. 1:30 PDMS.

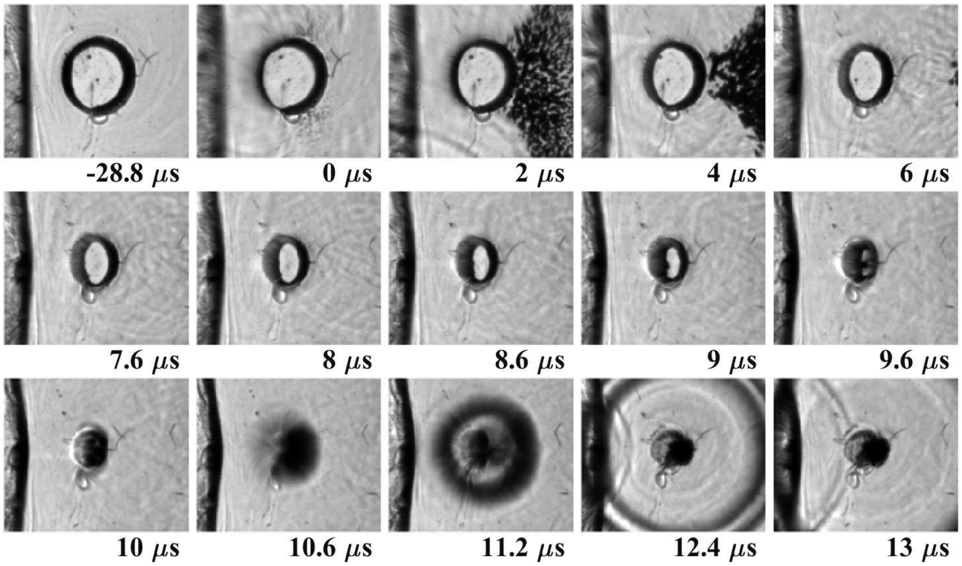

Figure B.43: Test #641. 1:30 PDMS.

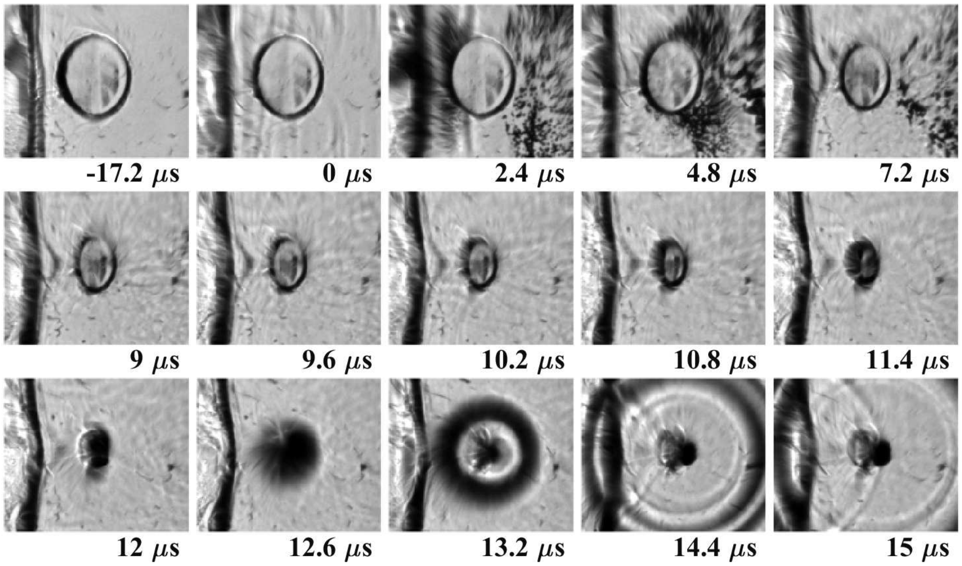

-17.2 μs
0 μs
2.4 μs
4.8 μs
7.2 μs
9 μs
9.6 μs
10.2 μs
10.8 μs
11.4 μs
12 μs
12.6 μs
13.2 μs
14.4 μs
15 μs

Figure B.44: Test #643. 1:30 PDMS.

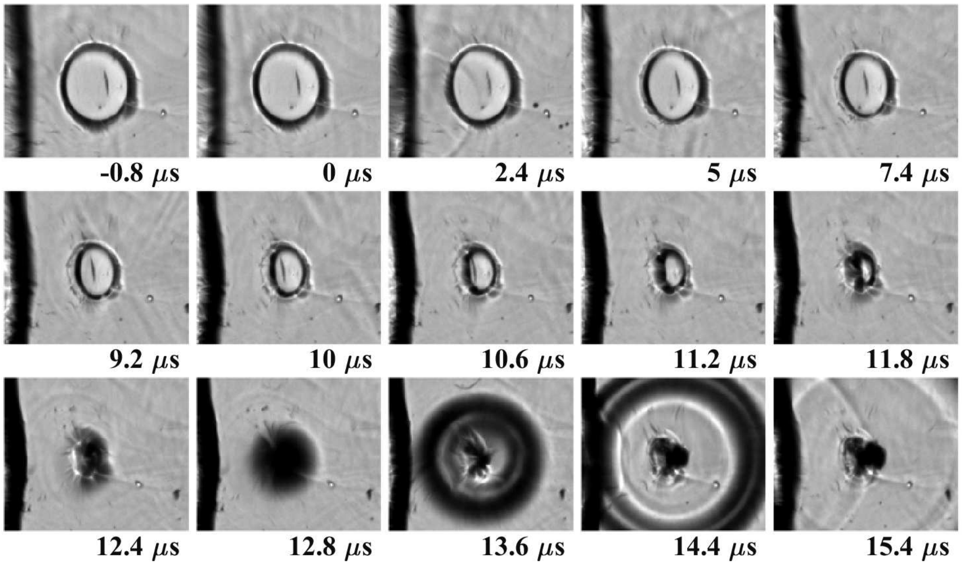

-0.8 μs
0 μs
2.4 μs
5 μs
7.4 μs
9.2 μs
10 μs
10.6 μs
11.2 μs
11.8 μs
12.4 μs
12.8 μs
13.6 μs
14.4 μs
15.4 μs

Figure B.45: Test #576. 1:40 PDMS.

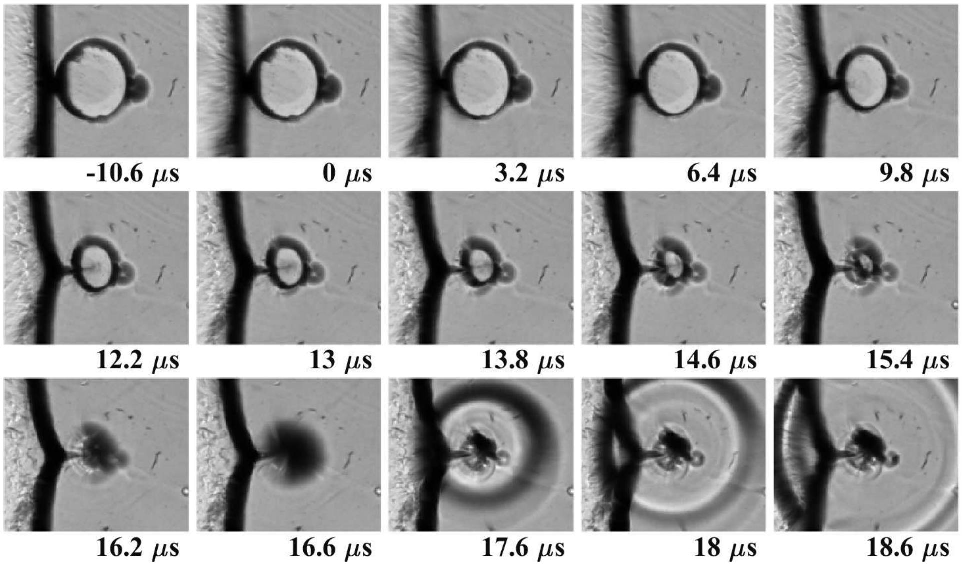

Figure B.46: Test #578. 1:40 PDMS.

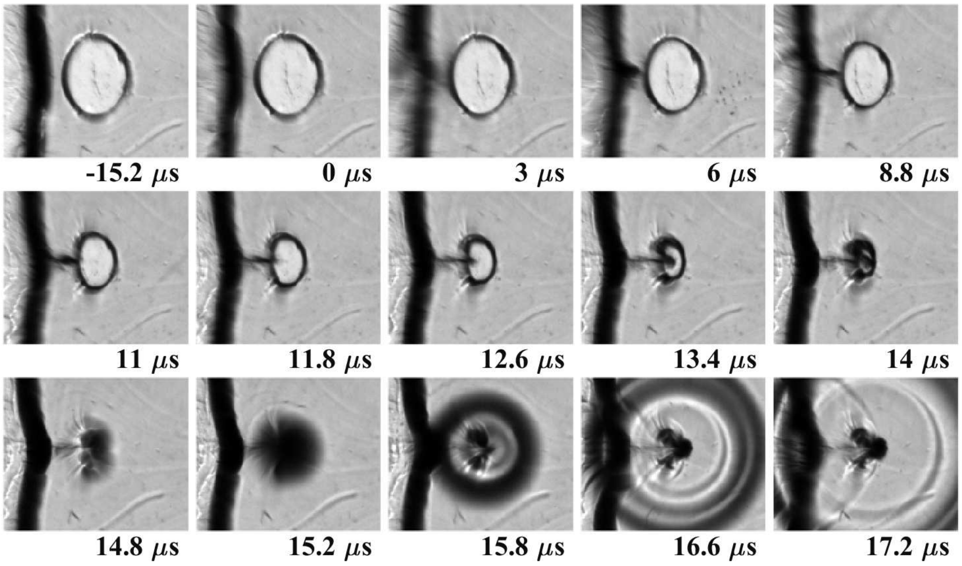

Figure B.47: Test #579. 1:40 PDMS.

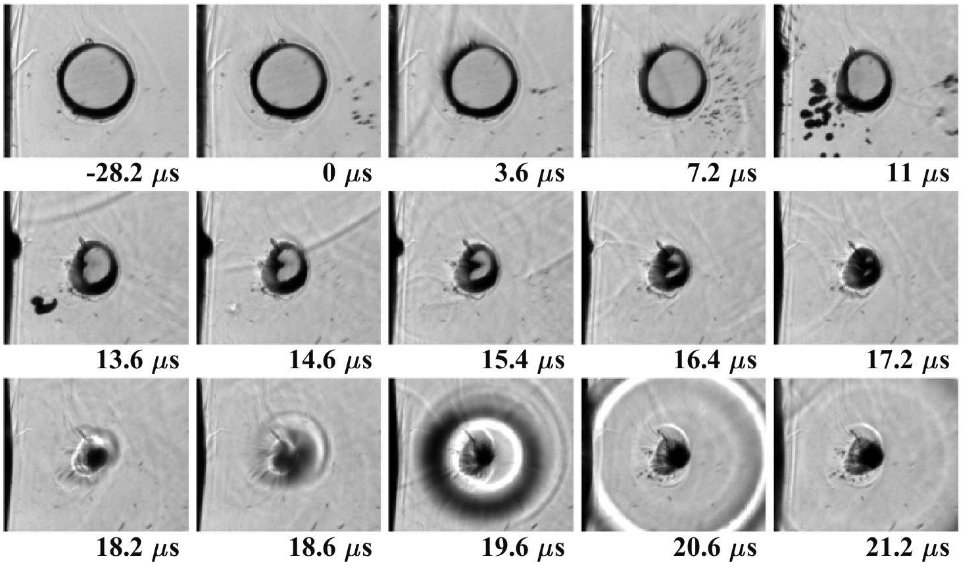
-28.2 μs
0 μs
3.6 μs
7.2 μs
11 μs
13.6 μs
14.6 μs
15.4 μs
16.4 μs
17.2 μs
18.2 μs
18.6 μs
19.6 μs
20.6 μs
21.2 μs

Figure B.48: Test #614. 1:40 PDMS.

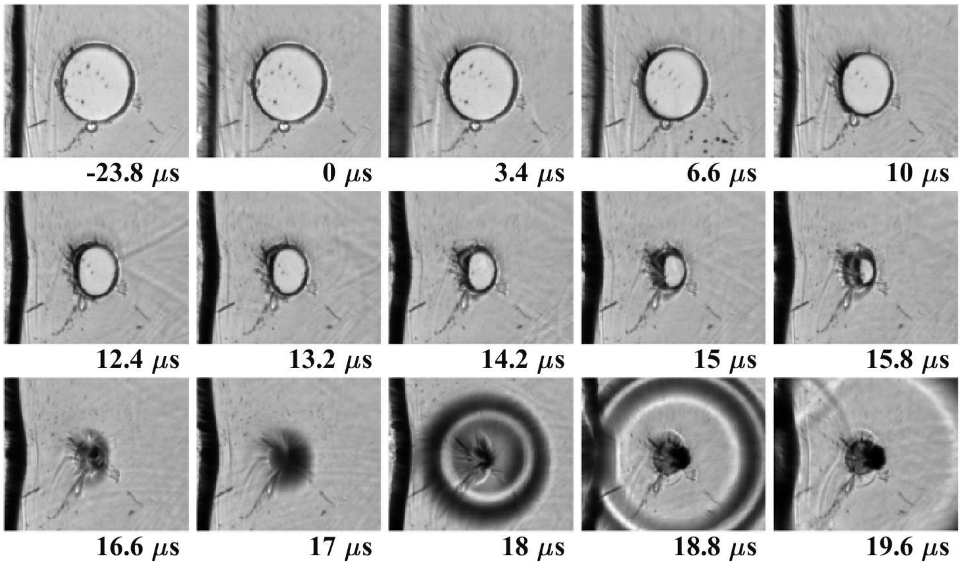
-23.8 μs
0 μs
3.4 μs
6.6 μs
10 μs
12.4 μs
13.2 μs
14.2 μs
15 μs
15.8 μs
16.6 μs
17 μs
18 μs
18.8 μs
19.6 μs

Figure B.49: Test #616. 1:40 PDMS.

B.4 Two Boundary

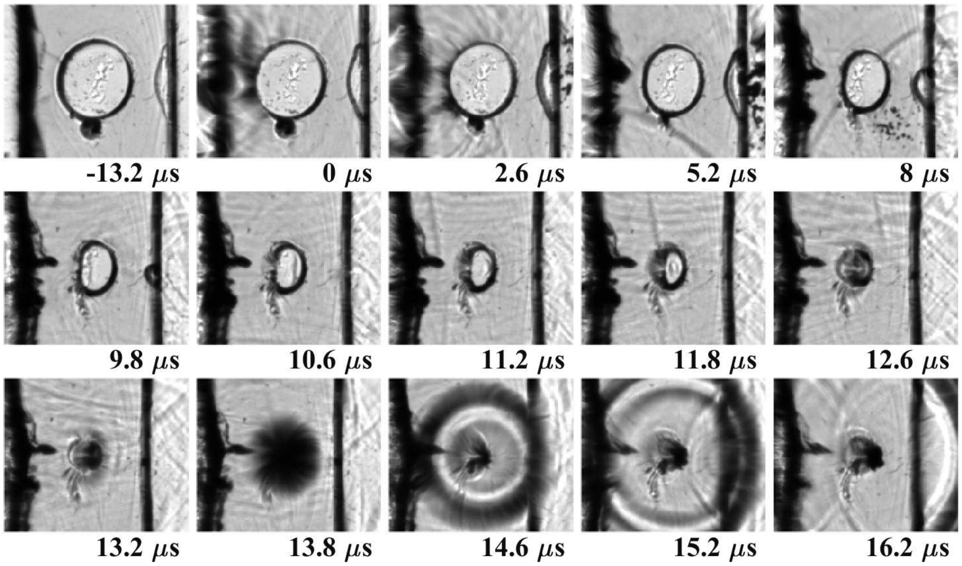

Figure B.50: Test #606. 1:20 PDMS.

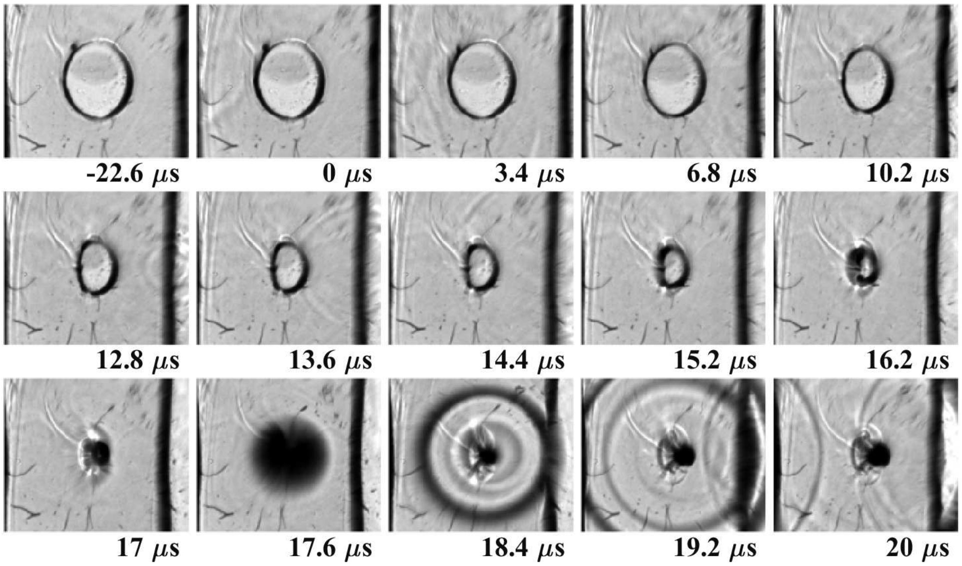

Figure B.51: Test #620. 1:20 PDMS.

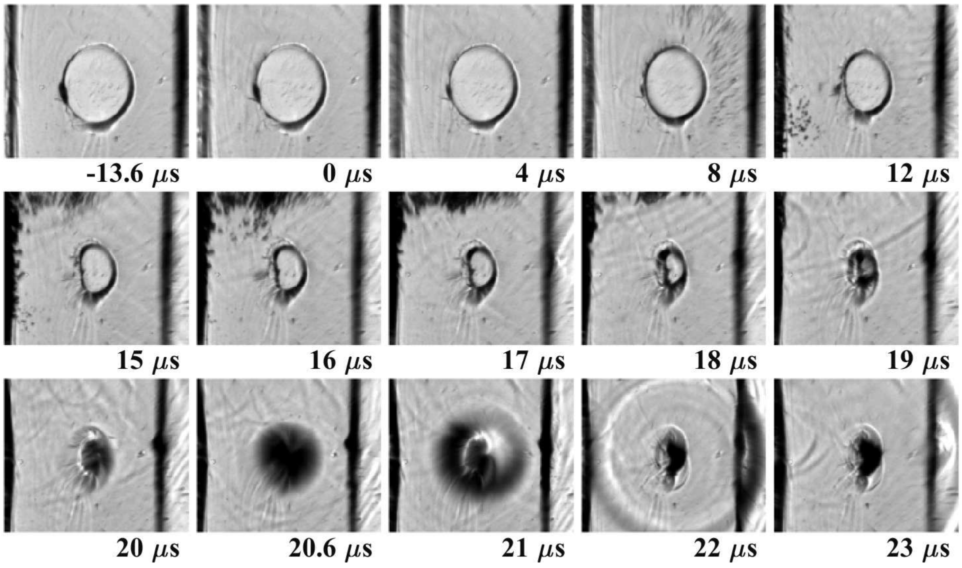

Figure B.52: Test #622. 1:20 PDMS.

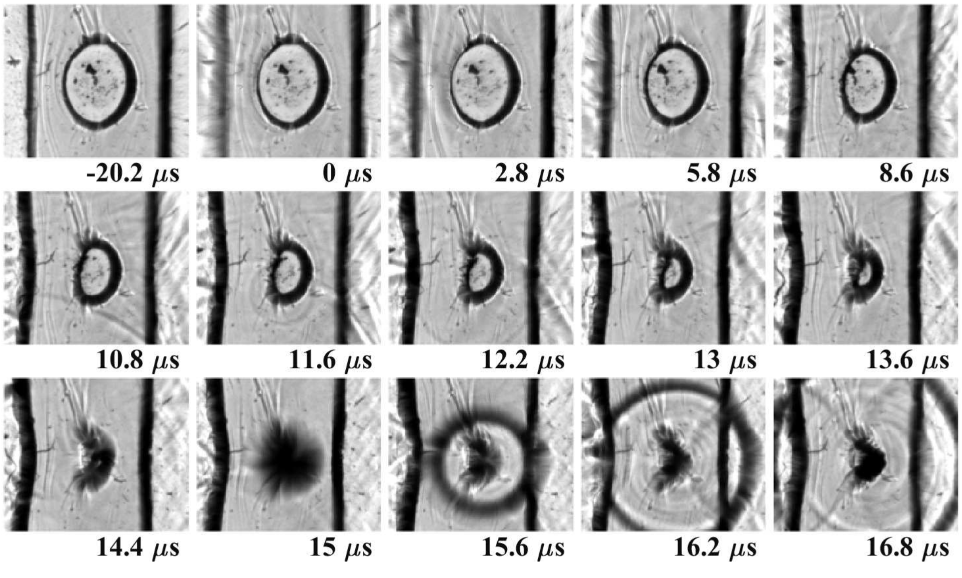

Figure B.53: Test #637. 1:20 PDMS.

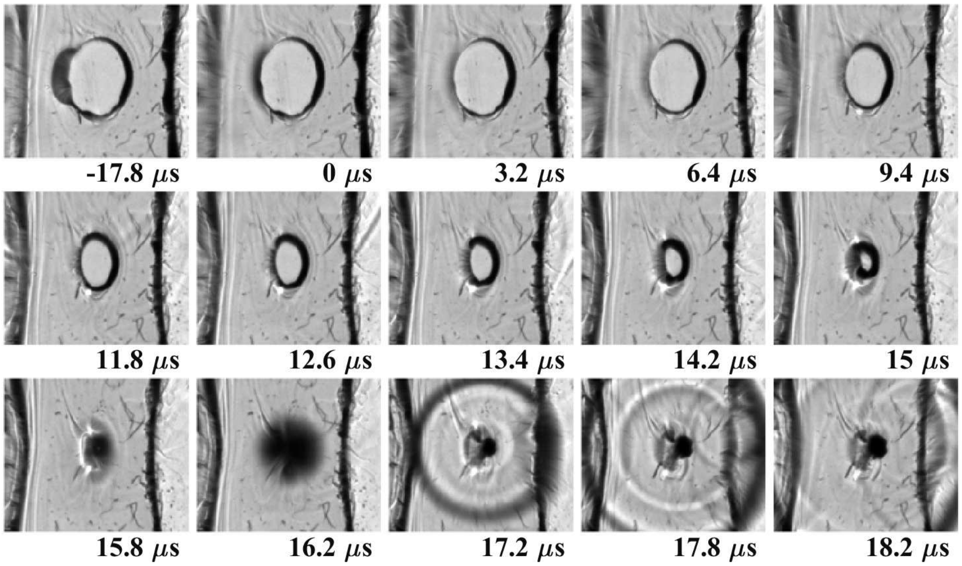

Figure B.54: Test #619. 1:30 PDMS.

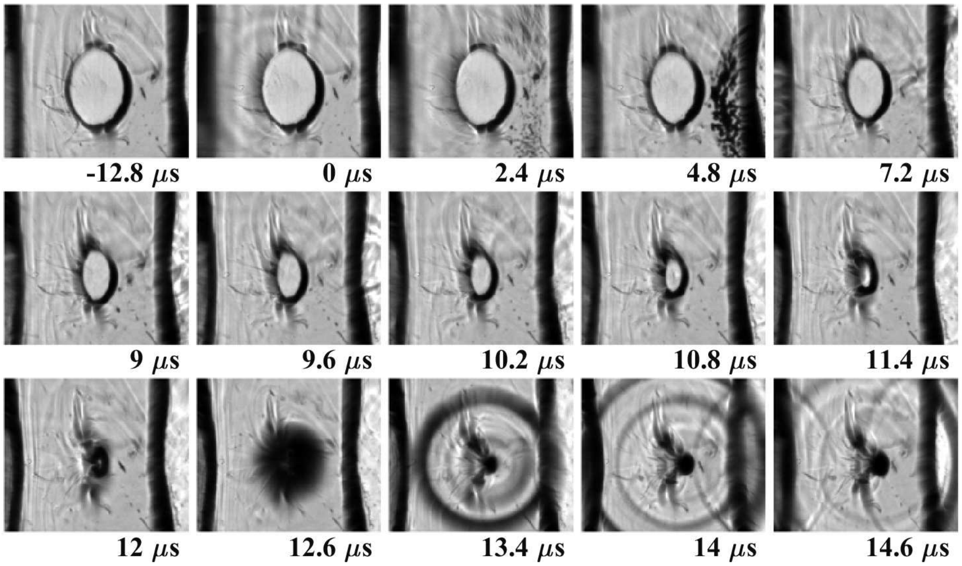

Figure B.55: Test #621. 1:30 PDMS.

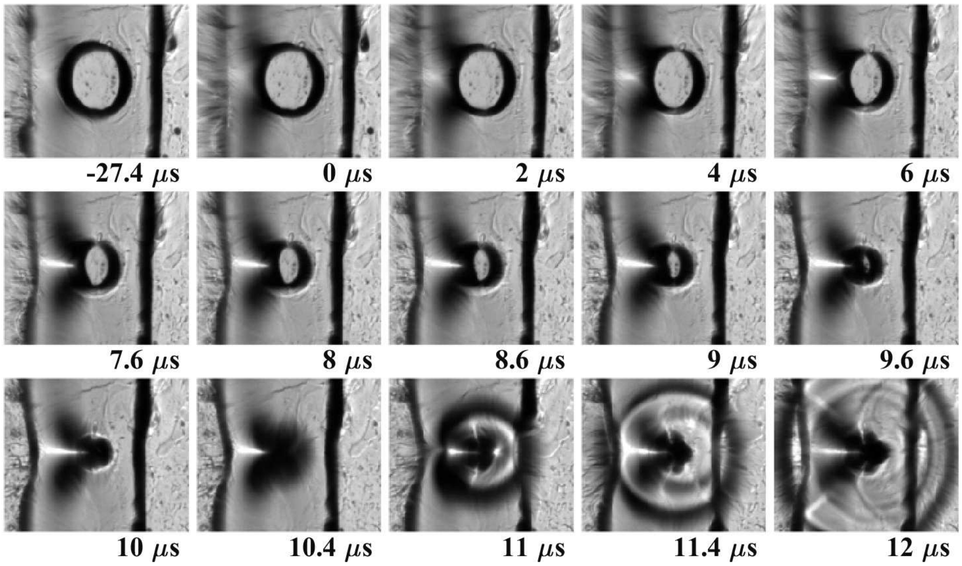

Figure B.56: Test #634. 1:30 PDMS.

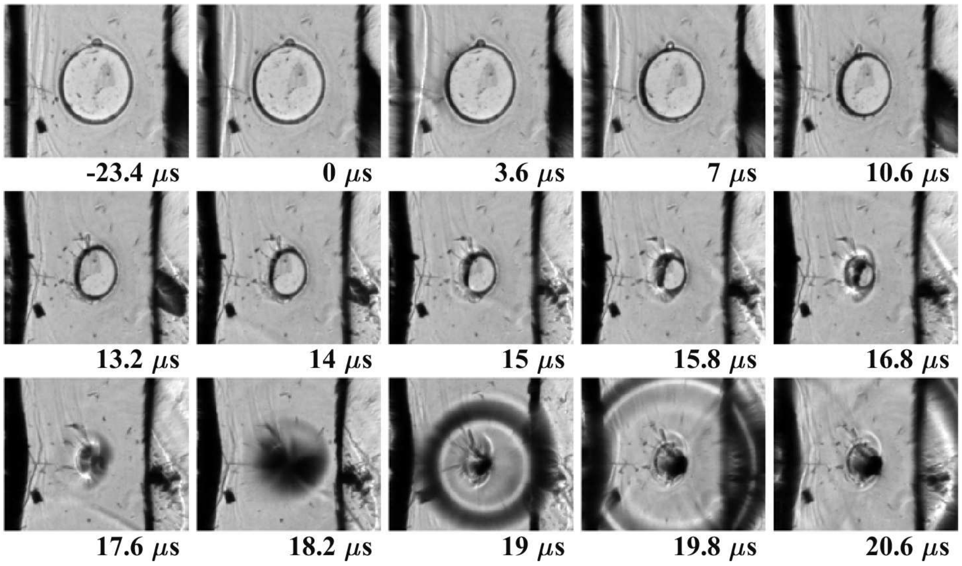

Figure B.57: Test #635. 1:30 PDMS.

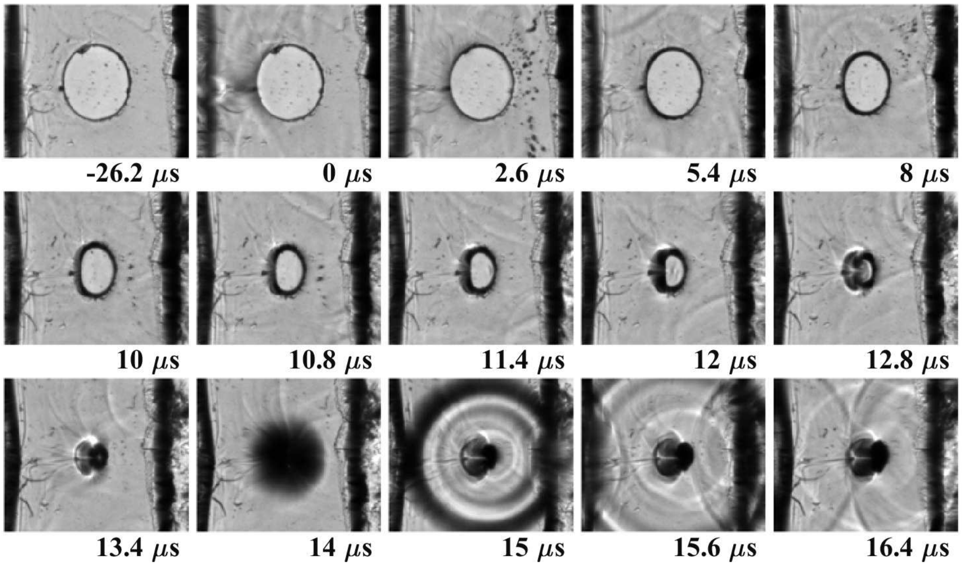

Figure B.58: Test #618. 1:40 PDMS.

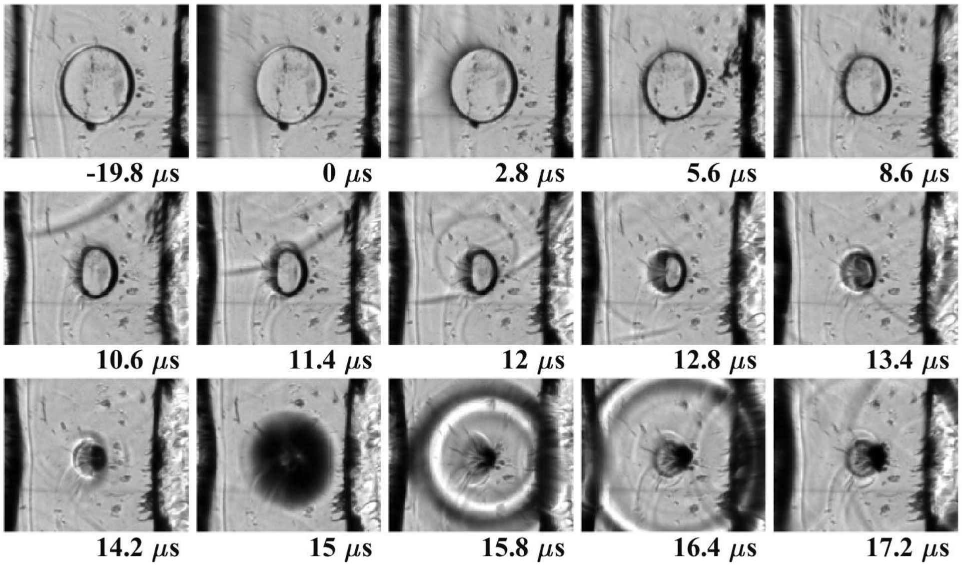

Figure B.59: Test #633. 1:40 PDMS.

B.5 Aluminum Boundary

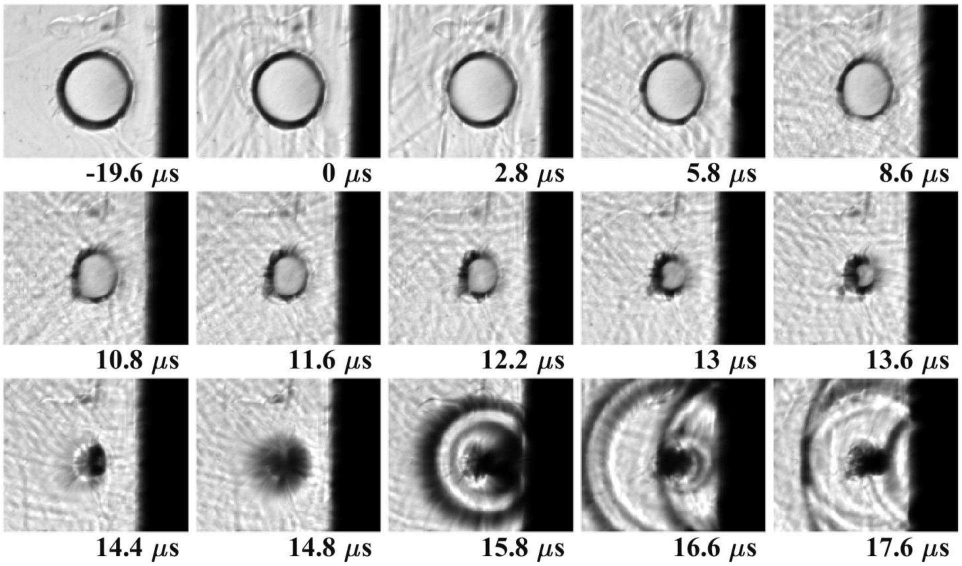

Figure B.60: Test #653.

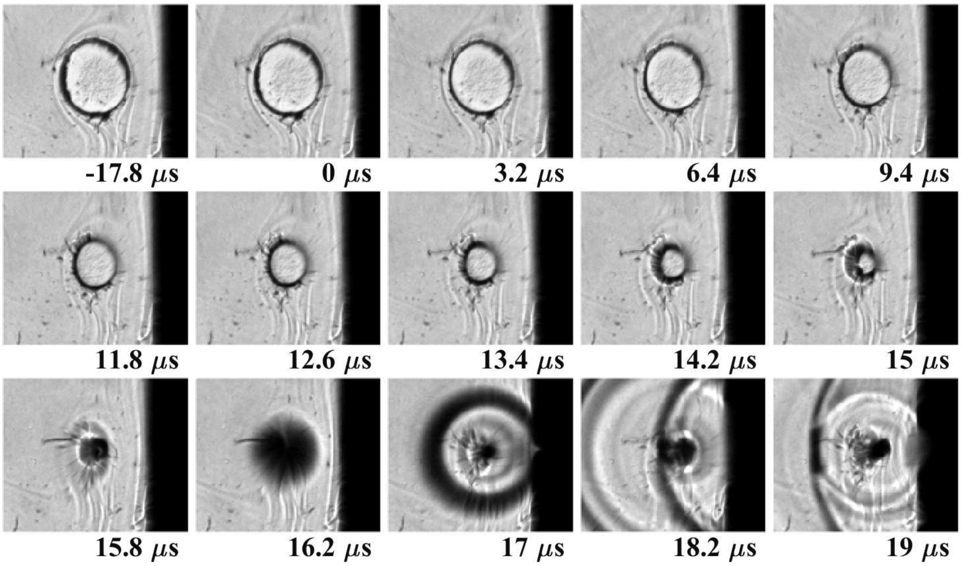

Figure B.61: Test #654.

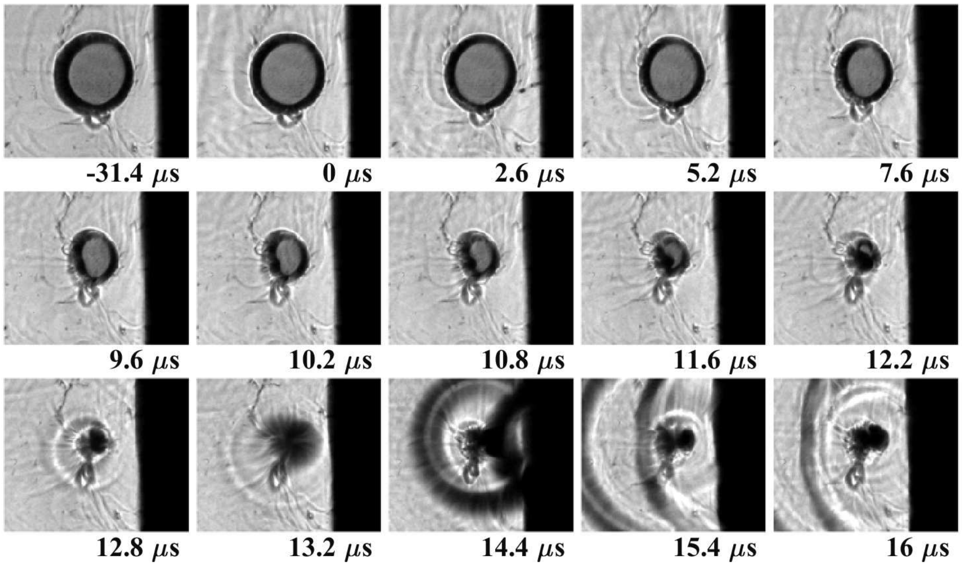

Figure B.62: Test #657.

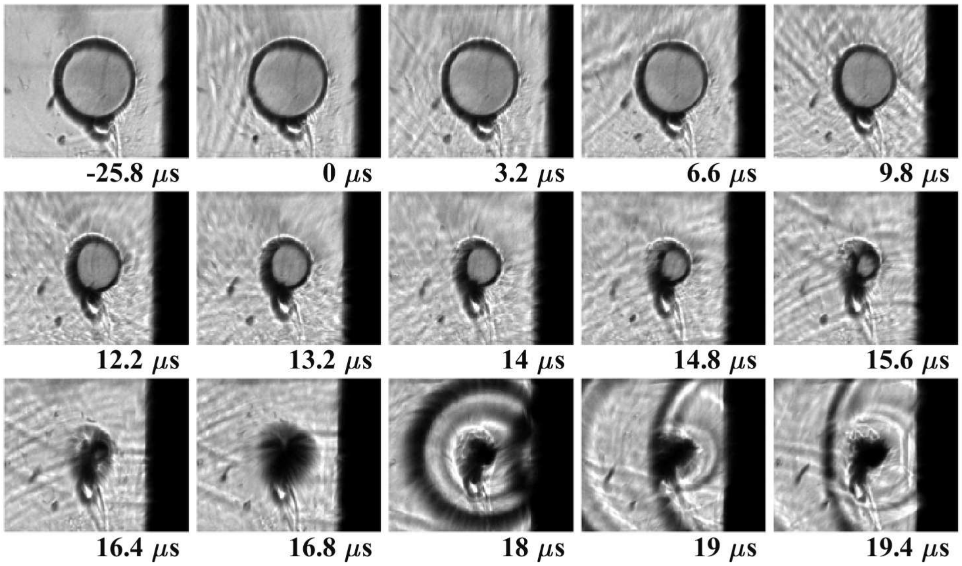

Figure B.63: Test #658.

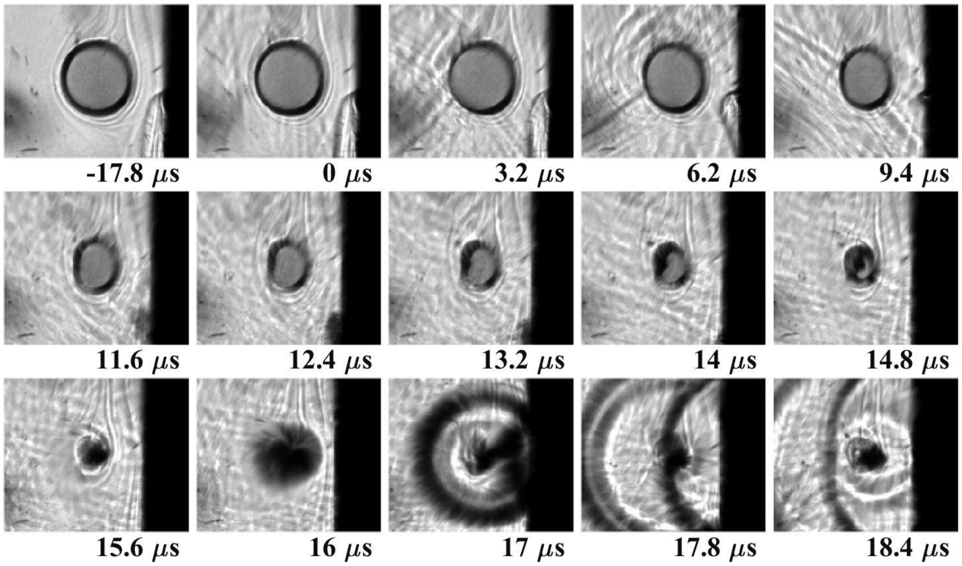

Figure B.64: Test #660.

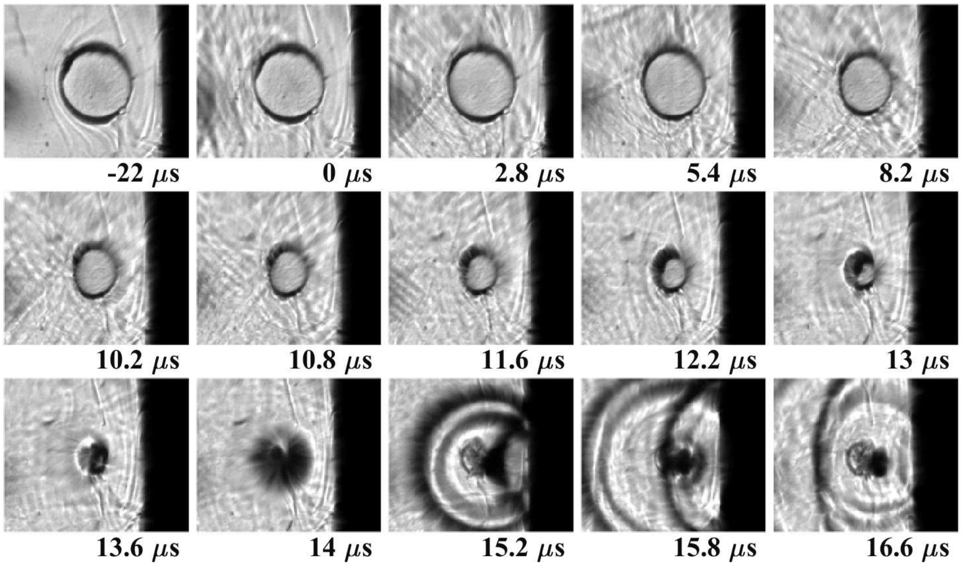

Figure B.65: Test #661.

APPENDIX C

SHADOWGRAPH TEST PARAMETER TABLES

C.1 No Boundary

Table C.1: Summary of impact condition, geometry, and collapse conditions of all high speed video tests with no boundary.

		Measured in photo				Measured in video							
Test	v_I (m/s)	D_o	h_o	h_1	h_2	$D_{o,out}$	D_o	W	H	$t_{c,o}$	$t_{c,f}$	t_c	Jet
560	26.3	2.44	10.3	—	—	2.22	1.73	1.76	1.69	29.4	43.4	14	J
561	26.4	2.48	9.96	—	—	2.57	2.10	2.08	2.18	25.8	41.8	16	N
562	26.4	2.42	9.63	—	—	2.19	1.95	1.91	2.05	20.4	35.6	15.2	J
563	25.8	2.60	10.32	—	—	2.27	1.93	1.97	1.89	21.8	36.2	14.4	J
564	25.5	2.43	10.1	—	—	2.27	1.89	1.89	1.93	29.8	45.2	15.4	J
626	26.0	2.24	9.42	—	—	2.67	1.68	1.69	1.65	24.2	37.2	13	J
627	25.9	2.62	10.4	—	—	2.51	1.66	1.67	1.65	27.2	39.2	12	J
629	25.3	2.47	8.93	—	—	2.38	1.79	1.83	1.73	25.6	37.6	12	J
630	25.6	2.46	9.46	—	—	2.47	1.80	1.84	1.79	20.6	31.8	11.2	J
631	25.6	2.46	9.38	—	—	2.43	1.67	1.67	1.67	14.4	25.6	11.2	J
662	26.5	2.41	9.21	—	—	2.42	1.88	2.10	1.75	26.2	40	13.8	U
663	26.2	2.26	8.94	—	—	2.32	2.05	2.00	2.16	24.2	39.2	15	N
664	26.0	2.36	9.05	—	—	2.34	1.86	1.81	1.89	26.2	40.8	14.6	J
665	25.8	2.15	9.2	—	—	2.69	1.83	1.87	1.77	36.4	50.6	14.2	J
666	26.3	2.39	8.81	—	—	2.41	1.89	1.95	1.87	30.6	46.6	16	J

C.2 Upstream Boundary

Table C.2: Summary of impact condition, geometry, and collapse conditions of all high speed video tests with upstream boundary with 40:1 PDMS.

		Measured in photo				Measured in video							
Test	v_I (m/s)	$D_{o,out}$	h_o	h_1	h_2	$D_{o,out}$	D_o	W	H	$t_{c,o}$	$t_{c,f}$	t_c	Jet
574	26.0	2.44	9.18	2.07	—	2.67	2.1	2.09	2.21	23.6	39.4	15.8	J
575	25.9	2.33	9.06	2.35	—	2.32	2.13	2.03	2.3	20.8	33.8	13	N
576	25.6	2.3	9.35	2.55	—	2.48	1.98	1.84	2.09	21	33.4	12.4	N
577	25.9	2.26	9.6	2.62	—	2.33	2.06	1.92	2.24	21.8	38.4	16.6	N
578	26.0	2.33	7.91	1.79	—	2.42	1.94	1.79	2.19	20.4	37	16.6	N
579	25.5	2.1	8.95	2.17	—	2.33	1.96	1.75	2.28	25.6	40.2	14.6	U
592	26.0	2.25	9.38	2.59	—	2.37	2.08	1.98	2.22	21.2	41.8	20.6	N
614	26.0	2.3	9.69	2.99	—	2.32	1.89	1.96	1.88	37	56.6	19.6	J
615	26.0	2.54	9.26	2.3	—	2.42	2.24	2.24	2.26	42.8	57.4	14.6	N
616	25.7	2.52	9.46	2.58	—	2.39	2.14	2.03	2.22	32.6	50.6	18	N

Table C.3: Summary of impact condition, geometry, and collapse conditions of all high speed video tests with upstream boundary with 30:1 PDMS.

		Measured in photo				Measured in video							
Test	v_I (m/s)	$D_{o,out}$	h_o	h_1	h_2	$D_{o,out}$	D_o	W	H	$t_{c,o}$	$t_{c,f}$	t_c	Jet
580	25.4	2.39	9.03	2.08	—	2.84	2.03	1.95	2.18	19	32.8	13.8	N
581	26	2.43	9.05	2.08	—	2.47	2.05	1.89	2.31	21.4	36.4	15	U
582	25.9	2.47	9.42	2.61	—	2.29	1.87	1.67	2.16	20.8	31.2	10.4	N
584	25.7	2.41	9.63	2.48	—	2.3	2.08	2.05	2.18	13.4	30.4	17	N
585	26.2	2.41	9.85	2.77	—	2.32	2.01	1.74	2.37	20.2	34	13.8	N
593	25.5	2.41	9.45	2.46	—	2.48	2.01	1.88	2.22	16	32	16	N
623	25.6	2.22	9.78	2.63	—	2.59	2	1.95	2.03	22.6	37.4	14.8	J
624	25.3	2.37	9.59	2.78	—	2.47	2.04	1.9	2.2	28.4	42.8	14.4	N
625	25.5	2.51	9.61	2.84	—	2.46	2.06	2.09	2.09	27	40.4	13.4	U
636	25.5	2.46	9.59	2.94	—	2.45	1.96	1.96	1.94	34.4	47.8	13.4	J
641	25.4	2.18	8.88	2.47	—	2.33	1.72	1.59	1.89	39	49	10	J
642	25.9	2.39	9.48	2.83	—	2.32	1.96	1.89	1.99	25.4	37.4	12	U
643	25.2	2.29	8.19	2.08	—	2.44	2.12	1.93	2.39	28.4	39.4	11	N

Table C.4: Summary of impact condition, geometry, and collapse conditions of all high speed video tests with upstream boundary with 20:1 PDMS.

		Measured in photo				Measured in video							
Test	v_I (m/s)	$D_{o,out}$	h_o	h_1	h_2	$D_{o,out}$	D_o	W	H	$t_{c,o}$	$t_{c,f}$	t_c	Jet
565	25.9	2.43	10.7	2.95	—	2.21	1.47	1.42	1.65	37	48	11	J
567	26.1	2.74	11.6	2.9	—	2.23	2.06	2.01	2.22	37.4	51.2	13.8	N
569	25.4	2.61	11.1	2.76	—	2.22	1.91	1.84	1.97	21.6	36.8	15.2	J
570	26	2.37	9.93	2.35	—	2.3	2.01	2.01	2.05	26.2	39	12.8	J
571	—	2.43	10.09	2.05	—	2.73	1.58	1.59	1.57	30.8	44.2	13.4	J
572	26	2.04	10.2	2.4	—	2.51	1.71	1.65	1.78	29.4	43.8	14.4	U
573	26.5	2.27	9.05	2.05	—	2.19	1.62	1.65	1.59	25.6	38.8	13.2	J
603	25.1	2.38	10.2	2.86	—	2.52	1.95	1.94	2	28.6	40	11.4	N
604	24.8	2.34	9.5	2.89	—	2.5	1.92	1.75	2.24	28.8	43.6	14.8	U
605	25.8	2.37	9.6	2.13	—	2.89	2.18	2.03	2.4	21.8	36.4	14.6	N

C.3 Downstream Boundary

Table C.5: Summary of impact condition, geometry, and collapse conditions of all high speed video tests with downstream boundary with 40:1 PDMS.

		Measured in photo				Measured in video							
Test	v_I (m/s)	D_o	h_o	h_1	h_2	$D_{o,out}$	D_o	W	H	$t_{c,o}$	$t_{c,f}$	t_c	Jet
588	26.1	2.37	10.4	—	2.3	2.34	2.05	1.9	2.26	14.4	27.6	13.2	N
589	26	2.57	9.97	—	2.81	2.31	2.04	1.92	2.28	13	26.2	13.2	N
596	26	2.34	9.05	—	2.52	2.41	1.99	1.77	2.26	24.6	38.8	14.2	N
597	25.7	2.42	10.2	—	2.33	2.3	2.11	2.07	2.09	19.8	35	15.2	U
598	25.4	2.45	9.26	—	2.26	2.32	2.15	2.13	2.17	20.6	42.2	21.6	J
650	25.9	2.31	9.24	—	2.49	2.3	1.89	1.77	2	17.8	28.8	11	U
651	25.1	2.43	8.77	—	2.53	2.41	2.05	1.92	2.22	18.4	29.4	11	U
652	25.4	2.38	9.38	—	2.14	2.32	1.97	1.77	2.3	17.2	31.4	14.2	N

Table C.6: Summary of impact condition, geometry, and collapse conditions of all high speed video tests with downstream boundary with 30:1 PDMS.

		Measured in photo				Measured in video							
Test	v_I (m/s)	D_o	h_o	h_1	h_2	$D_{o,out}$	D_o	W	H	$t_{c,o}$	$t_{c,f}$	t_c	Jet
587	26.2	2.35	9.69	—	2.39	2.29	2.03	1.88	2.19	14.4	30	15.6	J
590	26.4	2.47	9.87	—	2.75	2.51	2	1.96	2.17	12.2	29.2	17	N
595	25.7	2.38	10.2	—	2.11	2.27	1.71	1.56	1.9	20.4	32.6	12.2	N
599	25.6	2.42	9.92	—	2.74	2.61	2.12	2.11	2.17	33	51	18	N
638	26	2.48	9.81	—	2.52	2.38	2.1	2	2.22	25.4	41.2	15.8	N
647	26.2	2.46	10.2	—	2.74	2.45	1.9	1.81	1.91	14.2	32.6	18.4	J
648	25.8	2.37	9.19	—	2.53	2.44	1.9	1.87	1.93	10.4	24.2	13.8	J
649	25.8	2.4	9.55	—	2.49	2.45	2.05	1.97	2.16	10.8	25.2	14.4	N
671	26.4	2.35	9.75	—	2.44	2.42	1.92	1.93	2.02	25.4	43	17.6	J
672	26	2.3	9.52	—	2.38	2.34	2.07	2.08	2.1	24.8	45.4	20.6	N
673	26	2.45	9.76	—	2.46	2.32	2.06	1.95	2.24	28.4	45	16.6	N

Table C.7: Summary of impact condition, geometry, and collapse conditions of all high speed video tests with downstream boundary with 20:1 PDMS.

		Measured in photo				Measured in video							
Test	v_I (m/s)	D_o	h_o	h_1	h_2	$D_{o,out}$	D_o	W	H	$t_{c,o}$	$t_{c,f}$	t_c	Jet
591	26	2.35	9.74	—	2.27	2.4	2	1.81	2.28	15	32.8	17.8	N
594	25.3	2.33	10.3	—	1.76	2.26	2.08	2	2.21	17.6	42.4	24.8	N
601	25.7	2.29	9.64	—	2.61	2.35	1.84	1.81	1.94	26.6	46.8	20.2	J
602	25.9	2.28	9.69	—	3.19	2.34	2.1	2.11	2.09	24.8	44.6	19.8	N
639	25.6	2.46	9.49	—	2.55	2.4	2.03	1.94	2.15	31.8	45	13.2	N
640	25.9	2.45	9.7	—	2.22	2.32	1.92	1.83	2.03	30	46.4	16.4	J
644	25.6	2.48	8.95	—	2.11	2.32	2.04	1.83	2.42	21.4	38	16.6	N
645	25.9	2.38	9.26	—	2.36	2.35	1.91	2.23	2.48	12.6	24.6	12	N
646	25.5	2.39	9.23	—	2.68	2.38	1.74	1.68	1.81	17.8	34	16.2	J
668	26.5	2.36	10.4	—	1.87	2.29	2.08	1.95	2.2	31	46	15	N
669	26	2.37	9.85	—	2.34	2.2	1.96	1.87	2.08	24.4	42.2	17.8	N
670	26.5	2.64	9.82	—	2.4	2.65	2.3	2.24	2.39	27.8	41.6	13.8	J

Table C.8: Summary of impact condition, geometry, and collapse conditions of all high speed video tests with downstream boundary with aluminum.

		Measured in photo				Measured in video							
Test	v_I (m/s)	D_o	h_o	h_1	h_2	$D_{o,out}$	D_o	W	H	$t_{c,o}$	$t_{c,f}$	t_c	Jet
653	26.5	—	—	—	—	2.28	1.88	1.87	1.92	27.6	44.2	16.6	U
654	26	2.3	9.29	—	2.37	2.31	1.97	1.83	2.12	27	43.8	16.8	U
656	26.2	2.27	9.76	—	2.22	2.29	1.95	1.87	2.08	25.4	42.2	16.8	U
657	26.9	2.16	9.42	—	2.24	2.49	1.83	1.76	1.92	37.6	54.4	16.8	J
658	26.1	2.32	10.1	—	2.38	2.54	2.14	2.16	2.18	35.8	52.4	16.6	U
659	26.1	2.13	10.1	—	2.27	2.37	1.84	1.9	1.8	32.2	44	11.8	U
660	26	2.25	9.9	—	2.32	2.25	1.87	1.86	1.88	26.2	43.6	17.4	J
661	26.1	2.36	9.53	—	2.24	2.36	2.03	2.08	2.04	32.2	45.8	13.6	N

C.4 Two Boundary

Table C.9: Summary of impact condition, geometry, and collapse conditions of all high speed video tests where the void was between two boundaries with 40:1 PDMS.

		Measured in photo				Measured in video							
Test	v_I (m/s)	$D_{o,out}$	h_o	h_1	h_2	$D_{o,out}$	D_o	W	H	$t_{c,o}$	$t_{c,f}$	t_c	Jet
610	26.1	2.49	9.81	3.19	2.72	2.47	2.06	2.05	2.03	27.6	45.4	17.8	N
612	25.8	2.31	9.28	2.67	2.6	2.42	2.02	1.9	2.13	35.8	59.4	23.6	N
617	26	—	—	—	—	2.44	1.97	1.92	2.07	41.2	56.6	15.4	J
618	25.8	2.34	9.58	2.85	2.85	2.28	2.07	1.96	2.22	36.8	49.8	13	N
632	25.6	2.46	8.53	2.51	2.55	2.42	2.11	2.09	2.17	24.6	38.4	13.8	U
633	26	2.44	8.86	2.67	2.68	2.4	2.09	1.96	2.26	30.8	44.2	13.4	N

Table C.10: Summary of impact condition, geometry, and collapse conditions of all high speed video tests where the void was between two boundaries with 30:1 PDMS.

		Measured in photo				Measured in video							
Test	v_I (m/s)	$D_{o,out}$	h_o	h_1	h_2	$D_{o,out}$	D_o	W	H	$t_{c,o}$	$t_{c,f}$	t_c	Jet
608	26.2	2.47	9	2.65	2.64	2.47	2.11	2.02	2.24	25.8	42.2	16.4	J
619	25.8	2.47	8.93	2.56	2.56	2.35	1.97	1.77	2.28	27.8	43.8	16	N
621	26	2.41	10.1	3.35	3.1	2.34	1.91	1.63	2.35	23.8	35	11.2	N
634	25.3	2.14	8.64	2.13	2.08	2.34	1.64	1.46	1.81	37.6	47.6	10	N
635	25.6	2.4	9.22	2.73	2.53	2.39	2.13	2.32	2.47	32.8	51.2	18.4	N

Table C.11: Summary of impact condition, geometry, and collapse conditions of all high speed video tests where the void was between two boundaries with 20:1 PDMS.

		Measured in photo				Measured in video							
Test	v_I (m/s)	$D_{o,out}$	h_o	h_1	h_2	$D_{o,out}$	D_o	W	H	$t_{c,o}$	$t_{c,f}$	t_c	Jet
606	26.2	2.43	9.26	2.64	2.62	2.4	2.1	1.98	2.22	22.8	36.6	13.8	N
611	25.9	2.3	9.15	2.74	2.8	2.22	1.97	1.88	2.07	39	52.2	13.2	U
620	25.6	2.32	8.79	2.55	2.02	2.34	2	1.84	2.3	33	49.8	16.8	N
622	25.8	2.35	9.39	2.97	2.94	2.41	2.08	1.94	2.24	22.8	43.8	21	U
637	25.8	2.57	9.68	2.36	2.11	2.5	2.06	1.83	2.38	30.6	44.8	14.2	N

APPENDIX D

COMPLETE SHADOWGRAPH AREA DATA AND DERIVATIVES

D.1 No Boundary

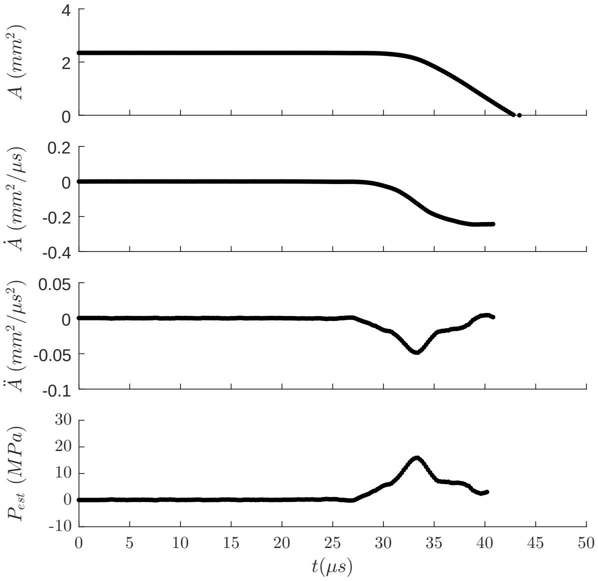

Figure D.1: Test #560

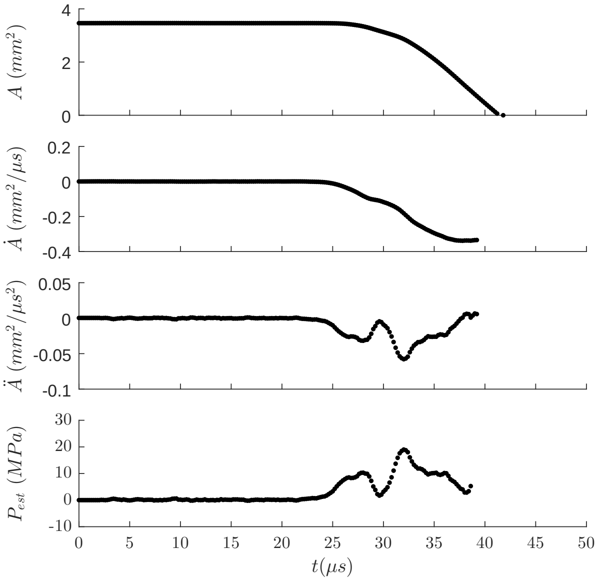

Figure D.2: Test #561

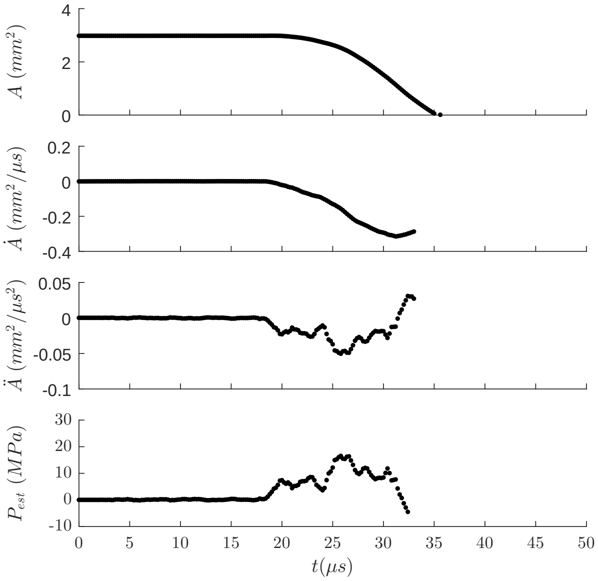

Figure D.3: Test #562.

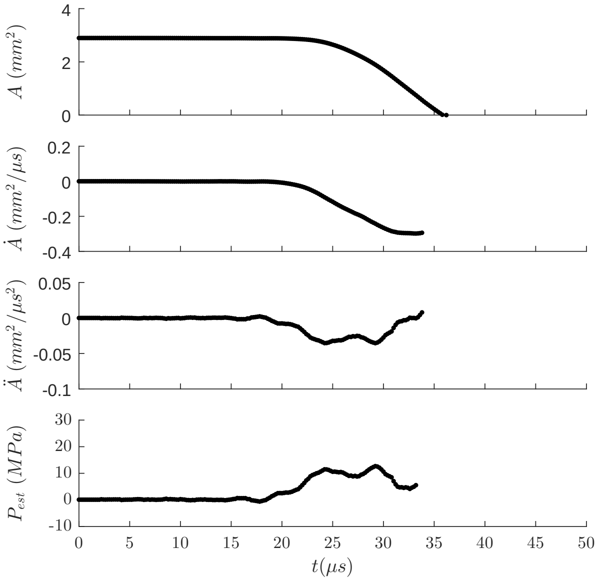

Figure D.4: Test #563.

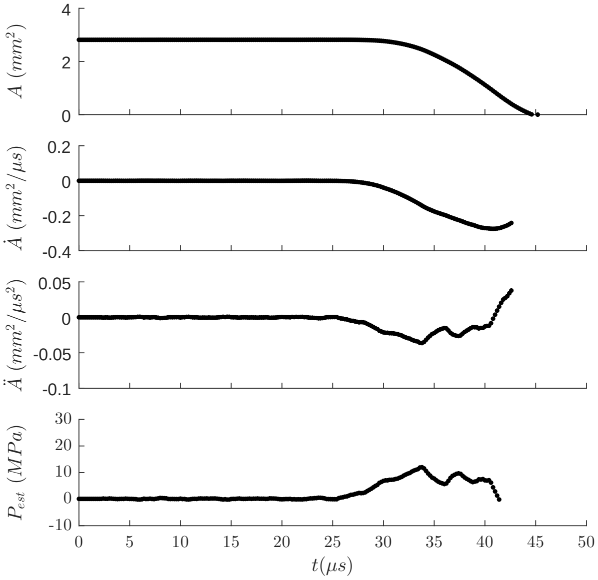

Figure D.5: Test #564.

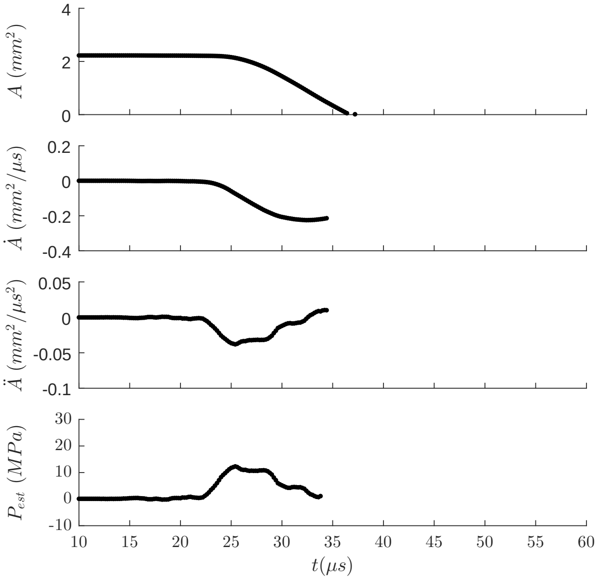

Figure D.6: Test #626.

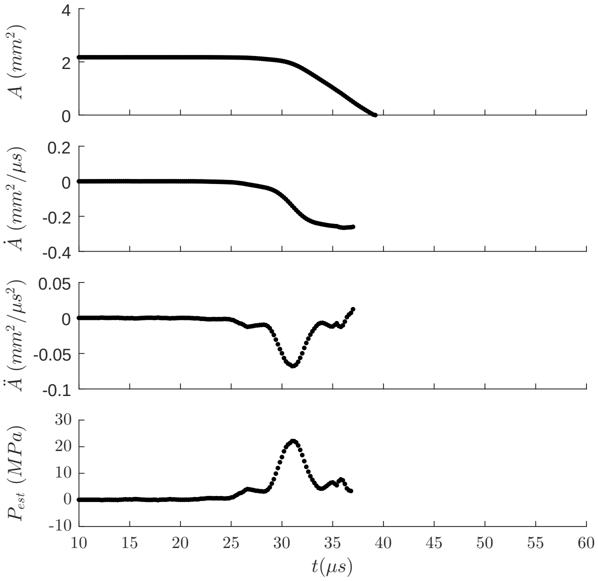

Figure D.7: Test #627.

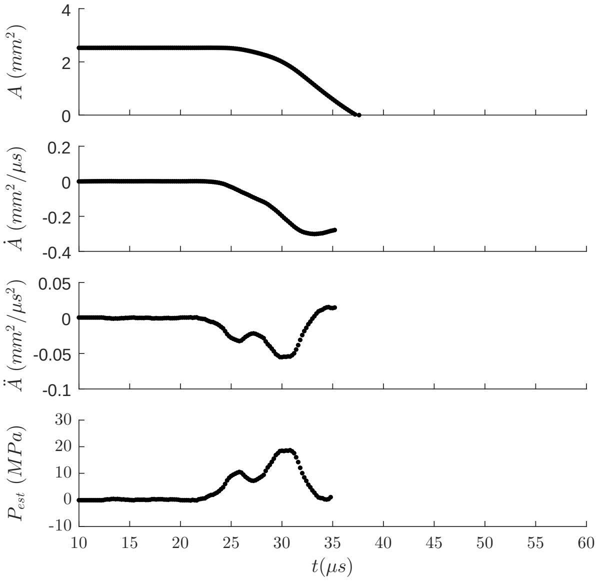

Figure D.8: Test #629.

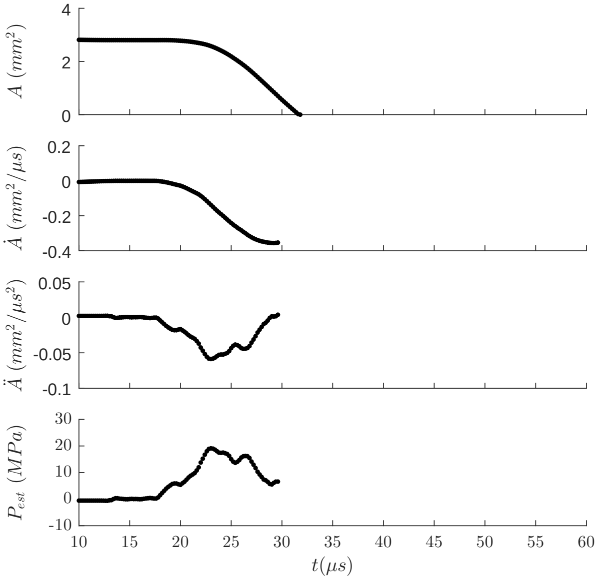

Figure D.9: Test #630.

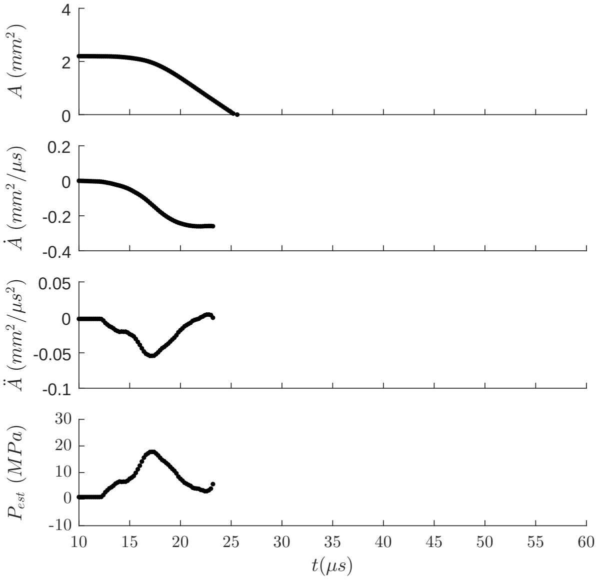

Figure D.10: Test #631.

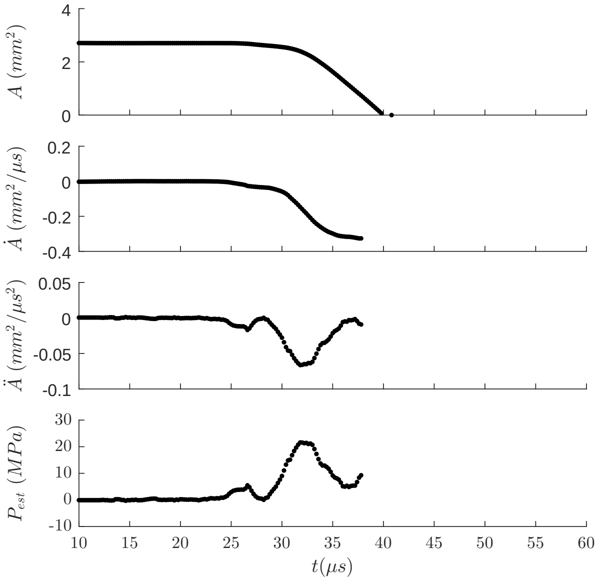

Figure D.11: Test #664.

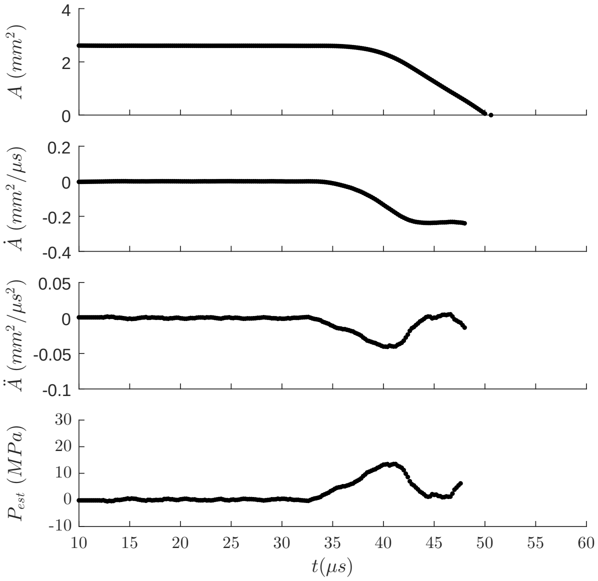

Figure D.12: Test #665.

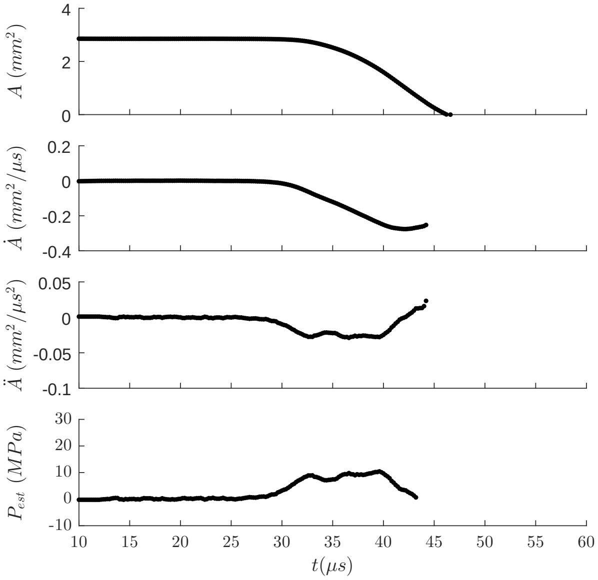

Figure D.13: Test #666.

D.2 Downstream Boundary

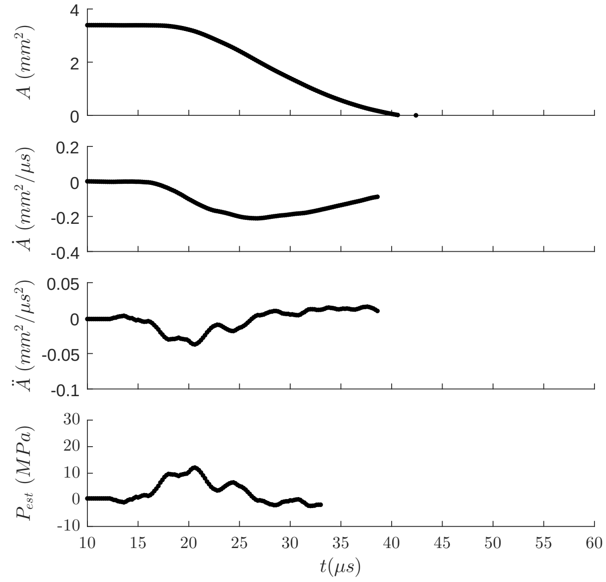

Figure D.14: Test #594. 1:20 PDMS.

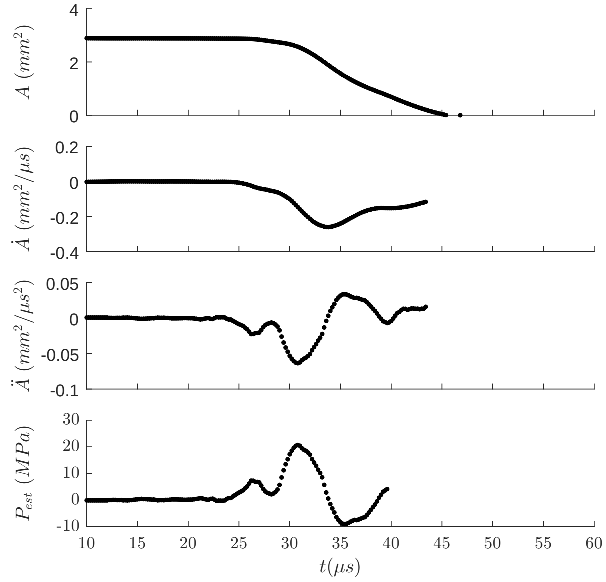

Figure D.15: Test #601. 1:20 PDMS.

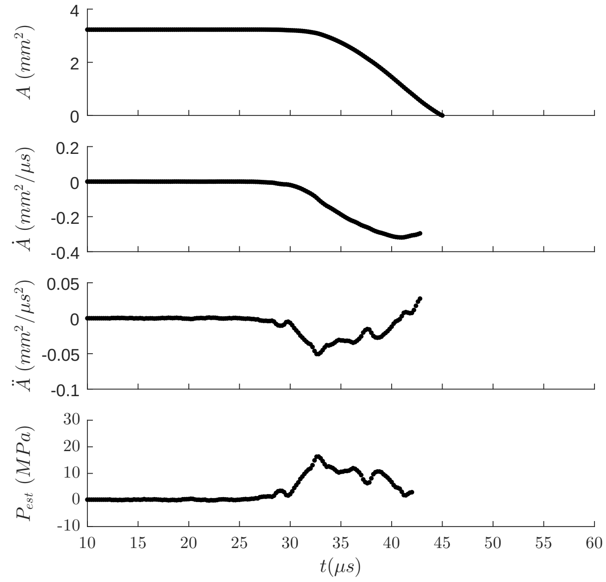

Figure D.16: Test #639. 1:20 PDMS.

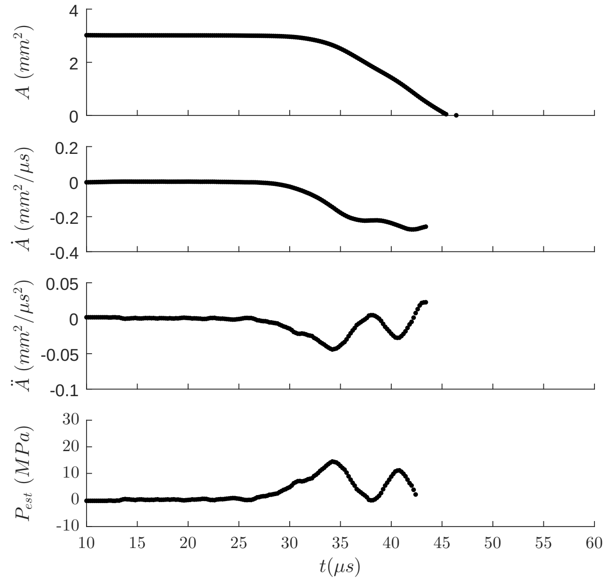

Figure D.17: Test #640. 1:20 PDMS.

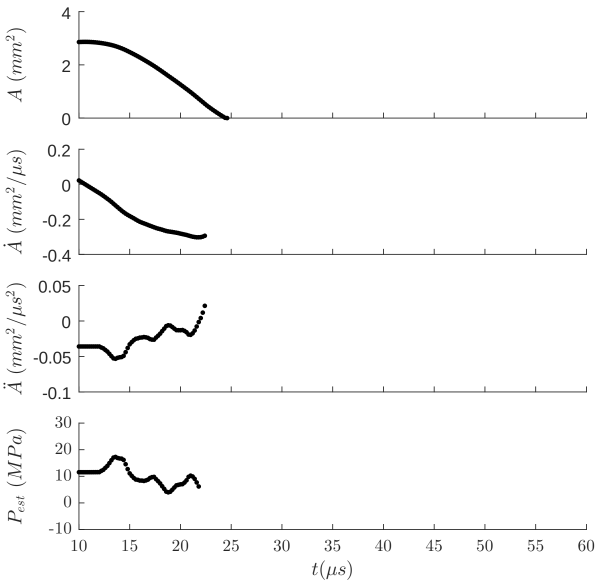

Figure D.18: Test #645. 1:20 PDMS.

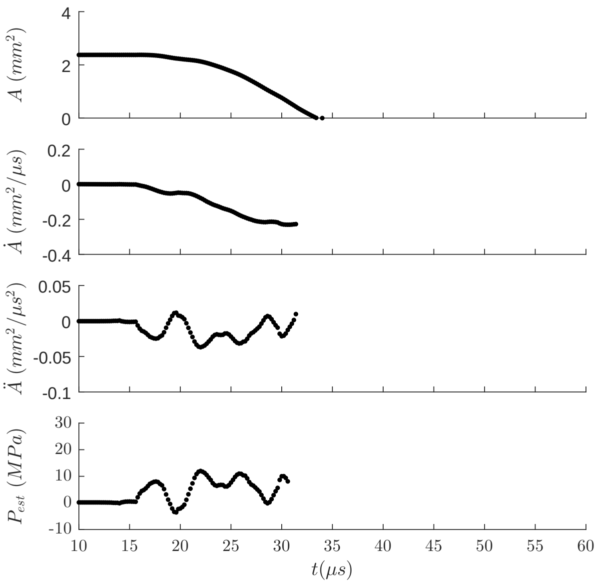

Figure D.19: Test #646. 1:20 PDMS.

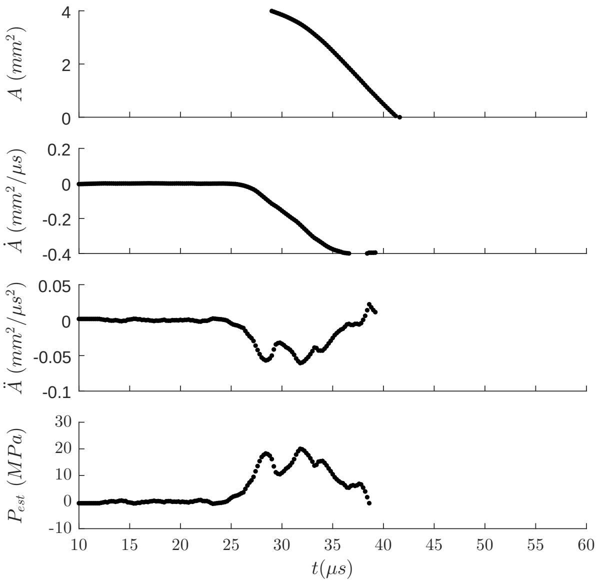

Figure D.20: Test #670. 1:20 PDMS.

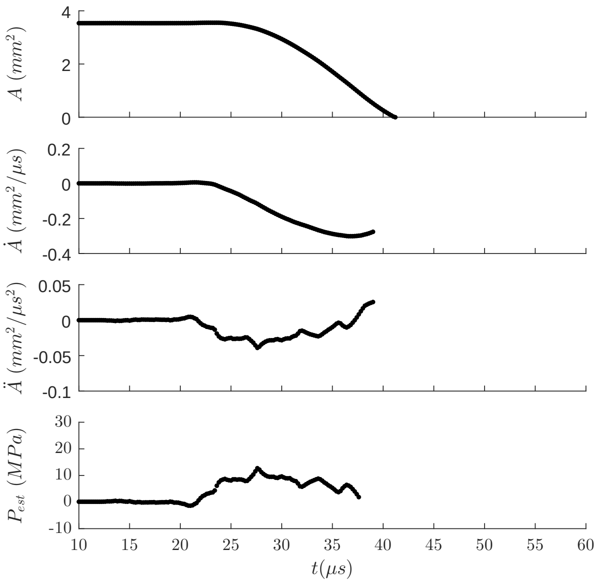

Figure D.21: Test #638. 1:30 PDMS.

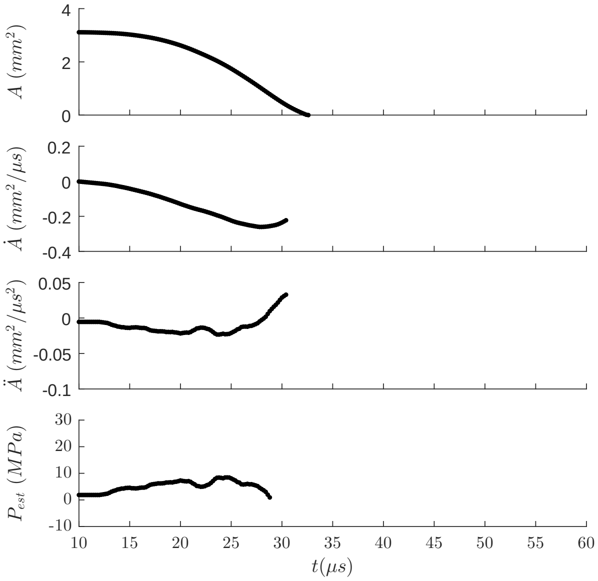

Figure D.22: Test #647. 1:30 PDMS.

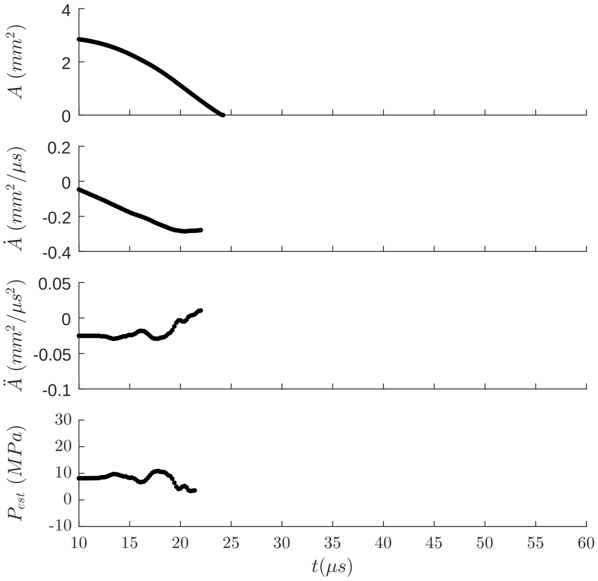

Figure D.23: Test #648. 1:30 PDMS.

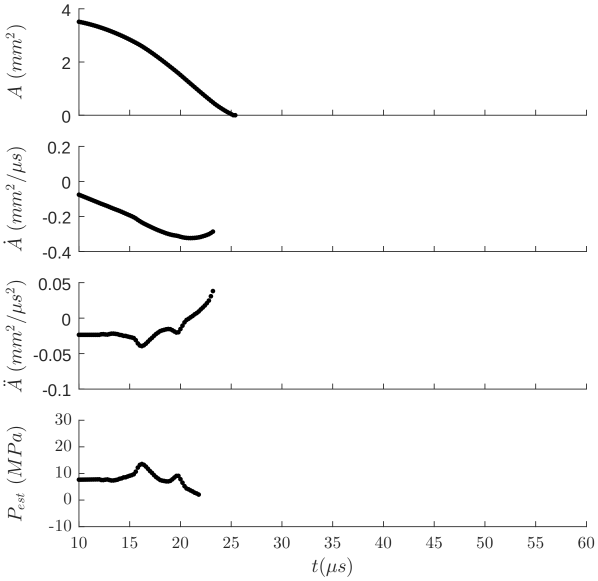

Figure D.24: Test #649. 1:30 PDMS.

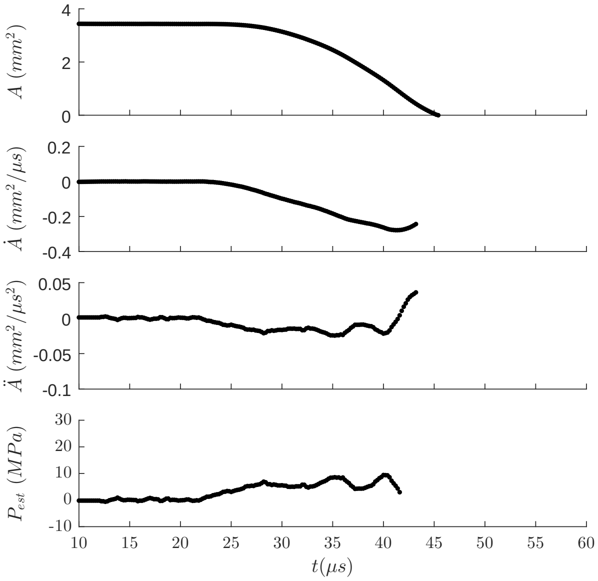

Figure D.25: Test #672. 1:30 PDMS.

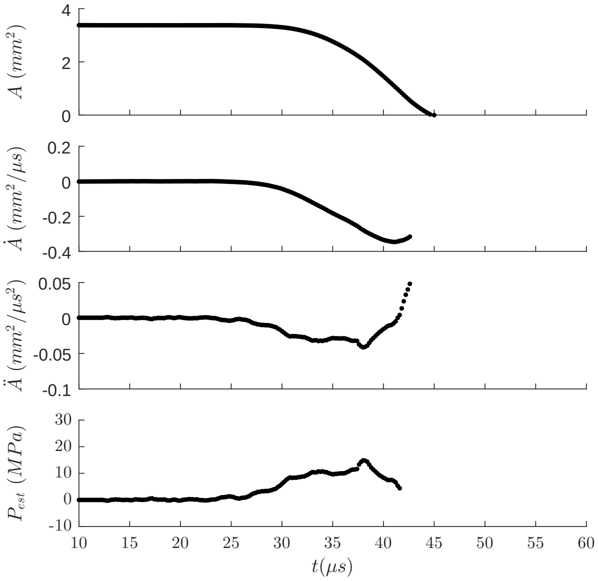

Figure D.26: Test #673. 1:30 PDMS.

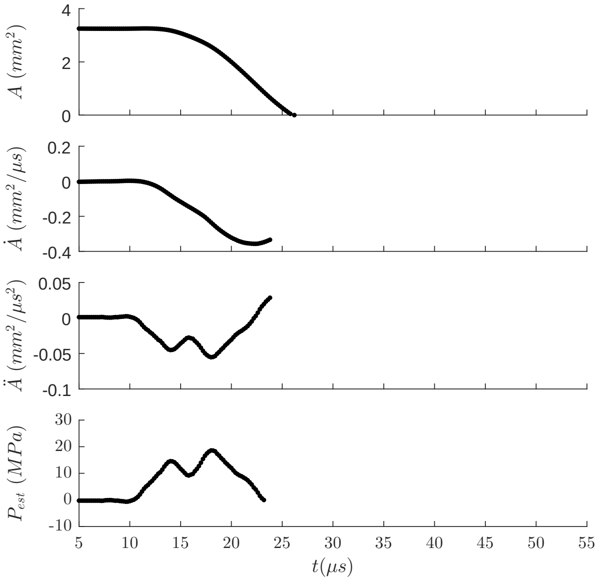

Figure D.27: Test #589. 1:40 PDMS.

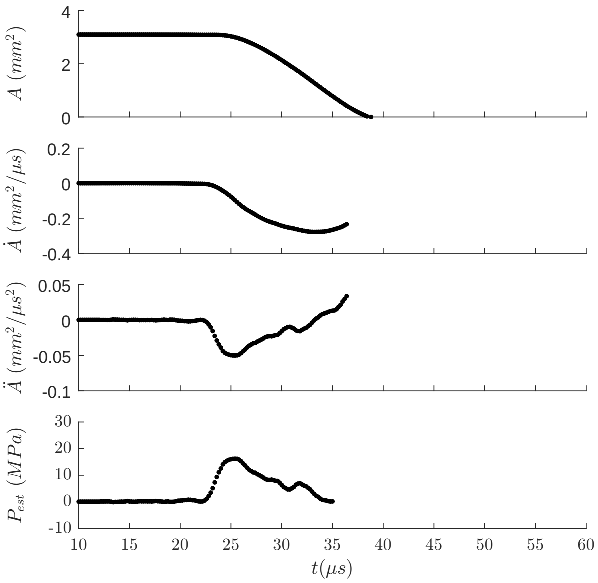

Figure D.28: Test #596. 1:40 PDMS.

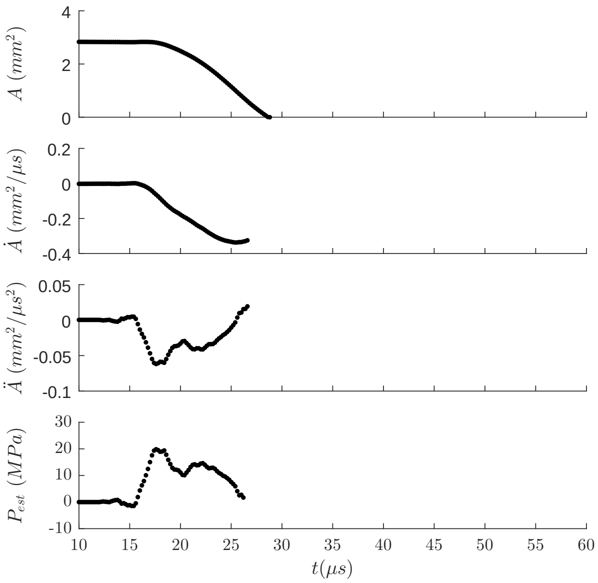

Figure D.29: Test #650. 1:40 PDMS.

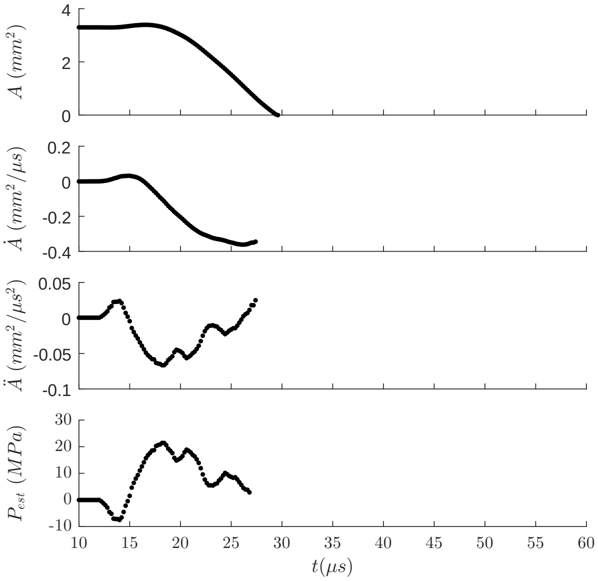

Figure D.30: Test #651. 1:40 PDMS.

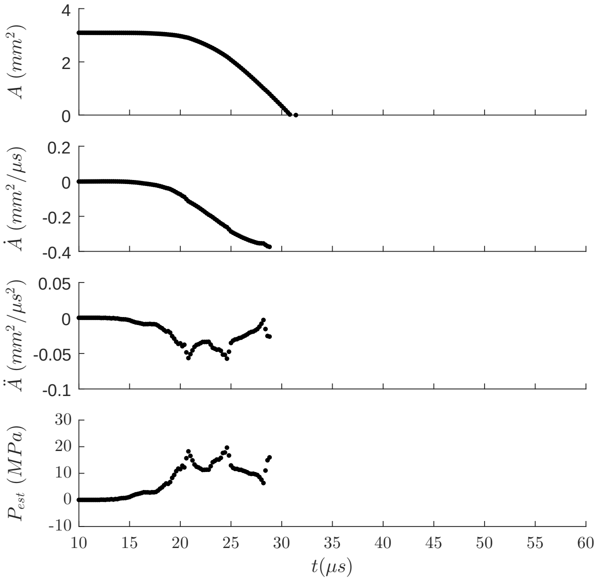

Figure D.31: Test #652. 1:40 PDMS.

D.3 Upstream Boundary

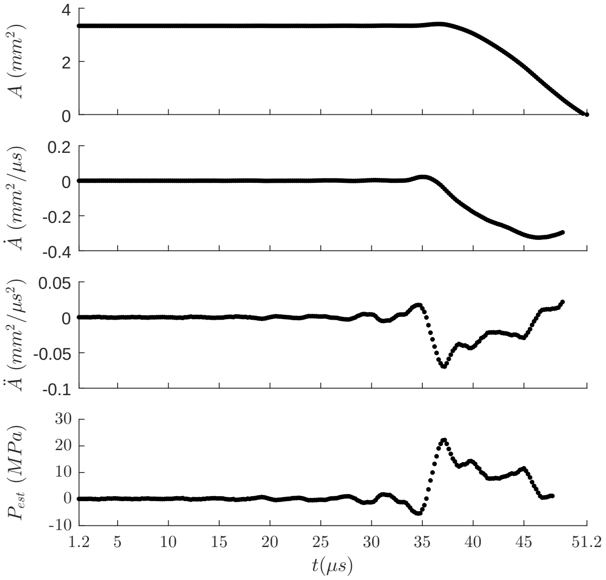

Figure D.32: Test #567. 1:20 PDMS.

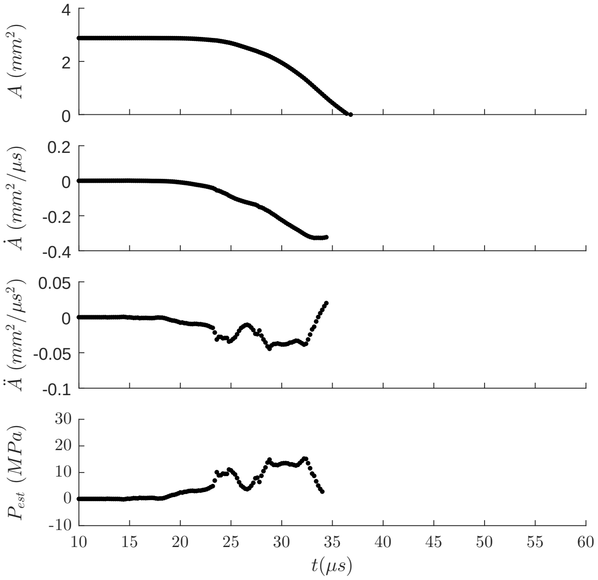

Figure D.33: Test #569. 1:20 PDMS.

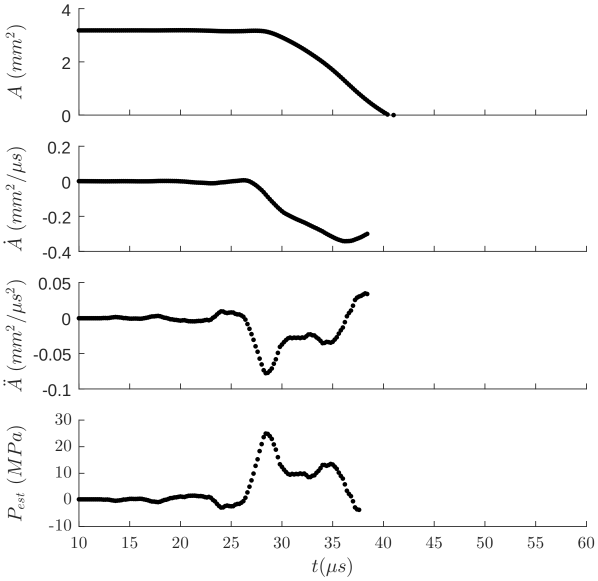

Figure D.34: Test #570. 1:20 PDMS.

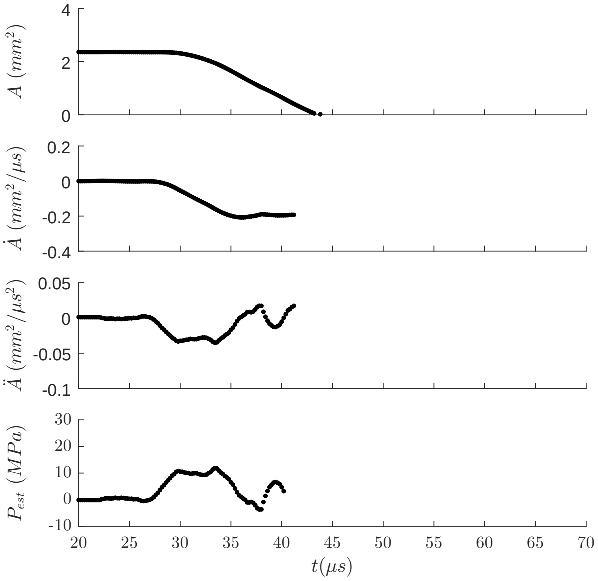

Figure D.35: Test #572. 1:20 PDMS.

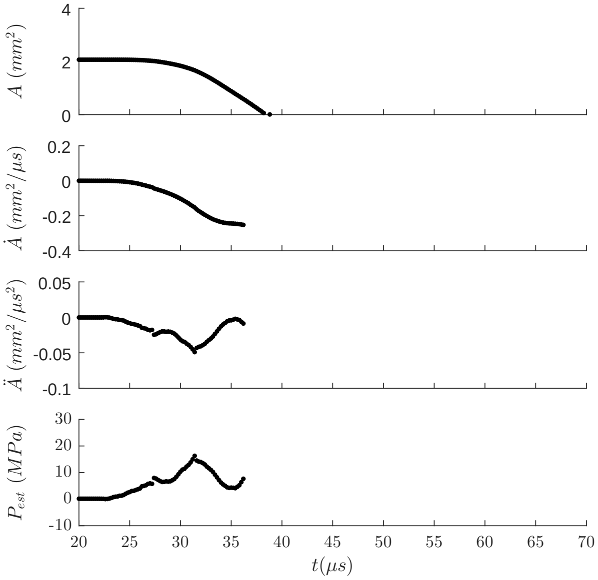

Figure D.36: Test #573. 1:20 PDMS.

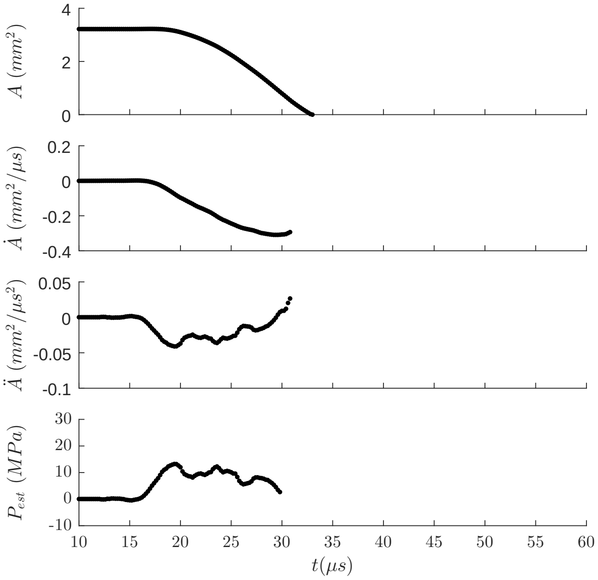

Figure D.37: Test #580. 1:30 PDMS.

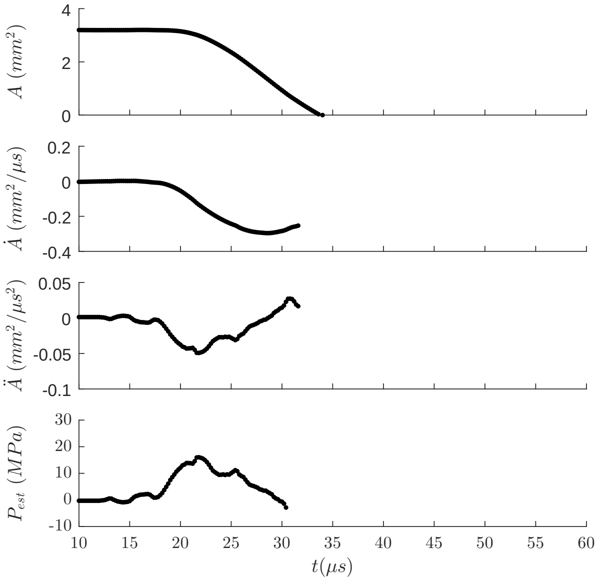

Figure D.38: Test #585. 1:30 PDMS.

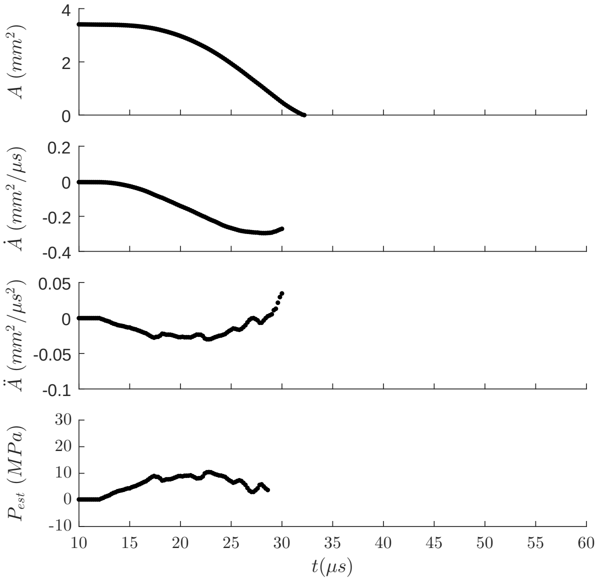

Figure D.39: Test #593. 1:30 PDMS.

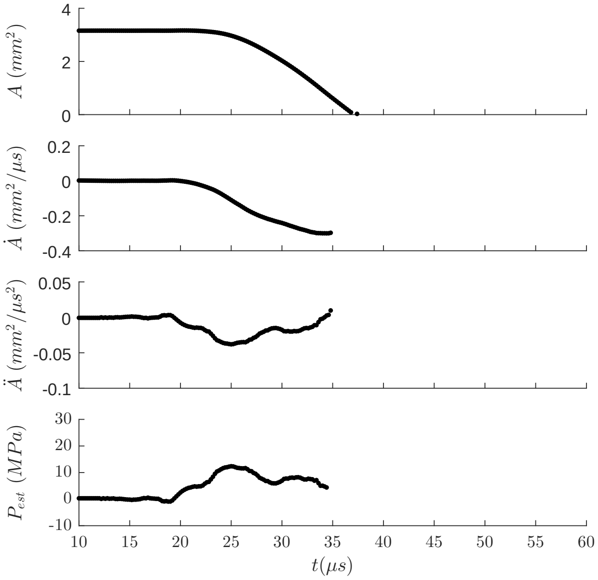

Figure D.40: Test #623. 1:30 PDMS.

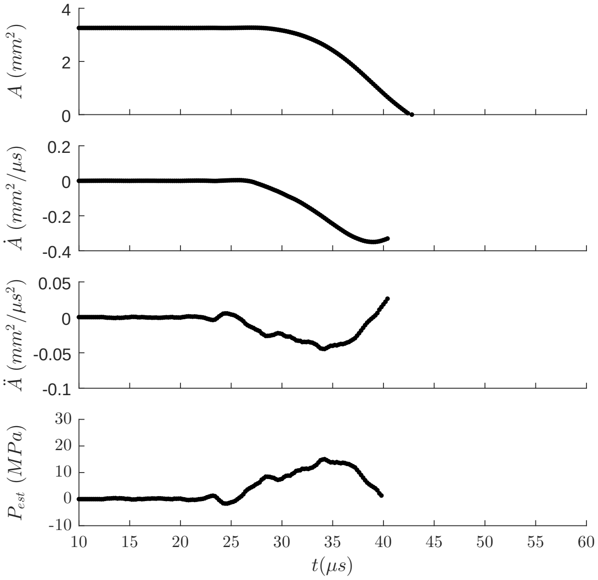

Figure D.41: Test #624. 1:30 PDMS.

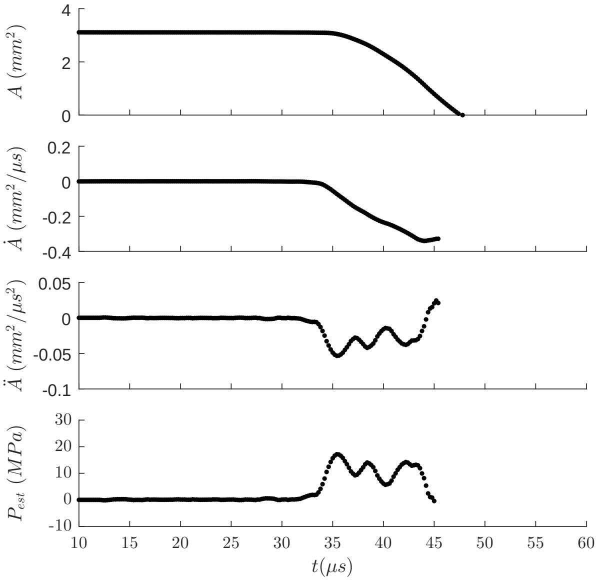

Figure D.42: Test #636. 1:30 PDMS.

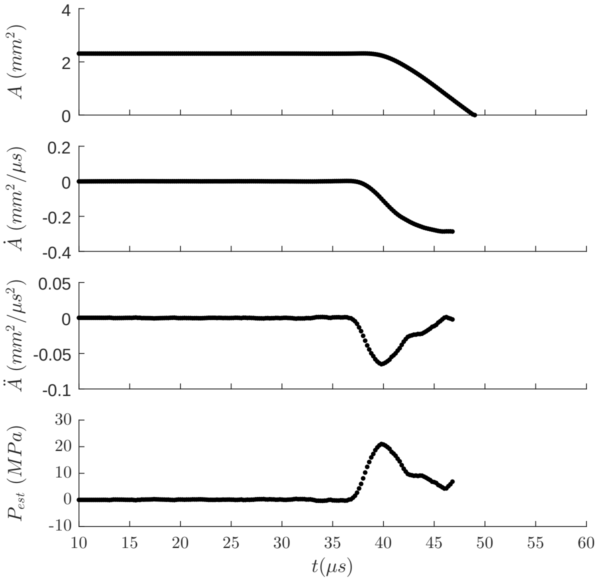

Figure D.43: Test #641. 1:30 PDMS.

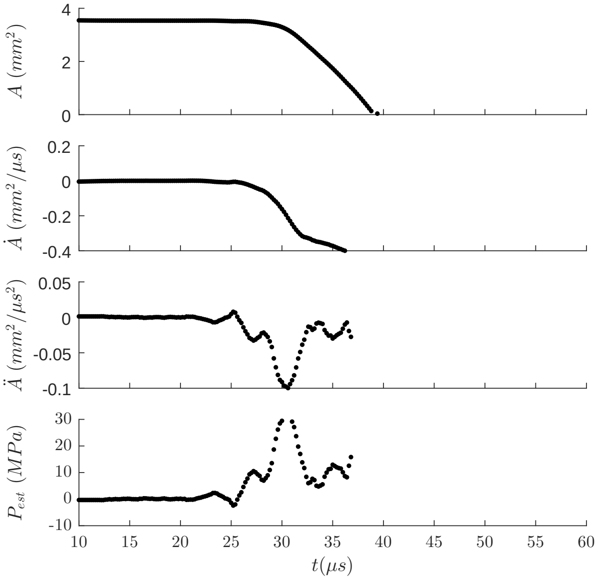

Figure D.44: Test #643. 1:30 PDMS.

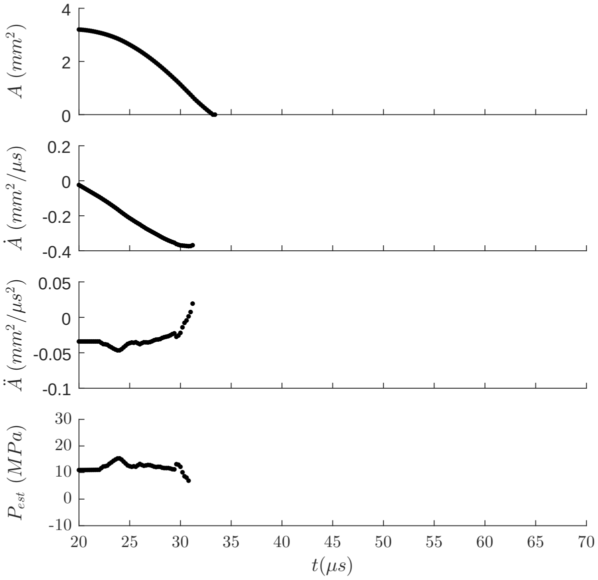

Figure D.45: Test #576. 1:40 PDMS.

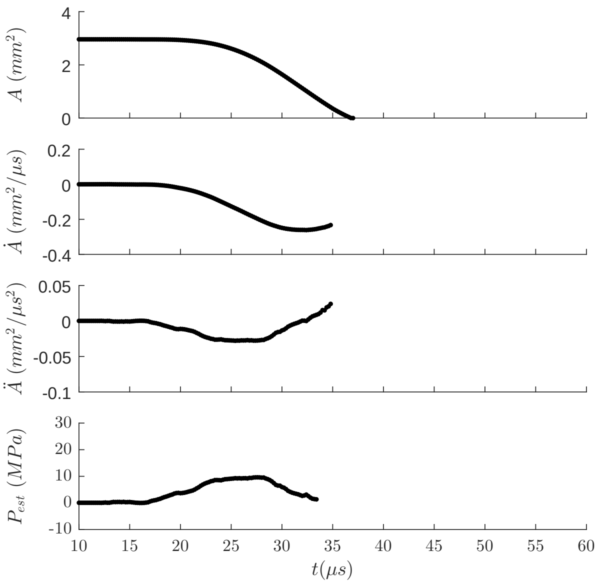

Figure D.46: Test #578. 1:40 PDMS.

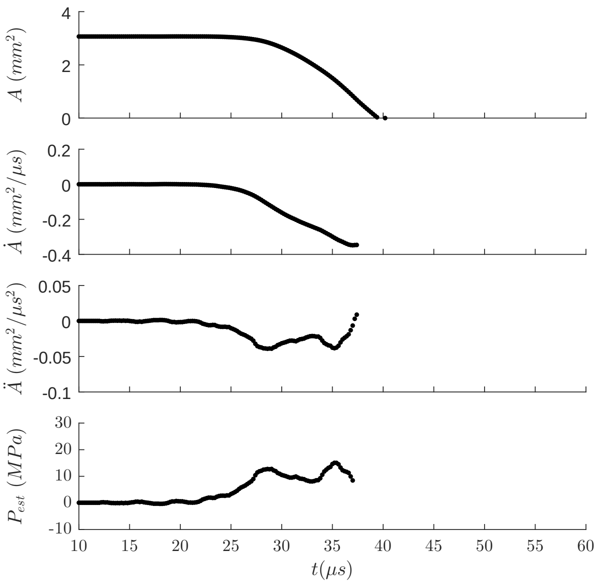

Figure D.47: Test #579. 1:40 PDMS.

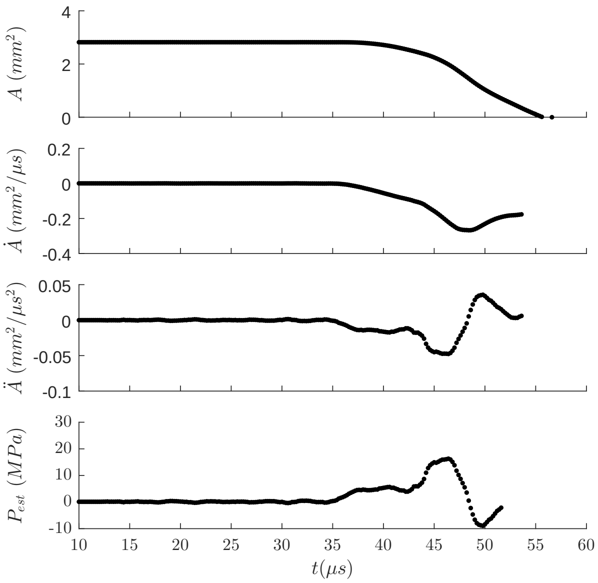

Figure D.48: Test #614. 1:40 PDMS.

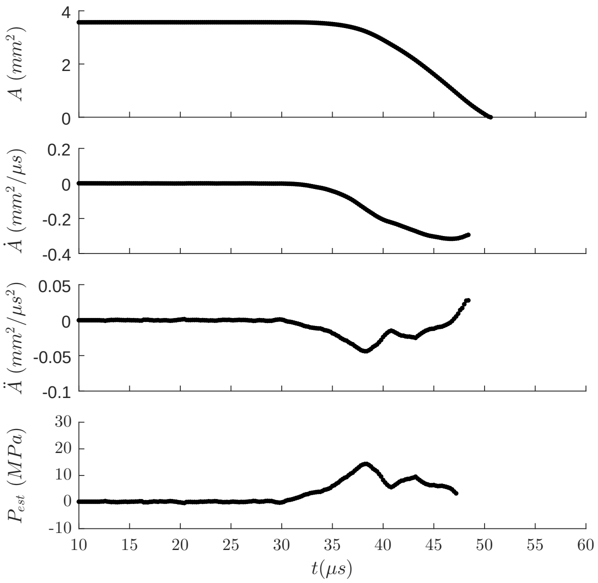

Figure D.49: Test #616. 1:40 PDMS.

D.4 Two Boundary

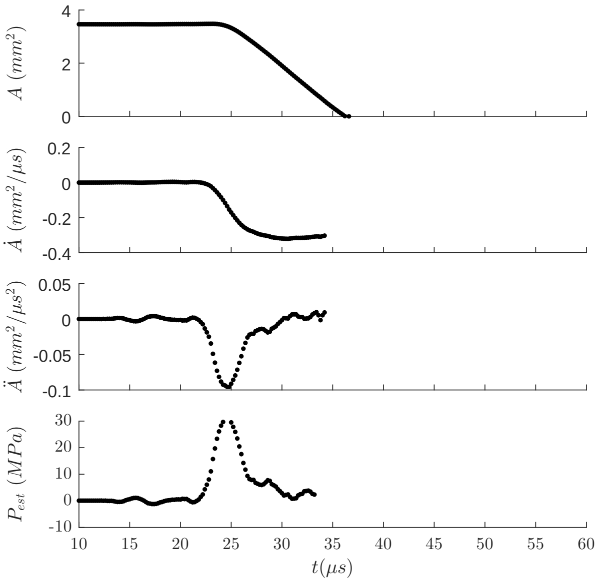

Figure D.50: Test #606. 1:20 PDMS.

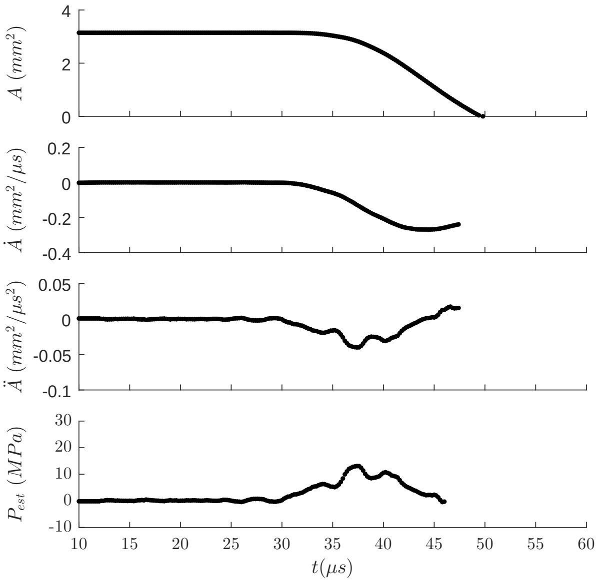

Figure D.51: Test #620. 1:20 PDMS.

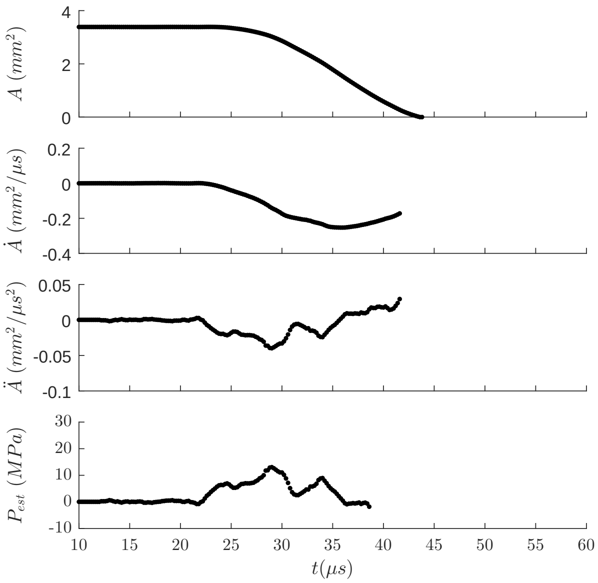

Figure D.52: Test #622. 1:20 PDMS.

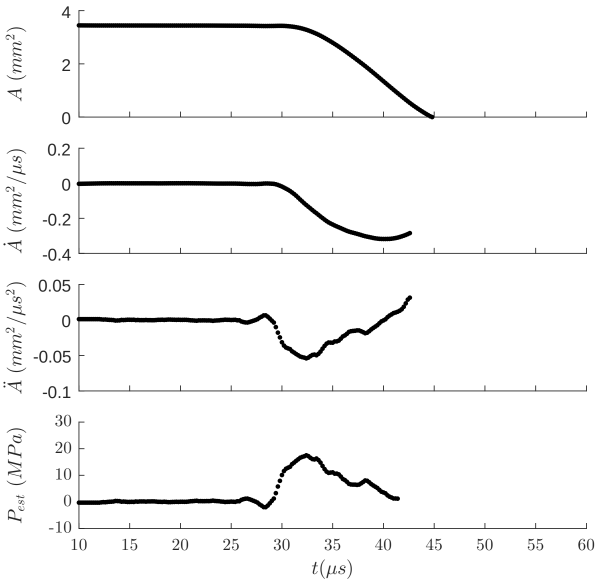

Figure D.53: Test #637. 1:20 PDMS.

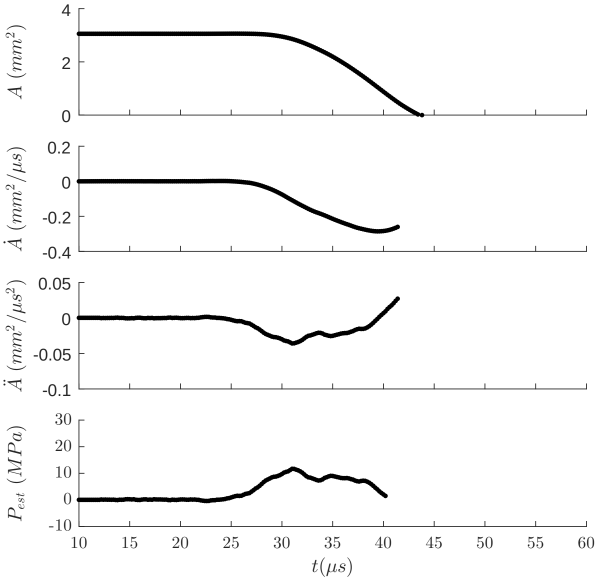

Figure D.54: Test #619. 1:30 PDMS.

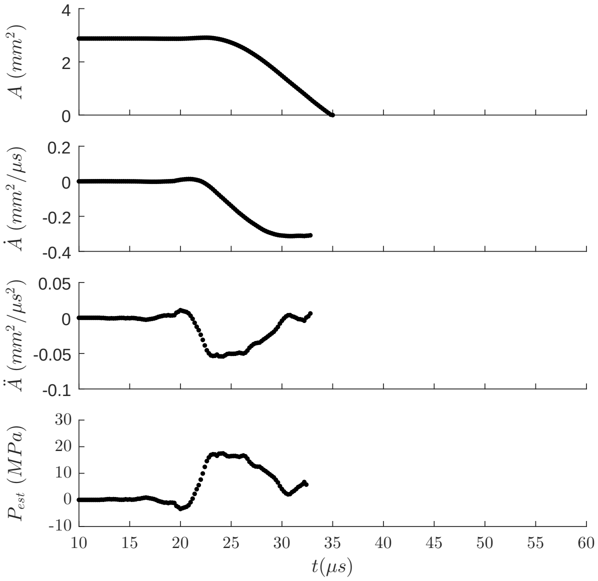

Figure D.55: Test #621. 1:30 PDMS.

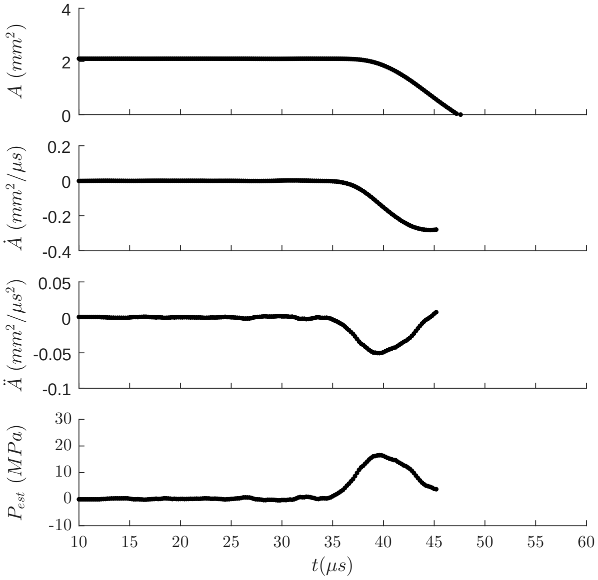

Figure D.56: Test #634. 1:30 PDMS.

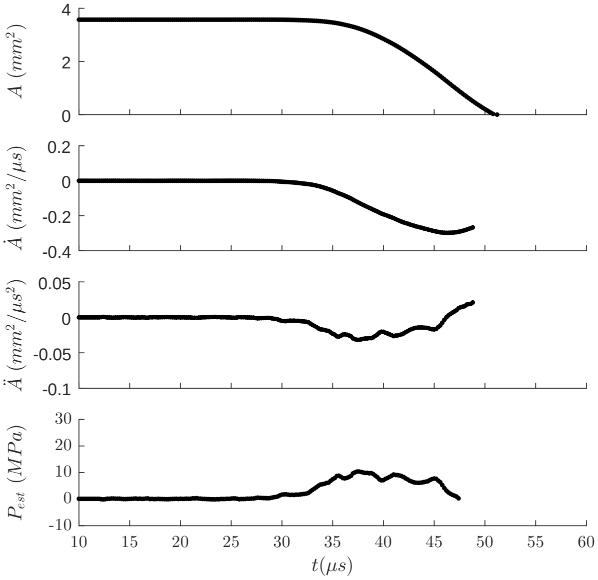

Figure D.57: Test #635. 1:30 PDMS.

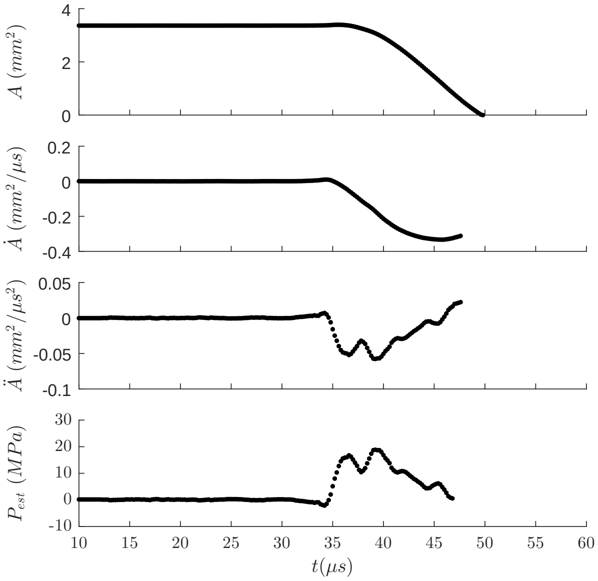

Figure D.58: Test #618. 1:40 PDMS.

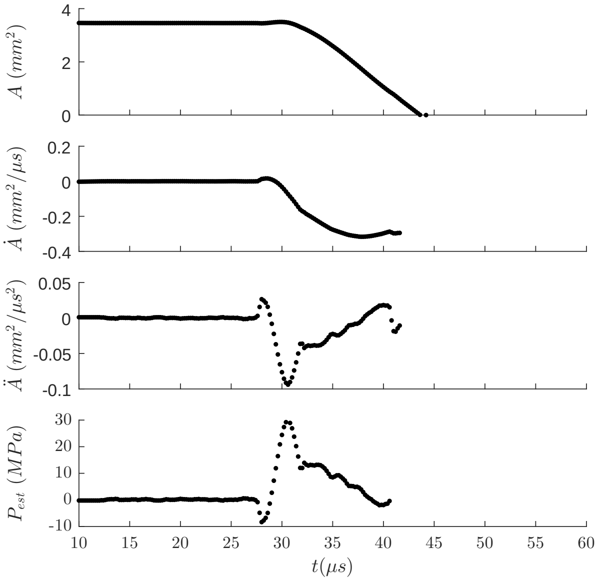

Figure D.59: Test #633. 1:40 PDMS.

D.5 Aluminum Boundary

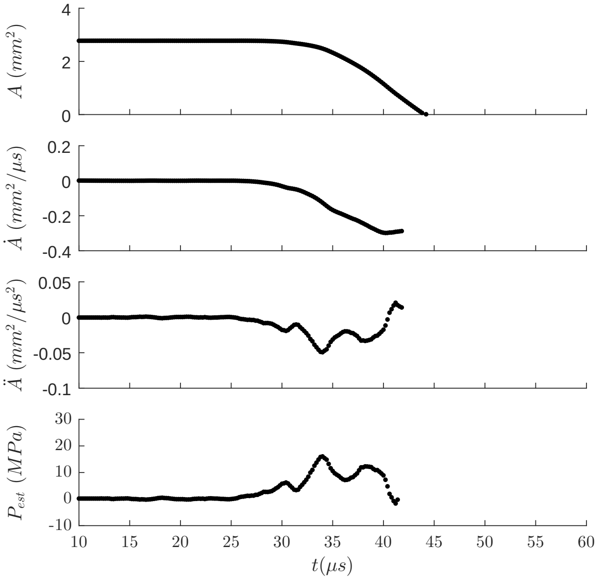

Figure D.60: Test #653.

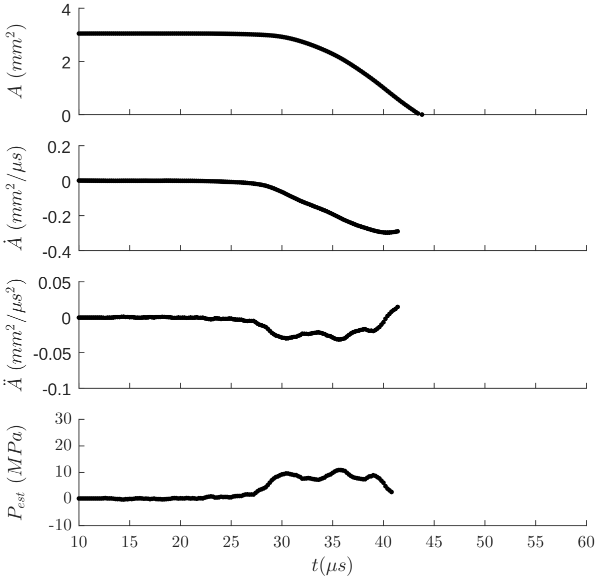

Figure D.61: Test #654.

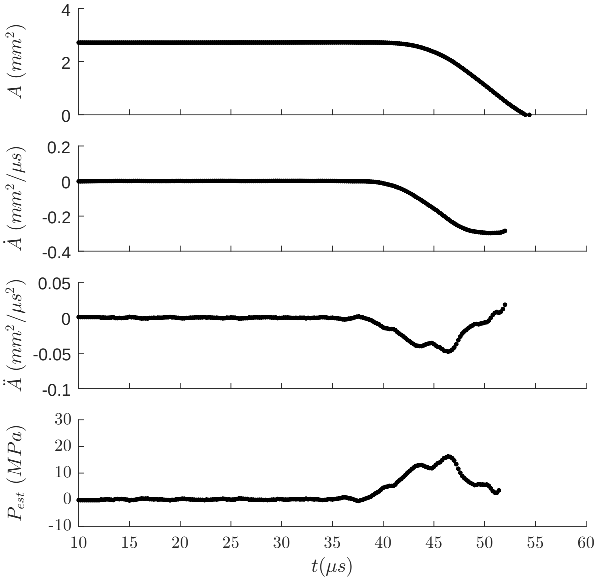

Figure D.62: Test #657.

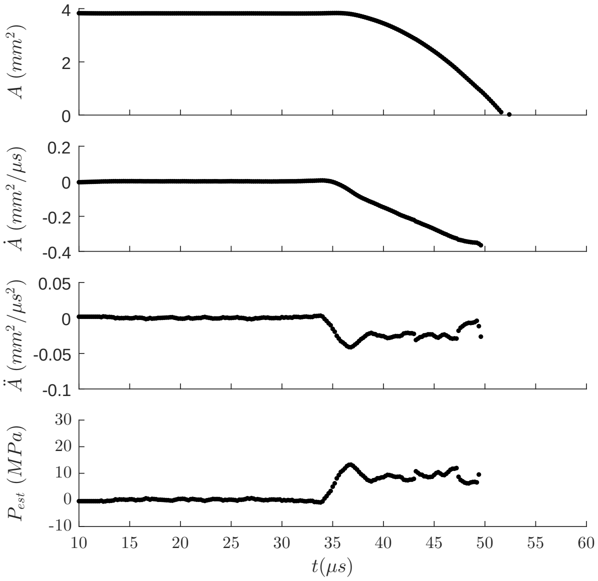

Figure D.63: Test #658.

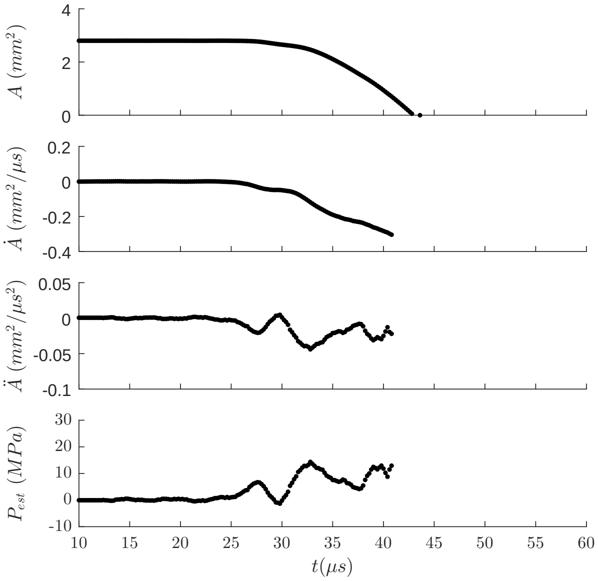

Figure D.64: Test #660.

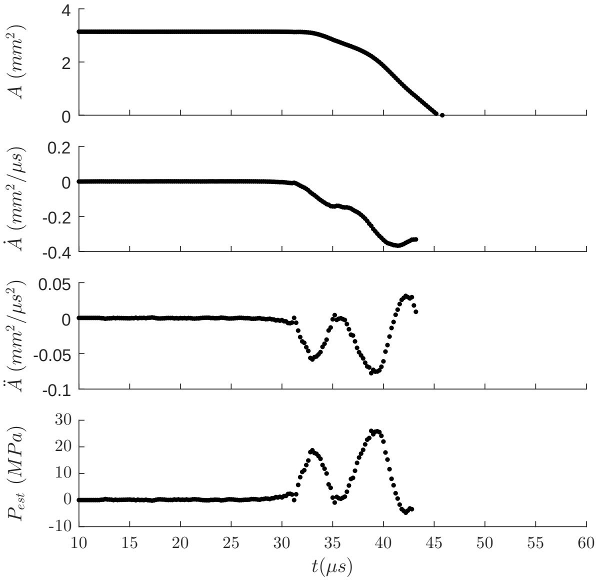

Figure D.65: Test #661.

APPENDIX E

COMPLETE SHADOWGRAPH EXPERIMENT-THEORY COMPARISONS

E.1 No Boundary

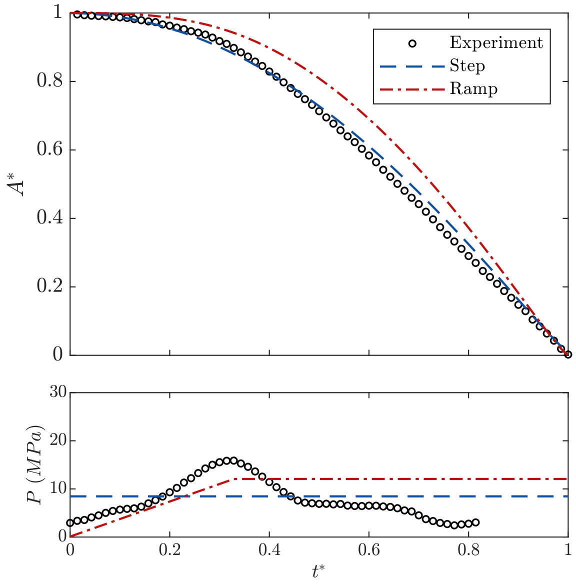

Figure E.1: Test #560

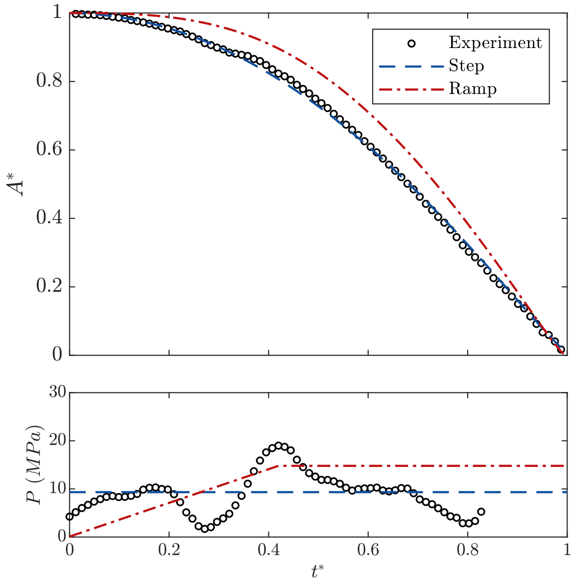

Figure E.2: Test #561

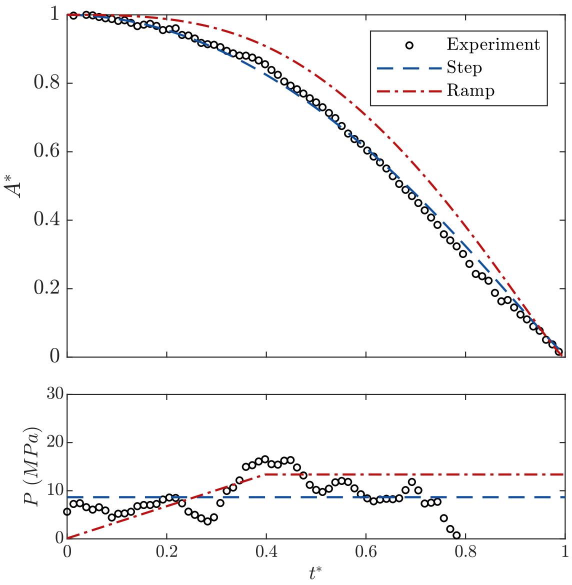

Figure E.3: Test #562.

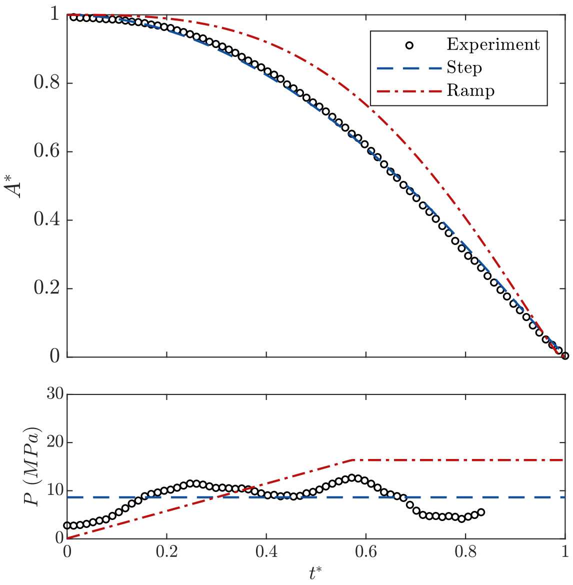

Figure E.4: Test #563.

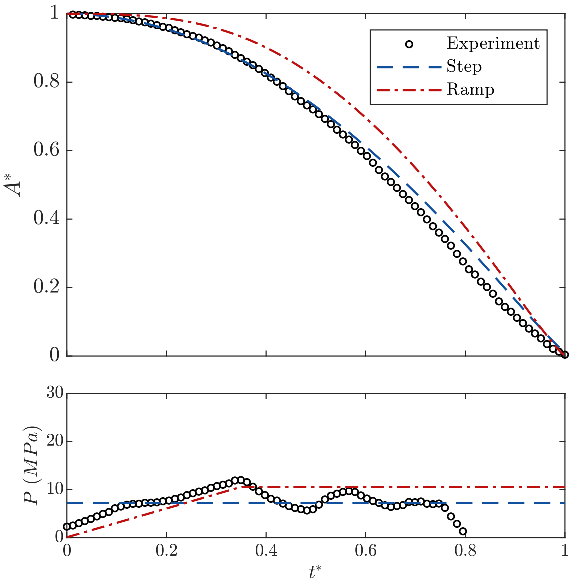

Figure E.5: Test #564.

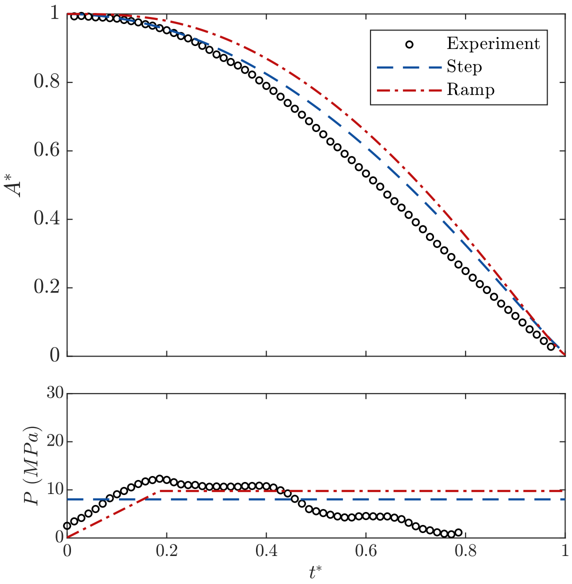

Figure E.6: Test #626.

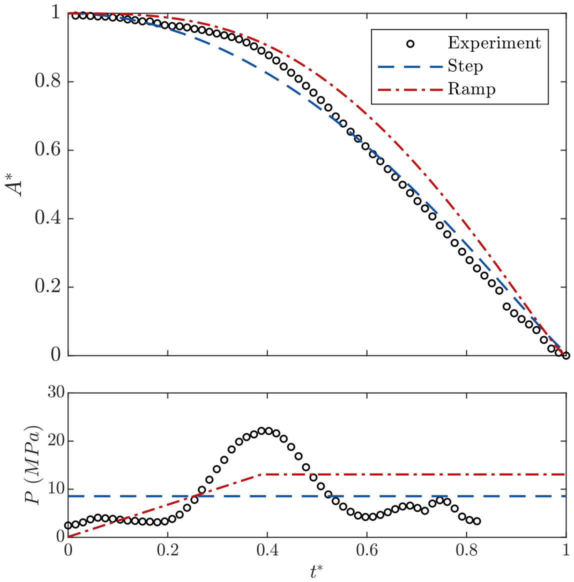

Figure E.7: Test #627.

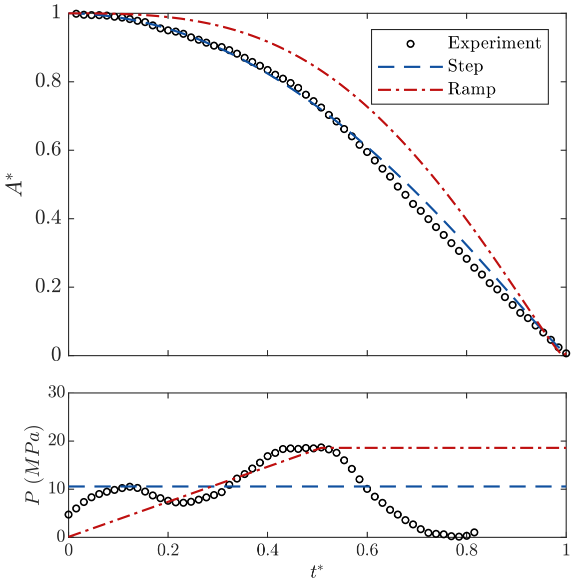

Figure E.8: Test #629.

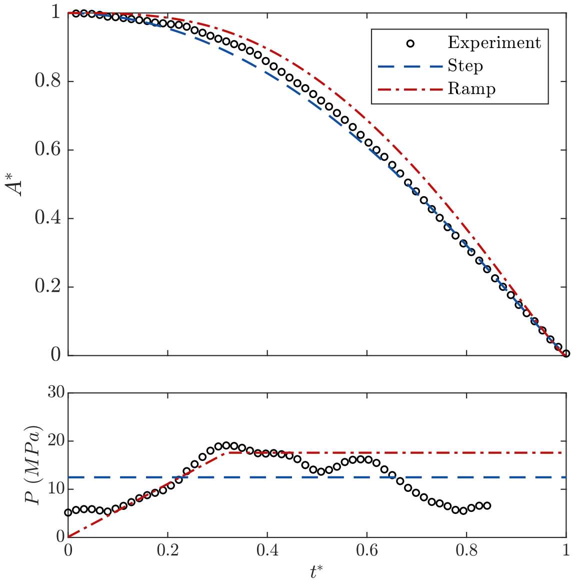

Figure E.9: Test #630.

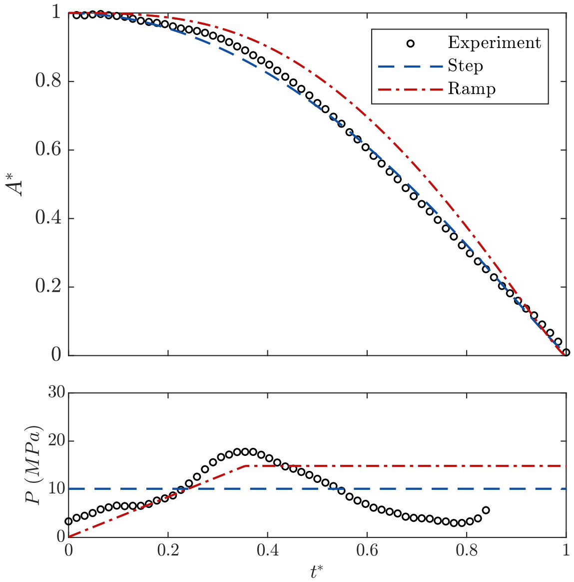

Figure E.10: Test #631.

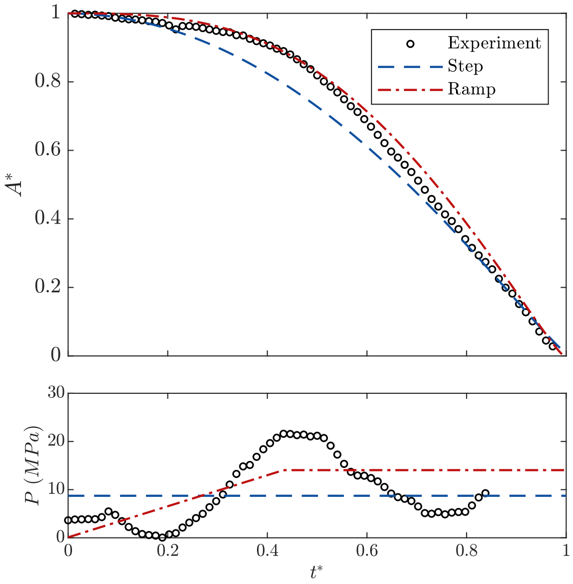

Figure E.11: Test #664.

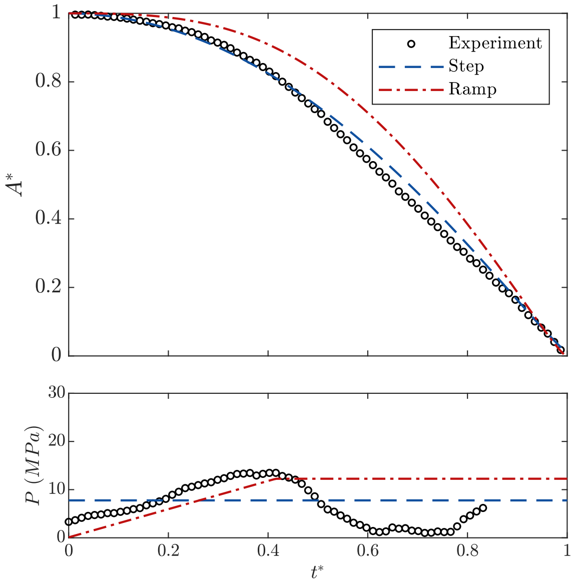

Figure E.12: Test #665.

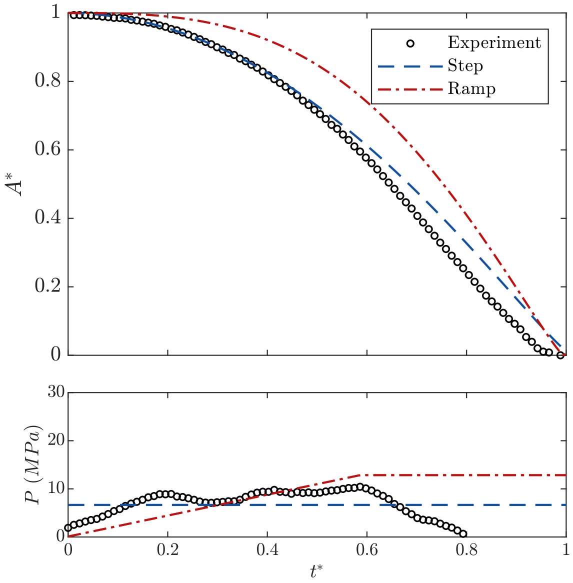

Figure E.13: Test #666.

E.2 Downstream Boundary

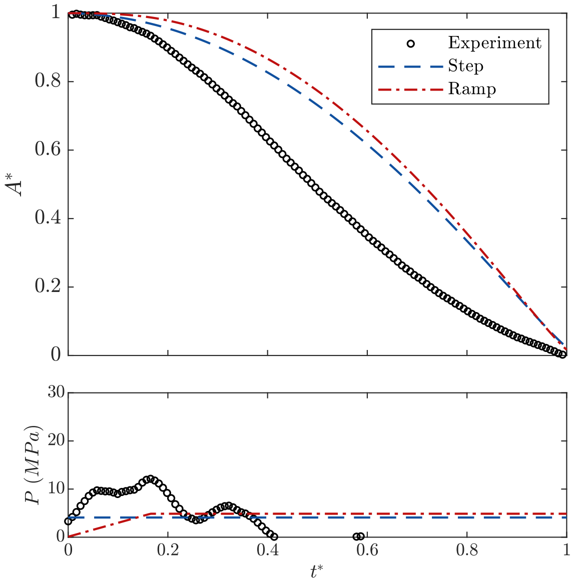

Figure E.14: Test #594. 1:20 PDMS.

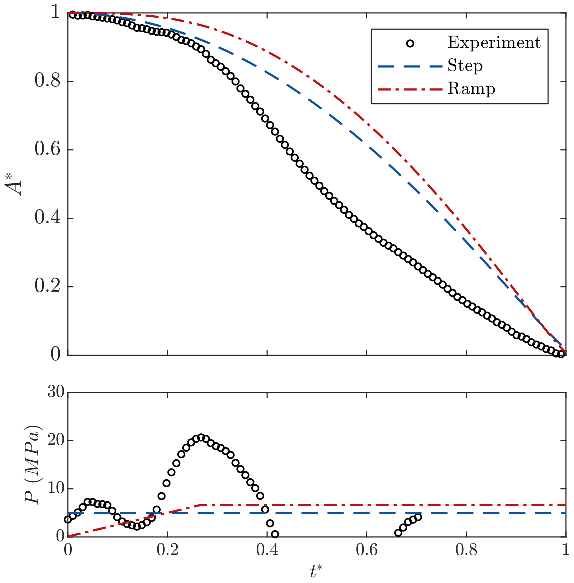

Figure E.15: Test #601. 1:20 PDMS.

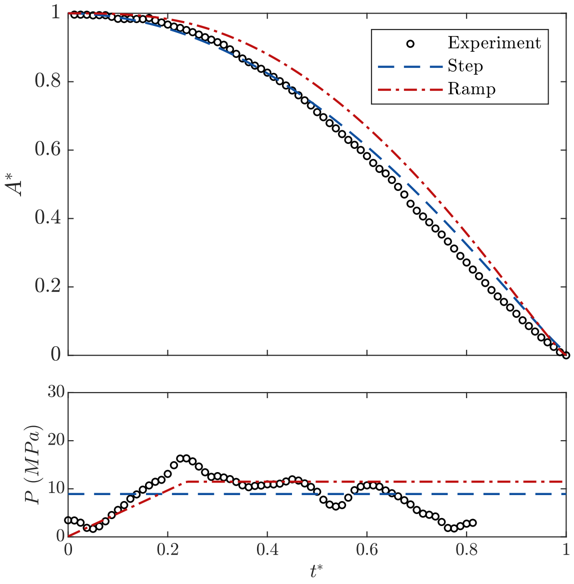

Figure E.16: Test #639. 1:20 PDMS.

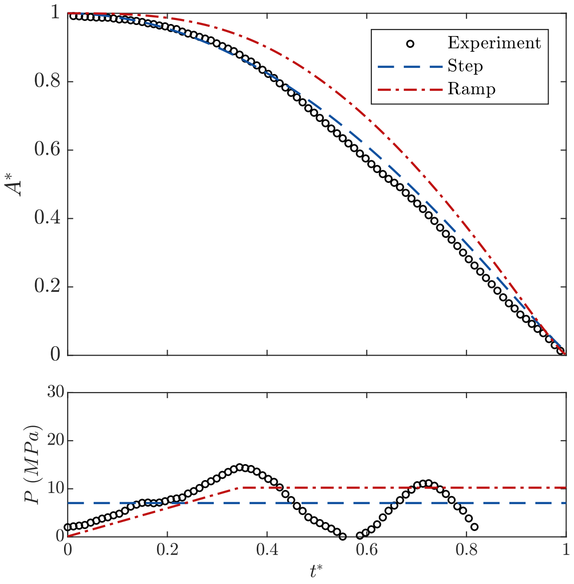

Figure E.17: Test #640. 1:20 PDMS.

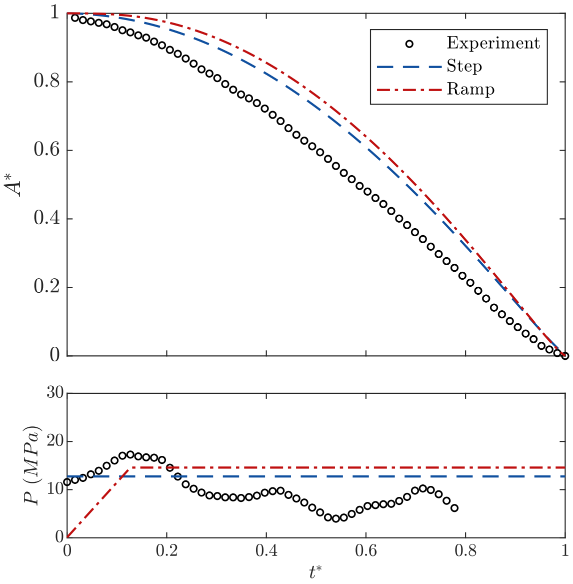

Figure E.18: Test #645. 1:20 PDMS.

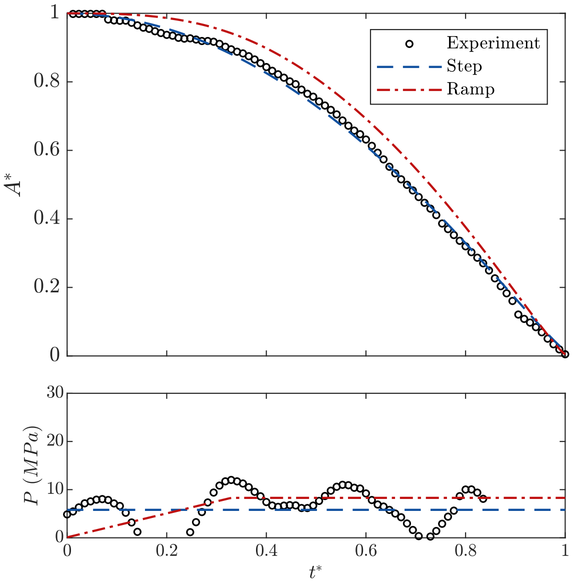

Figure E.19: Test #646. 1:20 PDMS.

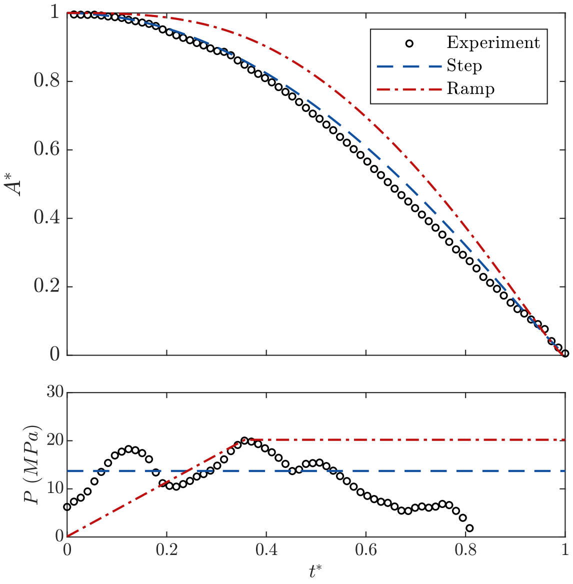

Figure E.20: Test #670. 1:20 PDMS.

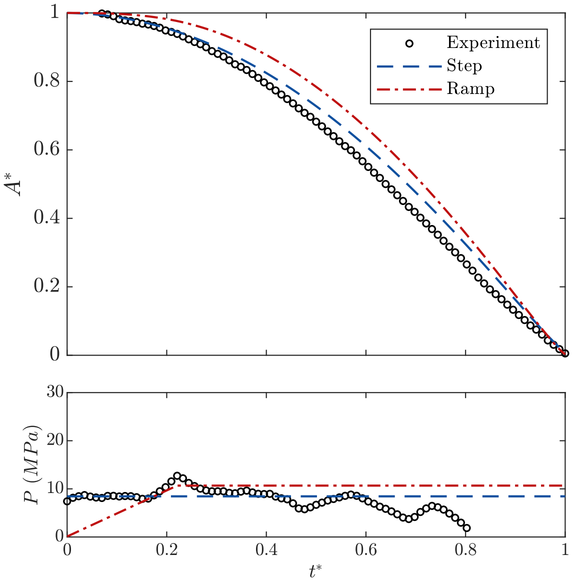

Figure E.21: Test #638. 1:30 PDMS.

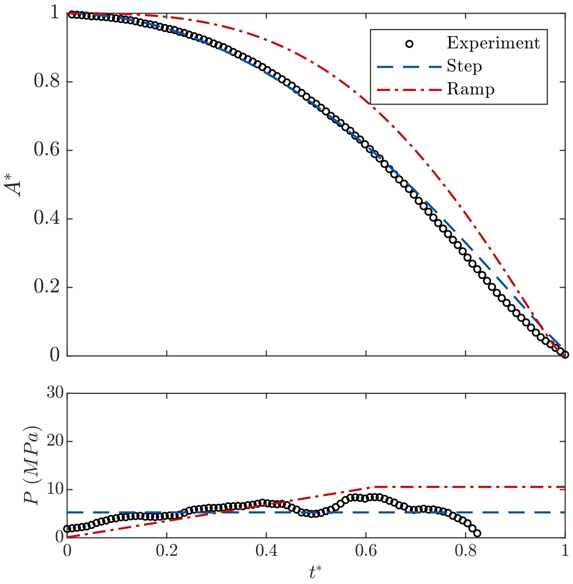

Figure E.22: Test #647. 1:30 PDMS.

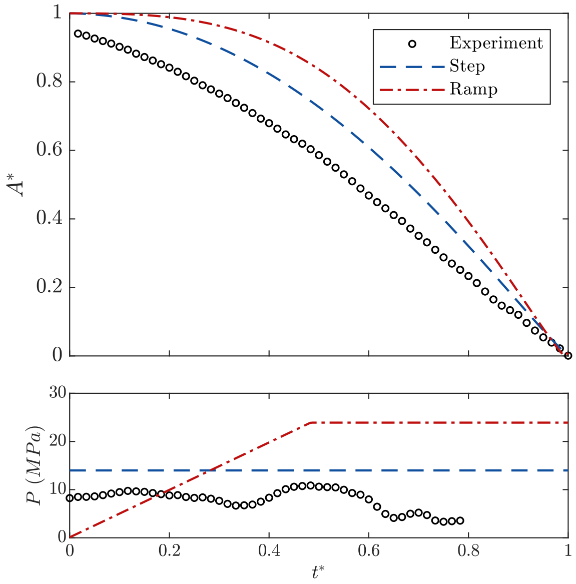

Figure E.23: Test #648. 1:30 PDMS.

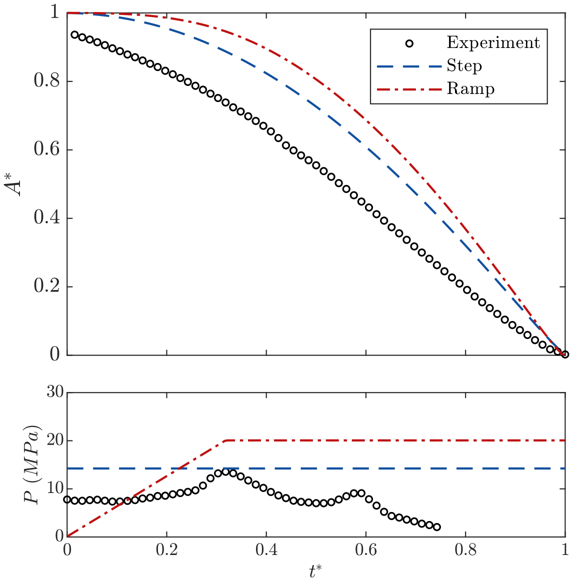

Figure E.24: Test #649. 1:30 PDMS.

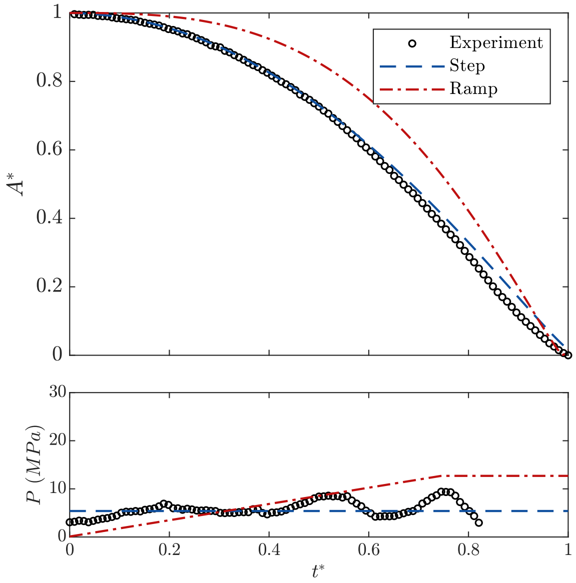

Figure E.25: Test #672. 1:30 PDMS.

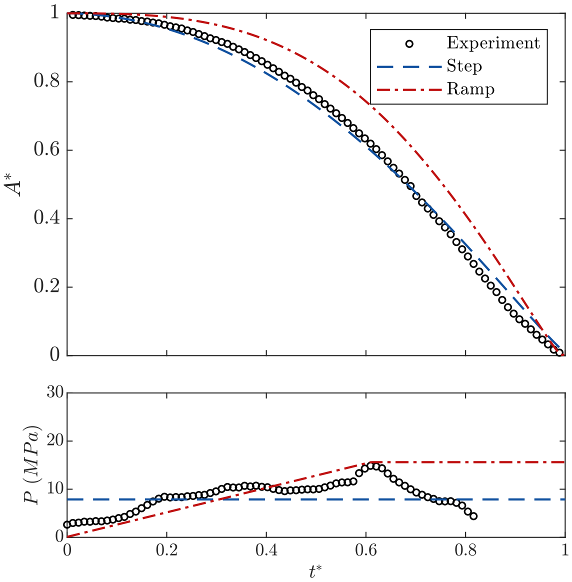

Figure E.26: Test #673. 1:30 PDMS.

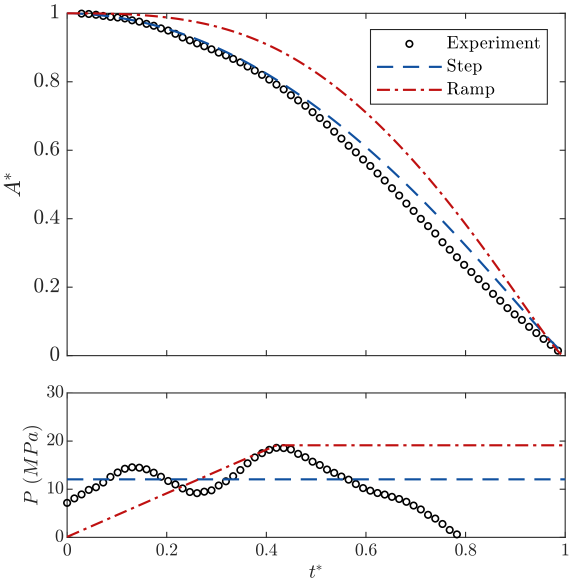

Figure E.27: Test #589. 1:40 PDMS.

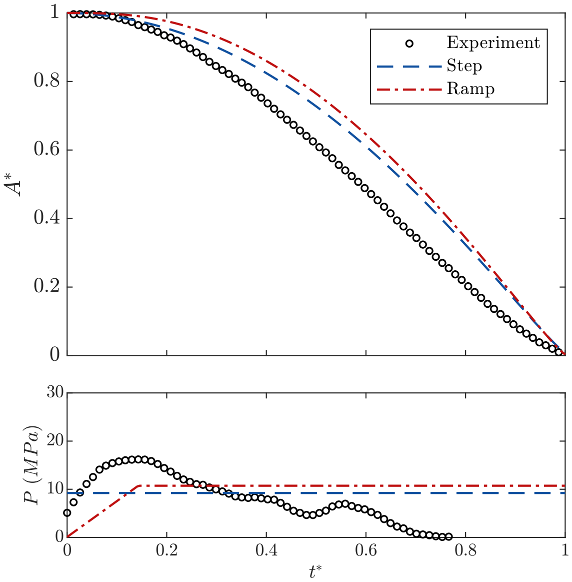

Figure E.28: Test #596. 1:40 PDMS.

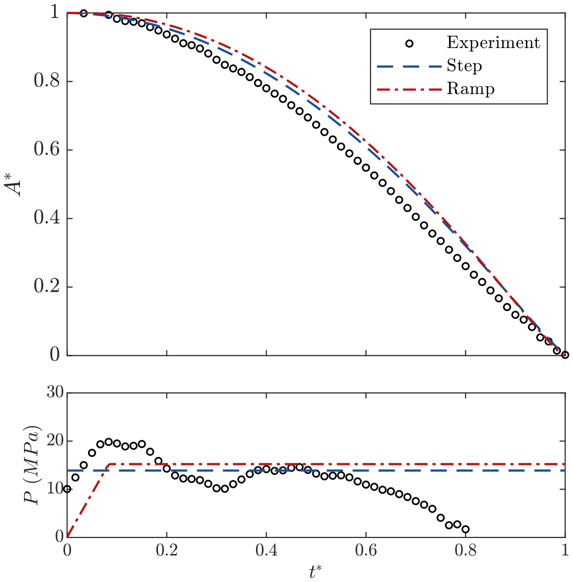

Figure E.29: Test #650. 1:40 PDMS.

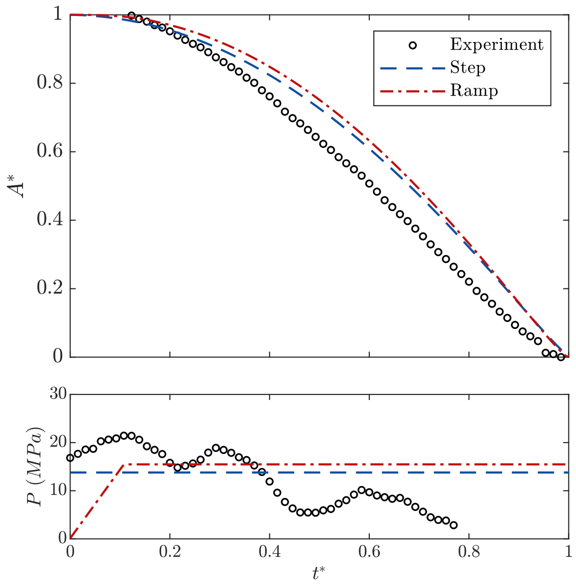

Figure E.30: Test #651. 1:40 PDMS.

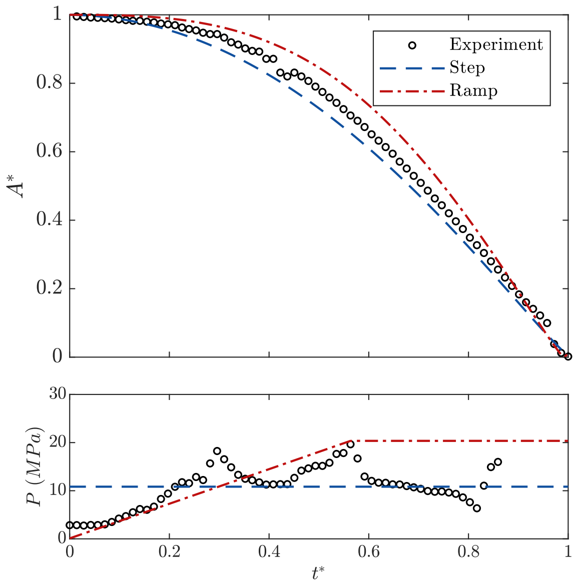

Figure E.31: Test #652. 1:40 PDMS.

E.3 Upstream Boundary

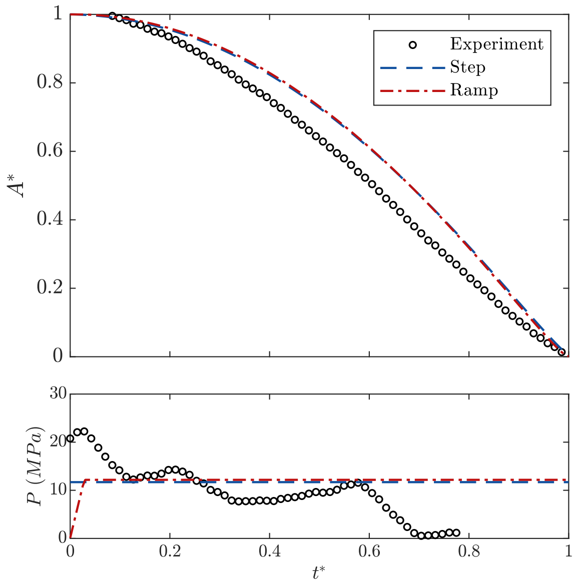

Figure E.32: Test #567. 1:20 PDMS.

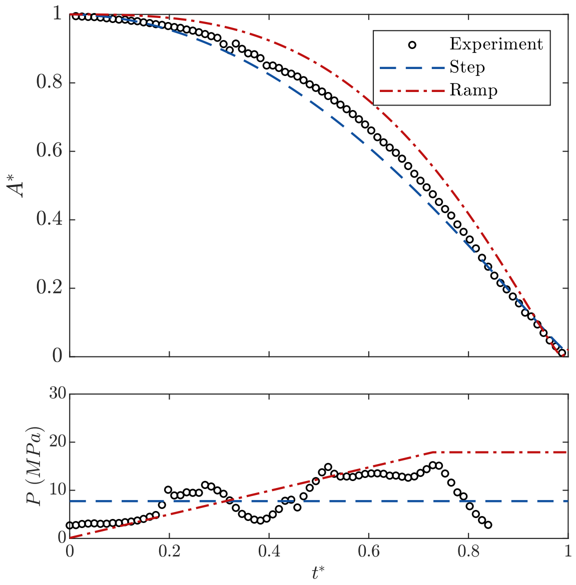

Figure E.33: Test #569. 1:20 PDMS.

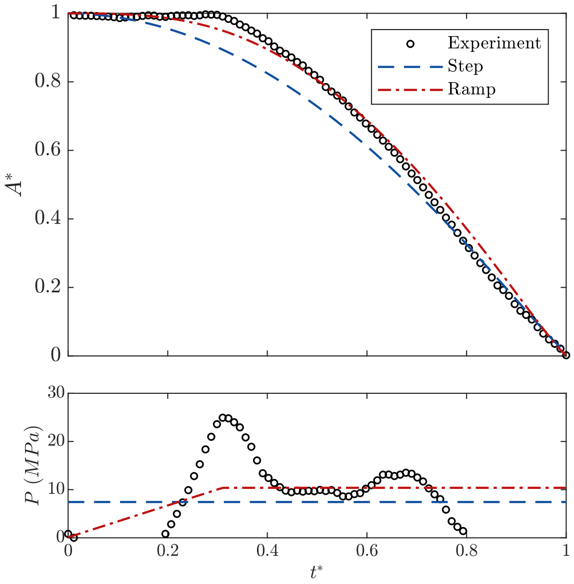

Figure E.34: Test #570. 1:20 PDMS.

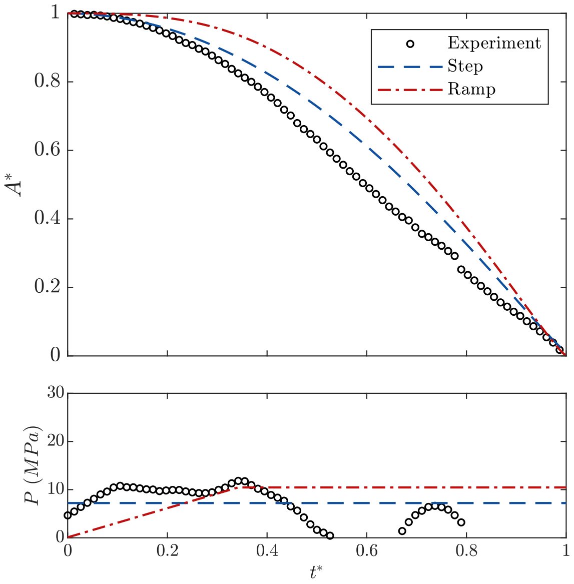

Figure E.35: Test #572. 1:20 PDMS.

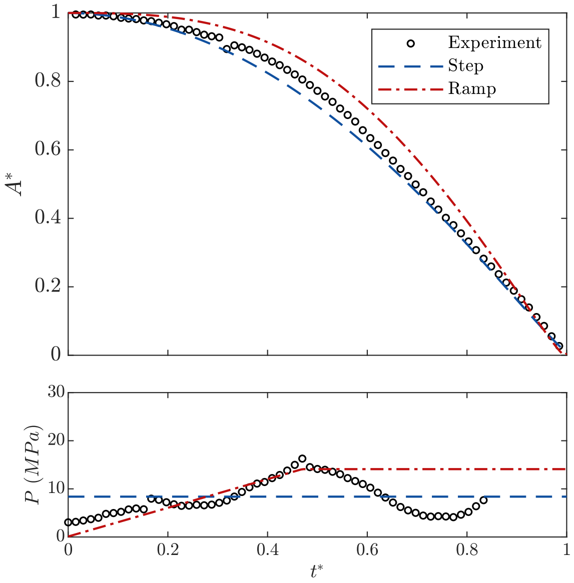

Figure E.36: Test #573. 1:20 PDMS.

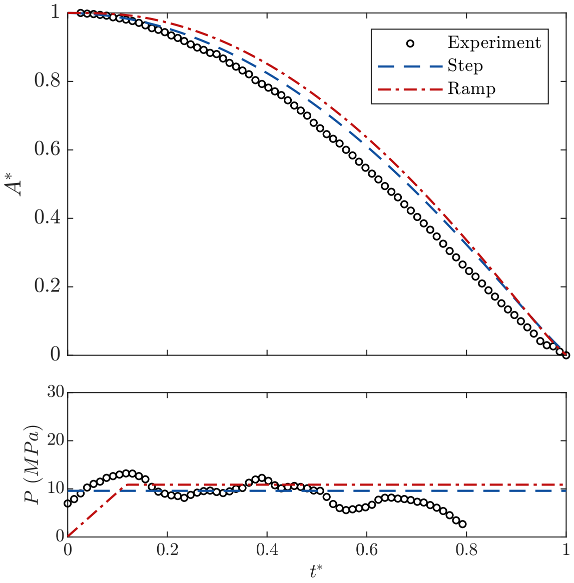

Figure E.37: Test #580. 1:30 PDMS.

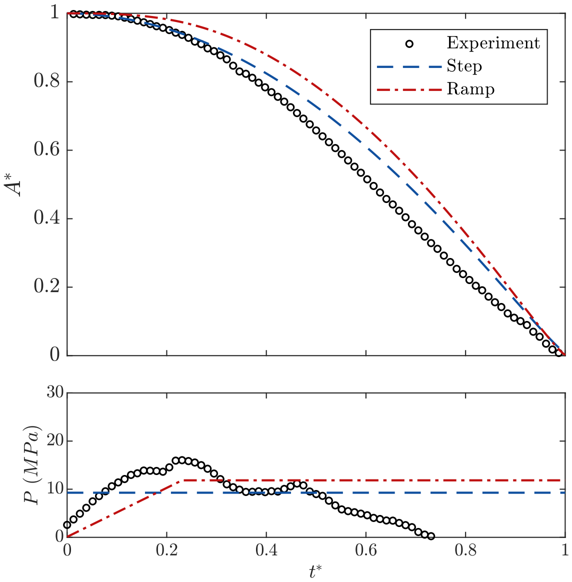

Figure E.38: Test #585. 1:30 PDMS.

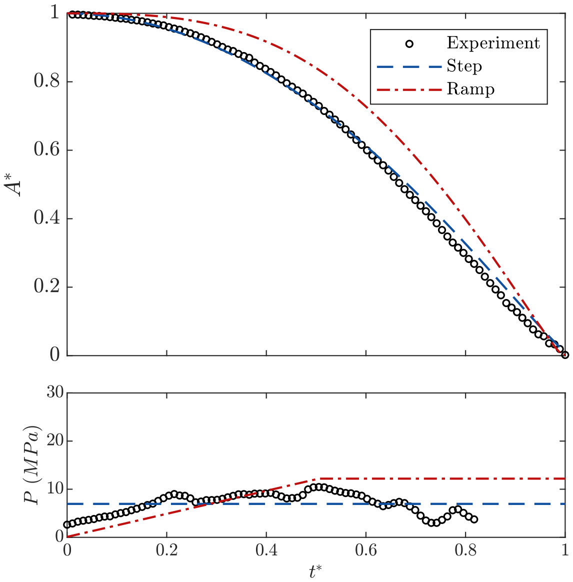

Figure E.39: Test #593. 1:30 PDMS.

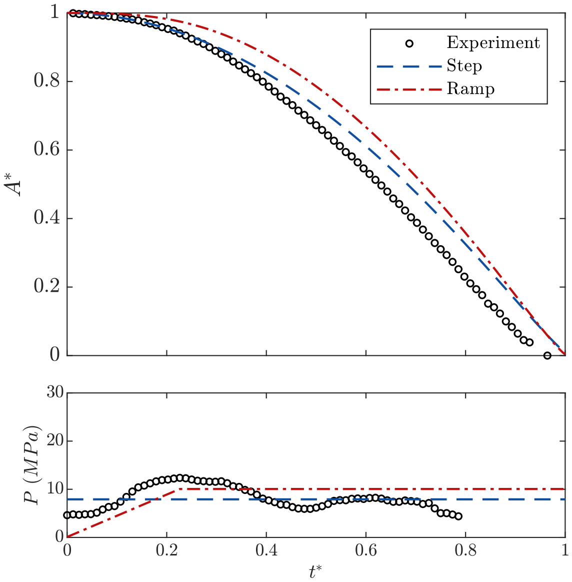

Figure E.40: Test #623. 1:30 PDMS.

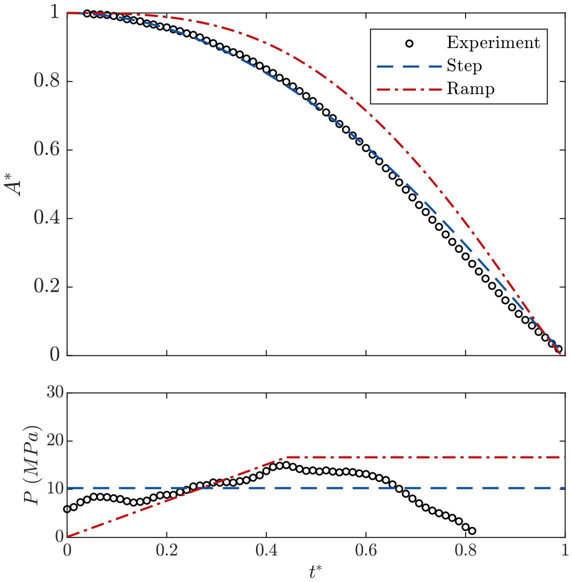

Figure E.41: Test #624. 1:30 PDMS.

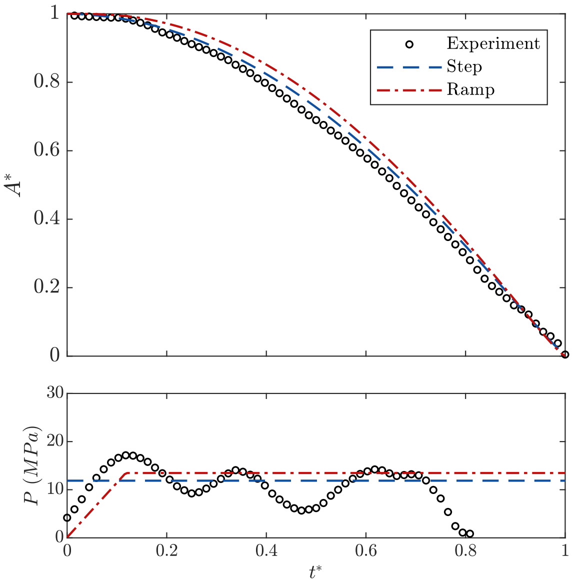

Figure E.42: Test #636. 1:30 PDMS.

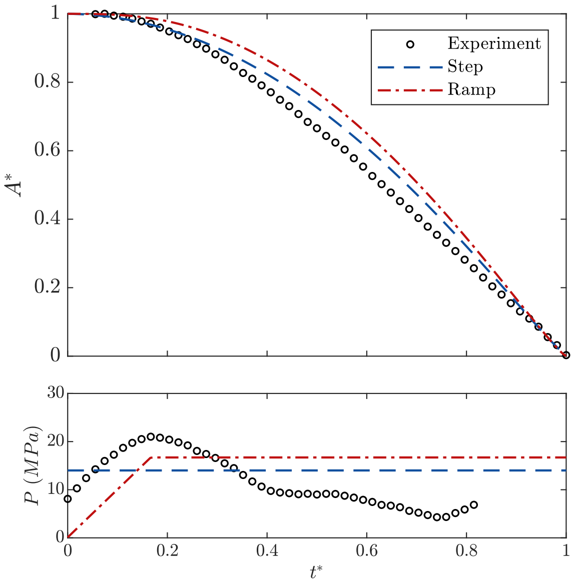

Figure E.43: Test #641. 1:30 PDMS.

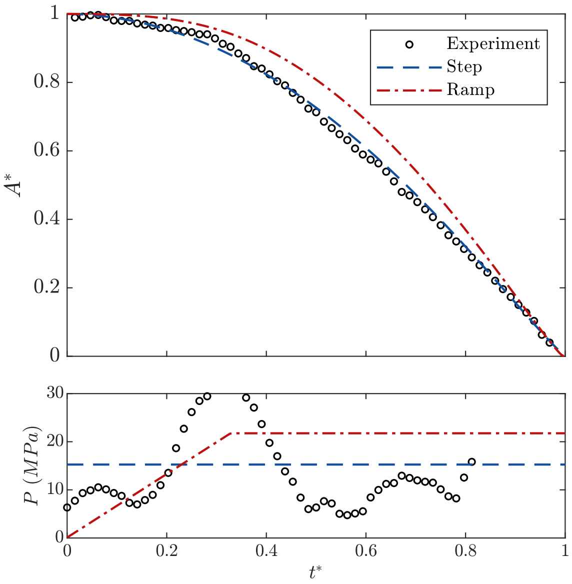

Figure E.44: Test #643. 1:30 PDMS.

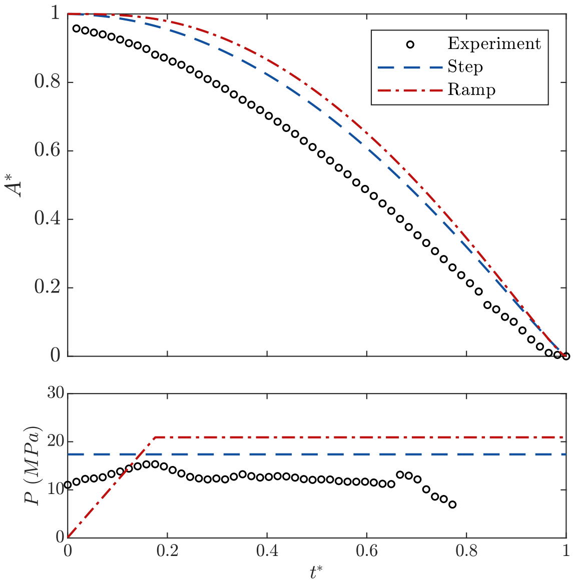

Figure E.45: Test #576. 1:40 PDMS.

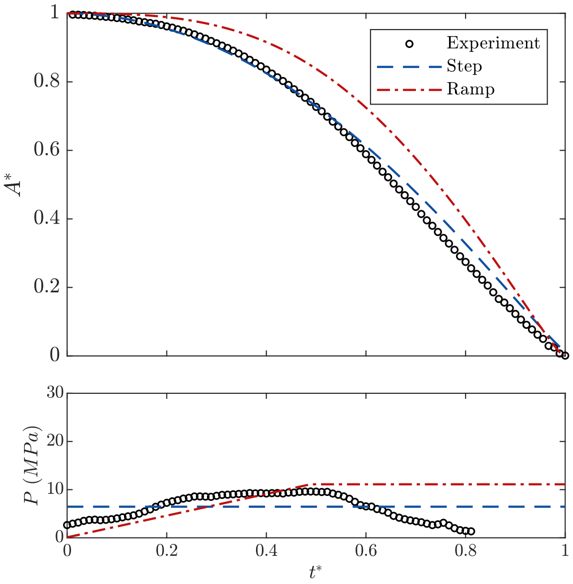

Figure E.46: Test #578. 1:40 PDMS.

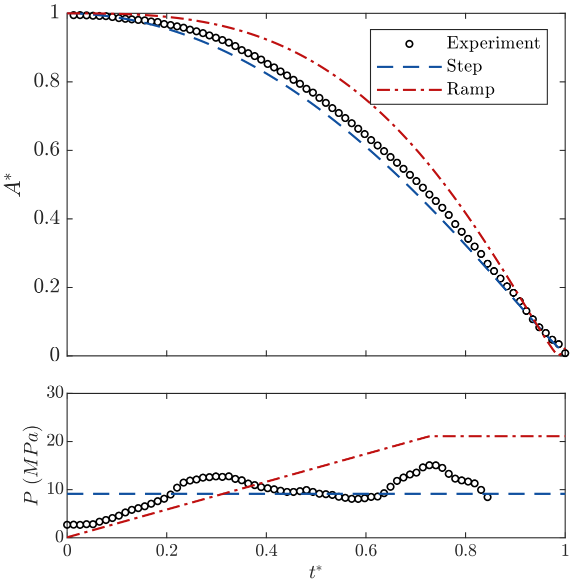

Figure E.47: Test #579. 1:40 PDMS.

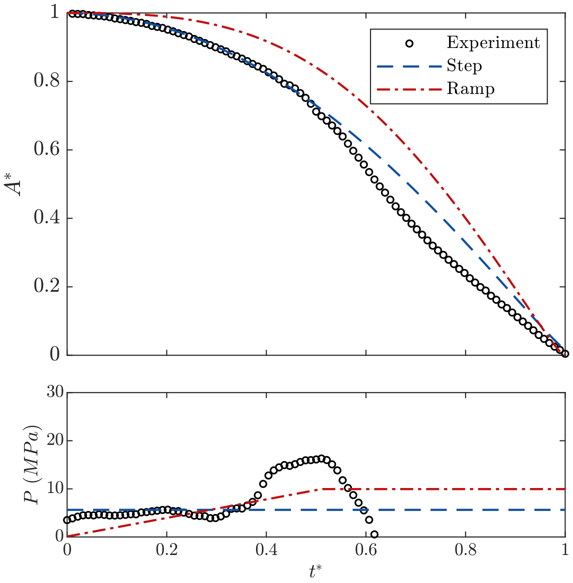

Figure E.48: Test #614. 1:40 PDMS.

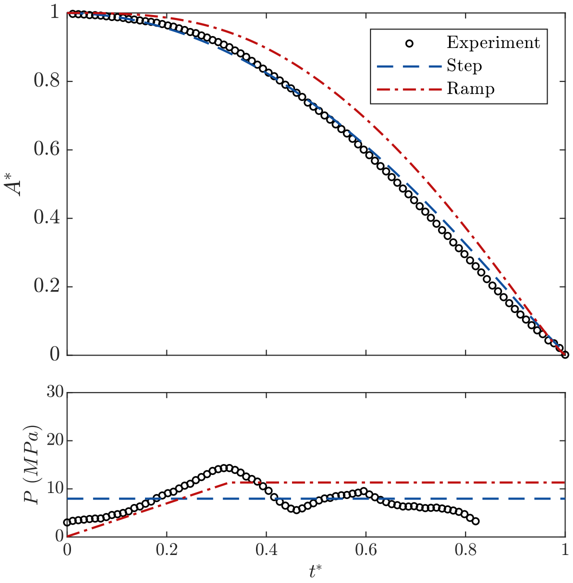

Figure E.49: Test #616. 1:40 PDMS.

E.4 Two Boundary

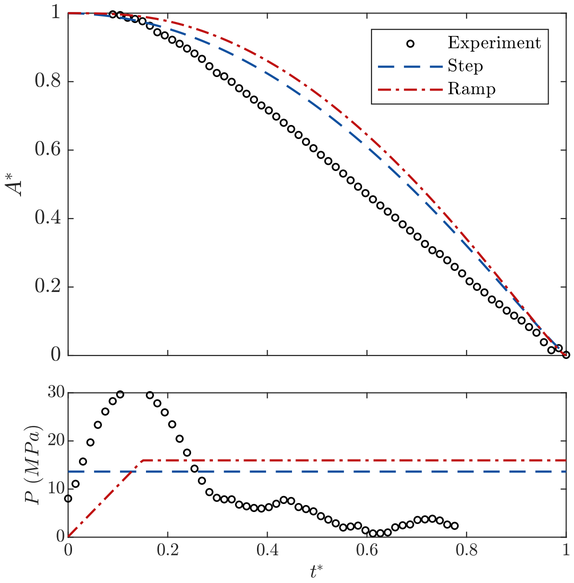

Figure E.50: Test #606. 1:20 PDMS.

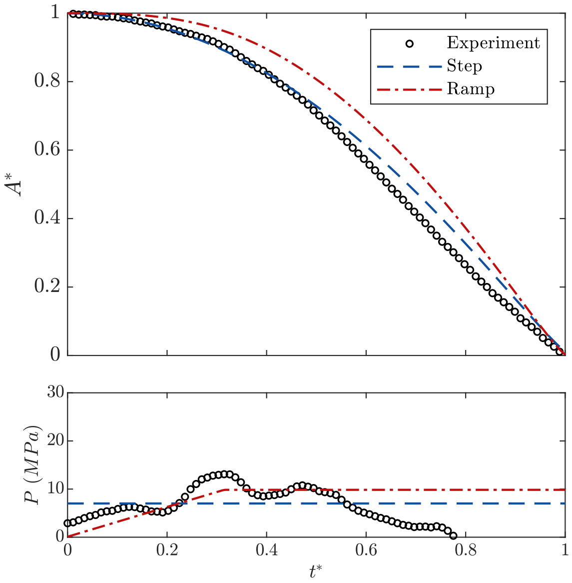

Figure E.51: Test #620. 1:20 PDMS.

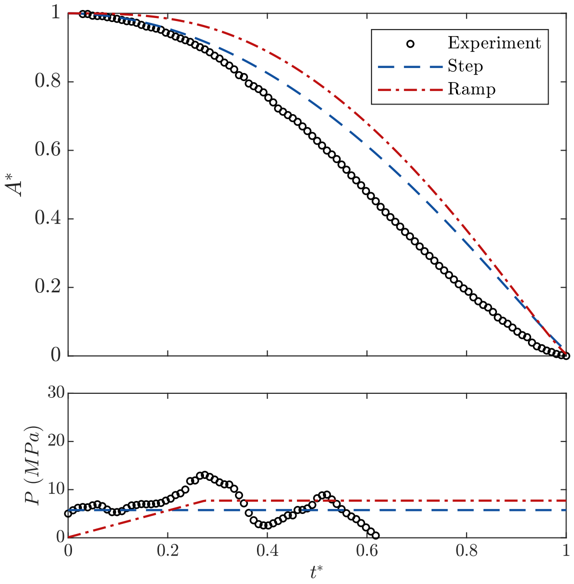

Figure E.52: Test #622. 1:20 PDMS.

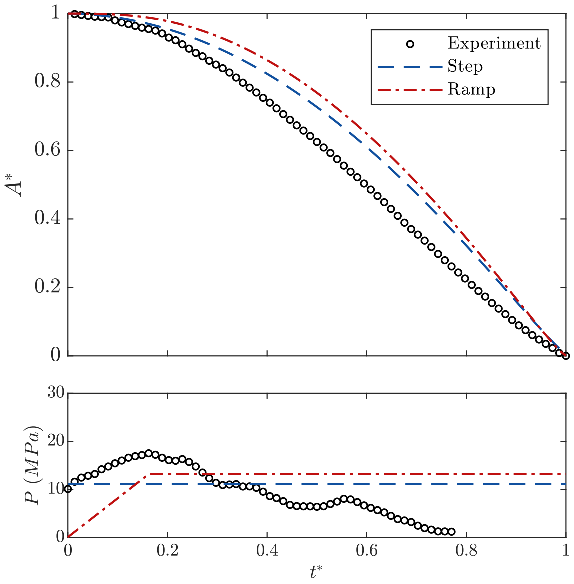

Figure E.53: Test #637. 1:20 PDMS.

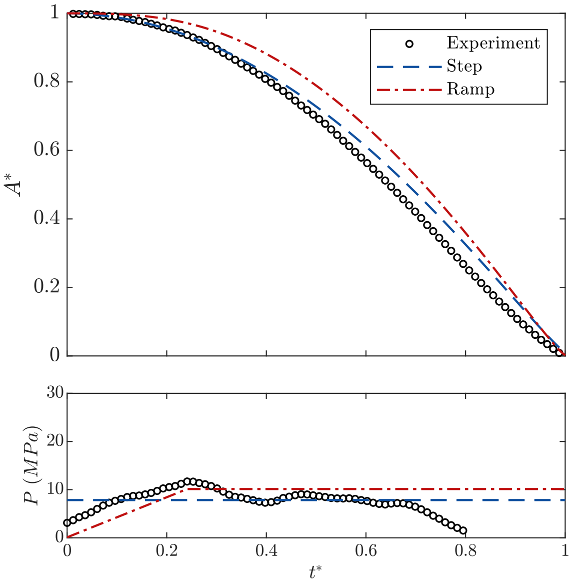

Figure E.54: Test #619. 1:30 PDMS.

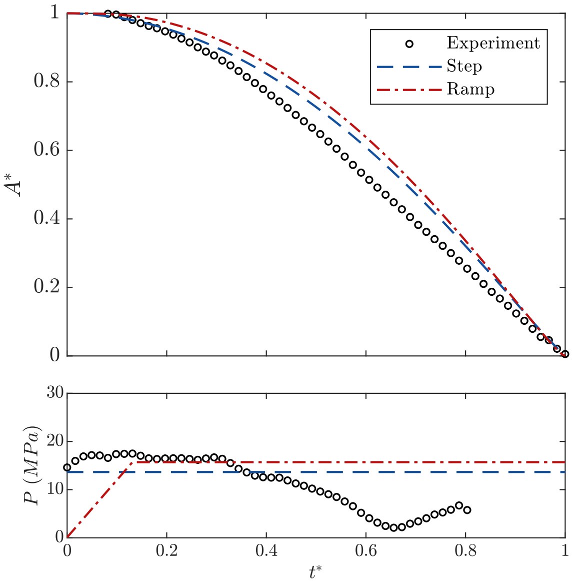

Figure E.55: Test #621. 1:30 PDMS.

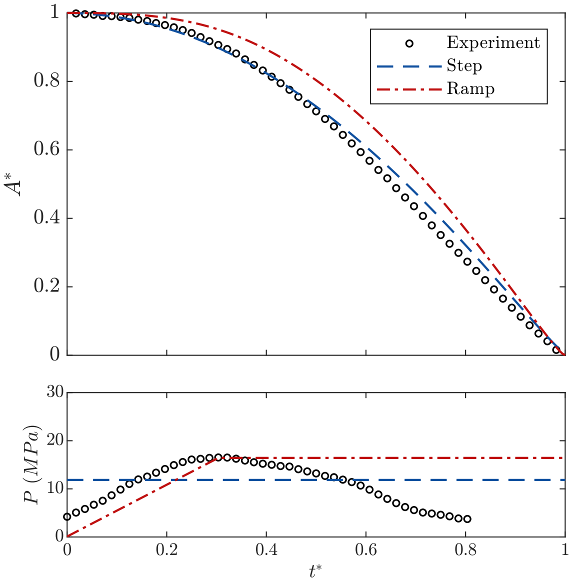

Figure E.56: Test #634. 1:30 PDMS.

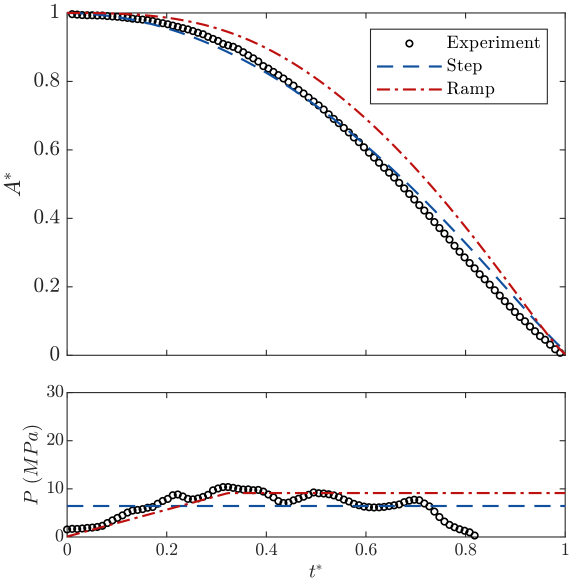

Figure E.57: Test #635. 1:30 PDMS.

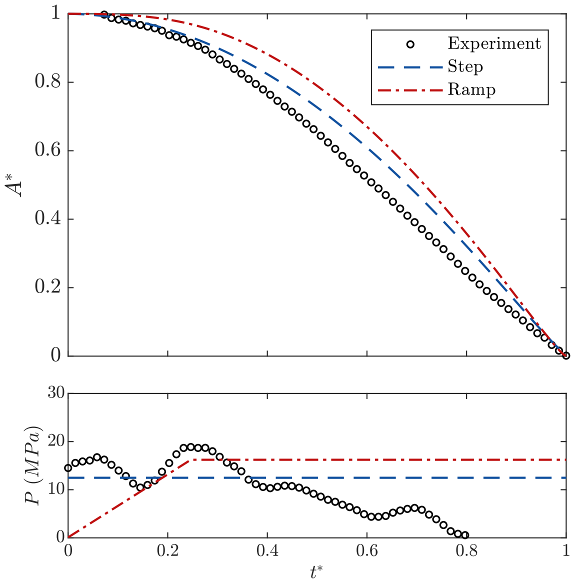

Figure E.58: Test #618. 1:40 PDMS.

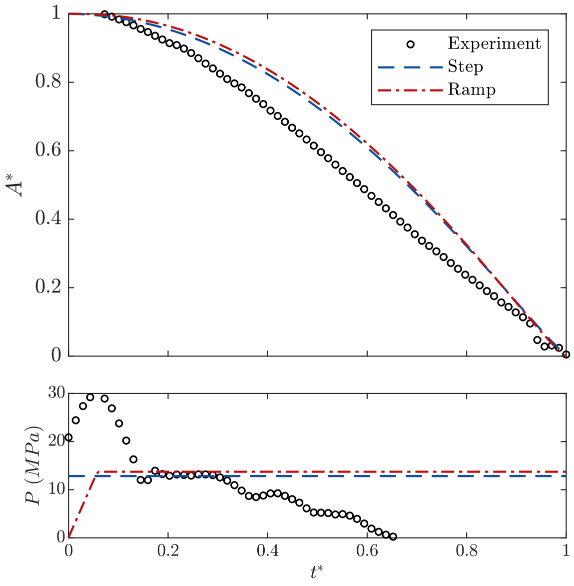

Figure E.59: Test #633. 1:40 PDMS.

E.5 Aluminum Boundary

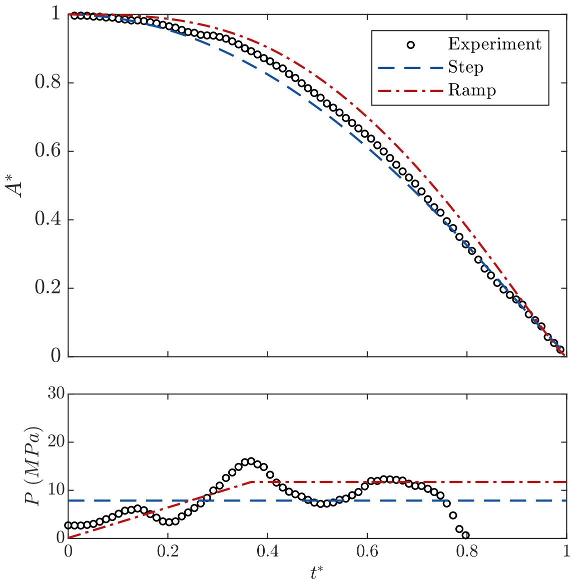

Figure E.60: Test #653.

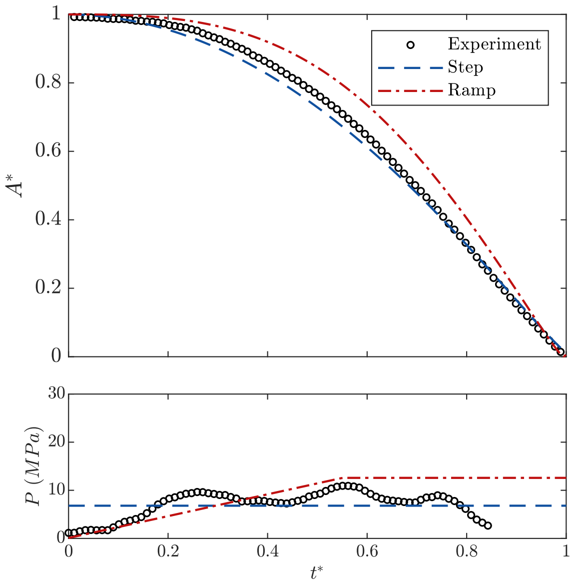

Figure E.61: Test #654.

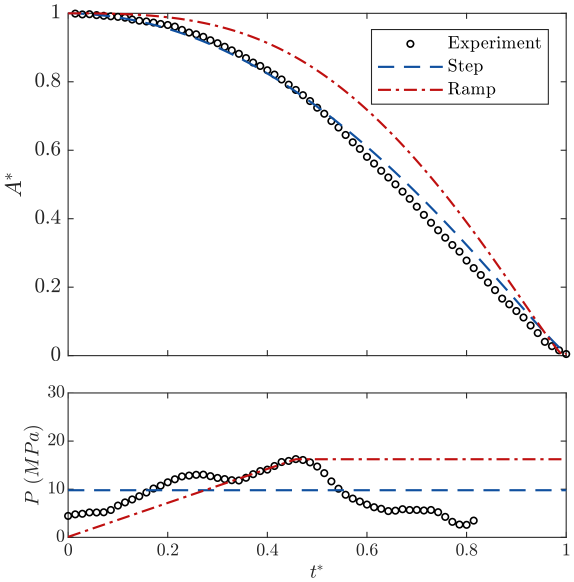

Figure E.62: Test #657.

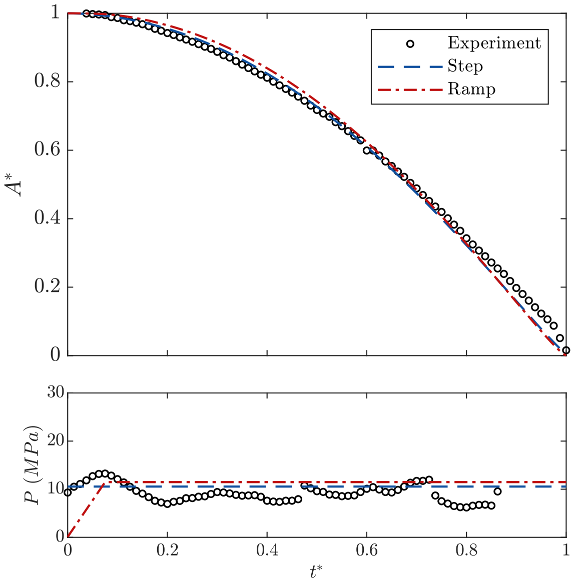

Figure E.63: Test #658.

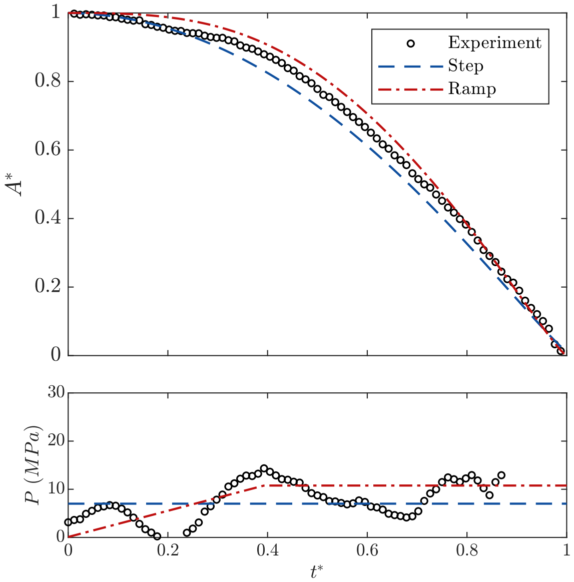

Figure E.64: Test #660.

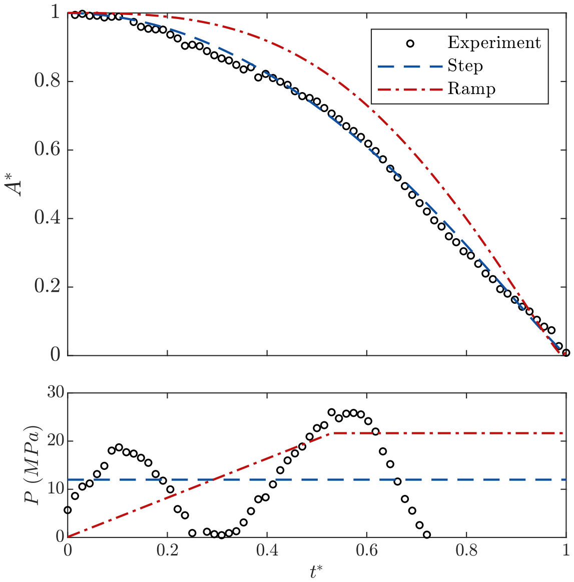

Figure E.65: Test #661.

APPENDIX F

PARTICLE SHADOW VELOCIMETRY: COMPLETE DATA AND MODELS

F.1 No Boundary

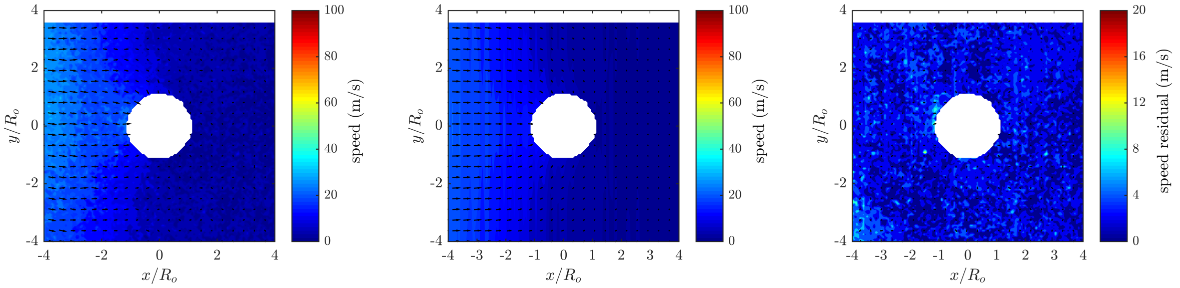

(a) Data (b) Model (c) Residuals

Figure F.1: Test# 746. A^* =1.00; x_c^* =0.02; S_{max} =31.4; S_{avg} =8.8; K =27.6; Q =48.8; Avg S_{res} =2.59.

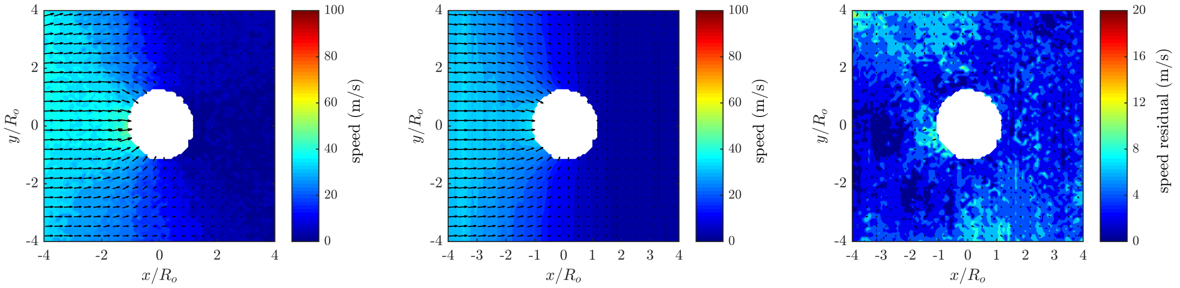

(a) Data (b) Model (c) Residuals

Figure F.2: Test# 702. A^* =0.99; x_c^* =0.07; S_{max} =47.1; S_{avg} =15.4; K =15.4; Q =53.6; Avg S_{res} =3.81.

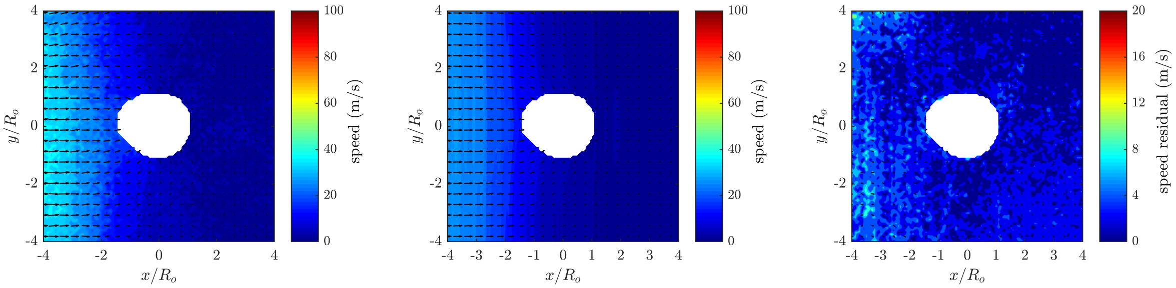

(a) Data (b) Model (c) Residuals

Figure F.3: Test# 824. A^* =0.98; x_c^* =0.02; S_{max} =48.5; S_{avg} =14.2; K =34.8; Q =52.7; Avg S_{res} =2.97.

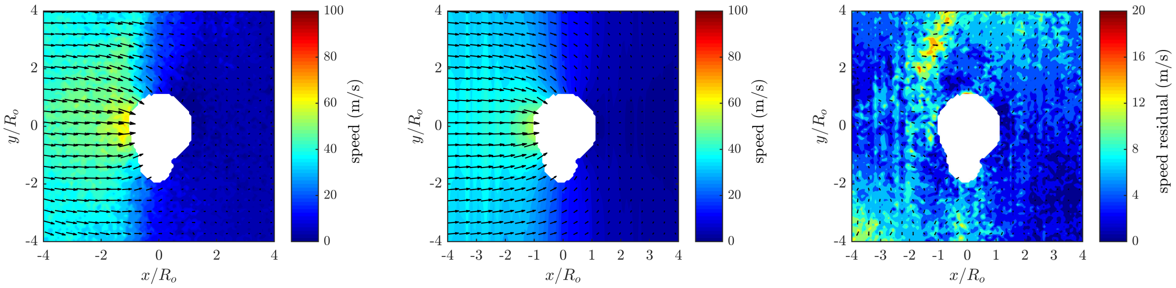

(a) Data (b) Model (c) Residuals

Figure F.4: Test# 836. A^* =0.94; x_c^* =0.10; S_{max} =69.5; S_{avg} =21.8; K =6.0; Q =8.4; Avg S_{res} =5.20.

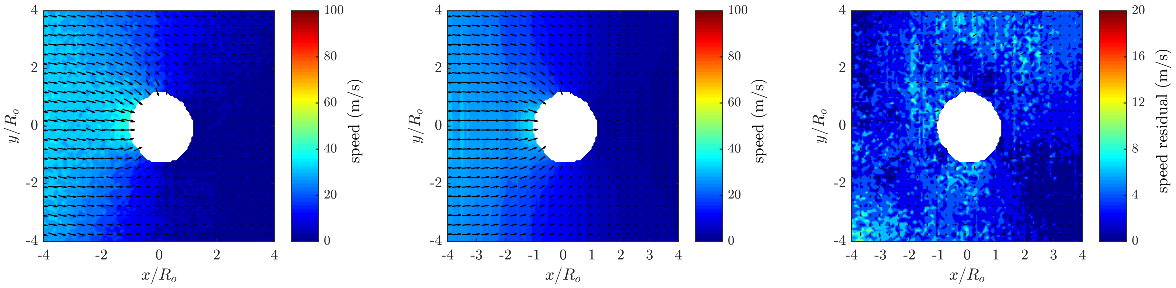

(a) Data (b) Model (c) Residuals

Figure F.5: Test# 756. A^* =0.93; x_c^* =0.09; S_{max} =45.3; S_{avg} =13.9; K =17.9; Q =37.6; Avg S_{res} =3.61.

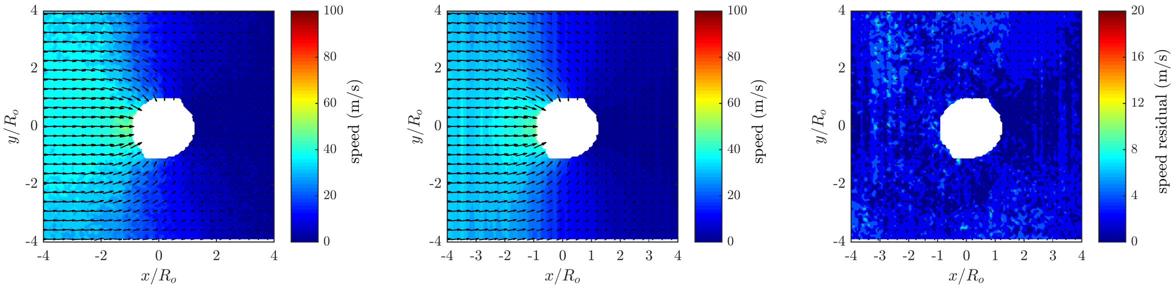

(a) Data (b) Model (c) Residuals

Figure F.6: Test# 752. A^* =0.90; x_c^* =0.18; S_{max} =51.6; S_{avg} =16.7; K =16.4; Q =50.5; Avg S_{res} =2.40.

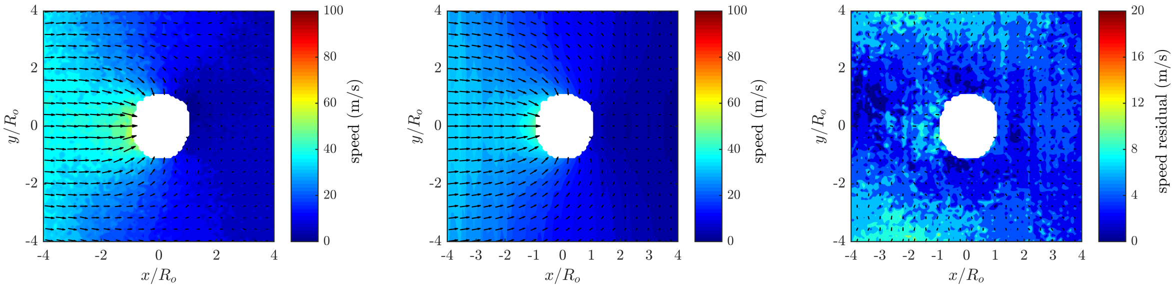

(a) Data (b) Model (c) Residuals

Figure F.7: Test# 849. A^* =0.89; x_c^* =0.09; S_{max} =59.6; S_{avg} =19.3; K =11.8; Q =36.0; Avg S_{res} =4.69.

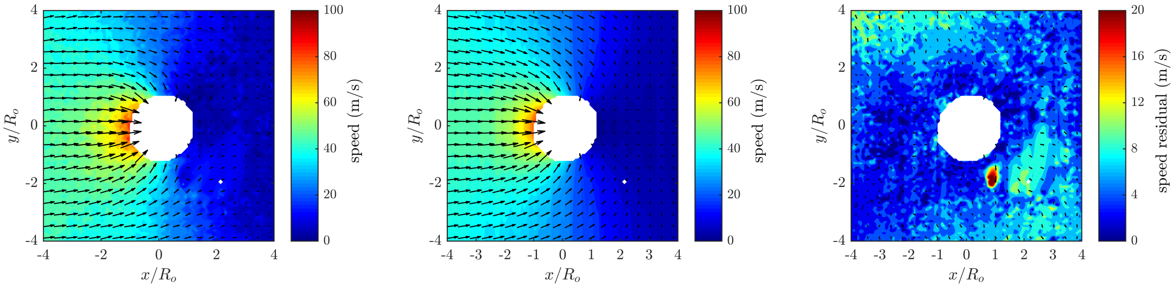

(a) Data (b) Model (c) Residuals

Figure F.8: Test# 842. A^* =0.89; x_c^* =0.13; S_{max} =85.9; S_{avg} =24.8; K =16.7; Q =49.2; Avg S_{res} =5.28.

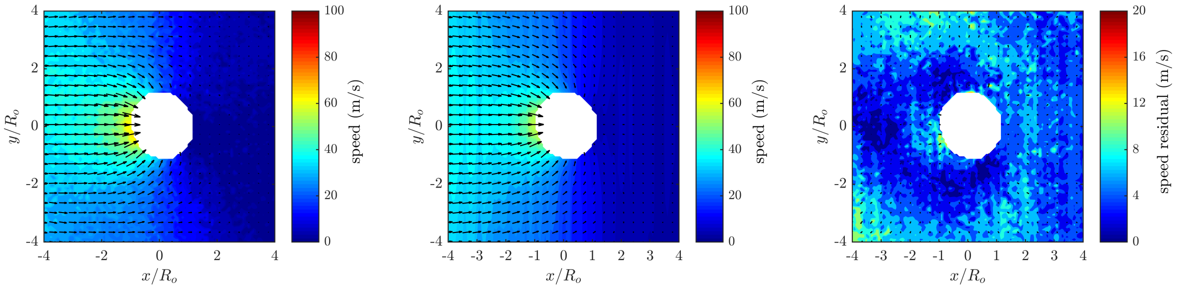

(a) Data (b) Model (c) Residuals

Figure F.9: Test# 701. A^* =0.87; x_c^* =0.15; S_{max} =67.4; S_{avg} =15.9; K =4.1; Q =50.3; Avg S_{res} =4.93.

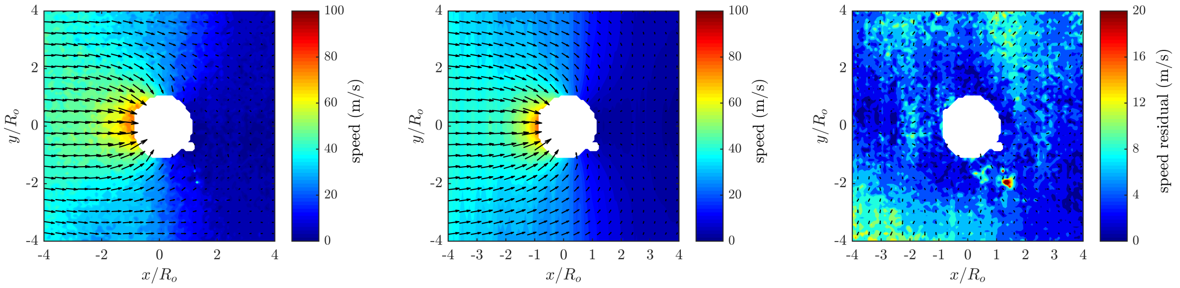

(a) Data (b) Model (c) Residuals

Figure F.10: Test# 745. A^* =0.86; x_c^* =0.12; S_{max} =77.6; S_{avg} =21.7; K =14.0; Q =43.4; Avg S_{res} =5.05.

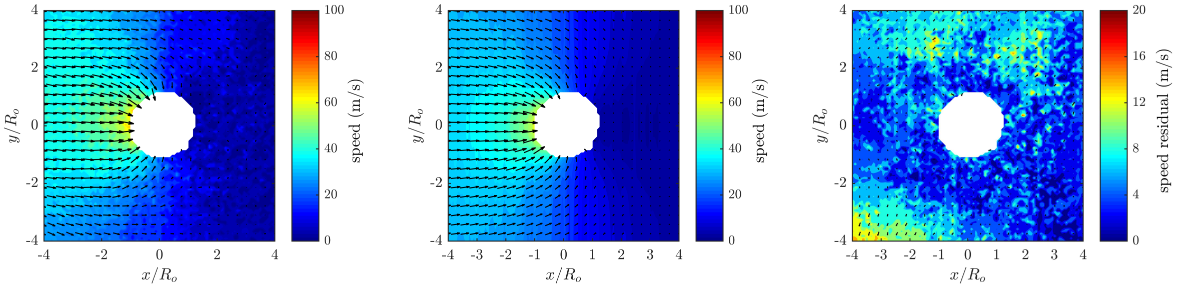

(a) Data (b) Model (c) Residuals

Figure F.11: Test# 823. A^* =0.86; x_c^* =0.10; S_{max} =70.6; S_{avg} =20.0; K =17.1; Q =48.2; Avg S_{res} =6.06.

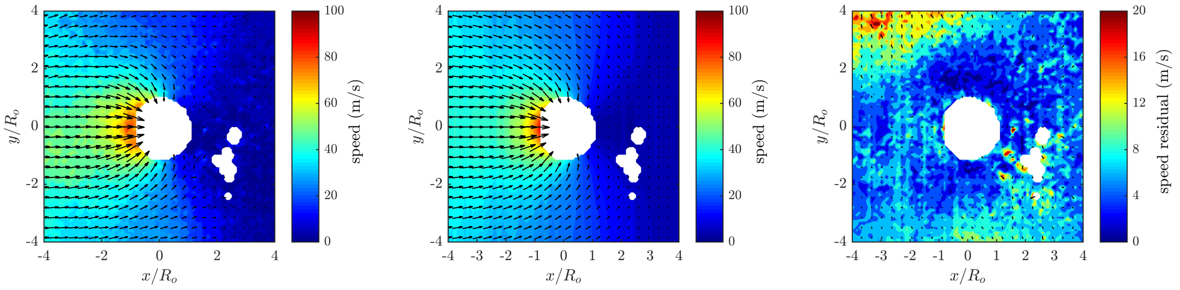

(a) Data

(b) Model

(c) Residuals

Figure F.12: Test# 704. A^* =0.81; x_c^* =0.16; S_{max} =81.2; S_{avg} =19.5; K =21.4; Q =43.5; Avg S_{res} =6.54.

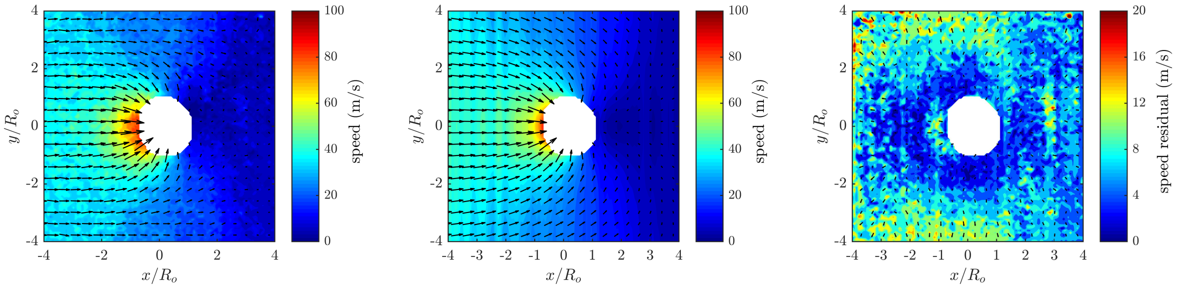

(a) Data

(b) Model

(c) Residuals

Figure F.13: Test# 843. A^* =0.74; x_c^* =0.24; S_{max} =85.9; S_{avg} =23.6; K =13.0; Q =33.2; Avg S_{res} =7.31.

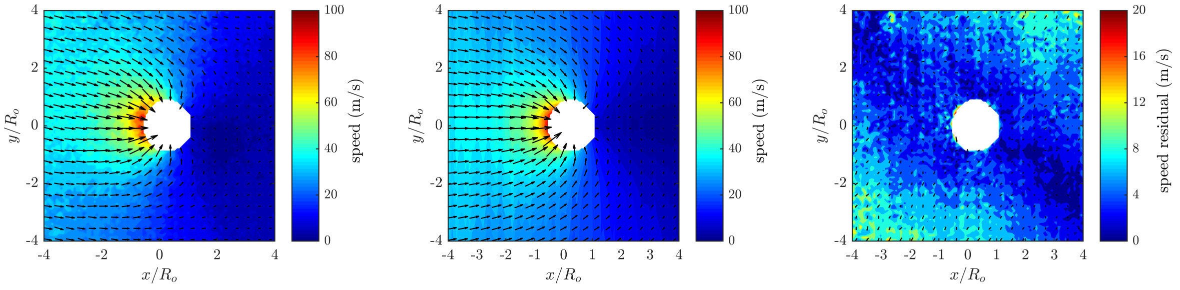

(a) Data

(b) Model

(c) Residuals

Figure F.14: Test# 689. A^* =0.56; x_c^* =0.32; S_{max} =87.2; S_{avg} =18.2; K =17.2; Q =46.0; Avg S_{res} =5.05.

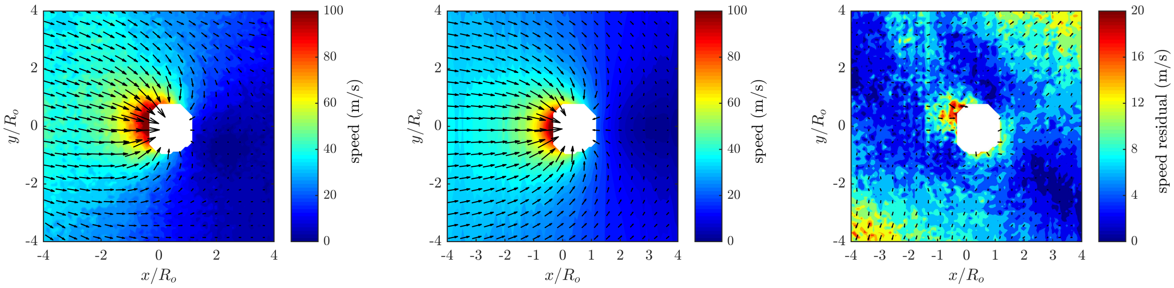

(a) Data (b) Model (c) Residuals

Figure F.15: Test# 750. $A^* = 0.50$; $x_c^* = 0.38$; $S_{max} = 124.2$; $S_{avg} = 20.9$; $K = 27.2$; $Q = 57.5$; Avg $S_{res} = 6.94$.

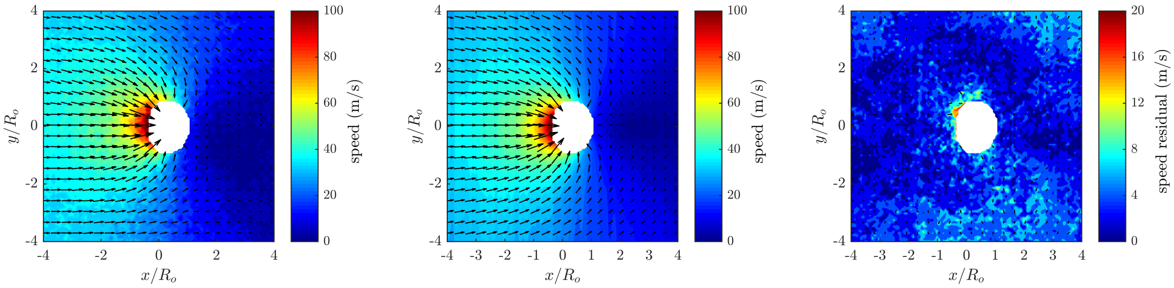

(a) Data (b) Model (c) Residuals

Figure F.16: Test# 751. $A^* = 0.48$; $x_c^* = 0.37$; $S_{max} = 109.2$; $S_{avg} = 19.9$; $K = 22.0$; $Q = 57.5$; Avg $S_{res} = 3.73$.

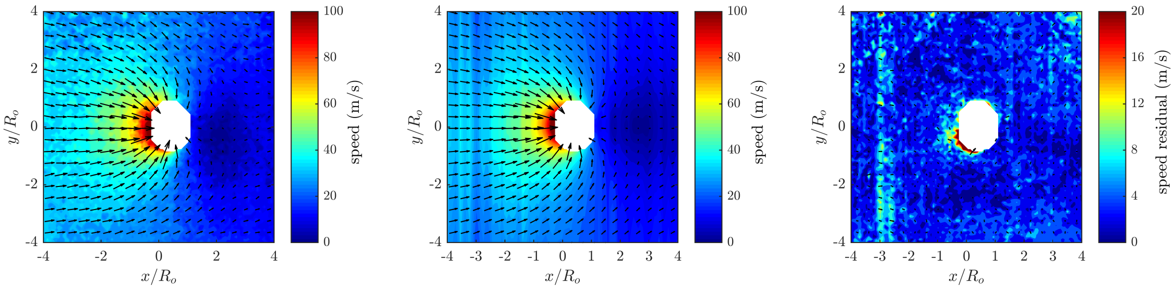

(a) Data (b) Model (c) Residuals

Figure F.17: Test# 687. $A^* = 0.44$; $x_c^* = 0.44$; $S_{max} = 128.3$; $S_{avg} = 20.5$; $K = 14.4$; $Q = 52.6$; Avg $S_{res} = 4.82$.

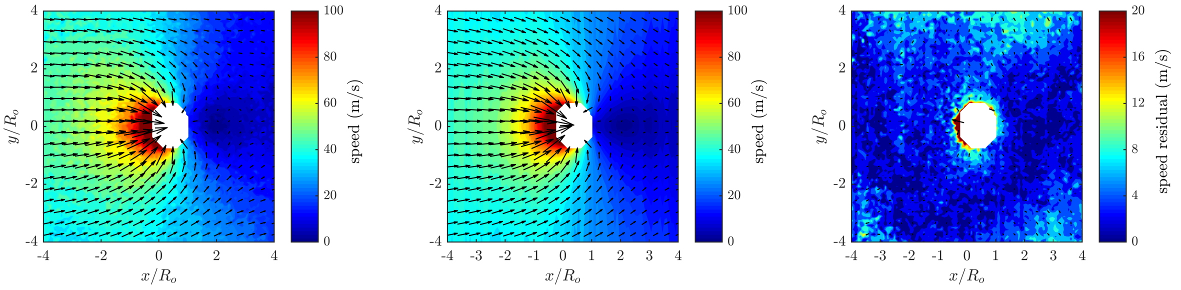

(a) Data (b) Model (c) Residuals

Figure F.18: Test# 699. $A^* = 0.39$; $x_c^* = 0.48$; $S_{max} = 129.5$; $S_{avg} = 25.8$; $K = 17.7$; $Q = 45.8$; Avg $S_{res} = 4.37$.

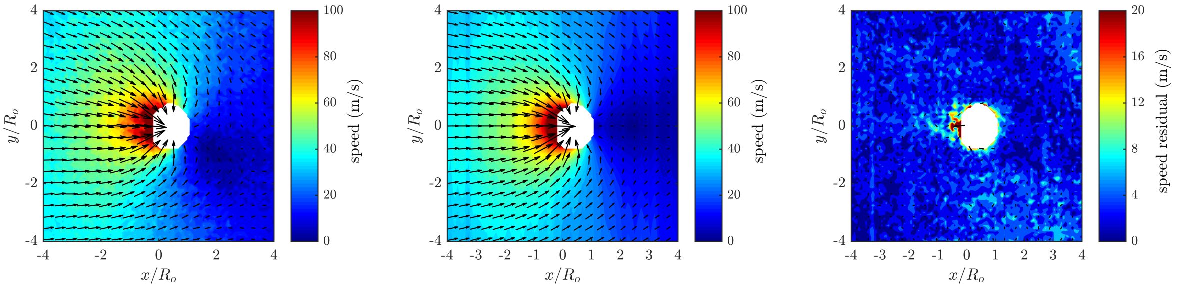

(a) Data (b) Model (c) Residuals

Figure F.19: Test# 688. $A^* = 0.38$; $x_c^* = 0.48$; $S_{max} = 144.8$; $S_{avg} = 23.8$; $K = 22.7$; $Q = 54.2$; Avg $S_{res} = 4.35$.

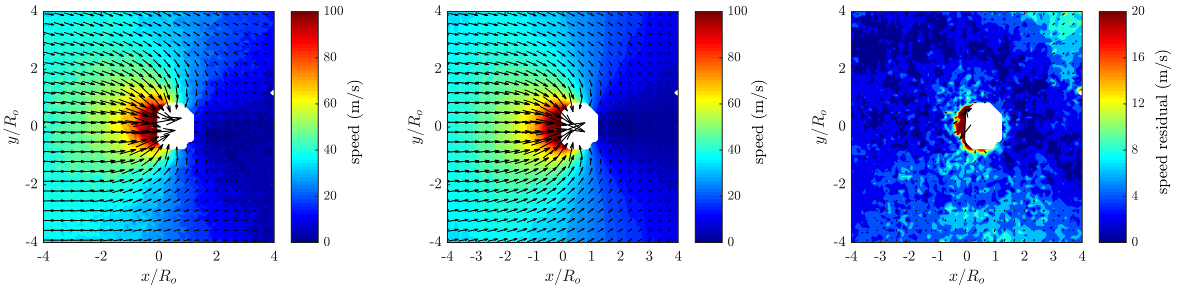

(a) Data (b) Model (c) Residuals

Figure F.20: Test# 694. $A^* = 0.37$; $x_c^* = 0.52$; $S_{max} = 172.8$; $S_{avg} = 22.2$; $K = 27.7$; $Q = 44.5$; Avg $S_{res} = 4.46$.

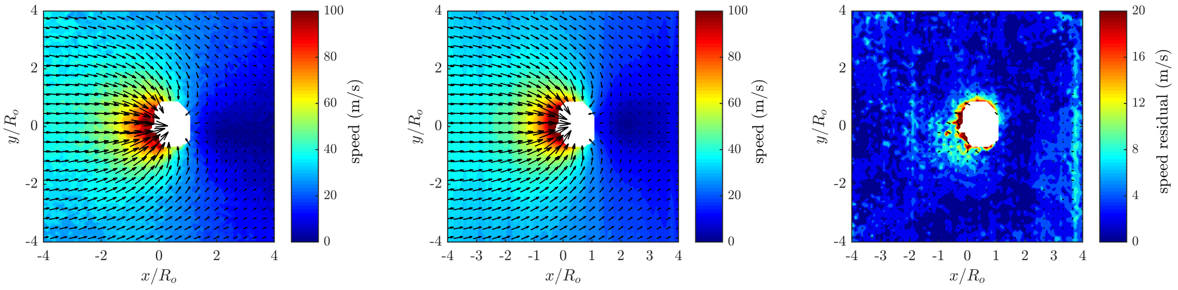

(a) Data (b) Model (c) Residuals

Figure F.21: Test# 693. $A^* = 0.35$; $x_c^* = 0.52$; $S_{max} = 138.8$; $S_{avg} = 21.8$; $K = 31.8$; $Q = 46.2$; Avg $S_{res} = 4.11$.

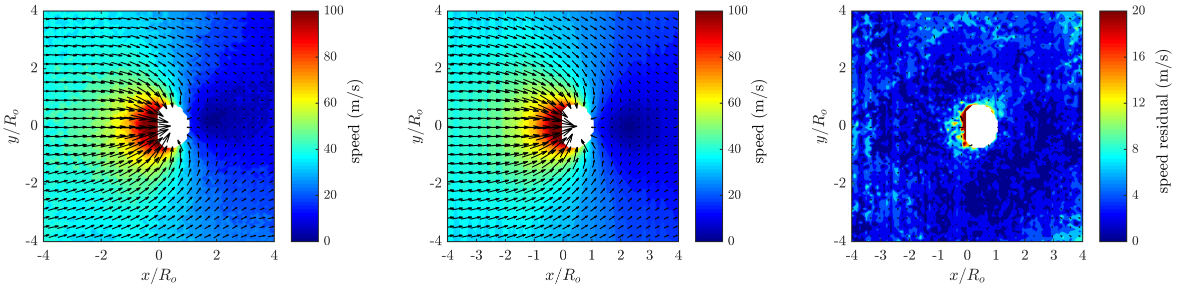

(a) Data (b) Model (c) Residuals

Figure F.22: Test# 822. $A^* = 0.29$; $x_c^* = 0.53$; $S_{max} = 152.8$; $S_{avg} = 29.0$; $K = 9.6$; $Q = 38.4$; Avg $S_{res} = 3.71$.

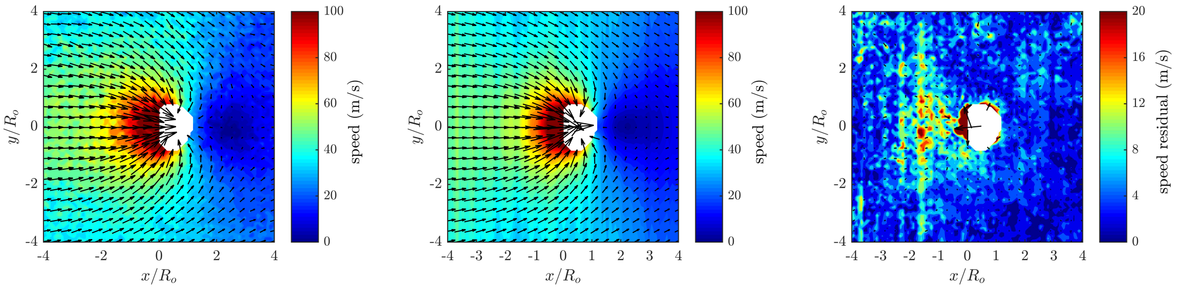

(a) Data (b) Model (c) Residuals

Figure F.23: Test# 703. $A^* = 0.28$; $x_c^* = 0.60$; $S_{max} = 136.1$; $S_{avg} = 26.7$; $K = 25.4$; $Q = 43.1$; Avg $S_{res} = 5.62$.

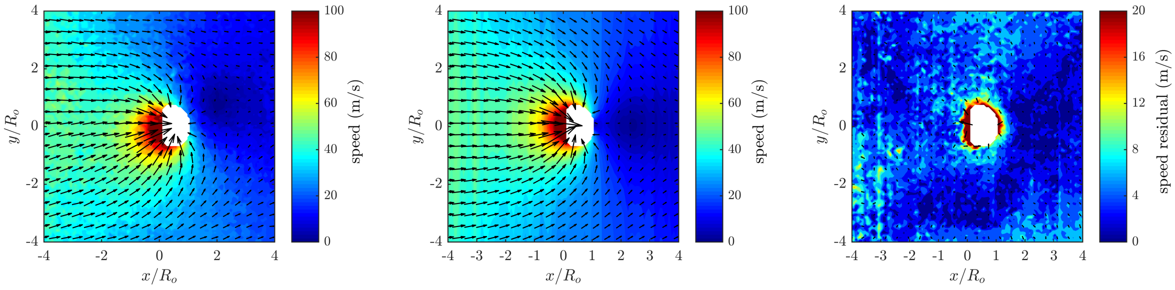

(a) Data (b) Model (c) Residuals

Figure F.24: Test# 840. $A^* = 0.24$; $x_c^* = 0.62$; $S_{max} = 123.5$; $S_{avg} = 30.5$; $K = 21.9$; $Q = 34.5$; Avg $S_{res} = 4.75$.

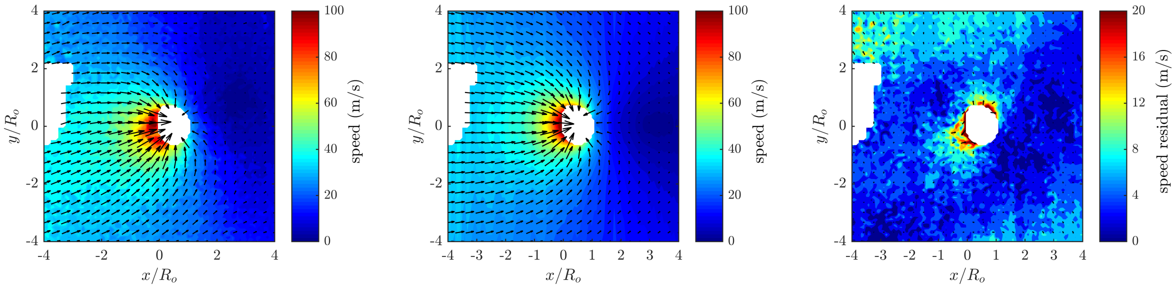

(a) Data (b) Model (c) Residuals

Figure F.25: Test# 700. $A^* = 0.22$; $x_c^* = 0.59$; $S_{max} = 110.1$; $S_{avg} = 17.1$; $K = 16.5$; $Q = 50.7$; Avg $S_{res} = 5.16$.

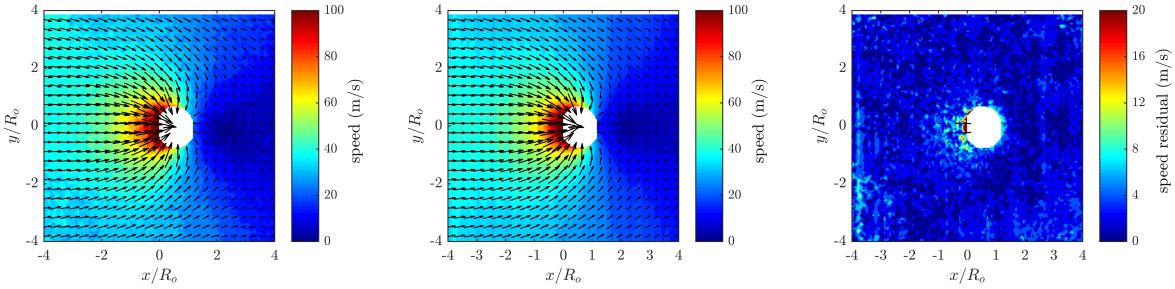

(a) Data (b) Model (c) Residuals

Figure F.26: Test# 761. $A^* = 0.15$; $x_c^* = 0.69$; $S_{max} = 133.2$; $S_{avg} = 26.9$; $K = 12.8$; $Q = 24.3$; Avg $S_{res} = 2.86$.

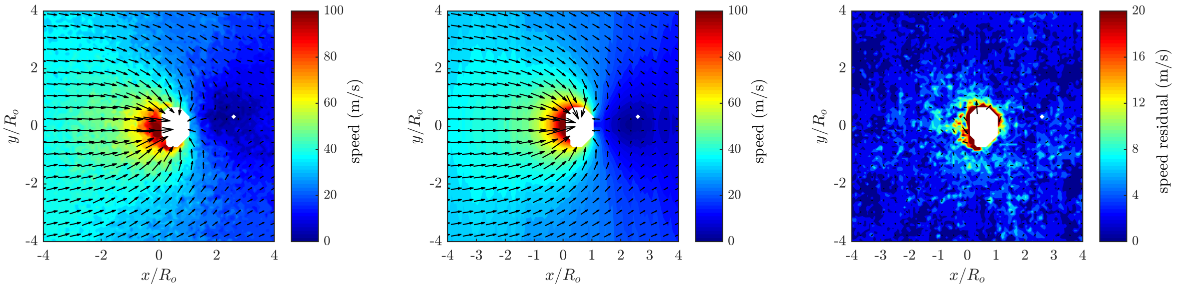

(a) Data (b) Model (c) Residuals

Figure F.27: Test# 838. A^* =0.13; x_c^* =0.72; S_{max} =113.9; S_{avg} =30.4; K =27.6; Q =48.8; Avg S_{res} =3.06.

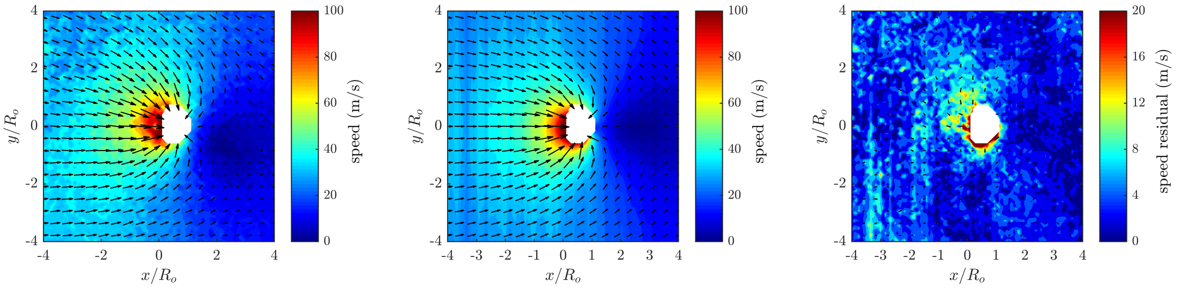

(a) Data (b) Model (c) Residuals

Figure F.28: Test# 686. A^* =0.09; x_c^* =0.70; S_{max} =126.6; S_{avg} =20.7; K =19.1; Q =33.3; Avg S_{res} =4.67.

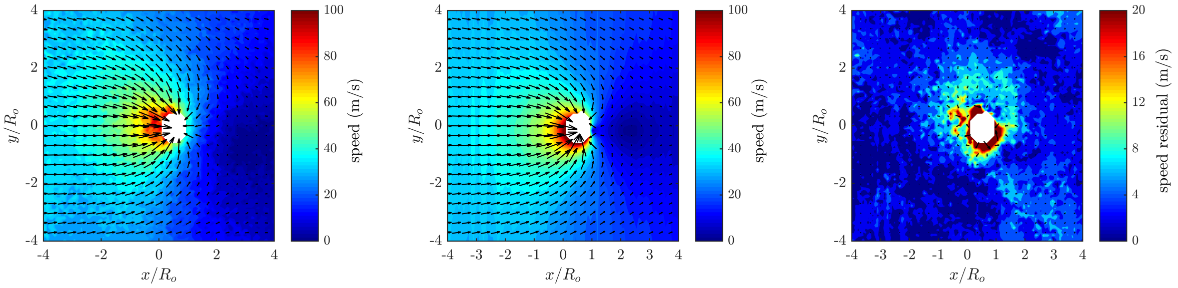

(a) Data (b) Model (c) Residuals

Figure F.29: Test# 692. A^* =0.06; x_c^* =0.79; S_{max} =100.0; S_{avg} =19.0; K =11.7; Q =45.4; Avg S_{res} =3.82.

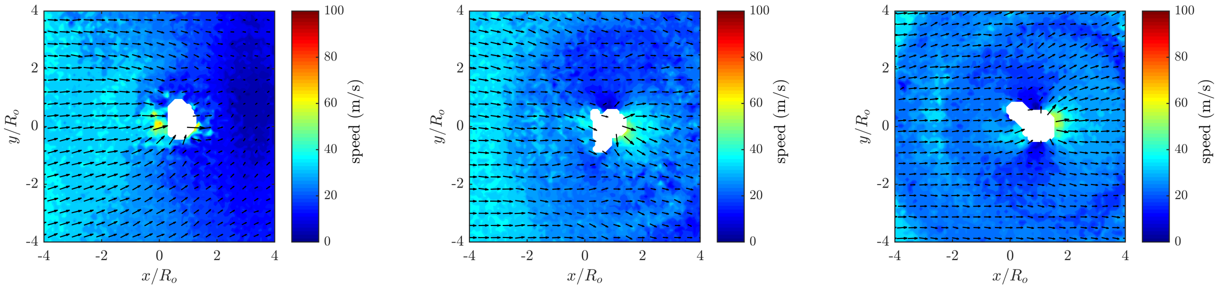

(a) Test# 684. A^* =0.00; x_c^* =0.84; S_{max} =74.1; S_{avg} =19.1.

(b) Test# 685. A^* =0.00; x_c^* =1.04; S_{max} =60.2; S_{avg} =21.7.

(c) Test# 691. A^* =0.00; x_c^* =1.08; S_{max} =58.2; S_{avg} =24.6.

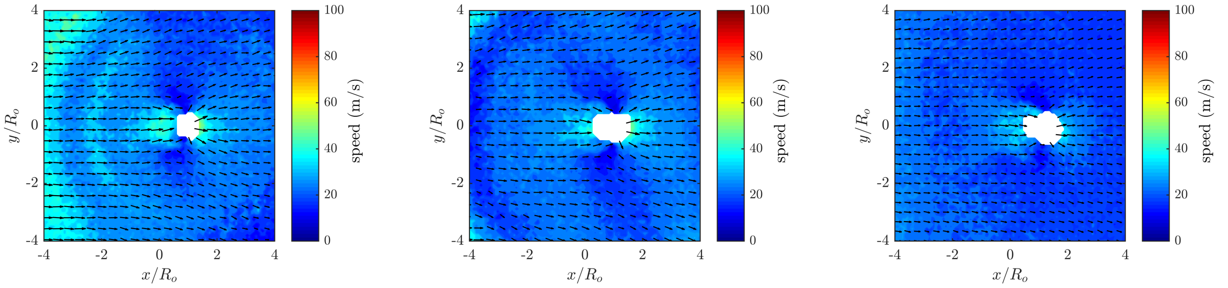

(d) Test# 760. A^* =0.00; x_c^* =1.16; S_{max} =55.4; S_{avg} =25.3.

(e) Test# 690. A^* =0.00; x_c^* =1.25; S_{max} =55.0; S_{avg} =20.1.

(f) Test# 753. A^* =0.00; x_c^* =1.32; S_{max} =40.0; S_{avg} =19.4.

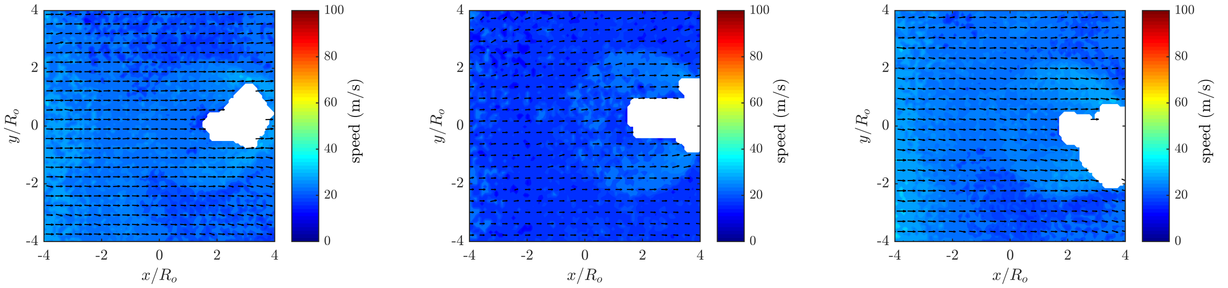

(g) Test# 696. A^* =0.00; x_c^* =3.16; S_{max} =53.1; S_{avg} =21.4.

(h) Test# 697. A^* =0.00; x_c^* =3.29; S_{max} =36.1; S_{avg} =17.1.

(i) Test# 695. A^* =0.00; x_c^* =3.35; S_{max} =49.4; S_{avg} =21.9.

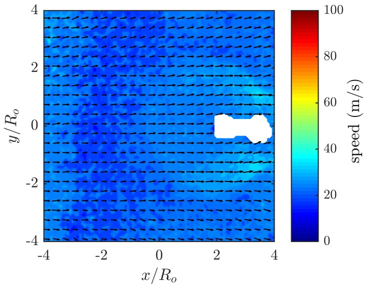

(j) Test# 698. A^* =0.00; x_c^* =3.47; S_{max} =45.4; S_{avg} =21.6.

Figure F.30: Raw data for tests 684–698. Void boundary could not be identified reliably(<3%), or test was after collapse, so model could not be computed.

F.2 Downstream Boundary

F.2.1 Downstream 20:1 PDMS

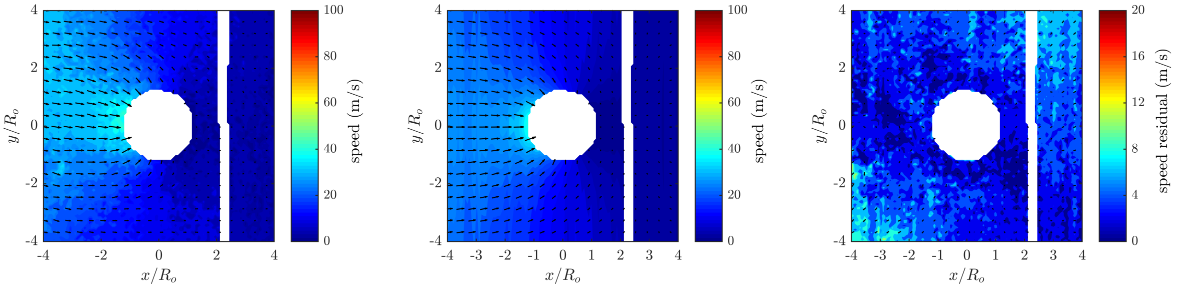

(a) Data (b) Model (c) Residuals

Figure F.31: Test# 809. $A^* = 1.04$; $x_c^* = 0.02$; $S_{max} = 45.1$; $S_{avg} = 15.8$; $K = 7.1$; $Q = 19.2$; Avg $S_{res} = 4.31$.

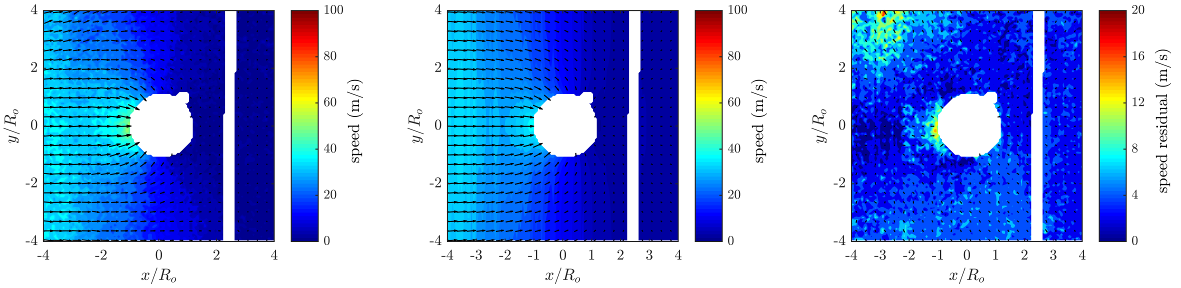

(a) Data (b) Model (c) Residuals

Figure F.32: Test# 728. $A^* = 1.00$; $x_c^* = 0.09$; $S_{max} = 51.1$; $S_{avg} = 13.5$; $K = 24.3$; $Q = 50.7$; Avg $S_{res} = 4.07$.

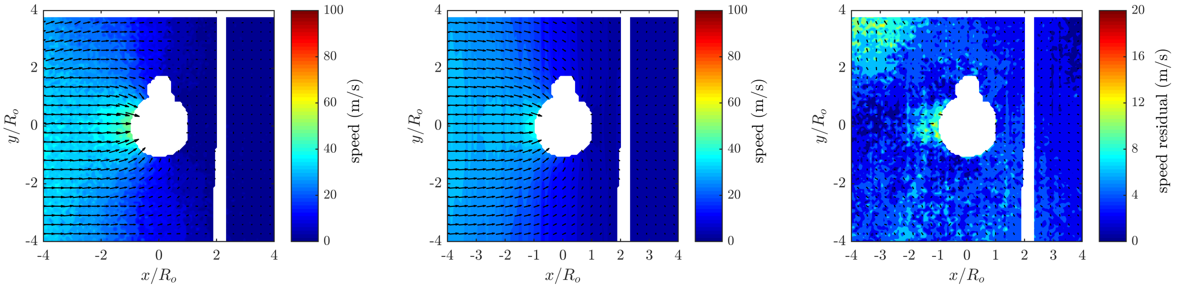

(a) Data (b) Model (c) Residuals

Figure F.33: Test# 743. $A^* = 0.95$; $x_c^* = 0.08$; $S_{max} = 51.4$; $S_{avg} = 14.7$; $K = 18.3$; $Q = 29.4$; Avg $S_{res} = 3.98$.

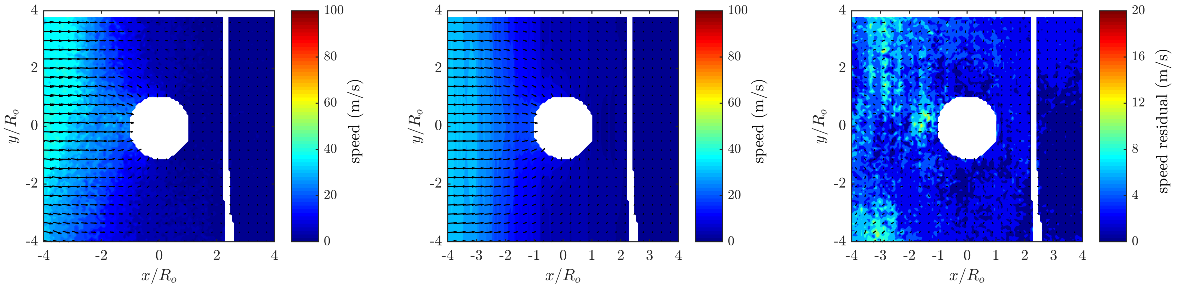

(a) Data (b) Model (c) Residuals

Figure F.34: Test# 742. A^* =0.95; x_c^* =0.05; S_{max} =41.6; S_{avg} =10.7; K =19.1; Q =52.7; Avg S_{res} =3.07.

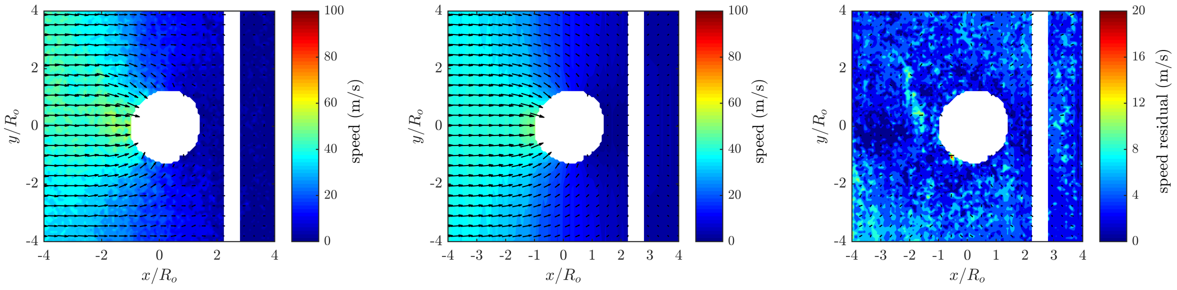

(a) Data (b) Model (c) Residuals

Figure F.35: Test# 764. A^* =0.93; x_c^* =0.15; S_{max} =58.9; S_{avg} =18.8; K =12.4; Q =54.1; Avg S_{res} =3.91.

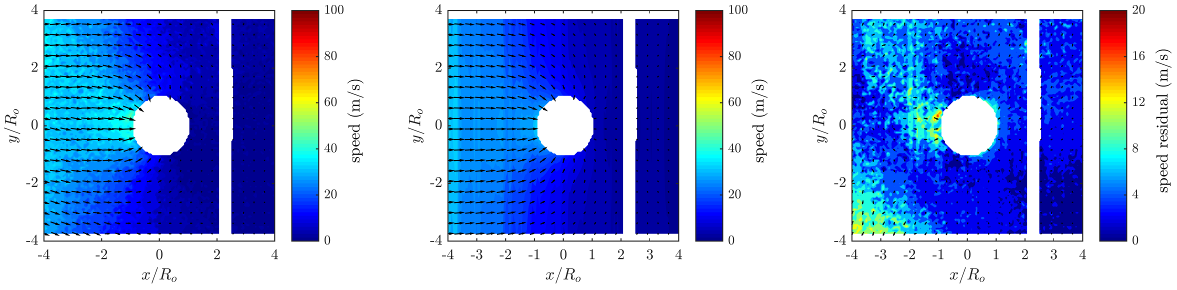

(a) Data (b) Model (c) Residuals

Figure F.36: Test# 749. A^* =0.90; x_c^* =0.10; S_{max} =47.4; S_{avg} =13.7; K =5.3; Q =12.9; Avg S_{res} =4.11.

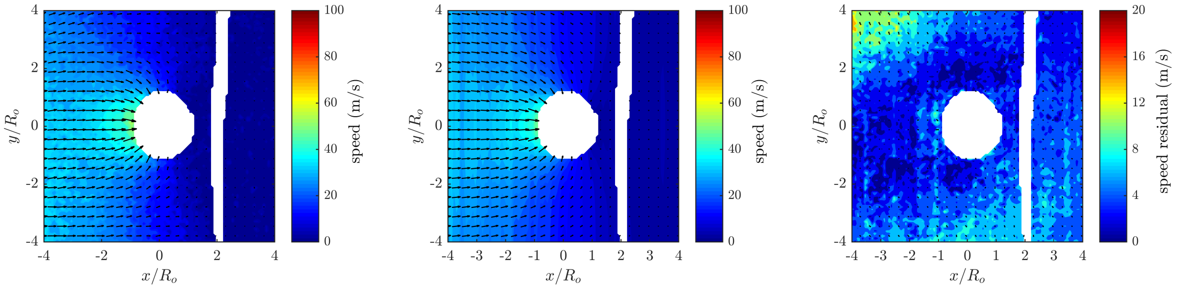

(a) Data (b) Model (c) Residuals

Figure F.37: Test# 717. $A^* = 0.89$; $x_c^* = 0.14$; $S_{max} = 52.7$; $S_{avg} = 15.3$; $K = 28.8$; $Q = 53.7$; Avg $S_{res} = 4.65$.

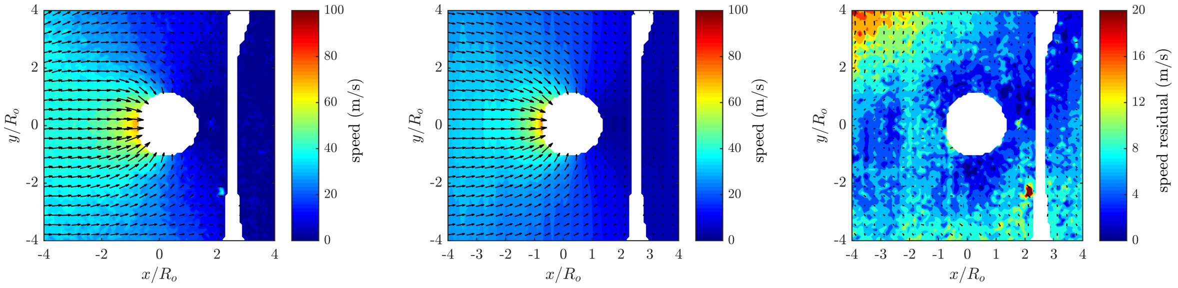

(a) Data (b) Model (c) Residuals

Figure F.38: Test# 718. $A^* = 0.79$; $x_c^* = 0.23$; $S_{max} = 74.7$; $S_{avg} = 17.4$; $K = 13.6$; $Q = 53.8$; Avg $S_{res} = 6.32$.

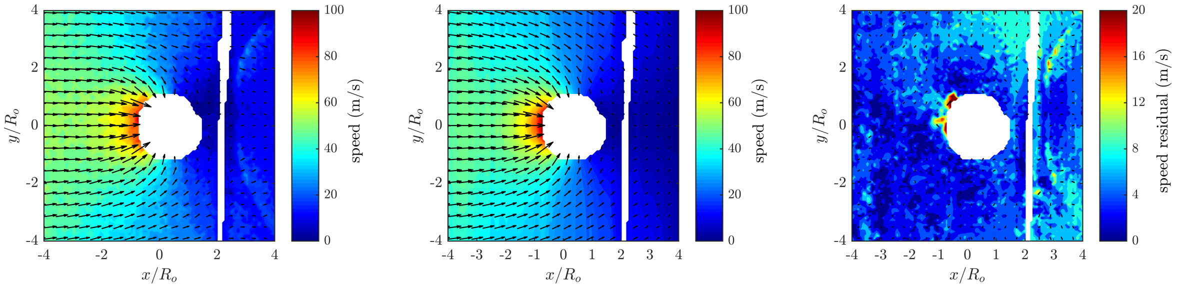

(a) Data (b) Model (c) Residuals

Figure F.39: Test# 912. $A^* = 0.68$; $x_c^* = 0.23$; $S_{max} = 96.9$; $S_{avg} = 25.6$; $K = 24.3$; $Q = 52.0$; Avg $S_{res} = 4.73$.

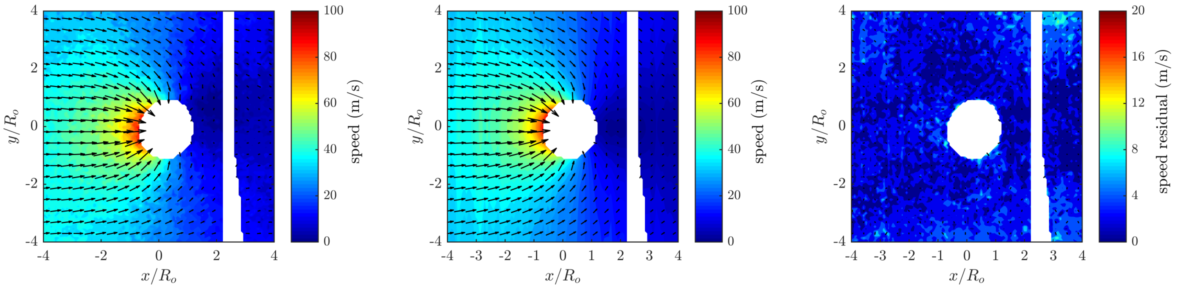

(a) Data (b) Model (c) Residuals

Figure F.40: Test# 894. A^* =0.63; x_c^* =0.31; S_{max} =92.5; S_{avg} =23.6; K =20.3; Q =45.4; Avg S_{res} =3.31.

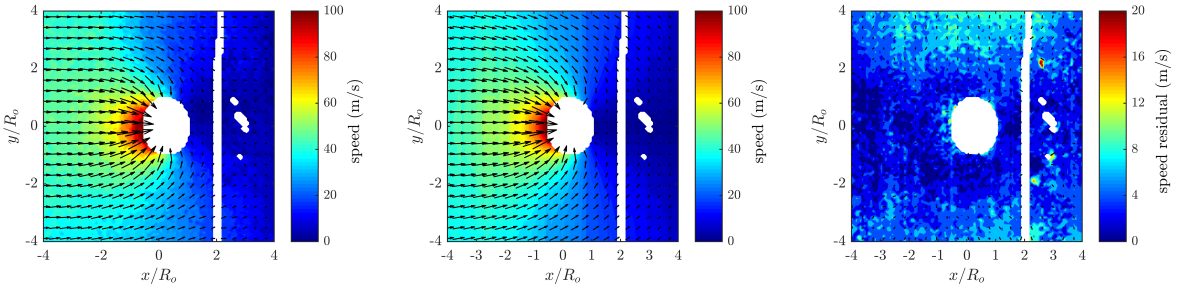

(a) Data (b) Model (c) Residuals

Figure F.41: Test# 813. A^* =0.62; x_c^* =0.33; S_{max} =115.4; S_{avg} =26.4; K =14.7; Q =20.0; Avg S_{res} =4.33.

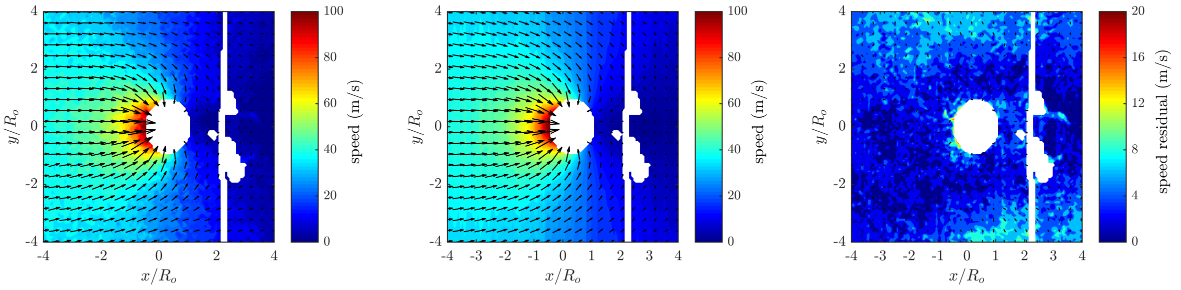

(a) Data (b) Model (c) Residuals

Figure F.42: Test# 727. A^* =0.55; x_c^* =0.37; S_{max} =110.2; S_{avg} =19.5; K =13.7; Q =38.3; Avg S_{res} =3.79.

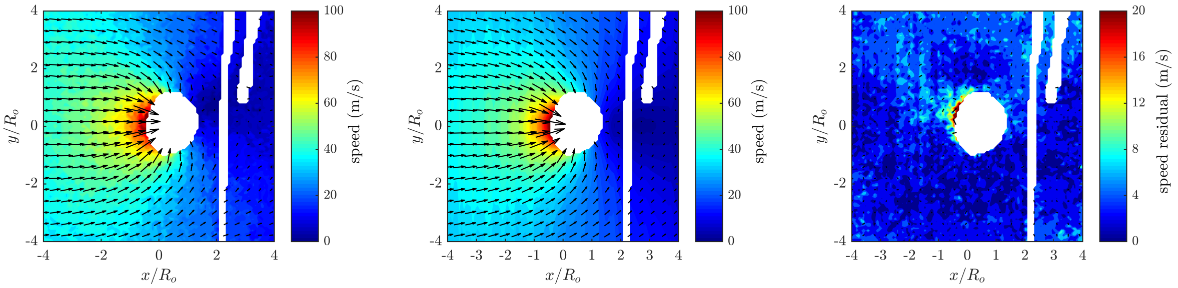

(a) Data (b) Model (c) Residuals

Figure F.43: Test# 893. A^* =0.42; x_c^* =0.40; S_{max} =113.4; S_{avg} =25.3; K =9.9; Q =36.9; Avg S_{res} =3.73.

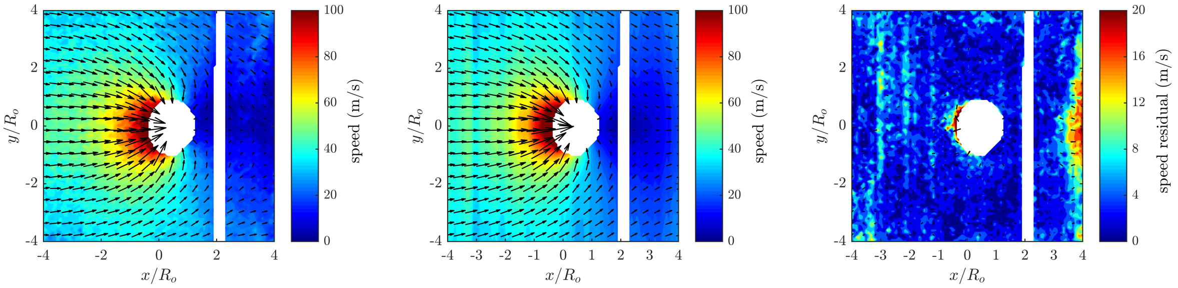

(a) Data (b) Model (c) Residuals

Figure F.44: Test# 795. A^* =0.42; x_c^* =0.41; S_{max} =126.2; S_{avg} =30.1; K =22.2; Q =52.5; Avg S_{res} =5.11.

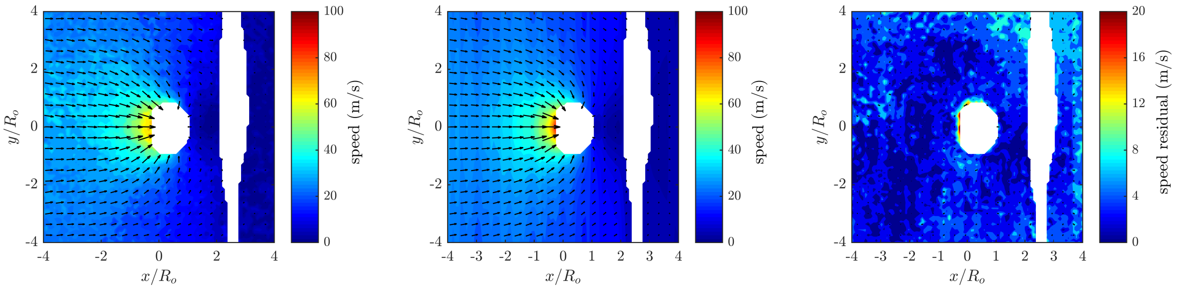

(a) Data (b) Model (c) Residuals

Figure F.45: Test# 706. A^* =0.41; x_c^* =0.43; S_{max} =70.6; S_{avg} =15.9; K =2.3; Q =4.2; Avg S_{res} =4.19.

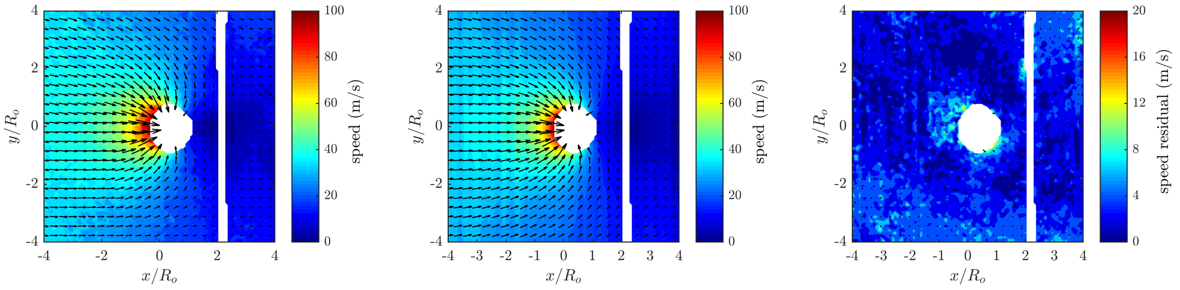

(a) Data (b) Model (c) Residuals

Figure F.46: Test# 911. $A^* = 0.40$; $x_c^* = 0.49$; $S_{max} = 108.2$; $S_{avg} = 23.5$; $K = 26.7$; $Q = 60.3$; Avg $S_{res} = 3.69$.

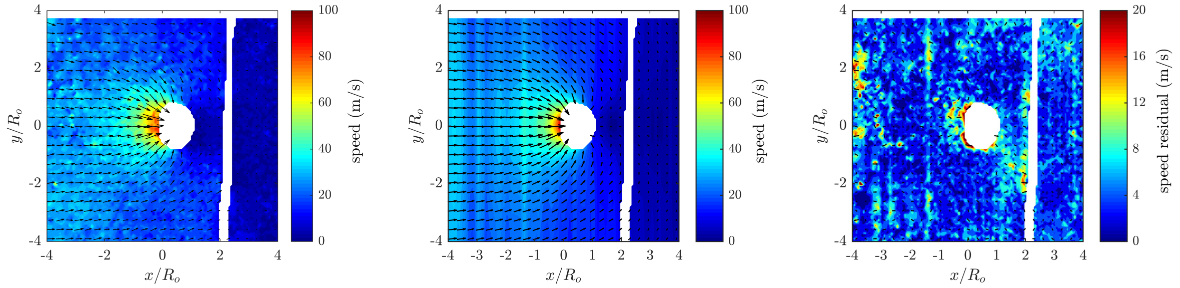

(a) Data (b) Model (c) Residuals

Figure F.47: Test# 765. $A^* = 0.37$; $x_c^* = 0.55$; $S_{max} = 87.0$; $S_{avg} = 16.3$; $K = 19.3$; $Q = 42.9$; Avg $S_{res} = 4.79$.

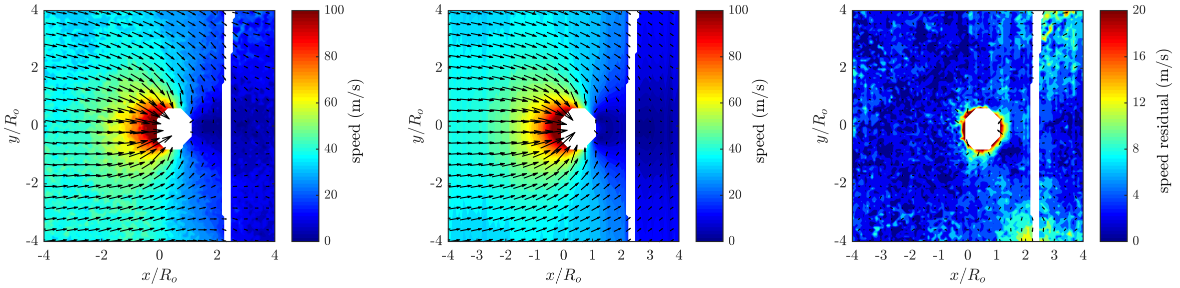

(a) Data (b) Model (c) Residuals

Figure F.48: Test# 895. $A^* = 0.25$; $x_c^* = 0.66$; $S_{max} = 132.8$; $S_{avg} = 30.1$; $K = 25.2$; $Q = 36.6$; Avg $S_{res} = 4.52$.

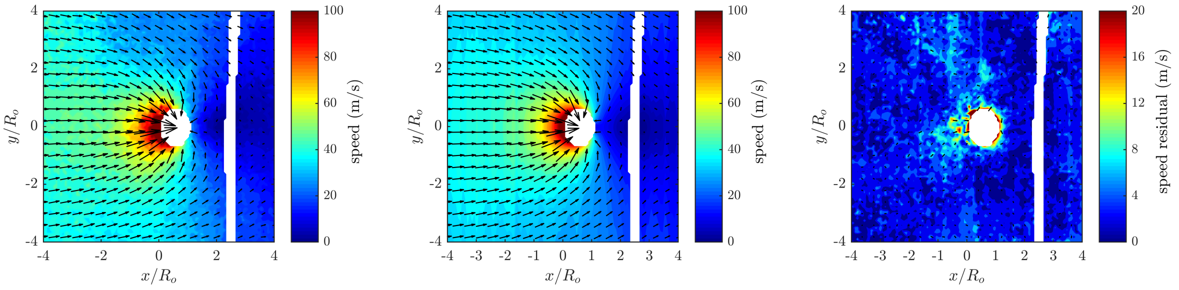

(a) Data (b) Model (c) Residuals

Figure F.49: Test# 910. $A^* = 0.14$; $x_c^* = 0.77$; $S_{max} = 131.7$; $S_{avg} = 28.0$; $K = 13.0$; $Q = 44.7$; Avg $S_{res} = 3.51$.

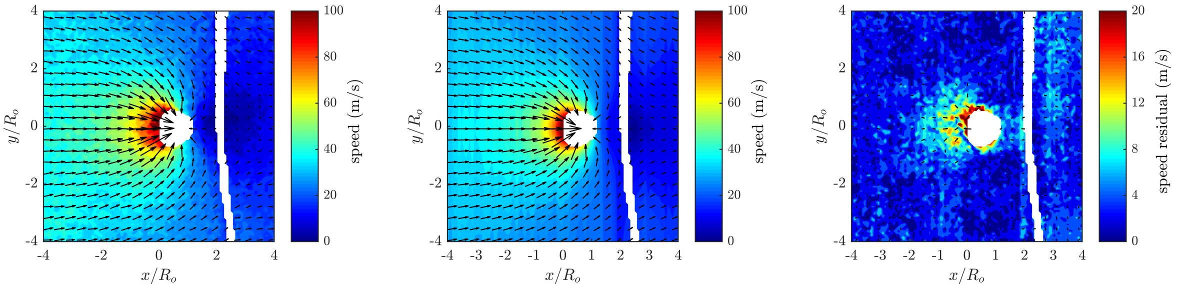

(a) Data (b) Model (c) Residuals

Figure F.50: Test# 896. $A^* = 0.10$; $x_c^* = 0.67$; $S_{max} = 115.7$; $S_{avg} = 23.9$; $K = 19.2$; $Q = 41.1$; Avg $S_{res} = 3.59$.

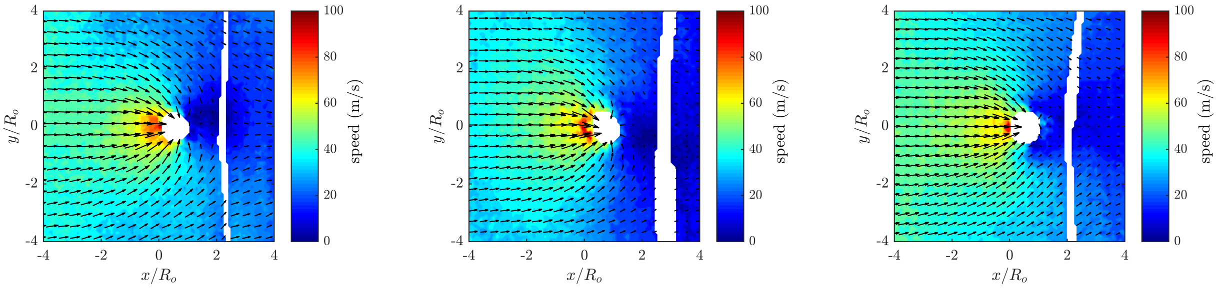

(a) Test# 909. A^* =0.02; x_c^* =0.76; S_{max} =89.4; S_{avg} =29.5.

(b) Test# 707. A^* =0.01; x_c^* =0.86; S_{max} =106.6; S_{avg} =20.6.

(c) Test# 871. A^* =0.01; x_c^* =0.79; S_{max} =96.6; S_{avg} =29.4.

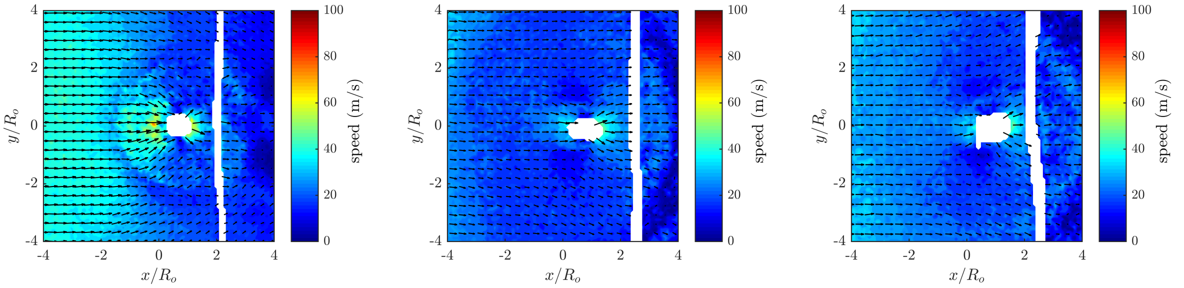

(d) Test# 817. A^* =0.00; x_c^* =0.90; S_{max} =74.8; S_{avg} =25.2.

(e) Test# 784. A^* =0.00; x_c^* =0.98; S_{max} =51.0; S_{avg} =18.2.

(f) Test# 705. A^* =0.00; x_c^* =1.12; S_{max} =47.6; S_{avg} =17.7.

Figure F.51: Raw data for tests 909-705. Void boundary could not be identified reliably(<3%), or test was after collapse, so model could not be computed.

F.2.2 Downstream 30:1 PDMS

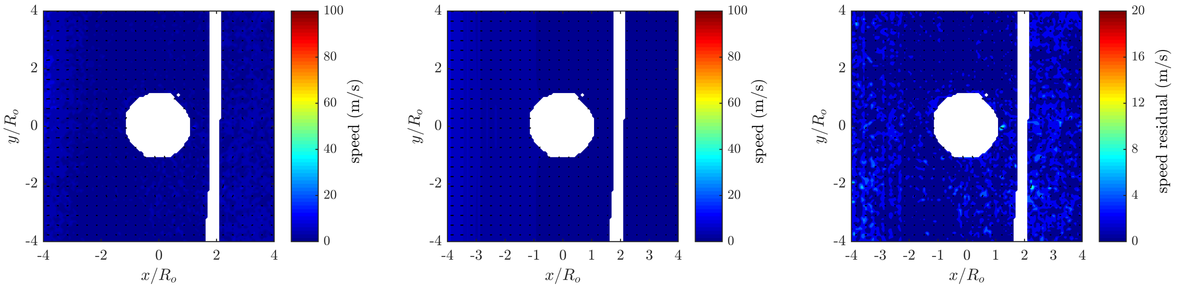

(a) Data

(b) Model

(c) Residuals

Figure F.52: Test# 726. A^* =1.00; x_c^* =0.02; S_{max} =23.5; S_{avg} =3.8; K =15.5; Q =45.0; Avg S_{res} =1.73.

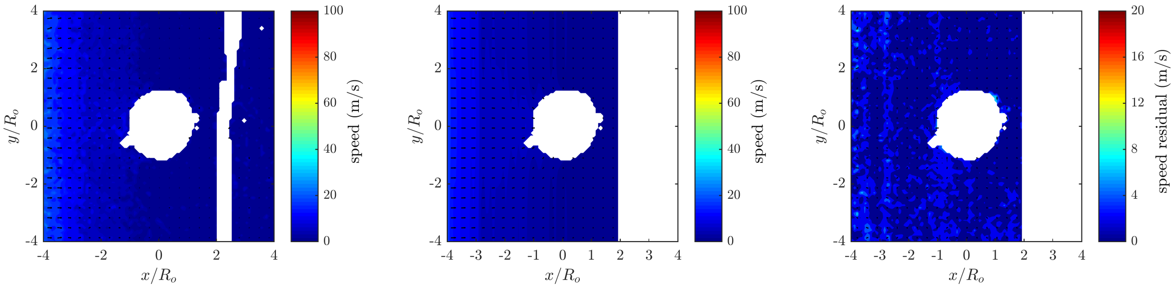

(a) Data (b) Model (c) Residuals

Figure F.53: Test# 715. A^* =0.99; x_c^* =0.01; S_{max} =40.2; S_{avg} =8.1; K =10.2; Q =40.3; Avg S_{res} =2.34.

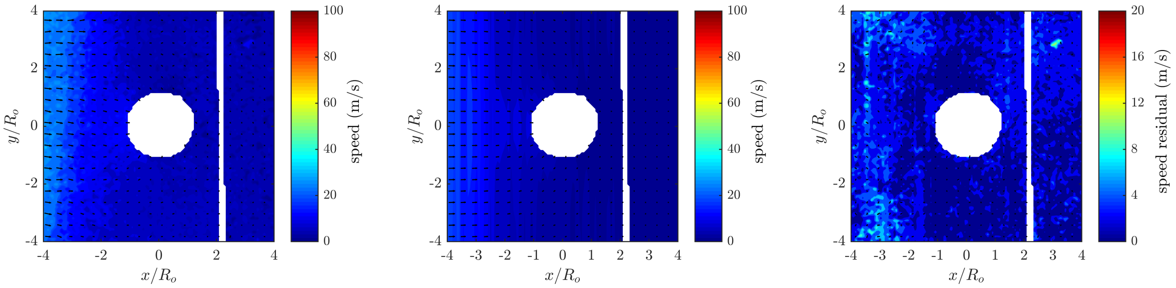

(a) Data (b) Model (c) Residuals

Figure F.54: Test# 897. A^* =0.99; x_c^* =0.04; S_{max} =45.9; S_{avg} =11.5; K =10.9; Q =29.4; Avg S_{res} =2.74.

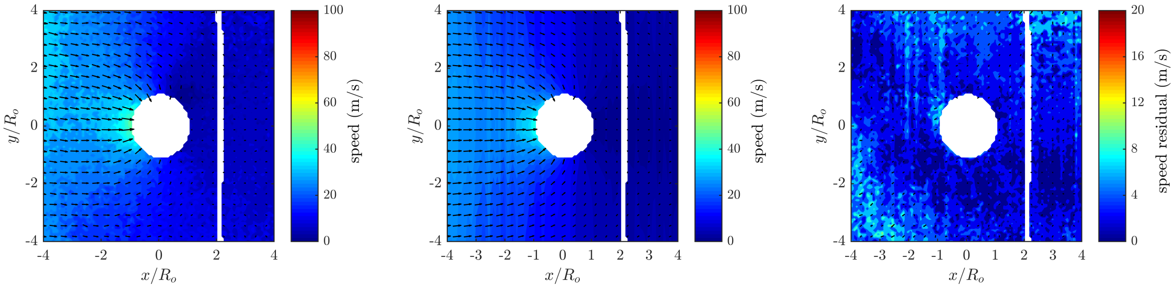

(a) Data (b) Model (c) Residuals

Figure F.55: Test# 799. A^* =0.86; x_c^* =0.09; S_{max} =48.9; S_{avg} =17.8; K =29.5; Q =51.7; Avg S_{res} =3.74.

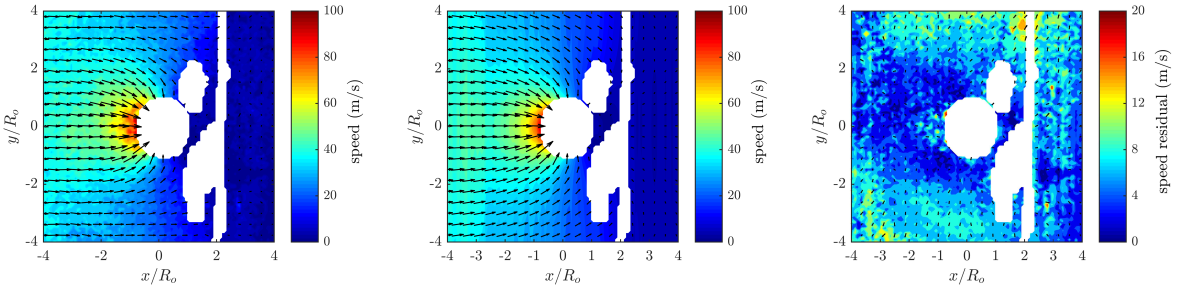

(a) Data (b) Model (c) Residuals

Figure F.56: Test# 740. A^* =0.81; x_c^* =0.18; S_{max} =96.9; S_{avg} =21.1; K =6.9; Q =39.3; Avg S_{res} =5.63.

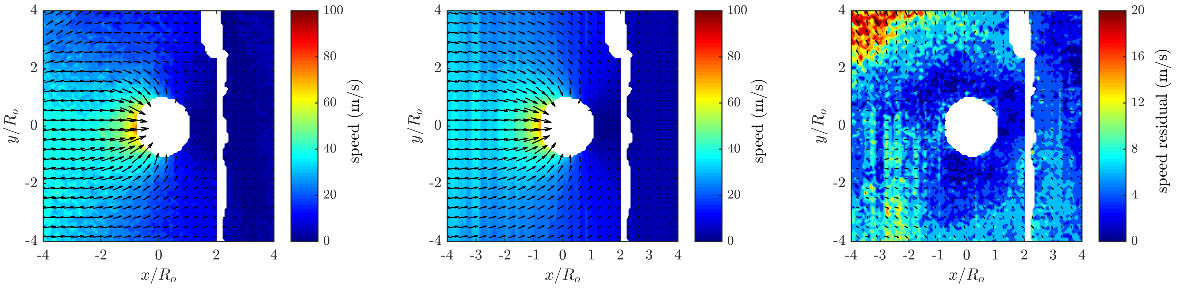

(a) Data (b) Model (c) Residuals

Figure F.57: Test# 725. A^* =0.75; x_c^* =0.23; S_{max} =81.3; S_{avg} =16.4; K =8.7; Q =30.7; Avg S_{res} =5.30.

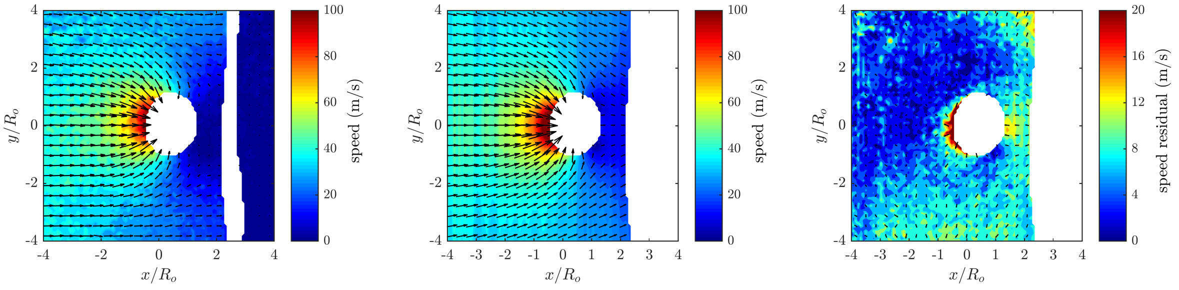

(a) Data (b) Model (c) Residuals

Figure F.58: Test# 716. A^* =0.61; x_c^* =0.36; S_{max} =106.3; S_{avg} =21.0; K =6.9; Q =26.1; Avg S_{res} =6.56.

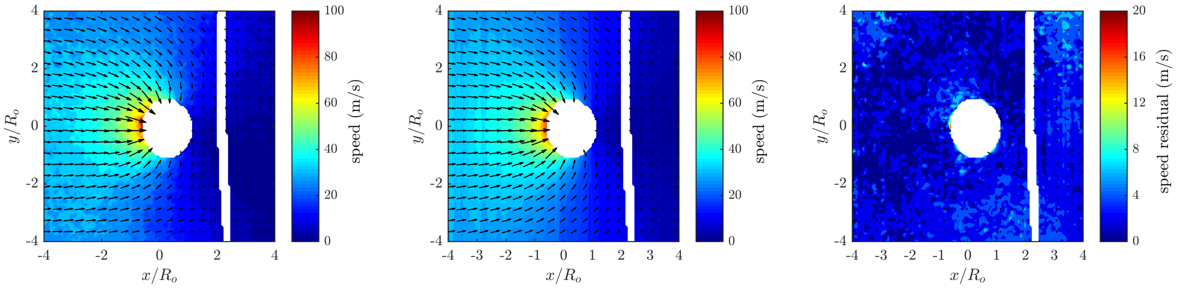

(a) Data (b) Model (c) Residuals

Figure F.59: Test# 762. $A^* = 0.59$; $x_c^* = 0.32$; $S_{max} = 102.0$; $S_{avg} = 20.2$; $K = 19.4$; $Q = 55.1$; Avg $S_{res} = 3.08$.

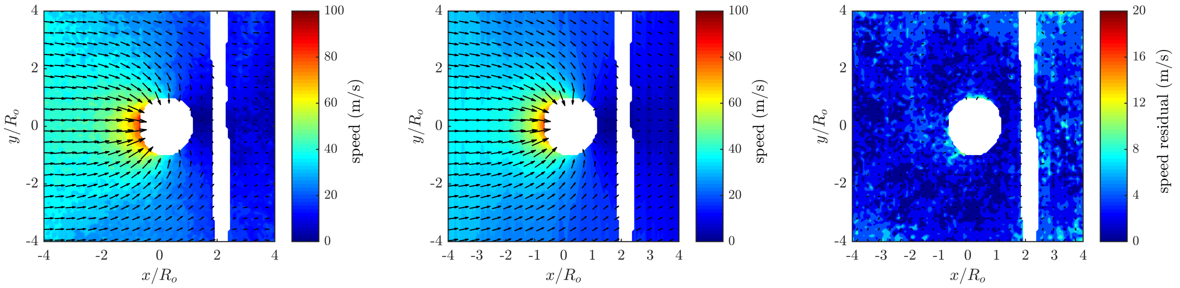

(a) Data (b) Model (c) Residuals

Figure F.60: Test# 900. $A^* = 0.57$; $x_c^* = 0.32$; $S_{max} = 89.6$; $S_{avg} = 23.5$; $K = 22.5$; $Q = 43.3$; Avg $S_{res} = 3.53$.

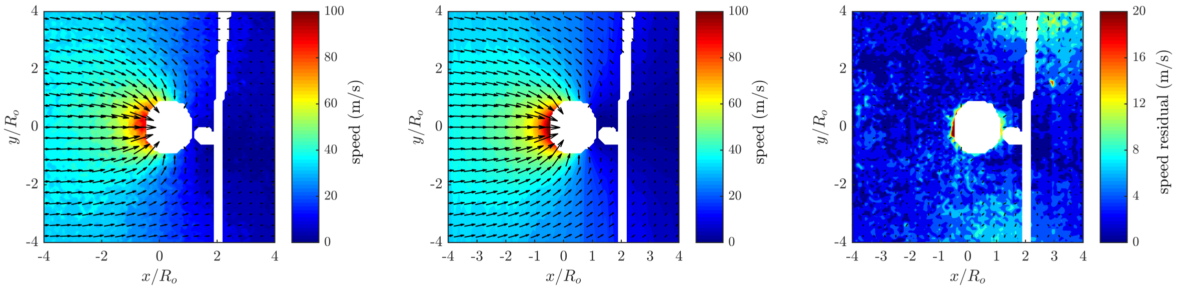

(a) Data (b) Model (c) Residuals

Figure F.61: Test# 741. $A^* = 0.54$; $x_c^* = 0.38$; $S_{max} = 94.8$; $S_{avg} = 20.9$; $K = 20.2$; $Q = 63.6$; Avg $S_{res} = 3.74$.

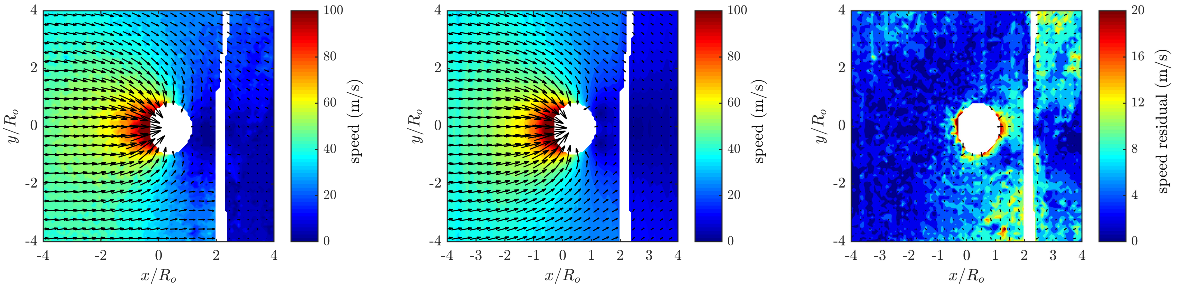

(a) Data (b) Model (c) Residuals

Figure F.62: Test# 788. A^* =0.41; x_c^* =0.48; S_{max} =133.2; S_{avg} =29.6; K =2.6; Q =6.1; Avg S_{res} =4.65.

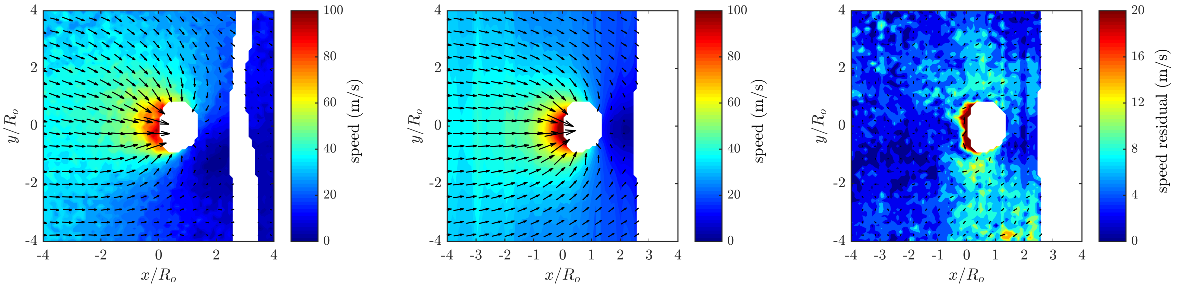

(a) Data (b) Model (c) Residuals

Figure F.63: Test# 714. A^* =0.20; x_c^* =0.55; S_{max} =98.9; S_{avg} =21.5; K =17.7; Q =52.4; Avg S_{res} =6.02.

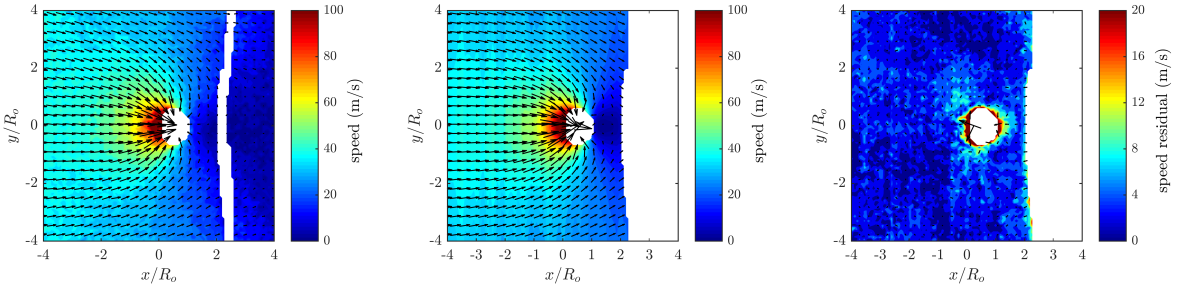

(a) Data (b) Model (c) Residuals

Figure F.64: Test# 713. A^* =0.16; x_c^* =0.67; S_{max} =127.2; S_{avg} =21.2; K =24.5; Q =44.3; Avg S_{res} =3.72.

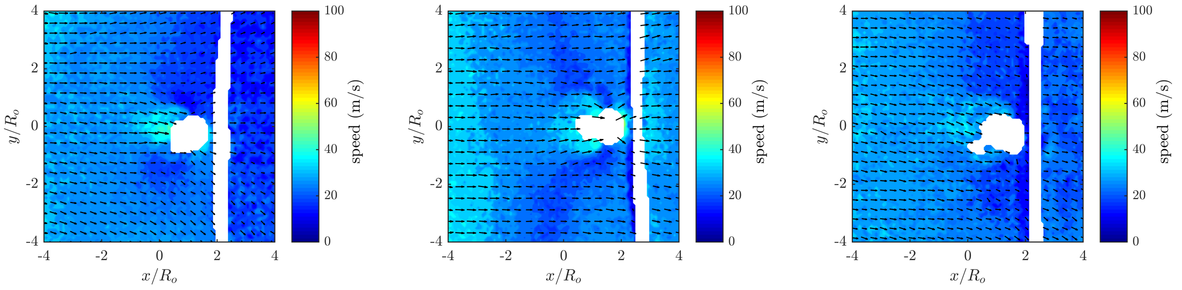

(a) Test# 711. A^* =0.00; x_c^* =1.17; S_{max} =53.7; S_{avg} =20.8.
(b) Test# 899. A^* =0.00; x_c^* =1.44; S_{max} =55.3; S_{avg} =26.3.
(c) Test# 898. A^* =0.00; x_c^* =1.48; S_{max} =41.7; S_{avg} =24.3.

Figure F.65: Raw data for tests 711-898. Void boundary could not be identified reliably(<3%), or test was after collapse, so model could not be computed.

F.2.3 Downstream 40:1 PDMS

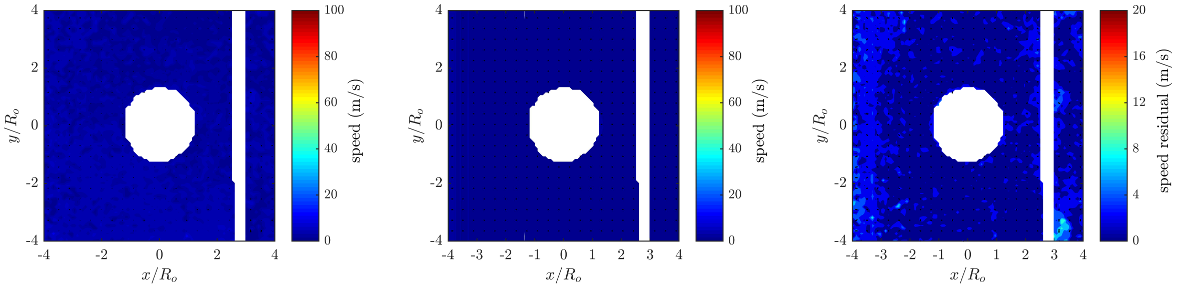

(a) Data
(b) Model
(c) Residuals

Figure F.66: Test# 832. A^* =1.01; x_c^* =0.01; S_{max} =18.5; S_{avg} =4.1; K =11.5; Q =44.9; Avg S_{res} =2.29.

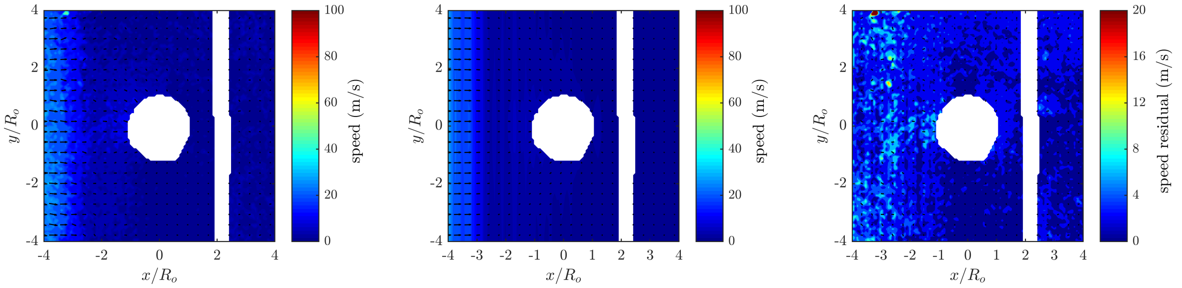

(a) Data
(b) Model
(c) Residuals

Figure F.67: Test# 733. A^* =1.00; x_c^* =0.03; S_{max} =48.8; S_{avg} =7.5; K =14.8; Q =42.1; Avg S_{res} =2.72.

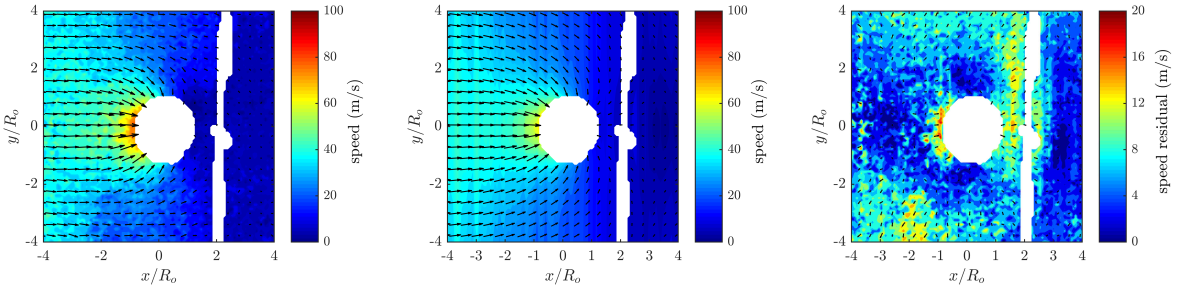

(a) Data (b) Model (c) Residuals

Figure F.68: Test# 875. $A^* = 0.77$; $x_c^* = 0.19$; $S_{max} = 79.3$; $S_{avg} = 19.3$; $K = 25.2$; $Q = 49.7$; Avg $S_{res} = 5.68$.

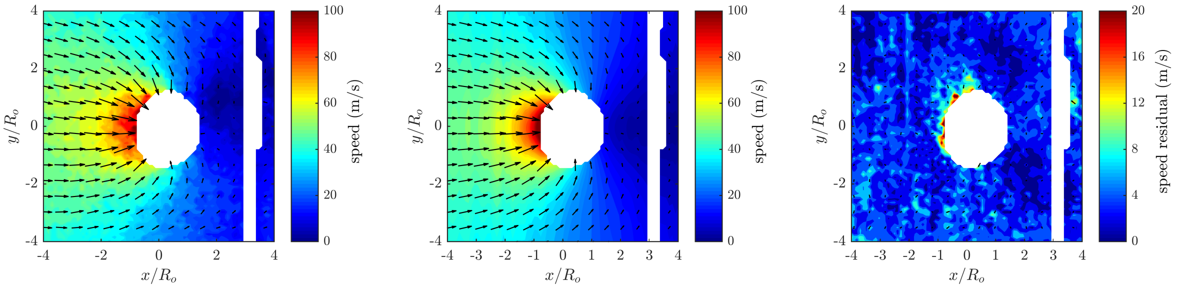

(a) Data (b) Model (c) Residuals

Figure F.69: Test# 916. $A^* = 0.76$; $x_c^* = 0.18$; $S_{max} = 103.7$; $S_{avg} = 26.1$; $K = 18.0$; $Q = 43.5$; Avg $S_{res} = 4.77$.

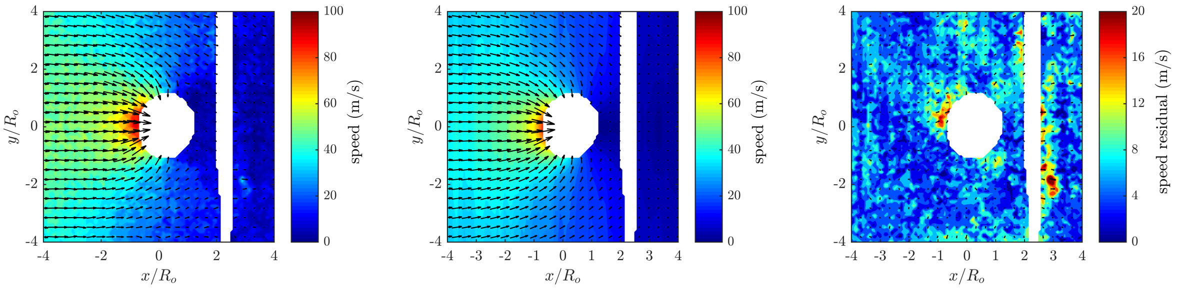

(a) Data (b) Model (c) Residuals

Figure F.70: Test# 873. $A^* = 0.67$; $x_c^* = 0.25$; $S_{max} = 90.7$; $S_{avg} = 24.0$; $K = 1.8$; $Q = 6.3$; Avg $S_{res} = 5.56$.

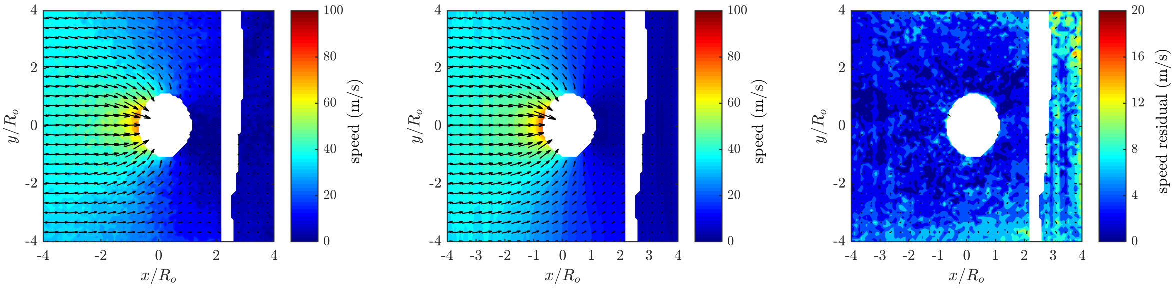

(a) Data (b) Model (c) Residuals

Figure F.71: Test# 710. A^* =0.67; x_c^* =0.29; S_{max} =77.5; S_{avg} =20.3; K =26.4; Q =52.4; Avg S_{res} =4.51.

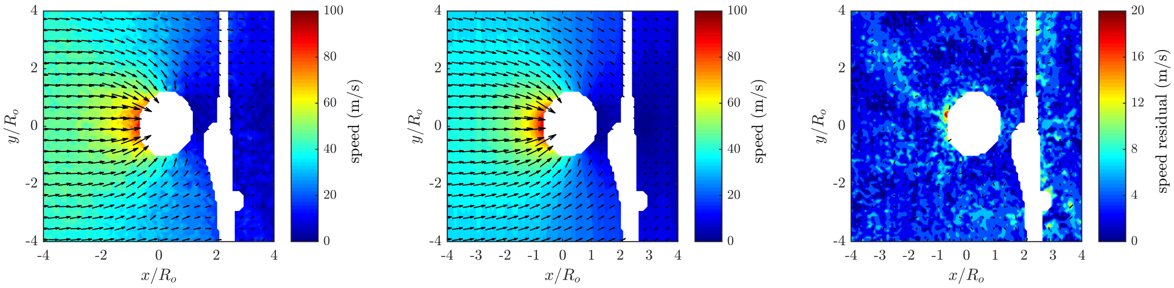

(a) Data (b) Model (c) Residuals

Figure F.72: Test# 903. A^* =0.63; x_c^* =0.30; S_{max} =95.5; S_{avg} =27.0; K =22.7; Q =65.9; Avg S_{res} =3.82.

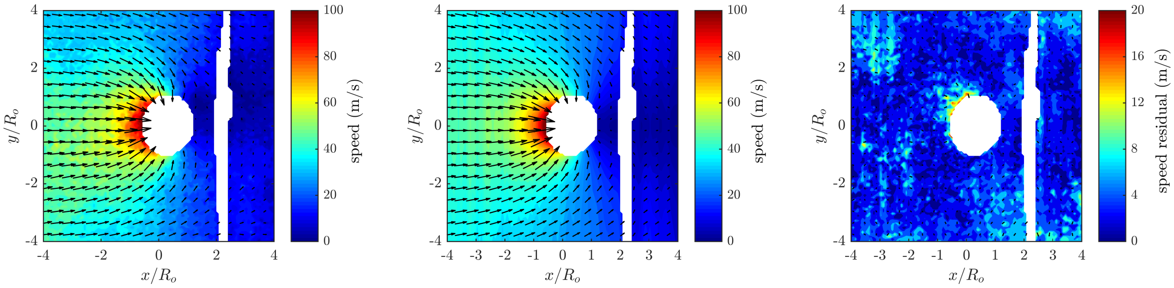

(a) Data (b) Model (c) Residuals

Figure F.73: Test# 874. A^* =0.59; x_c^* =0.32; S_{max} =111.2; S_{avg} =25.0; K =9.4; Q =17.6; Avg S_{res} =4.27.

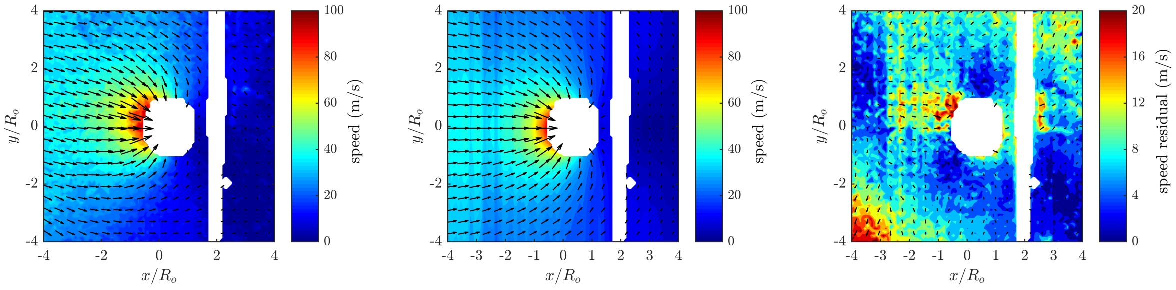

(a) Data (b) Model (c) Residuals

Figure F.74: Test# 735. $A^* = 0.59$; $x_c^* = 0.35$; $S_{max} = 98.2$; $S_{avg} = 19.0$; $K = 2.2$; $Q = 2.9$; Avg $S_{res} = 7.73$.

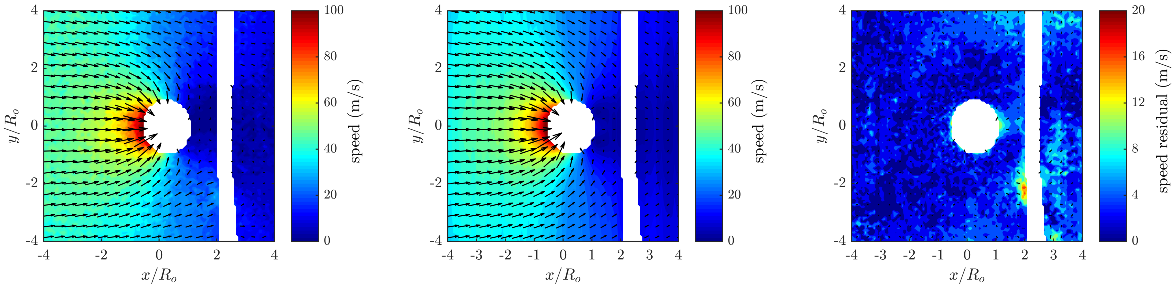

(a) Data (b) Model (c) Residuals

Figure F.75: Test# 913. $A^* = 0.56$; $x_c^* = 0.35$; $S_{max} = 118.4$; $S_{avg} = 25.8$; $K = 21.7$; $Q = 56.5$; Avg $S_{res} = 3.57$.

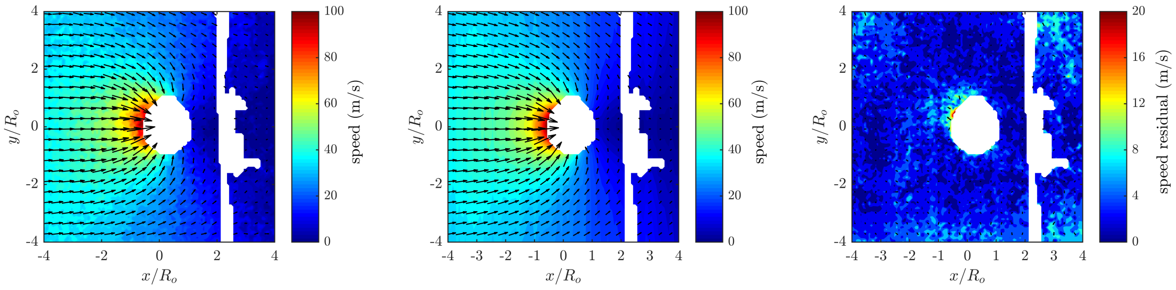

(a) Data (b) Model (c) Residuals

Figure F.76: Test# 780. $A^* = 0.56$; $x_c^* = 0.32$; $S_{max} = 101.3$; $S_{avg} = 24.1$; $K = 19.5$; $Q = 57.1$; Avg $S_{res} = 3.45$.

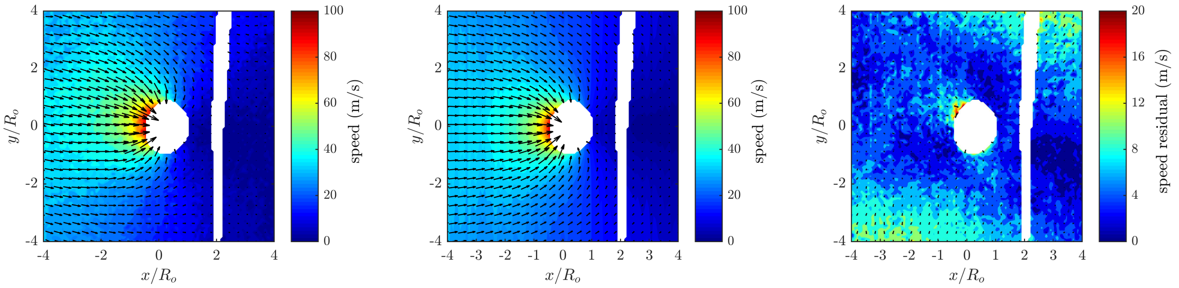

(a) Data (b) Model (c) Residuals

Figure F.77: Test# 709. $A^* = 0.54$; $x_c^* = 0.34$; $S_{max} = 95.6$; $S_{avg} = 18.3$; $K = 9.8$; $Q = 47.1$; Avg $S_{res} = 5.44$.

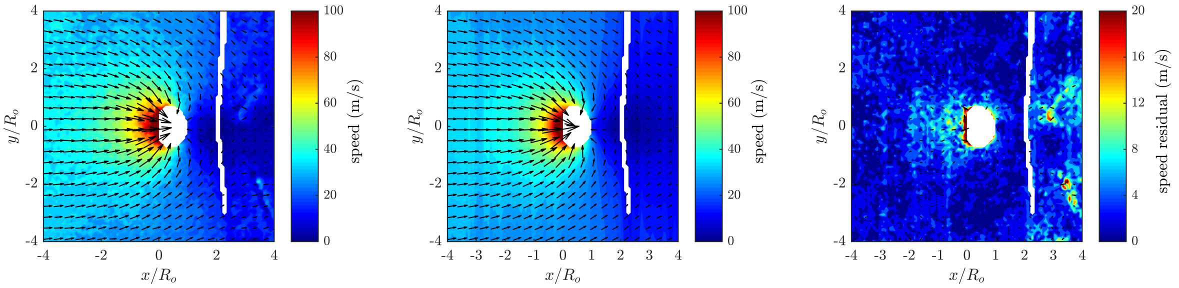

(a) Data (b) Model (c) Residuals

Figure F.78: Test# 763. $A^* = 0.21$; $x_c^* = 0.58$; $S_{max} = 139.8$; $S_{avg} = 24.1$; $K = 22.3$; $Q = 56.7$; Avg $S_{res} = 3.16$.

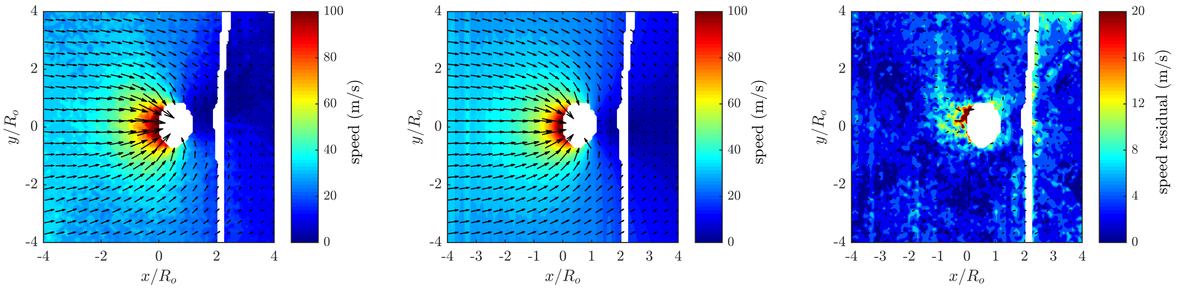

(a) Data (b) Model (c) Residuals

Figure F.79: Test# 876. $A^* = 0.18$; $x_c^* = 0.66$; $S_{max} = 136.6$; $S_{avg} = 19.0$; $K = 2.0$; $Q = 0.6$; Avg $S_{res} = 3.84$.

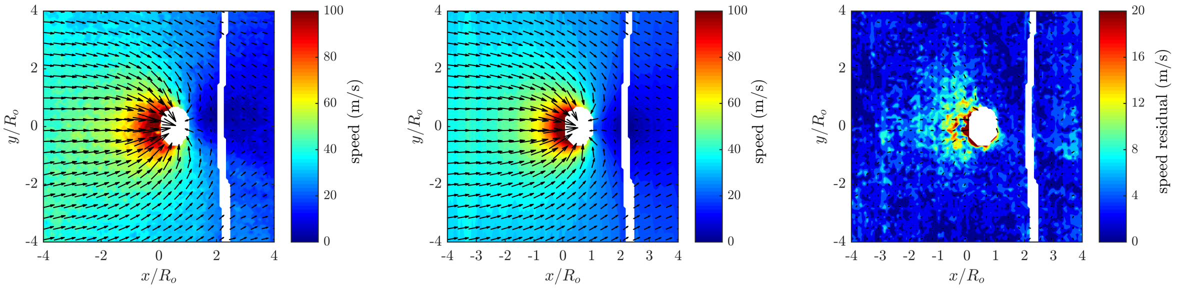

(a) Data (b) Model (c) Residuals

Figure F.80: Test# 905. $A^* = 0.10$; $x_c^* = 0.68$; $S_{max} = 135.6$; $S_{avg} = 30.1$; $K = 9.1$; $Q = 17.2$; Avg $S_{res} = 3.59$.

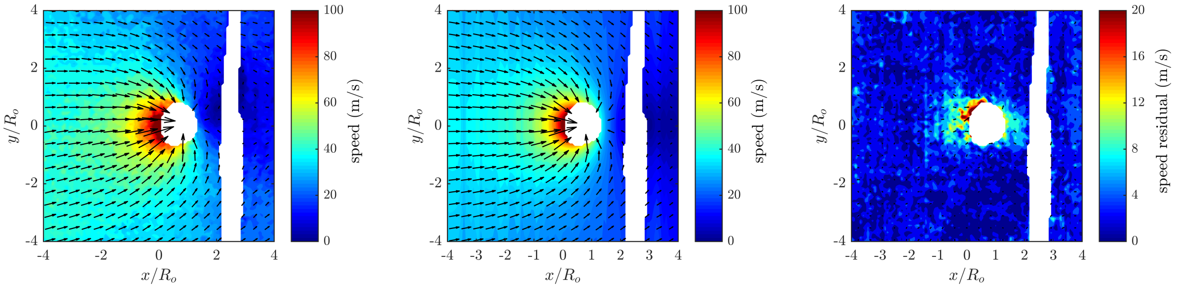

(a) Data (b) Model (c) Residuals

Figure F.81: Test# 907. $A^* = 0.08$; $x_c^* = 0.67$; $S_{max} = 124.8$; $S_{avg} = 27.2$; $K = 15.9$; $Q = 29.4$; Avg $S_{res} = 3.24$.

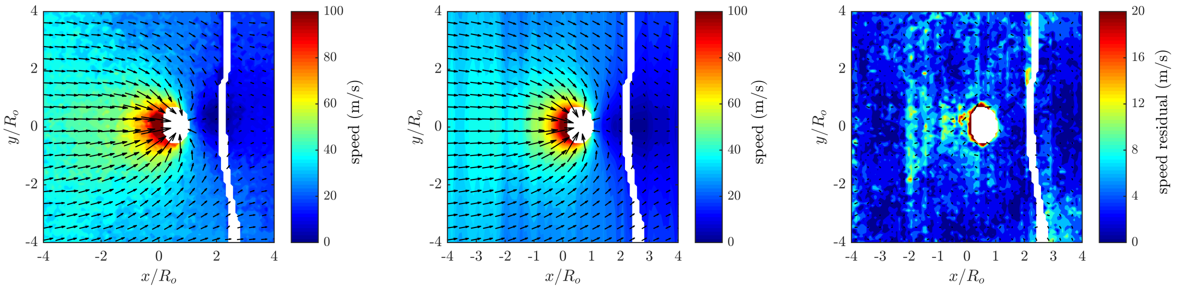

(a) Data (b) Model (c) Residuals

Figure F.82: Test# 915. $A^* = 0.07$; $x_c^* = 0.69$; $S_{max} = 126.7$; $S_{avg} = 27.3$; $K = 13.1$; $Q = 41.9$; Avg $S_{res} = 4.37$.

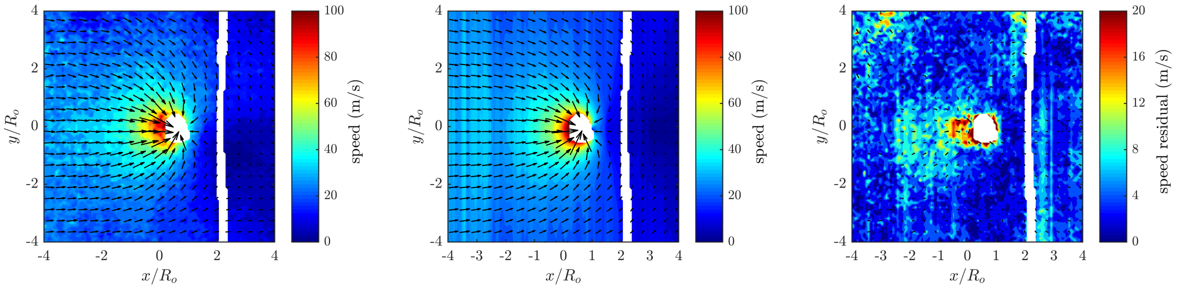

(a) Data (b) Model (c) Residuals

Figure F.83: Test# 737. $A^* = 0.04$; $x_c^* = 0.82$; $S_{max} = 100.9$; $S_{avg} = 18.3$; $K = 11.8$; $Q = 51.4$; Avg $S_{res} = 4.65$.

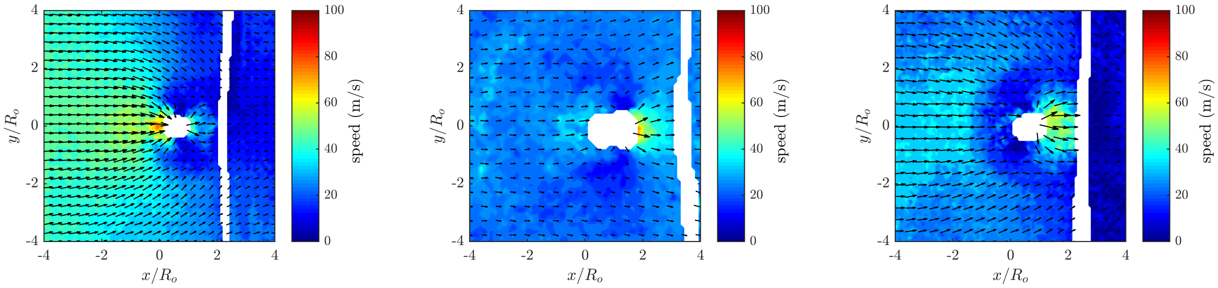

(a) Test# 914. $A^* = 0.01$; $x_c^* = 0.91$; $S_{max} = 81.0$; $S_{avg} = 28.5$.

(b) Test# 904. $A^* = 0.00$; $x_c^* = 0.87$; $S_{max} = 74.5$; $S_{avg} = 23.6$.

(c) Test# 736. $A^* = 0.00$; $x_c^* = 0.94$; $S_{max} = 65.3$; $S_{avg} = 18.8$.

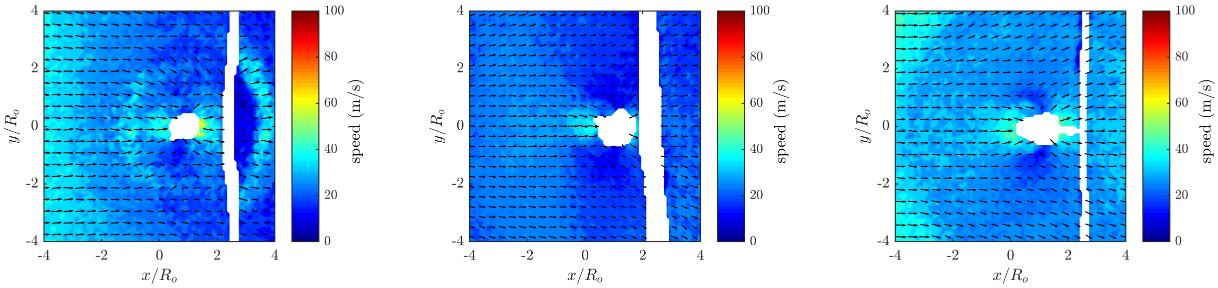

(d) Test# 908. $A^* = 0.00$; $x_c^* = 0.98$; $S_{max} = 67.5$; $S_{avg} = 22.9$.

(e) Test# 708. $A^* = 0.00$; $x_c^* = 1.22$; $S_{max} = 41.9$; $S_{avg} = 20.1$.

(f) Test# 906. $A^* = 0.00$; $x_c^* = 1.26$; $S_{max} = 50.7$; $S_{avg} = 27.7$.

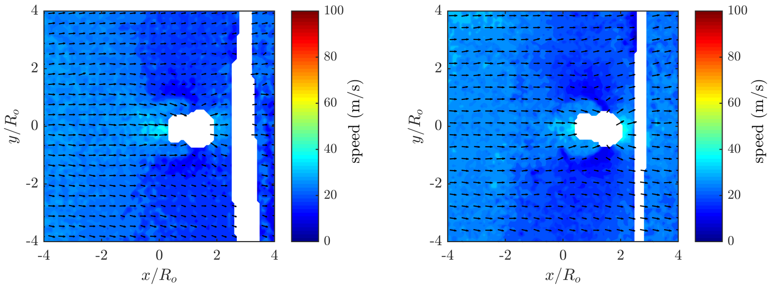

(g) Test# 902. $A^* = 0.00$; $x_c^* = 1.29$; $S_{max} = 39.6$; $S_{avg} = 21.6$.

(h) Test# 901. $A^* = 0.00$; $x_c^* = 1.29$; $S_{max} = 42.4$; $S_{avg} = 22.6$.

Figure F.84: Raw data for tests 914-901. Void boundary could not be identified reliably(<3%), or test was after collapse, so model could not be computed.

F.2.4 Downstream Aluminum

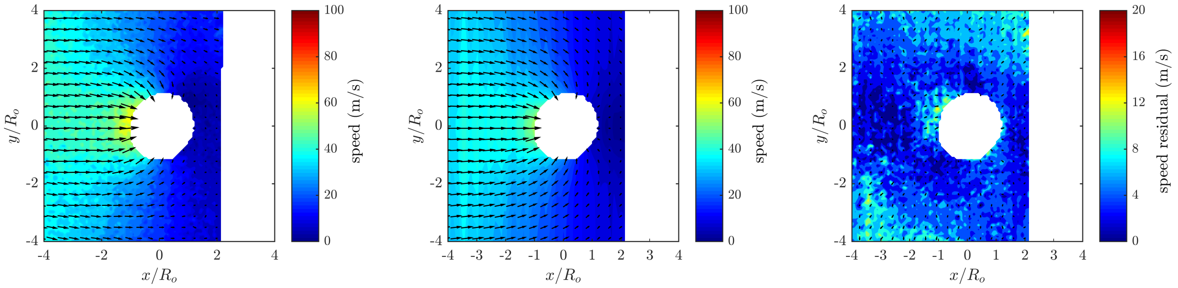

(a) Data (b) Model (c) Residuals

Figure F.85: Test# 882. A^* =0.89; x_c^* =0.11; S_{max} =65.0; S_{avg} =29.1; K =1.7; Q =0.8; Avg S_{res} =5.13.

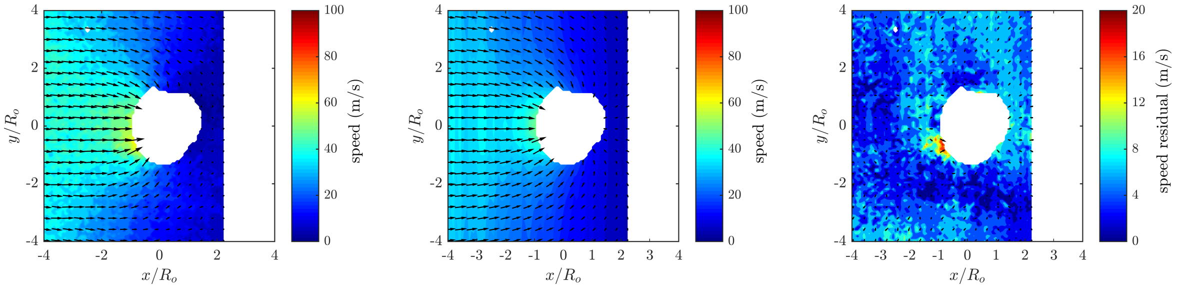

(a) Data (b) Model (c) Residuals

Figure F.86: Test# 877. A^* =0.81; x_c^* =0.12; S_{max} =62.3; S_{avg} =28.6; K =23.1; Q =36.3; Avg S_{res} =5.34.

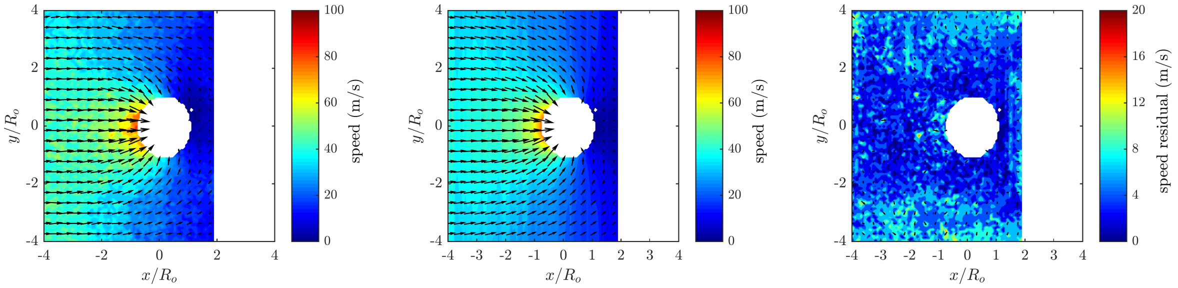

(a) Data (b) Model (c) Residuals

Figure F.87: Test# 879. A^* =0.70; x_c^* =0.23; S_{max} =82.5; S_{avg} =32.9; K =25.4; Q =42.0; Avg S_{res} =5.14.

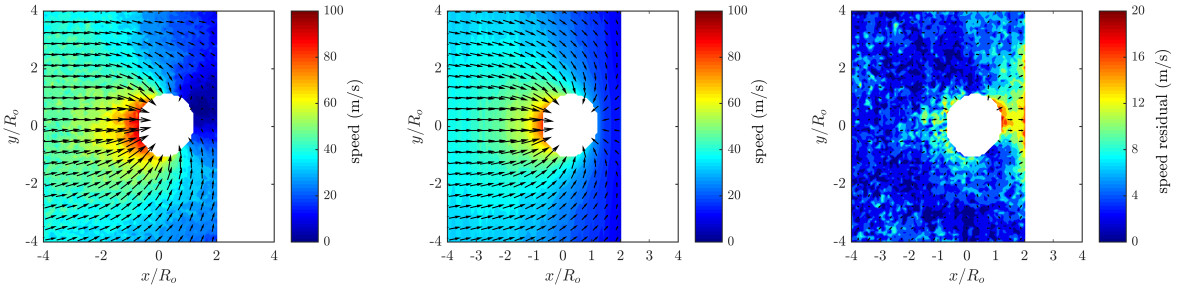

(a) Data (b) Model (c) Residuals

Figure F.88: Test# 884. A^* =0.60; x_c^* =0.33; S_{max} =104.7; S_{avg} =38.3; K =19.7; Q =36.6; Avg S_{res} =4.79.

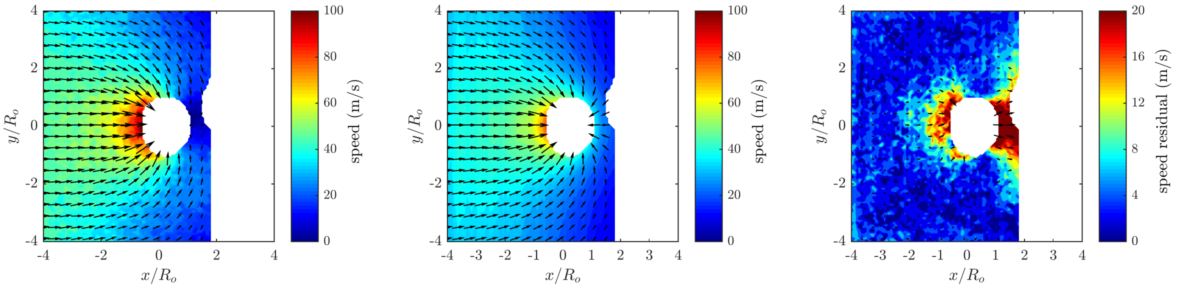

(a) Data (b) Model (c) Residuals

Figure F.89: Test# 878. A^* =0.57; x_c^* =0.28; S_{max} =126.8; S_{avg} =37.8; K =1.6; Q =9.5; Avg S_{res} =5.13.

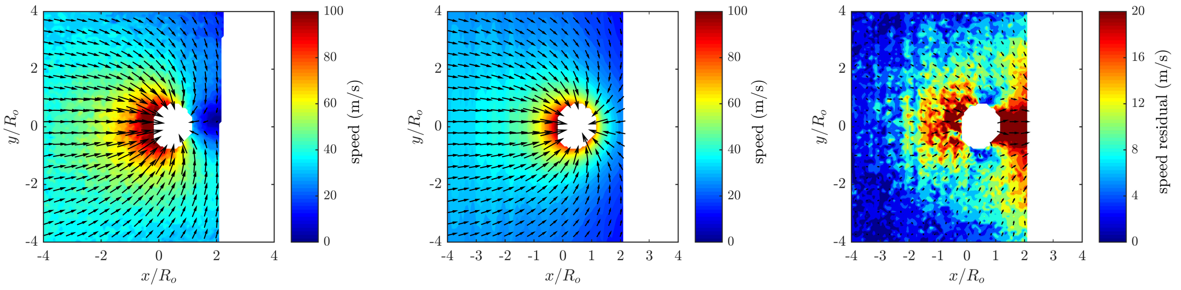

(a) Data (b) Model (c) Residuals

Figure F.90: Test# 881. A^* =0.21; x_c^* =0.56; S_{max} =131.6; S_{avg} =40.4; K =7.9; Q =29.2; Avg S_{res} =6.84.

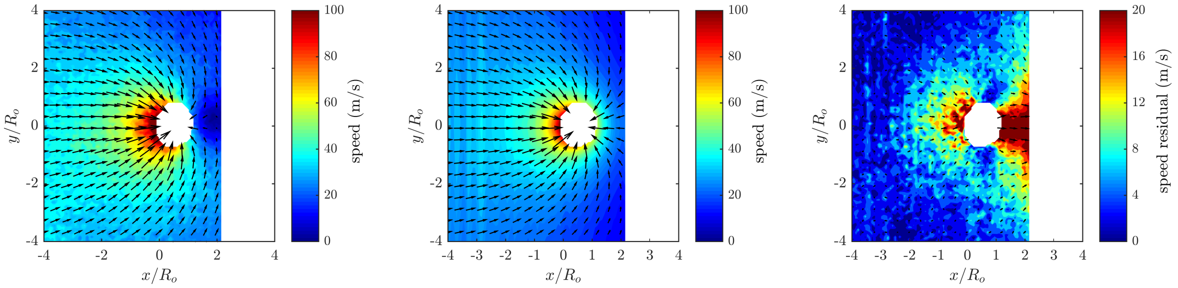

(a) Data (b) Model (c) Residuals

Figure F.91: Test# 880. A^* =0.14; x_c^* =0.53; S_{max} =127.4; S_{avg} =33.6; K =14.3; Q =46.1; Avg S_{res} =5.19.

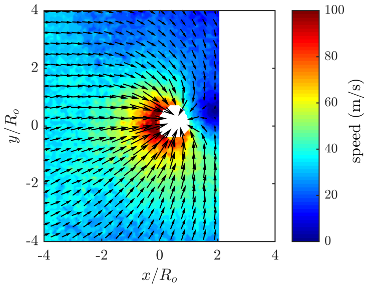

(a) Test# 883. A^* =0.04; x_c^* =0.75; S_{max} =122.3; S_{avg} =36.2.

Figure F.92: Raw data for tests 883-883. Void boundary could not be identified reliably(<3%), or test was after collapse, so model could not be computed.

F.3 Upstream Boundary

F.3.1 Upstream 20:1 PDMS

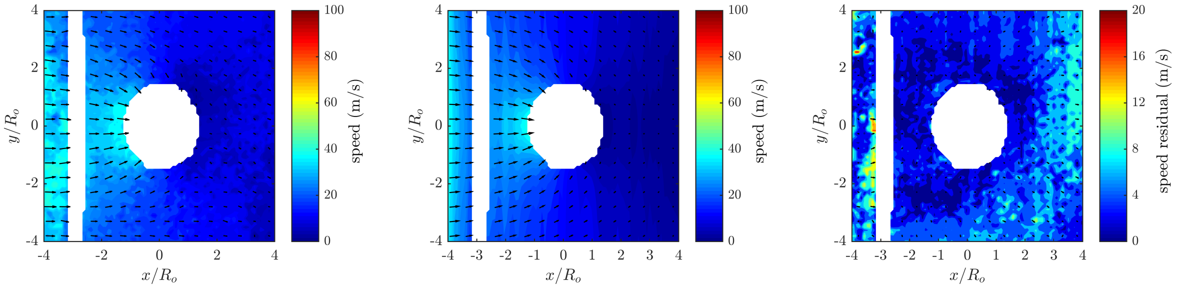

(a) Data (b) Model (c) Residuals

Figure F.93: Test# 816. A^* =1.01; x_c^* =0.01; S_{max} =57.1; S_{avg} =19.9; K =23.7; Q =59.4; Avg S_{res} =5.78.

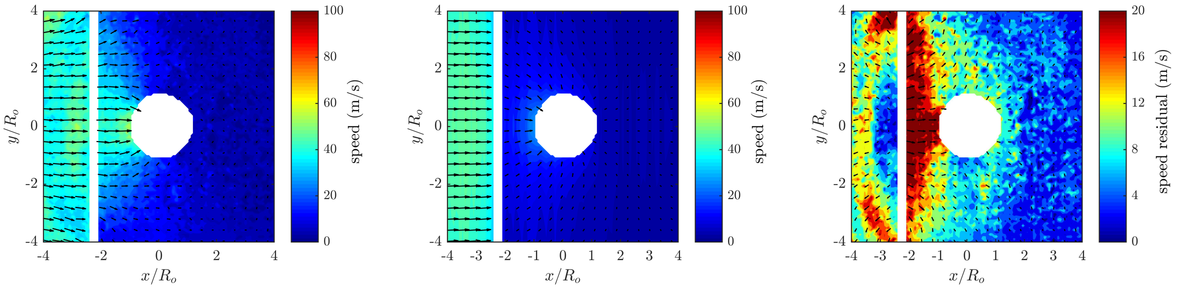

(a) Data (b) Model (c) Residuals

Figure F.94: Test# 803. $A^* = 1.01$; $x_c^* = 0.08$; $S_{max} = 60.2$; $S_{avg} = 20.5$; $K = 11.9$; $Q = 18.2$; Avg $S_{res} = 7.84$.

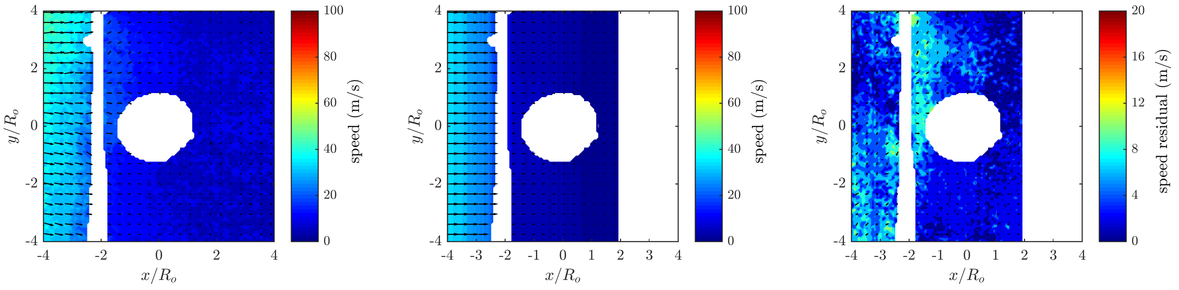

(a) Data (b) Model (c) Residuals

Figure F.95: Test# 868. $A^* = 1.00$; $x_c^* = 0.02$; $S_{max} = 55.1$; $S_{avg} = 15.3$; $K = 19.0$; $Q = 47.5$; Avg $S_{res} = 4.22$.

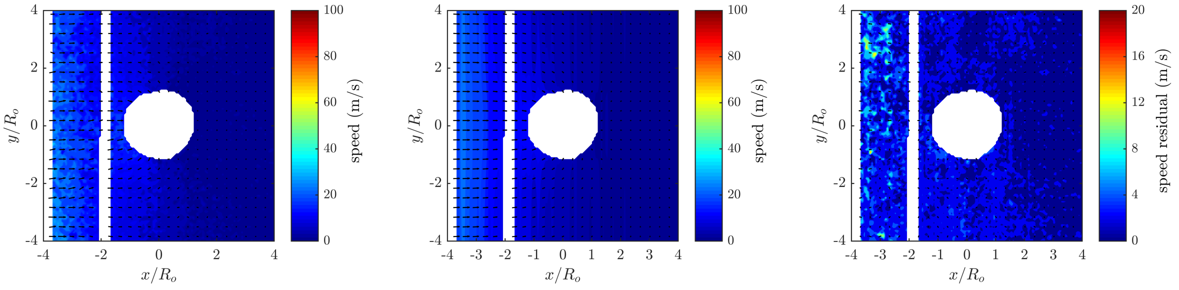

(a) Data (b) Model (c) Residuals

Figure F.96: Test# 729. $A^* = 0.99$; $x_c^* = 0.04$; $S_{max} = 32.4$; $S_{avg} = 5.0$; $K = 20.3$; $Q = 40.8$; Avg $S_{res} = 1.91$.

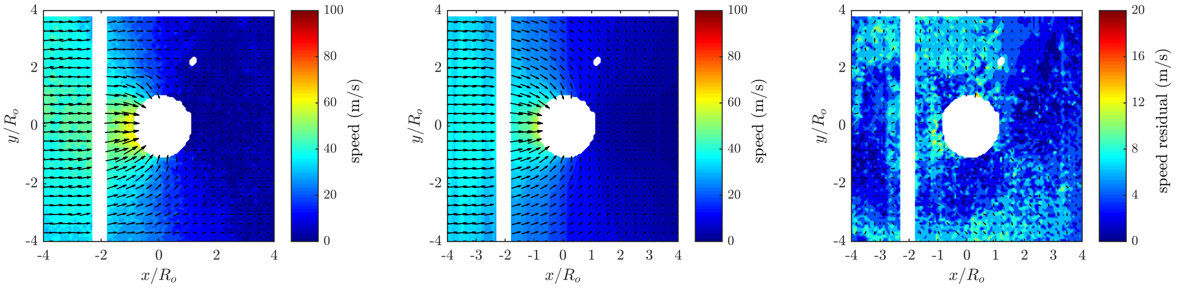

(a) Data (b) Model (c) Residuals

Figure F.97: Test# 804. A^* =0.88; x_c^* =0.13; S_{max} =69.1; S_{avg} =19.0; K =22.1; Q =62.5; Avg S_{res} =4.76.

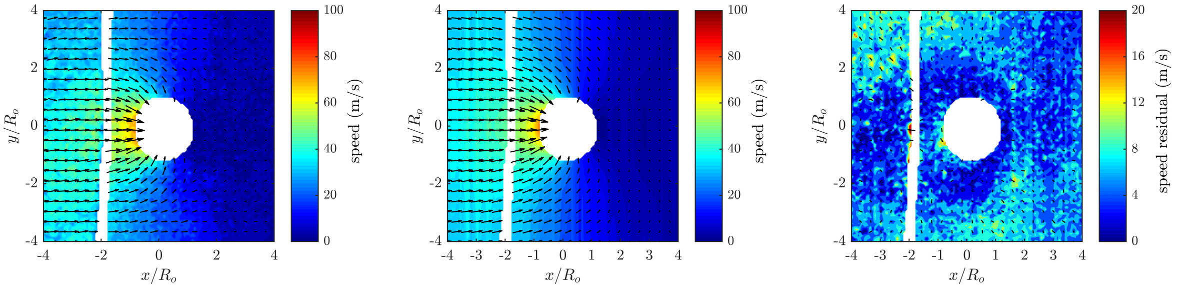

(a) Data (b) Model (c) Residuals

Figure F.98: Test# 767. A^* =0.86; x_c^* =0.18; S_{max} =73.8; S_{avg} =20.5; K =21.1; Q =51.6; Avg S_{res} =5.60.

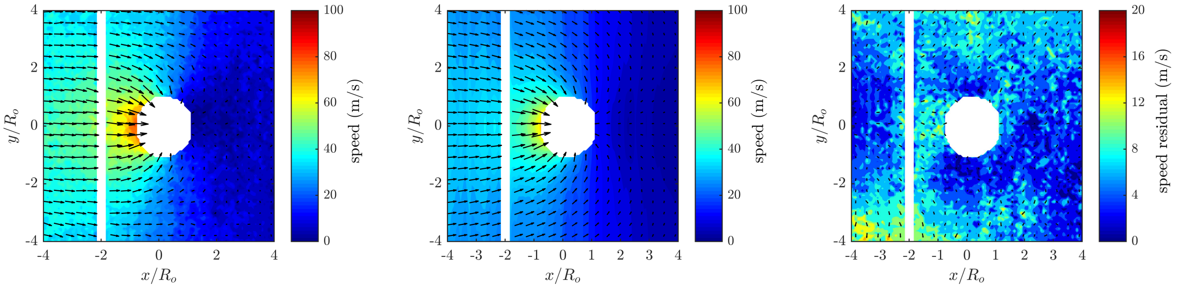

(a) Data (b) Model (c) Residuals

Figure F.99: Test# 858. A^* =0.73; x_c^* =0.23; S_{max} =82.4; S_{avg} =22.2; K =0.5; Q =26.2; Avg S_{res} =5.76.

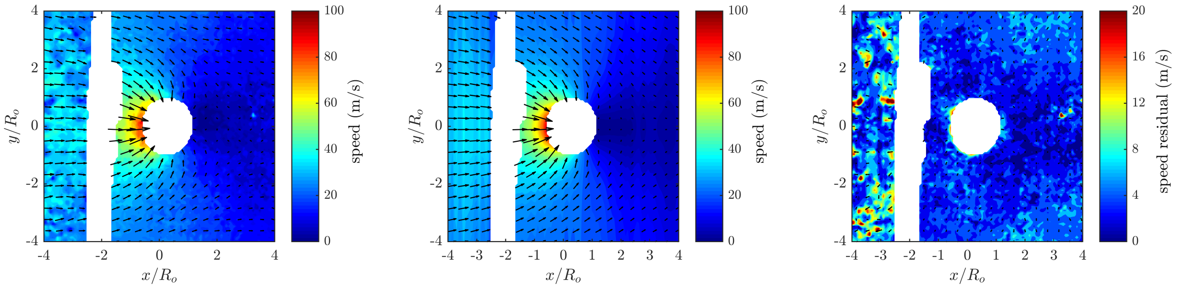

(a) Data (b) Model (c) Residuals

Figure F.100: Test# 793. A^* =0.63; x_c^* =0.32; S_{max} =88.2; S_{avg} =20.5; K =31.1; Q =53.8; Avg S_{res} =5.21.

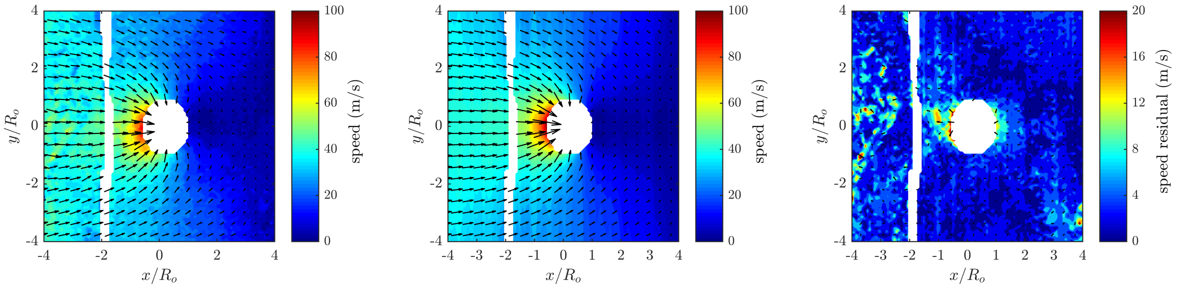

(a) Data (b) Model (c) Residuals

Figure F.101: Test# 805. A^* =0.58; x_c^* =0.29; S_{max} =87.1; S_{avg} =24.4; K =24.6; Q =42.3; Avg S_{res} =3.79.

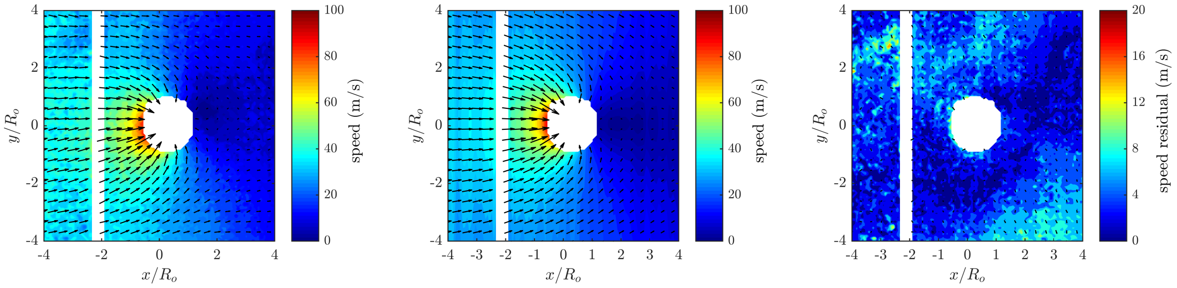

(a) Data (b) Model (c) Residuals

Figure F.102: Test# 815. A^* =0.56; x_c^* =0.38; S_{max} =87.0; S_{avg} =24.4; K =10.0; Q =46.7; Avg S_{res} =4.47.

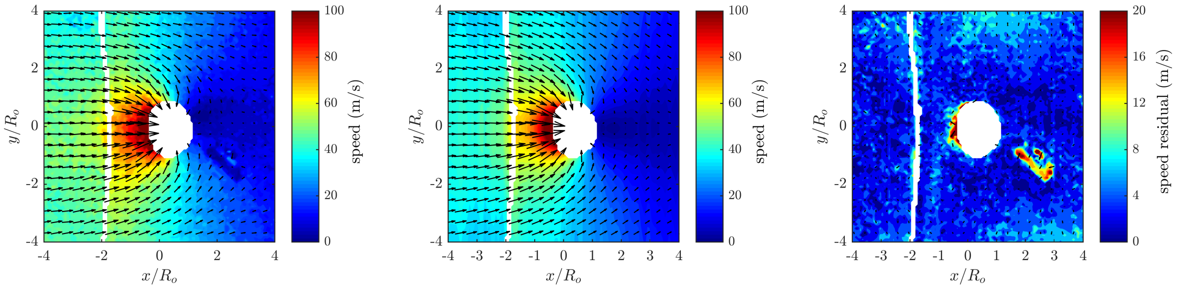

(a) Data (b) Model (c) Residuals

Figure F.103: Test# 811. $A^* = 0.54$; $x_c^* = 0.41$; $S_{max} = 124.5$; $S_{avg} = 31.8$; $K = 10.6$; $Q = 38.3$; Avg $S_{res} = 4.22$.

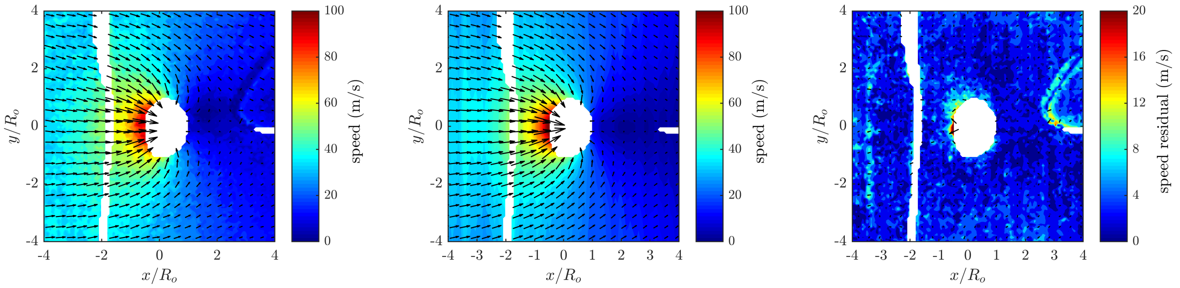

(a) Data (b) Model (c) Residuals

Figure F.104: Test# 810. $A^* = 0.49$; $x_c^* = 0.33$; $S_{max} = 95.4$; $S_{avg} = 25.3$; $K = 19.2$; $Q = 51.8$; Avg $S_{res} = 3.58$.

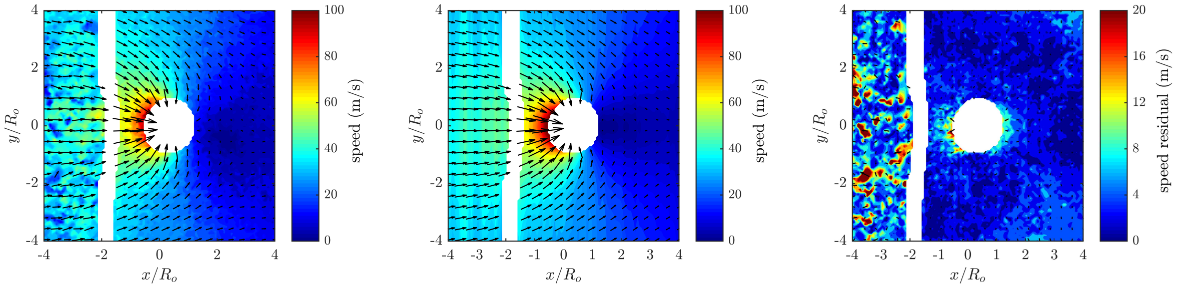

(a) Data (b) Model (c) Residuals

Figure F.105: Test# 755. $A^* = 0.46$; $x_c^* = 0.39$; $S_{max} = 103.6$; $S_{avg} = 24.5$; $K = 13.1$; $Q = 21.2$; Avg $S_{res} = 5.32$.

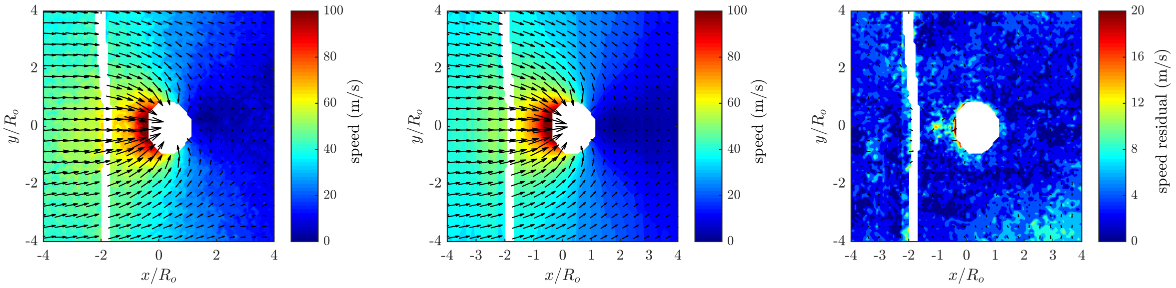

(a) Data (b) Model (c) Residuals

Figure F.106: Test# 814. $A^* = 0.45$; $x_c^* = 0.42$; $S_{max} = 120.2$; $S_{avg} = 31.2$; $K = 14.9$; $Q = 46.1$; Avg $S_{res} = 3.78$.

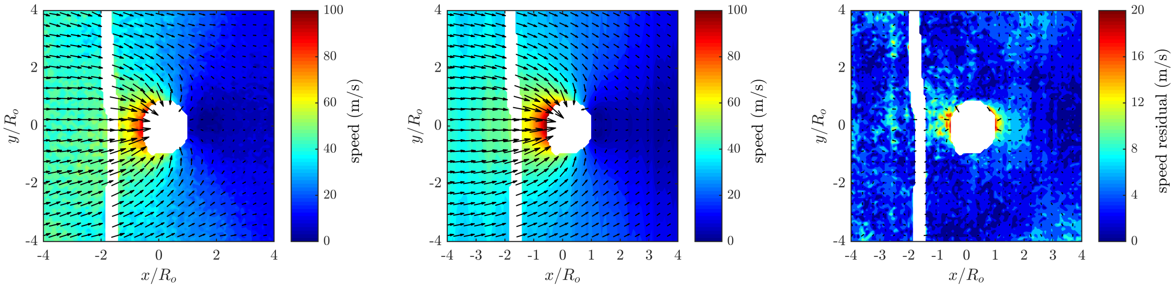

(a) Data (b) Model (c) Residuals

Figure F.107: Test# 859. $A^* = 0.45$; $x_c^* = 0.37$; $S_{max} = 92.3$; $S_{avg} = 25.5$; $K = 3.0$; $Q = 8.1$; Avg $S_{res} = 3.97$.

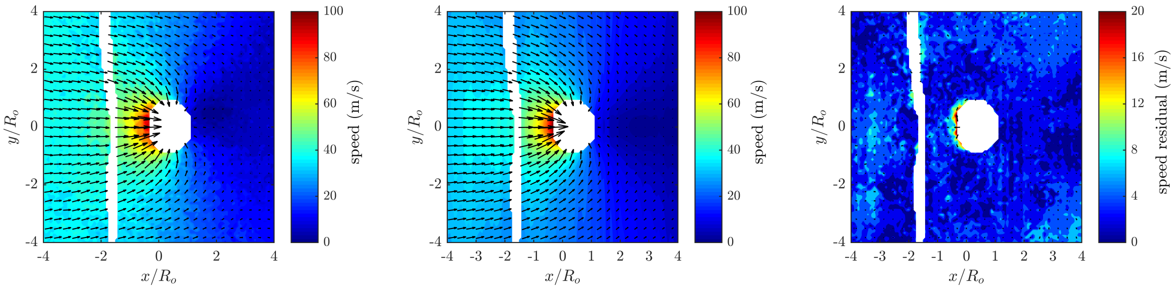

(a) Data (b) Model (c) Residuals

Figure F.108: Test# 860. $A^* = 0.42$; $x_c^* = 0.41$; $S_{max} = 95.2$; $S_{avg} = 23.7$; $K = 23.5$; $Q = 37.0$; Avg $S_{res} = 3.73$.

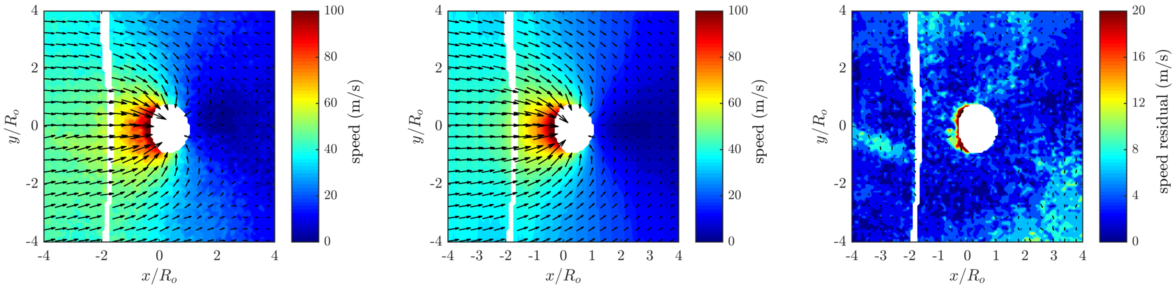

(a) Data (b) Model (c) Residuals

Figure F.109: Test# 794. $A^* = 0.40$; $x_c^* = 0.42$; $S_{max} = 116.8$; $S_{avg} = 31.8$; $K = 28.7$; $Q = 49.1$; Avg $S_{res} = 4.51$.

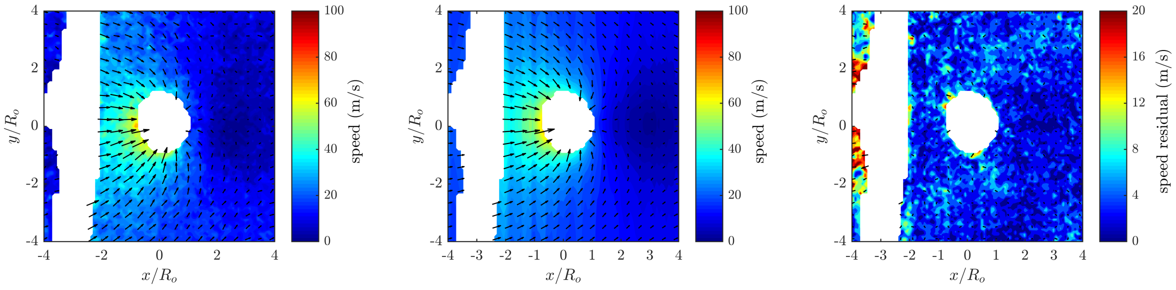

(a) Data (b) Model (c) Residuals

Figure F.110: Test# 744. $A^* = 0.39$; $x_c^* = 0.34$; $S_{max} = 72.9$; $S_{avg} = 14.5$; $K = 23.0$; $Q = 55.4$; Avg $S_{res} = 5.26$.

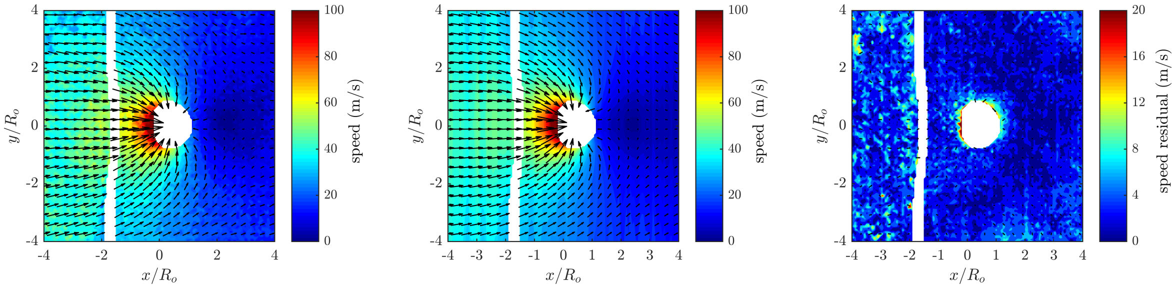

(a) Data (b) Model (c) Residuals

Figure F.111: Test# 758. $A^* = 0.38$; $x_c^* = 0.52$; $S_{max} = 125.2$; $S_{avg} = 29.7$; $K = 8.4$; $Q = 38.6$; Avg $S_{res} = 3.78$.

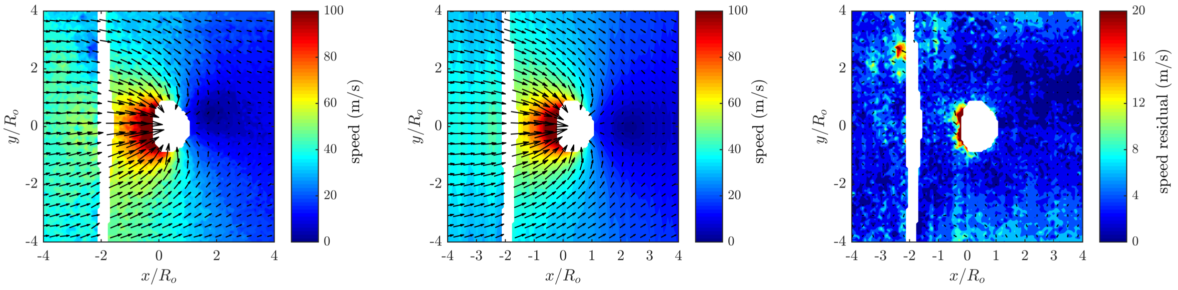

(a) Data (b) Model (c) Residuals

Figure F.112: Test# 807. A^* =0.37; x_c^* =0.44; S_{max} =160.5; S_{avg} =33.8; K =14.7; Q =30.1; Avg S_{res} =4.05.

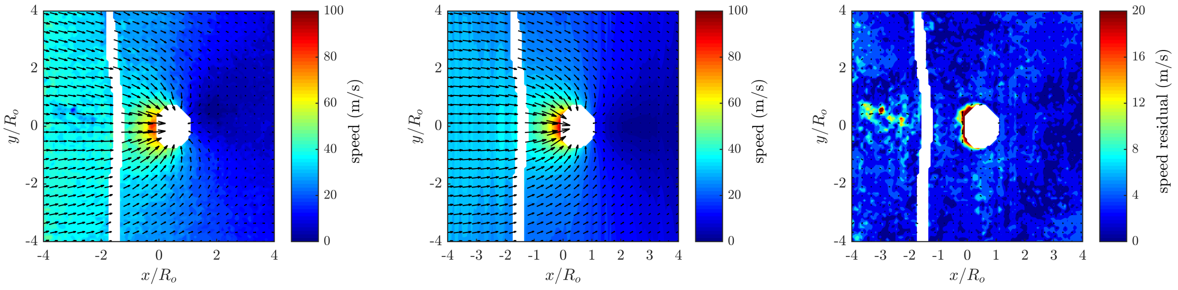

(a) Data (b) Model (c) Residuals

Figure F.113: Test# 866. A^* =0.20; x_c^* =0.54; S_{max} =84.4; S_{avg} =21.2; K =24.1; Q =42.4; Avg S_{res} =3.38.

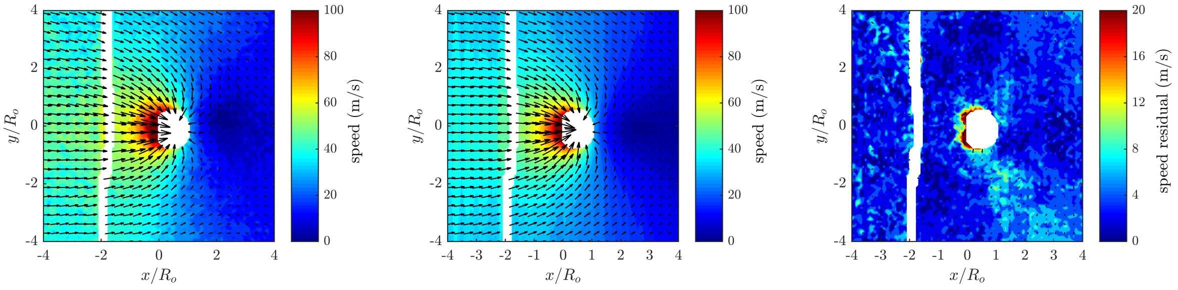

(a) Data (b) Model (c) Residuals

Figure F.114: Test# 867. A^* =0.19; x_c^* =0.60; S_{max} =129.7; S_{avg} =27.4; K =9.6; Q =40.2; Avg S_{res} =4.29.

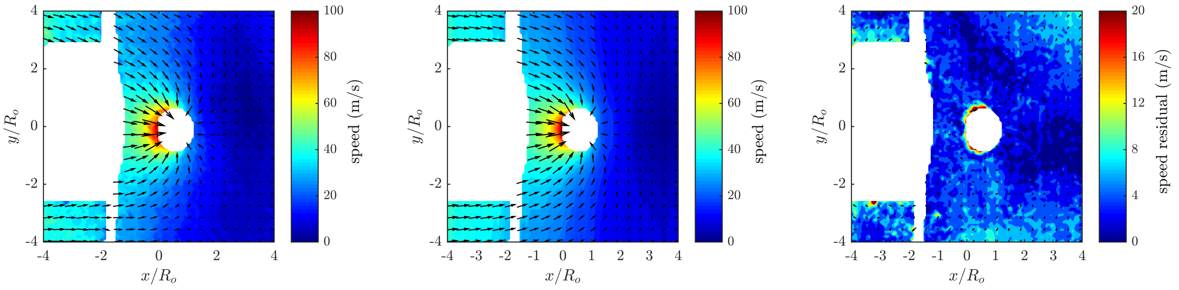

(a) Data (b) Model (c) Residuals

Figure F.115: Test# 792. A^* =0.16; x_c^* =0.64; S_{max} =95.3; S_{avg} =22.2; K =19.9; Q =58.2; Avg S_{res} =5.05.

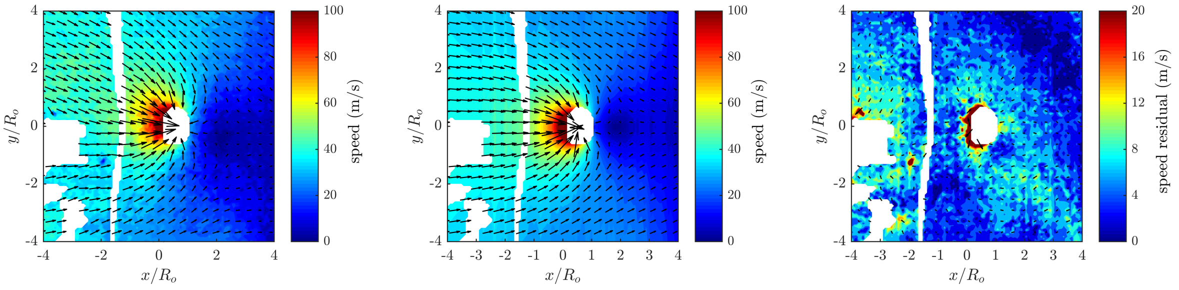

(a) Data (b) Model (c) Residuals

Figure F.116: Test# 730. A^* =0.12; x_c^* =0.67; S_{max} =140.7; S_{avg} =20.6; K =11.9; Q =39.4; Avg S_{res} =5.17.

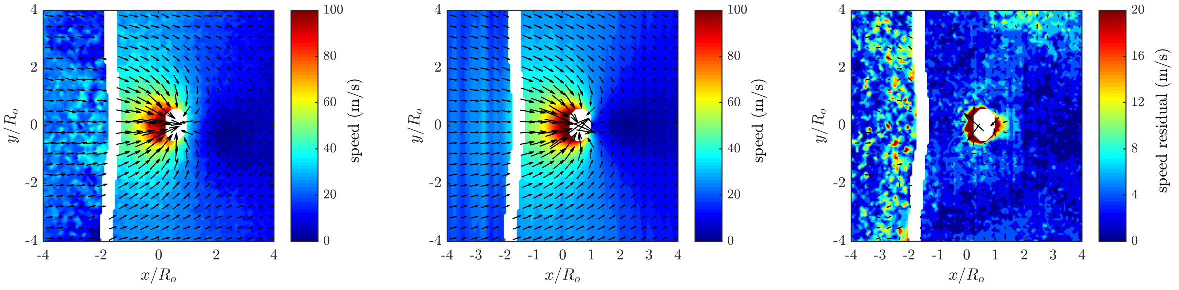

(a) Data (b) Model (c) Residuals

Figure F.117: Test# 766. A^* =0.08; x_c^* =0.74; S_{max} =140.8; S_{avg} =22.7; K =24.2; Q =40.8; Avg S_{res} =4.97.

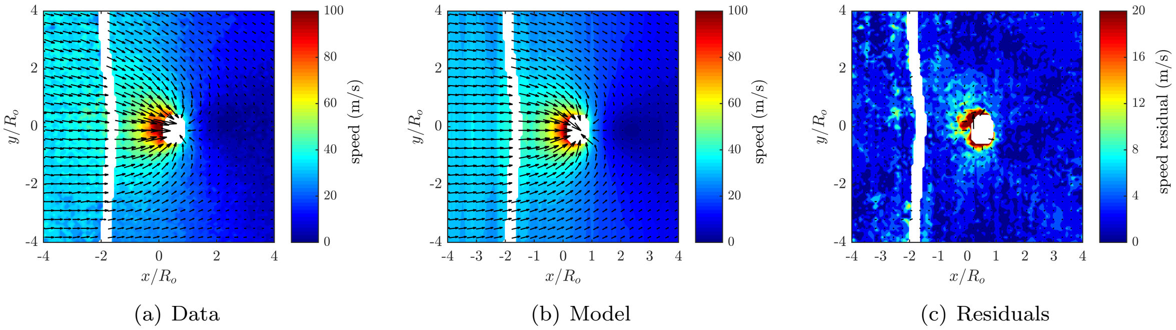

(a) Data (b) Model (c) Residuals

Figure F.118: Test# 865. $A^* = 0.06$; $x_c^* = 0.71$; $S_{max} = 113.7$; $S_{avg} = 21.8$; $K = 30.0$; $Q = 41.6$; Avg $S_{res} = 3.48$.

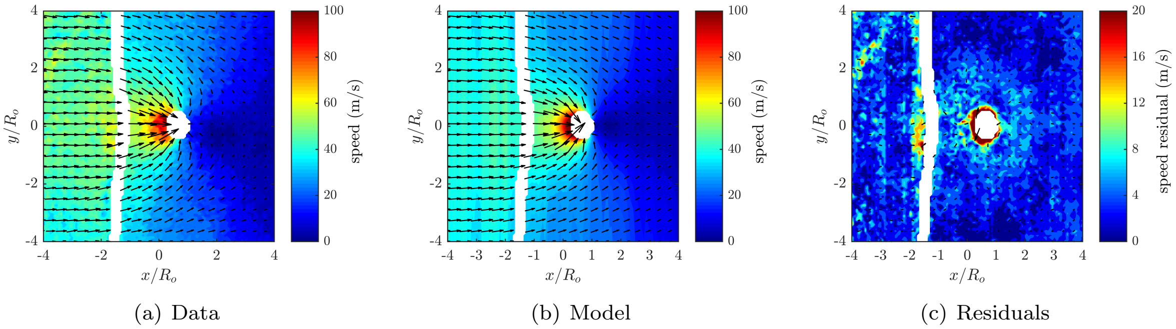

(a) Data (b) Model (c) Residuals

Figure F.119: Test# 759. $A^* = 0.03$; $x_c^* = 0.83$; $S_{max} = 113.5$; $S_{avg} = 29.0$; $K = 10.0$; $Q = 26.9$; Avg $S_{res} = 4.19$.

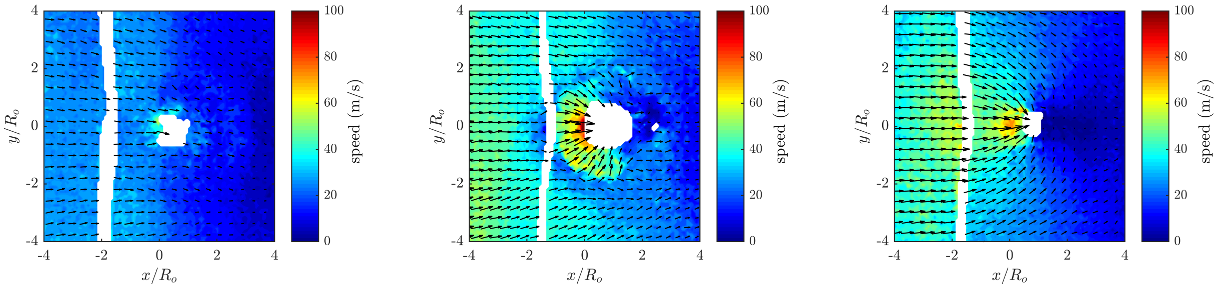

(a) Test# 808. A^* =0.00; x_c^* =0.57; S_{max} =55.4; S_{avg} =17.7.

(b) Test# 806. A^* =0.00; x_c^* =0.73; S_{max} =112.8; S_{avg} =31.4.

(c) Test# 754. A^* =0.00; x_c^* =0.93; S_{max} =78.8; S_{avg} =27.2.

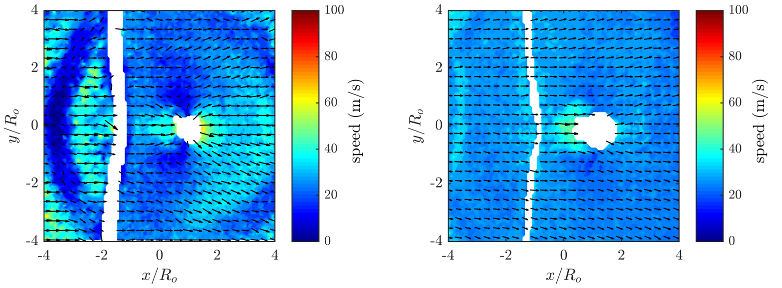

(d) Test# 757. A^* =0.00; x_c^* =1.17; S_{max} =75.0; S_{avg} =26.9.

(e) Test# 812. A^* =0.00; x_c^* =1.27; S_{max} =51.6; S_{avg} =26.0.

Figure F.120: Raw data for tests 808-812. Void boundary could not be identified reliably(<3%), or test was after collapse, so model could not be computed.

F.3.2 Upstream 30:1 PDMS

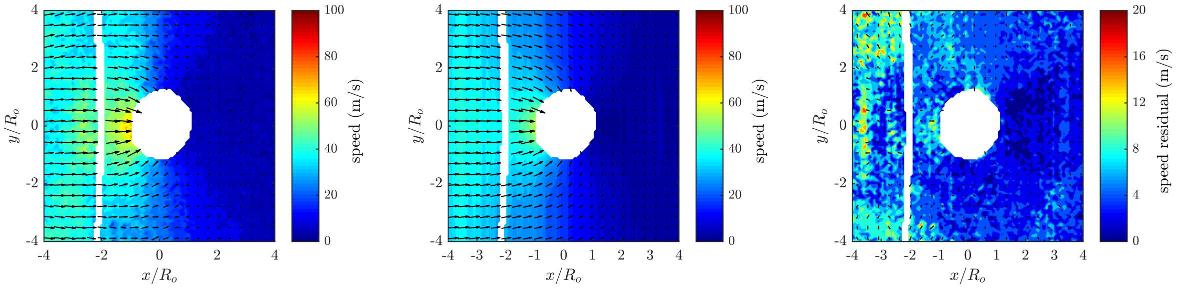

(a) Data

(b) Model

(c) Residuals

Figure F.121: Test# 848. A^* =0.96; x_c^* =0.04; S_{max} =70.5; S_{avg} =22.2; K =20.8; Q =56.4; Avg S_{res} =5.20.

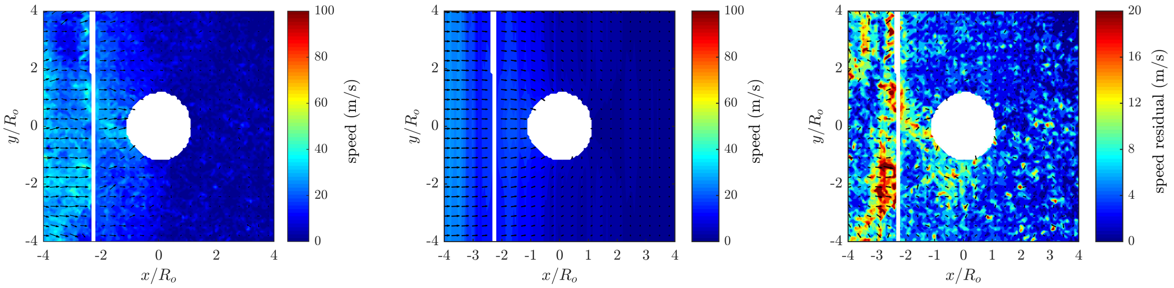

(a) Data (b) Model (c) Residuals

Figure F.122: Test# 724. A^* =0.96; x_c^* =0.04; S_{max} =49.5; S_{avg} =12.3; K =5.4; Q =51.1; Avg S_{res} =5.64.

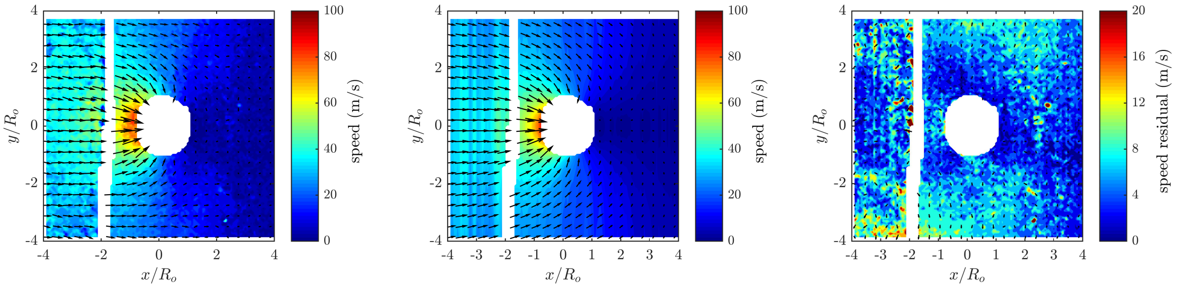

(a) Data (b) Model (c) Residuals

Figure F.123: Test# 738. A^* =0.78; x_c^* =0.18; S_{max} =84.8; S_{avg} =18.4; K =9.5; Q =35.9; Avg S_{res} =5.43.

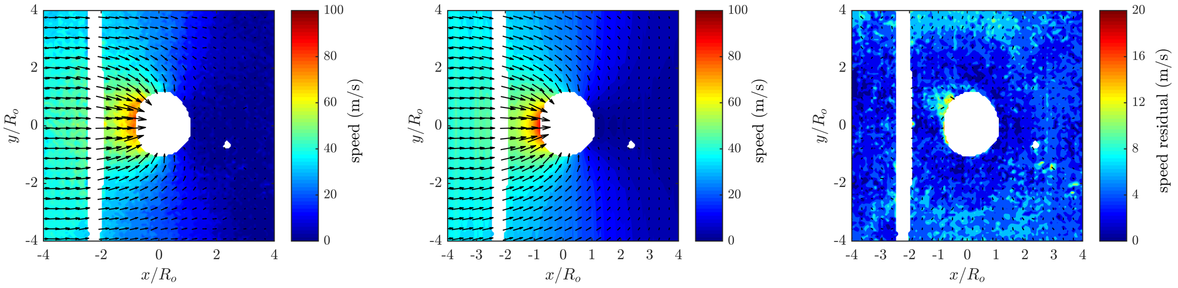

(a) Data (b) Model (c) Residuals

Figure F.124: Test# 723. A^* =0.77; x_c^* =0.18; S_{max} =84.2; S_{avg} =16.9; K =21.5; Q =39.8; Avg S_{res} =3.91.

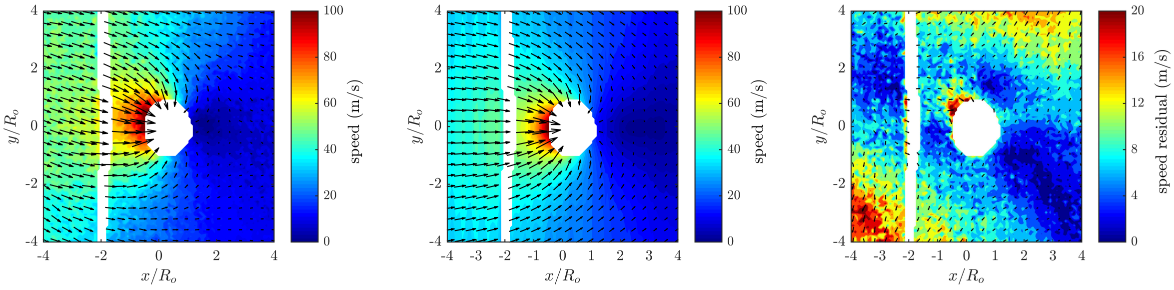

(a) Data (b) Model (c) Residuals

Figure F.125: Test# 847. $A^* = 0.54$; $x_c^* = 0.36$; $S_{max} = 112.2$; $S_{avg} = 27.9$; $K = 19.0$; $Q = 39.6$; Avg $S_{res} = 8.29$.

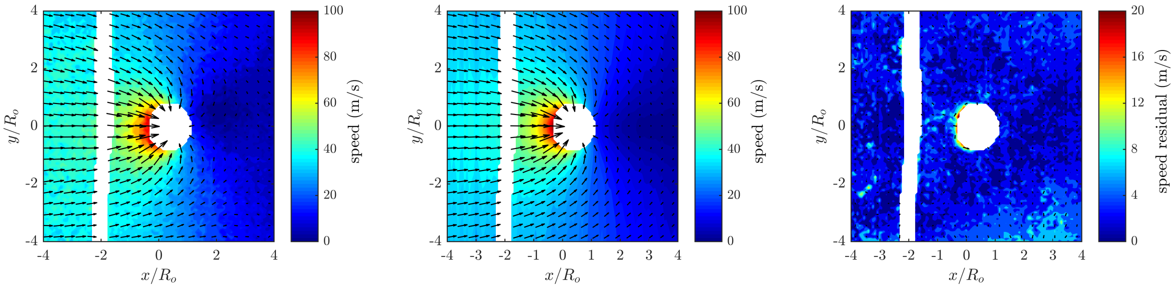

(a) Data (b) Model (c) Residuals

Figure F.126: Test# 798. $A^* = 0.40$; $x_c^* = 0.48$; $S_{max} = 97.7$; $S_{avg} = 24.8$; $K = 24.0$; $Q = 55.2$; Avg $S_{res} = 3.40$.

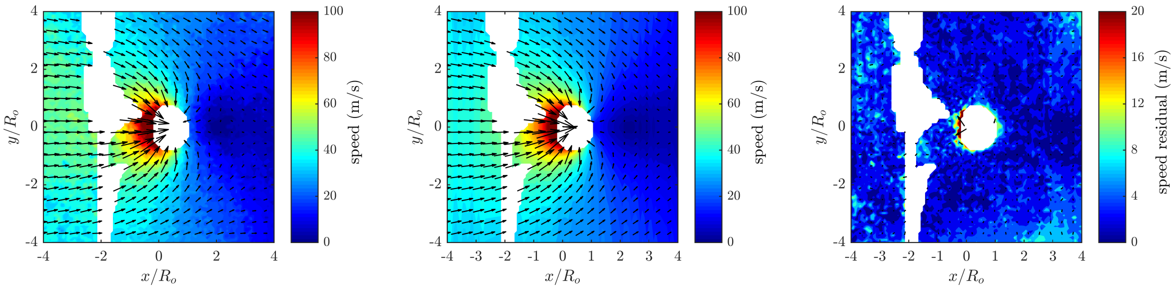

(a) Data (b) Model (c) Residuals

Figure F.127: Test# 796. $A^* = 0.32$; $x_c^* = 0.52$; $S_{max} = 131.5$; $S_{avg} = 30.1$; $K = 8.5$; $Q = 16.1$; Avg $S_{res} = 3.82$.

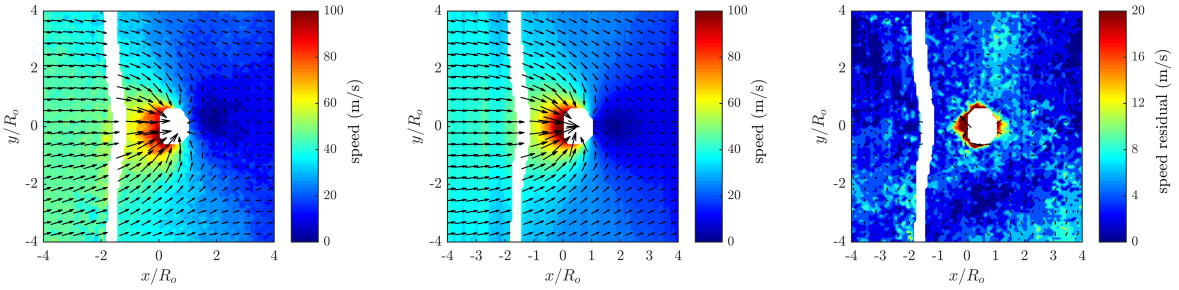

(a) Data (b) Model (c) Residuals

Figure F.128: Test# 790. A^* =0.20; x_c^* =0.63; S_{max} =115.7; S_{avg} =31.7; K =19.6; Q =32.1; Avg S_{res} =4.43.

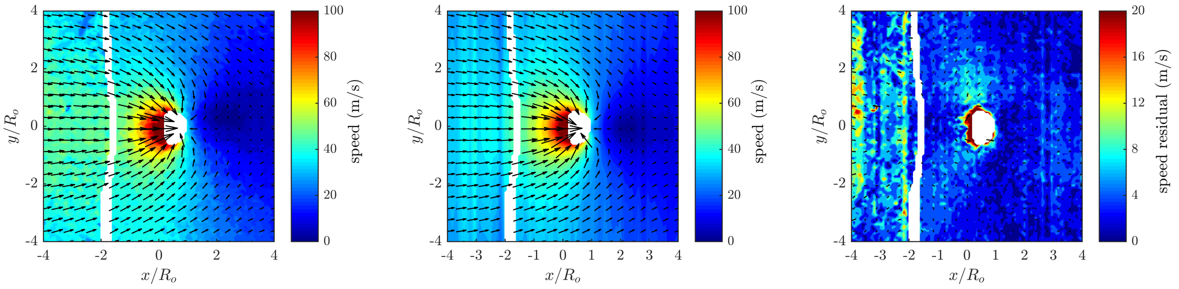

(a) Data (b) Model (c) Residuals

Figure F.129: Test# 797. A^* =0.09; x_c^* =0.66; S_{max} =140.7; S_{avg} =28.3; K =21.8; Q =45.2; Avg S_{res} =4.35.

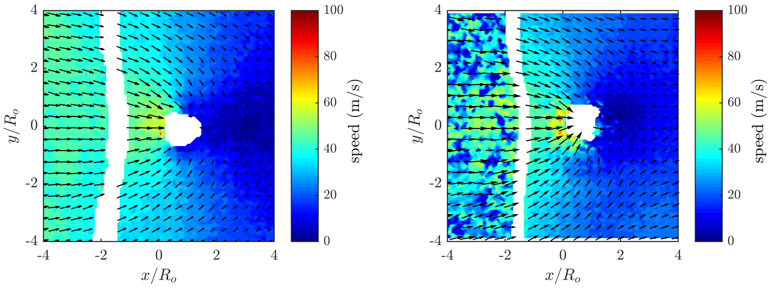

(a) Test# 789. A^* =0.02; x_c^* =0.80; S_{max} =82.8; S_{avg} =29.9.

(b) Test# 739. A^* =0.00; x_c^* =0.88; S_{max} =82.0; S_{avg} =23.9.

Figure F.130: Raw data for tests 789-739. Void boundary could not be identified reliably(<3%), or test was after collapse, so model could not be computed.

F.3.3 Upstream 40:1 PDMS

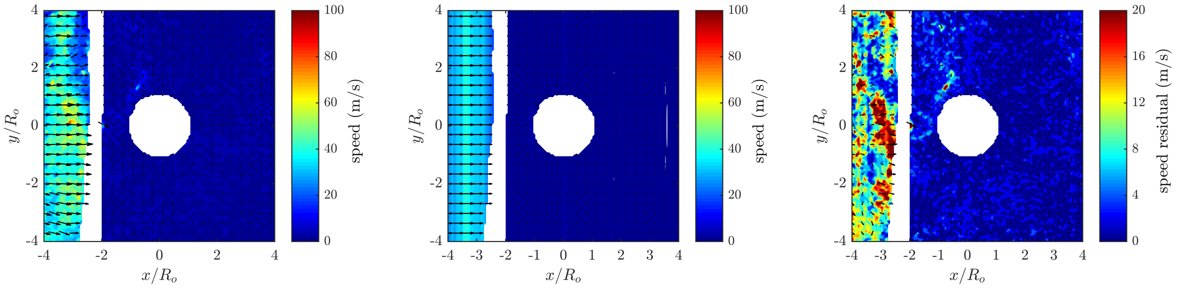

(a) Data (b) Model (c) Residuals

Figure F.131: Test# 719. A^* =1.01; x_c^* =0.01; S_{max} =87.8; S_{avg} =10.6; K =14.3; Q =28.6; Avg S_{res} =4.19.

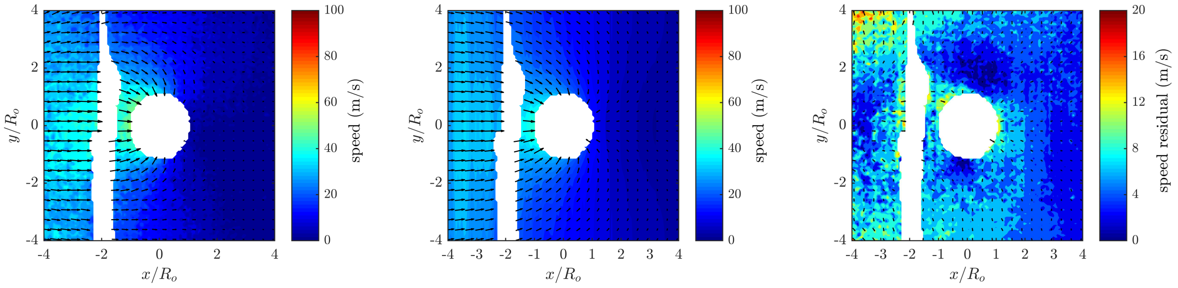

(a) Data (b) Model (c) Residuals

Figure F.132: Test# 720. A^* =0.78; x_c^* =0.19; S_{max} =51.2; S_{avg} =12.8; K =3.4; Q =66.0; Avg S_{res} =4.93.

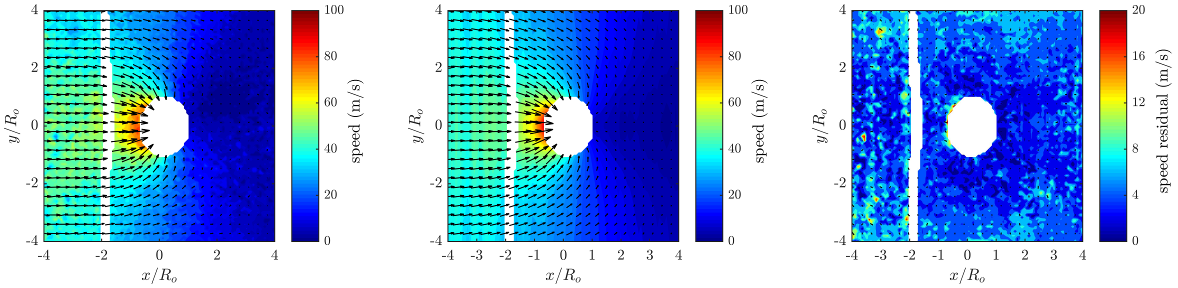

(a) Data (b) Model (c) Residuals

Figure F.133: Test# 870. A^* =0.66; x_c^* =0.22; S_{max} =85.3; S_{avg} =19.9; K =20.0; Q =53.3; Avg S_{res} =4.84.

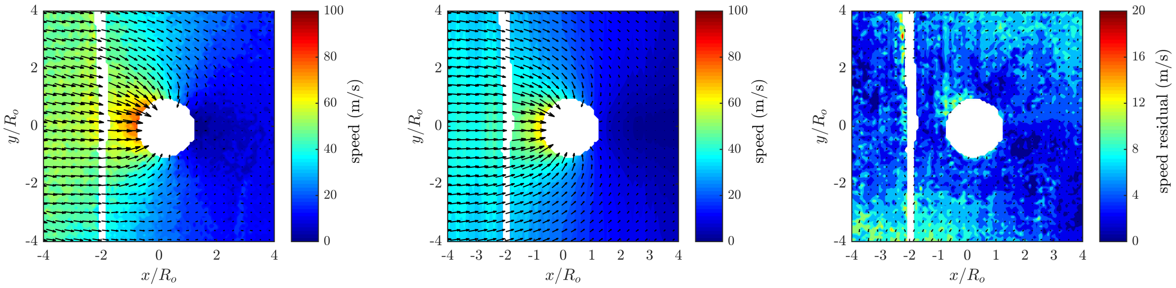

(a) Data (b) Model (c) Residuals

Figure F.134: Test# 869. A^{*} =0.65; x_c^{*} =0.32; S_{max} =82.1; S_{avg} =27.6; K =1.0; Q =4.1; Avg S_{res} =5.37.

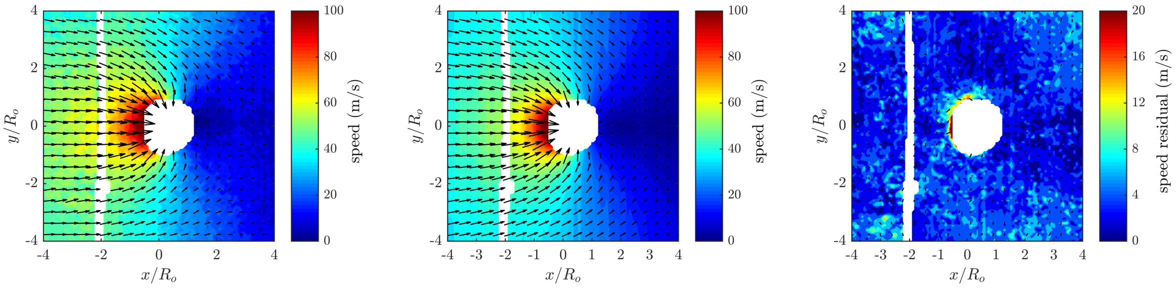

(a) Data (b) Model (c) Residuals

Figure F.135: Test# 846. A^{*} =0.60; x_c^{*} =0.29; S_{max} =111.2; S_{avg} =30.0; K =15.3; Q =47.6; Avg S_{res} =4.12.

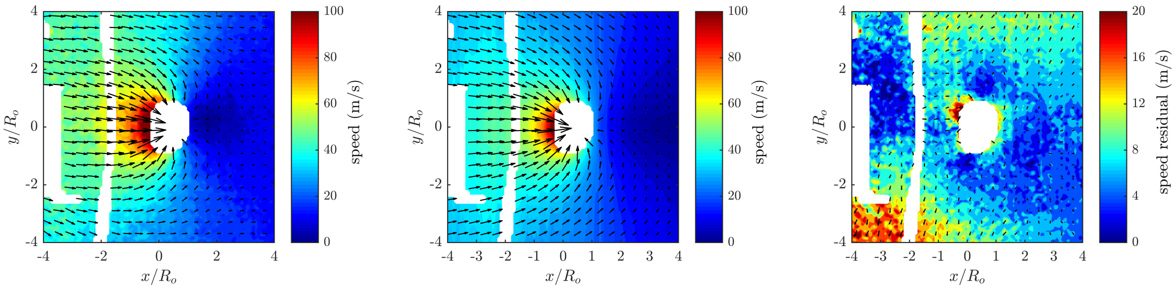

(a) Data (b) Model (c) Residuals

Figure F.136: Test# 845. A^{*} =0.41; x_c^{*} =0.41; S_{max} =123.0; S_{avg} =23.6; K =19.4; Q =23.9; Avg S_{res} =7.32.

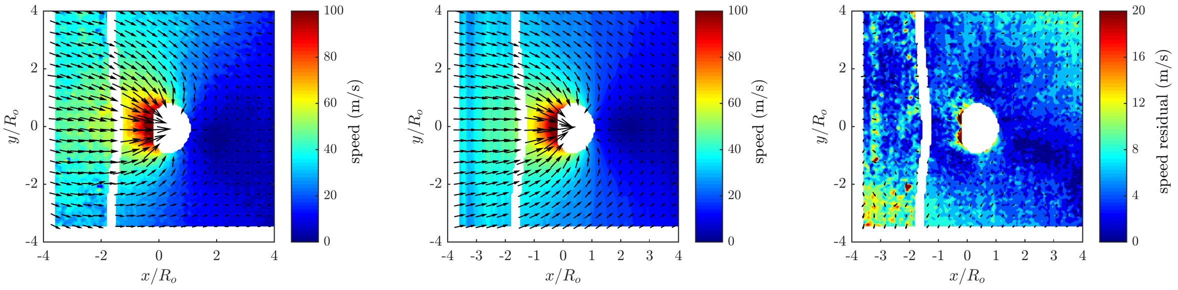

(a) Data (b) Model (c) Residuals

Figure F.137: Test# 731. $A^* = 0.38$; $x_c^* = 0.46$; $S_{max} = 150.7$; $S_{avg} = 26.5$; $K = 19.2$; $Q = 43.5$; Avg $S_{res} = 5.57$.

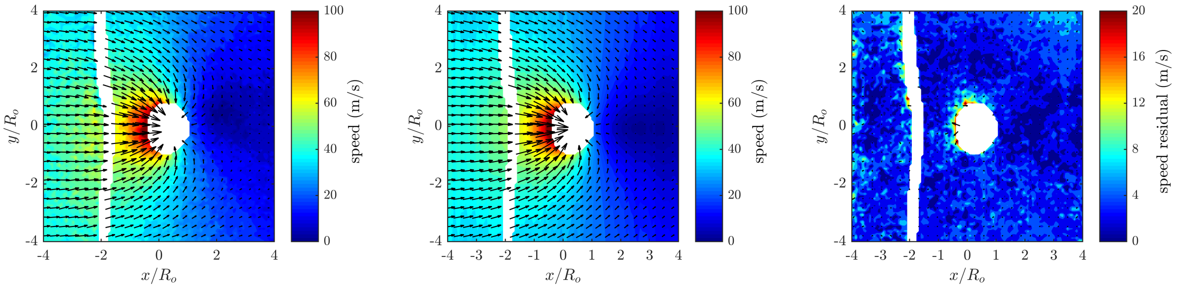

(a) Data (b) Model (c) Residuals

Figure F.138: Test# 830. $A^* = 0.38$; $x_c^* = 0.40$; $S_{max} = 107.9$; $S_{avg} = 24.3$; $K = 2.7$; $Q = 9.6$; Avg $S_{res} = 3.97$.

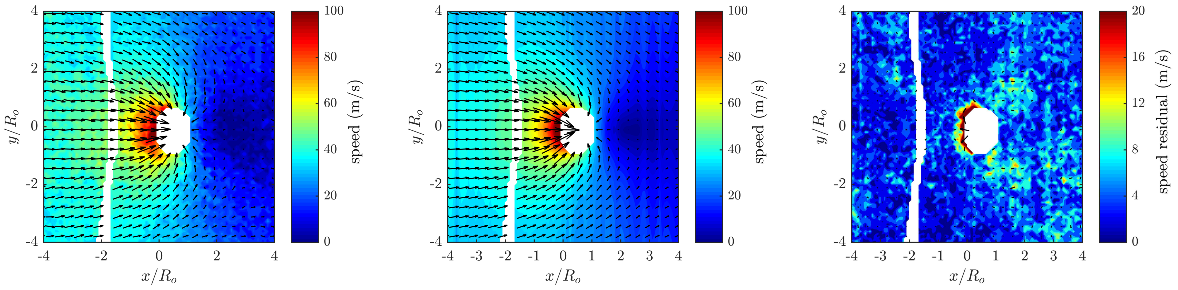

(a) Data (b) Model (c) Residuals

Figure F.139: Test# 831. $A^* = 0.21$; $x_c^* = 0.54$; $S_{max} = 118.3$; $S_{avg} = 25.4$; $K = 29.6$; $Q = 51.5$; Avg $S_{res} = 4.72$.

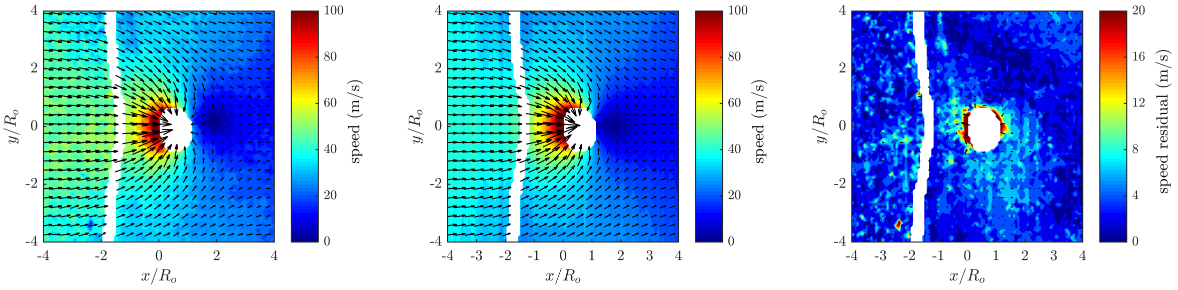

(a) Data (b) Model (c) Residuals

Figure F.140: Test# 802. $A^* = 0.13$; $x_c^* = 0.69$; $S_{max} = 133.7$; $S_{avg} = 32.6$; $K = 19.7$; $Q = 49.5$; Avg $S_{res} = 3.91$.

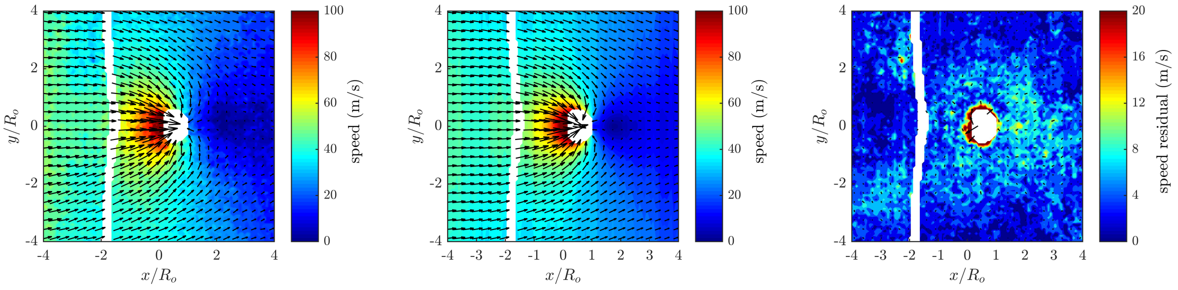

(a) Data (b) Model (c) Residuals

Figure F.141: Test# 829. $A^* = 0.06$; $x_c^* = 0.75$; $S_{max} = 135.1$; $S_{avg} = 30.0$; $K = 15.4$; $Q = 49.6$; Avg $S_{res} = 4.13$.

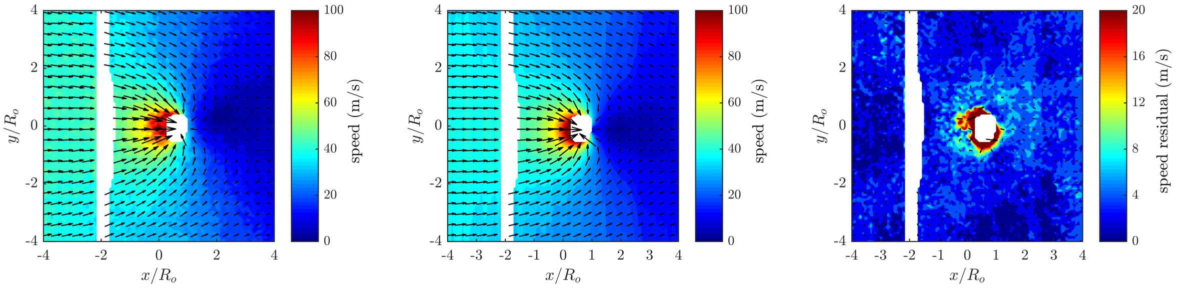

(a) Data (b) Model (c) Residuals

Figure F.142: Test# 800. $A^* = 0.04$; $x_c^* = 0.83$; $S_{max} = 105.1$; $S_{avg} = 27.6$; $K = 25.3$; $Q = 54.9$; Avg $S_{res} = 3.81$.

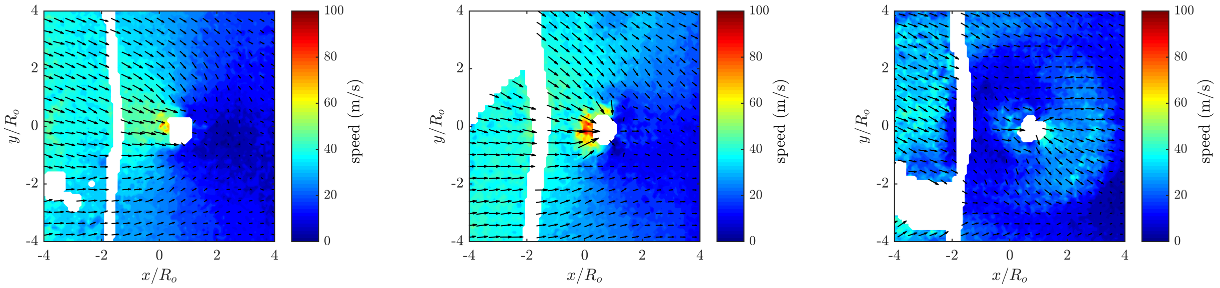

(a) Test# 844. A^* =0.01; x_c^* =0.81; S_{max} =85.4; S_{avg} =22.6.

(b) Test# 786. A^* =0.01; x_c^* =0.86; S_{max} =105.1; S_{avg} =23.5.

(c) Test# 722. A^* =0.00; x_c^* =0.80; S_{max} =53.4; S_{avg} =14.8.

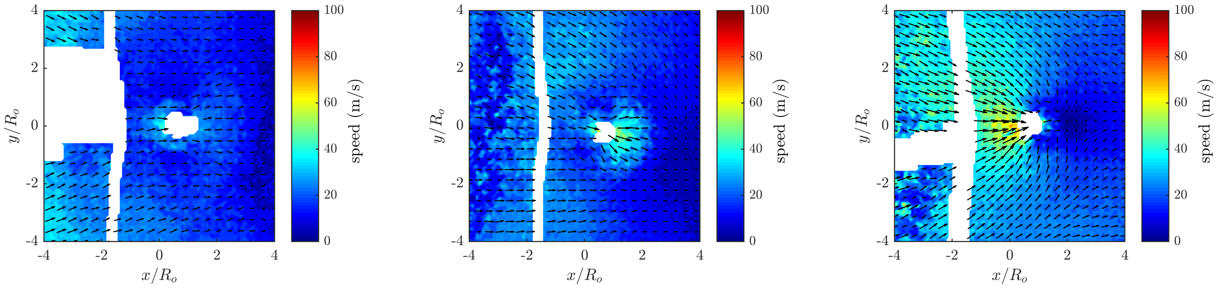

(d) Test# 734. A^* =0.00; x_c^* =0.86; S_{max} =45.0; S_{avg} =16.0.

(e) Test# 781. A^* =0.00; x_c^* =0.88; S_{max} =62.1; S_{avg} =17.6.

(f) Test# 732. A^* =0.00; x_c^* =0.89; S_{max} =74.9; S_{avg} =24.1.

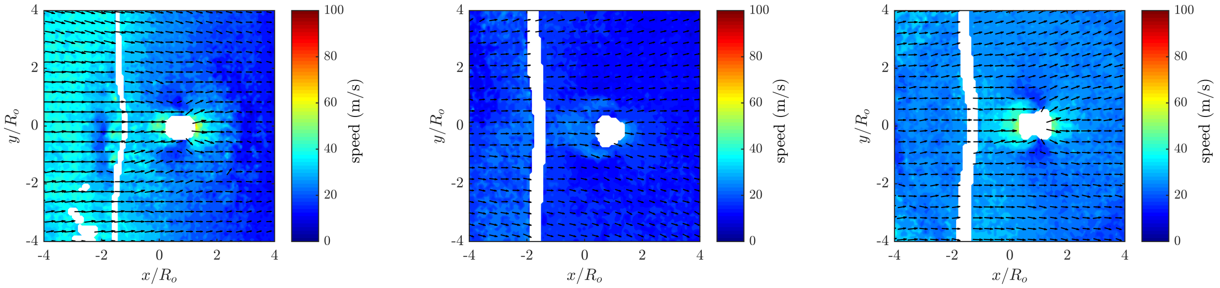

(g) Test# 783. A^* =0.00; x_c^* =0.99; S_{max} =73.9; S_{avg} =25.6.

(h) Test# 782. A^* =0.00; x_c^* =0.99; S_{max} =38.8; S_{avg} =13.3.

(i) Test# 785. A^* =0.00; x_c^* =1.23; S_{max} =54.0; S_{avg} =25.5.

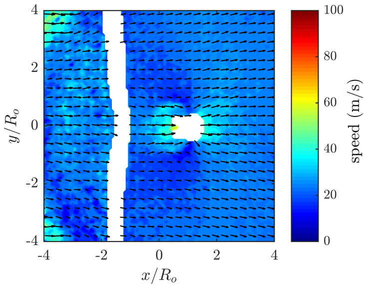

(j) Test# 801. A^* =0.00; x_c^* =1.29; S_{max} =59.6; S_{avg} =23.1.

Figure F.143: Raw data for tests 844-801. Void boundary could not be identified reliably(<3%), or test was after collapse, so model could not be computed.

F.4 Two Boundary

F.4.1 Two Boundary 20:1 PDMS

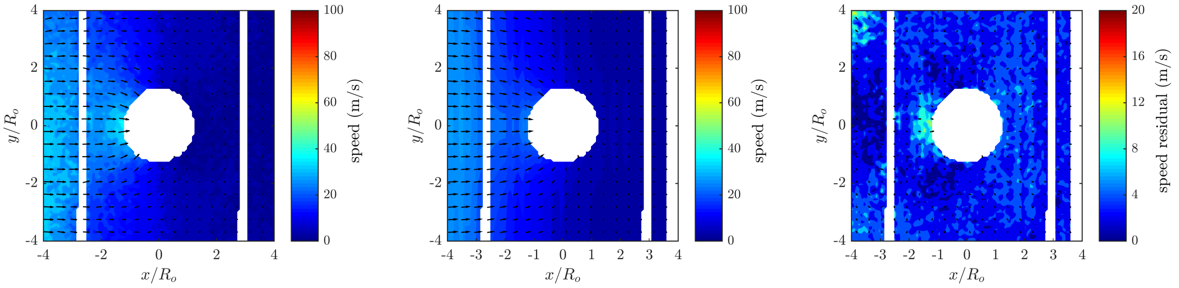

(a) Data (b) Model (c) Residuals

Figure F.144: Test# 835. $A^* = 1.04$; $x_c^* = 0.02$; $S_{max} = 48.1$; $S_{avg} = 13.2$; $K = 4.0$; $Q = 8.6$; Avg $S_{res} = 4.21$.

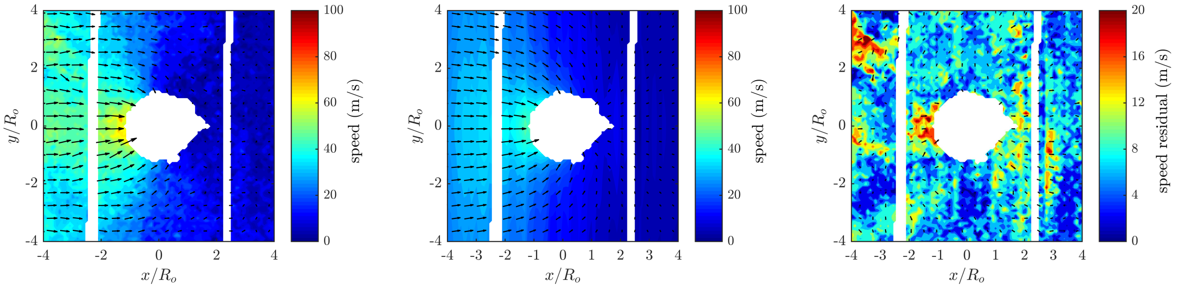

(a) Data (b) Model (c) Residuals

Figure F.145: Test# 887. $A^* = 0.98$; $x_c^* = 0.06$; $S_{max} = 71.7$; $S_{avg} = 21.2$; $K = 33.1$; $Q = 48.2$; Avg $S_{res} = 7.05$.

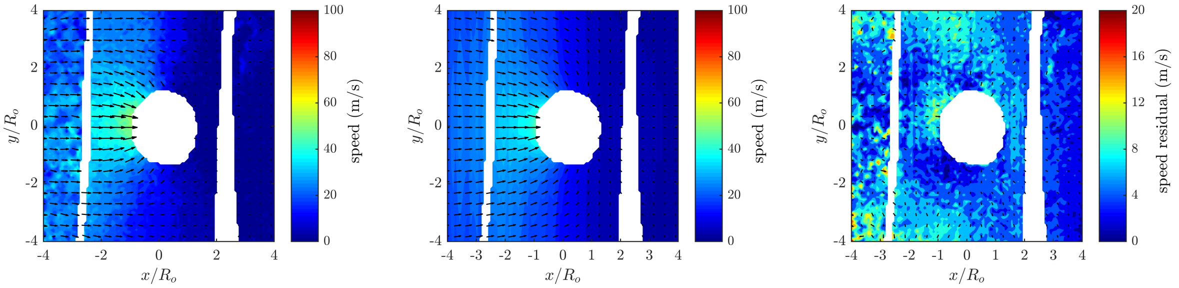

(a) Data (b) Model (c) Residuals

Figure F.146: Test# 777. $A^* = 0.92$; $x_c^* = 0.07$; $S_{max} = 54.6$; $S_{avg} = 14.8$; $K = 21.3$; $Q = 51.2$; Avg $S_{res} = 5.95$.

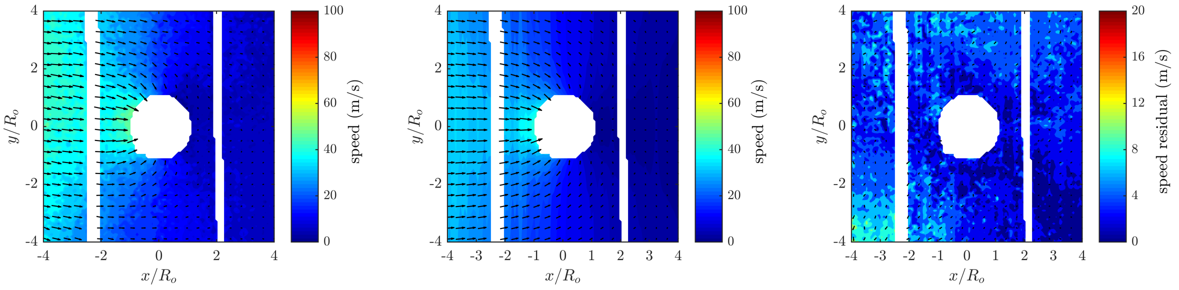

(a) Data (b) Model (c) Residuals

Figure F.147: Test# 852. $A^* = 0.92$; $x_c^* = 0.11$; $S_{max} = 53.5$; $S_{avg} = 20.5$; $K = 27.6$; $Q = 53.0$; Avg $S_{res} = 4.17$.

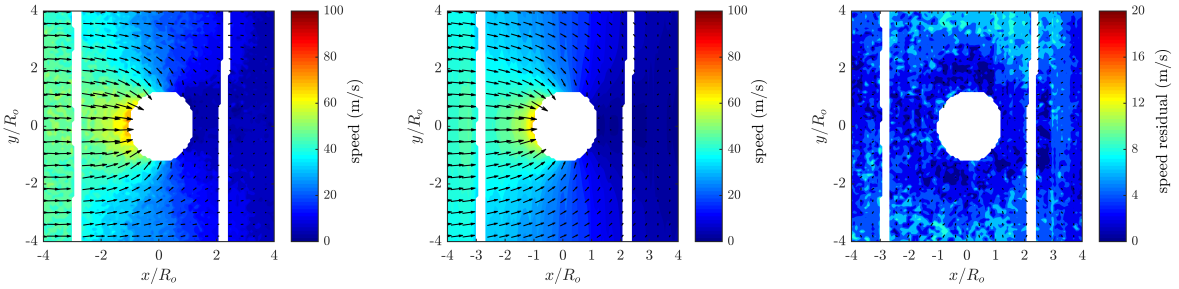

(a) Data (b) Model (c) Residuals

Figure F.148: Test# 919. $A^* = 0.89$; $x_c^* = 0.10$; $S_{max} = 74.2$; $S_{avg} = 22.9$; $K = 11.7$; $Q = 43.4$; Avg $S_{res} = 4.17$.

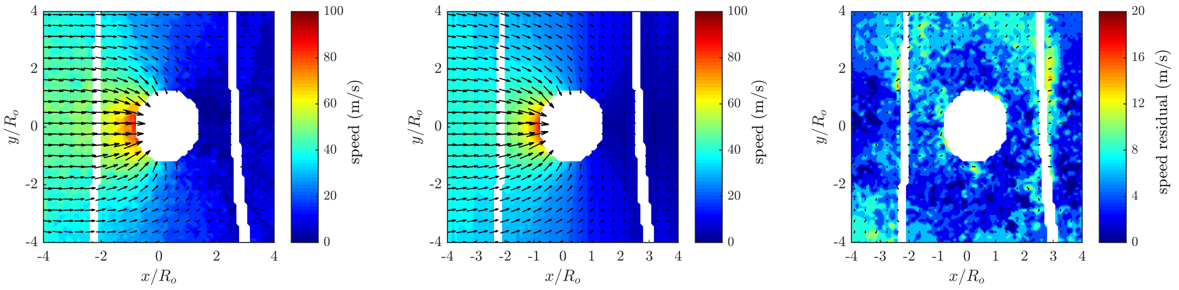

(a) Data (b) Model (c) Residuals

Figure F.149: Test# 851. $A^* = 0.88$; $x_c^* = 0.13$; $S_{max} = 91.6$; $S_{avg} = 23.1$; $K = 10.2$; $Q = 19.0$; Avg $S_{res} = 5.18$.

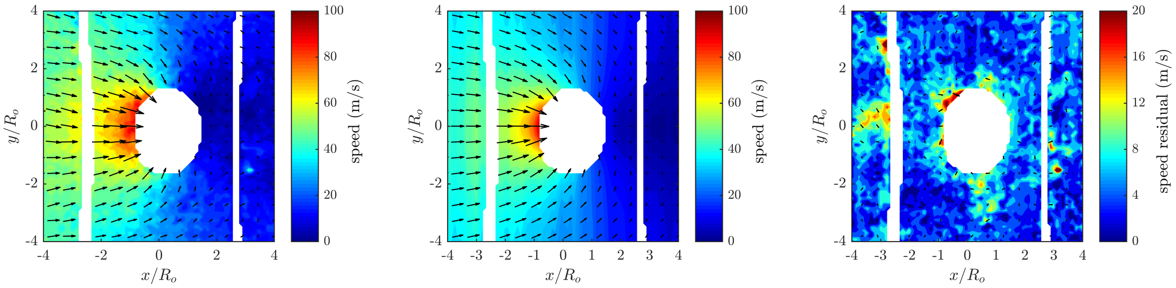

(a) Data (b) Model (c) Residuals

Figure F.150: Test# 891. A^* =0.81; x_c^* =0.14; S_{max} =95.3; S_{avg} =24.6; K =3.2; Q =2.7; Avg S_{res} =5.30.

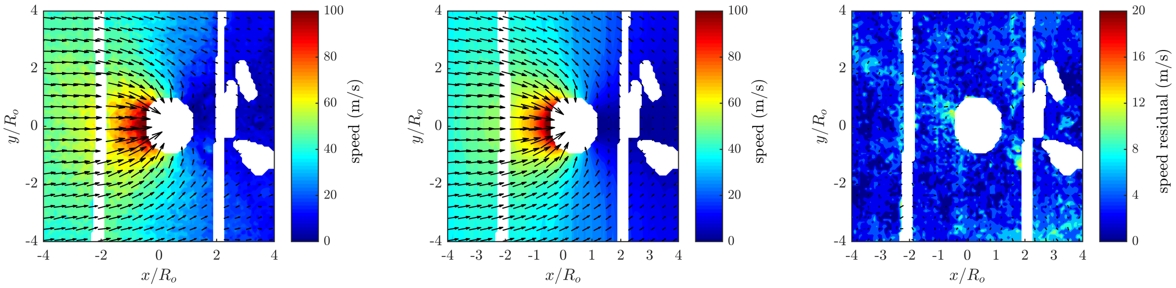

(a) Data (b) Model (c) Residuals

Figure F.151: Test# 886. A^* =0.47; x_c^* =0.45; S_{max} =133.2; S_{avg} =30.9; K =14.3; Q =24.0; Avg S_{res} =3.86.

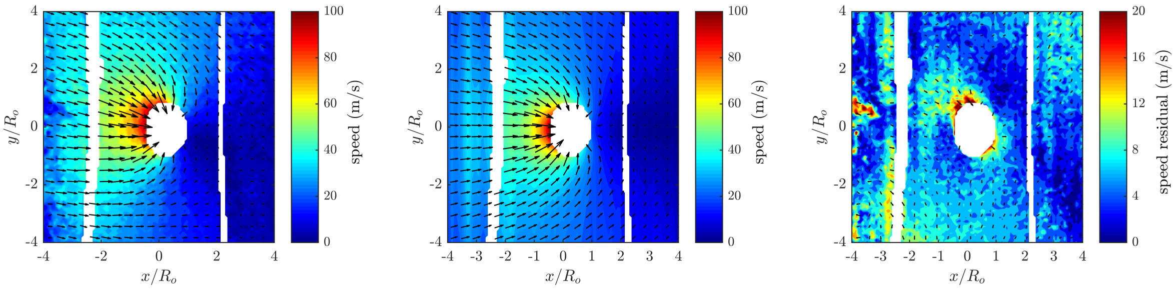

(a) Data (b) Model (c) Residuals

Figure F.152: Test# 776. A^* =0.46; x_c^* =0.36; S_{max} =100.5; S_{avg} =19.7; K =12.4; Q =47.2; Avg S_{res} =6.57.

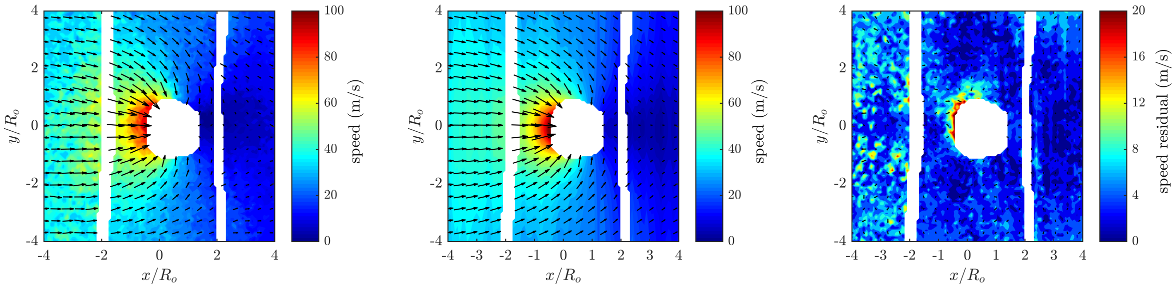

(a) Data (b) Model (c) Residuals

Figure F.153: Test# 853. $A^* = 0.43$; $x_c^* = 0.37$; $S_{max} = 94.2$; $S_{avg} = 25.8$; $K = 15.5$; $Q = 22.4$; Avg $S_{res} = 4.81$.

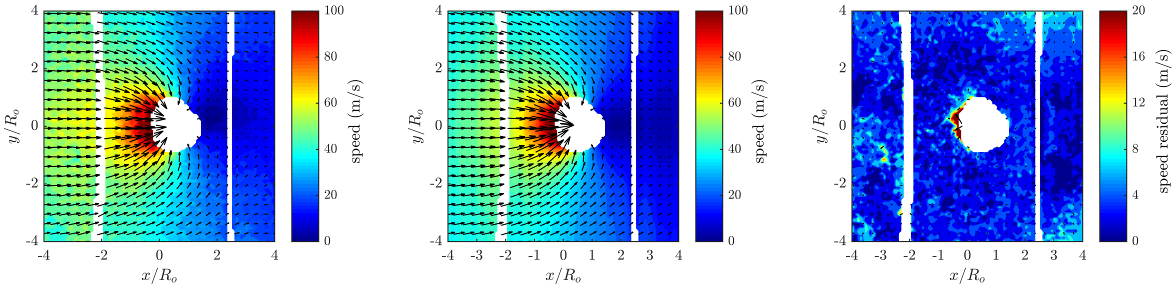

(a) Data (b) Model (c) Residuals

Figure F.154: Test# 920. $A^* = 0.40$; $x_c^* = 0.50$; $S_{max} = 120.0$; $S_{avg} = 29.1$; $K = 13.6$; $Q = 44.3$; Avg $S_{res} = 4.57$.

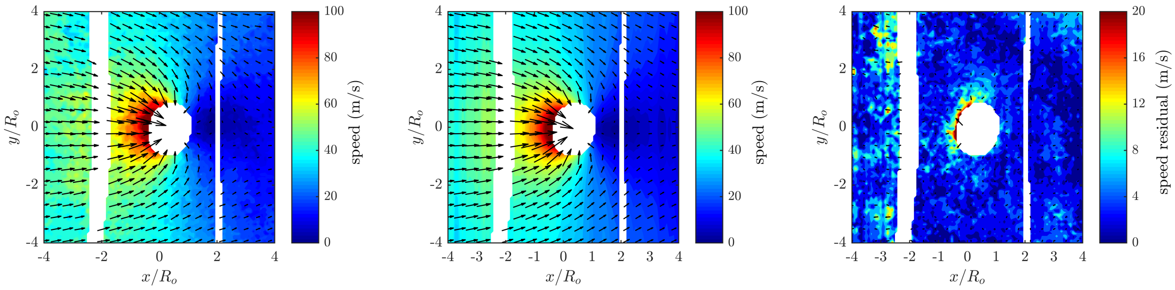

(a) Data (b) Model (c) Residuals

Figure F.155: Test# 917. $A^* = 0.36$; $x_c^* = 0.45$; $S_{max} = 126.2$; $S_{avg} = 30.4$; $K = 23.9$; $Q = 56.1$; Avg $S_{res} = 4.00$.

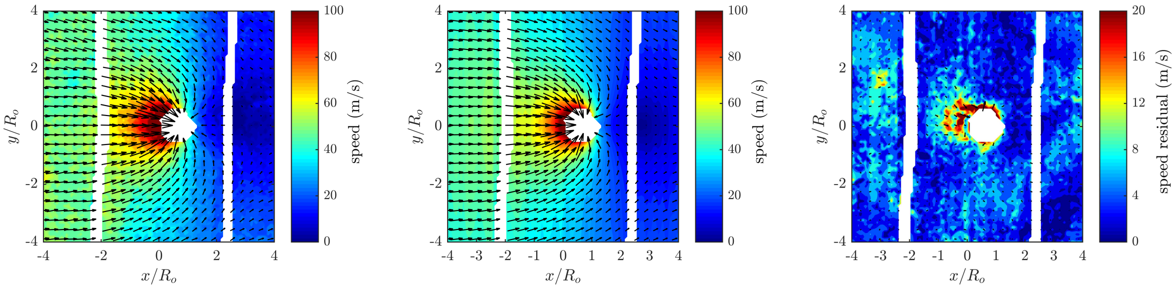

(a) Data (b) Model (c) Residuals

Figure F.156: Test# 918. A^* =0.06; x_c^* =0.84; S_{max} =137.2; S_{avg} =32.6; K =17.9; Q =48.8; Avg S_{res} =5.05.

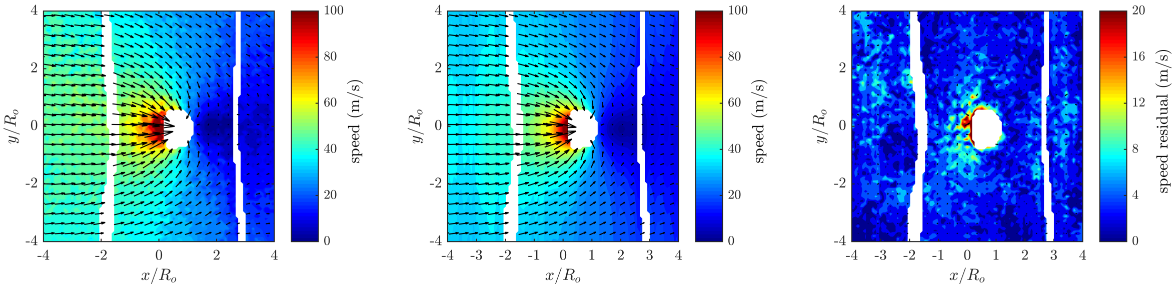

(a) Data (b) Model (c) Residuals

Figure F.157: Test# 850. A^* =0.05; x_c^* =0.71; S_{max} =114.7; S_{avg} =30.0; K =24.0; Q =52.3; Avg S_{res} =3.37.

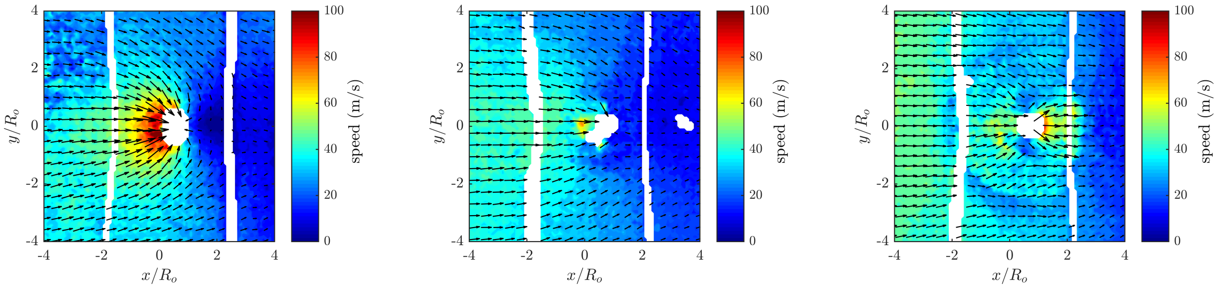

(a) Test# 889. A^* =0.03; x_c^* =0.66; S_{max} =125.8; S_{avg} =22.6.

(b) Test# 885. A^* =0.01; x_c^* =0.77; S_{max} =72.3; S_{avg} =25.2.

(c) Test# 833. A^* =0.00; x_c^* =0.82; S_{max} =91.8; S_{avg} =33.1.

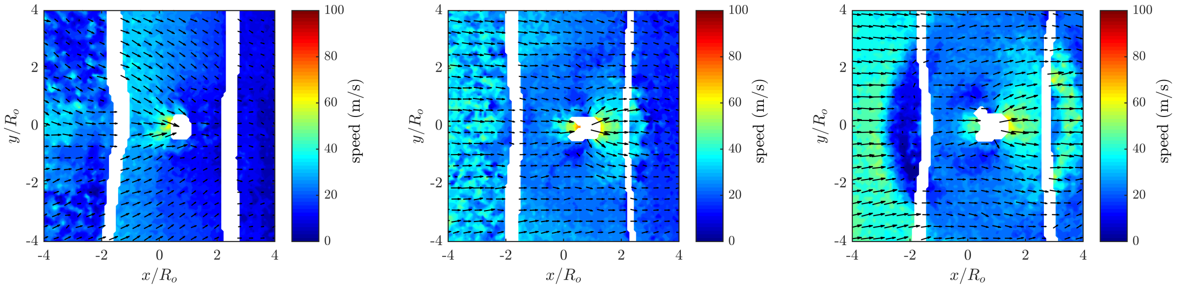

(d) Test# 779. A^* =0.00; x_c^* =0.86; S_{max} =66.4; S_{avg} =14.4.

(e) Test# 890. A^* =0.00; x_c^* =0.91; S_{max} =73.8; S_{avg} =24.2.

(f) Test# 892. A^* =0.00; x_c^* =0.91; S_{max} =67.9; S_{avg} =28.0.

Figure F.158: Raw data for tests 889-892. Void boundary could not be identified reliably(<3%), or test was after collapse, so model could not be computed.

F.4.2 Two Boundary 30:1 PDMS

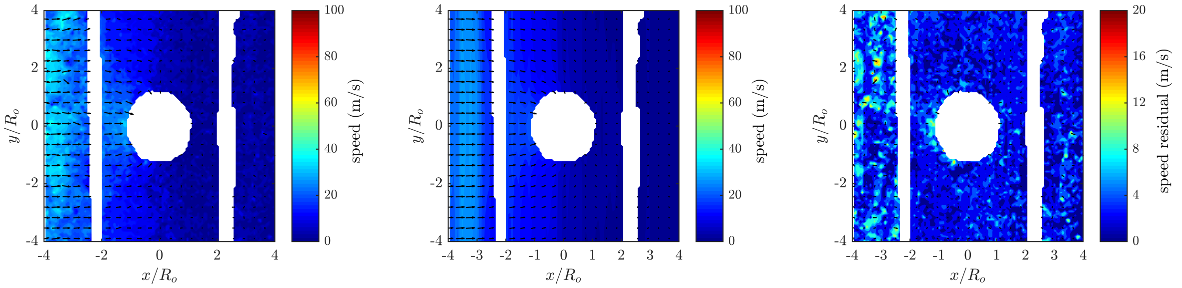

(a) Data

(b) Model

(c) Residuals

Figure F.159: Test# 771. A^* =0.98; x_c^* =0.03; S_{max} =42.0; S_{avg} =8.1; K =4.5; Q =12.6; Avg S_{res} =3.07.

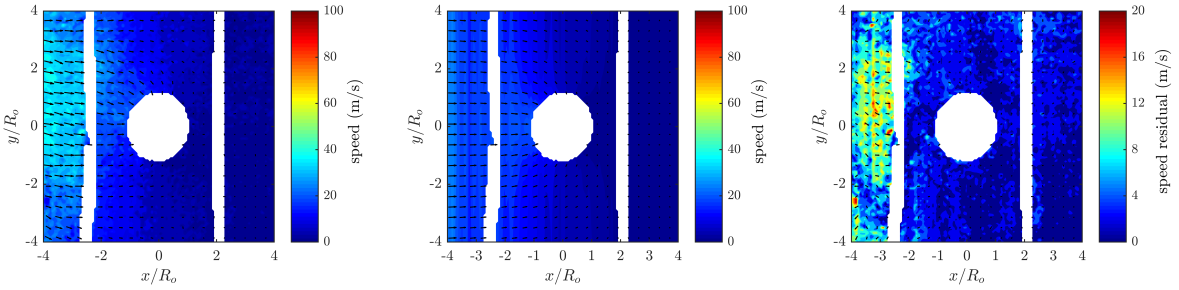

(a) Data (b) Model (c) Residuals

Figure F.160: Test# 770. $A^* = 0.95$; $x_c^* = 0.04$; $S_{max} = 44.8$; $S_{avg} = 10.1$; $K = 16.3$; $Q = 23.4$; Avg $S_{res} = 3.53$.

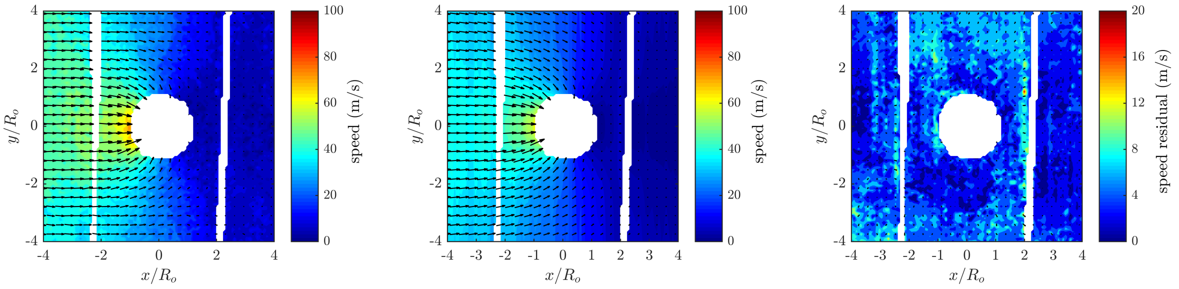

(a) Data (b) Model (c) Residuals

Figure F.161: Test# 862. $A^* = 0.92$; $x_c^* = 0.09$; $S_{max} = 73.6$; $S_{avg} = 22.1$; $K = 10.9$; $Q = 18.9$; Avg $S_{res} = 4.16$.

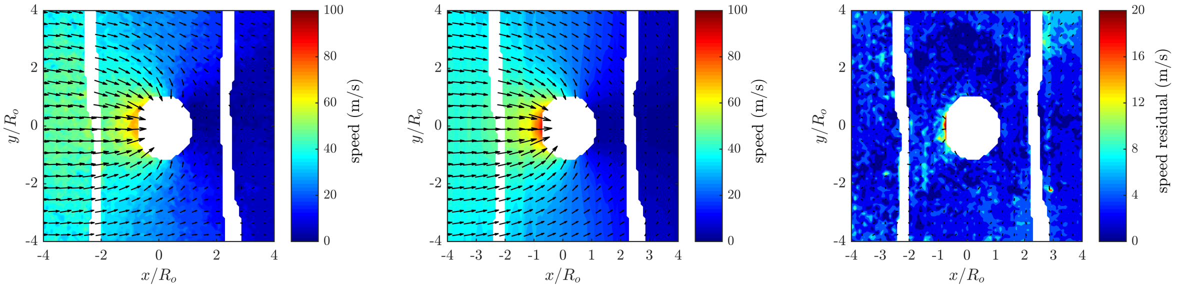

(a) Data (b) Model (c) Residuals

Figure F.162: Test# 827. $A^* = 0.73$; $x_c^* = 0.23$; $S_{max} = 74.4$; $S_{avg} = 23.5$; $K = 9.2$; $Q = 38.2$; Avg $S_{res} = 3.86$.

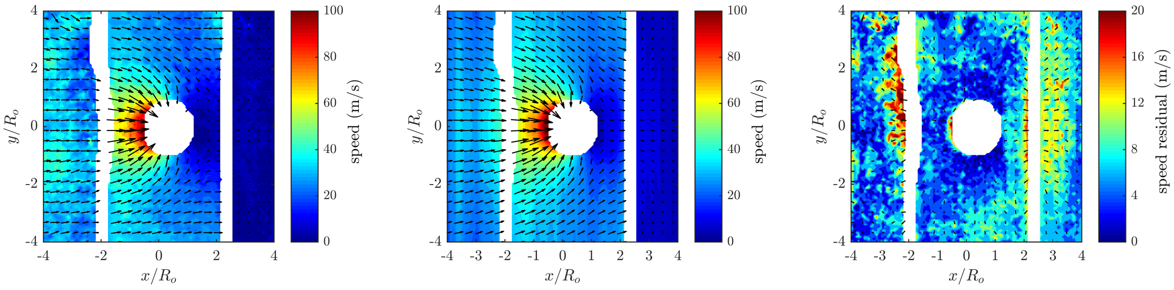

(a) Data (b) Model (c) Residuals

Figure F.163: Test# 768. $A^* = 0.62$; $x_c^* = 0.32$; $S_{max} = 108.5$; $S_{avg} = 20.6$; $K = 14.3$; $Q = 47.3$; Avg $S_{res} = 6.46$.

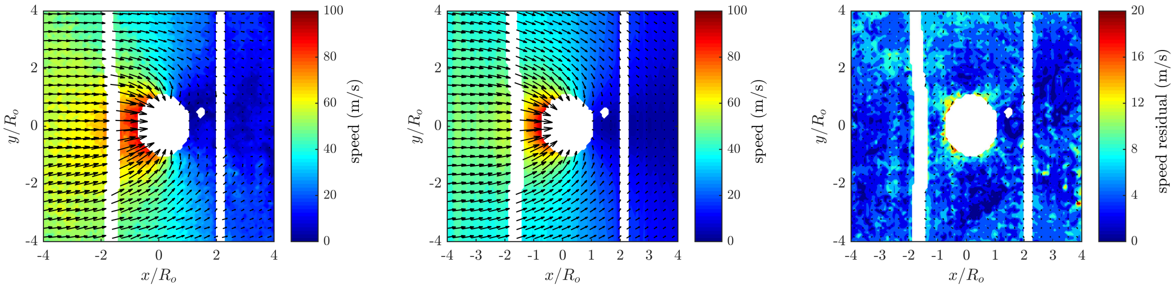

(a) Data (b) Model (c) Residuals

Figure F.164: Test# 861. $A^* = 0.56$; $x_c^* = 0.30$; $S_{max} = 95.2$; $S_{avg} = 26.3$; $K = 10.3$; $Q = 36.8$; Avg $S_{res} = 4.46$.

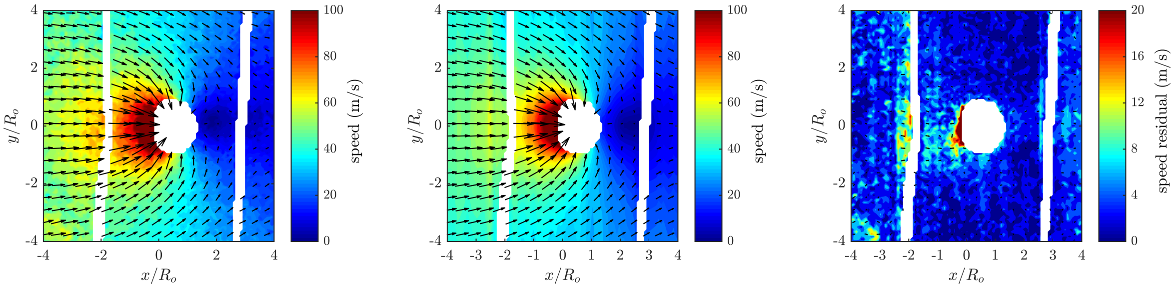

(a) Data (b) Model (c) Residuals

Figure F.165: Test# 864. $A^* = 0.42$; $x_c^* = 0.49$; $S_{max} = 136.8$; $S_{avg} = 33.0$; $K = 28.1$; $Q = 46.2$; Avg $S_{res} = 3.86$.

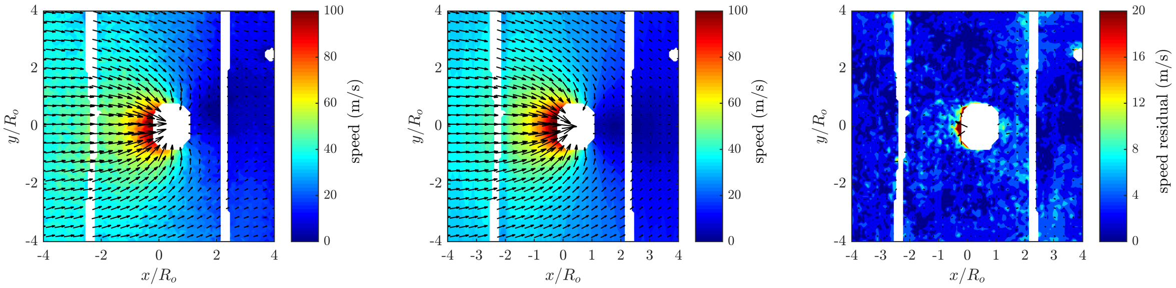

(a) Data (b) Model (c) Residuals

Figure F.166: Test# 828. $A^* = 0.37$; $x_c^* = 0.50$; $S_{max} = 114.5$; $S_{avg} = 26.1$; $K = 9.1$; $Q = 20.7$; Avg $S_{res} = 3.43$.

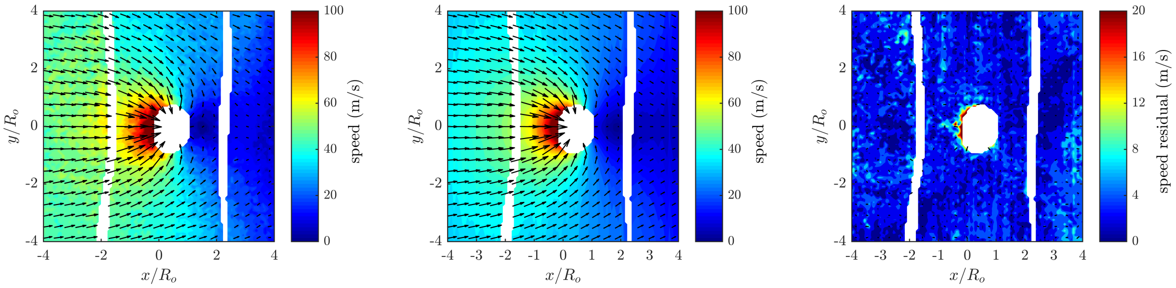

(a) Data (b) Model (c) Residuals

Figure F.167: Test# 863. $A^* = 0.26$; $x_c^* = 0.50$; $S_{max} = 133.9$; $S_{avg} = 30.7$; $K = 5.6$; $Q = 11.2$; Avg $S_{res} = 3.44$.

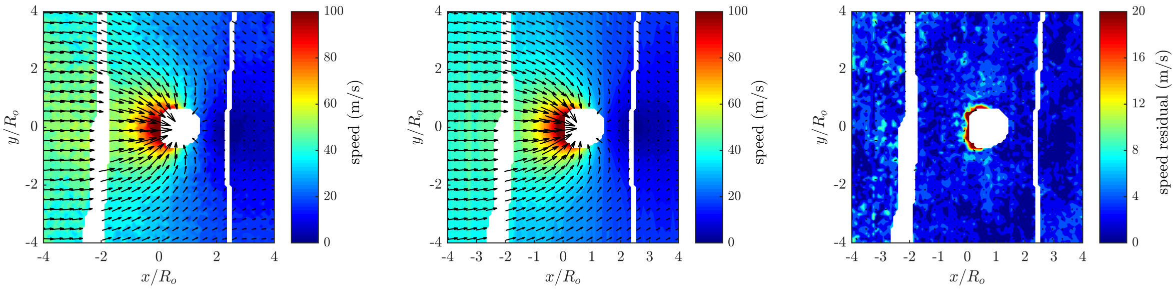

(a) Data (b) Model (c) Residuals

Figure F.168: Test# 825. $A^* = 0.17$; $x_c^* = 0.64$; $S_{max} = 126.6$; $S_{avg} = 29.1$; $K = 10.6$; $Q = 43.4$; Avg $S_{res} = 3.46$.

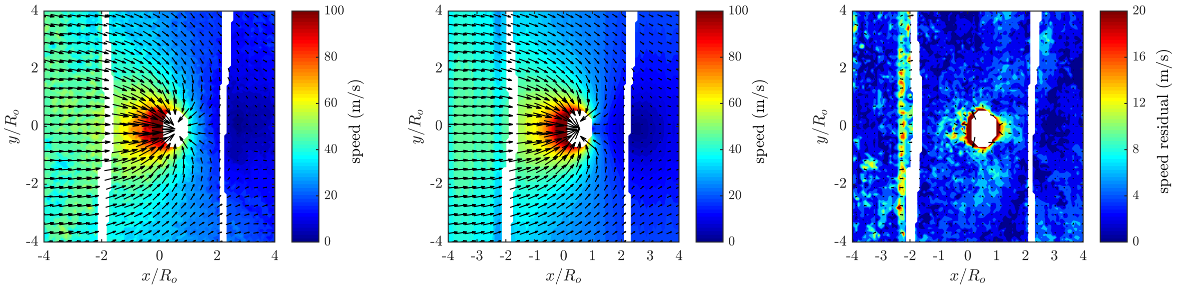

(a) Data (b) Model (c) Residuals

Figure F.169: Test# 826. A^* =0.13; x_c^* =0.71; S_{max} =136.1; S_{avg} =29.2; K =23.9; Q =49.8; Avg S_{res} =4.25.

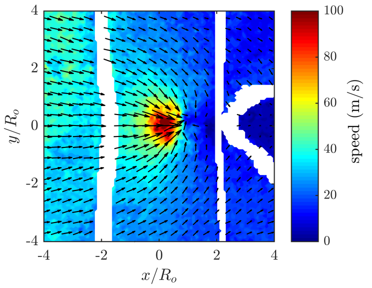

(a) Test# 769. A^* =0.02; x_c^* =0.77; S_{max} =126.0; S_{avg} =19.1.

Figure F.170: Raw data for tests 769-769. Void boundary could not be identified reliably(<3%), or test was after collapse, so model could not be computed.

F.4.3 Two Boundary 40:1 PDMS

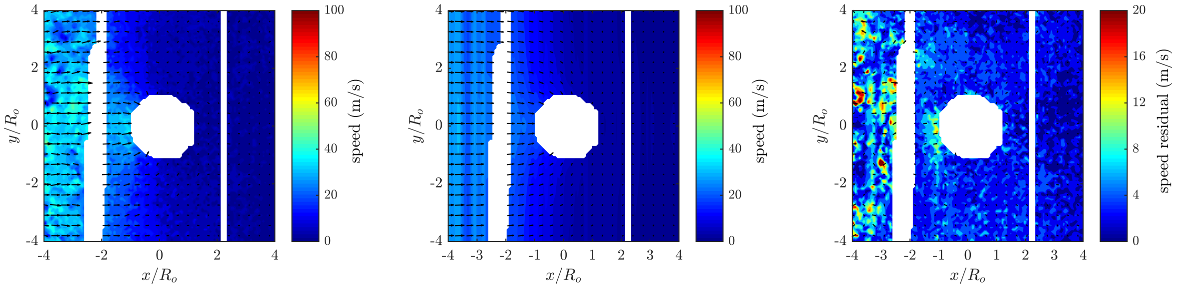

(a) Data (b) Model (c) Residuals

Figure F.171: Test# 775. A^* =0.96; x_c^* =0.05; S_{max} =50.3; S_{avg} =11.1; K =16.8; Q =57.3; Avg S_{res} =3.73.

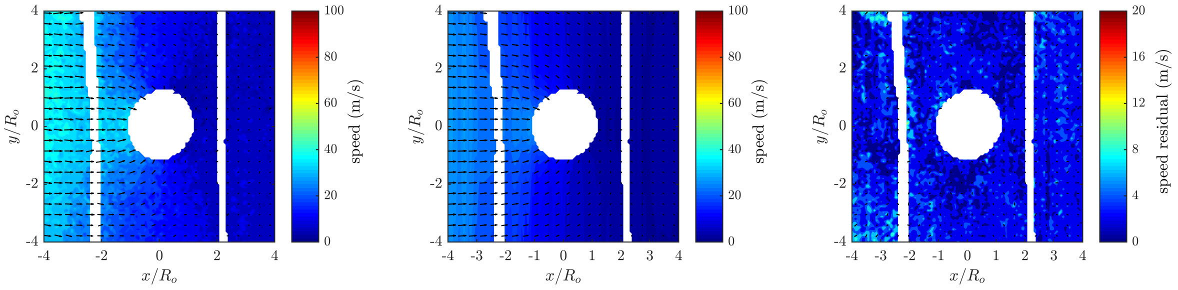

(a) Data (b) Model (c) Residuals

Figure F.172: Test# 857. A^{*} =0.94; x_c^{*} =0.06; S_{max} =46.3; S_{avg} =16.4; K =7.7; Q =18.6; Avg S_{res} =3.20.

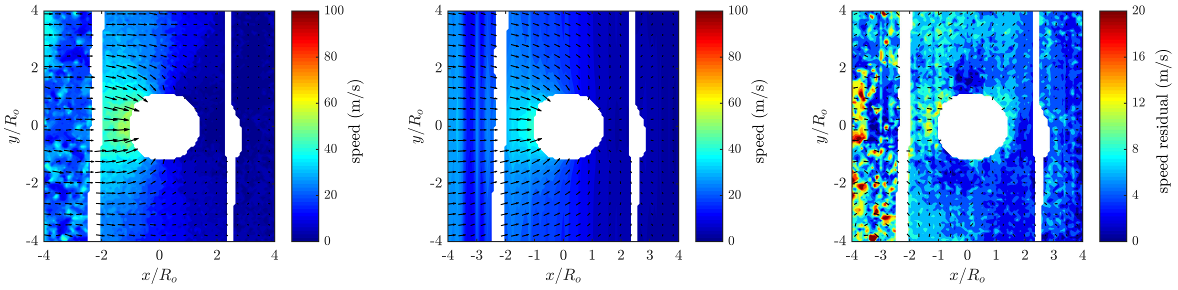

(a) Data (b) Model (c) Residuals

Figure F.173: Test# 772. A^{*} =0.93; x_c^{*} =0.10; S_{max} =55.3; S_{avg} =14.2; K =4.3; Q =0.1; Avg S_{res} =5.96.

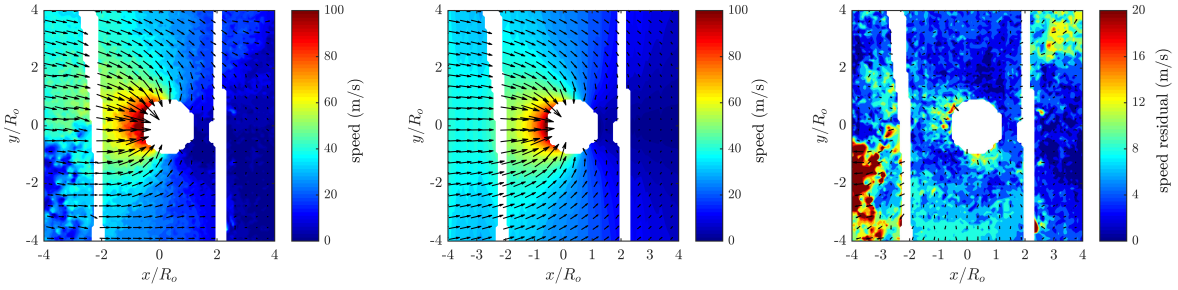

(a) Data (b) Model (c) Residuals

Figure F.174: Test# 774. A^{*} =0.66; x_c^{*} =0.34; S_{max} =112.5; S_{avg} =20.6; K =8.6; Q =50.5; Avg S_{res} =6.41.

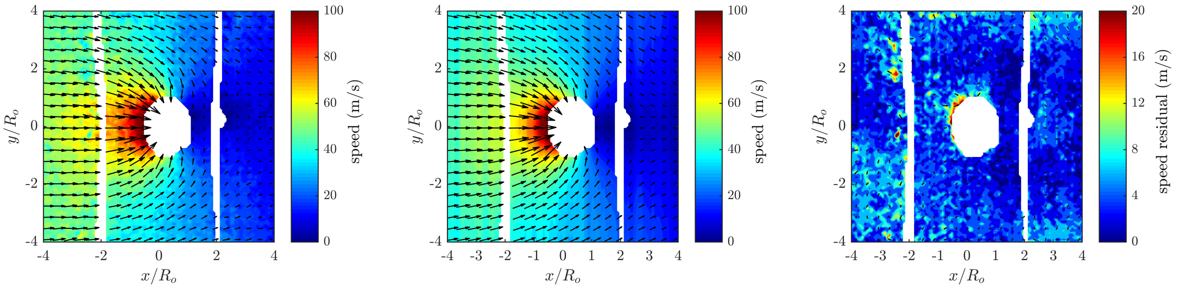

(a) Data (b) Model (c) Residuals

Figure F.175: Test# 856. $A^* = 0.54$; $x_c^* = 0.35$; $S_{max} = 118.2$; $S_{avg} = 26.4$; $K = 15.4$; $Q = 49.1$; Avg $S_{res} = 4.38$.

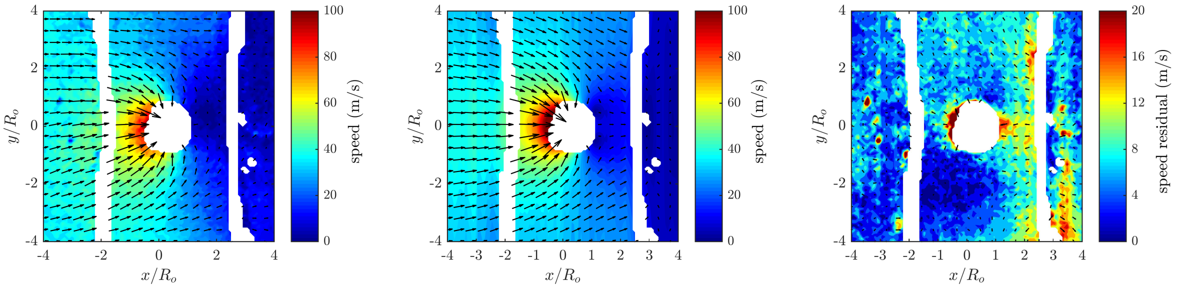

(a) Data (b) Model (c) Residuals

Figure F.176: Test# 820. $A^* = 0.44$; $x_c^* = 0.39$; $S_{max} = 119.2$; $S_{avg} = 22.9$; $K = 17.1$; $Q = 51.1$; Avg $S_{res} = 6.39$.

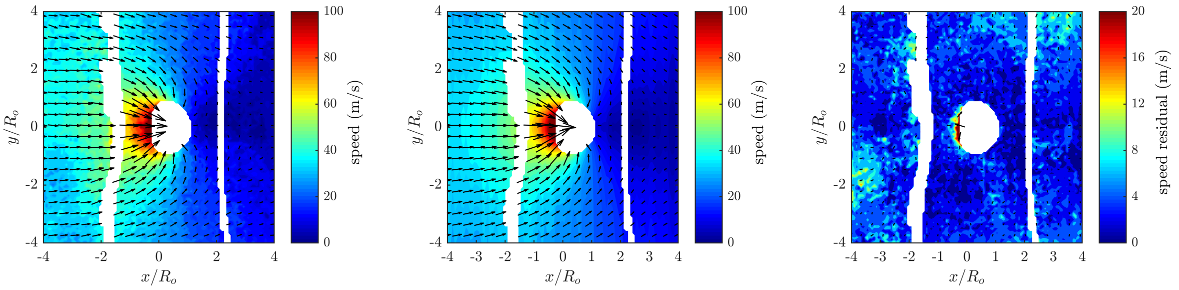

(a) Data (b) Model (c) Residuals

Figure F.177: Test# 819. $A^* = 0.40$; $x_c^* = 0.44$; $S_{max} = 112.4$; $S_{avg} = 22.2$; $K = 25.0$; $Q = 63.4$; Avg $S_{res} = 4.08$.

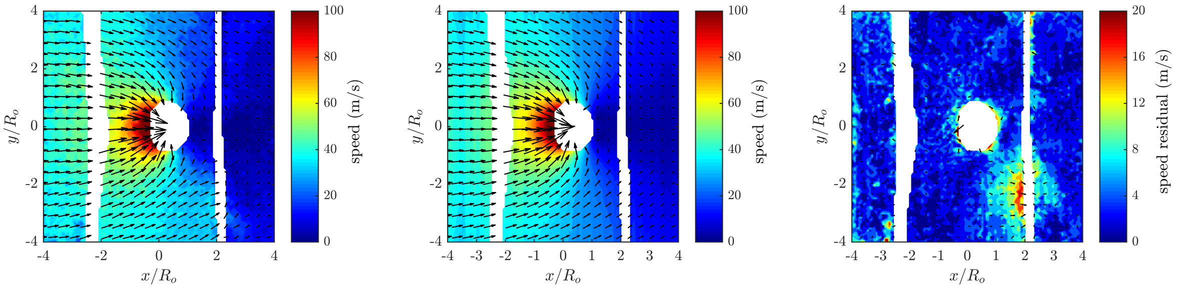

(a) Data (b) Model (c) Residuals

Figure F.178: Test# 821. A^* =0.40; x_c^* =0.47; S_{max} =135.7; S_{avg} =25.2; K =22.7; Q =44.6; Avg S_{res} =4.01.

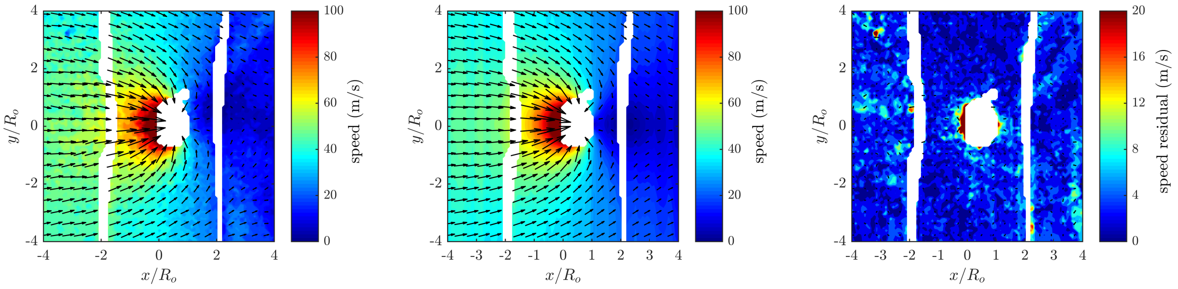

(a) Data (b) Model (c) Residuals

Figure F.179: Test# 854. A^* =0.26; x_c^* =0.58; S_{max} =136.1; S_{avg} =30.8; K =19.0; Q =49.1; Avg S_{res} =3.87.

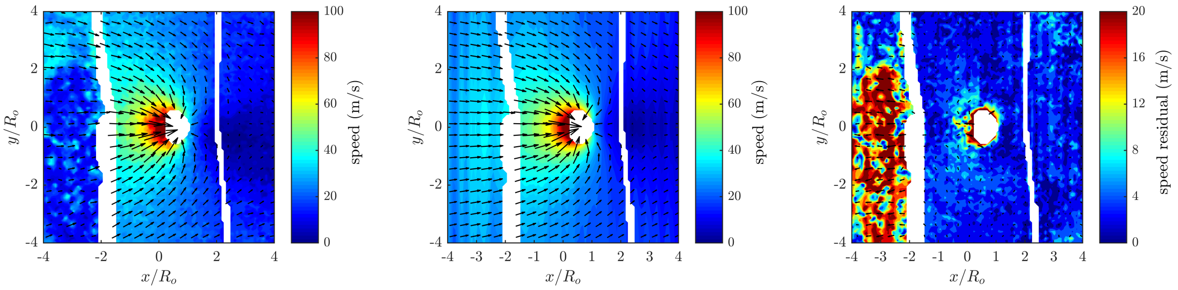

(a) Data (b) Model (c) Residuals

Figure F.180: Test# 773. A^* =0.11; x_c^* =0.75; S_{max} =140.7; S_{avg} =21.3; K =1.6; Q =0.3; Avg S_{res} =6.31.

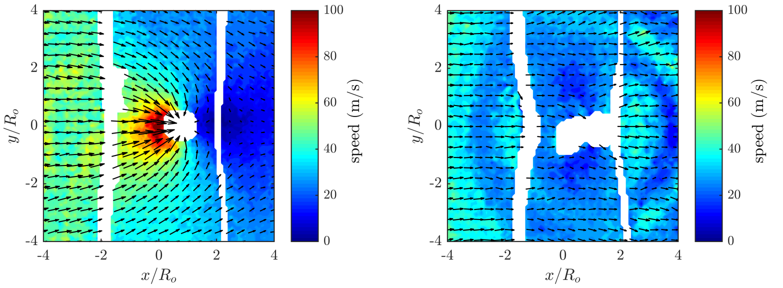

(a) Test# 855. A^* =0.02; x_c^* =0.92; S_{max} =123.7; S_{avg} =33.8.

(b) Test# 818. A^* =0.00; x_c^* =1.26; S_{max} =61.6; S_{avg} =30.5.

Figure F.181: Raw data for tests 855-818. Void boundary could not be identified reliably(<3%), or test was after collapse, so model could not be computed.

APPENDIX G

PARTICLE SHADOW VELOCIMETRY: MODEL FITTING CURVES

G.1 No Boundary

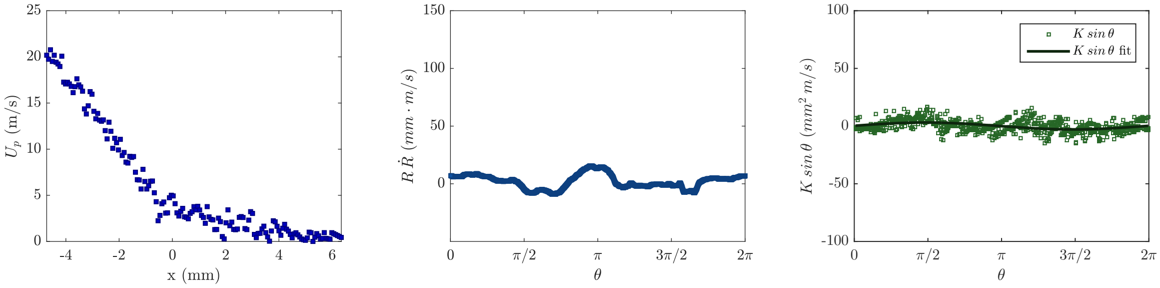

(a) Wave flow at edges.

(b) $R \cdot \dot{R}$ on interface.

(c) $K\, sin\theta$ fit.

Figure G.1: Test# 746. A^* =1.00; x_c^* =0.02; S_{max} =31.4; $U_p(x=0)$ =3.6.

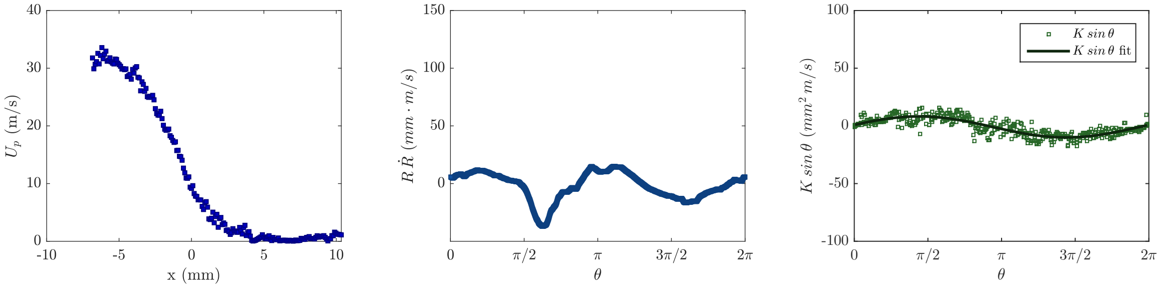

(a) Wave flow at edges.

(b) $R \cdot \dot{R}$ on interface.

(c) $K\, sin\theta$ fit.

Figure G.2: Test# 702. A^* =0.99; x_c^* =0.07; S_{max} =47.1; $U_p(x=0)$ =9.7.

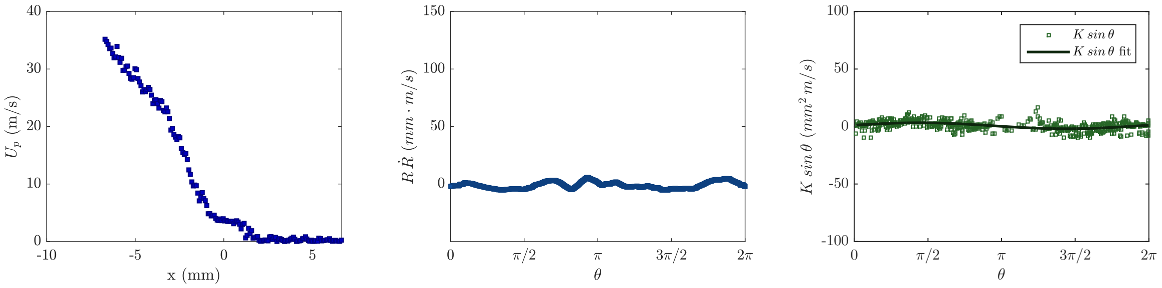

(a) Wave flow at edges.

(b) $R \cdot \dot{R}$ on interface.

(c) $K\ sin\theta$ fit.

Figure G.3: Test# 824. A^* =0.98; x_c^* =0.02; S_{max} =48.5; $U_p(x=0)$ =3.8.

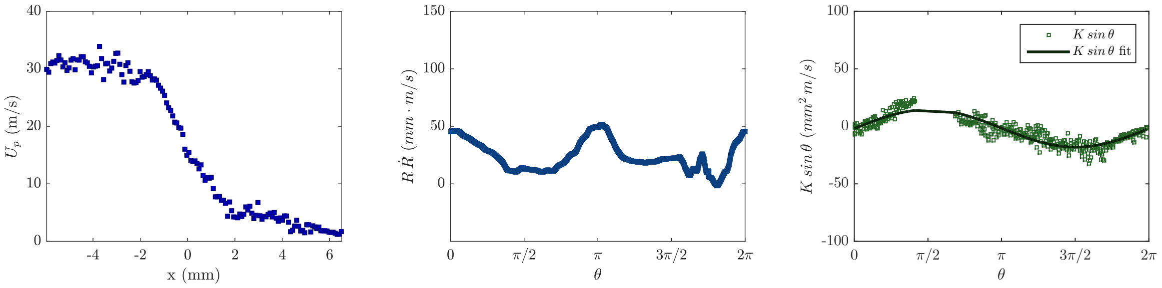

(a) Wave flow at edges.

(b) $R \cdot \dot{R}$ on interface.

(c) $K\ sin\theta$ fit.

Figure G.4: Test# 836. A^* =0.94; x_c^* =0.10; S_{max} =69.5; $U_p(x=0)$ =16.6.

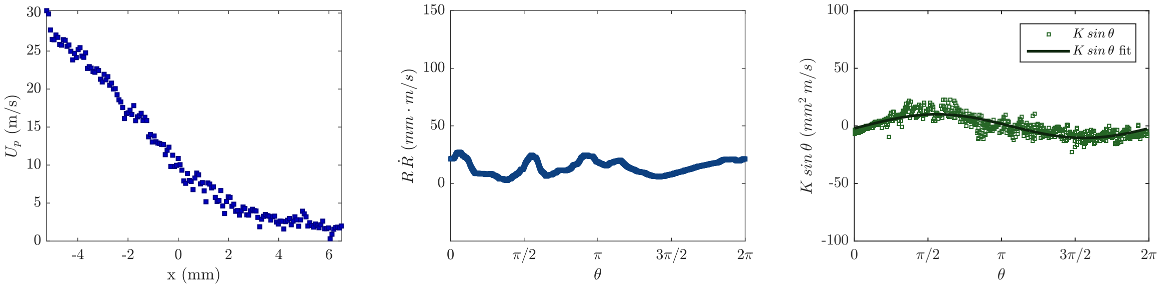

(a) Wave flow at edges.

(b) $R \cdot \dot{R}$ on interface.

(c) $K\ sin\theta$ fit.

Figure G.5: Test# 756. A^* =0.93; x_c^* =0.09; S_{max} =45.3; $U_p(x=0)$ =9.8.

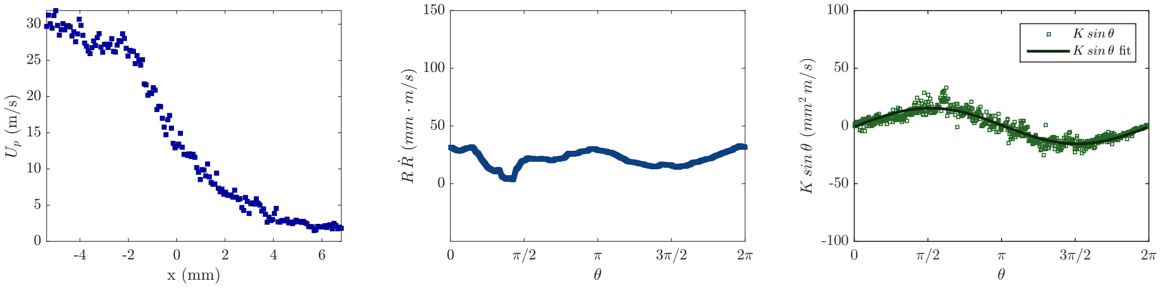

(a) Wave flow at edges. (b) $R \cdot \dot{R}$ on interface. (c) $K\ sin\theta$ fit.

Figure G.6: Test# 752. A^* =0.90; x_c^* =0.18; S_{max} =51.6; $U_p(x = 0)$ =14.0.

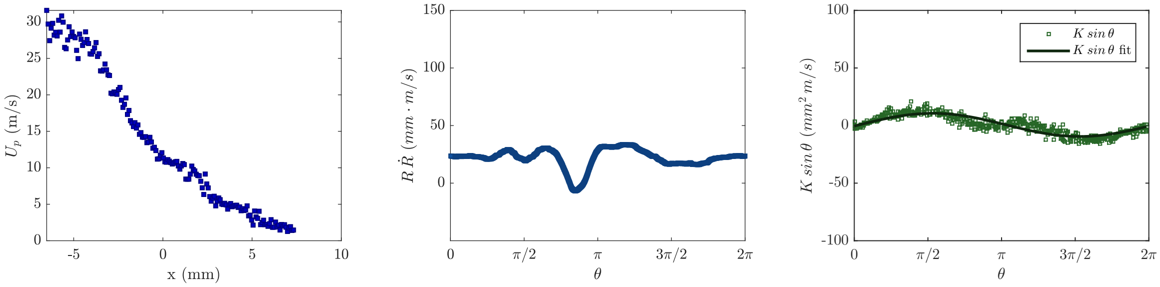

(a) Wave flow at edges. (b) $R \cdot \dot{R}$ on interface. (c) $K\ sin\theta$ fit.

Figure G.7: Test# 849. A^* =0.89; x_c^* =0.09; S_{max} =59.6; $U_p(x = 0)$ =11.4.

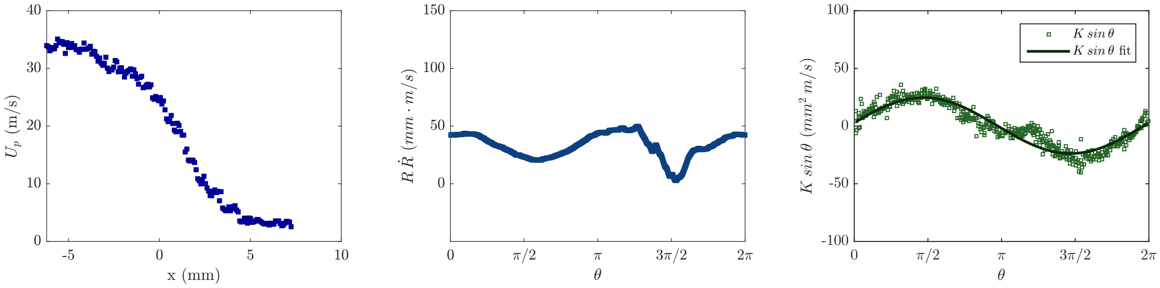

(a) Wave flow at edges. (b) $R \cdot \dot{R}$ on interface. (c) $K\ sin\theta$ fit.

Figure G.8: Test# 842. A^* =0.89; x_c^* =0.13; S_{max} =85.9; $U_p(x = 0)$ =24.3.

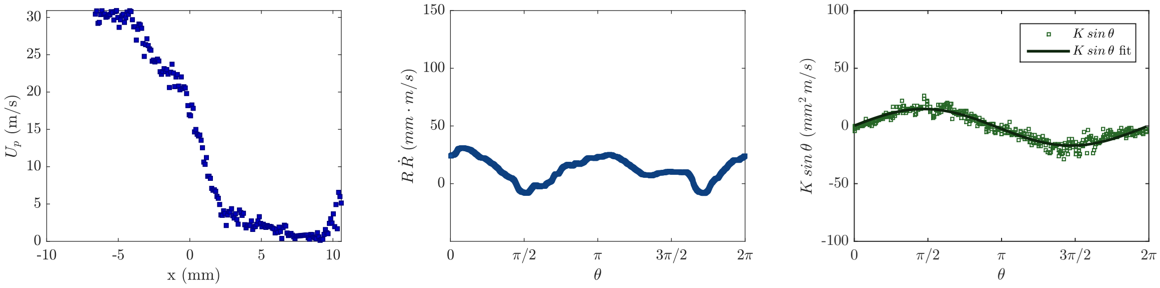

(a) Wave flow at edges.

(b) $R \cdot \dot{R}$ on interface.

(c) $K\ sin\theta$ fit.

Figure G.9: Test# 701. $A^* =0.87$; $x_c^* =0.15$; $S_{max} =67.4$; $U_p(x=0) =18.0$.

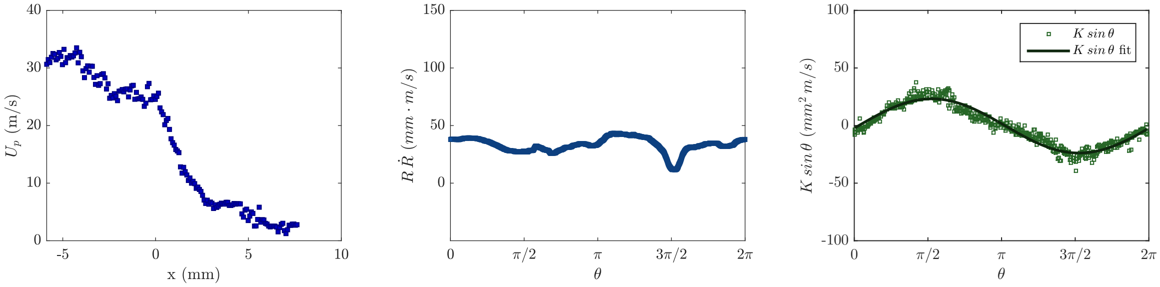

(a) Wave flow at edges.

(b) $R \cdot \dot{R}$ on interface.

(c) $K\ sin\theta$ fit.

Figure G.10: Test# 745. $A^* =0.86$; $x_c^* =0.12$; $S_{max} =77.6$; $U_p(x=0) =23.9$.

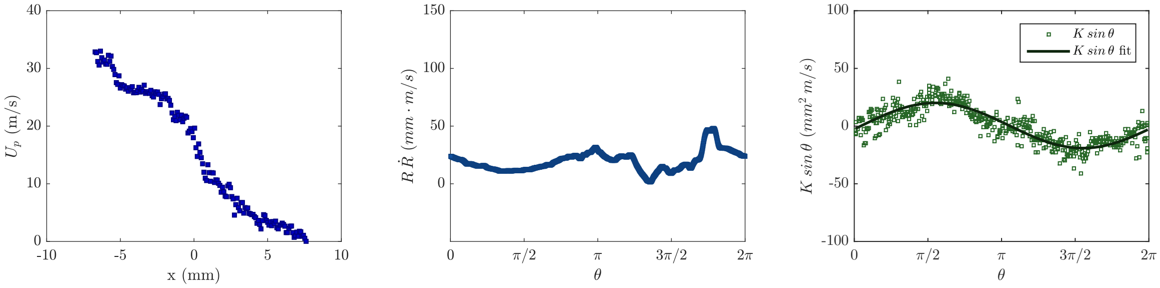

(a) Wave flow at edges.

(b) $R \cdot \dot{R}$ on interface.

(c) $K\ sin\theta$ fit.

Figure G.11: Test# 823. $A^* =0.86$; $x_c^* =0.10$; $S_{max} =70.6$; $U_p(x=0) =18.0$.

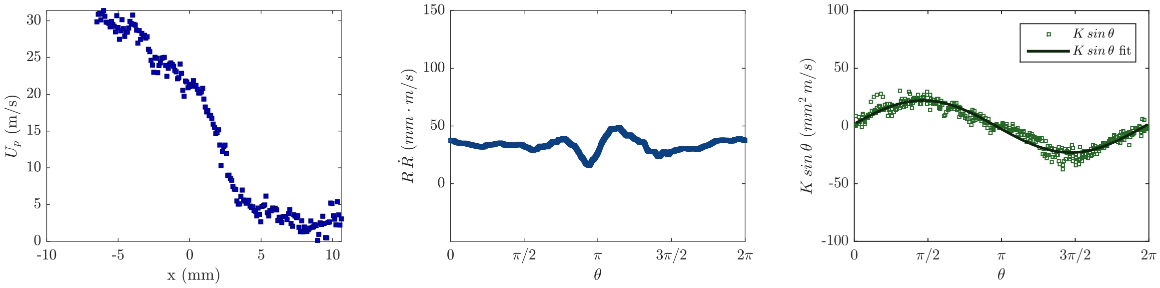

(a) Wave flow at edges.

(b) $R \cdot \dot{R}$ on interface.

(c) $K\ sin\theta$ fit.

Figure G.12: Test# 704. $A^* = 0.81$; $x_c^* = 0.16$; $S_{max} = 81.2$; $U_p(x=0) = 21.4$.

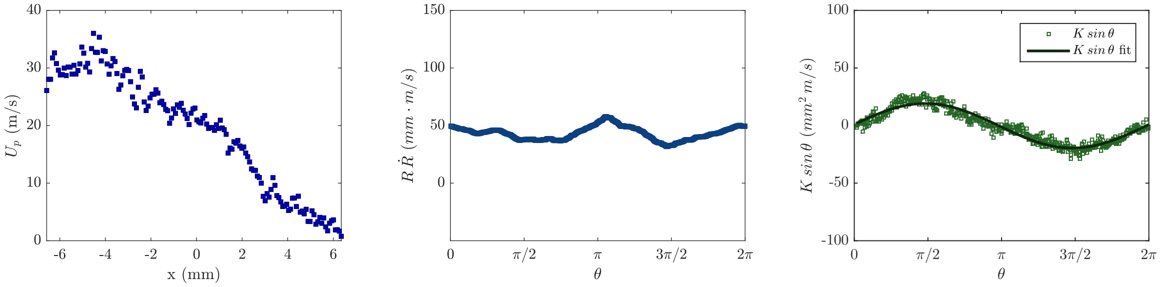

(a) Wave flow at edges.

(b) $R \cdot \dot{R}$ on interface.

(c) $K\ sin\theta$ fit.

Figure G.13: Test# 843. $A^* = 0.74$; $x_c^* = 0.24$; $S_{max} = 85.9$; $U_p(x=0) = 21.2$.

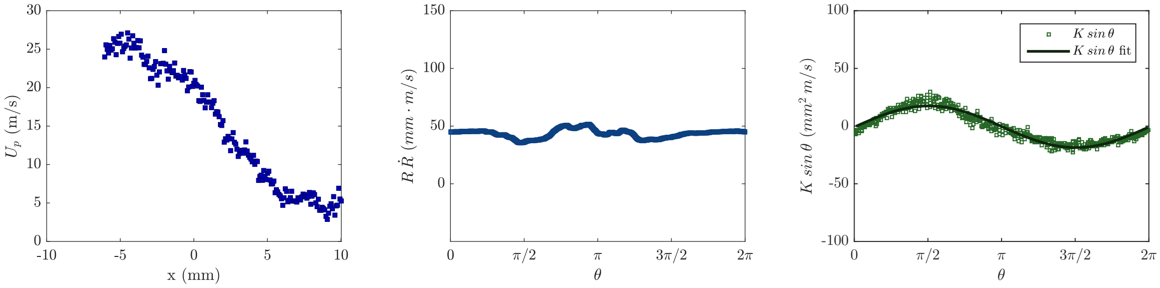

(a) Wave flow at edges.

(b) $R \cdot \dot{R}$ on interface.

(c) $K\ sin\theta$ fit.

Figure G.14: Test# 689. $A^* = 0.56$; $x_c^* = 0.32$; $S_{max} = 87.2$; $U_p(x=0) = 20.3$.

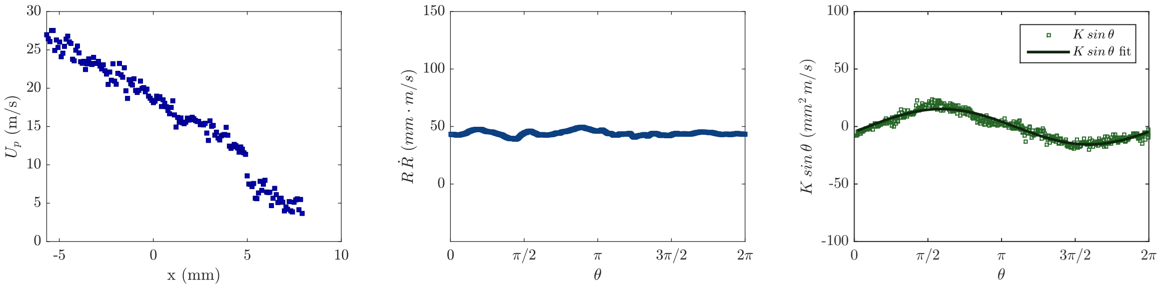

(a) Wave flow at edges.

(b) $R \cdot \dot{R}$ on interface.

(c) $K\ sin\theta$ fit.

Figure G.15: Test# 750. $A^* = 0.50$; $x_c^* = 0.38$; $S_{max} = 124.2$; $U_p(x = 0) = 18.8$.

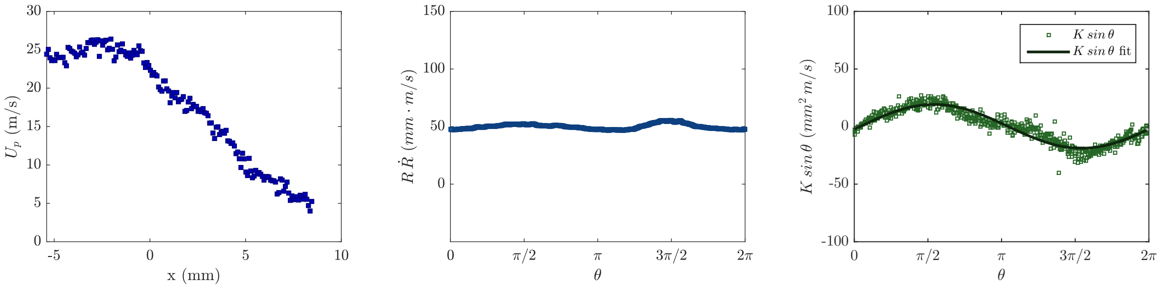

(a) Wave flow at edges.

(b) $R \cdot \dot{R}$ on interface.

(c) $K\ sin\theta$ fit.

Figure G.16: Test# 751. $A^* = 0.48$; $x_c^* = 0.37$; $S_{max} = 109.2$; $U_p(x = 0) = 22.4$.

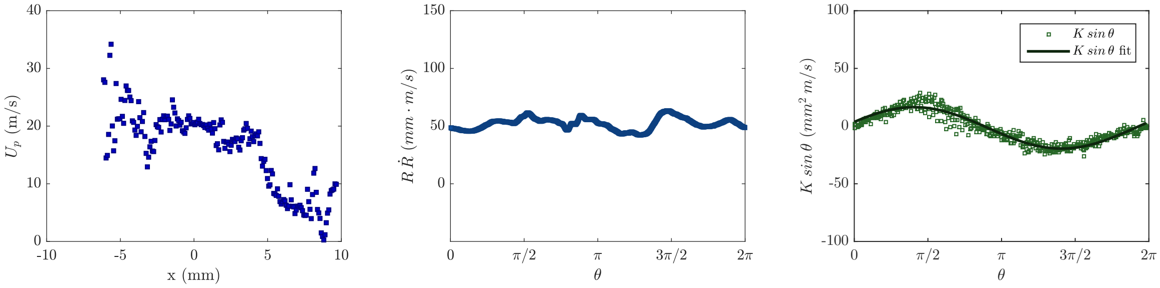

(a) Wave flow at edges.

(b) $R \cdot \dot{R}$ on interface.

(c) $K\ sin\theta$ fit.

Figure G.17: Test# 687. $A^* = 0.44$; $x_c^* = 0.44$; $S_{max} = 128.3$; $U_p(x = 0) = 20.5$.

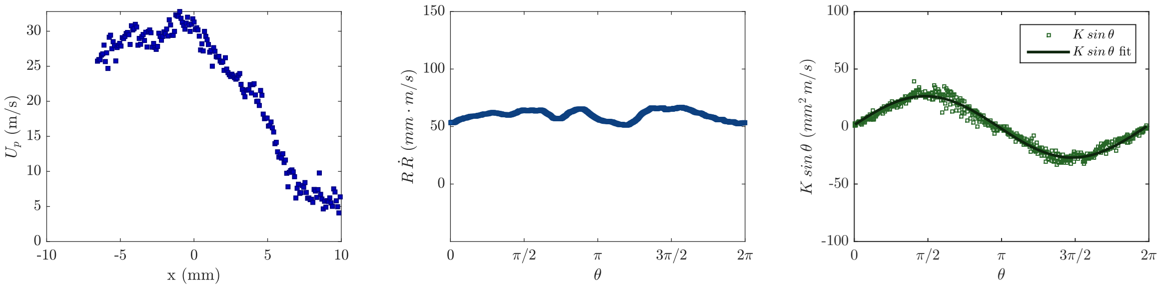

(a) Wave flow at edges.

(b) $R \cdot \dot{R}$ on interface.

(c) $K\ sin\theta$ fit.

Figure G.18: Test# 699. $A^* = 0.39$; $x_c^* = 0.48$; $S_{max} = 129.5$; $U_p(x = 0) = 30.1$.

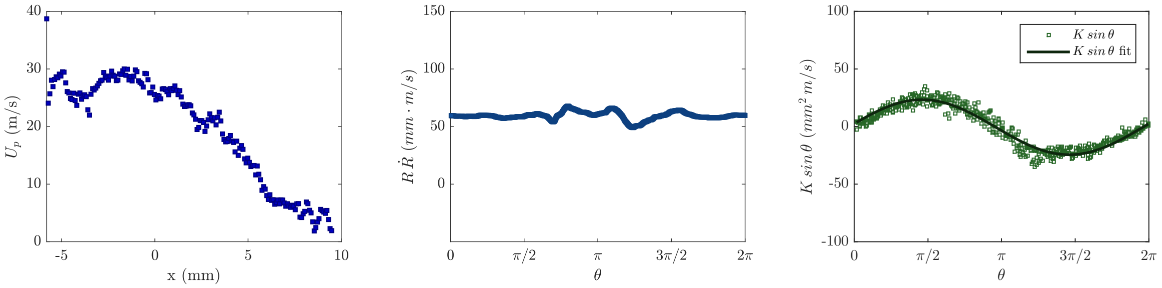

(a) Wave flow at edges.

(b) $R \cdot \dot{R}$ on interface.

(c) $K\ sin\theta$ fit.

Figure G.19: Test# 688. $A^* = 0.38$; $x_c^* = 0.48$; $S_{max} = 144.8$; $U_p(x = 0) = 26.5$.

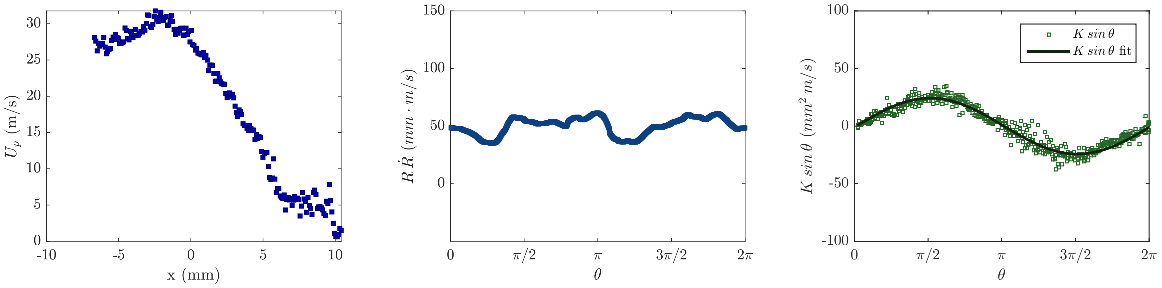

(a) Wave flow at edges.

(b) $R \cdot \dot{R}$ on interface.

(c) $K\ sin\theta$ fit.

Figure G.20: Test# 694. $A^* = 0.37$; $x_c^* = 0.52$; $S_{max} = 172.8$; $U_p(x = 0) = 27.6$.

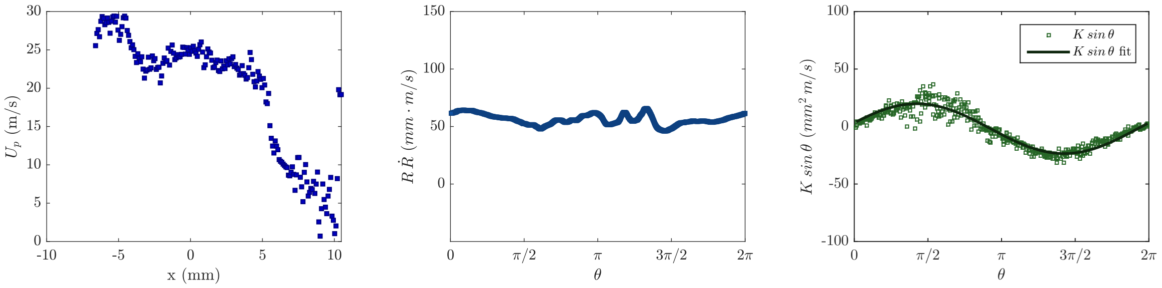

(a) Wave flow at edges.

(b) $R \cdot \dot{R}$ on interface.

(c) $K\ sin\theta$ fit.

Figure G.21: Test# 693. $A^* =0.35$; $x_c^* =0.52$; $S_{max} =138.8$; $U_p(x=0) =24.9$.

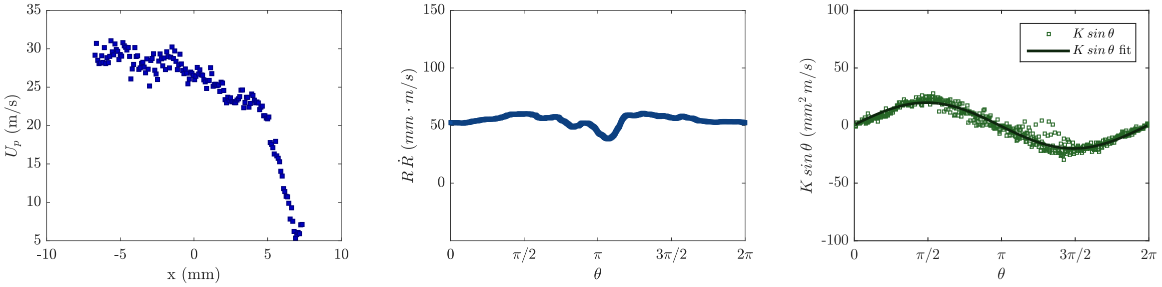

(a) Wave flow at edges.

(b) $R \cdot \dot{R}$ on interface.

(c) $K\ sin\theta$ fit.

Figure G.22: Test# 822. $A^* =0.29$; $x_c^* =0.53$; $S_{max} =152.8$; $U_p(x=0) =26.6$.

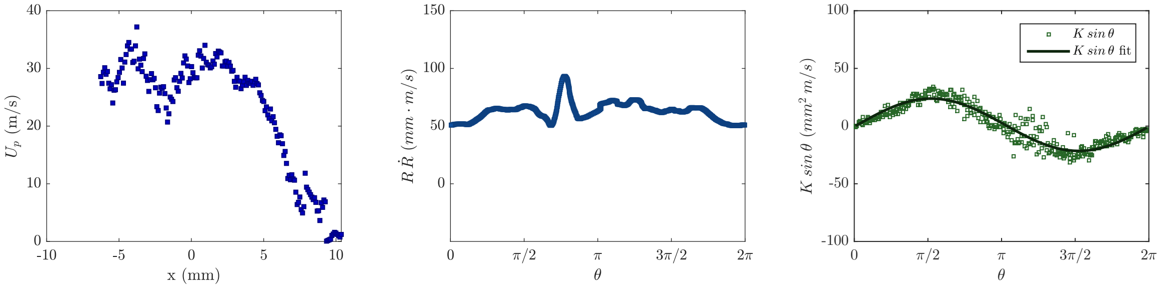

(a) Wave flow at edges.

(b) $R \cdot \dot{R}$ on interface.

(c) $K\ sin\theta$ fit.

Figure G.23: Test# 703. $A^* =0.28$; $x_c^* =0.60$; $S_{max} =136.1$; $U_p(x=0) =30.1$.

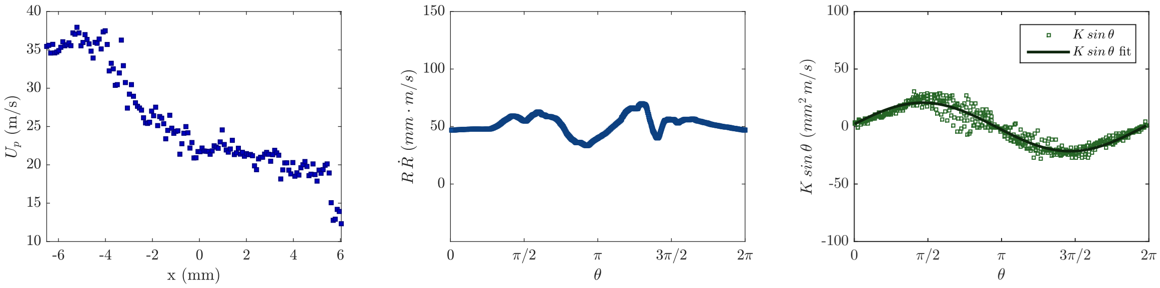

(a) Wave flow at edges.

(b) $R \cdot \dot{R}$ on interface.

(c) $K\ sin\theta$ fit.

Figure G.24: Test# 840. A^* =0.24; x_c^* =0.62; S_{max} =123.5; $U_p(x=0)$ =22.2.

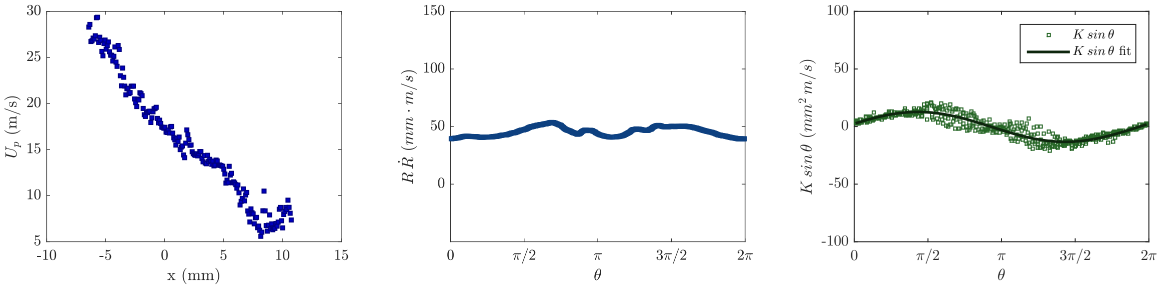

(a) Wave flow at edges.

(b) $R \cdot \dot{R}$ on interface.

(c) $K\ sin\theta$ fit.

Figure G.25: Test# 700. A^* =0.22; x_c^* =0.59; S_{max} =110.1; $U_p(x=0)$ =17.4.

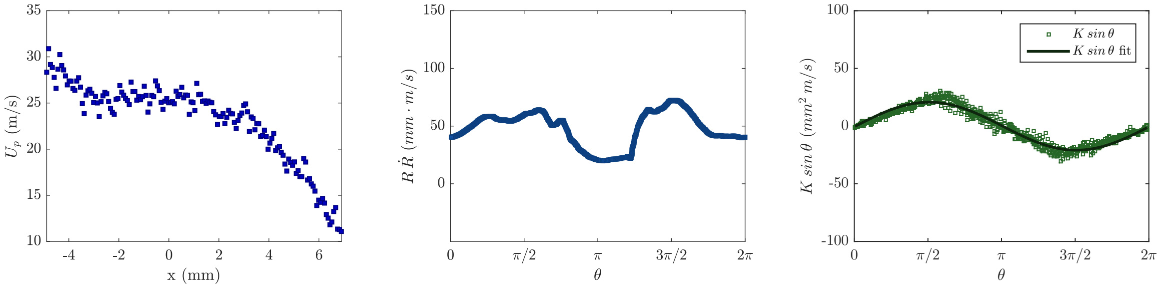

(a) Wave flow at edges.

(b) $R \cdot \dot{R}$ on interface.

(c) $K\ sin\theta$ fit.

Figure G.26: Test# 761. A^* =0.15; x_c^* =0.69; S_{max} =133.2; $U_p(x=0)$ =25.7.

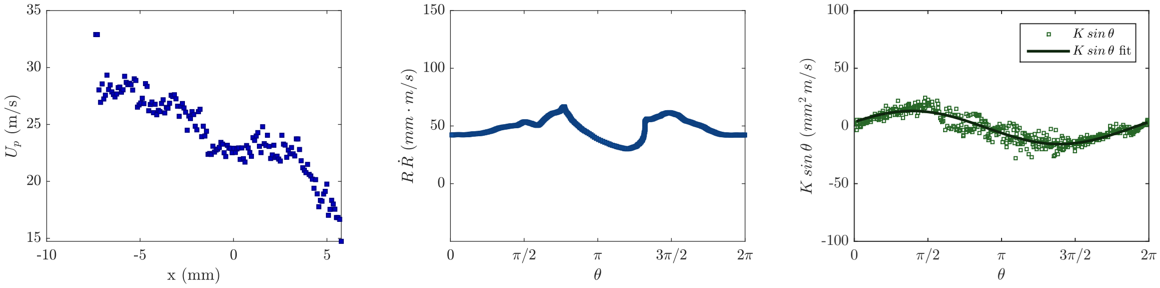

(a) Wave flow at edges. (b) $R \cdot \dot{R}$ on interface. (c) $K\ sin\theta$ fit.

Figure G.27: Test# 838. A^* =0.13; x_c^* =0.72; S_{max} =113.9; $U_p(x=0)$ =22.6.

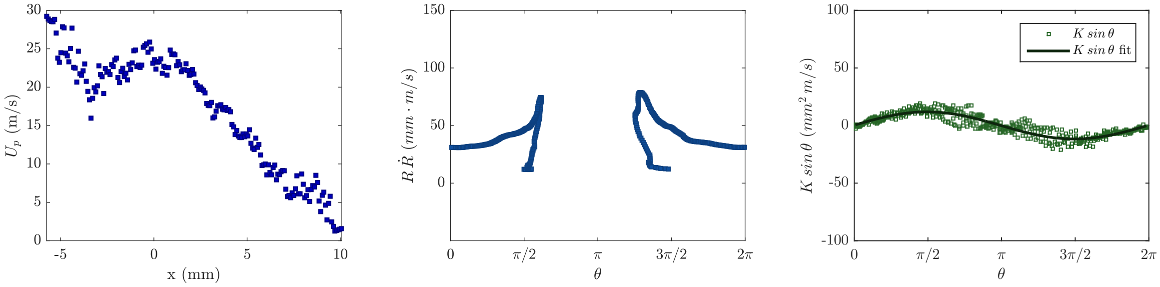

(a) Wave flow at edges. (b) $R \cdot \dot{R}$ on interface. (c) $K\ sin\theta$ fit.

Figure G.28: Test# 686. A^* =0.09; x_c^* =0.70; S_{max} =126.6; $U_p(x=0)$ =23.9.

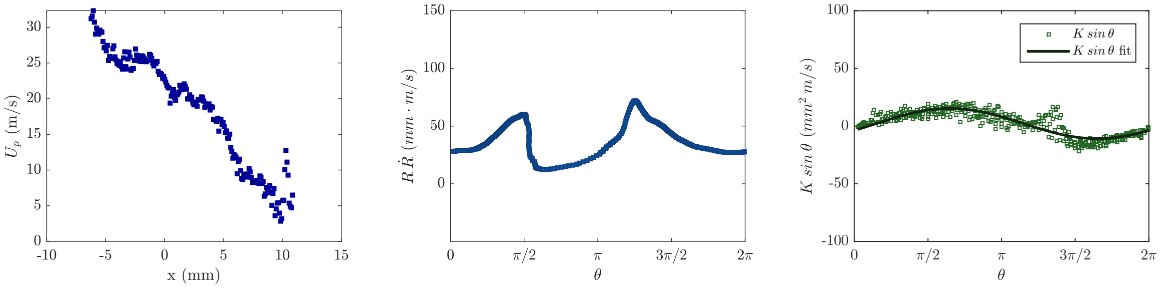

(a) Wave flow at edges. (b) $R \cdot \dot{R}$ on interface. (c) $K\ sin\theta$ fit.

Figure G.29: Test# 692. A^* =0.06; x_c^* =0.79; S_{max} =100.0; $U_p(x=0)$ =22.4.

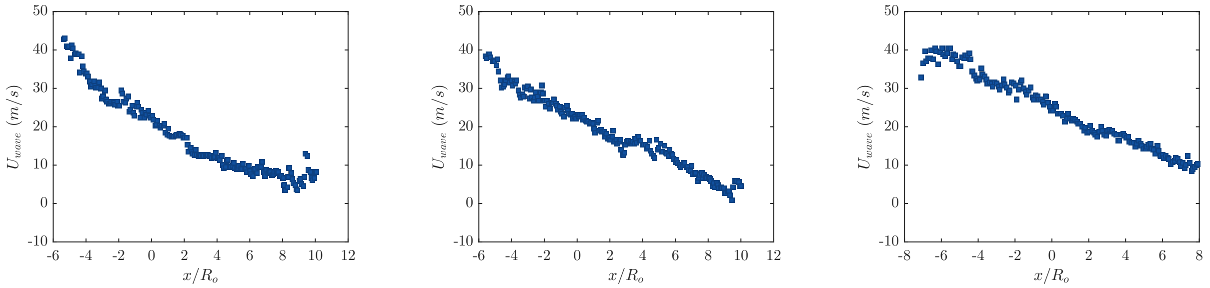

(a) Test# 684. A^* =0.00; x_c^* =0.84; S_{max} =74.1.

(b) Test# 685. A^* =0.00; x_c^* =1.04; S_{max} =60.2.

(c) Test# 691. A^* =0.00; x_c^* =1.08; S_{max} =58.2.

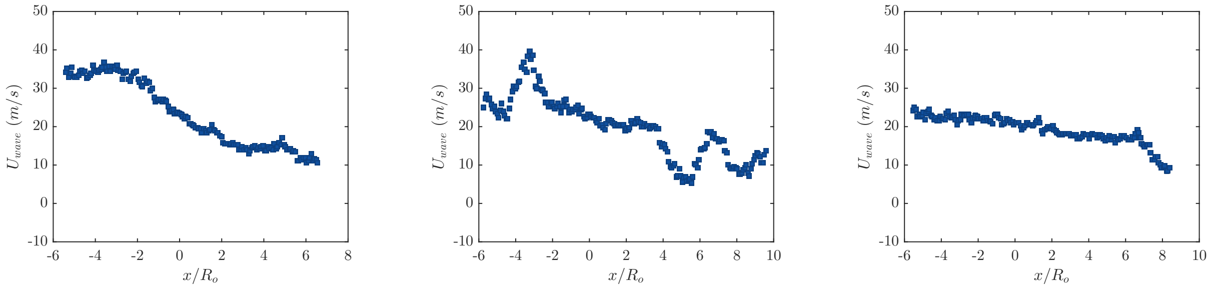

(d) Test# 760. A^* =0.00; x_c^* =1.16; S_{max} =55.4.

(e) Test# 690. A^* =0.00; x_c^* =1.25; S_{max} =55.0.

(f) Test# 753. A^* =0.00; x_c^* =1.32; S_{max} =40.0.

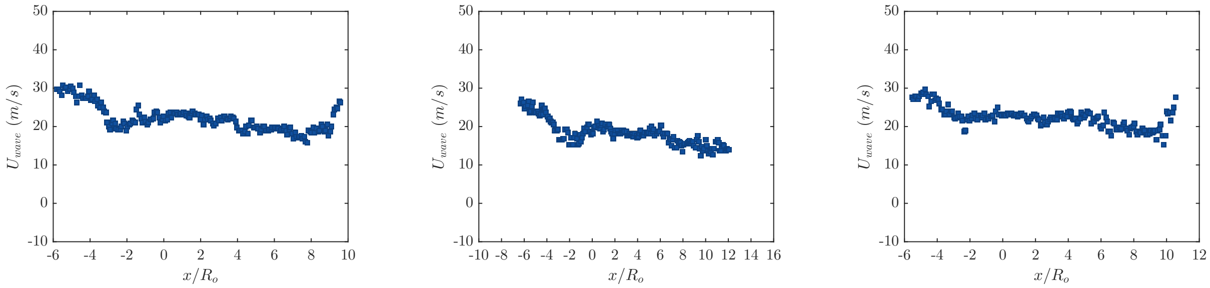

(g) Test# 696. A^* =0.00; x_c^* =3.16; S_{max} =53.1.

(h) Test# 697. A^* =0.00; x_c^* =3.29; S_{max} =36.1.

(i) Test# 695. A^* =0.00; x_c^* =3.35; S_{max} =49.4.

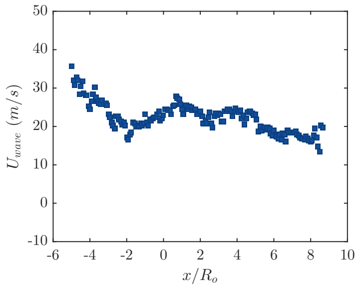

(j) Test# 698. A^* =0.00; x_c^* =3.47; S_{max} =45.4.

Figure G.30: Wave flow velocity distribution for tests 684–698. Void boundary could not be identified reliably(<3%), or test was after collapse, so outgoing wave prevented accurate U_p evaluation.

G.2 Downstream Boundary

G.2.1 Downstream 20:1 PDMS

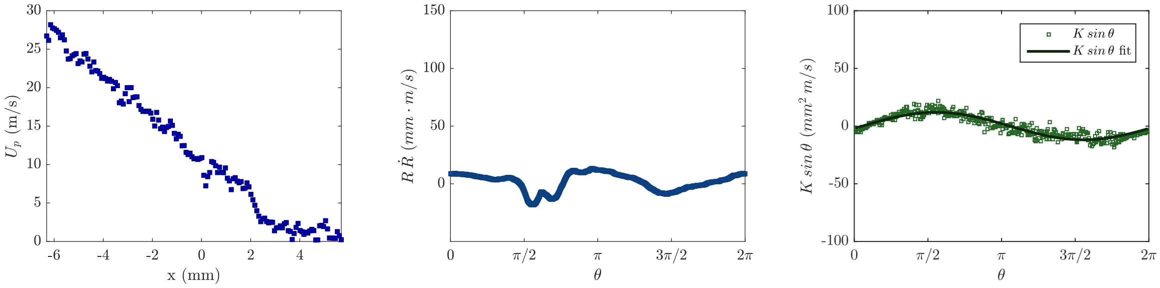

(a) Wave flow at edges. (b) $R \cdot \dot{R}$ on interface (c) $K\ sin\theta$ fit.

Figure G.31: Test# 809 $A^* = 1.04$, $x_c^* = 0.02$, $S_{max} = 45.1$, $U_p(x = 0) = 10.1$.

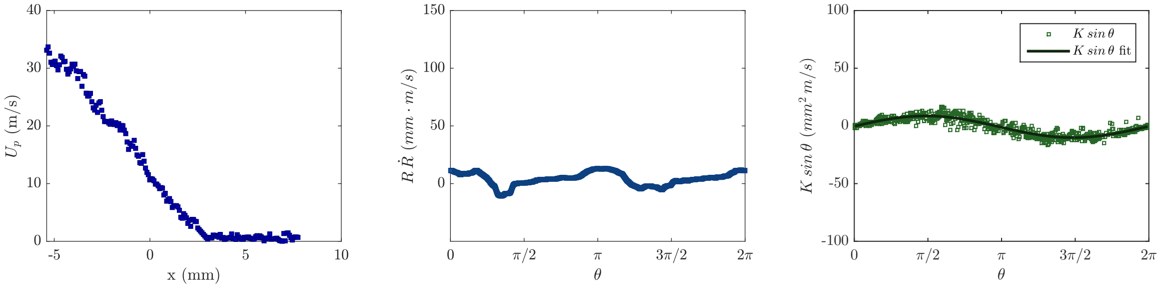

(a) Wave flow at edges. (b) $R \cdot \dot{R}$ on interface (c) $K\ sin\theta$ fit.

Figure G.32: Test# 728 $A^* = 1.00$, $x_c^* = 0.09$, $S_{max} = 51.1$, $U_p(x = 0) = 11.6$.

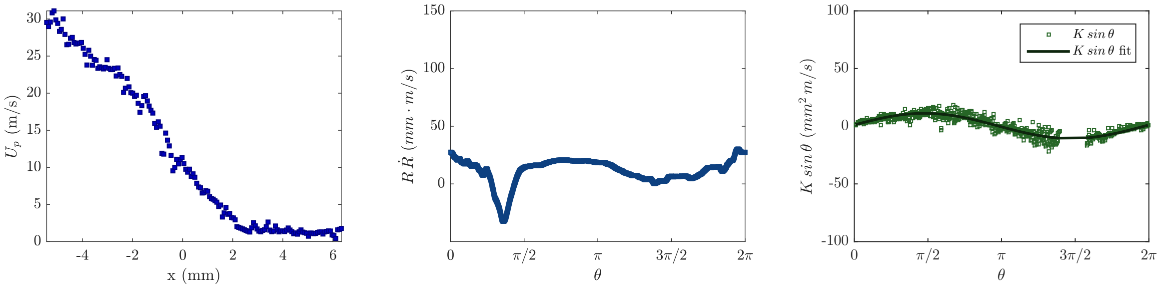

(a) Wave flow at edges. (b) $R \cdot \dot{R}$ on interface (c) $K\ sin\theta$ fit.

Figure G.33: Test# 743 $A^* = 0.95$, $x_c^* = 0.08$, $S_{max} = 51.4$, $U_p(x = 0) = 10.3$.

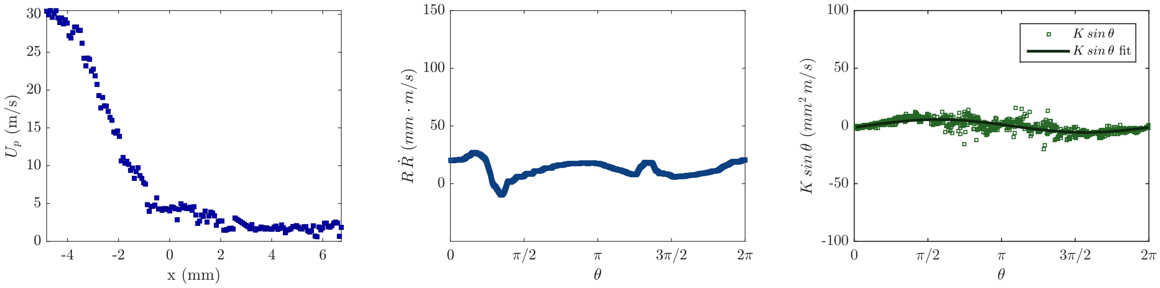

(a) Wave flow at edges. (b) $R \cdot \dot{R}$ on interface (c) $K\ sin\theta$ fit.

Figure G.34: Test# 742 $A^* =$0.95, $x_c^* = $0.05, $S_{max} = $41.6, $U_p(x = 0) = $4.3.

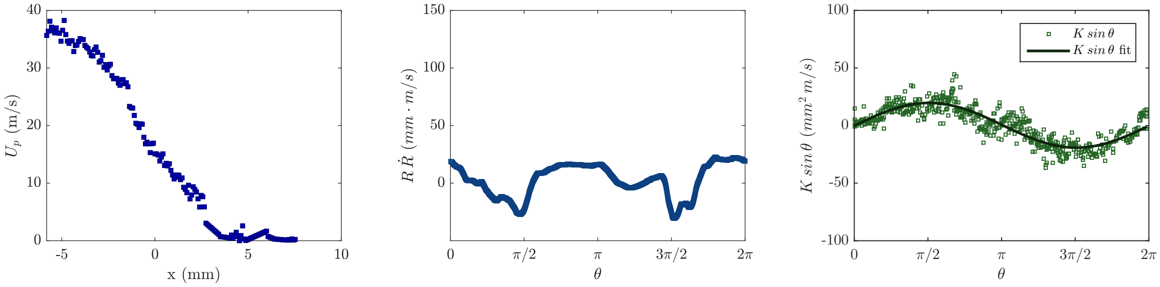

(a) Wave flow at edges. (b) $R \cdot \dot{R}$ on interface (c) $K\ sin\theta$ fit.

Figure G.35: Test# 764 $A^* = $0.93, $x_c^* = $0.15, $S_{max} = $58.9, $U_p(x = 0) = $15.5.

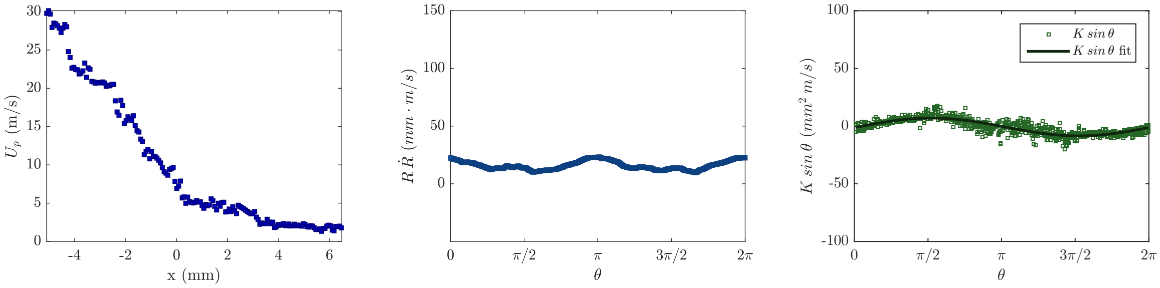

(a) Wave flow at edges. (b) $R \cdot \dot{R}$ on interface (c) $K\ sin\theta$ fit.

Figure G.36: Test# 749 $A^* = $0.90, $x_c^* = $0.10, $S_{max} = $47.4, $U_p(x = 0) = $7.5.

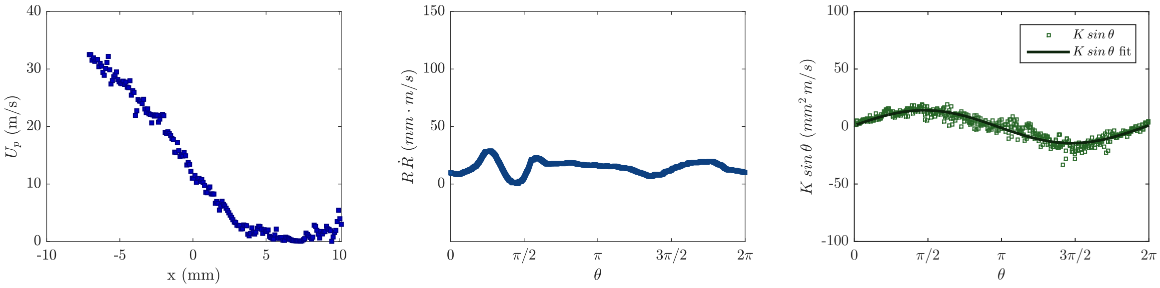

(a) Wave flow at edges.

(b) $R \cdot \dot{R}$ on interface

(c) $K\ sin\theta$ fit.

Figure G.37: Test# 717 A^* =0.89, x_c^* =0.14, S_{max} =52.7, $U_p(x = 0)$ =12.3.

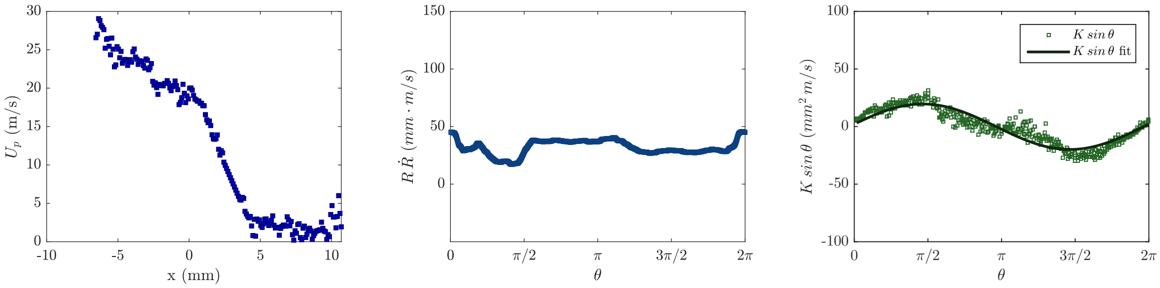

(a) Wave flow at edges.

(b) $R \cdot \dot{R}$ on interface

(c) $K\ sin\theta$ fit.

Figure G.38: Test# 718 A^* =0.79, x_c^* =0.23, S_{max} =74.7, $U_p(x = 0)$ =19.0.

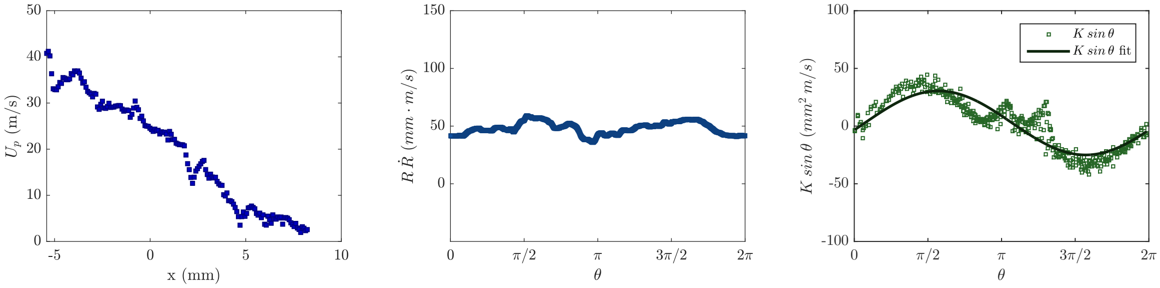

(a) Wave flow at edges.

(b) $R \cdot \dot{R}$ on interface

(c) $K\ sin\theta$ fit.

Figure G.39: Test# 912 A^* =0.68, x_c^* =0.23, S_{max} =96.9, $U_p(x = 0)$ =25.0.

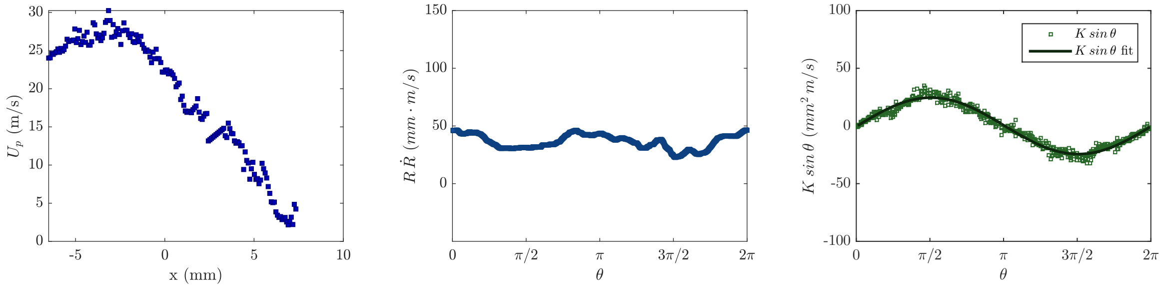

(a) Wave flow at edges.

(b) $R \cdot \dot{R}$ on interface

(c) $K\ sin\theta$ fit.

Figure G.40: Test# 894 $A^* = 0.63$, $x_c^* = 0.31$, $S_{max} = 92.5$, $U_p(x = 0) = 22.6$.

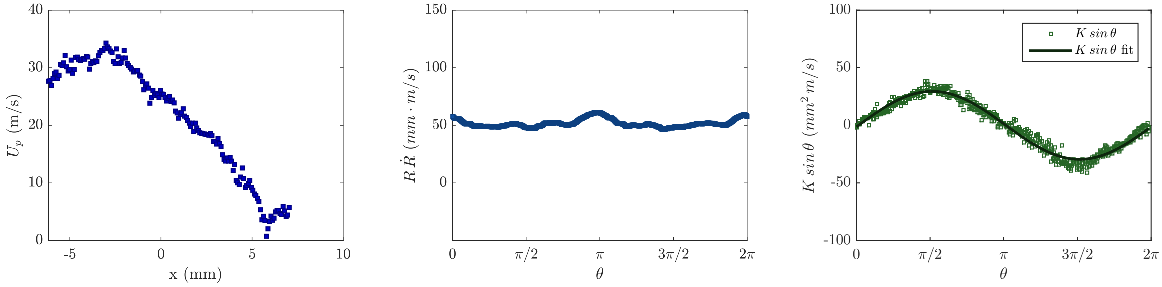

(a) Wave flow at edges.

(b) $R \cdot \dot{R}$ on interface

(c) $K\ sin\theta$ fit.

Figure G.41: Test# 813 $A^* = 0.62$, $x_c^* = 0.33$, $S_{max} = 115.4$, $U_p(x = 0) = 25.0$.

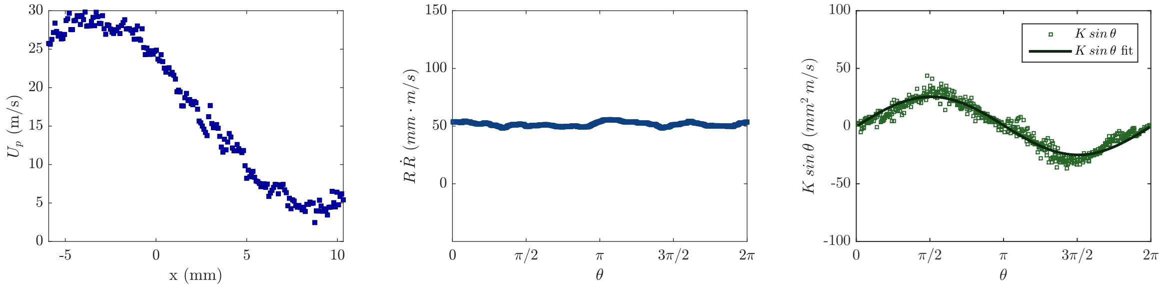

(a) Wave flow at edges.

(b) $R \cdot \dot{R}$ on interface

(c) $K\ sin\theta$ fit.

Figure G.42: Test# 727 $A^* = 0.55$, $x_c^* = 0.37$, $S_{max} = 110.2$, $U_p(x = 0) = 23.9$.

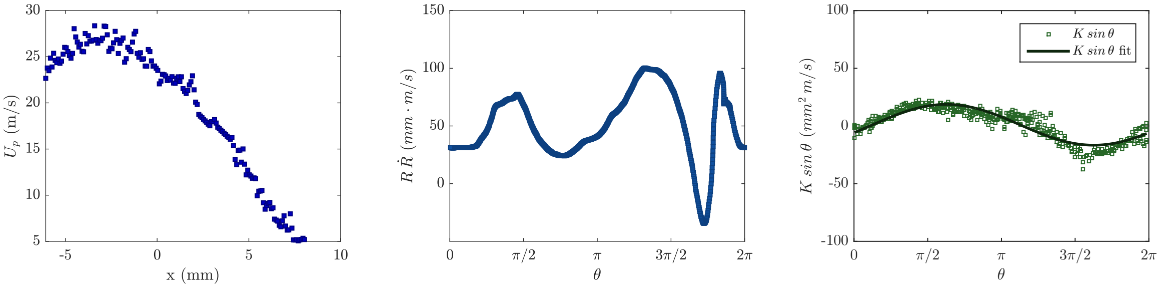

(a) Wave flow at edges.

(b) $R \cdot \dot{R}$ on interface

(c) $K\ sin\theta$ fit.

Figure G.43: Test# 893 $A^* = 0.42$, $x_c^* = 0.40$, $S_{max} = 113.4$, $U_p(x=0) = 23.6$.

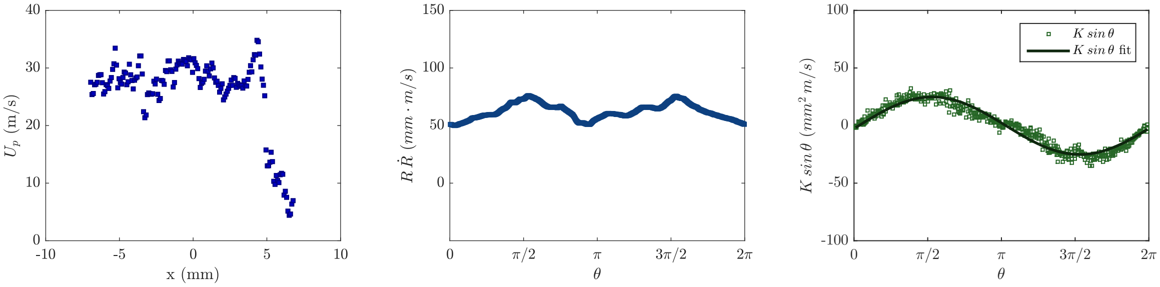

(a) Wave flow at edges.

(b) $R \cdot \dot{R}$ on interface

(c) $K\ sin\theta$ fit.

Figure G.44: Test# 795 $A^* = 0.42$, $x_c^* = 0.41$, $S_{max} = 126.2$, $U_p(x=0) = 30.2$.

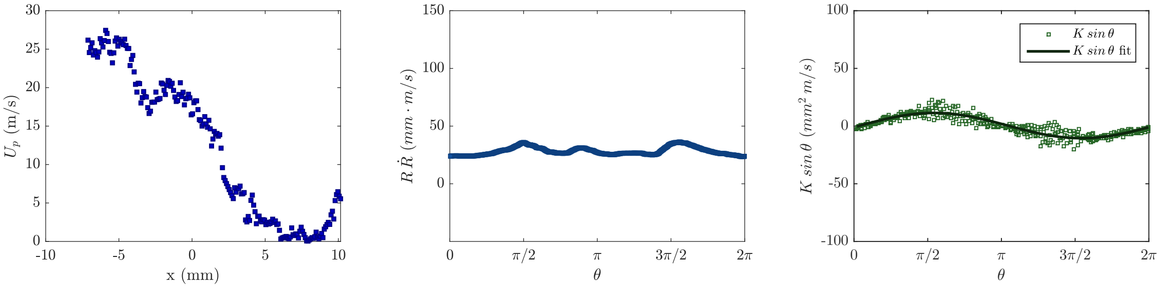

(a) Wave flow at edges.

(b) $R \cdot \dot{R}$ on interface

(c) $K\ sin\theta$ fit.

Figure G.45: Test# 706 $A^* = 0.41$, $x_c^* = 0.43$, $S_{max} = 70.6$, $U_p(x=0) = 17.6$.

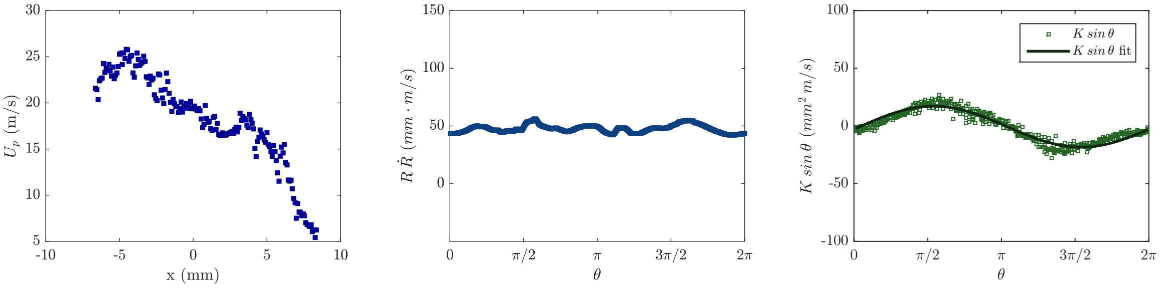

(a) Wave flow at edges.

(b) $R \cdot \dot{R}$ on interface

(c) $K\ sin\theta$ fit.

Figure G.46: Test# 911 $A^* = 0.40$, $x_c^* = 0.49$, $S_{max} = 108.2$, $U_p(x=0) = 19.3$.

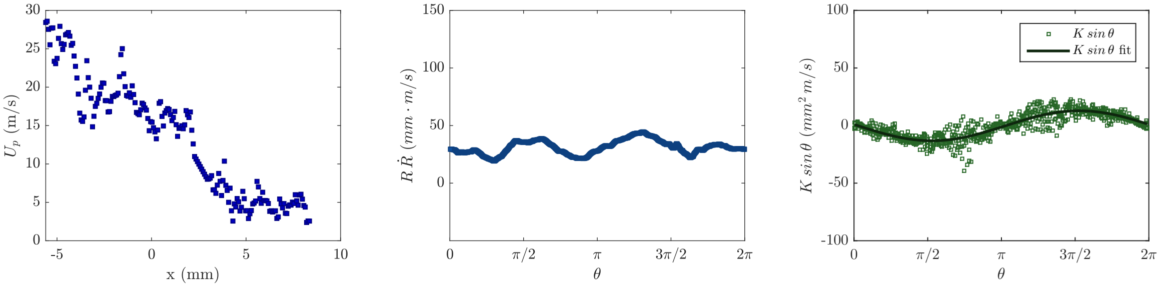

(a) Wave flow at edges.

(b) $R \cdot \dot{R}$ on interface

(c) $K\ sin\theta$ fit.

Figure G.47: Test# 765 $A^* = 0.37$, $x_c^* = 0.55$, $S_{max} = 87.0$, $U_p(x=0) = 16.0$.

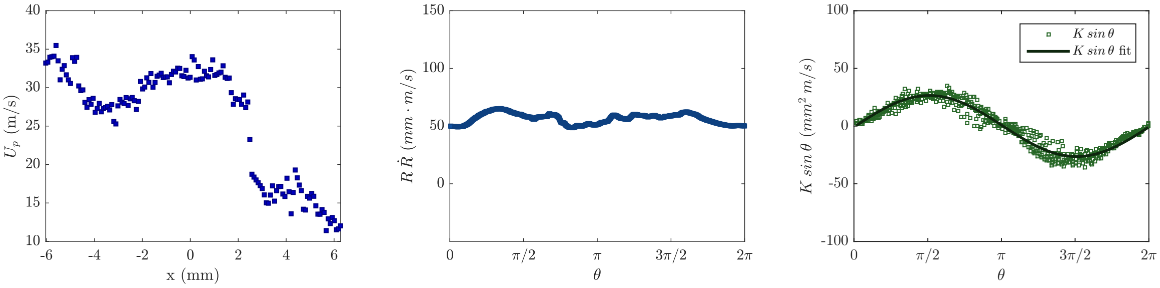

(a) Wave flow at edges.

(b) $R \cdot \dot{R}$ on interface

(c) $K\ sin\theta$ fit.

Figure G.48: Test# 895 $A^* = 0.25$, $x_c^* = 0.66$, $S_{max} = 132.8$, $U_p(x=0) = 32.0$.

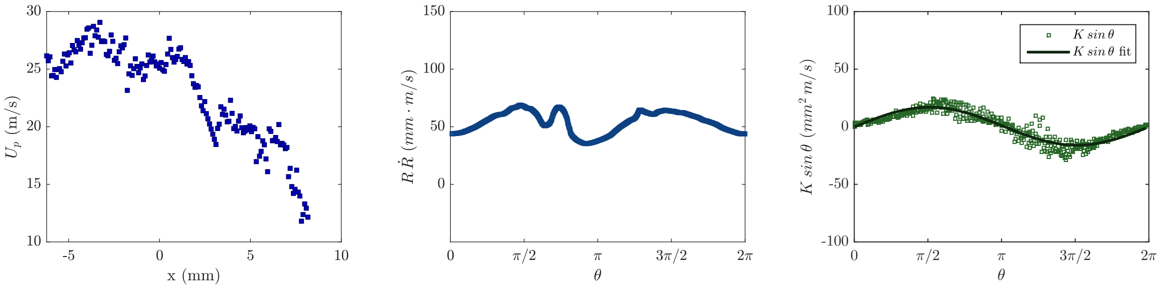

(a) Wave flow at edges.

(b) $R \cdot \dot{R}$ on interface

(c) $K\ sin\theta$ fit.

Figure G.49: Test# 910 A^* =0.14, x_c^* =0.77, S_{max} =131.7, $U_p(x=0)$ =25.8.

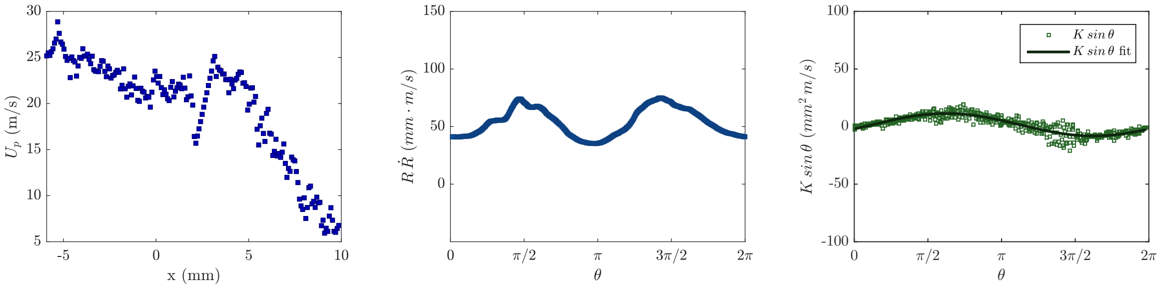

(a) Wave flow at edges.

(b) $R \cdot \dot{R}$ on interface

(c) $K\ sin\theta$ fit.

Figure G.50: Test# 896 A^* =0.10, x_c^* =0.67, S_{max} =115.7, $U_p(x=0)$ =21.5.

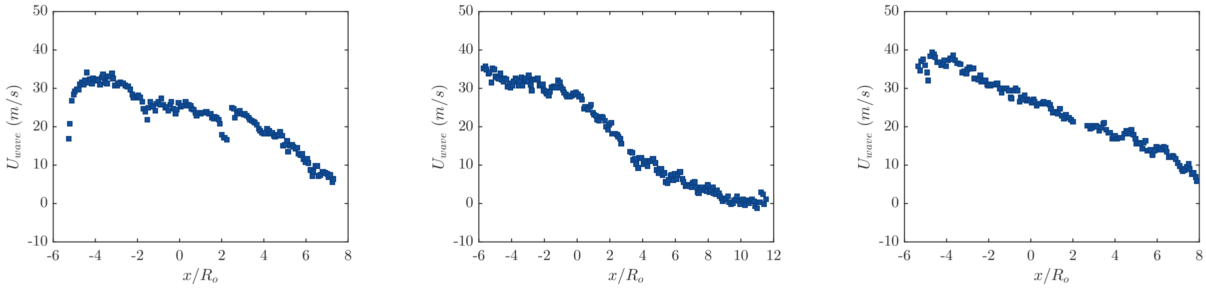

(a) Test# 909. A^* =0.02; x_c^* =0.76; S_{max} =89.4.
(b) Test# 707. A^* =0.01; x_c^* =0.86; S_{max} =106.6.
(c) Test# 871. A^* =0.01; x_c^* =0.79; S_{max} =96.6.

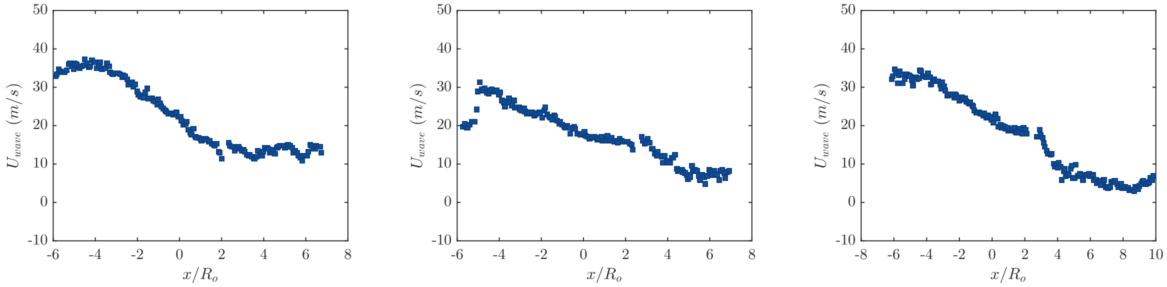

(d) Test# 817. A^* =0.00; x_c^* =0.90; S_{max} =74.8.
(e) Test# 784. A^* =0.00; x_c^* =0.98; S_{max} =51.0.
(f) Test# 705. A^* =0.00; x_c^* =1.12; S_{max} =47.6.

Figure G.51: Wave flow velocity distribution for tests 909–705. Void boundary could not be identified reliably(<3%), or test was after collapse, so outgoing waves prevented accurate U_p evaluation.

G.2.2 Downstream 30:1 PDMS

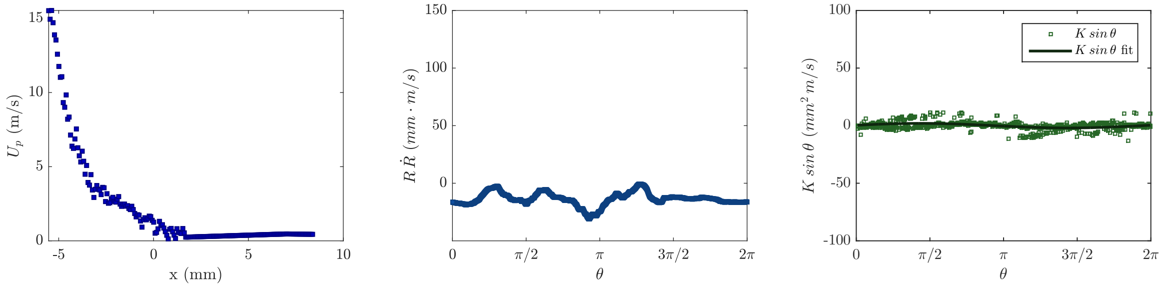

(a) Wave flow at edges.
(b) $R \cdot \dot{R}$ on interface
(c) $K\ sin\theta$ fit.

Figure G.52: Test# 726 A^* =1.00, x_c^* =0.02, S_{max} =23.5, $U_p(x=0)$ =1.2.

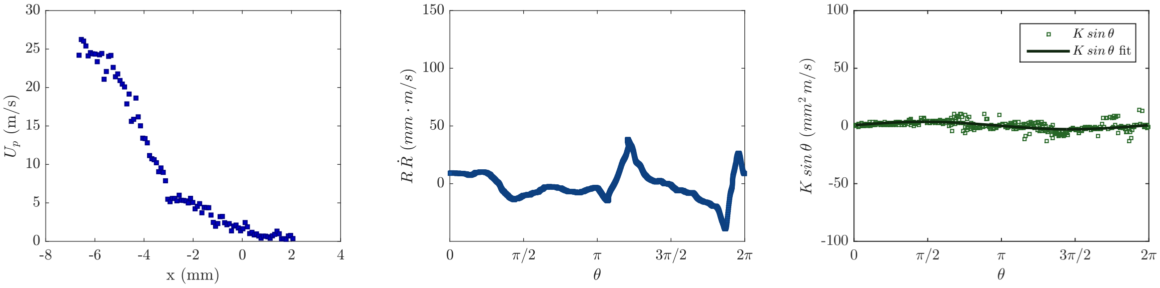

(a) Wave flow at edges.

(b) $R\cdot\dot{R}$ on interface

(c) $K\ sin\theta$ fit.

Figure G.53: Test# 715 A^* =0.99, x_c^* =0.01, S_{max} =40.2, $U_p(x=0)$ =1.6.

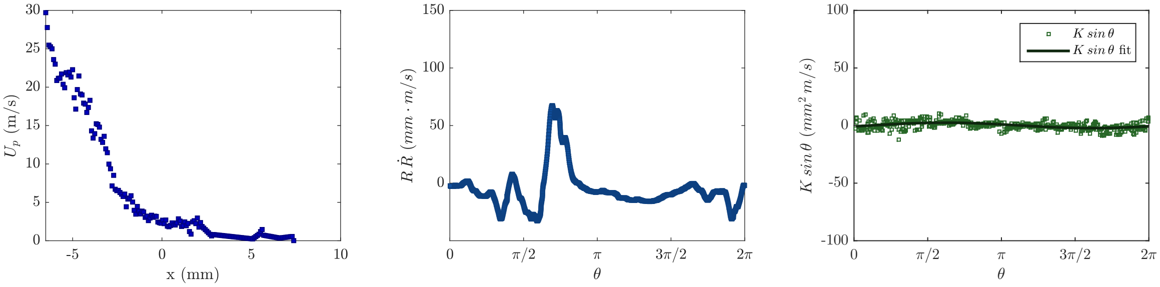

(a) Wave flow at edges.

(b) $R\cdot\dot{R}$ on interface

(c) $K\ sin\theta$ fit.

Figure G.54: Test# 897 A^* =0.99, x_c^* =0.04, S_{max} =45.9, $U_p(x=0)$ =2.5.

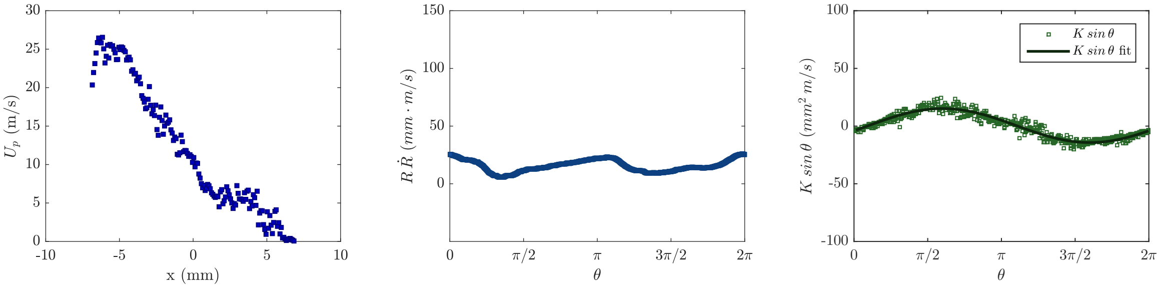

(a) Wave flow at edges.

(b) $R\cdot\dot{R}$ on interface

(c) $K\ sin\theta$ fit.

Figure G.55: Test# 799 A^* =0.86, x_c^* =0.09, S_{max} =48.9, $U_p(x=0)$ =10.1.

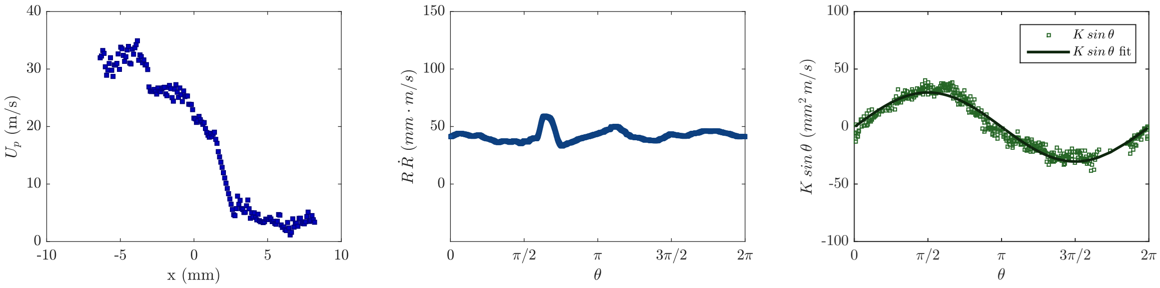

(a) Wave flow at edges.

(b) $R \cdot \dot{R}$ on interface

(c) $K\ sin\theta$ fit.

Figure G.56: Test# 740 $A^* = 0.81$, $x_c^* = 0.18$, $S_{max} = 96.9$, $U_p(x = 0) = 22.6$.

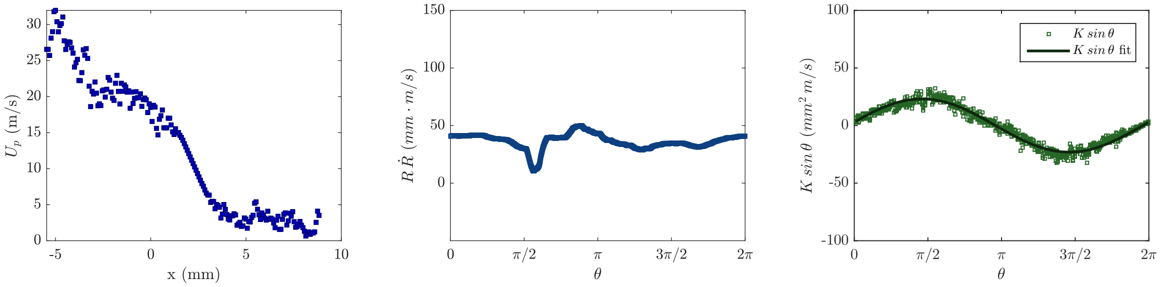

(a) Wave flow at edges.

(b) $R \cdot \dot{R}$ on interface

(c) $K\ sin\theta$ fit.

Figure G.57: Test# 725 $A^* = 0.75$, $x_c^* = 0.23$, $S_{max} = 81.3$, $U_p(x = 0) = 18.1$.

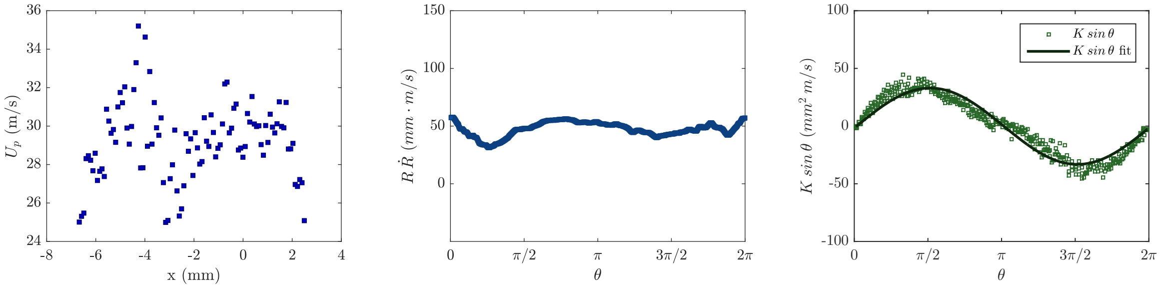

(a) Wave flow at edges.

(b) $R \cdot \dot{R}$ on interface

(c) $K\ sin\theta$ fit.

Figure G.58: Test# 716 $A^* = 0.61$, $x_c^* = 0.36$, $S_{max} = 106.3$, $U_p(x = 0) = 30.1$.

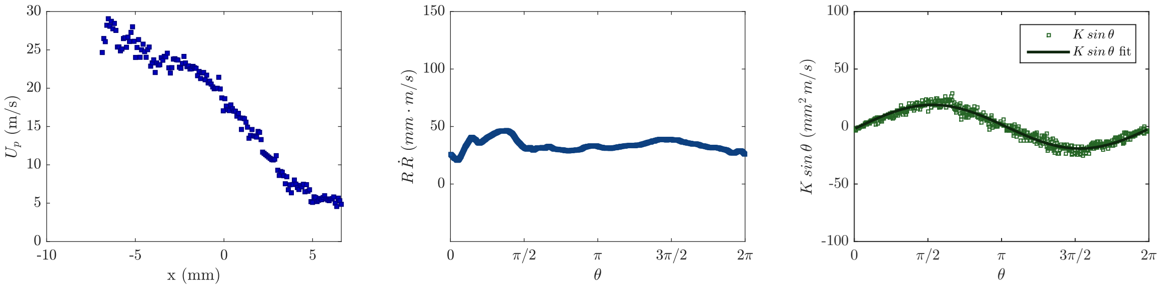

(a) Wave flow at edges.

(b) $R \cdot \dot{R}$ on interface

(c) $K\ sin\theta$ fit.

Figure G.59: Test# 762 $A^* = 0.59$, $x_c^* = 0.32$, $S_{max} = 102.0$, $U_p(x = 0) = 18.7$.

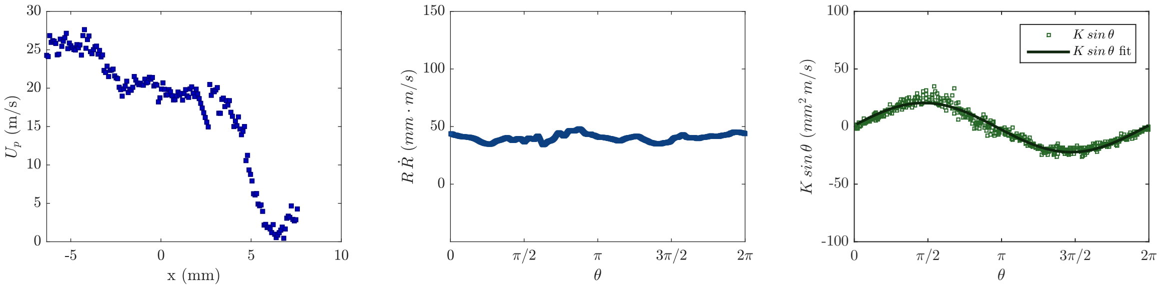

(a) Wave flow at edges.

(b) $R \cdot \dot{R}$ on interface

(c) $K\ sin\theta$ fit.

Figure G.60: Test# 900 $A^* = 0.57$, $x_c^* = 0.32$, $S_{max} = 89.6$, $U_p(x = 0) = 19.8$.

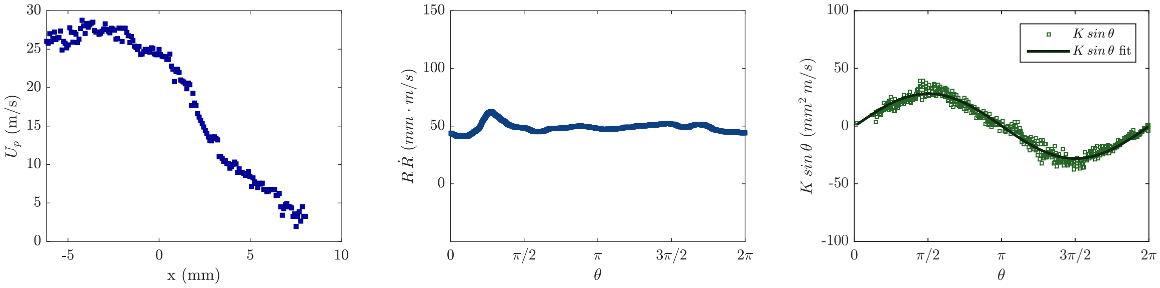

(a) Wave flow at edges.

(b) $R \cdot \dot{R}$ on interface

(c) $K\ sin\theta$ fit.

Figure G.61: Test# 741 $A^* = 0.54$, $x_c^* = 0.38$, $S_{max} = 94.8$, $U_p(x = 0) = 24.4$.

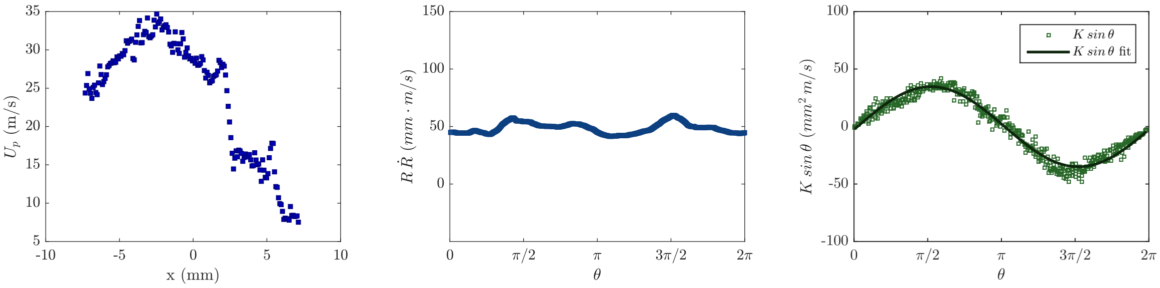

(a) Wave flow at edges. (b) $R \cdot \dot{R}$ on interface (c) $K\ sin\theta$ fit.

Figure G.62: Test# 788 $A^* = 0.41$, $x_c^* = 0.48$, $S_{max} = 133.2$, $U_p(x=0) = 28.8$.

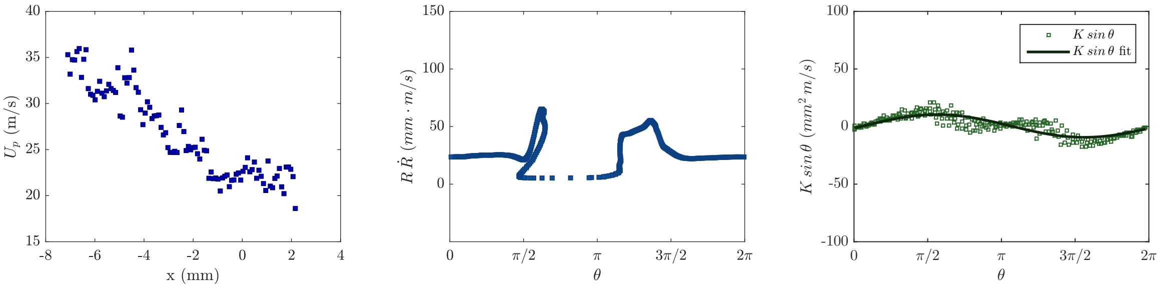

(a) Wave flow at edges. (b) $R \cdot \dot{R}$ on interface (c) $K\ sin\theta$ fit.

Figure G.63: Test# 714 $A^* = 0.20$, $x_c^* = 0.55$, $S_{max} = 98.9$, $U_p(x=0) = 22.4$.

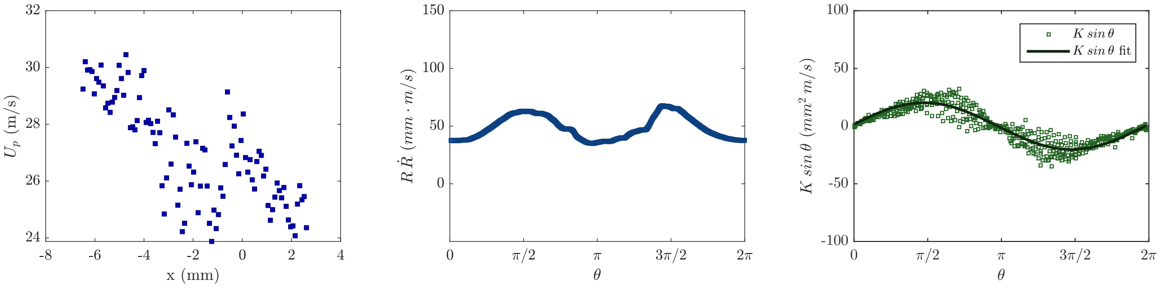

(a) Wave flow at edges. (b) $R \cdot \dot{R}$ on interface (c) $K\ sin\theta$ fit.

Figure G.64: Test# 713 $A^* = 0.16$, $x_c^* = 0.67$, $S_{max} = 127.2$, $U_p(x=0) = 27.1$.

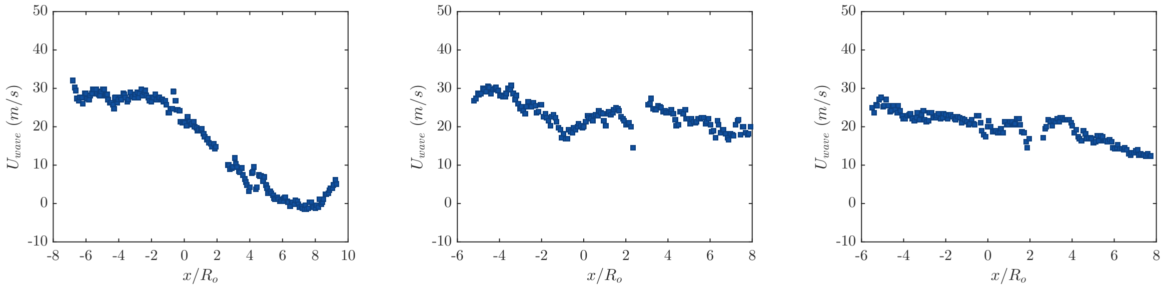

(a) Test# 711. A^* =0.00; x_c^* =1.17; S_{max} =53.7.

(b) Test# 899. A^* =0.00; x_c^* =1.44; S_{max} =55.3.

(c) Test# 898. A^* =0.00; x_c^* =1.48; S_{max} =41.7.

Figure G.65: Wave flow velocity distribution for tests 711–898. Void boundary could not be identified reliably(<3%), or test was after collapse, so outgoing waves prevented accurate U_p evaluation.

G.2.3 Downstream 40:1 PDMS

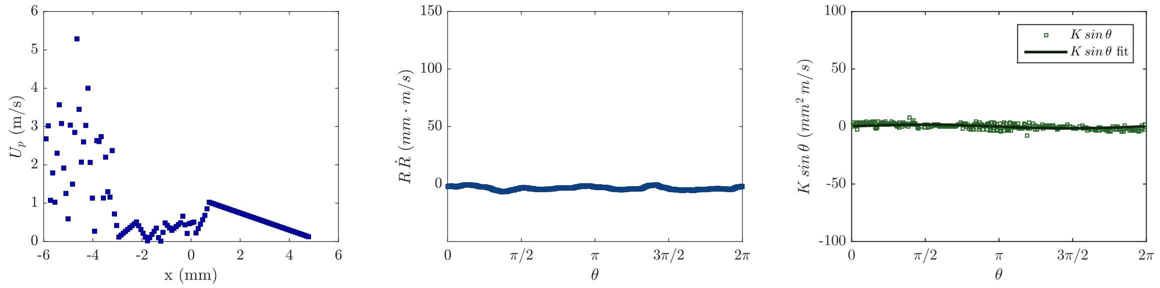

(a) Wave flow at edges.

(b) $R \cdot \dot{R}$ on interface

(c) $K\ sin\theta$ fit.

Figure G.66: Test# 832 A^* =1.01, x_c^* =0.01, S_{max} =18.5, $U_p(x=0)$ =0.5.

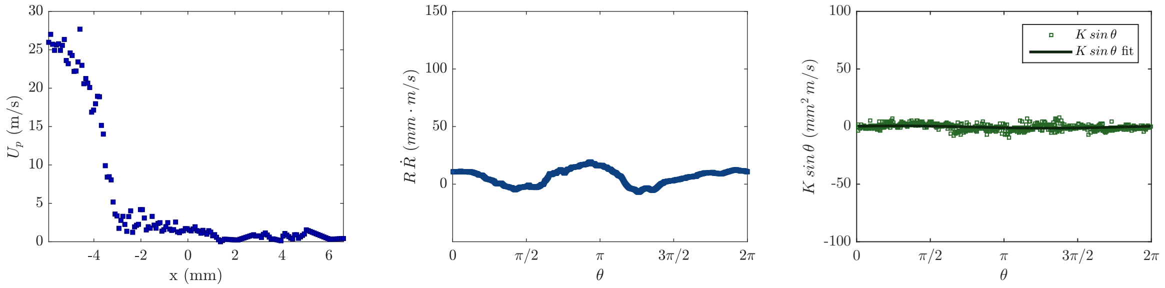

(a) Wave flow at edges.

(b) $R \cdot \dot{R}$ on interface

(c) $K\ sin\theta$ fit.

Figure G.67: Test# 733 A^* =1.00, x_c^* =0.03, S_{max} =48.8, $U_p(x=0)$ =1.6.

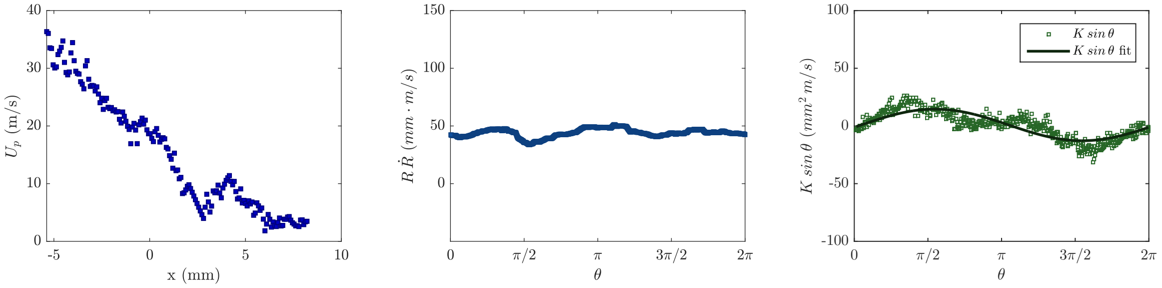

(a) Wave flow at edges. (b) $R \cdot \dot{R}$ on interface (c) $K\,sin\theta$ fit.

Figure G.68: Test# 875 A^{*} =0.77, x_c^{*} =0.19, S_{max} =79.3, $U_p(x=0)$ =19.1.

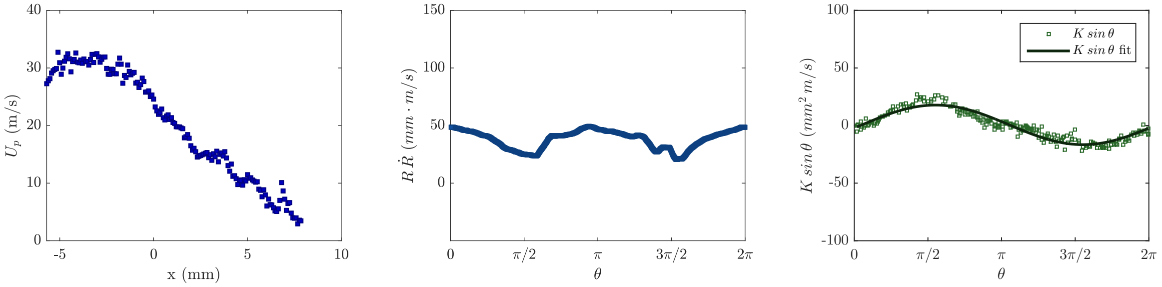

(a) Wave flow at edges. (b) $R \cdot \dot{R}$ on interface (c) $K\,sin\theta$ fit.

Figure G.69: Test# 916 A^{*} =0.76, x_c^{*} =0.18, S_{max} =103.7, $U_p(x=0)$ =24.2.

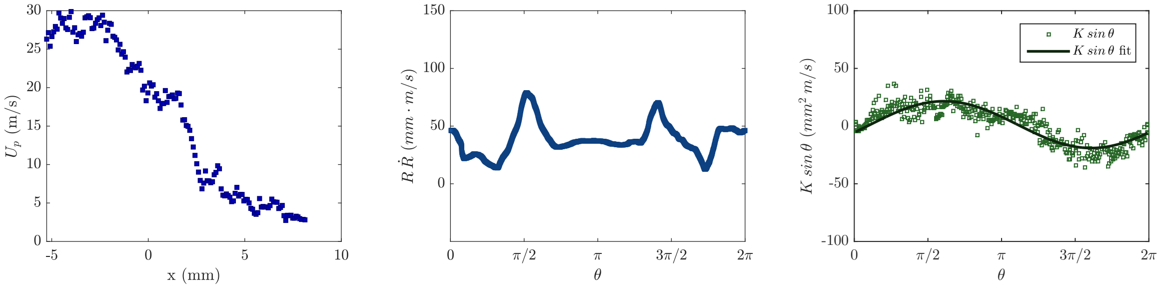

(a) Wave flow at edges. (b) $R \cdot \dot{R}$ on interface (c) $K\,sin\theta$ fit.

Figure G.70: Test# 873 A^{*} =0.67, x_c^{*} =0.25, S_{max} =90.7, $U_p(x=0)$ =20.2.

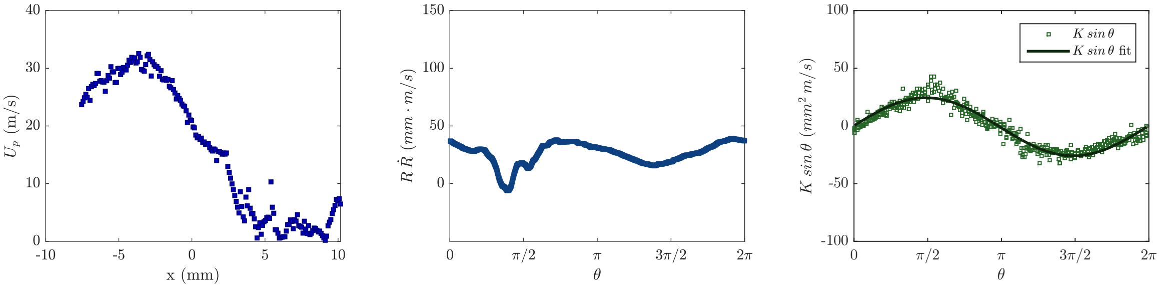

(a) Wave flow at edges.

(b) $R \cdot \dot{R}$ on interface

(c) $K\ sin\theta$ fit.

Figure G.71: Test# 710 A^* =0.67, x_c^* =0.29, S_{max} =77.5, $U_p(x=0)$ =20.5.

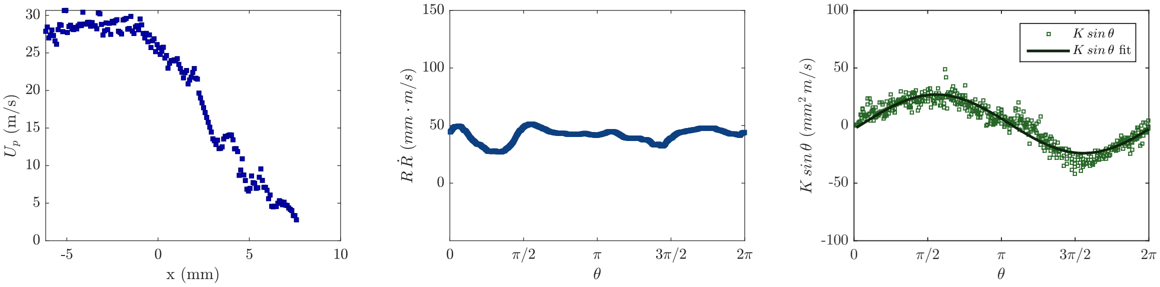

(a) Wave flow at edges.

(b) $R \cdot \dot{R}$ on interface

(c) $K\ sin\theta$ fit.

Figure G.72: Test# 903 A^* =0.63, x_c^* =0.30, S_{max} =95.5, $U_p(x=0)$ =25.4.

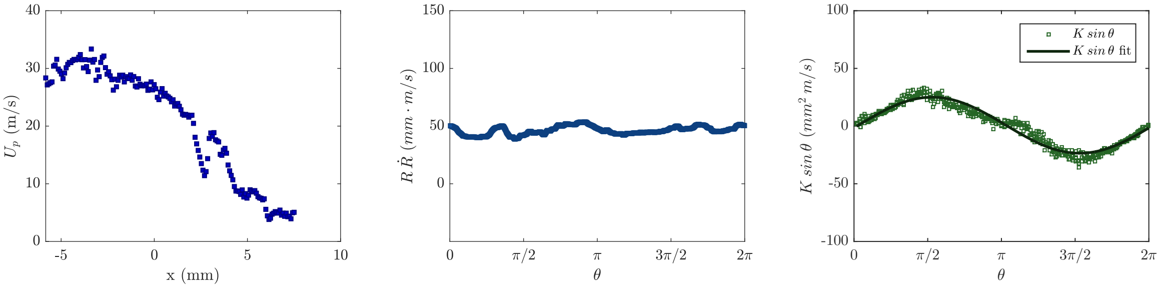

(a) Wave flow at edges.

(b) $R \cdot \dot{R}$ on interface

(c) $K\ sin\theta$ fit.

Figure G.73: Test# 874 A^* =0.59, x_c^* =0.32, S_{max} =111.2, $U_p(x=0)$ =26.3.

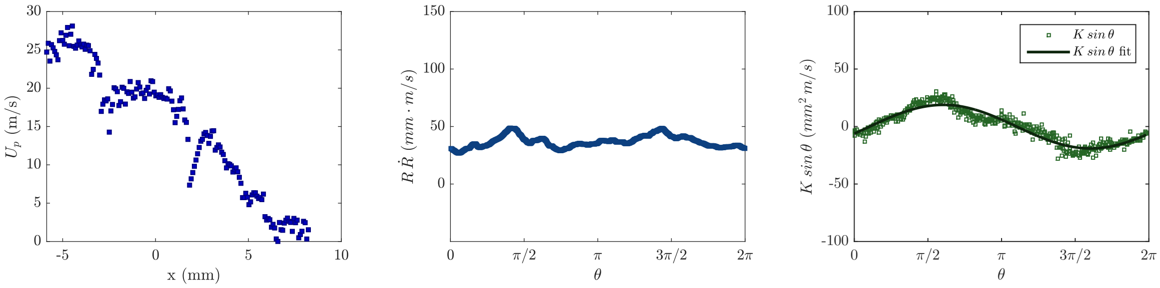

(a) Wave flow at edges.

(b) $R \cdot \dot{R}$ on interface

(c) $K\,sin\theta$ fit.

Figure G.74: Test# 735 $A^* =0.59$, $x_c^* =0.35$, $S_{max} =98.2$, $U_p(x=0) =19.3$.

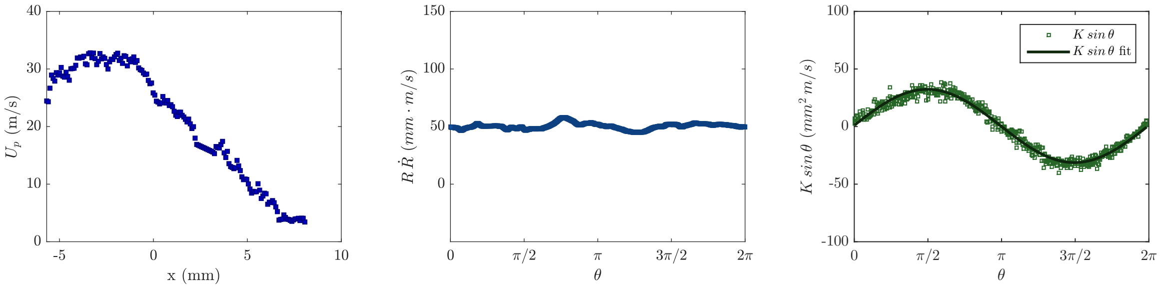

(a) Wave flow at edges.

(b) $R \cdot \dot{R}$ on interface

(c) $K\,sin\theta$ fit.

Figure G.75: Test# 913 $A^* =0.56$, $x_c^* =0.35$, $S_{max} =118.4$, $U_p(x=0) =26.5$.

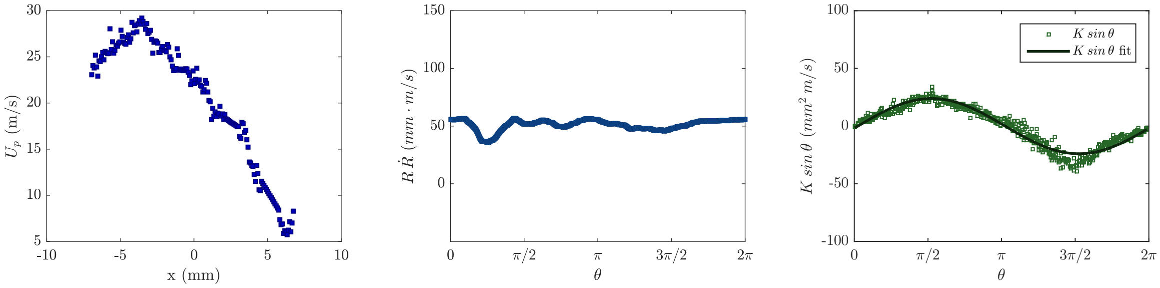

(a) Wave flow at edges.

(b) $R \cdot \dot{R}$ on interface

(c) $K\,sin\theta$ fit.

Figure G.76: Test# 780 $A^* =0.56$, $x_c^* =0.32$, $S_{max} =101.3$, $U_p(x=0) =22.6$.

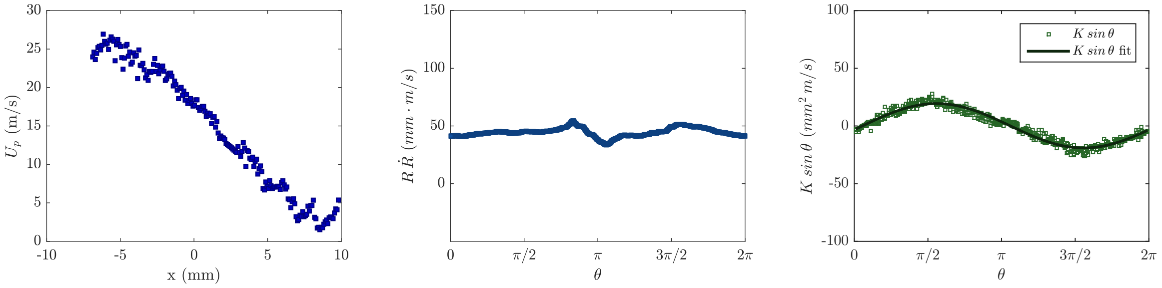

(a) Wave flow at edges.
(b) $R \cdot \dot{R}$ on interface
(c) $K\ sin\theta$ fit.

Figure G.77: Test# 709 A^* =0.54, x_c^* =0.34, S_{max} =95.6, $U_p(x = 0)$ =17.9.

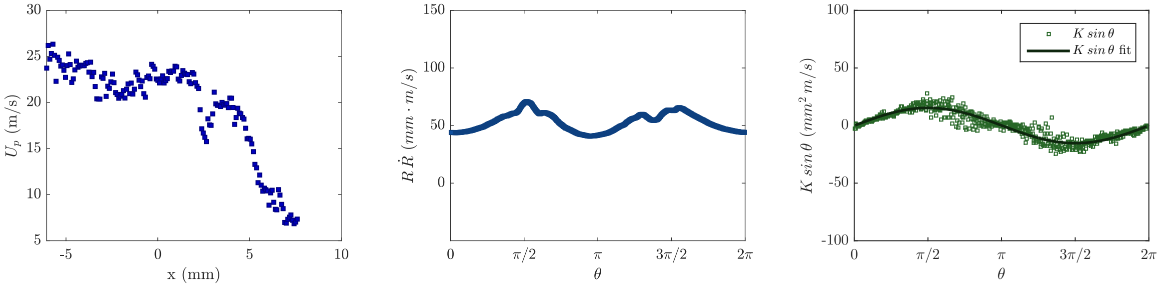

(a) Wave flow at edges.
(b) $R \cdot \dot{R}$ on interface
(c) $K\ sin\theta$ fit.

Figure G.78: Test# 763 A^* =0.21, x_c^* =0.58, S_{max} =139.8, $U_p(x = 0)$ =22.9.

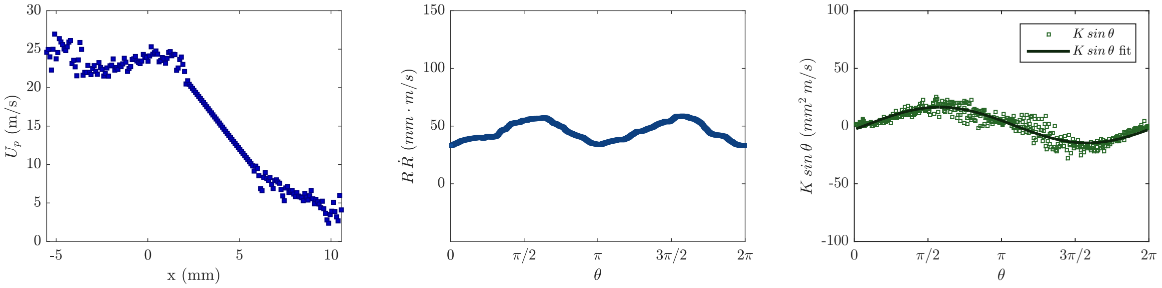

(a) Wave flow at edges.
(b) $R \cdot \dot{R}$ on interface
(c) $K\ sin\theta$ fit.

Figure G.79: Test# 876 A^* =0.18, x_c^* =0.66, S_{max} =136.6, $U_p(x = 0)$ =24.0.

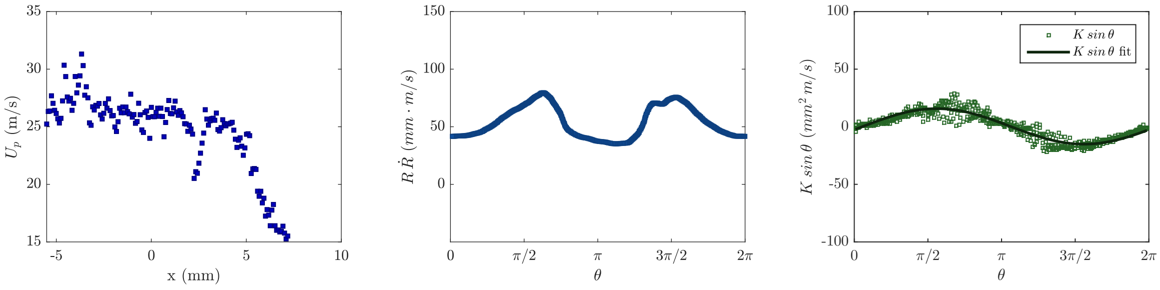

(a) Wave flow at edges.

(b) $R \cdot \dot{R}$ on interface

(c) $K\ sin\theta$ fit.

Figure G.80: Test# 905 $A^* = 0.10$, $x_c^* = 0.68$, $S_{max} = 135.6$, $U_p(x = 0) = 25.8$.

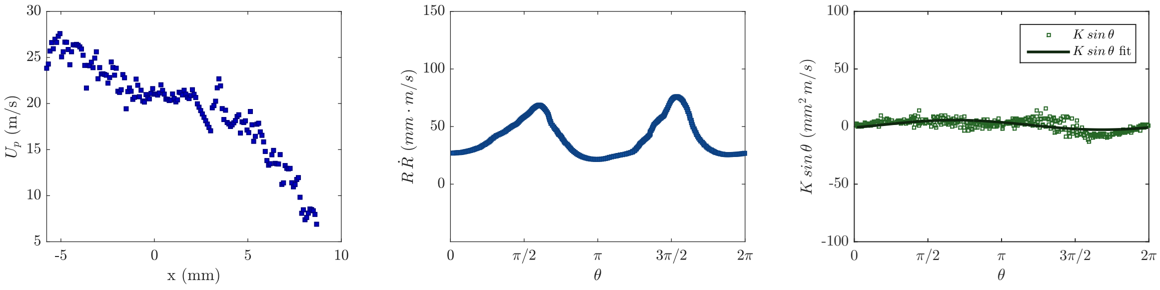

(a) Wave flow at edges.

(b) $R \cdot \dot{R}$ on interface

(c) $K\ sin\theta$ fit.

Figure G.81: Test# 907 $A^* = 0.08$, $x_c^* = 0.67$, $S_{max} = 124.8$, $U_p(x = 0) = 21.0$.

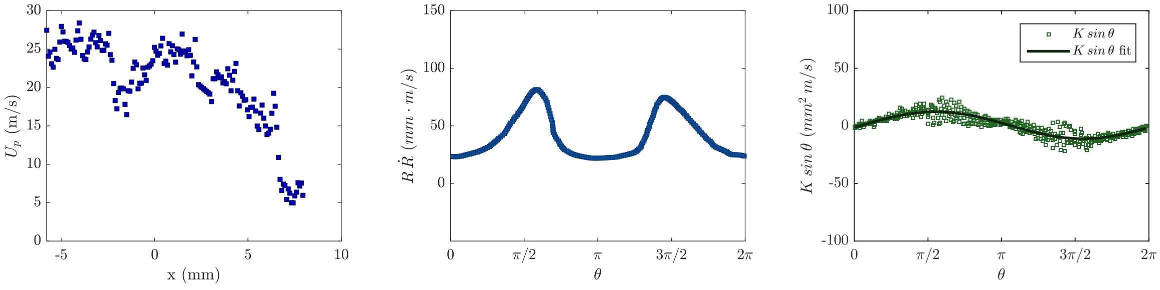

(a) Wave flow at edges.

(b) $R \cdot \dot{R}$ on interface

(c) $K\ sin\theta$ fit.

Figure G.82: Test# 915 $A^* = 0.07$, $x_c^* = 0.69$, $S_{max} = 126.7$, $U_p(x = 0) = 23.6$.

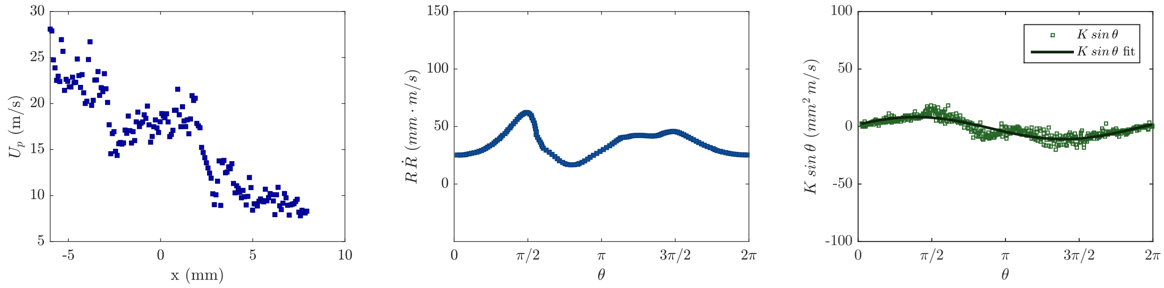

(a) Wave flow at edges. (b) $R \cdot \dot{R}$ on interface (c) $K\ sin\theta$ fit.

Figure G.83: Test# 737 A^* =0.04, x_c^* =0.82, S_{max} =100.9, $U_p(x=0)$ =17.6.

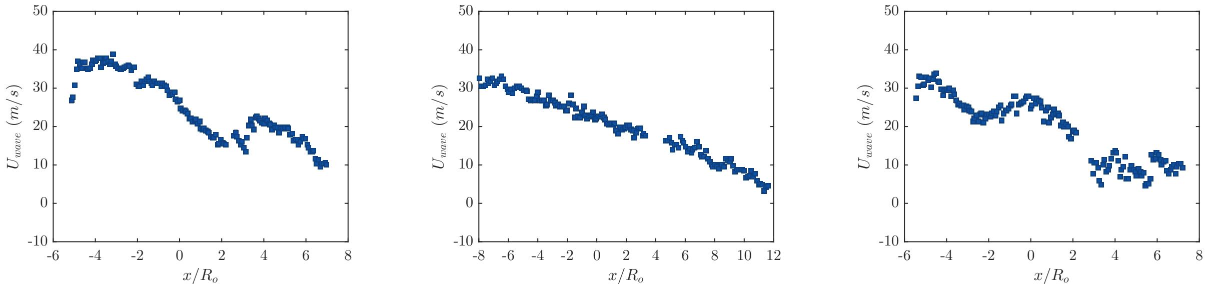

(a) Test# 914. A^* =0.01; x_c^* =0.91; S_{max} =81.0.
(b) Test# 904. A^* =0.00; x_c^* =0.87; S_{max} =74.5.
(c) Test# 736. A^* =0.00; x_c^* =0.94; S_{max} =65.3.

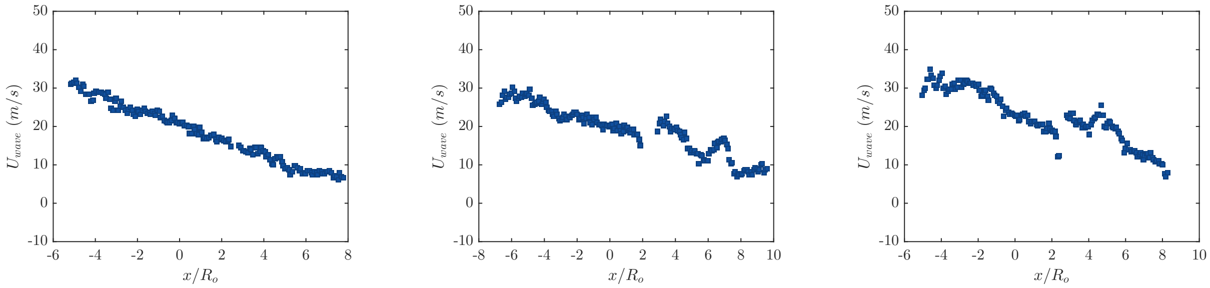

(d) Test# 908. A^* =0.00; x_c^* =0.98; S_{max} =67.5.
(e) Test# 708. A^* =0.00; x_c^* =1.22; S_{max} =41.9.
(f) Test# 906. A^* =0.00; x_c^* =1.26; S_{max} =50.7.

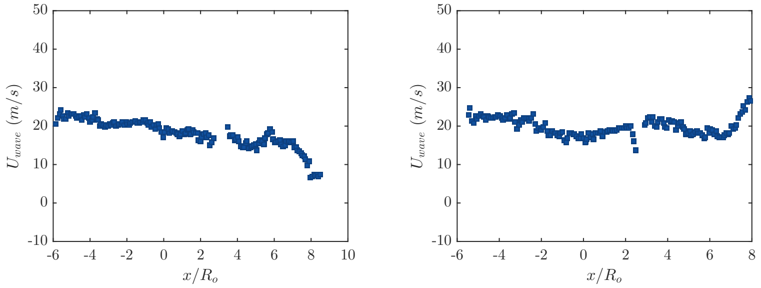

(g) Test# 902. A^* =0.00; x_c^* =1.29; S_{max} =39.6.
(h) Test# 901. A^* =0.00; x_c^* =1.29; S_{max} =42.4.

Figure G.84: Wave flow velocity distribution for tests 914–901. Void boundary could not be identified reliably(<3%), or test was after collapse, so outgoing waves prevented accurate U_p evaluation.

G.2.4 Downstream Aluminum

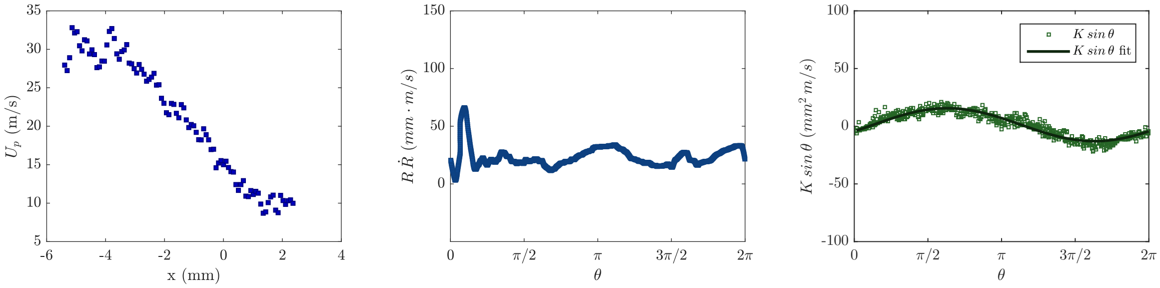

(a) Wave flow at edges.

(b) $R \cdot \dot{R}$ on interface

(c) $K\ sin\theta$ fit.

Figure G.85: Test# 882 A^* =0.89, x_c^* =0.11, S_{max} =65.0, $U_p(x=0)$ =15.1.

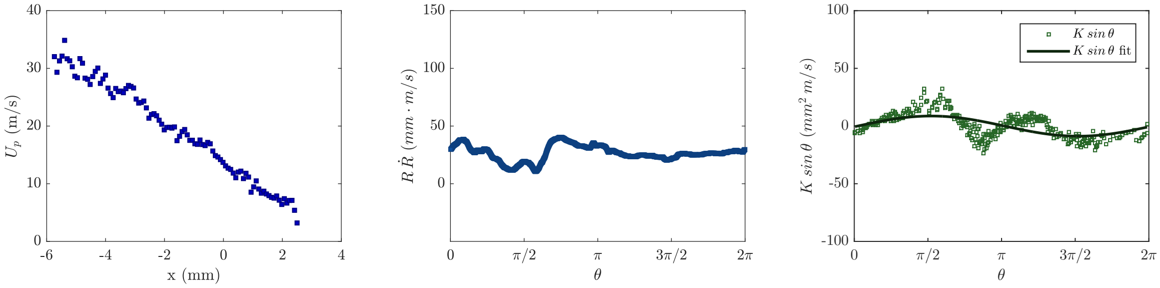

(a) Wave flow at edges.

(b) $R \cdot \dot{R}$ on interface

(c) $K\ sin\theta$ fit.

Figure G.86: Test# 877 A^* =0.81, x_c^* =0.12, S_{max} =62.3, $U_p(x=0)$ =13.9.

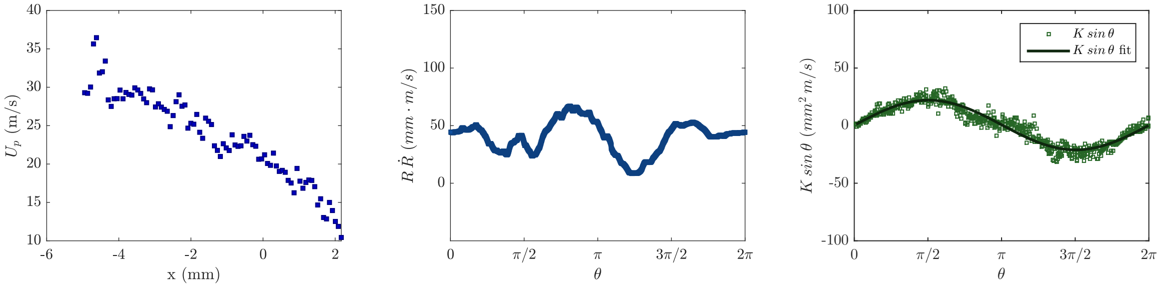

(a) Wave flow at edges.

(b) $R \cdot \dot{R}$ on interface

(c) $K\ sin\theta$ fit.

Figure G.87: Test# 879 A^* =0.70, x_c^* =0.23, S_{max} =82.5, $U_p(x=0)$ =21.3.

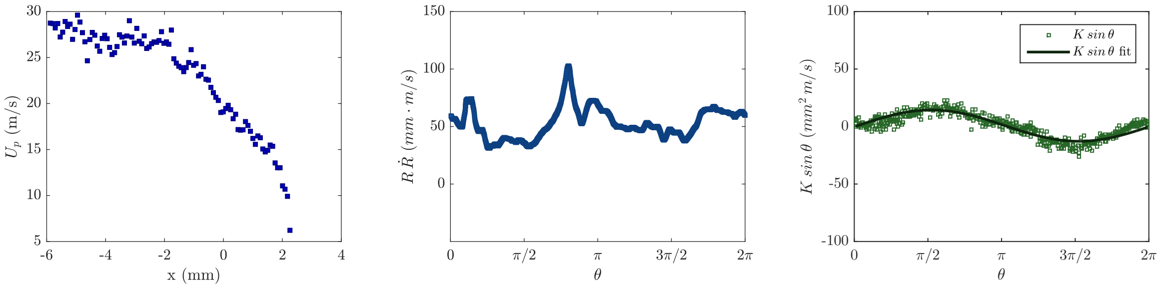

(a) Wave flow at edges. (b) $R \cdot \dot{R}$ on interface (c) $K\,sin\theta$ fit.

Figure G.88: Test# 884 $A^* = 0.60$, $x_c^* = 0.33$, $S_{max} = 104.7$, $U_p(x=0) = 19.8$.

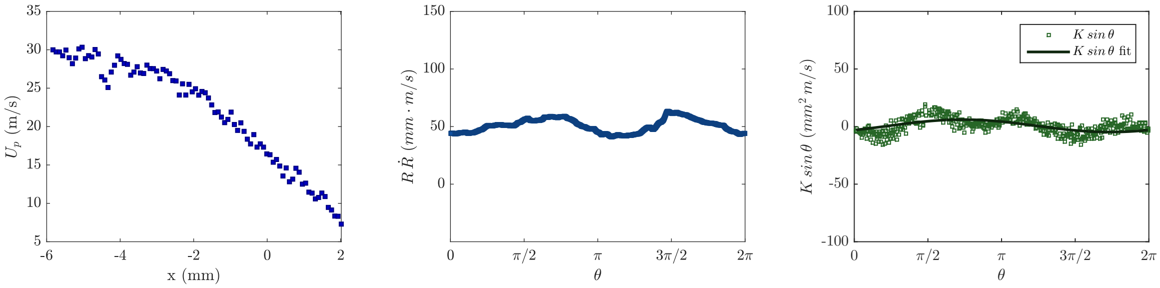

(a) Wave flow at edges. (b) $R \cdot \dot{R}$ on interface (c) $K\,sin\theta$ fit.

Figure G.89: Test# 878 $A^* = 0.57$, $x_c^* = 0.28$, $S_{max} = 126.8$, $U_p(x=0) = 16.4$.

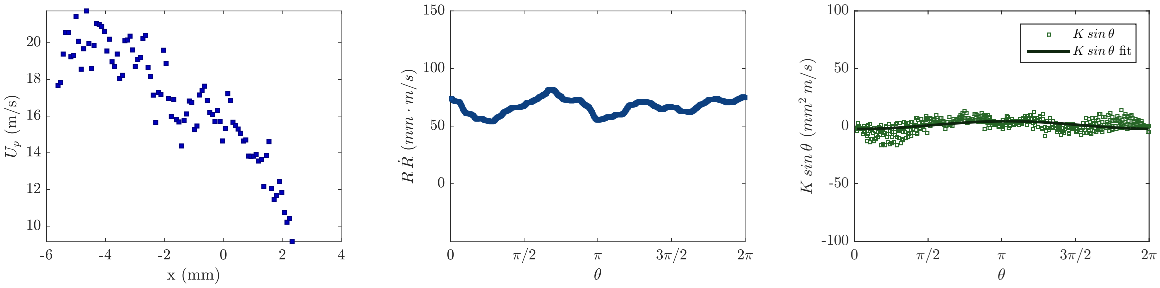

(a) Wave flow at edges. (b) $R \cdot \dot{R}$ on interface (c) $K\,sin\theta$ fit.

Figure G.90: Test# 881 $A^* = 0.21$, $x_c^* = 0.56$, $S_{max} = 131.6$, $U_p(x=0) = 16.0$.

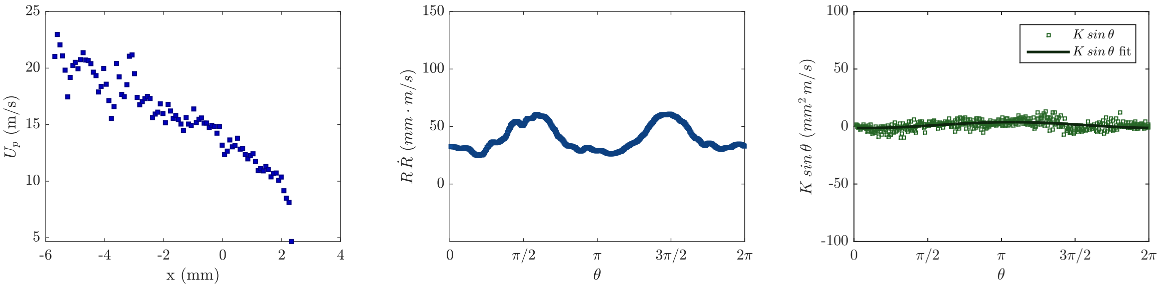

(a) Wave flow at edges.

(b) $R \cdot \dot{R}$ on interface

(c) $K\ sin\theta$ fit.

Figure G.91: Test# 880 $A^* = 0.14$, $x_c^* = 0.53$, $S_{max} = 127.4$, $U_p(x=0) = 13.9$.

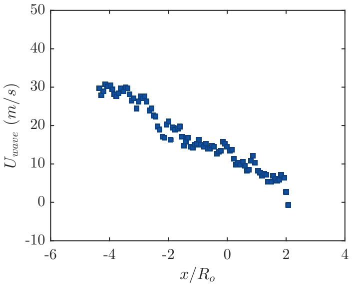

(a) Test# 883. $A^* = 0.04$; $x_c^* = 0.75$; $S_{max} = 122.3$.

Figure G.92: Wave flow velocity distribution for test 883. Void boundary could not be identified reliably(<3%), or test was after collapse, so outgoing waves prevented accurate U_p evaluation.

G.3 Upstream Boundary

G.3.1 Upstream 20:1 PDMS

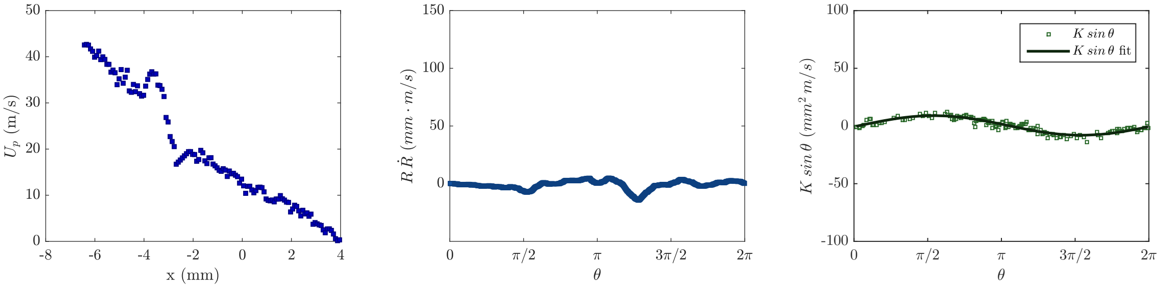

(a) Wave flow at edges.

(b) $R \cdot \dot{R}$ on interface

(c) $K\ sin\theta$ fit.

Figure G.93: Test# 816 $A^* = 1.01$, $x_c^* = 0.01$, $S_{max} = 57.1$, $U_p(x=0) = 12.8$.

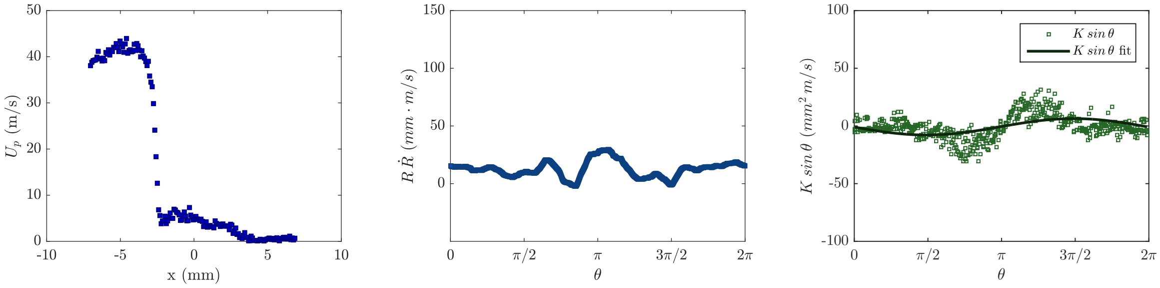

(a) Wave flow at edges. (b) $R \cdot \dot{R}$ on interface (c) $K\ sin\theta$ fit.

Figure G.94: Test# 803 $A^* = 1.01$, $x_c^* = 0.08$, $S_{max} = 60.2$, $U_p(x=0) = 4.9$.

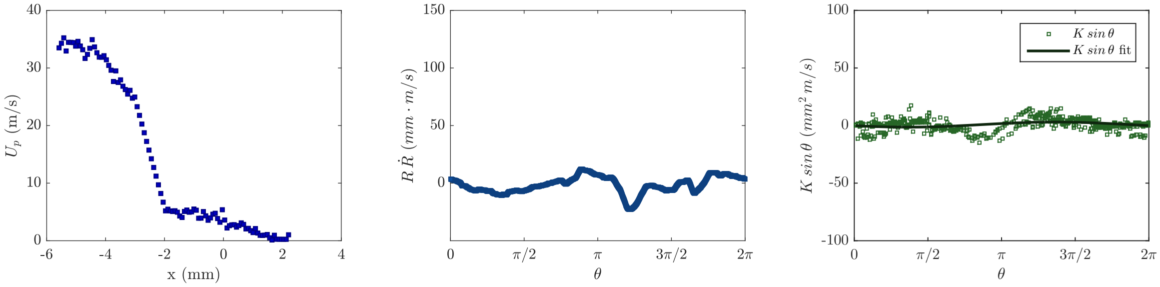

(a) Wave flow at edges. (b) $R \cdot \dot{R}$ on interface (c) $K\ sin\theta$ fit.

Figure G.95: Test# 868 $A^* = 1.00$, $x_c^* = 0.02$, $S_{max} = 55.1$, $U_p(x=0) = 3.5$.

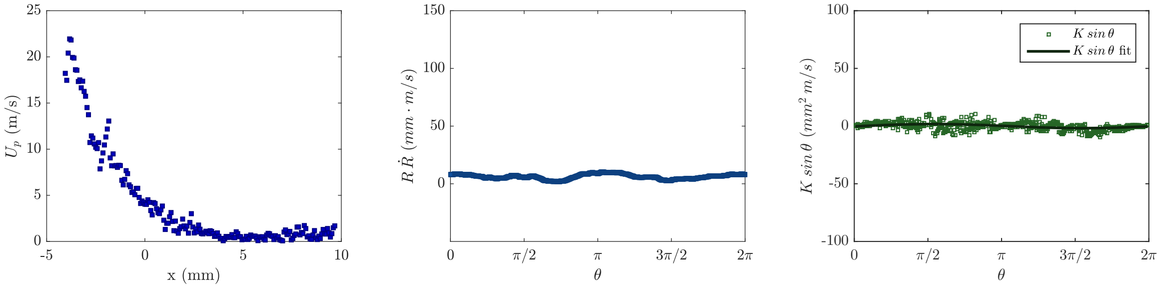

(a) Wave flow at edges. (b) $R \cdot \dot{R}$ on interface (c) $K\ sin\theta$ fit.

Figure G.96: Test# 729 $A^* = 0.99$, $x_c^* = 0.04$, $S_{max} = 32.4$, $U_p(x=0) = 4.4$.

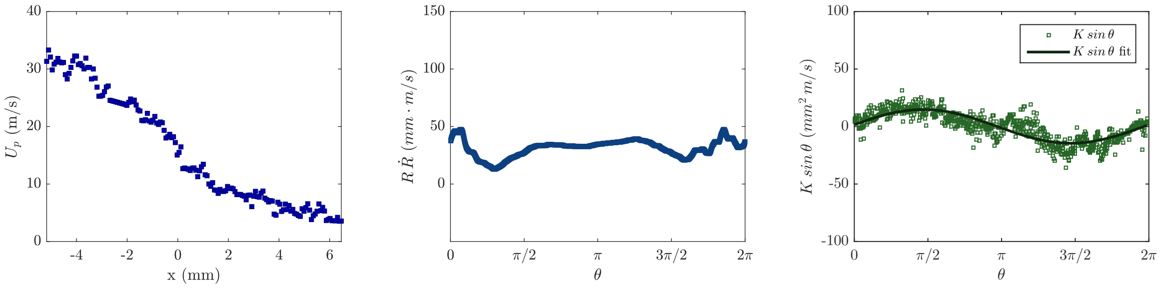

(a) Wave flow at edges.

(b) $R \cdot \dot{R}$ on interface

(c) $K\ sin\theta$ fit.

Figure G.97: Test# 804 $A^* = 0.88$, $x_c^* = 0.13$, $S_{max} = 69.1$, $U_p(x=0) = 15.8$.

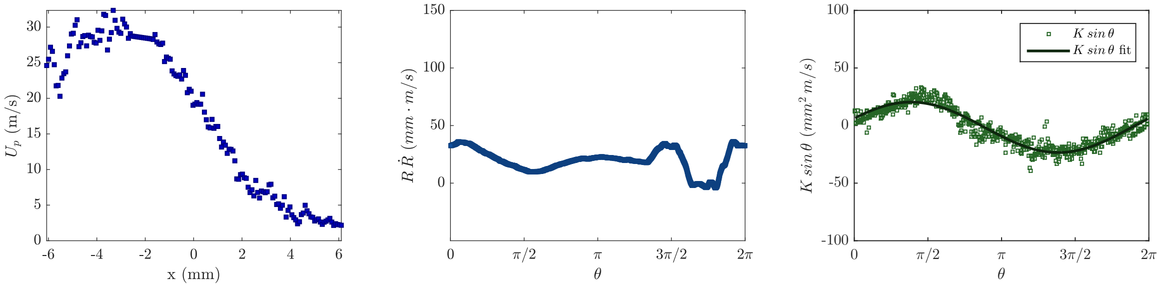

(a) Wave flow at edges.

(b) $R \cdot \dot{R}$ on interface

(c) $K\ sin\theta$ fit.

Figure G.98: Test# 767 $A^* = 0.86$, $x_c^* = 0.18$, $S_{max} = 73.8$, $U_p(x=0) = 20.5$.

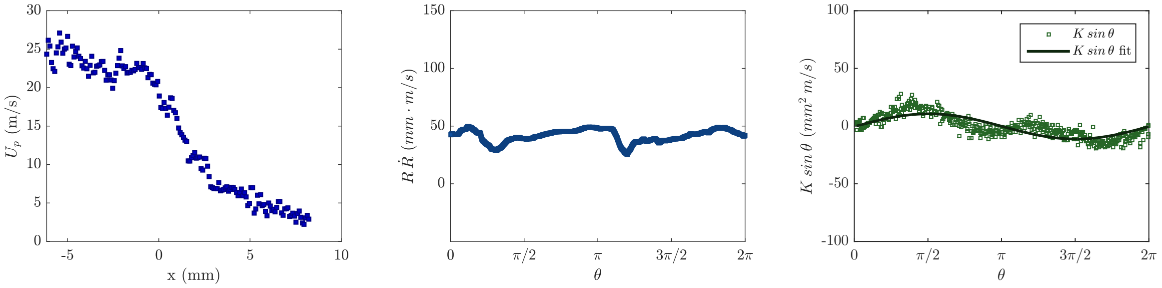

(a) Wave flow at edges.

(b) $R \cdot \dot{R}$ on interface

(c) $K\ sin\theta$ fit.

Figure G.99: Test# 858 $A^* = 0.73$, $x_c^* = 0.23$, $S_{max} = 82.4$, $U_p(x=0) = 19.2$.

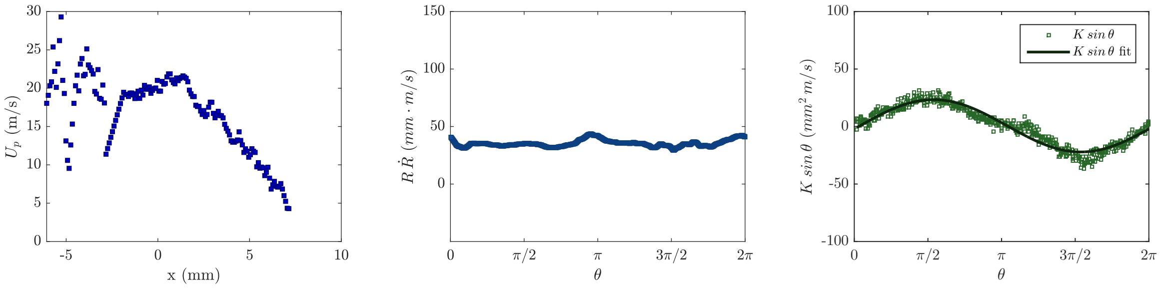

(a) Wave flow at edges.

(b) $R \cdot \dot{R}$ on interface

(c) $K\ sin\theta$ fit.

Figure G.100: Test# 793 $A^* =0.63$, $x_c^* =0.32$, $S_{max} =88.2$, $U_p(x=0) =20.3$.

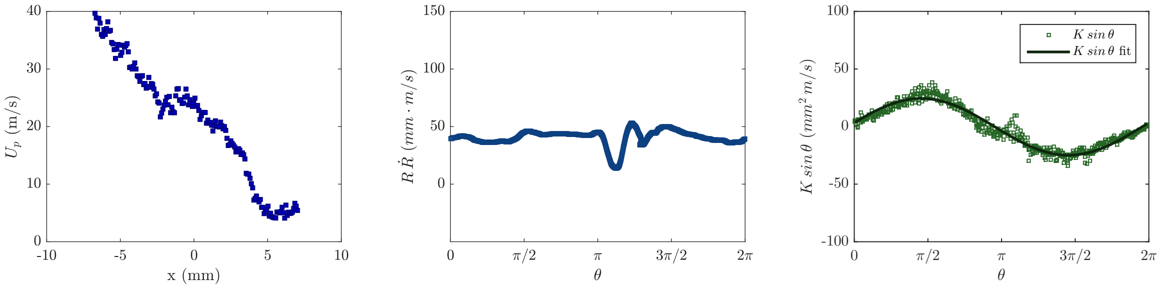

(a) Wave flow at edges.

(b) $R \cdot \dot{R}$ on interface

(c) $K\ sin\theta$ fit.

Figure G.101: Test# 805 $A^* =0.58$, $x_c^* =0.29$, $S_{max} =87.1$, $U_p(x=0) =23.8$.

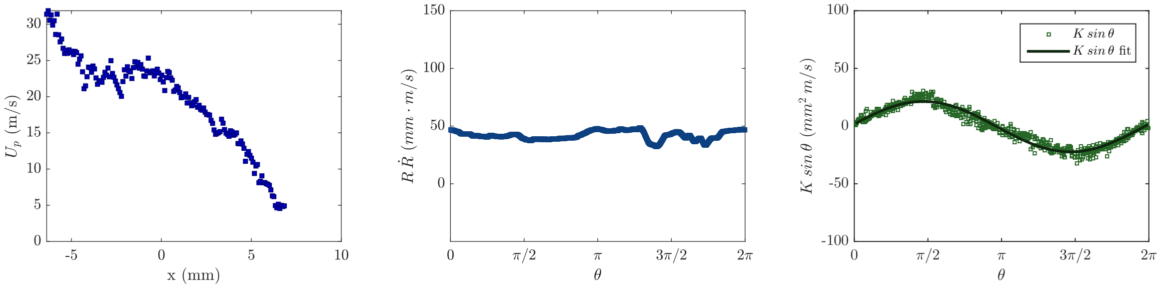

(a) Wave flow at edges.

(b) $R \cdot \dot{R}$ on interface

(c) $K\ sin\theta$ fit.

Figure G.102: Test# 815 $A^* =0.56$, $x_c^* =0.38$, $S_{max} =87.0$, $U_p(x=0) =22.9$.

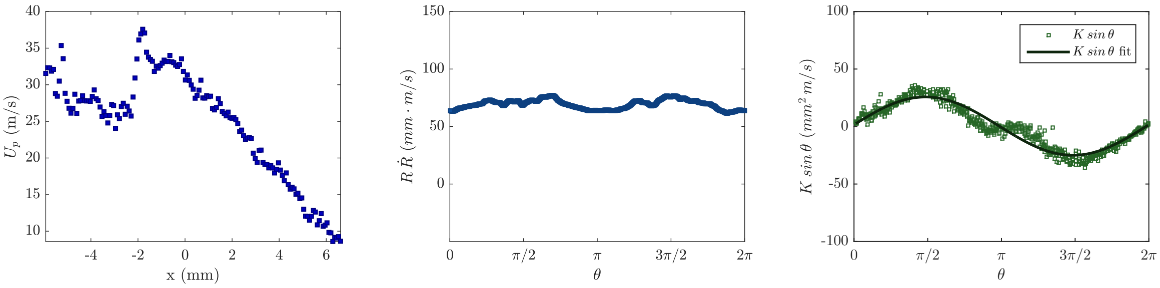

(a) Wave flow at edges.

(b) $R \cdot \dot{R}$ on interface

(c) $K\ sin\theta$ fit.

Figure G.103: Test# 811 $A^* = 0.54$, $x_c^* = 0.41$, $S_{max} = 124.5$, $U_p(x = 0) = 31.2$.

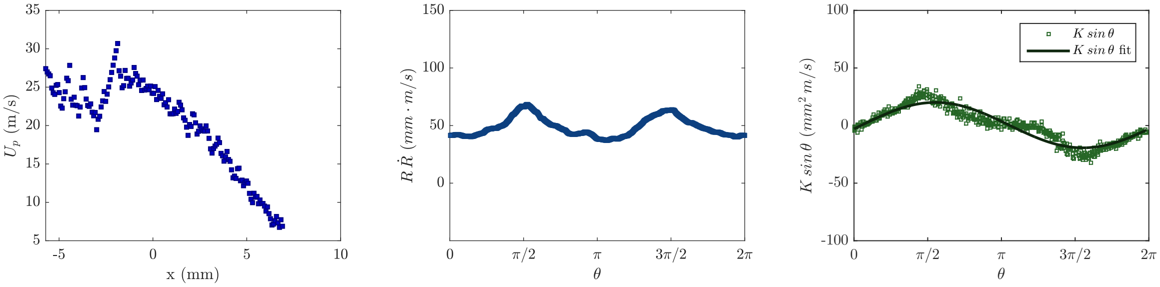

(a) Wave flow at edges.

(b) $R \cdot \dot{R}$ on interface

(c) $K\ sin\theta$ fit.

Figure G.104: Test# 810 $A^* = 0.49$, $x_c^* = 0.33$, $S_{max} = 95.4$, $U_p(x = 0) = 24.4$.

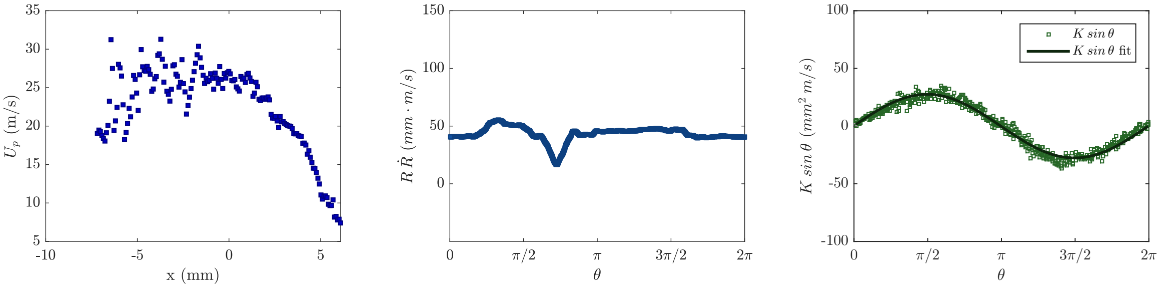

(a) Wave flow at edges.

(b) $R \cdot \dot{R}$ on interface

(c) $K\ sin\theta$ fit.

Figure G.105: Test# 755 $A^* = 0.46$, $x_c^* = 0.39$, $S_{max} = 103.6$, $U_p(x = 0) = 26.0$.

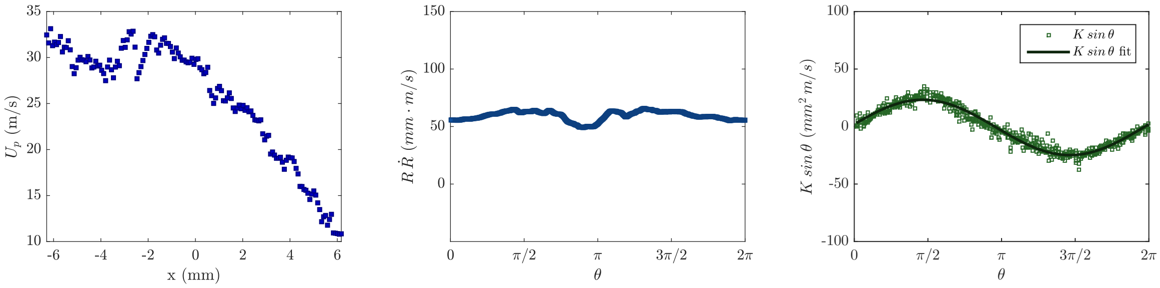

(a) Wave flow at edges.

(b) $R \cdot \dot{R}$ on interface

(c) $K\ sin\theta$ fit.

Figure G.106: Test# 814 A^* =0.45, x_c^* =0.42, S_{max} =120.2, $U_p(x=0)$ =29.1.

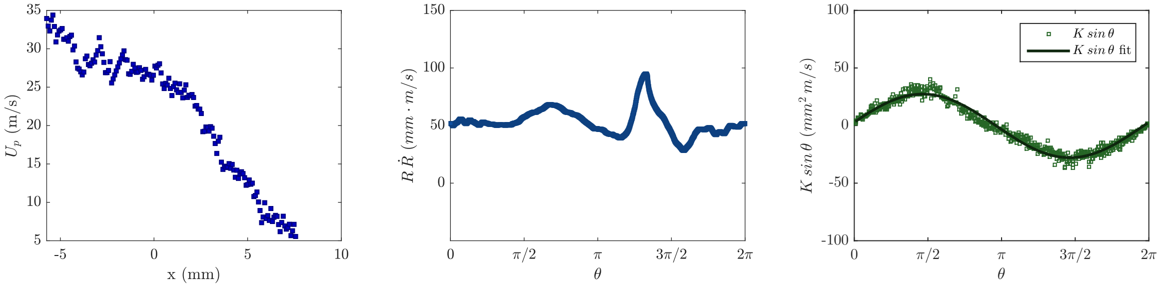

(a) Wave flow at edges.

(b) $R \cdot \dot{R}$ on interface

(c) $K\ sin\theta$ fit.

Figure G.107: Test# 859 A^* =0.45, x_c^* =0.37, S_{max} =92.3, $U_p(x=0)$ =26.7.

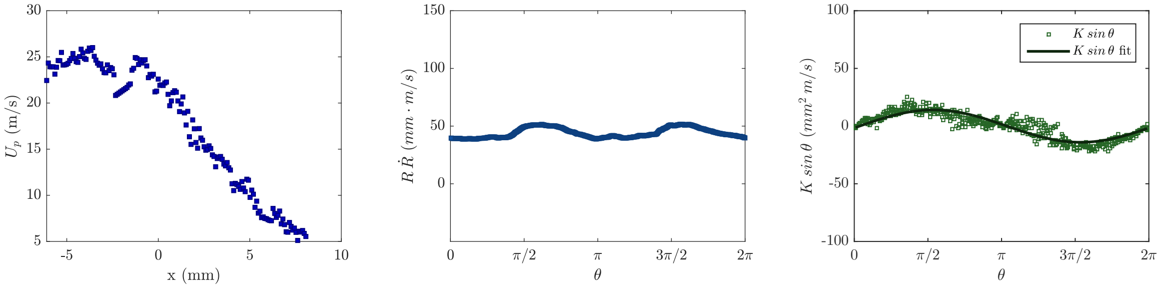

(a) Wave flow at edges.

(b) $R \cdot \dot{R}$ on interface

(c) $K\ sin\theta$ fit.

Figure G.108: Test# 860 A^* =0.42, x_c^* =0.41, S_{max} =95.2, $U_p(x=0)$ =22.1.

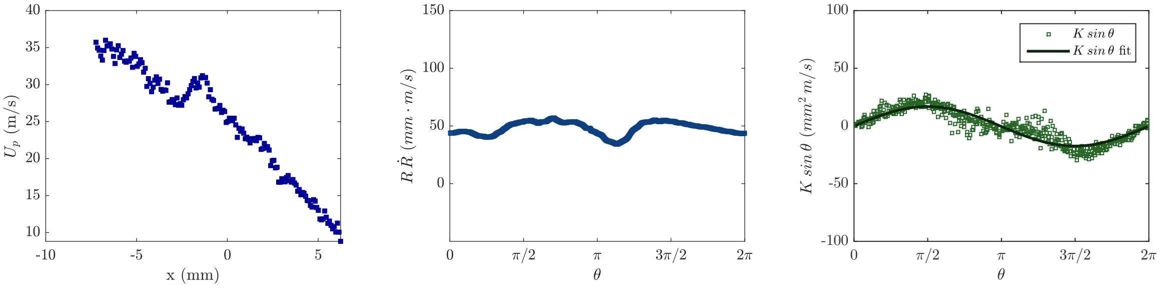

(a) Wave flow at edges. (b) $R \cdot \dot{R}$ on interface (c) $K\ sin\theta$ fit.

Figure G.109: Test# 794 $A^* = 0.40$, $x_c^* = 0.42$, $S_{max} = 116.8$, $U_p(x = 0) = 25.5$.

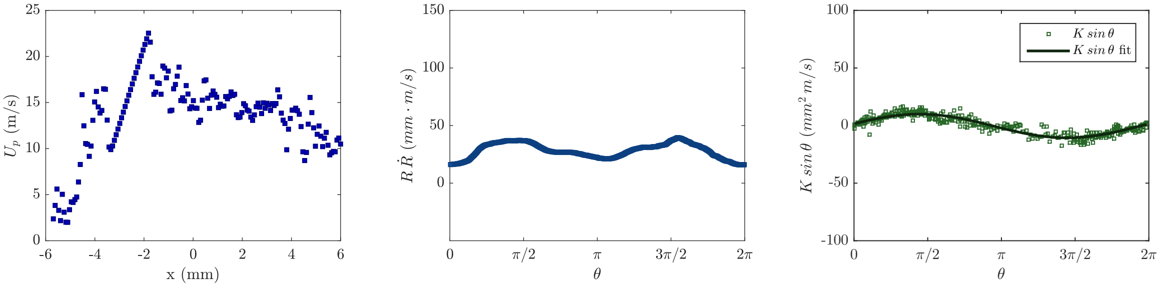

(a) Wave flow at edges. (b) $R \cdot \dot{R}$ on interface (c) $K\ sin\theta$ fit.

Figure G.110: Test# 744 $A^* = 0.39$, $x_c^* = 0.34$, $S_{max} = 72.9$, $U_p(x = 0) = 15.2$.

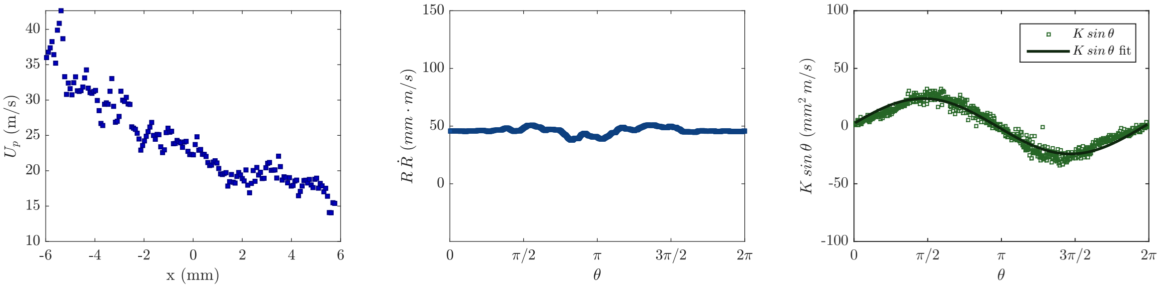

(a) Wave flow at edges. (b) $R \cdot \dot{R}$ on interface (c) $K\ sin\theta$ fit.

Figure G.111: Test# 758 $A^* = 0.38$, $x_c^* = 0.52$, $S_{max} = 125.2$, $U_p(x = 0) = 23.1$.

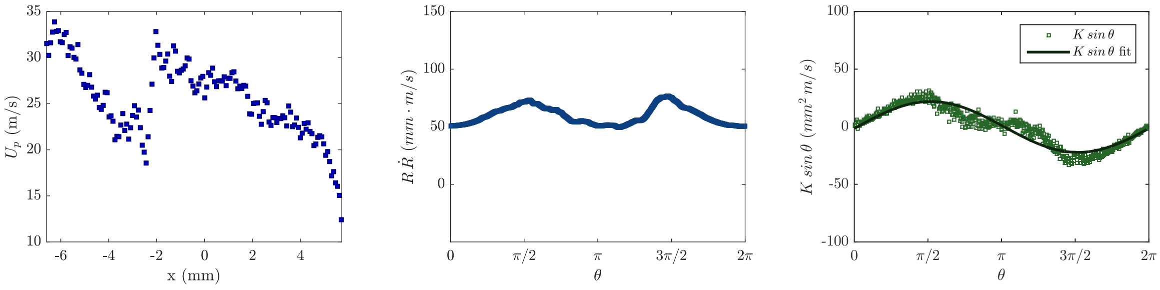

(a) Wave flow at edges.

(b) $R \cdot \dot{R}$ on interface

(c) $K\ sin\theta$ fit.

Figure G.112: Test# 807 A^* =0.37, x_c^* =0.44, S_{max} =160.5, $U_p(x=0)$ =27.3.

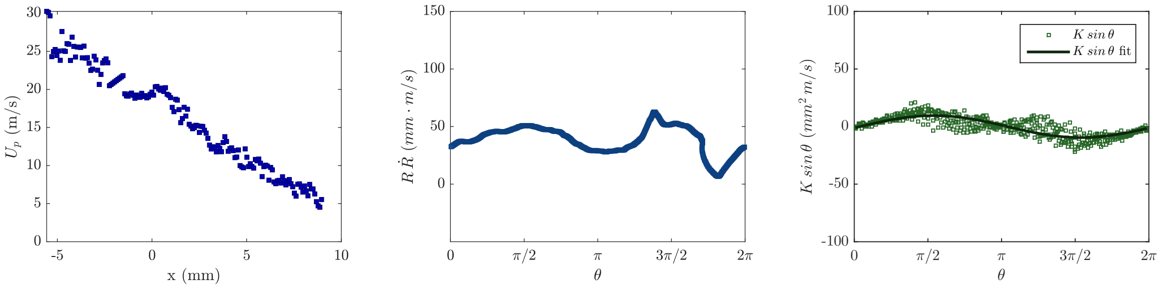

(a) Wave flow at edges.

(b) $R \cdot \dot{R}$ on interface

(c) $K\ sin\theta$ fit.

Figure G.113: Test# 866 A^* =0.20, x_c^* =0.54, S_{max} =84.4, $U_p(x=0)$ =19.6.

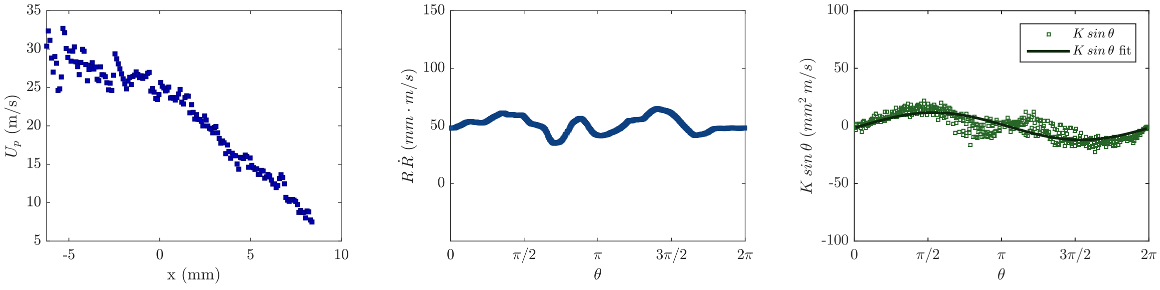

(a) Wave flow at edges.

(b) $R \cdot \dot{R}$ on interface

(c) $K\ sin\theta$ fit.

Figure G.114: Test# 867 A^* =0.19, x_c^* =0.60, S_{max} =129.7, $U_p(x=0)$ =24.8.

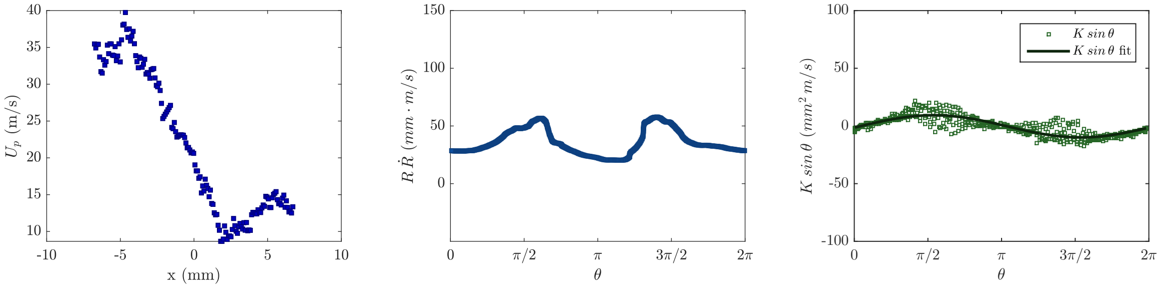

(a) Wave flow at edges. (b) $R \cdot \dot{R}$ on interface (c) $K\ sin\theta$ fit.

Figure G.115: Test# 792 A^* =0.16, x_c^* =0.64, S_{max} =95.3, $U_p(x = 0)$ =19.5.

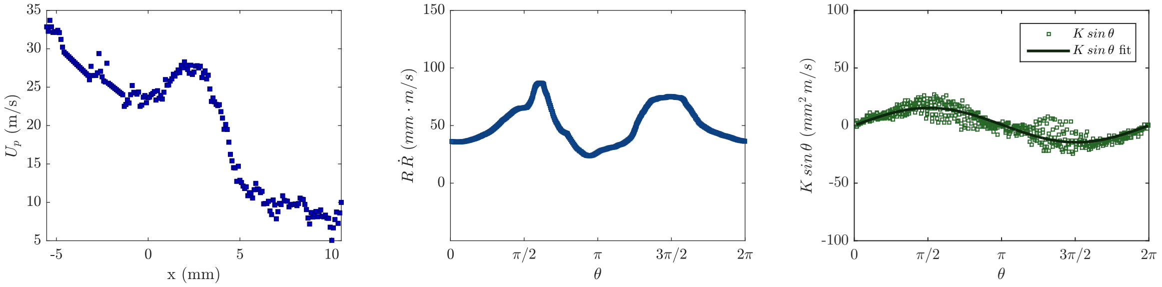

(a) Wave flow at edges. (b) $R \cdot \dot{R}$ on interface (c) $K\ sin\theta$ fit.

Figure G.116: Test# 730 A^* =0.12, x_c^* =0.67, S_{max} =140.7, $U_p(x = 0)$ =23.7.

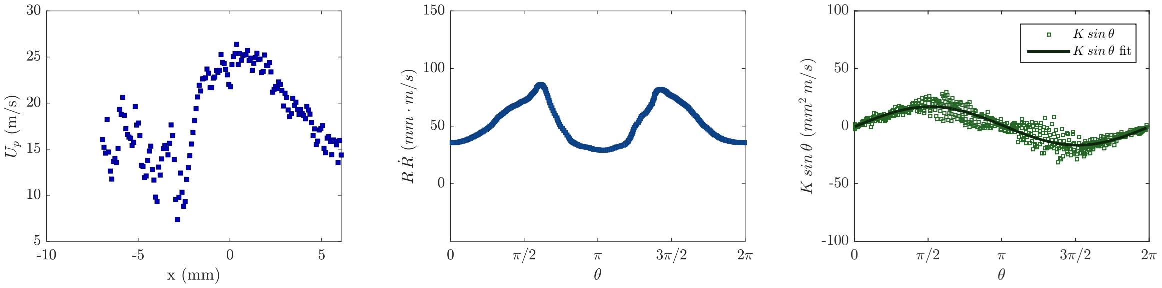

(a) Wave flow at edges. (b) $R \cdot \dot{R}$ on interface (c) $K\ sin\theta$ fit.

Figure G.117: Test# 766 A^* =0.08, x_c^* =0.74, S_{max} =140.8, $U_p(x = 0)$ =24.2.

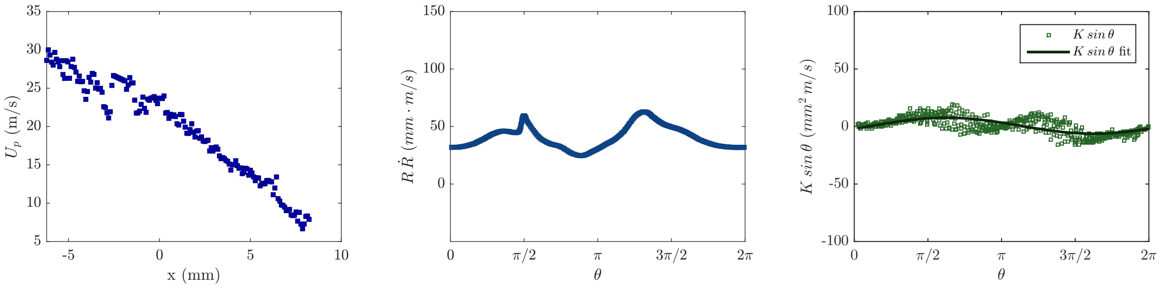

(a) Wave flow at edges.

(b) $R \cdot \dot{R}$ on interface

(c) $K\ sin\theta$ fit.

Figure G.118: Test# 865 $A^* = 0.06$, $x_c^* = 0.71$, $S_{max} = 113.7$, $U_p(x = 0) = 23.1$.

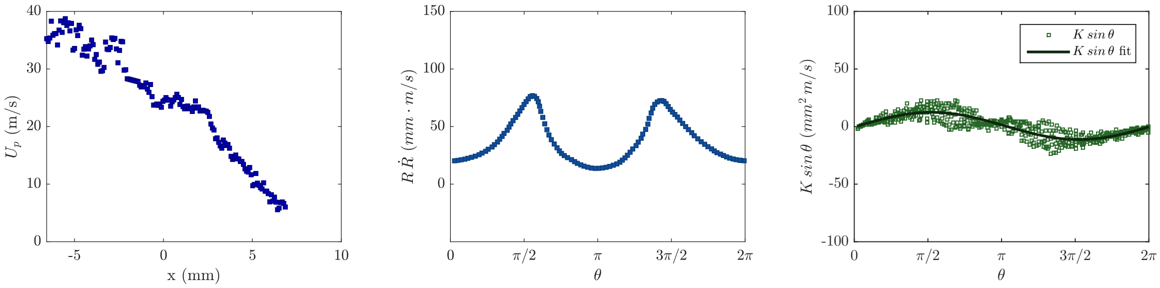

(a) Wave flow at edges.

(b) $R \cdot \dot{R}$ on interface

(c) $K\ sin\theta$ fit.

Figure G.119: Test# 759 $A^* = 0.03$, $x_c^* = 0.83$, $S_{max} = 113.5$, $U_p(x = 0) = 24.2$.

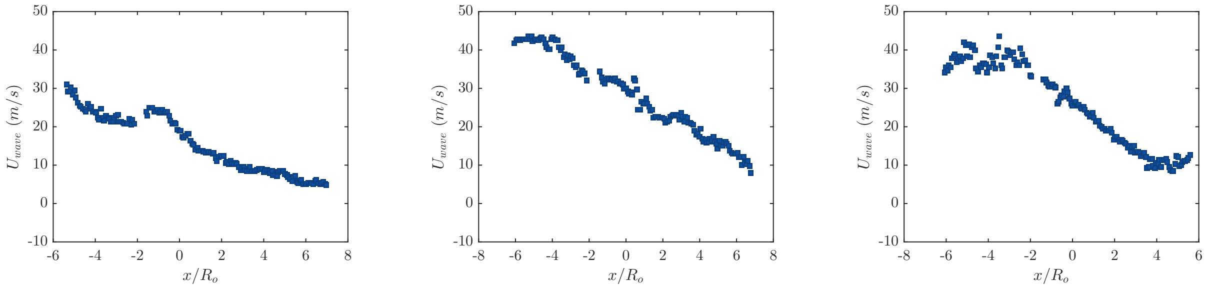

(a) Test# 808. A^* =0.00; x_c^* =0.57; S_{max} =55.4.

(b) Test# 806. A^* =0.00; x_c^* =0.73; S_{max} =112.8.

(c) Test# 754. A^* =0.00; x_c^* =0.93; S_{max} =78.8.

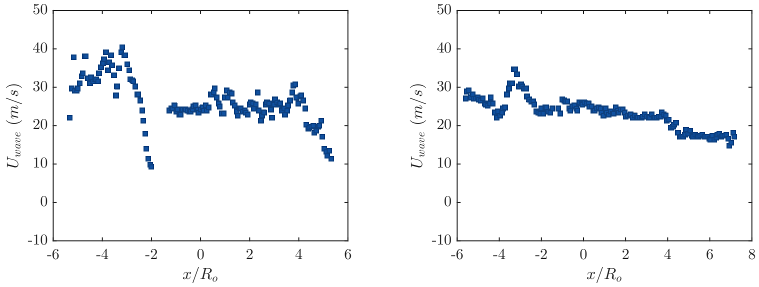

(d) Test# 757. A^* =0.00; x_c^* =1.17; S_{max} =75.0.

(e) Test# 812. A^* =0.00; x_c^* =1.27; S_{max} =51.6.

Figure G.120: Wave flow velocity distribution for tests 808–812. Void boundary could not be identified reliably(<3%), or test was after collapse, so outgoing waves prevented accurate U_p evaluation.

G.3.2 Upstream 30:1 PDMS

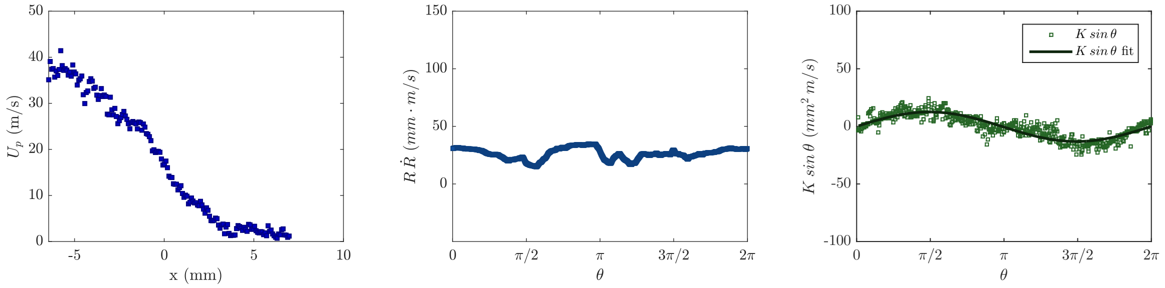

(a) Wave flow at edges.

(b) $R \cdot \dot{R}$ on interface

(c) $K\ sin\theta$ fit.

Figure G.121: Test# 848 A^* =0.96, x_c^* =0.04, S_{max} =70.5, $U_p(x = 0)$ =16.6.

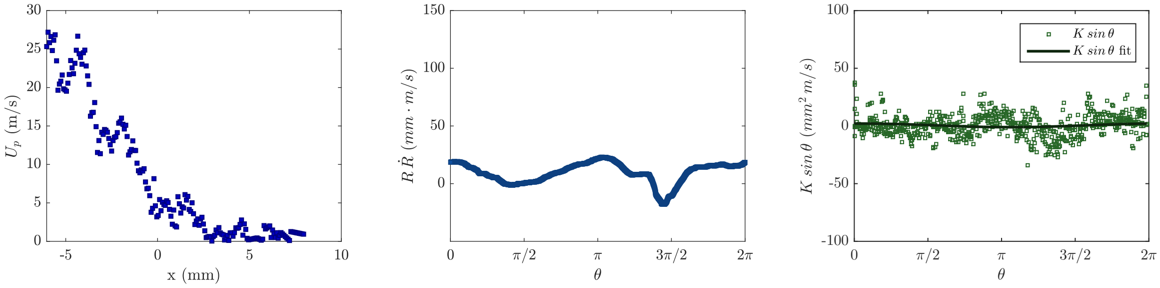

(a) Wave flow at edges. (b) $R \cdot \dot{R}$ on interface (c) $K\ sin\theta$ fit.

Figure G.122: Test# 724 $A^* = 0.96$, $x_c^* = 0.04$, $S_{max} = 49.5$, $U_p(x = 0) = 5.0$.

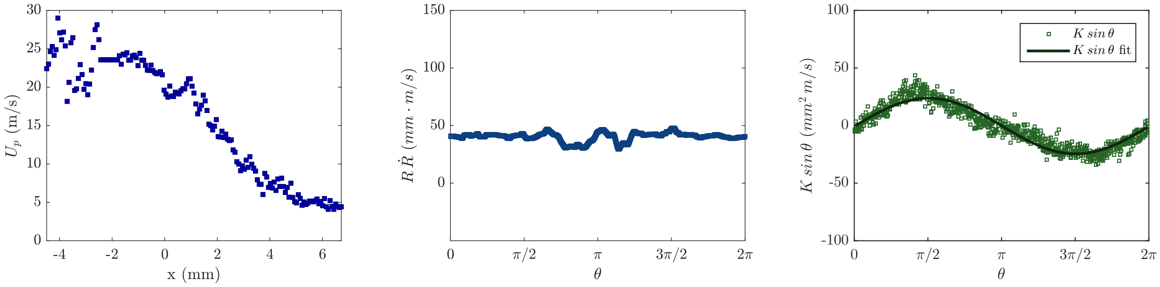

(a) Wave flow at edges. (b) $R \cdot \dot{R}$ on interface (c) $K\ sin\theta$ fit.

Figure G.123: Test# 738 $A^* = 0.78$, $x_c^* = 0.18$, $S_{max} = 84.8$, $U_p(x = 0) = 20.5$.

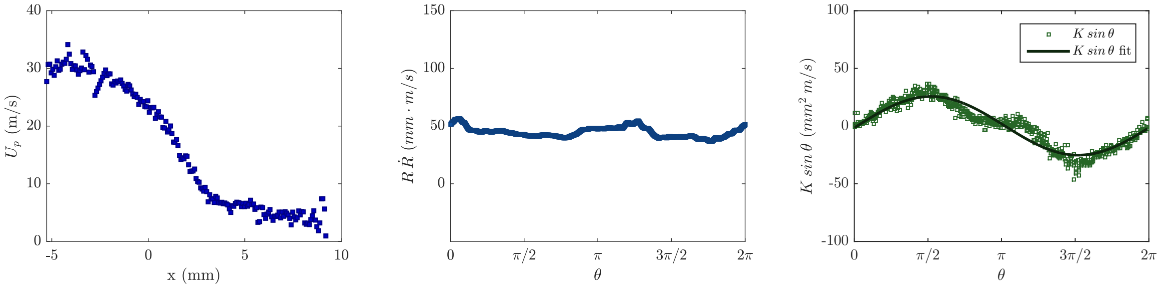

(a) Wave flow at edges. (b) $R \cdot \dot{R}$ on interface (c) $K\ sin\theta$ fit.

Figure G.124: Test# 723 $A^* = 0.77$, $x_c^* = 0.18$, $S_{max} = 84.2$, $U_p(x = 0) = 23.4$.

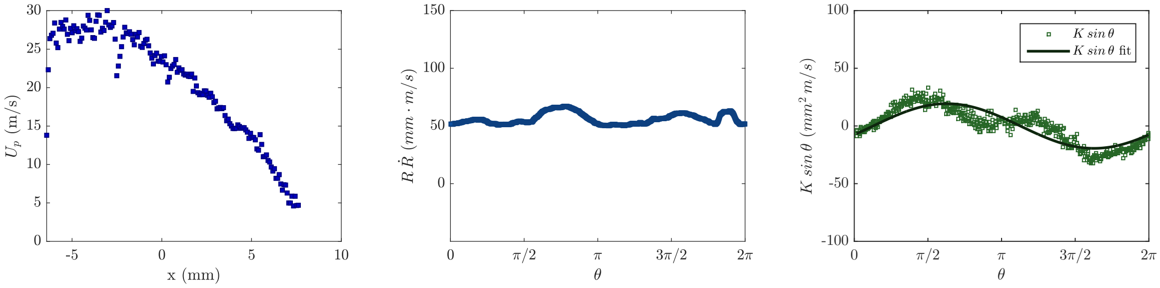

(a) Wave flow at edges. (b) $R \cdot \dot{R}$ on interface (c) $K\,sin\theta$ fit.

Figure G.125: Test# 847 A^* =0.54, x_c^* =0.36, S_{max} =112.2, $U_p(x=0)$ =23.3.

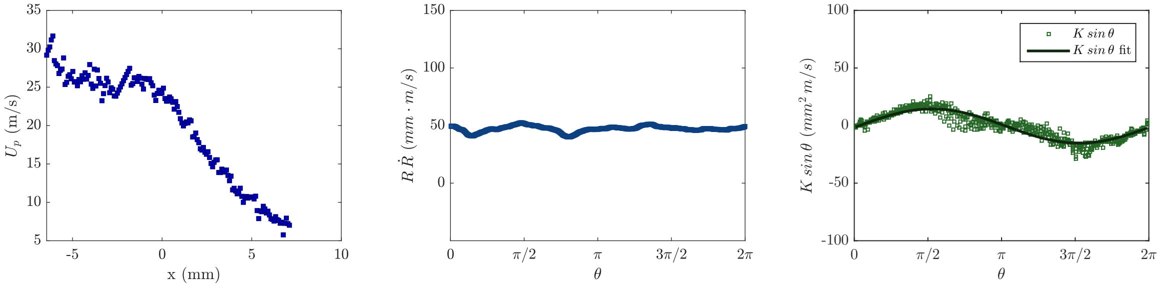

(a) Wave flow at edges. (b) $R \cdot \dot{R}$ on interface (c) $K\,sin\theta$ fit.

Figure G.126: Test# 798 A^* =0.40, x_c^* =0.48, S_{max} =97.7, $U_p(x=0)$ =24.0.

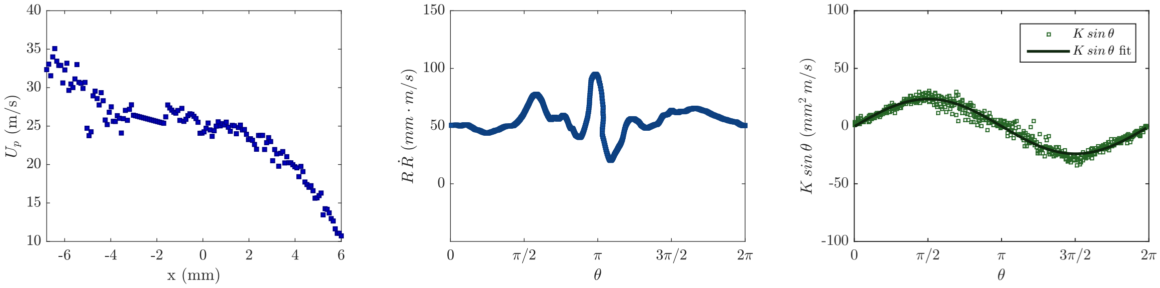

(a) Wave flow at edges. (b) $R \cdot \dot{R}$ on interface (c) $K\,sin\theta$ fit.

Figure G.127: Test# 796 A^* =0.32, x_c^* =0.52, S_{max} =131.5, $U_p(x=0)$ =25.2.

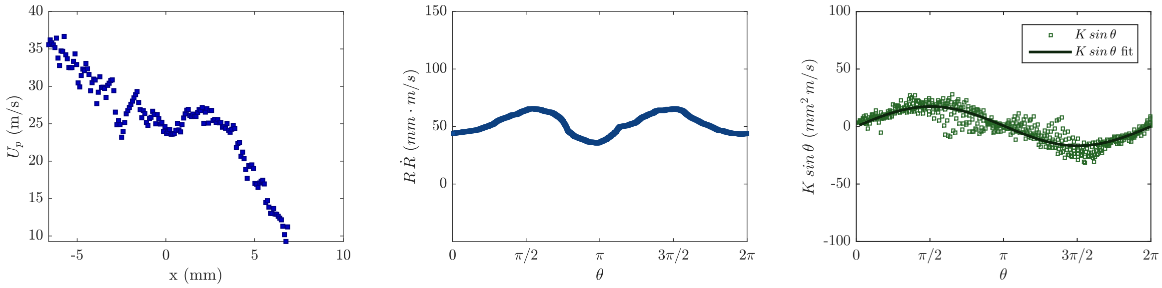

(a) Wave flow at edges. (b) $R \cdot \dot{R}$ on interface (c) $K\ sin\theta$ fit.

Figure G.128: Test# 790 A^* =0.20, x_c^* =0.63, S_{max} =115.7, $U_p(x = 0)$ =24.5.

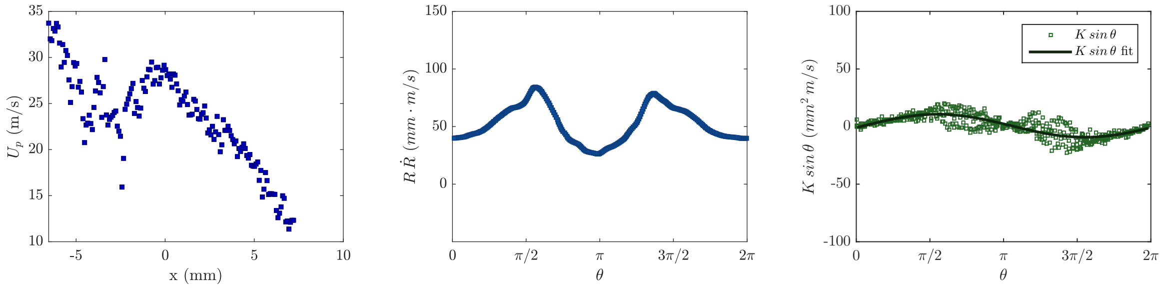

(a) Wave flow at edges. (b) $R \cdot \dot{R}$ on interface (c) $K\ sin\theta$ fit.

Figure G.129: Test# 797 A^* =0.09, x_c^* =0.66, S_{max} =140.7, $U_p(x = 0)$ =28.0.

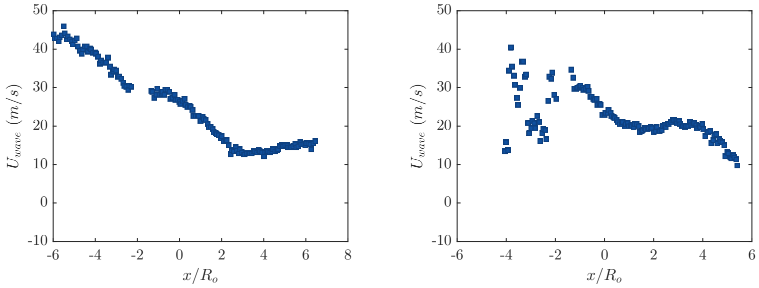

(a) Test# 789. A^* =0.02; x_c^* =0.80; S_{max} =82.8. (b) Test# 739. A^* =0.00; x_c^* =0.88; S_{max} =82.0.

Figure G.130: Wave flow velocity distribution for tests 789–739. Void boundary could not be identified reliably(<3%), or test was after collapse, so outgoing waves prevented accurate U_p evaluation.

G.3.3 Upstream 40:1 PDMS

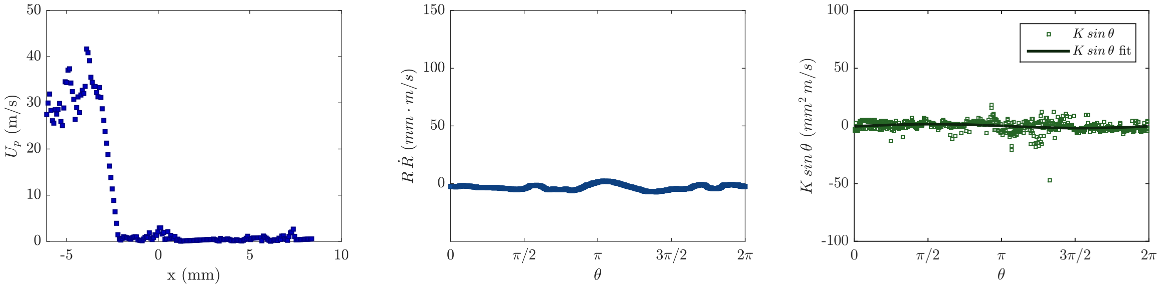

(a) Wave flow at edges. (b) $R \cdot \dot{R}$ on interface (c) $K\ sin\theta$ fit.

Figure G.131: Test# 719 $A^* =1.01$, $x_c^* =0.01$, $S_{max} =87.8$, $U_p(x=0) =1.4$.

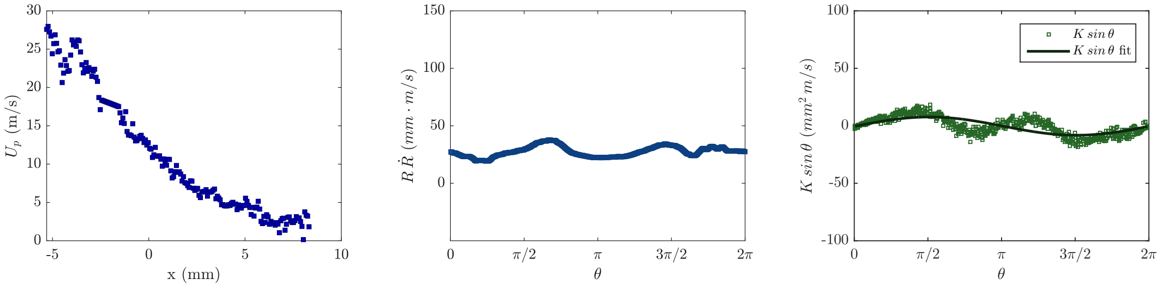

(a) Wave flow at edges. (b) $R \cdot \dot{R}$ on interface (c) $K\ sin\theta$ fit.

Figure G.132: Test# 720 $A^* =0.78$, $x_c^* =0.19$, $S_{max} =51.2$, $U_p(x=0) =12.4$.

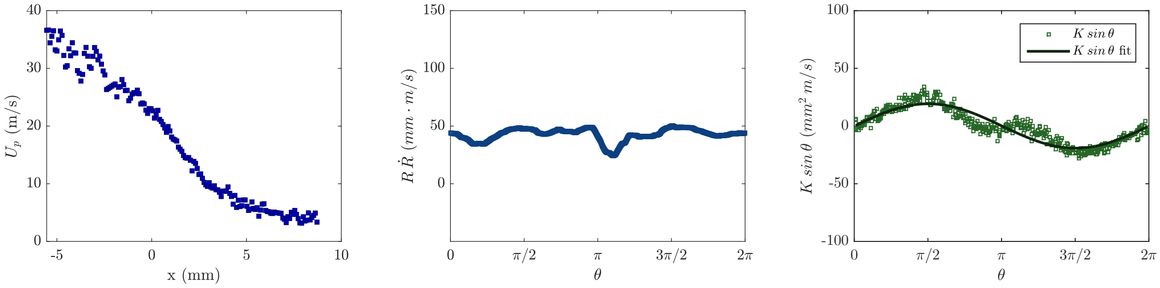

(a) Wave flow at edges. (b) $R \cdot \dot{R}$ on interface (c) $K\ sin\theta$ fit.

Figure G.133: Test# 870 $A^* =0.66$, $x_c^* =0.22$, $S_{max} =85.3$, $U_p(x=0) =22.6$.

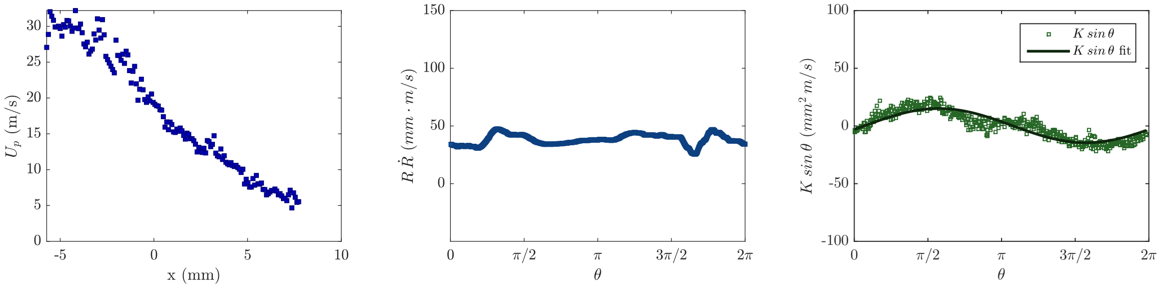

(a) Wave flow at edges. (b) $R \cdot \dot{R}$ on interface (c) $K\ sin\theta$ fit.

Figure G.134: Test# 869 $A^* = 0.65$, $x_c^* = 0.32$, $S_{max} = 82.1$, $U_p(x=0) = 19.3$.

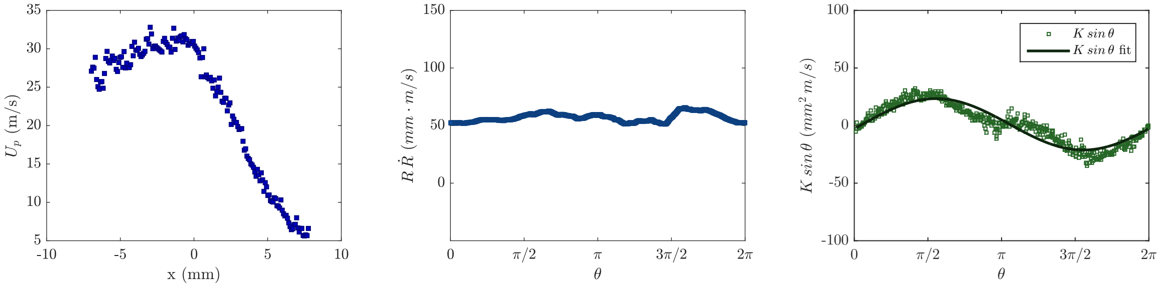

(a) Wave flow at edges. (b) $R \cdot \dot{R}$ on interface (c) $K\ sin\theta$ fit.

Figure G.135: Test# 846 $A^* = 0.60$, $x_c^* = 0.29$, $S_{max} = 111.2$, $U_p(x=0) = 30.1$.

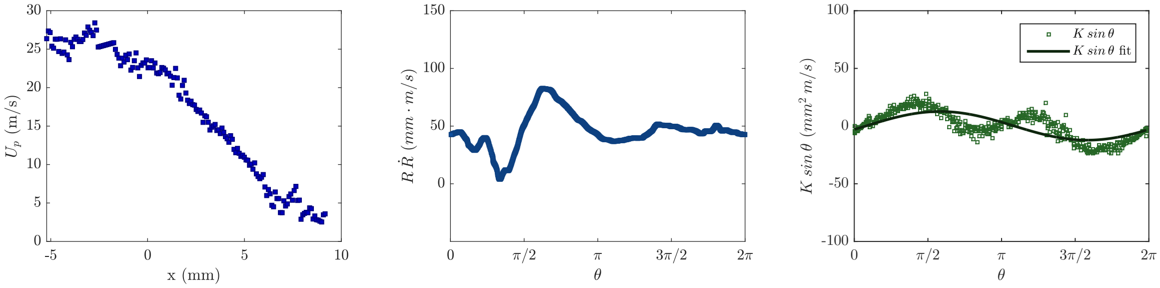

(a) Wave flow at edges. (b) $R \cdot \dot{R}$ on interface (c) $K\ sin\theta$ fit.

Figure G.136: Test# 845 $A^* = 0.41$, $x_c^* = 0.41$, $S_{max} = 123.0$, $U_p(x=0) = 22.8$.

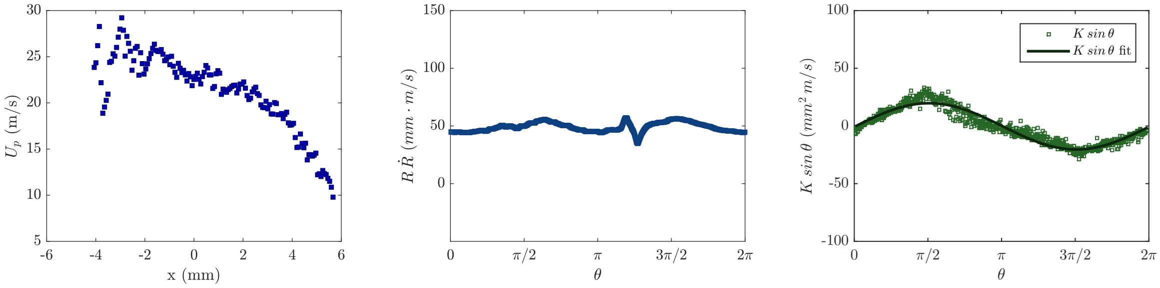

(a) Wave flow at edges. (b) $R \cdot \dot{R}$ on interface (c) $K\ sin\theta$ fit.

Figure G.137: Test# 731 A^* =0.38, x_c^* =0.46, S_{max} =150.7, $U_p(x=0)$ =22.9.

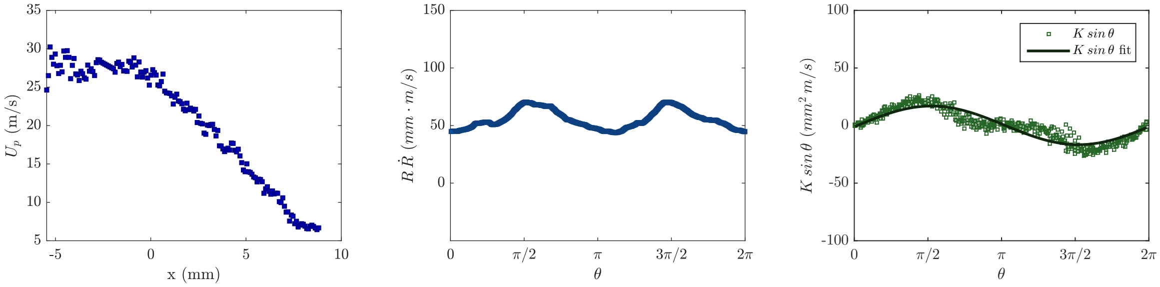

(a) Wave flow at edges. (b) $R \cdot \dot{R}$ on interface (c) $K\ sin\theta$ fit.

Figure G.138: Test# 830 A^* =0.38, x_c^* =0.40, S_{max} =107.9, $U_p(x=0)$ =26.5.

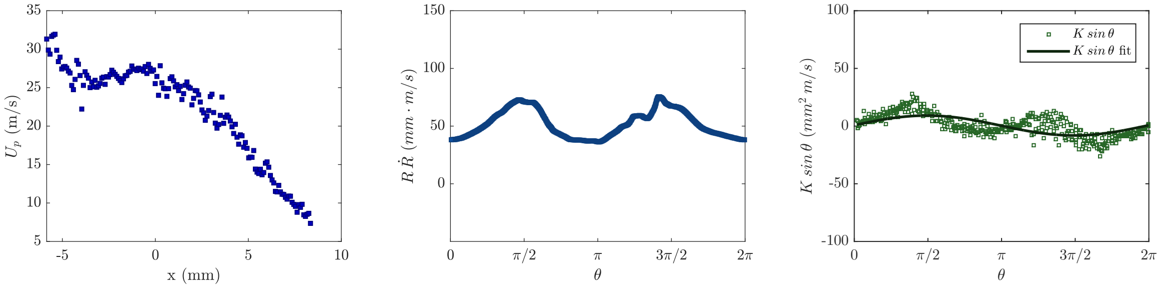

(a) Wave flow at edges. (b) $R \cdot \dot{R}$ on interface (c) $K\ sin\theta$ fit.

Figure G.139: Test# 831 A^* =0.21, x_c^* =0.54, S_{max} =118.3, $U_p(x=0)$ =26.3.

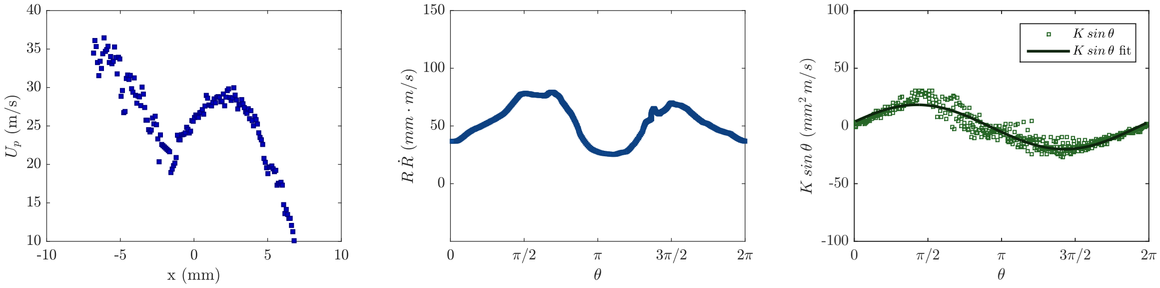

(a) Wave flow at edges. (b) $R \cdot \dot{R}$ on interface (c) $K\, sin\theta$ fit.

Figure G.140: Test# 802 $A^* = 0.13$, $x_c^* = 0.69$, $S_{max} = 133.7$, $U_p(x=0) = 25.7$.

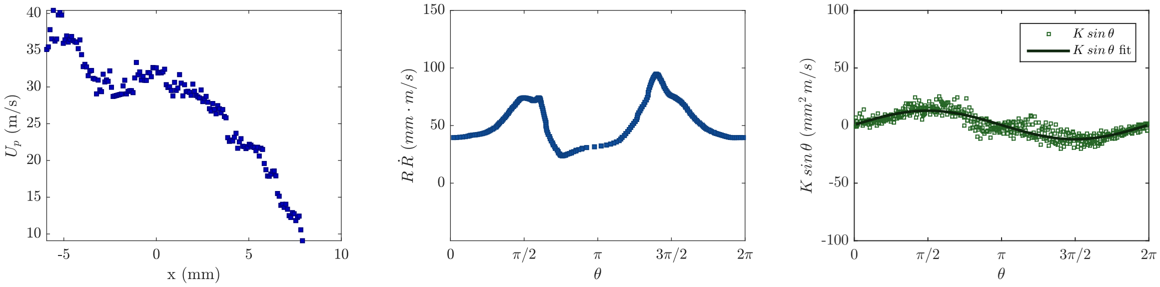

(a) Wave flow at edges. (b) $R \cdot \dot{R}$ on interface (c) $K\, sin\theta$ fit.

Figure G.141: Test# 829 $A^* = 0.06$, $x_c^* = 0.75$, $S_{max} = 135.1$, $U_p(x=0) = 31.7$.

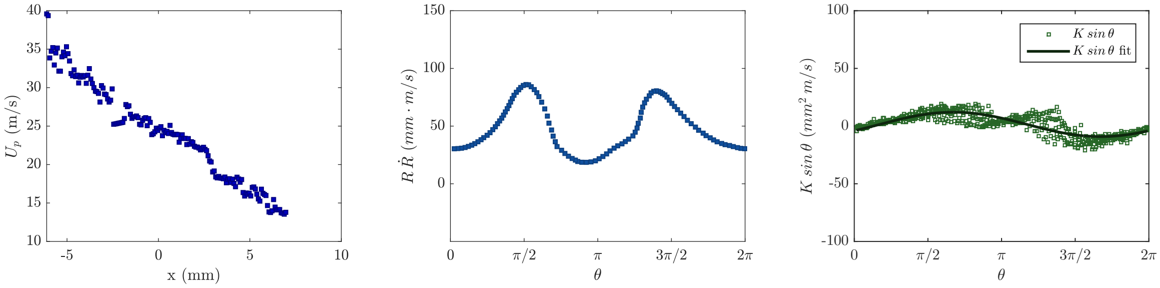

(a) Wave flow at edges. (b) $R \cdot \dot{R}$ on interface (c) $K\, sin\theta$ fit.

Figure G.142: Test# 800 $A^* = 0.04$, $x_c^* = 0.83$, $S_{max} = 105.1$, $U_p(x=0) = 24.5$.

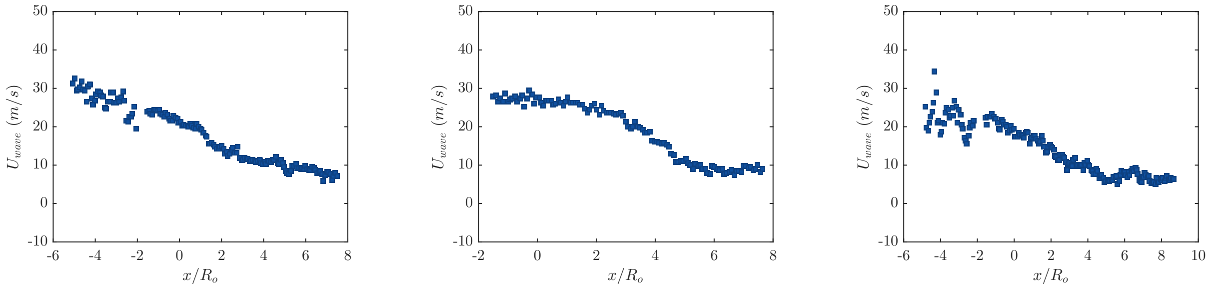

(a) Test# 844. A^* =0.01; x_c^* =0.81; S_{max} =85.4.

(b) Test# 786. A^* =0.01; x_c^* =0.86; S_{max} =105.1.

(c) Test# 722. A^* =0.00; x_c^* =0.80; S_{max} =53.4.

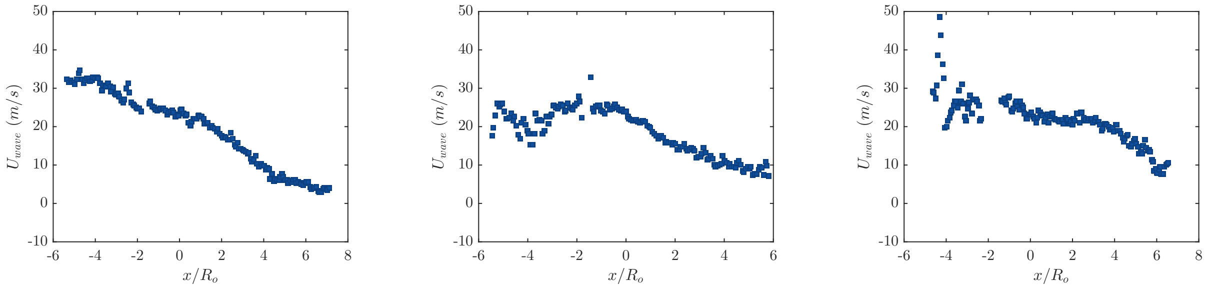

(d) Test# 734. A^* =0.00; x_c^* =0.86; S_{max} =45.0.

(e) Test# 781. A^* =0.00; x_c^* =0.88; S_{max} =62.1.

(f) Test# 732. A^* =0.00; x_c^* =0.89; S_{max} =74.9.

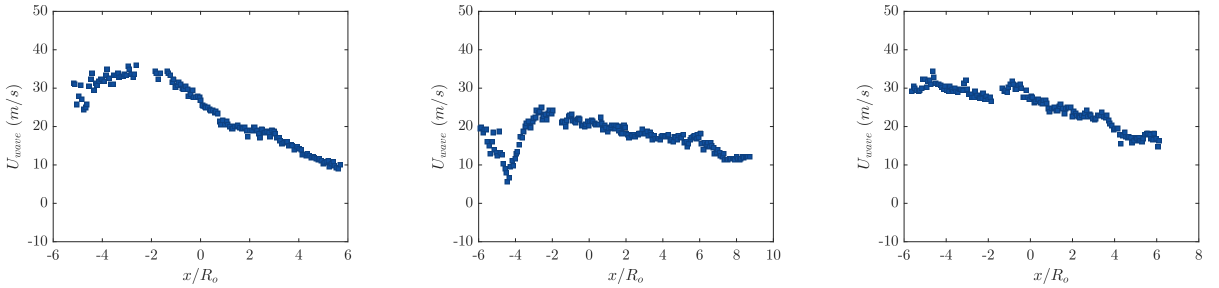

(g) Test# 783. A^* =0.00; x_c^* =0.99; S_{max} =73.9.

(h) Test# 782. A^* =0.00; x_c^* =0.99; S_{max} =38.8.

(i) Test# 785. A^* =0.00; x_c^* =1.23; S_{max} =54.0.

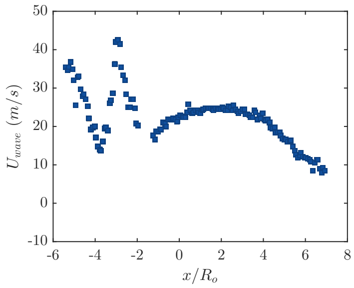

(j) Test# 801. A^* =0.00; x_c^* =1.29; S_{max} =59.6.

Figure G.143: Wave flow velocity distribution for tests 844–801. Void boundary could not be identified reliably(<3%), or test was after collapse, so outgoing waves prevented accurate U_p evaluation.

G.4 Two Boundary

G.4.1 Two Boundary 20:1 PDMS

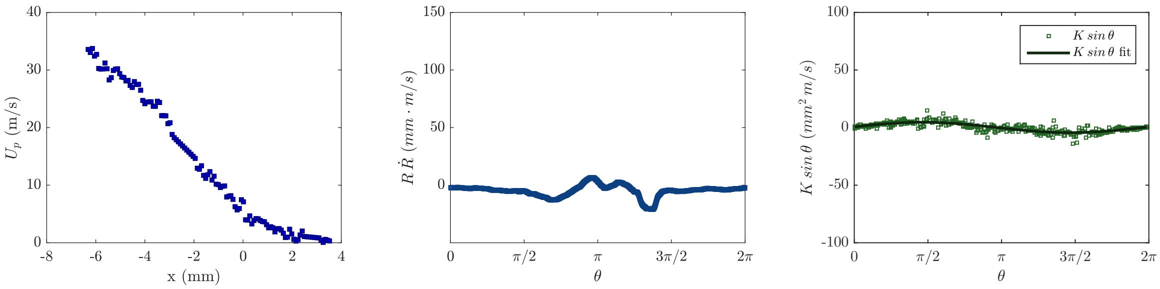

(a) Wave flow at edges. (b) $R \cdot \dot{R}$ on interface (c) $K\,sin\theta$ fit.

Figure G.144: Test# 835 $A^* = 1.04$, $x_c^* = 0.02$, $S_{max} = 48.1$, $U_p(x=0) = 5.6$.

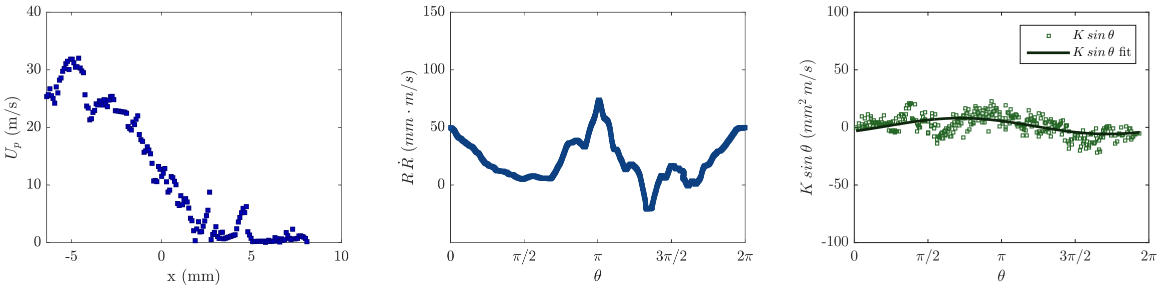

(a) Wave flow at edges. (b) $R \cdot \dot{R}$ on interface (c) $K\,sin\theta$ fit.

Figure G.145: Test# 887 $A^* = 0.98$, $x_c^* = 0.06$, $S_{max} = 71.7$, $U_p(x=0) = 11.7$.

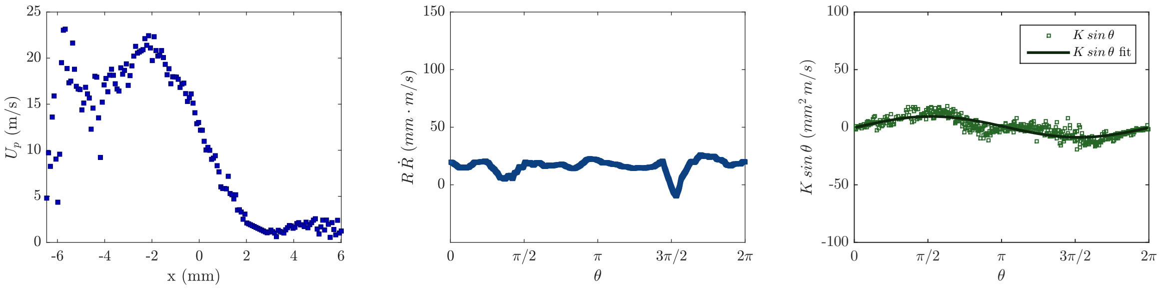

(a) Wave flow at edges. (b) $R \cdot \dot{R}$ on interface (c) $K\,sin\theta$ fit.

Figure G.146: Test# 777 $A^* = 0.92$, $x_c^* = 0.07$, $S_{max} = 54.6$, $U_p(x=0) = 12.9$.

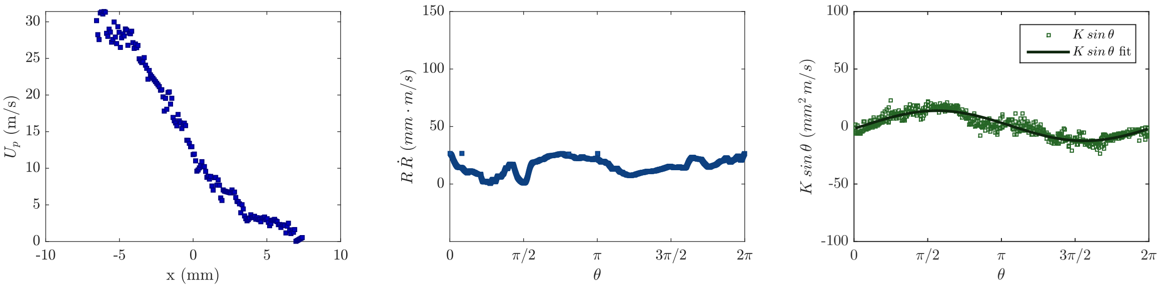

(a) Wave flow at edges. (b) $R \cdot \dot{R}$ on interface (c) $K\ sin\theta$ fit.

Figure G.147: Test# 852 $A^* = 0.92$, $x_c^* = 0.11$, $S_{max} = 53.5$, $U_p(x=0) = 12.3$.

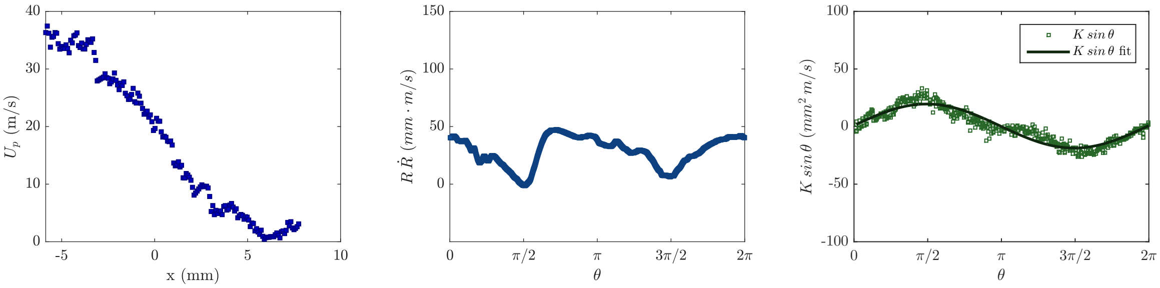

(a) Wave flow at edges. (b) $R \cdot \dot{R}$ on interface (c) $K\ sin\theta$ fit.

Figure G.148: Test# 919 $A^* = 0.89$, $x_c^* = 0.10$, $S_{max} = 74.2$, $U_p(x=0) = 20.5$.

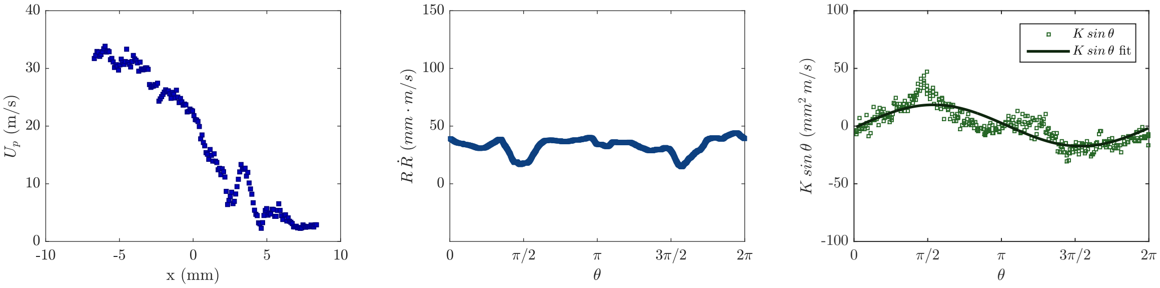

(a) Wave flow at edges. (b) $R \cdot \dot{R}$ on interface (c) $K\ sin\theta$ fit.

Figure G.149: Test# 851 $A^* = 0.88$, $x_c^* = 0.13$, $S_{max} = 91.6$, $U_p(x=0) = 21.7$.

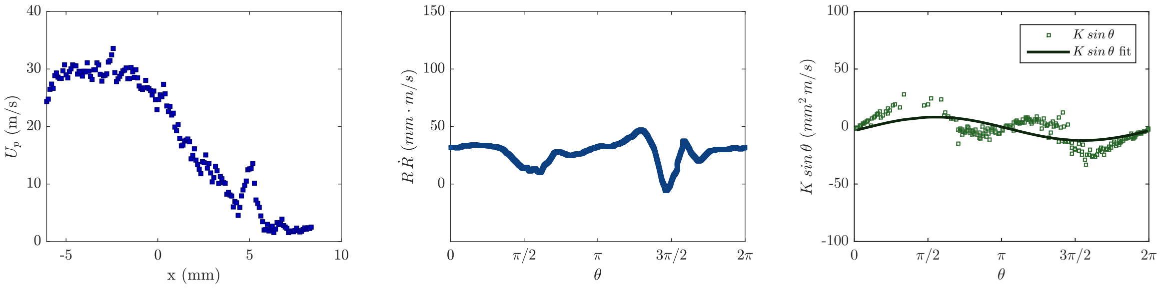

(a) Wave flow at edges. (b) $R \cdot \dot{R}$ on interface (c) $K\ sin\theta$ fit.

Figure G.150: Test# 891 $A^* =0.81$, $x_c^* =0.14$, $S_{max} =95.3$, $U_p(x=0) =25.4$.

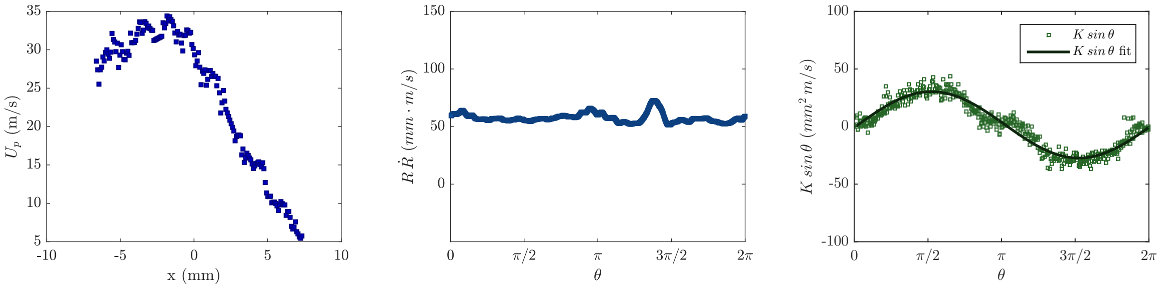

(a) Wave flow at edges. (b) $R \cdot \dot{R}$ on interface (c) $K\ sin\theta$ fit.

Figure G.151: Test# 886 $A^* =0.47$, $x_c^* =0.45$, $S_{max} =133.2$, $U_p(x=0) =29.7$.

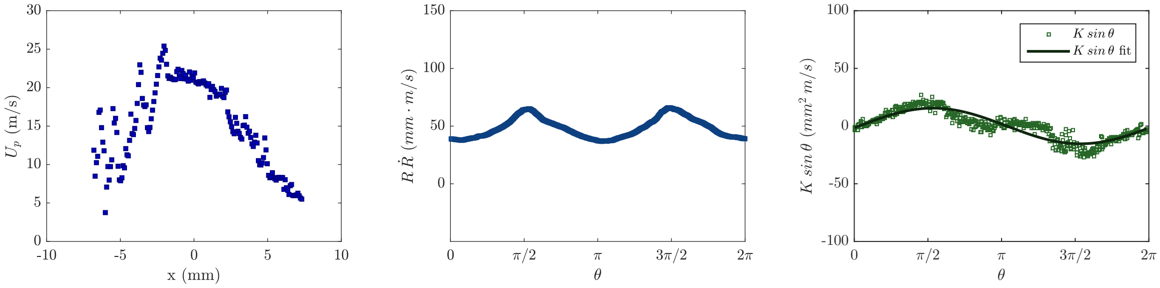

(a) Wave flow at edges. (b) $R \cdot \dot{R}$ on interface (c) $K\ sin\theta$ fit.

Figure G.152: Test# 776 $A^* =0.46$, $x_c^* =0.36$, $S_{max} =100.5$, $U_p(x=0) =21.1$.

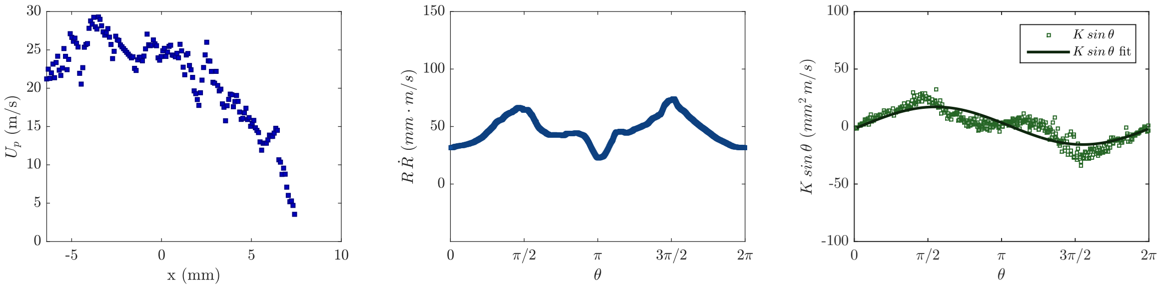

(a) Wave flow at edges. (b) $R \cdot \dot{R}$ on interface (c) $K\ sin\theta$ fit.

Figure G.153: Test# 853 $A^* = 0.43$, $x_c^* = 0.37$, $S_{max} = 94.2$, $U_p(x = 0) = 25.0$.

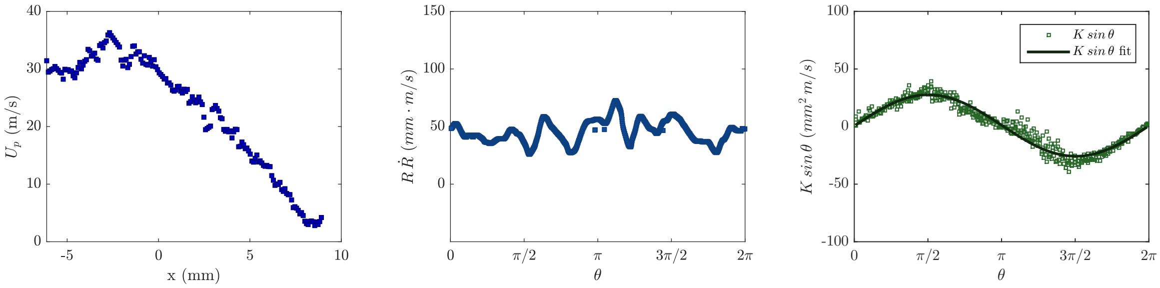

(a) Wave flow at edges. (b) $R \cdot \dot{R}$ on interface (c) $K\ sin\theta$ fit.

Figure G.154: Test# 920 $A^* = 0.40$, $x_c^* = 0.50$, $S_{max} = 120.0$, $U_p(x = 0) = 29.5$.

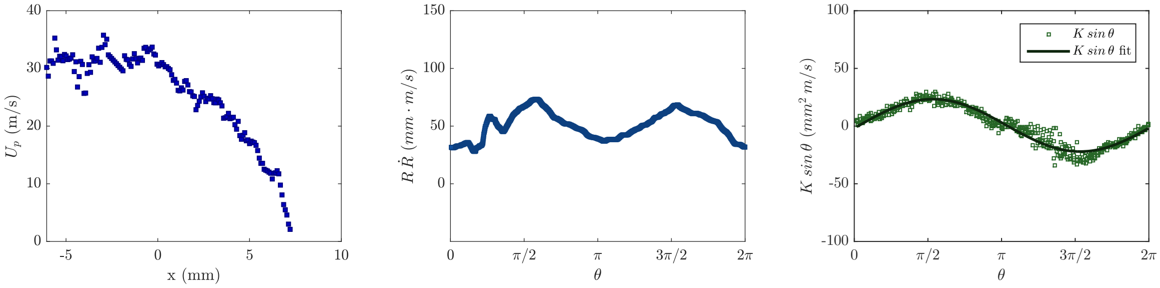

(a) Wave flow at edges. (b) $R \cdot \dot{R}$ on interface (c) $K\ sin\theta$ fit.

Figure G.155: Test# 917 $A^* = 0.36$, $x_c^* = 0.45$, $S_{max} = 126.2$, $U_p(x = 0) = 31.7$.

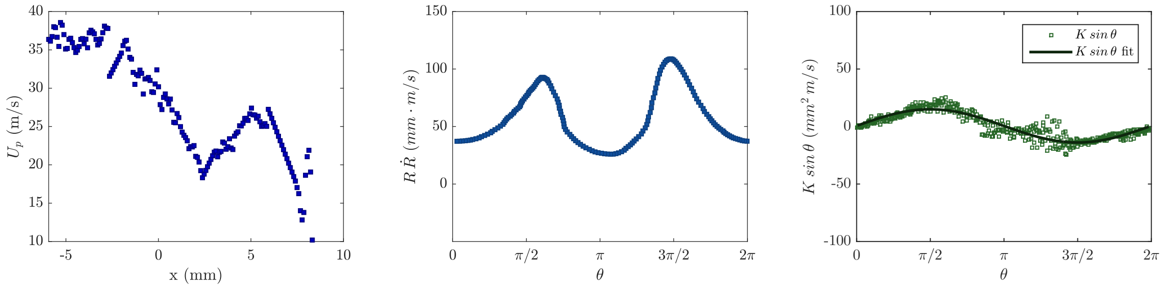

(a) Wave flow at edges.

(b) $R \cdot \dot{R}$ on interface

(c) $K\ sin\theta$ fit.

Figure G.156: Test# 918 A^* =0.06, x_c^* =0.84, S_{max} =137.2, $U_p(x = 0)$ =29.6.

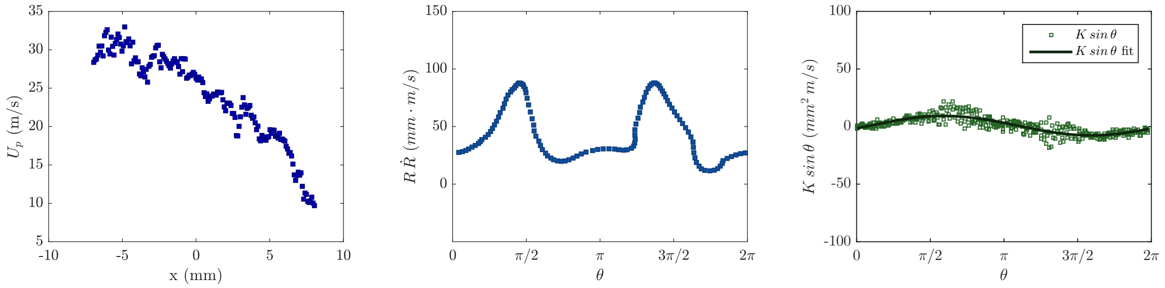

(a) Wave flow at edges.

(b) $R \cdot \dot{R}$ on interface

(c) $K\ sin\theta$ fit.

Figure G.157: Test# 850 A^* =0.05, x_c^* =0.71, S_{max} =114.7, $U_p(x = 0)$ =26.1.

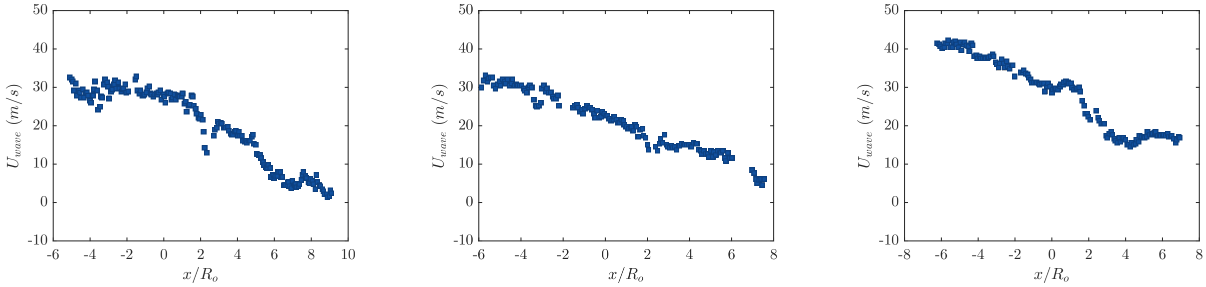

(a) Test# 889. A^* =0.03; x_c^* =0.66; S_{max} =125.8.
(b) Test# 885. A^* =0.01; x_c^* =0.77; S_{max} =72.3.
(c) Test# 833. A^* =0.00; x_c^* =0.82; S_{max} =91.8.

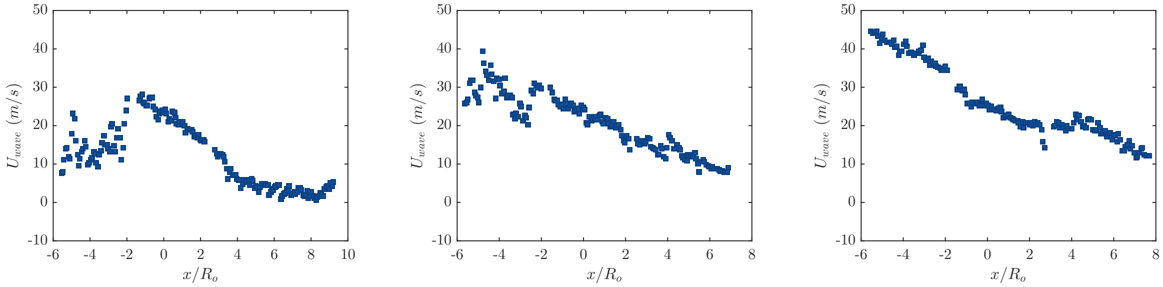

(d) Test# 779. A^* =0.00; x_c^* =0.86; S_{max} =66.4.
(e) Test# 890. A^* =0.00; x_c^* =0.91; S_{max} =73.8.
(f) Test# 892. A^* =0.00; x_c^* =0.91; S_{max} =67.9.

Figure G.158: Wave flow velocity distribution for tests 889–892. Void boundary could not be identified reliably(<3%), or test was after collapse, so outgoing waves prevented accurate U_p evaluation.

G.4.2 Two Boundary 30:1 PDMS

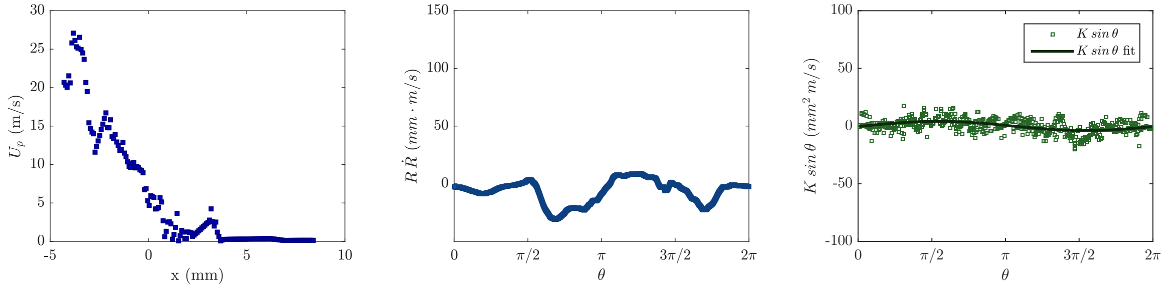

(a) Wave flow at edges.
(b) $R \cdot \dot{R}$ on interface
(c) $K\,sin\theta$ fit.

Figure G.159: Test# 771 A^* =0.98, x_c^* =0.03, S_{max} =42.0, $U_p(x=0)$ =6.7.

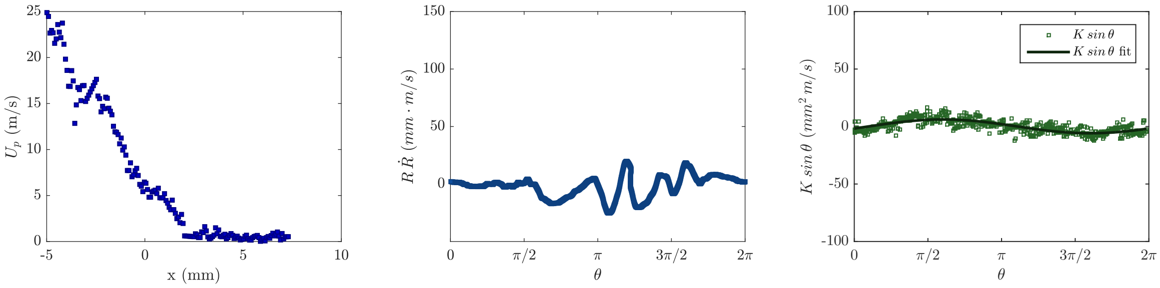

(a) Wave flow at edges.   (b) $R \cdot \dot{R}$ on interface   (c) $K\ sin\theta$ fit.

Figure G.160: Test# 770 A^* =0.95, x_c^* =0.04, S_{max} =44.8, $U_p(x=0)$ =6.2.

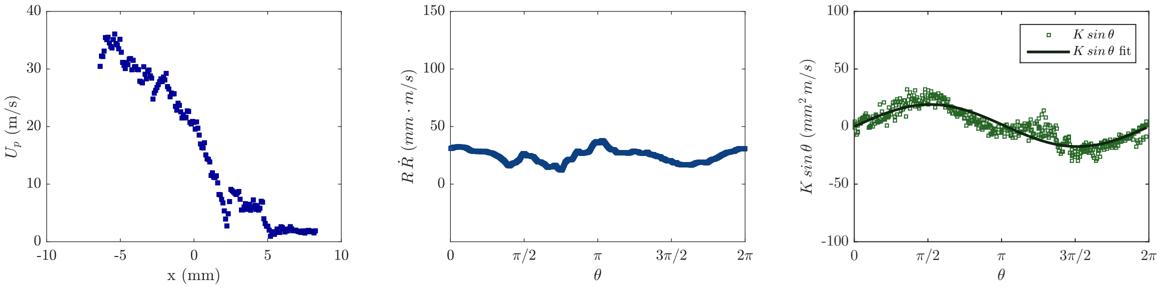

(a) Wave flow at edges.   (b) $R \cdot \dot{R}$ on interface   (c) $K\ sin\theta$ fit.

Figure G.161: Test# 862 A^* =0.92, x_c^* =0.09, S_{max} =73.6, $U_p(x=0)$ =20.0.

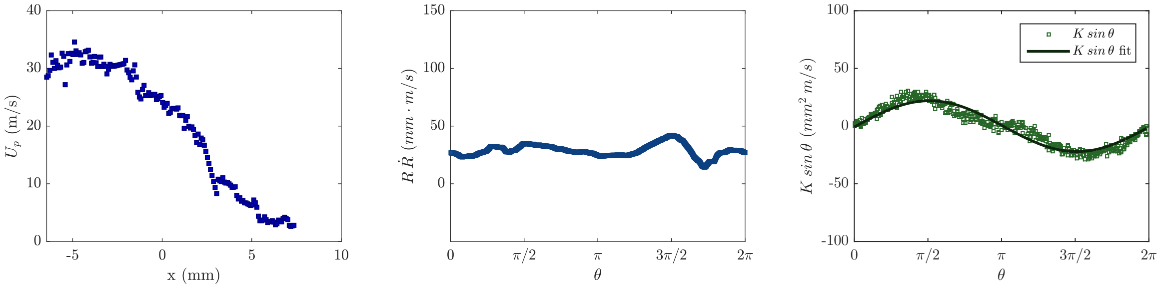

(a) Wave flow at edges.   (b) $R \cdot \dot{R}$ on interface   (c) $K\ sin\theta$ fit.

Figure G.162: Test# 827 A^* =0.73, x_c^* =0.23, S_{max} =74.4, $U_p(x=0)$ =24.1.

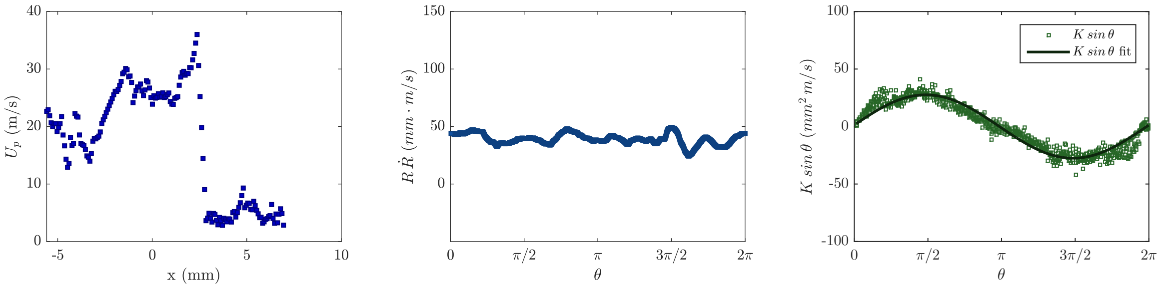

(a) Wave flow at edges.

(b) $R \cdot \dot{R}$ on interface

(c) $K\,sin\theta$ fit.

Figure G.163: Test# 768 $A^* = 0.62$, $x_c^* = 0.32$, $S_{max} = 108.5$, $U_p(x=0) = 25.8$.

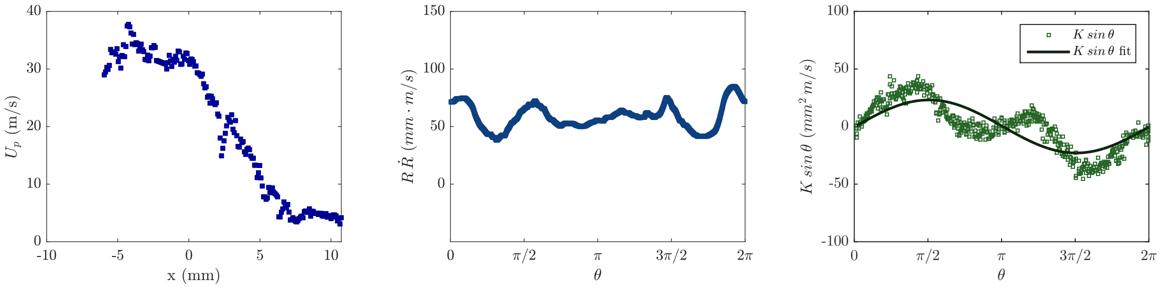

(a) Wave flow at edges.

(b) $R \cdot \dot{R}$ on interface

(c) $K\,sin\theta$ fit.

Figure G.164: Test# 861 $A^* = 0.56$, $x_c^* = 0.30$, $S_{max} = 95.2$, $U_p(x=0) = 31.4$.

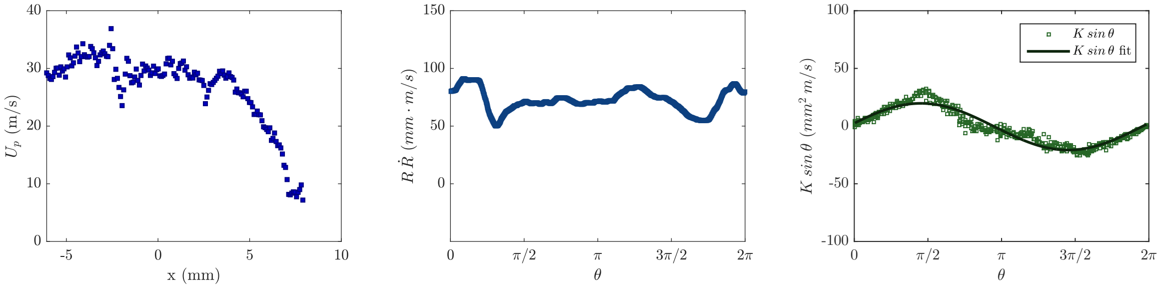

(a) Wave flow at edges.

(b) $R \cdot \dot{R}$ on interface

(c) $K\,sin\theta$ fit.

Figure G.165: Test# 864 $A^* = 0.42$, $x_c^* = 0.49$, $S_{max} = 136.8$, $U_p(x=0) = 29.8$.

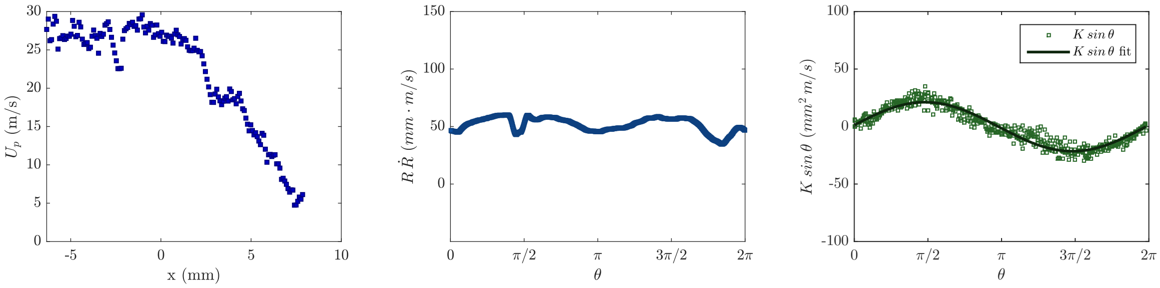

(a) Wave flow at edges. (b) $R \cdot \dot{R}$ on interface (c) $K\ sin\theta$ fit.

Figure G.166: Test# 828 $A^* = 0.37$, $x_c^* = 0.50$, $S_{max} = 114.5$, $U_p(x=0) = 27.0$.

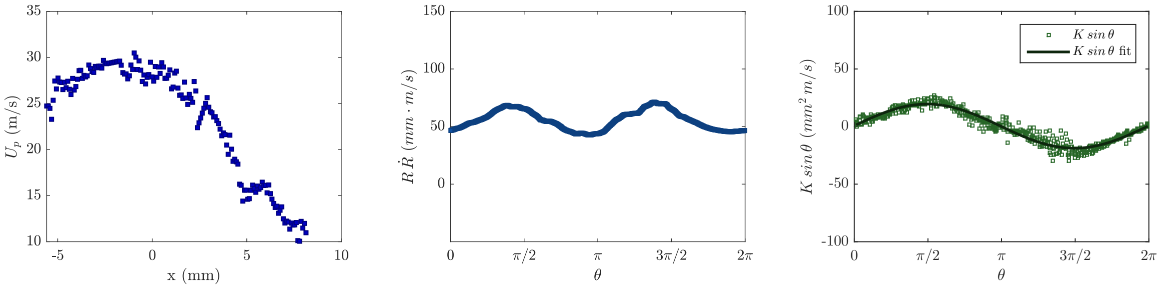

(a) Wave flow at edges. (b) $R \cdot \dot{R}$ on interface (c) $K\ sin\theta$ fit.

Figure G.167: Test# 863 $A^* = 0.26$, $x_c^* = 0.50$, $S_{max} = 133.9$, $U_p(x=0) = 28.3$.

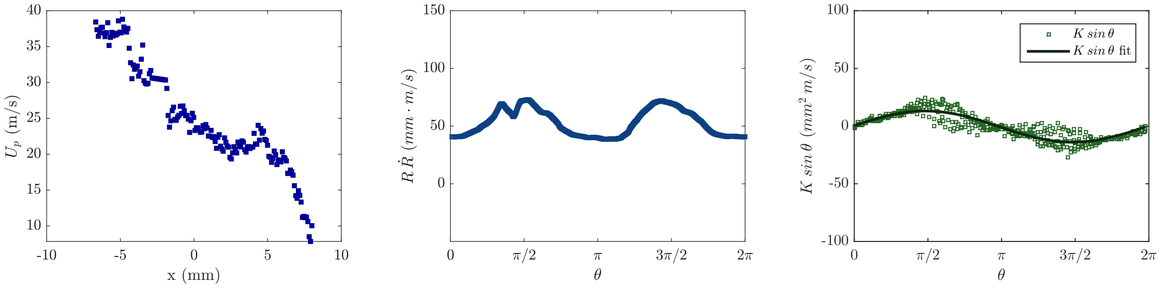

(a) Wave flow at edges. (b) $R \cdot \dot{R}$ on interface (c) $K\ sin\theta$ fit.

Figure G.168: Test# 825 $A^* = 0.17$, $x_c^* = 0.64$, $S_{max} = 126.6$, $U_p(x=0) = 24.3$.

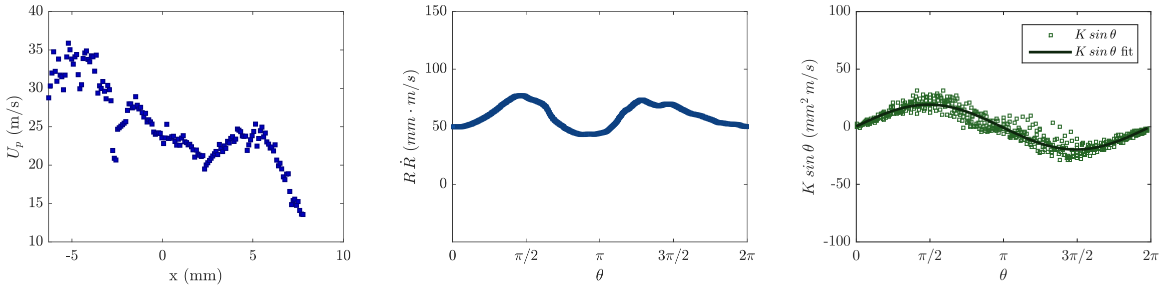

(a) Wave flow at edges. (b) $R \cdot \dot{R}$ on interface (c) $K\ sin\theta$ fit.

Figure G.169: Test# 826 A^* =0.13, x_c^* =0.71, S_{max} =136.1, $U_p(x = 0)$ =24.1.

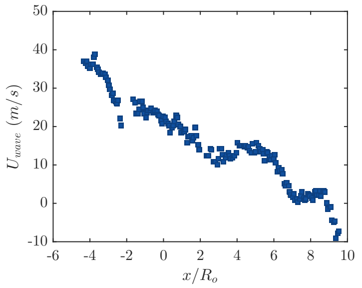

(a) Test# 769. A^* =0.02; x_c^* =0.77; S_{max} =126.0.

Figure G.170: Wave flow velocity distribution for test 769. Void boundary could not be identified reliably(<3%), or test was after collapse, so outgoing waves prevented accurate U_p evaluation.

G.4.3 Two Boundary 40:1 PDMS

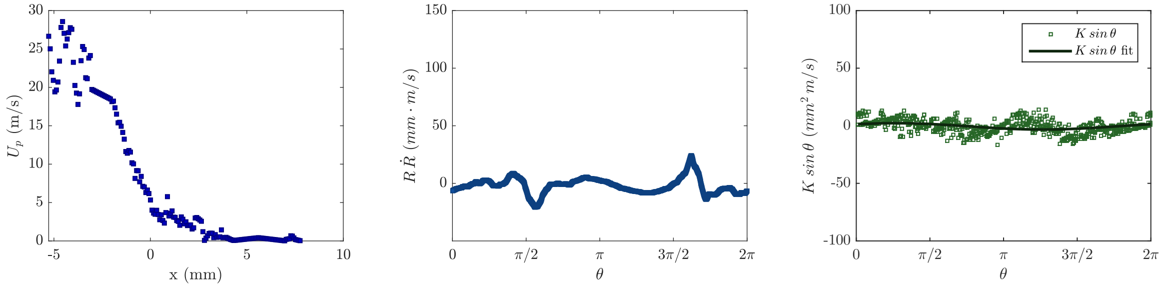

(a) Wave flow at edges. (b) $R \cdot \dot{R}$ on interface (c) $K\ sin\theta$ fit.

Figure G.171: Test# 775 A^* =0.96, x_c^* =0.05, S_{max} =50.3, $U_p(x = 0)$ =5.3.

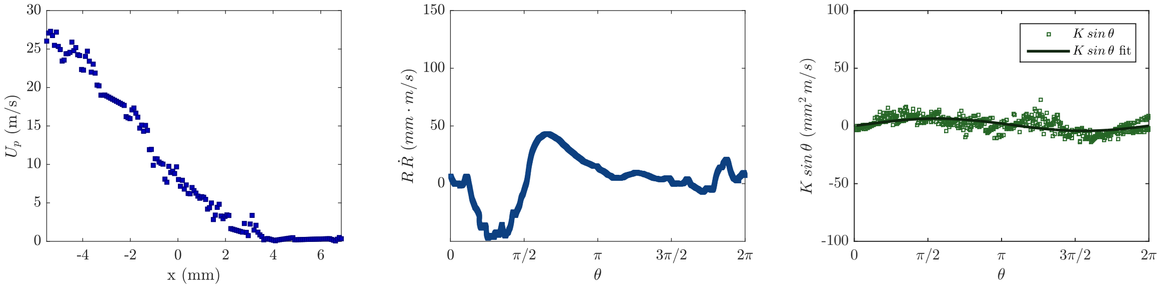

(a) Wave flow at edges. (b) $R \cdot \dot{R}$ on interface (c) $K\ sin\theta$ fit.

Figure G.172: Test# 857 A^* =0.94, x_c^* =0.06, S_{max} =46.3, $U_p(x=0)$ =7.9.

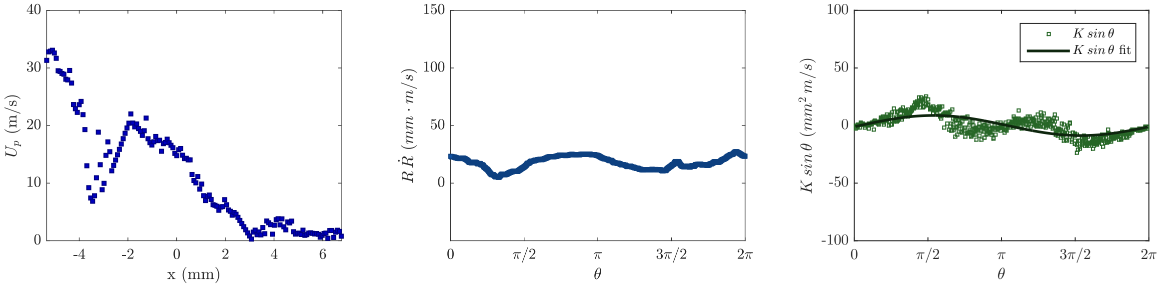

(a) Wave flow at edges. (b) $R \cdot \dot{R}$ on interface (c) $K\ sin\theta$ fit.

Figure G.173: Test# 772 A^* =0.93, x_c^* =0.10, S_{max} =55.3, $U_p(x=0)$ =15.6.

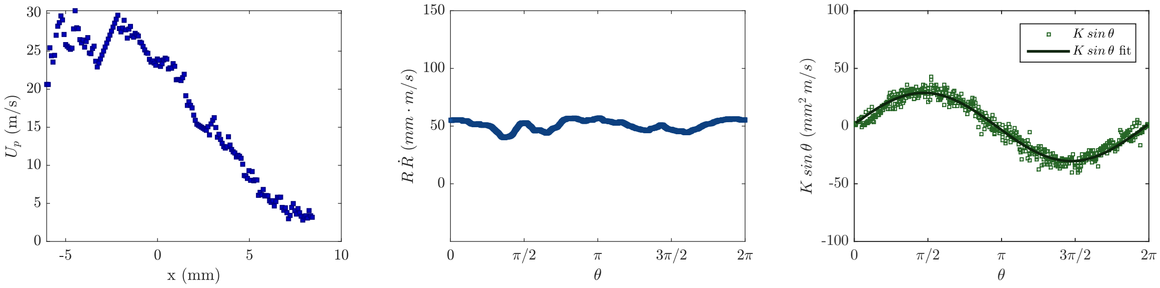

(a) Wave flow at edges. (b) $R \cdot \dot{R}$ on interface (c) $K\ sin\theta$ fit.

Figure G.174: Test# 774 A^* =0.66, x_c^* =0.34, S_{max} =112.5, $U_p(x=0)$ =23.7.

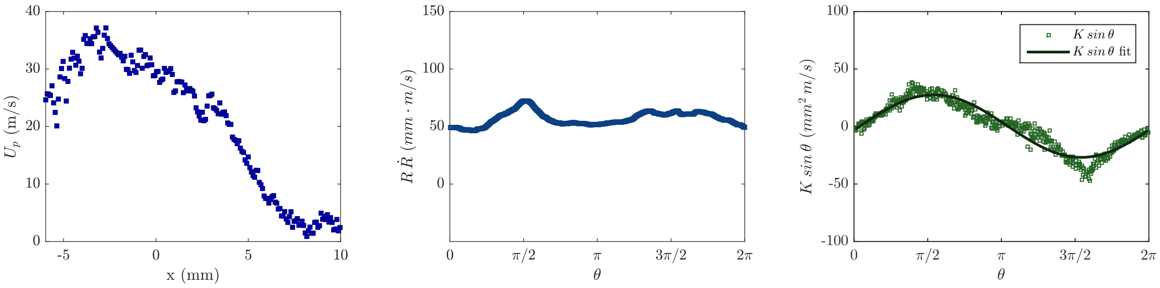

(a) Wave flow at edges.

(b) $R \cdot \dot{R}$ on interface

(c) $K\ sin\theta$ fit.

Figure G.175: Test# 856 $A^* = 0.54$, $x_c^* = 0.35$, $S_{max} = 118.2$, $U_p(x=0) = 29.8$.

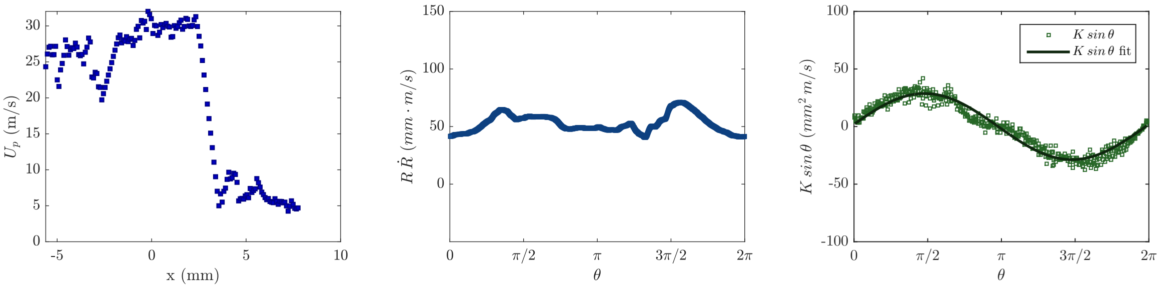

(a) Wave flow at edges.

(b) $R \cdot \dot{R}$ on interface

(c) $K\ sin\theta$ fit.

Figure G.176: Test# 820 $A^* = 0.44$, $x_c^* = 0.39$, $S_{max} = 119.2$, $U_p(x=0) = 30.1$.

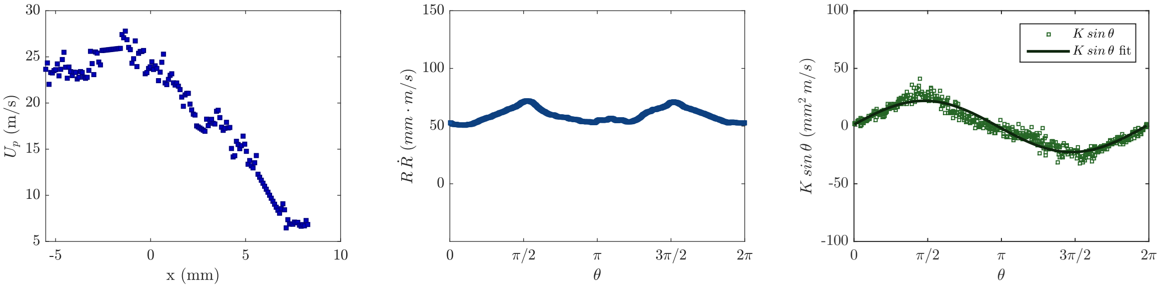

(a) Wave flow at edges.

(b) $R \cdot \dot{R}$ on interface

(c) $K\ sin\theta$ fit.

Figure G.177: Test# 819 $A^* = 0.40$, $x_c^* = 0.44$, $S_{max} = 112.4$, $U_p(x=0) = 24.2$.

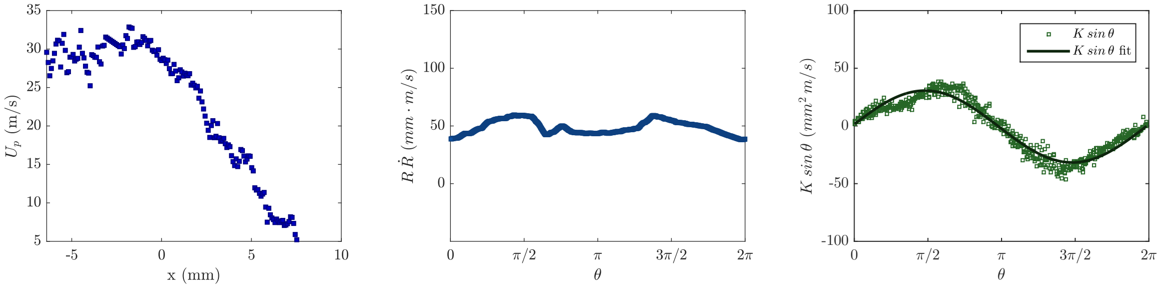

(a) Wave flow at edges. (b) $R \cdot \dot{R}$ on interface (c) $K\ sin\theta$ fit.

Figure G.178: Test# 821 $A^* = 0.40$, $x_c^* = 0.47$, $S_{max} = 135.7$, $U_p(x=0) = 28.8$.

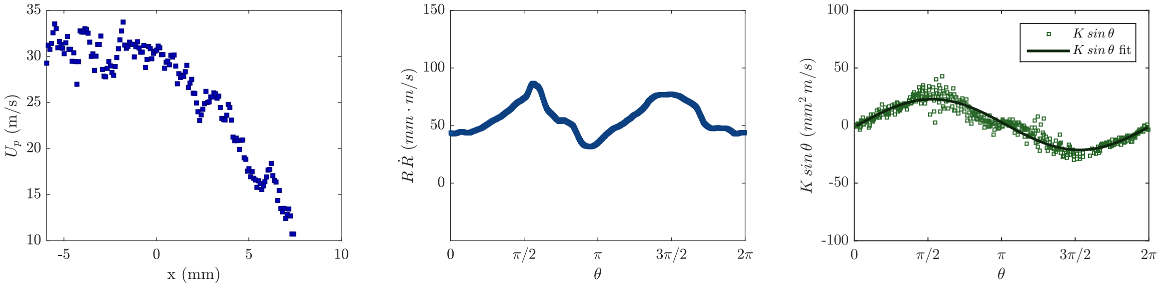

(a) Wave flow at edges. (b) $R \cdot \dot{R}$ on interface (c) $K\ sin\theta$ fit.

Figure G.179: Test# 854 $A^* = 0.26$, $x_c^* = 0.58$, $S_{max} = 136.1$, $U_p(x=0) = 30.1$.

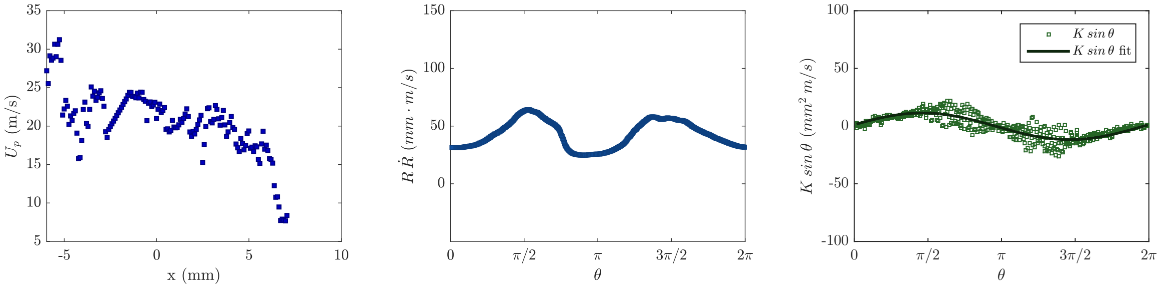

(a) Wave flow at edges. (b) $R \cdot \dot{R}$ on interface (c) $K\ sin\theta$ fit.

Figure G.180: Test# 773 $A^* = 0.11$, $x_c^* = 0.75$, $S_{max} = 140.7$, $U_p(x=0) = 22.0$.

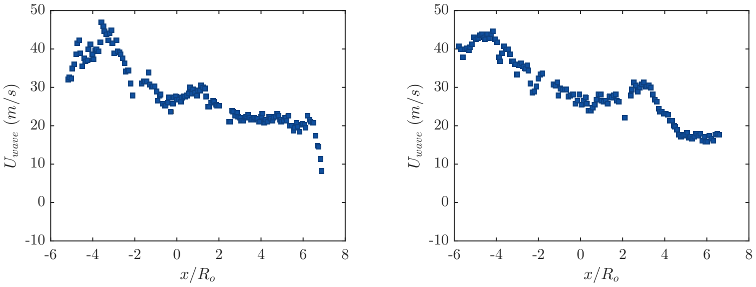

(a) Test# 855. A^* =0.02; x_c^* =0.92; S_{max} =123.7.

(b) Test# 818. A^* =0.00; x_c^* =1.26; S_{max} =61.6.

Figure G.181: Wave flow velocity distribution for tests 855–818. Void boundary could not be identified reliably(<3%), or test was after collapse, so outgoing waves prevented accurate U_p evaluation.

APPENDIX H

PARTICLE SHADOW VELOCIMETRY: TEST PARAMETER TABLES

This section presents a number of geometric, flow, and model properties for each test particle shadow velocimetry (PSV) test conducted. Tests are arranged by area ratio and void centroid displacement. The tabulated variables are as follows:

Test#	—	A reference number assigned each test.
R_o	mm	Initial radius. Measured in pre-shot image.
A^*	$^{A}/_{A_o}$	Area ratio.
$\dot{A}$	$mm^2/\mu s$	Area rate of change with time.
x_c^*	$^{x_c}/_{R_o}$	Void centroid displacement (from initial).
$\dot{x_c}$	m/s	Void centroid velocity (from difference between frames).

U_I	m/s	Impact velocity.
$U_{p,max}$	m/s	Maximum velocity in measured waveform at edge.
$U_{p,x=0}$	m/s	Value of velocity in measured waveform at edge at $x = 0$.
$U_{p,min}$	m/s	Minimum velocity in measured waveform at edge.
dU_p/dx	$(m/s)/mm$	Velocity gradient in waveform measured at edge.

K	$mm^2 \cdot m/s$	Doublet strength.
R_K^2	—	Coefficient of determination of least squares fit to obtain K.
Q	$mm \cdot m/s$	Source (sink) strength.
S_{max}	m/s	Maximum flow speed in experimental flowfield data.
S_{avg}	m/s	Mean flow speed in experimental flowfield data.
STD	m/s	Square root of sum of squares of residual velocities.
MAR	m/s	Mean Absolute Residual.

H.1 No Boundary

Table H.1: Geometric properties and wave speed properties of tests for the no boundary case.

Test#	R_o	A^*	$\dot{A}$	x_c^*	$\dot{x}_c$	U_I	$U_{p,max}$	$U_{p,x=0}$	$U_{p,min}$	dU_p/dx
746	1.15	1.00	0.02	0.02	10.2	26.2	19.6	3.6	0.32	1.03
702	1.11	0.99	-0.01	0.07	25.2	25.6	29.6	9.7	0.28	5.68
824	1.14	0.98	-0.01	0.02	9.0	26.0	26.2	3.8	0.03	1.03
836	1.12	0.94	0.16	0.10	45.0	26.2	32.7	16.6	1.92	9.01
756	1.12	0.93	0.09	0.09	24.8	26.1	25.7	9.8	2.07	4.65
752	1.15	0.90	0.13	0.18	28.3	26.1	29.8	14.0	1.70	5.10
849	1.06	0.89	0.14	0.09	32.5	26.1	27.5	11.4	4.41	1.84
842	1.06	0.89	0.21	0.13	56.3	26.4	33.7	24.3	4.94	5.36
701	1.09	0.87	0.08	0.15	41.6	25.5	30.5	18.0	0.81	6.47
745	1.10	0.86	0.21	0.12	50.1	25.9	32.6	23.9	5.93	3.96
823	1.12	0.86	0.12	0.10	35.5	26.2	26.7	18.0	3.64	6.91
704	1.06	0.81	0.21	0.16	51.4	26.0	29.8	21.4	4.85	1.31
843	1.09	0.74	0.27	0.24	57.3	26.0	33.3	21.2	5.73	2.01
689	1.12	0.56	0.28	0.32	49.1	26.1	26.2	20.3	9.43	2.17
750	1.04	0.50	0.28	0.38	65.5	26.0	25.4	18.8	12.02	1.61
751	1.15	0.48	0.32	0.37	53.8	26.0	26.3	22.4	12.87	5.17
687	1.06	0.44	0.33	0.44	63.7	26.5	24.9	20.5	13.85	0.28
699	1.13	0.39	0.38	0.48	78.8	26.8	32.3	30.1	20.19	3.24
688	1.08	0.38	0.38	0.48	74.6	26.0	29.8	26.5	16.52	2.29
694	1.08	0.37	0.33	0.52	82.7	26.0	31.4	27.6	15.12	3.13
693	1.11	0.35	0.36	0.52	78.5	25.9	27.1	24.9	20.32	0.09
822	1.15	0.29	0.35	0.53	80.0	26.2	30.0	26.6	22.47	0.01
703	1.03	0.28	0.41	0.60	114.2	26.0	34.7	30.1	22.41	0.93
840	1.08	0.24	0.34	0.63	83.5	26.0	36.7	22.2	12.26	1.60
683	1.07	0.23	0.21	0.58	66.5	26.3	18.7	16.1	10.58	2.41
700	1.07	0.22	0.30	0.59	69.7	26.4	25.7	17.4	10.25	0.98
761	1.15	0.15	0.33	0.69	83.4	26.2	28.9	25.7	19.98	0.41
838	1.06	0.13	0.35	0.72	109.9	26.0	27.4	22.6	19.83	0.68
686	1.01	0.09	0.31	0.70	86.9	26.1	26.0	23.9	14.83	2.94
692	1.09	0.06	0.26	0.79	96.9	26.0	26.9	22.4	17.27	3.75
684	1.04	0.00	—	0.84	-4.0	26.2	—	—	—	—
685	1.01	0.00	—	1.04	71.5	26.1	—	—	—	—
691	0.99	0.00	—	1.08	46.1	25.9	—	—	—	—
760	1.14	0.00	—	1.16	40.6	26.1	—	—	—	—
690	1.05	0.00	—	1.25	54.5	26.3	—	—	—	—
753	1.08	0.00	—	1.32	35.3	26.5	—	—	—	—
696	1.11	0.00	—	3.17	19.2	—	—	—	—	—
697	0.93	0.00	—	3.29	28.5	26.0	—	—	—	—
695	1.04	0.00	—	3.35	-16.4	26.0	—	—	—	—
698	1.14	0.00	—	3.47	-6.6	26.1	—	—	—	—

Table H.2: Model parameters and error measures of tests for the no boundary case.

Test#	A^*	K	R_K^2	Q	S_{max}	S_{avg}	STD	MAR
746	1.00	2.5	0.09	7.8	31	8.8	2.98	2.58
702	0.99	8.4	0.60	17.3	47	15.4	4.44	3.83
824	0.98	2.3	0.14	6.2	48	14.2	3.63	2.98
836	0.94	16.6	0.76	23.5	69	21.8	5.97	5.20
756	0.93	9.9	0.61	18.7	45	13.9	4.08	3.60
752	0.90	15.4	0.87	22.3	52	16.7	2.77	2.39
849	0.89	9.4	0.67	26.9	60	19.3	5.29	4.71
842	0.89	24.9	0.88	40.4	86	24.8	5.87	5.22
701	0.87	15.9	0.89	29.2	67	15.9	5.51	4.90
745	0.86	23.2	0.91	36.6	78	21.7	5.83	5.01
823	0.86	18.8	0.72	32.1	71	20.0	7.11	6.07
704	0.81	22.2	0.91	43.1	81	19.5	7.56	6.53
843	0.74	19.2	0.91	42.9	86	23.6	8.09	7.31
689	0.56	18.1	0.93	43.6	87	18.2	5.70	5.05
750	0.50	15.4	0.93	49.0	124	20.9	7.88	6.93
751	0.48	18.8	0.89	49.2	109	19.9	4.29	3.74
687	0.44	17.5	0.90	48.9	128	20.5	5.92	4.84
699	0.39	26.1	0.97	60.2	129	25.8	5.15	4.36
688	0.38	23.3	0.93	55.8	145	23.8	5.13	4.33
694	0.37	23.6	0.93	52.0	173	22.2	5.44	4.46
693	0.35	20.1	0.90	55.6	139	21.8	5.05	4.12
822	0.29	18.4	0.91	58.0	153	29.0	4.40	3.71
703	0.28	21.1	0.87	64.2	136	26.7	6.99	5.67
840	0.24	18.8	0.90	51.6	123	30.5	5.76	4.75
683	0.23	11.4	0.72	44.1	134	15.2	7.05	6.17
700	0.22	10.0	0.79	44.1	110	17.1	5.87	5.20
761	0.15	18.5	0.95	54.7	133	26.9	3.48	2.92
838	0.13	11.2	0.77	44.0	114	30.4	4.08	3.20
686	0.09	7.9	0.69	40.0	127	20.7	5.65	4.79
692	0.06	9.1	0.71	35.9	100	19.0	5.08	4.08
684	0.00	—	—	—	74	19.1	—	—
685	0.00	—	—	—	60	21.7	—	—
691	0.00	—	—	—	58	24.6	—	—
760	0.00	—	—	—	55	25.3	—	—
690	0.00	—	—	—	55	20.1	—	—
753	0.00	—	—	—	40	19.4	—	—

H.2 Downstream Boundary

H.2.1 Downstream Aluminum

Table H.3: Geometric properties and wave speed properties of tests for aluminum downstream boundary case.

Test#	R_o	A^*	$\dot{A}$	x_c^*	$\dot{x}_c$	U_I	$U_{p,max}$	$U_{p,x=0}$	$U_{p,min}$	dU_p/dx
882	1.11	0.89	0.15	0.11	42.9	26.1	31.5	15.1	8.02	5.73
877	1.12	0.81	0.17	0.12	31.6	26.4	29.0	13.9	5.37	5.48
879	1.14	0.70	0.25	0.23	46.2	26.0	31.0	21.3	12.14	4.36
884	1.12	0.60	0.35	0.33	52.8	26.1	28.1	19.8	10.18	4.83
878	1.12	0.57	0.32	0.28	51.8	26.2	28.5	16.4	8.51	5.26
881	1.12	0.21	0.42	0.56	91.6	26.1	20.8	16.0	10.40	1.26
880	1.09	0.14	0.26	0.53	75.3	26.1	20.6	13.9	8.11	2.19
883	1.14	0.05	—	0.75	91.6	26.3	—	—	—	—

Table H.4: Model parameters and error measures of tests for aluminum downstream boundary case.

Test#	A^*	K	R_K^2	Q	S_{max}	S_{avg}	STD	MAR
882	0.89	13.8	0.87	28.6	65	29.1	5.73	5.13
877	0.81	8.7	0.32	30.5	62	28.6	5.78	5.32
879	0.70	21.6	0.91	39.6	82	32.9	5.75	5.11
884	0.60	13.6	0.83	53.9	105	38.3	5.51	4.79
878	0.57	5.4	0.31	51.2	127	37.8	6.42	5.12
881	0.21	3.5	0.40	62.3	132	40.4	9.09	7.39
880	0.14	2.6	0.26	53.2	127	33.6	6.76	5.29
883	0.05	—	—	—	122	36.2	—	—

H.2.2 Downstream 20:1 PDMS

Table H.5: Geometric properties and wave speed properties of tests for the 20:1 PDMS downstream boundary case.

Test#	R_o	A^*	$\dot{A}$	x_c^*	$\dot{x}_c$	U_I	$U_{p,max}$	$U_{p,x=0}$	$U_{p,min}$	dU_p/dx
809	0.99	1.04	0.01	0.02	-9.6	26.1	22.3	10.1	0.91	1.93
728	1.12	1.01	0.02	0.09	39.4	25.7	30.6	11.6	0.38	5.75
743	1.15	0.95	0.07	0.08	31.0	26.2	27.1	10.3	1.27	3.17
742	1.16	0.95	0.08	0.05	19.5	26.3	29.6	4.3	1.52	0.56
764	1.22	0.93	0.02	0.15	46.5	26.1	34.9	15.5	0.52	4.28
749	1.17	0.90	0.10	0.10	26.6	26.0	26.6	7.5	1.98	5.57
717	1.11	0.89	0.09	0.14	34.5	25.9	26.8	12.3	1.31	4.44
718	1.11	0.79	0.21	0.23	45.4	25.9	24.3	19.0	2.51	0.37
912	1.10	0.68	0.31	0.23	56.6	26.3	36.7	25.0	8.34	3.77
748	0.78	0.68	0.13	0.21	41.6	26.0	19.8	10.0	2.82	0.67
894	1.10	0.63	0.23	0.31	59.0	26.4	29.1	22.6	12.05	3.21
813	1.13	0.62	0.33	0.33	60.0	26.0	33.6	25.0	10.67	0.43
727	1.15	0.56	0.33	0.37	55.1	25.9	29.5	23.9	11.85	2.30
872	1.12	0.45	0.29	0.42	49.6	26.4	19.4	13.4	4.86	2.10
893	1.09	0.42	0.33	0.40	51.1	26.5	28.1	23.6	14.70	2.54
795	1.08	0.42	0.39	0.41	77.1	25.6	33.2	30.2	22.88	3.51
706	0.99	0.41	0.18	0.43	45.4	26.0	24.2	17.6	2.72	2.46
911	1.12	0.40	0.30	0.49	67.8	26.0	25.3	19.3	14.05	1.35
765	1.16	0.37	0.19	0.55	56.9	26.1	26.4	16.0	4.13	1.45
895	1.14	0.25	0.37	0.66	101.3	26.5	33.4	32.0	14.94	0.27
910	1.10	0.14	0.37	0.77	118.4	26.8	28.6	25.8	19.56	0.55
896	1.10	0.10	0.35	0.67	112.9	26.3	25.3	21.5	18.36	0.52
909	1.12	0.02	—	0.76	-224.7	26.6	—	—	—	—
707	1.04	0.01	—	0.86	3.0	26.0	—	—	—	—
871	1.07	0.01	—	0.79	-114.9	26.1	—	—	—	—
817	1.15	0.00	—	0.90	6.9	26.1	—	—	—	—
784	1.13	0.00	—	0.98	16.6	26.0	—	—	—	—
705	1.08	0.00	—	1.12	19.8	25.7	—	—	—	—

Table H.6: Model parameters and error measures of tests for the 20:1 PDMS downstream boundary case.

Test#	A^*	K	R_K^2	Q	S_{max}	S_{avg}	STD	MAR
809	1.04	11.9	0.83	18.3	45	15.8	4.85	4.31
728	1.01	8.6	0.74	17.2	51	13.5	4.50	4.02
743	0.95	10.1	0.77	18.5	51	14.7	4.45	3.95
742	0.95	5.1	0.41	11.1	42	10.7	3.67	3.08
764	0.93	19.4	0.74	23.9	59	18.8	4.41	3.91
749	0.90	7.1	0.61	18.6	47	13.7	4.78	4.13
717	0.89	14.2	0.84	23.8	53	15.3	5.54	4.64
718	0.79	19.2	0.79	36.6	75	17.4	7.57	6.32
912	0.68	28.6	0.82	44.7	97	25.6	5.61	4.75
748	0.68	1.5	0.12	25.3	54	11.4	4.58	4.10
894	0.63	24.5	0.97	44.5	92	23.6	3.79	3.33
813	0.62	29.6	0.97	51.7	115	26.4	4.92	4.33
727	0.56	25.1	0.93	49.7	110	19.5	4.36	3.79
872	0.45	12.0	0.86	39.6	100	17.6	6.54	5.61
893	0.42	16.9	0.81	52.3	113	25.3	4.23	3.74
795	0.42	24.7	0.95	63.3	126	30.1	6.17	5.11
706	0.41	10.2	0.83	29.5	71	15.9	4.72	4.21
911	0.40	17.2	0.92	45.7	108	23.5	4.22	3.69
765	0.37	11.7	0.76	32.9	87	16.3	5.68	4.80
895	0.25	23.5	0.94	51.9	133	30.2	5.33	4.51
910	0.14	12.5	0.88	48.3	132	28.0	4.26	3.64
896	0.10	6.2	0.72	42.5	116	23.9	4.72	3.91
909	0.02	—	—	—	89	29.5	—	—
707	0.01	—	—	—	107	20.6	—	—
871	0.01	—	—	—	97	29.4	—	—
817	0.00	—	—	—	75	25.2	—	—
784	0.00	—	—	—	51	18.2	—	—
705	0.00	—	—	—	48	17.7	—	—

H.2.3 Downstream 30:1 PDMS

Table H.7: Geometric properties and wave speed properties of tests for the 30:1 PDMS downstream boundary case.

Test#	R_o	A^*	$\dot{A}$	x_c^*	$\dot{x}_c$	U_I	$U_{p,max}$	$U_{p,x=0}$	$U_{p,min}$	dU_p/dx
726	1.14	1.00	-0.09	0.02	-3.6	26.2	7.3	1.2	0.21	0.80
715	1.07	0.99	-0.01	0.01	6.4	25.3	15.8	1.6	0.26	1.08
897	1.12	0.99	-0.06	0.04	10.9	26.3	18.1	2.5	0.44	1.16
799	1.16	0.86	0.10	0.09	29.9	25.9	23.2	10.1	3.97	4.37
740	1.15	0.81	0.27	0.18	52.3	26.1	34.1	22.6	3.98	5.03
725	1.14	0.75	0.23	0.23	43.7	26.0	27.2	18.1	3.20	4.07
716	1.06	0.61	0.31	0.36	56.6	26.1	33.7	30.1	24.98	0.38
762	1.10	0.59	0.21	0.32	50.5	26.1	24.8	18.7	6.81	3.55
900	1.11	0.57	0.25	0.32	58.4	26.2	26.6	19.8	14.22	1.54
741	1.12	0.54	0.31	0.38	55.4	26.0	28.5	24.4	9.33	1.10
788	1.11	0.41	0.31	0.49	80.7	26.1	34.1	28.8	14.88	1.04
714	0.84	0.20	0.23	0.55	80.4	26.0	31.3	22.4	17.41	0.94
713	1.15	0.16	0.32	0.67	79.3	25.9	29.2	27.1	23.53	1.79
711	1.09	0.00	—	1.17	43.2	26.0	—	—	—	—
899	1.09	0.00	—	1.44	-76.4	26.0	—	—	—	—
898	1.13	0.00	—	1.48	-14.3	26.4	—	—	—	—

Table H.8: Model parameters and error measures of tests for the 30:1 PDMS downstream boundary case.

Test#	A^*	K	R_K^2	Q	S_{max}	S_{avg}	STD	MAR
726	1.00	1.8	0.11	0.4	24	3.8	2.06	1.72
715	0.99	3.1	0.31	2.3	40	8.1	2.79	2.31
897	0.99	2.3	0.17	4.1	46	11.5	3.29	2.74
799	0.86	14.7	0.91	20.0	49	17.8	4.22	3.73
740	0.81	29.6	0.94	41.5	97	21.1	6.23	5.63
725	0.75	23.0	0.95	36.2	81	16.4	6.32	5.29
716	0.61	33.8	0.92	48.3	106	21.0	7.48	6.60
762	0.59	19.0	0.95	39.6	102	20.2	3.48	3.08
900	0.57	21.0	0.95	43.3	90	23.5	4.04	3.53
741	0.54	28.1	0.97	46.2	95	20.9	4.35	3.74
788	0.41	33.9	0.96	52.4	133	29.6	5.50	4.62
714	0.20	8.0	0.60	36.5	99	21.5	6.99	6.03
713	0.16	14.0	0.87	44.8	127	21.2	4.57	3.83

H.2.4 Downstream 40:1 PDMS

Table H.9: Geometric properties and wave speed properties of tests for the 40:1 PDMS downstream boundary case.

Test#	R_o	A^*	$\dot{A}$	x_c^*	$\dot{x}_c$	U_I	$U_{p,max}$	$U_{p,x=0}$	$U_{p,min}$	dU_p/dx
832	0.97	1.01	-0.02	0.01	2.0	25.3	3.0	0.5	0.07	0.16
733	1.16	1.00	0.04	0.03	12.3	25.9	20.3	1.6	0.14	0.30
875	1.10	0.77	0.28	0.19	47.6	26.6	32.2	19.2	3.19	3.15
916	0.79	0.76	0.25	0.18	74.8	26.3	32.3	24.2	11.02	4.50
873	1.09	0.67	0.25	0.25	56.4	26.6	29.4	20.2	5.62	4.00
710	1.13	0.67	0.17	0.29	55.1	26.0	32.2	20.5	2.96	5.67
903	1.11	0.63	0.26	0.30	58.6	26.3	30.1	25.4	11.47	3.06
874	1.05	0.59	0.30	0.32	62.2	26.2	32.3	26.3	9.82	1.61
735	1.07	0.59	0.23	0.35	50.0	26.3	26.3	19.3	8.73	1.13
913	1.15	0.56	0.32	0.35	64.6	26.3	32.7	26.5	13.01	6.06
780	1.14	0.56	0.32	0.32	61.1	25.7	28.9	22.6	11.98	1.73
709	1.15	0.54	0.28	0.34	49.0	26.2	24.4	17.9	9.62	1.14
763	1.13	0.21	0.34	0.58	87.9	25.9	24.3	22.9	17.13	0.56
876	1.11	0.18	0.29	0.66	81.9	26.0	25.7	24.0	20.77	0.97
905	1.11	0.11	0.36	0.68	92.7	26.8	29.8	25.8	22.04	0.97
907	1.06	0.08	0.26	0.67	82.9	26.3	26.3	21.0	16.56	0.66
915	1.05	0.07	0.27	0.69	108.1	26.4	27.4	23.6	17.59	2.66
737	1.12	0.04	0.23	0.83	91.1	26.1	24.3	17.6	9.59	0.70
914	1.17	0.01	—	0.91	-48.6	25.9	—	—	—	—
904	0.72	0.00	—	0.87	54.6	26.3	—	—	—	—
736	1.08	0.00	—	0.94	8.1	26.1	—	—	—	—
908	1.10	0.00	—	0.98	35.3	26.5	—	—	—	—
708	1.07	0.00	—	1.22	-8.9	25.3	—	—	—	—
906	1.09	0.00	—	1.26	13.9	26.5	—	—	—	—
902	1.03	0.00	—	1.29	56.3	26.0	—	—	—	—
901	1.01	0.00	—	1.29	-88.7	26.2	—	—	—	—

Table H.10: Model parameters and error measures of tests for the 40:1 PDMS downstream boundary case.

Test#	A^*	K	R_K^2	Q	S_{max}	S_{avg}	STD	MAR
832	1.01	1.7	0.24	0.0	18	4.1	2.87	2.29
733	1.00	0.8	0.04	4.2	49	7.5	3.33	2.72
875	0.77	12.6	0.61	37.6	79	19.3	6.52	5.63
916	0.76	18.2	0.90	46.6	104	26.1	5.45	4.82
873	0.67	19.8	0.74	40.4	91	24.0	6.19	5.54
710	0.67	25.4	0.92	36.7	77	20.3	5.15	4.52
903	0.63	25.6	0.89	43.2	95	27.0	4.31	3.83
874	0.59	24.5	0.94	50.7	111	25.0	4.84	4.26
735	0.59	18.5	0.89	47.5	98	19.0	8.83	7.73
913	0.56	31.8	0.98	46.2	118	25.8	4.11	3.56
780	0.56	23.9	0.94	49.8	101	24.1	3.95	3.45
709	0.54	19.2	0.96	41.1	96	18.3	6.08	5.44
763	0.21	12.3	0.83	46.7	140	24.1	4.02	3.26
876	0.18	10.8	0.76	44.6	137	19.0	4.66	3.95
905	0.11	10.4	0.87	47.1	136	30.1	5.61	4.52
907	0.08	2.4	0.16	48.8	125	27.2	3.88	3.25
915	0.07	6.3	0.67	41.0	127	27.3	5.49	4.58
737	0.04	7.2	0.86	33.8	101	18.3	5.79	4.76
914	0.01	—	—	—	81	28.5	—	—
904	0.00	—	—	—	75	23.6	—	—
736	0.00	—	—	—	65	18.8	—	—
908	0.00	—	—	—	67	22.9	—	—
708	0.00	—	—	—	42	20.1	—	—
906	0.00	—	—	—	51	27.7	—	—
902	0.00	—	—	—	40	21.6	—	—
901	0.00	—	—	—	42	22.6	—	—

H.3 Upstream Boundary

H.3.1 Upstream 20:1 PDMS

Table H.11: Geometric properties and wave speed properties of tests for 20:1 PDMS upstream boundary case.

Test#	R_o	A^*	$\dot{A}$	x_c^*	$\dot{x}_c$	U_I	$U_{p,max}$	$U_{p,x=0}$	$U_{p,min}$	dU_p/dx
816	0.82	1.01	-0.01	0.01	9.8	26	36.1	12.8	0	3.3
803	1.14	1.01	0.08	0.08	22.7	25.2	42.2	4.9	0.1	1.36
868	1.15	1	-0.01	0.02	5.9	26	33	3.5	0	2.13
729	1.1	0.99	0.04	0.04	6.6	26.1	20.8	4.4	0.3	1.9
804	1.16	0.88	0.2	0.13	35.2	26	31.8	15.8	1.9	8.68
767	1.12	0.86	0.12	0.18	52.7	25.4	31.6	20.5	2.9	5.85
858	1.14	0.73	0.27	0.23	47.2	26	24.4	19.2	6.4	4.61
793	1.12	0.63	0.22	0.32	45.1	25.9	23.6	20.3	12.7	1.5
805	1.11	0.58	0.25	0.29	43.6	25.9	31	23.8	7.4	3.34
815	1.16	0.56	0.27	0.38	53.6	25.9	25.1	22.9	14	0.99
811	1.08	0.54	0.44	0.41	66.9	26.4	36.4	31.2	16.9	4.87
810	1.09	0.49	0.31	0.33	50.4	25.9	28.1	24.4	13.9	1.95
755	1.09	0.46	0.27	0.39	60.3	26.3	29.8	26	16.9	1.33
814	1.12	0.45	0.38	0.42	65.8	25.9	32.6	29.1	17.6	2.02
859	1.13	0.45	0.35	0.37	67.5	26.2	31.1	26.7	14.1	0.18
860	1.13	0.42	0.28	0.41	49.9	26	25.8	22.1	10.9	2.23
794	1.1	0.4	0.3	0.42	57.2	25.9	31	25.5	14.8	2.88
744	0.88	0.39	0.18	0.34	51.2	26.1	20.1	15.2	9.7	0.12
758	1.12	0.38	0.3	0.52	62.2	26	32.8	23.1	13.9	1.4
807	1.15	0.38	0.38	0.44	72.7	26.1	30.8	27.3	19.9	0.91
866	1.13	0.2	0.26	0.54	39.8	26.9	26	19.6	11.5	1.09
867	1.13	0.19	0.34	0.6	71.2	26	29.1	24.8	15.4	1.25
792	1.06	0.16	0.25	0.64	53	25.9	36.7	19.5	4.1	6.01
730	1.13	0.12	0.33	0.67	67.6	25.8	28.3	23.7	18.6	0.5
766	1.16	0.08	0.34	0.74	107.6	26.2	25.7	24.2	8.9	1.31
865	1.16	0.07	0.27	0.71	80.5	26.1	26.7	23.1	14.7	2.04
759	1.17	0.03	0.22	0.83	92.7	26.3	35.1	24.2	14	0.36
808	1.12	0	—	0.57	104.6	25.9	—	—	—	—
806	1.09	0	—	0.73	107.3	26.1	—	—	—	—
754	1.14	0	—	0.93	16.3	26.1	—	—	—	—
757	1.11	0	—	1.17	26.8	25.9	—	—	—	—
812	1.11	0	—	1.27	40.6	26.1	—	—	—	—

Table H.12: Model parameters and error measures of tests for 20:1 PDMS upstream boundary case.

Test#	A^*	K	R_K^2	Q	S_{max}	S_{avg}	STD	MAR
816	1.01	8.4	0.84	16.5	57	19.9	6.88	5.84
803	1.01	9.8	0.26	19.3	60	20.5	9.43	7.84
868	1	2.8	0.09	3.2	55	15.3	4.89	4.26
729	0.99	1.2	0.05	6.1	32	5	2.36	1.9
804	0.88	14.1	0.62	29.9	69	19	5.35	4.75
767	0.86	21.8	0.87	33.8	74	20.5	6.13	5.49
858	0.73	10.5	0.56	38.7	82	22.2	6.43	5.76
793	0.63	22.7	0.92	44.6	88	20.5	6.09	5.21
805	0.58	24.6	0.94	42.3	87	24.4	4.63	3.79
815	0.56	21.6	0.95	45.2	87	24.4	5.16	4.47
811	0.54	25.4	0.91	54.9	125	31.8	4.93	4.22
810	0.49	19.8	0.88	49.5	95	25.3	4.1	3.58
755	0.46	27.1	0.97	53.0	104	24.5	6.95	5.32
814	0.45	23.8	0.95	55.4	120	31.2	4.37	3.79
859	0.45	27.4	0.97	48.7	92	25.5	4.59	3.97
860	0.42	13.2	0.78	43.5	95	23.7	4.17	3.74
794	0.4	16.3	0.78	50.9	117	31.8	5.15	4.5
744	0.39	10.2	0.85	37.0	73	14.5	6.45	5.28
758	0.38	23.4	0.94	52.0	125	29.7	4.52	3.78
807	0.38	21.8	0.87	62.4	161	33.8	4.82	4.05
866	0.2	5.0	0.35	34.9	84	21.2	3.95	3.44
867	0.19	7.8	0.39	50.9	130	27.4	4.97	4.34
792	0.16	5.7	0.49	38.8	95	22.2	6.1	5.29
730	0.12	8.1	0.57	47.2	141	20.6	6.09	5.28
766	0.08	9.2	0.7	44.6	141	22.7	6.35	5.18
865	0.07	2.4	0.17	33.3	114	21.8	4.76	3.9
759	0.03	4.3	0.52	26.7	114	29	6.5	5.38
808	0	—	—	—	55	17.7	—	—
806	0	—	—	—	113	31.4	—	—
754	0	—	—	—	79	27.2	—	—
757	0	—	—	—	75	26.9	—	—
812	0	—	—	—	52	26	—	—

H.3.2 Upstream 30:1 PDMS

Table H.13: Geometric properties and wave speed properties of tests for 30:1 PDMS upstream boundary case.

Test#	R_o	A^*	$\dot{A}$	x_c^*	$\dot{x}_c$	U_I	$U_{p,max}$	$U_{p,x=0}$	$U_{p,min}$	dU_p/dx
848	1.14	0.96	0.17	0.04	32.9	26.2	34.3	16.6	1.4	7.86
724	1.14	0.96	0.06	0.04	18.7	26.1	25.1	5	0.3	0.99
738	1.15	0.78	0.26	0.18	44.2	25.1	27.8	20.5	6.7	4.86
723	1.12	0.77	0.28	0.18	51.7	26.1	32.6	23.4	5.9	2.67
847	1.18	0.54	0.36	0.36	61	26.2	29.4	23.3	14.7	2.17
798	1.12	0.4	0.3	0.48	53.3	25.9	27.4	24	11.3	1.58
796	1.13	0.32	0.35	0.52	74.8	25.8	28.1	25.2	18.9	2.17
790	1.12	0.2	0.34	0.63	74.5	26	31.4	24.5	20.6	1.47
797	1.11	0.09	0.33	0.66	86.8	25.9	29.3	28	18.8	0.67
789	1.11	0.02	—	0.8	16.5	25.7	—	—	—	—
739	1.12	0	—	0.88	20.6	26.3	—	—	—	—

Table H.14: Model parameters and error measures of tests for 30:1 PDMS upstream boundary case.

Test#	A^*	K	R_K^2	Q	S_{max}	S_{avg}	STD	MAR
848	0.96	11.6	0.63	24.2	71	22.2	6.04	5.2
724	0.96	3.4	0.04	9.6	50	12.3	7.11	5.63
738	0.78	24.0	0.87	42.2	85	18.5	6.35	5.4
723	0.77	25.4	0.9	42.1	84	16.9	4.46	3.92
847	0.54	19.5	0.77	55.1	112	27.9	9.49	8.28
798	0.4	13.6	0.82	46.2	98	24.8	3.91	3.43
796	0.32	22.6	0.94	59.4	132	30.1	4.52	3.82
790	0.2	12.0	0.66	46.8	116	31.7	5.24	4.43
797	0.09	3.7	0.23	43.4	141	28.3	5.89	4.9
789	0.02	—	—	—	83	29.9	—	—
739	0	—	—	—	82	23.9	—	—

H.3.3 Upstream 40:1 PDMS

Table H.15: Geometric properties and wave speed properties of tests for the 40:1 PDMS upstream boundary case.

Test#	R_o	A^*	$\dot{A}$	x_c^*	$\dot{x}_c$	U_I	$U_{p,max}$	$U_{p,x=0}$	$U_{p,min}$	dU_p/dx
719	1.14	1.01	-0.02	0.01	2.7	25.8	38.3	1.4	0.1	0.65
720	1.07	0.78	0.17	0.19	33.1	25.6	26	12.4	0.6	2.95
870	1.12	0.66	0.27	0.23	48.7	26.2	33.6	22.6	7.2	3.5
869	1.14	0.65	0.24	0.32	57.3	26.2	30.9	19.3	8.8	3.96
846	1.13	0.6	0.36	0.29	62.5	26.1	32.2	30.1	13.6	3.22
721	1.14	0.55	0.31	0.37	59.5	26.2	19.3	14.6	8.9	2.81
845	1.12	0.41	0.3	0.42	65	26.2	27.7	22.8	13	0.96
731	1.13	0.38	0.31	0.46	66.7	25.9	28.1	22.9	15.5	0.1
830	1.11	0.38	0.36	0.4	56.2	26	29	26.5	16.8	1.3
787	1.14	0.29	0.33	0.54	57.4	25.9	16.6	14	10.8	2.68
831	1.07	0.21	0.33	0.54	57.8	25.9	28.1	26.3	19	2.79
802	1.12	0.13	0.37	0.69	95.2	25.8	30.8	25.7	19.7	2.67
829	1.15	0.06	0.38	0.75	137.5	26	36	31.7	22.4	0.36
800	1.13	0.04	0.3	0.83	120	25.9	31.8	24.5	17.2	1.03
844	1.12	0.01	—	0.81	24.8	26.2	—	—	—	—
786	1.06	0.01	—	0.86	33.2	26	—	—	—	—
722	1.01	0	—	0.8	32.3	26.4	—	—	—	—
734	1.11	0	—	0.86	44	—	—	—	—	—
781	1.15	0	—	0.88	77.9	26	—	—	—	—
732	1.13	0	—	0.89	20.1	26.1	—	—	—	—
783	1.18	0	—	0.99	58.8	25.8	—	—	—	—
782	1.12	0	—	0.99	1.3	26.3	—	—	—	—
785	1.14	0	—	1.23	51.2	26	—	—	—	—
801	1.18	0	—	1.29	55.1	25.7	—	—	—	—

Table H.16: Model parameters and error measures of tests for the 40:1 PDMS upstream boundary case.

Test#	A^*	K	R_K^2	Q	S_{max}	S_{avg}	STD	MAR
719	1.01	2.2	0.08	1.0	88	10.6	6.14	4.2
720	0.78	7.0	0.39	29.0	51	12.8	5.78	4.95
870	0.66	19.1	0.83	43.5	85	19.9	5.39	4.84
869	0.65	14.8	0.78	42.1	82	27.6	5.98	5.37
846	0.6	22.4	0.86	56.7	111	30	4.62	4.11
721	0.55	14.3	0.86	46.0	114	17.8	8.65	7.82
845	0.41	12.4	0.53	54.1	123	23.6	8.36	7.32
731	0.38	19.6	0.92	53.3	151	26.5	6.35	5.58
830	0.38	16.5	0.81	57.1	108	24.3	4.47	3.95
787	0.29	9.4	0.65	43.3	104	16.4	6.42	5.77
831	0.21	5.1	0.19	47.8	118	25.4	5.36	4.71
802	0.13	12.8	0.77	49.5	134	32.6	4.73	4.03
829	0.06	7.1	0.58	39.6	135	30	5.96	5
800	0.04	4.8	0.45	30.7	105	27.6	5.81	4.96
844	0.01	—	—	—	85	22.6	—	—
786	0.01	—	—	—	105	23.5	—	—
722	0	—	—	—	53	14.8	—	—
734	0	—	—	—	45	16	—	—
781	0	—	—	—	62	17.6	—	—
732	0	—	—	—	75	24.1	—	—
783	0	—	—	—	74	25.6	—	—
782	0	—	—	—	39	13.3	—	—
785	0	—	—	—	54	25.5	—	—
801	0	—	—	—	60	23.1	—	—

H.4 Two Boundary

H.4.1 Two Boundary 20:1 PDMS

Table H.17: Geometric properties and wave speed properties of tests for the 20:1 PDMS two boundary case.

Test#	R_o	A^*	$\dot{A}$	x_c^*	$\dot{x}_c$	U_I	$U_{p,max}$	$U_{p,x=0}$	$U_{p,min}$	dU_p/dx
835	0.98	1.04	-0.03	0.02	-4.0	26.0	26.8	5.6	0.00	3.78
834	1.10	1.01	-0.03	0.00	4.4	25.9	10.9	1.7	0.13	1.48
887	1.00	0.98	0.14	0.06	34.7	26.0	27.1	11.7	0.60	2.43
777	1.04	0.93	0.10	0.07	37.5	25.6	21.9	12.9	0.20	7.10
852	1.13	0.92	0.10	0.11	29.3	26.0	27.9	12.3	2.99	5.71
919	1.02	0.89	0.19	0.10	43.7	26.2	35.6	20.5	3.39	3.76
851	0.97	0.88	0.21	0.13	55.7	25.9	31.5	21.7	4.85	4.06
891	0.81	0.81	0.17	0.14	59.8	26.0	32.0	25.4	6.03	1.95
778	1.05	0.75	0.26	0.19	50.2	25.7	16.8	15.6	3.32	0.25
886	1.15	0.47	0.37	0.45	72.8	26.3	34.0	29.7	14.96	6.24
776	1.11	0.46	0.31	0.36	59.2	26.0	24.4	21.1	11.33	0.78
853	1.05	0.43	0.30	0.37	64.5	26.2	28.9	25.0	16.73	0.75
920	1.09	0.40	0.32	0.50	62.9	26.4	35.5	29.5	17.85	3.98
917	1.07	0.36	0.33	0.45	75.9	27.1	34.5	31.7	20.03	3.48
918	1.11	0.06	0.37	0.84	112.3	26.4	37.7	29.6	19.79	2.85
850	1.06	0.05	0.27	0.71	124.3	26.4	30.6	26.1	18.60	1.65
889	1.08	0.03	—	0.66	73.3	26.4	—	—	—	—
885	1.09	0.01	—	0.77	129.9	26.4	—	—	—	—
833	1.05	0.00	—	0.82	11.0	26.2	—	—	—	—
779	1.11	0.00	—	0.86	15.5	25.9	—	—	—	—
890	1.15	0.00	—	0.91	11.5	26.4	—	—	—	—
892	1.08	0.00	—	0.91	44.7	26.0	—	—	—	—

Table H.18: Model parameters and error measures of tests for the 20:1 PDMS two boundary case.

Test#	A^*	K	R_K^2	Q	S_{max}	S_{avg}	STD	MAR
835	1.04	3.6	0.42	12.5	48	13.2	4.75	4.22
834	1.01	4.9	0.35	0.3	44	10.0	2.96	2.46
887	0.98	5.5	0.15	25.0	72	21.2	7.82	6.97
777	0.93	8.5	0.57	20.0	55	14.8	6.95	5.89
852	0.92	12.6	0.79	21.0	53	20.5	4.74	4.15
919	0.89	18.9	0.87	33.0	74	22.9	4.58	4.13
851	0.88	17.7	0.67	37.7	92	23.1	5.84	5.19
891	0.81	13.6	0.46	41.0	95	24.6	5.96	5.29
778	0.75	8.1	0.29	38.2	79	14.1	8.68	7.60
886	0.47	28.6	0.94	53.5	133	30.9	4.41	3.85
776	0.46	15.5	0.80	49.6	101	19.7	7.40	6.56
853	0.43	16.2	0.73	50.4	94	25.8	5.60	4.80
920	0.40	26.0	0.93	55.4	120	29.1	5.23	4.54
917	0.36	21.9	0.93	54.1	126	30.4	4.79	3.99
918	0.06	11.5	0.85	44.6	137	32.6	6.77	5.90
850	0.05	2.6	0.40	34.5	115	30.0	4.69	3.89
889	0.03	—	—	—	126	22.6	—	—
885	0.01	—	—	—	72	25.2	—	—
833	0.00	—	—	—	92	33.1	—	—
779	0.00	—	—	—	66	14.4	—	—
890	0.00	—	—	—	74	24.2	—	—
892	0.00	—	—	—	68	28.0	—	—

H.4.2 Two Boundary 30:1 PDMS

Table H.19: Geometric properties and wave speed properties of tests for the 30:1 PDMS two boundary case.

Test#	R_o	A^*	$\dot{A}$	x_c^*	$\dot{x}_c$	U_I	$U_{p,max}$	$U_{p,x=0}$	$U_{p,min}$	dU_p/dx
771	1.09	0.98	-0.05	0.03	9.4	25.9	26.2	6.7	0.17	5.99
770	1.10	0.95	-0.01	0.04	6.9	26.0	22.7	6.2	0.36	2.54
862	1.13	0.92	0.15	0.09	40.2	26.3	31.2	20.0	4.60	5.23
827	1.06	0.73	0.18	0.23	48.7	26.0	32.6	24.1	7.65	2.80
768	1.11	0.62	0.25	0.32	62.1	26.0	33.0	25.8	3.18	1.50
861	1.16	0.56	0.39	0.30	50.1	26.2	37.0	31.4	15.02	1.71
864	1.01	0.42	0.46	0.49	73.2	25.9	34.5	29.8	25.12	1.11
828	1.11	0.37	0.33	0.51	68.1	26.0	29.0	27.0	18.09	1.53
863	1.11	0.26	0.36	0.50	84.4	26.4	29.9	28.3	19.18	1.05
825	1.07	0.17	0.34	0.64	74.6	25.9	34.7	24.3	16.04	2.03
826	1.16	0.13	0.39	0.72	87.2	26.0	34.4	24.1	16.01	1.29
769	1.06	0.02	—	0.77	87.0	26.3	—	—	—	—

Table H.20: Model parameters and error measures of tests for the 30:1 PDMS two boundary case.

Test#	A^*	K	R_K^2	Q	S_{max}	S_{avg}	STD	MAR
771	0.98	2.8	0.09	8.3	42	8.1	3.71	3.06
770	0.95	5.8	0.49	8.1	45	10.1	4.65	3.51
862	0.92	18.1	0.78	29.2	74	22.1	4.67	4.14
827	0.73	22.2	0.90	39.7	74	23.5	4.31	3.85
768	0.62	27.9	0.91	48.6	108	20.6	7.28	6.44
861	0.56	23.5	0.64	55.7	95	26.3	5.07	4.47
864	0.42	20.1	0.90	63.3	137	33.0	4.69	3.86
828	0.37	19.9	0.91	51.1	114	26.1	3.94	3.42
863	0.26	18.1	0.92	52.3	134	30.7	3.93	3.44
825	0.17	8.3	0.64	50.4	127	29.1	4.19	3.62
826	0.13	13.7	0.80	53.4	136	29.2	5.60	4.61
769	0.02	—	—	—	126	19.1	—	—

H.4.3 Two Boundary 40:1 PDMS

Table H.21: Geometric properties and wave speed properties of tests for the 40:1 PDMS two boundary case.

Test#	R_o	A^*	$\dot{A}$	x_c^*	$\dot{x}_c$	U_I	$U_{p,max}$	$U_{p,x=0}$	$U_{p,min}$	dU_p/dx
775	1.13	0.96	-0.01	0.05	34.9	25.8	27.2	5.3	0.09	5.62
857	1.11	0.94	0.05	0.06	25.0	26.1	25.0	7.9	0.16	2.53
772	1.07	0.93	0.11	0.10	33.2	25.7	26.5	15.6	0.86	3.43
774	1.14	0.66	0.32	0.34	65.6	26.0	29.1	23.7	11.40	0.90
856	1.11	0.54	0.36	0.35	71.2	26.0	36.5	29.8	17.62	2.52
820	1.07	0.44	0.34	0.39	59.5	26.1	31.4	30.1	6.32	0.56
819	1.15	0.40	0.38	0.44	60.9	25.7	27.2	24.2	15.50	1.87
821	1.16	0.40	0.31	0.47	71.0	26.0	32.5	28.8	15.21	3.34
854	1.07	0.26	0.37	0.58	80.9	25.9	33.0	30.1	20.80	0.36
773	1.11	0.11	0.28	0.75	72.1	26.0	24.6	22.0	16.16	1.94
855	1.13	0.02	—	0.93	83.4	26.0	—	—	—	—
818	1.02	0.00	—	1.26	56.3	26.0	—	—	—	—

Table H.22: Model parameters and error measures of tests for the 40:1 PDMS two boundary case.

Test#	A^*	K	R_K^2	Q	S_{max}	S_{avg}	STD	MAR
775	0.96	1.9	0.04	9.1	50	11.1	4.67	3.69
857	0.94	5.2	0.29	12.6	46	16.4	3.55	3.17
772	0.93	7.6	0.34	23.4	55	14.2	7.21	5.93
774	0.66	29.6	0.95	51.4	112	20.6	8.18	6.41
856	0.54	27.3	0.91	57.5	118	26.4	5.10	4.38
820	0.44	28.5	0.95	48.9	119	22.9	7.20	6.36
819	0.40	21.6	0.93	52.4	112	22.2	4.71	4.07
821	0.40	30.7	0.94	53.7	136	25.2	4.77	4.01
854	0.26	19.8	0.88	57.1	136	30.8	4.67	3.86
773	0.11	6.1	0.58	42.8	141	21.3	8.43	6.54
855	0.02	—	—	—	124	33.8	—	—
818	0.00	—	—	—	62	30.5	—	—